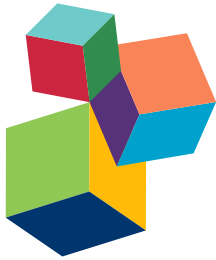


DEEP CARBON IN EARTH: EARLY CAREER SCIENTIST CONTRIBUTIONS TO THE DEEP CARBON OBSERVATORY

EDITED BY: Donato Giovannelli, Benjamin A. Black, Alyia D. Cox and
Cody S. Sheik

PUBLISHED IN: *Frontiers in Earth Science*, *Frontiers in Chemistry*, *Frontiers in
Microbiology* and *Frontiers in Environmental Science*





Frontiers Copyright Statement

© Copyright 2007-2017 Frontiers Media SA. All rights reserved.

All content included on this site, such as text, graphics, logos, button icons, images, video/audio clips, downloads, data compilations and software, is the property of or is licensed to Frontiers Media SA ("Frontiers") or its licensees and/or subcontractors. The copyright in the text of individual articles is the property of their respective authors, subject to a license granted to Frontiers.

The compilation of articles constituting this e-book, wherever published, as well as the compilation of all other content on this site, is the exclusive property of Frontiers. For the conditions for downloading and copying of e-books from Frontiers' website, please see the Terms for Website Use. If purchasing Frontiers e-books from other websites or sources, the conditions of the website concerned apply.

Images and graphics not forming part of user-contributed materials may not be downloaded or copied without permission.

Individual articles may be downloaded and reproduced in accordance with the principles of the CC-BY licence subject to any copyright or other notices. They may not be re-sold as an e-book.

As author or other contributor you grant a CC-BY licence to others to reproduce your articles, including any graphics and third-party materials supplied by you, in accordance with the Conditions for Website Use and subject to any copyright notices which you include in connection with your articles and materials.

All copyright, and all rights therein, are protected by national and international copyright laws.

The above represents a summary only. For the full conditions see the Conditions for Authors and the Conditions for Website Use.

ISSN 1664-8714

ISBN 978-2-88945-363-4

DOI 10.3389/978-2-88945-363-4

About Frontiers

Frontiers is more than just an open-access publisher of scholarly articles: it is a pioneering approach to the world of academia, radically improving the way scholarly research is managed. The grand vision of Frontiers is a world where all people have an equal opportunity to seek, share and generate knowledge. Frontiers provides immediate and permanent online open access to all its publications, but this alone is not enough to realize our grand goals.

Frontiers Journal Series

The Frontiers Journal Series is a multi-tier and interdisciplinary set of open-access, online journals, promising a paradigm shift from the current review, selection and dissemination processes in academic publishing. All Frontiers journals are driven by researchers for researchers; therefore, they constitute a service to the scholarly community. At the same time, the Frontiers Journal Series operates on a revolutionary invention, the tiered publishing system, initially addressing specific communities of scholars, and gradually climbing up to broader public understanding, thus serving the interests of the lay society, too.

Dedication to Quality

Each Frontiers article is a landmark of the highest quality, thanks to genuinely collaborative interactions between authors and review editors, who include some of the world's best academicians. Research must be certified by peers before entering a stream of knowledge that may eventually reach the public - and shape society; therefore, Frontiers only applies the most rigorous and unbiased reviews.

Frontiers revolutionizes research publishing by freely delivering the most outstanding research, evaluated with no bias from both the academic and social point of view.

By applying the most advanced information technologies, Frontiers is catapulting scholarly publishing into a new generation.

What are Frontiers Research Topics?

Frontiers Research Topics are very popular trademarks of the Frontiers Journals Series: they are collections of at least ten articles, all centered on a particular subject. With their unique mix of varied contributions from Original Research to Review Articles, Frontiers Research Topics unify the most influential researchers, the latest key findings and historical advances in a hot research area! Find out more on how to host your own Frontiers Research Topic or contribute to one as an author by contacting the Frontiers Editorial Office: researchtopics@frontiersin.org

DEEP CARBON IN EARTH: EARLY CAREER SCIENTIST CONTRIBUTIONS TO THE DEEP CARBON OBSERVATORY

Topic Editors:

Donato Giovannelli, Rutgers University, United States; National Research Council of Italy, Italy; Institute for Advanced Studies, United States and Tokyo Institute of Technology, Japan

Benjamin A. Black, City College of New York, United States

Alysia D. Cox, Montana Tech of the University of Montana, United States and Yachay Tech University, Ecuador

Cody S. Sheik, University of Minnesota Duluth, United States



Early Career Scientists (ECS) are the lifeblood of all scientific research programs and are the future of deep carbon science. As such, this issue highlights the research of ECS associated with the Deep Carbon Observatory (<http://www.deepcarb.net>). DCO-ECS sampling acidic waters in the caldera of Poás Volcano, Costa Rica. Photo credit Katie Pratt and Josh Wood for graphical design.

Since its inception, the Deep Carbon Observatory (DCO) has coalesced a multidisciplinary and international group of researchers focused on understanding and quantifying Earth's deep carbon budget. Carbon is the fourth most abundant element in the universe, and understanding carbon chemistry under a variety of environmental conditions impacts all aspects of planetary sciences, including planet formation, the form and function of planetary interiors, and the origin and diversity of life. DCO recognizes that integrating and promoting the contributions of early career scientists are integral to the advancement of knowledge regarding the quantities, movements, origins, and forms of Earth's deep carbon through field, experimental, analytical, and computational research. Early career scientists represent the future of deep carbon science and contribute substantially to ongoing research by implementing innovative ideas, challenging traditional working schemes, and bringing a globally interconnected perspective to the scientific community. This research topic highlights the contributions at the forefront of deep carbon research by DCO Early Career Scientist community. The manuscripts of this *Frontiers* e-volume bear evidence of the rapid advances in deep carbon science, and highlights the importance of approaching this field from a plethora of different angles integrating disciplines as diverse as mineralogy, geochemistry and microbiology. This integration is fundamental in understanding the movements and transformations of carbon across its deep cycle.

Citation: Giovannelli, D., Black, B. A., Cox, A. D., Sheik, C. S., eds. (2017). Deep Carbon in Earth: Early Career Scientist Contributions to the Deep Carbon Observatory. Lausanne: Frontiers Media. doi: 10.3389/978-2-88945-363-4

Table of Contents

- 06 Editorial: Deep Carbon in Earth: Early Career Scientist Contributions to the Deep Carbon Observatory**

Donato Giovannelli, Benjamin A. Black, Alycia D. Cox and Cody S. Sheik

Carbon Degassing at Volcanoes

- 08 Relationship between Diffuse CO₂ Degassing and Volcanic Activity. Case Study of the Poás, Irazú, and Turrialba Volcanoes, Costa Rica**

Matthieu Epiard, Geoffroy Avard, J. Maarten de Moor, María Martínez Cruz, Gustav Barrantes Castillo and Henriette Bakkar

- 22 Soil CO₂ Degassing Path along Volcano-Tectonic Structures in the Pico-Faial-São Jorge Islands (Azores Archipelago, Portugal)**

Fátima Viveiros, Márcio Marcos, Carlos Faria, João L. Gaspar, Teresa Ferreira and Catarina Silva

The Deep Earth

- 40 Transformations and Decomposition of MnCO₃ at Earth's Lower Mantle Conditions**

Eglantine Boulard, Yijin Liu, Ai L. Koh, Mary M. Reagan, Julien Stodolna, Guillaume Morard, Mohamed Mezouar and Wendy L. Mao

- 49 Structure and Dynamics of Confined C-O-H Fluids Relevant to the Subsurface: Application of Magnetic Resonance, Neutron Scattering, and Molecular Dynamics Simulations**

Siddharth S. Gautam, Salim Ok and David R. Cole

- 68 An Experimental Study of the Carbonation of Serpentinite and Partially Serpentinised Peridotites**

Alicja M. Lacinska, Michael T. Styles, Keith Bateman, Matthew Hall and Paul D. Brown

Activity of Subsurface Communities

- 88 Improved Measurement of Extracellular Enzymatic Activities in Subsurface Sediments Using Competitive Desorption Treatment**

Adrienne Hoarfrost, Rachel Snider and Carol Arnosti

- 99 Microbial Sulfide Filter along a Benthic Redox Gradient in the Eastern Gotland Basin, Baltic Sea**

Mustafa Yücel, Stefan Sommer, Andrew W. Dale and Olaf Pfannkuche

- 115 Electron Transfer between Electrically Conductive Minerals and Quinones**

Olga Taran

- 128 *Reactivation of Deep Subsurface Microbial Community in Response to Methane or Methanol Amendment***
Pauliina Rajala and Malin Bomberg
- 141 *Response of Deep Subsurface Microbial Community to Different Carbon Sources and Electron Acceptors during ~2 months Incubation in Microcosms***
Lotta Purkamo, Malin Bomberg, Mari Nyssönen, Lasse Ahonen, Ilmo Kukkonen and Merja Itävaara
- 155 *Guar Gum Stimulates Biogenic Sulfide Production at Elevated Pressures: Implications for Shale Gas Extraction***
Sophie L. Nixon, Leanne Walker, Matthew D. T. Streets, Bob Eden, Christopher Boothman, Kevin G. Taylor and Jonathan R. Lloyd

Serpentinization and the Carbon Cycle

- 166 *Serpentinization-Influenced Groundwater Harbors Extremely Low Diversity Microbial Communities Adapted to High pH***
Katrina I. Twing, William J. Brazelton, Michael D. Y. Kubo, Alex J. Hyer, Dawn Cardace, Tori M. Hoehler, Tom M. McCollom and Matthew O. Schrenk
- 182 *Methane Dynamics in a Tropical Serpentinizing Environment: The Santa Elena Ophiolite, Costa Rica***
Melitza Crespo-Medina, Katrina I. Twing, Ricardo Sánchez-Murillo, William J. Brazelton, Thomas M. McCollom and Matthew O. Schrenk

Carbon Through Space and Time

- 196 *Evaluating the Role of Seagrass in Cenozoic CO₂ Variations***
Marco Brandano, Marco Cuffaro, Giovanni Gaglianone, Patrizio Petricca, Vincenzo Stagno and Guillem Mateu-Vicens
- 205 *The Hyperarid Core of the Atacama Desert, an Extremely Dry and Carbon Deprived Habitat of Potential Interest for the Field of Carbon Science***
Armando Azua-Bustos, Carlos González-Silva and Gino Corsini

Building a Carbon Network

- 211 *Weaving a Knowledge Network for Deep Carbon Science***
Xiaogang Ma, Patrick West, Stephan Zednik, John Erickson, Ahmed Eleish, Yu Chen, Han Wang, Hao Zhong and Peter Fox



Editorial: Deep Carbon in Earth: Early Career Scientist Contributions to the Deep Carbon Observatory

Donato Giovannelli^{1, 2, 3, 4*}, **Benjamin A. Black**⁵, **Alysia D. Cox**^{6, 7} and **Cody S. Sheik**^{8, 9}

¹ Department of Marine and Coastal Science, Rutgers University, New Brunswick, NJ, United States, ² Institute of Marine Science, National Research Council of Italy, Ancona, Italy, ³ Program in Interdisciplinary Studies, Institute for Advanced Studies, Princeton, NJ, United States, ⁴ Earth-Life Science Institute, Tokyo Institute of Technology, Tokyo, Japan, ⁵ City College of New York, New York, NY, United States, ⁶ Department of Chemistry and Geochemistry, Montana Tech of the University of Montana, Butte, MT, United States, ⁷ Department of Geological Sciences and Engineering, Yachay Tech University, Urcuqui, Ecuador, ⁸ Department of Biology, University of Minnesota Duluth, Duluth, MN, United States, ⁹ Large Lakes Observatory, University of Minnesota Duluth, Duluth, MN, United States

Keywords: deep carbon cycle, subsurface, interdisciplinary, early career researcher, volcanism, geomicrobiology, geochemistry, carbon minerals

Editorial on the Research Topic

Deep Carbon in Earth: Early Career Scientist Contributions to the Deep Carbon Observatory

Since its inception, the Deep Carbon Observatory (DCO) has coalesced a multidisciplinary and international group of researchers focused on understanding and quantifying Earth's deep carbon budget. Carbon is the fourth most abundant element in the universe, and understanding carbon chemistry under a variety of environmental conditions impacts all aspects of planetary sciences. DCO recognizes that contributions of early career scientists are integral to the advancement of knowledge regarding the quantities, movements, origins, and forms of Earth's deep carbon. This research topic highlights the contributions of the DCO Early Career Scientist community.

CARBON DEGASSING AT VOLCANOES

OPEN ACCESS

Edited and reviewed by:

Martyn Tranter,

University of Bristol, United Kingdom

*Correspondence:

Donato Giovannelli

giovannelli@elsi.jp

Specialty section:

This article was submitted to

Geochemistry,

a section of the journal

Frontiers in Earth Science

Received: 17 October 2017

Accepted: 20 October 2017

Published: 03 November 2017

Citation:

Giovannelli D, Black BA, Cox AD and Sheik CS (2017) Editorial: Deep Carbon in Earth: Early Career Scientist Contributions to the Deep Carbon Observatory. *Front. Earth Sci.* 5:89.

doi: 10.3389/feart.2017.00089

Volcanoes are charismatic conduits of Earth's deep carbon, and contribute to gas emissions during eruption episodes and diffuse degassing. Diffuse degassing is a key feature of volcanoes, yet its relationship to volcanic activity is unclear. Epiard et al. show diffuse degassing represents up to 10% of the total CO₂ volcanic output, and find evidence for a shift in the patterns of degassing in the lead-up to eruptions. In a related contribution, Viveiros et al. highlight the pathways that CO₂ takes to reach the surface, and show diffuse degassing is concentrated along volcanic-tectonic structures rather than in the vicinity of the youngest volcanic edifices.

THE DEEP EARTH

Carbonates have been proposed as the principal oxidized carbon-bearing phases in the Earth's interior. Boulard et al. investigated the behavior of MnCO₃ at high temperature and pressure and report a phase transition from MnCO₃ into MnCO₃-II without an accompanying change in the manganese oxidation state until temperatures reached 1,400 K leading to the formation of manganese oxides and reduced carbon.

C-O-H volatiles are important throughout the lithosphere and are commonly found confined in pores, grain boundaries, and fractures. Gautam et al. present a systematic review of the use of nuclear magnetic resonance (NMR), neutron scattering (NS), and molecular dynamics (MD) simulations to show how application of these three techniques has shed light on the complex behavior of water, CO₂, and C-O-H volatiles.

In situ sequestration of CO₂ in mantle peridotites has been proposed as a method to alleviate the amount of anthropogenic CO₂ in the atmosphere. Lacinska et al. indicate

a rate of carbonation of $\sim 2\%$ in half a year, using natural ophiolites, suggesting that serpentinite might be a good host rock for CO_2 sequestration.

ACTIVITY OF SUBSURFACE COMMUNITIES

Microbial communities in deep subsurface environments comprise a significant portion of Earth's biomass, but the microbial activity in these habitats is largely unknown. Hoarfrost et al. present a new fluorescent method to measure extracellular enzymatic activities. The method improves recovery of the labeled substrate from sediment subsamples resulting in greater reliability of quantifying microbially catalyzed hydrolytic activities in sediments.

Yucel et al. show sediment sulfide accumulation is moderated by microbial oxidation at the sediment surface and FeS precipitation in deeper sediment layers. Microorganisms rely on electron flow to drive metabolism and biogeochemical cycles. Taran uses cyclic voltammetry to show that quinone, a microbially produced electron shuttle, interacts and exchanges electrons with pyrite thereby creating a cycle. Using mesocosm incubations, Rajala and Bomberg show rapid microbial response to methane and methanol amendments from two isolated groundwater fractures at 180 m and 500 m depths of the Outokumpu Deep Drill hole (Finland). Purkamo et al. used acetate to stimulate microbial community diversity and show treatments dominated by clostridial hydrogenotrophic thiosulfate reducers in fluids obtained from the same Outokumpu Deep Drill hole. Nixon et al. show guar gum stimulates biogenic sulfide production by sulfate-reducing microorganisms at elevated pressure. Their results have implications for the potential role in microbially induced corrosion during hydraulic fracturing operations.

SERPENTINIZATION AND THE CARBON CYCLE

Serpentinization is of particular interest for deep carbon science, as alteration of ultramafic rocks produce abundant reductants (H_2 and CH_4) that fuel life and sequester significant quantities of carbon. In a groundbreaking interdisciplinary study, Twing et al. show the Coast Range Ophiolite Microbial Observatory serpentinites are low in microbial diversity and dominated by members of the *Betaproteobacteria* and *Clostridia*, involved in hydrogen metabolism, carbon monoxide oxidation, carbon fixation, and acetogenesis. Crespo-Medina et al. report the Santa Elena Ophiolite communities are dominated by hydrogen, methane, and methanol oxidizers of the bacterial genera *Hydrogenophaga*, *Methylbacterium*, and *Methylibium* as well as methanogenic Archaea.

CARBON THROUGH TIME AND SPACE

Changes in the carbon cycle through deep time have astrobiological implications. Brandano et al. show the

importance of understanding the role of the slow carbon cycle through deep time using extant data of seagrass productivity along the Mediterranean Sea and integrating GPlate models. Azua-Bustos et al. present a compelling case for the study of the physiological and molecular mechanisms utilized by heterotrophic microorganisms to detect, mobilize, incorporate, and use carbon under extremely harsh conditions in the Atacama Desert in Chile with astrobiological significance.

BUILDING A CARBON NETWORK

Building a large community of interdisciplinary scientists focused on studying the different aspects of deep carbon science requires also creating a supporting infrastructure to foster community growth and facilitate information exchange. Ma et al. describe how the DCO has leveraged state of the art information technologies to establish a knowledge network, which promotes collaboration, reproducibility, accreditation, and stimulates new ideas across deep carbon related studies.

AUTHOR CONTRIBUTIONS

DG, BB, AC, and CS have all equally contributed to this editorial.

FUNDING

This publication was supported by Alfred P. Sloan Foundation grants G2014-13728 to DG, CS, and AC. DG was also supported by Alfred P. Sloan Foundation grant G2016-7206, National Science Foundation grant MCB 15-17567 and by the ELSI Origins Network (EON), which is supported by a grant from the John Templeton Foundation. The opinions expressed in this publication are those of the author(s) and do not necessarily reflect the views of the John Templeton Foundation. DG was also partly supported by a C-DEBI (Center for Dark Energy Biosphere Investigation) postdoctoral fellowship. BB was supported by National Science Foundation grant 1615147. AC was supported by NASA Exobiology Award NNX-16AJ61G.

ACKNOWLEDGMENTS

We are grateful to the Deep Carbon Observatory and the Alfred P. Sloan Foundation for their continuous support to early career scientists. We also wish to thank Katie Pratt for help in crafting the idea of this Research Topic. This is C-DEBI contribution 396.

Conflict of Interest Statement: The authors declare that the research was conducted in the absence of any commercial or financial relationships that could be construed as a potential conflict of interest.

Copyright © 2017 Giovannelli, Black, Cox and Sheik. This is an open-access article distributed under the terms of the Creative Commons Attribution License (CC BY). The use, distribution or reproduction in other forums is permitted, provided the original author(s) or licensor are credited and that the original publication in this journal is cited, in accordance with accepted academic practice. No use, distribution or reproduction is permitted which does not comply with these terms.



Relationship between Diffuse CO₂ Degassing and Volcanic Activity. Case Study of the Poás, Irazú, and Turrialba Volcanoes, Costa Rica

Matthieu Epiard^{1*}, Geoffroy Avard², J. Maarten de Moor², María Martínez Cruz², Gustav Barrantes Castillo³ and Henriette Bakkar⁴

¹ Geosciences Paris Sud Laboratory, Paris XI University, Orsay, France, ² Observatorio Vulcanológico y Sismológico de Costa Rica, Universidad Nacional, Heredia, Costa Rica, ³ Escuela de Ciencias Geográficas, Universidad Nacional, Heredia, Costa Rica, ⁴ Red Sismológica Nacional, Instituto Costarricense de Electricidad, San José, Costa Rica

OPEN ACCESS

Edited by:

Benjamin Alexander Black,
City College of New York (CUNY),
United States

Reviewed by:

Giancarlo Tamburello,
Istituto Nazionale di Geofisica e
Vulcanologia (INGV), Italy
Marc-Antoine Longpré,
Queens College (CUNY),
United States

*Correspondence:

Matthieu Epiard
matthieu.epiard@protonmail.com

Specialty section:

This article was submitted to
Geochemistry,
a section of the journal
Frontiers in Earth Science

Received: 01 April 2017

Accepted: 23 August 2017

Published: 11 October 2017

Citation:

Epiard M, Avard G, de Moor JM, Martínez Cruz M, Barrantes Castillo G and Bakkar H (2017) Relationship between Diffuse CO₂ Degassing and Volcanic Activity. Case Study of the Poás, Irazú, and Turrialba Volcanoes, Costa Rica. *Front. Earth Sci.* 5:71. doi: 10.3389/feart.2017.00071

Active volcanoes exhibit diffuse gas emanations through the ground, the most abundant species of which is CO₂. However, the relationship between diffuse degassing and volcanic activity is not often clear and some volcanoes may have low diffuse degassing levels despite having strong volcanic activity. The main goals of this study are to quantify diffuse CO₂ degassing and determine whether patterns exist in relation to volcanic activity through the study of Turrialba, Poás, and Irazú, three active volcanoes in Costa Rica which are at different stages of activity. Structural controls of spatial distribution of diffuse degassing were also investigated. Measurement campaigns were conducted using the accumulation chamber method coupled with 10 cm depth ground temperature sampling with the aim of estimating the total diffuse CO₂ degassing budget. The total amount of CO₂ emitted diffusely by each volcano is $\sim 113 \pm 46$ t/d over ~ 0.705 km² for Turrialba, 0.9 ± 0.5 t/d for Poás over ~ 0.734 km², 3.8 ± 0.9 t/d over ~ 0.049 km² for Irazú's main crater, and 15 ± 12 t/d over 0.0059 km² for Irazú's north flank. Turrialba and Poás volcano diffuse degassing budget represent about 10% of the whole gas output. Both volcanoes were in a transitional stage and the opening of new conduits may cause a loss in diffuse degassing and an increase of active degassing. Numerous diffuse degassing structures were also identified. At Turrialba, one of which was closely associated with the collapse of a crater wall in 2014 during the initiation of a new period of heightened eruptive activity. Similar structures were also observed on the outer slopes of the west crater, suggesting strong alteration and perhaps destabilization of the upper outer cone. Irazú's north flank is highly permeable and has experienced intense hydrothermal alteration.

Keywords: CO₂, diffuse degassing, gas ratio, Turrialba, Poas, Irazu, gas budget

INTRODUCTION

Carbon dioxide is a relatively inert and abundant magmatic gas (Gerlach and Graeber, 1985) that is relatively insoluble in melt and therefore exsolves at depth (Pan et al., 1991; Papale et al., 2006). CO₂ is emitted both actively through channelizing conduits (Aiuppa et al., 2014; de Moor et al., 2016b) and diffusely through the porous volcanic edifice

(Allard et al., 1991; Chiodini et al., 1996, 1998, 2001; Hernández et al., 1998, 2001; Hernández Perez et al., 2003). As a fluid, its transportation occurs in two different ways: (1) Diffusion according to the Maxwell–Stefan diffusion model which is used instead of Fick's law for multicomponent systems (Maxwell, 1965; Bird et al., 2001), and (2) viscous flow which is described by Darcy's law in a porous media (Bird et al., 2001). Gas transport is thus assumed to be the result of both diffusion and viscous flow contributions (Chiodini et al., 1998; Carapezza and Granieri, 2004).

Many studies on diffuse CO₂ degassing, which aim to establish a gas budget, have yielded varying results. Volcanic systems such as, La Fossa Crater volcano (Italy), which has mostly hydrothermal activity, was estimated to release 200 t/d of CO₂ with major gas flux centered on the crater's inner slope and the faults and cracks of its outer flanks (Chiodini et al., 1996). Other investigations at Teide volcano (Tenerife), which is in a quiescent stage, have shown a diffuse CO₂ output of 308 t/d, mostly of magmatic origin (Hernández et al., 1998). Salazar et al. (2001) measured a total output of 2,800 t/d at Cerro Negro (Nicaragua) which was in an active stage. Research at Satsuma Iwojima (Japan), which has relatively strong active degassing (300 t/d of SO₂ and 100 t/d of CO₂), has shown emissions of "only" 20 t/d of diffuse CO₂ (Shimoike et al., 2002). Finally, a study of the Usu-san volcano (Japan), which had an eruption from March 2000 until September 2001, has shown that CO₂ diffuse degassing increased substantially to 340 t/d 6 months before the eruption and decreased to 39 t/d 3 months after the start of the eruption (Hernández et al., 2001). Based on these studies there does not seem to be a clear relationship between diffuse degassing and volcanic activity.

Cause-effect relationships appear to exist in the diffuse/active ratio of carbon dioxide emissions and volcanic activity. Notsu et al. (2006) sampled CO₂ diffuse degassing data on the Fujisan volcano (Japan) and compared them with observations from other volcanoes (for example Mammoth Mountain, USA). Notsu et al. (2006) make the hypothesis that magma intrusion to shallow levels might lead to an increase in active degassing but a dramatic decrease in diffuse degassing. This idea is in accordance with observations made at the Usu-san volcano where a strong decrease in CO₂ diffuse degassing was observed after the start of the 2000–2001 eruption as mentioned above (Hernández et al., 2001; Notsu et al., 2006). If such a hypothesis is correct, this may lead to interesting and complementary applications in terms of volcanic monitoring. If magma is stored too deeply (more than 10 km deep), geophysical monitoring such as, geodetic, microgravimetry, and electromagnetic measurements, are not particularly effective. However, diffuse degassing may provide additional information when no other monitoring methods are available or suitable. For example, diffuse CO₂ degassing integrated with seismic analysis was used by Werner et al. (2014) to highlight the periodic injection of fresh magma underneath Mammoth Mountain. In our case, Turrialba volcano has experienced a reawakening process which has lasted ~20 years (Martini et al., 2010; de Moor et al., 2016a) and Poás' activity is particularly variable (Fischer et al., 2015; de Moor et al., 2016b) and seems to have stages of enhanced volcanic

activity and stages of quiescence that alternate every 6–12 years (Rymer et al., 2000, 2005, 2009). Diffuse degassing monitoring could thus be an interesting tool for long term monitoring (Allard et al., 1991; Chiodini et al., 1996, 1998, 2001; Giannanco et al., 1998; Hernández et al., 1998, 2001; Melián et al., 2001, 2010; Salazar et al., 2001; Shimoike et al., 2002; Hernández Perez et al., 2003; Carapezza and Granieri, 2004; Galindo et al., 2004; Lewicki et al., 2005; Notsu et al., 2006; Werner and Cardellini, 2006; Carapezza et al., 2009; Viveiros et al., 2010; Peltier et al., 2012; Werner et al., 2014).

The main aim of this study is thus to quantify total CO₂ flux emissions for Turrialba (10.0183°N, 83.7646°W; 3,340 m elevation), Poás (10.1980°N, 84.2307°W; 2,708 m elevation) and Irazú (09.9822°N, 83.8500°W; 3,432 m elevation) Costa Rican volcanoes, and compare the results with past estimations (Melián et al., 2001, 2010; Galindo et al., 2004; Aiuppa et al., 2014) in order to highlight the evolution of volcanic activity over time. Turrialba, Poás, and Irazú volcanoes are three active Costa Rican volcanoes near the capital city of San José. Despite 50 years of relative quiescence, Irazú is perhaps the most dangerous volcano in the country due to its proximity to San José and its frequent historical eruptive activity (Murata et al., 1966; Alvarado et al., 2013). Its last magmatic eruption occurred from March 19th 1963 until 1965. The ash fall area extended 24 km west of the volcano, including San José. Combined with rain, this led to landslides and mudflows (Murata et al., 1966). Poás is a very active volcano with continuous gas emissions (Fischer et al., 2015; de Moor et al., 2016b). Turrialba is currently an erupting volcano that has become active again during the last 20 years. Martini et al. (2010) compiled geophysical and geochemical data between 1996 and 2009, demonstrating the migration of the volcano from a hydrothermal stage to a magmatic stage. Other authors have provided evidence of volcanic cycles of Poás volcano (Rymer et al., 2000, 2005, 2009). But both volcanoes showed significant recent activity changes with episodes of frequent phreatic eruptions at Poás in 2006, 2011, 2014, and 2016 as reported by the Global Volcanism Program (Global Volcanism Program, 2006, 2011, 2013, 2015b), and the occurrence of phreatomagmatic eruptions at Turrialba volcano in 2010 and 2012 and frequent eruptive episodes since 2014 (Global Volcanism Program, 2010, 2012, 2013, 2015a; Campion et al., 2012; de Moor et al., 2016a; Rizzo et al., 2016).

Other information can be obtained from diffuse degassing investigations. For example, gas may be channelized by cracks or tectonic structures in many volcanic systems (Chiodini et al., 1998). For example, Werner and Cardellini (2006) determined the location of areas of increased permeability in the Rotorua geothermal system (New Zealand) and demonstrated structural controls on diffuse degassing. Investigation of diffuse degassing is a very useful tool for detecting hidden structures buried under younger volcanic products such as, faults and fractures (Barberi and Carapezza, 1994; Chiodini et al., 1996; Giannanco et al., 1998; Viveiros et al., 2010; Peltier et al., 2012) or ancient calderas or crater rims (Shimoike et al., 2002; Peltier et al., 2012). Observation of Diffuse Degassing Structures (DDS) may

be used to remotely monitor CO₂ precursors before an eruption or potentially to identify structures that may be responsible for future collapse events (Barberi and Carapezza, 1994; Carapezza et al., 2009). A secondary aim is to demonstrate the tectonic hidden structures of the volcanoes. Knowledge of structural fluid circulation controls is important for hazard assessments such as, evaluating possible eruptive scenarios or the probability of landslides.

METHODOLOGY

The accumulation chamber method has widely demonstrated its effectiveness for analyzing ground degassing (Chiodini et al., 1998; Carapezza and Granieri, 2004; Lewicki et al., 2005). We conducted diffuse soil flux measurements using this methodology using a WestSystem fluxmeter with two interchangeable chambers of different sizes. Both chambers were used for sampling, depending on field conditions. Carbon dioxide was sampled from the chamber for analysis by a LI-COR 820 CO₂ infrared gas analyser with an uncertainty comprised between 2 and 3% over each measurement. Gas was then injected back into the chamber (Chiodini et al., 1996, 1998). Sampling consists in measuring the concentration every second until an established constant flux is obtained (typically >2 min for a low flux). Calibration of the equipment was performed in the laboratory by injecting known and controlled CO₂ flux into the device. In addition, ground measurements were sampled at a depth of 10 cm with a multilogger thermocouple HH506RA.

Campaigns were conducted in July 2012 for Poás, in September 2013 for Turrialba and in May 2015 for Irazú's main crater and north flank, with respectively, 559, 636, 117, and 22 georeferenced points. Measurements were acquired in comparable weather conditions for each volcano. The spacing between each measurement point was between 15 and 50 m, depending mostly on topographic constraints. For example, data collected inside Irazú crater required mountaineering techniques and thus the data are patchy for this volcano. Due to the topographic and weather conditions at Irazú, a second WestSystem fluxmeter was used in order to optimize data acquisition. The detection device for the second fluxmeter is the same that the first fluxmeter (LI-COR 820 CO₂ infrared gas analyzer). The investigated area for each volcano was ~705,000 m² for Turrialba, 749,000 m² for Poás, 49 300 m² for Irazú's main crater and 5 880 m² for Irazú's north flank.

In order to establish geochemical maps of DDS and to infer a total gas budget, geostatistical interpolation of CO₂ and temperature was conducted. First, we removed measurement points for which no diffuse CO₂ was measured. For example, very high fluxes may be caused by fumaroles, i.e., active degassing, and should not be considered for the diffuse degassing investigation. These points are quite easy to distinguish using variogram analysis and were removed from the databases. Hence, the influence of points on the variogram was tested and problematic points were removed with the aim of minimizing

the nugget. The models used for spatial interpolation were estimated automatically. The spherical model or the Matérn model with M. Stein parameterization appeared to be the most appropriate. The relevance of Matérn model with M. Stein parameterization for geology and geostatistics was already investigated in past studies (Stein, 1999; Minasny and McBratney, 2005). Final variograms are shown in **Figures 1, 2**. We used for the interpolation sequential Gaussian simulations (sGs). Many geostatistical interpolation methods—such as, ordinary kriging—are reliable and were used, for example, by Chiodini et al. (2001). However, sGs appear to be the most suitable methodology for this purpose according to Cardellini et al. (2003) and Lewicki et al. (2005). sGs consist of the generation of a large number of possible and equally probable spatial distributions of the variable under consideration with respect to the histogram (Cardellini et al., 2003). Furthermore, the generation of a large number of variable events allows statistical uncertainty to be calculated (typically the mean plus or minus two standard deviations which contain 95.4% of the events). A degassing raster was created as a result and the total gas flux was computed by adding together all the raster cells.

The diffuse degassing data for volcanoes is known to be log-normally distributed and to exhibit a frequently overlapping polymodal distribution indicating different degassing sources (Chiodini et al., 1998, 2001; Cardellini et al., 2003). Basically, these sources are generally a background and endogenous sources and the data are assigned to those sources using a graphical statistical approach (Chiodini et al., 1998, 2001; Cardellini et al., 2003). The partitioning of these sources provides important information about the volcano's dynamic and volcanic activity. The unknown parameters that must be determined are the mean, the standard deviation and the contribution to the whole degassing flux of each source. However, they cannot be easily computed when there is a significant overlap of populations (Sinclair, 1974). Thus, these parameters must be computed and the graphical statistical procedure above mentioned involves probability plots according to the Sinclair approach (Sinclair, 1974, 1976). We can thus deduce a generic probability law on which the diffuse CO₂ degassing random variable depends. The reliability of the inferred probability law was then tested with a Monte Carlo simulation. A Monte Carlo simulation is a random sampling of a variable according to a determined probability law (Krauth, 2006). In this case, we randomly sampled the same amount of field sample data according to the inferred probability law, and compare the experimental histogram with the simulated Monte Carlo one.

RESULTS

Figures 3–5 show the measurement points and the spatial interpolation using sGs for Turrialba, Poás, and Irazú, respectively. Probability plots for CO₂ degassing data are shown in **Figure 6** and ground temperature ones are shown in **Figure 7**. Poás volcano ground temperature plot probably does not account for volcanic phenomena because the mean values are close to one another and all below 20°C. So we assume that the temperature populations for Poás are more likely to be

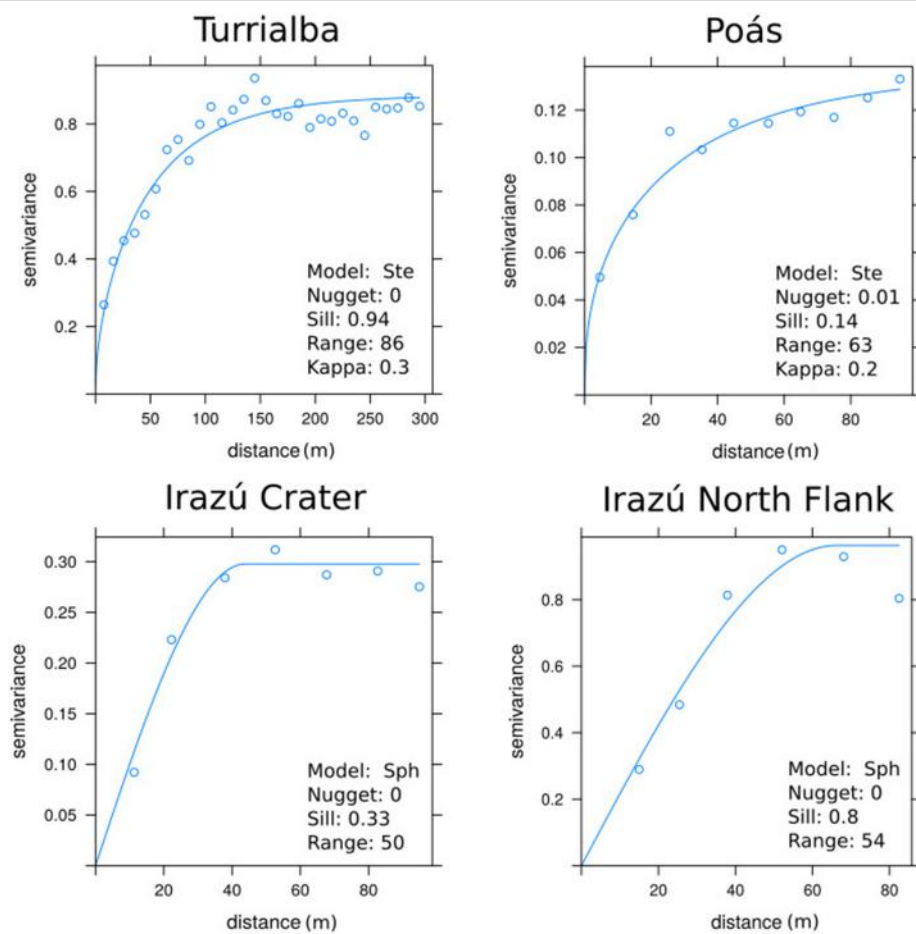


FIGURE 1 | Experimental variogram and fitted variogram model after removing nugget generating points for the CO₂ database of each volcano. “Sph” means Spherical model and “Ste” means Matérn model with M. Stein’s Parameterization. Kappa is the smoothing parameter of the Matérn model. The x-axis is the inter-distance between the points used to form the couples used to compute the semivariance.

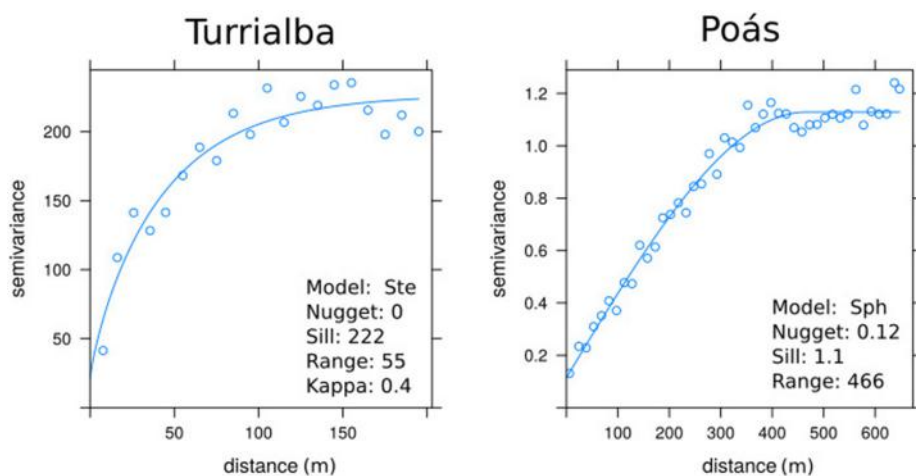


FIGURE 2 | Experimental variogram and fitted variogram model after removing nugget generating points for the 10 cm ground temperature database of Turrialba and Poás. “Sph” means Spherical model and “Ste” means Matérn model with M. Stein’s Parameterization. Kappa is the smoothing parameter of the Matérn model. The x-axis is the inter-distance between the points used to form the couples used to compute the semivariance.

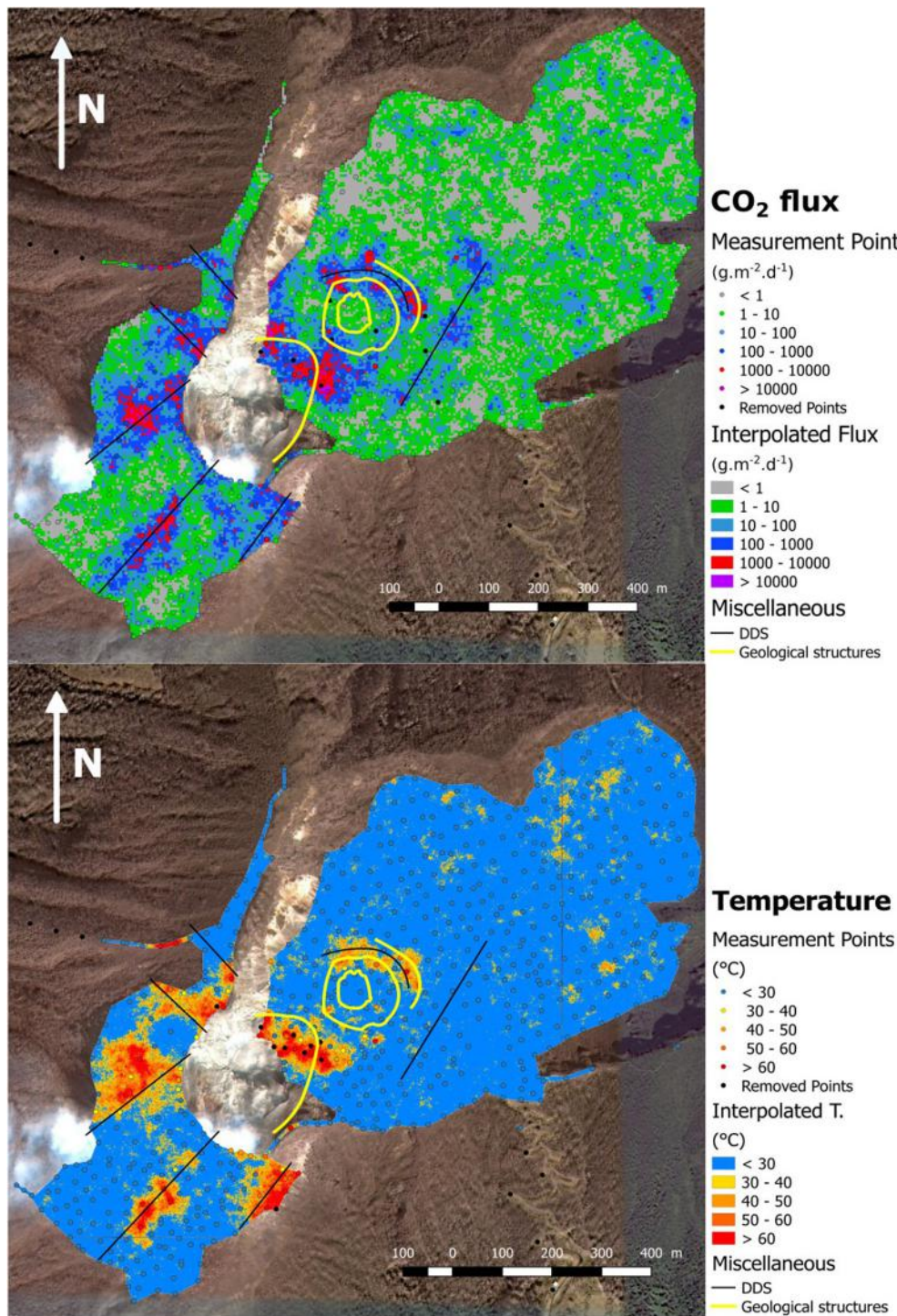


FIGURE 3 | Summit area of Turrialba volcano: measurement points and interpolation by sGs method of CO₂ flux with 5×5 m of resolution and ground temperature at 10 cm depth with 1×1 m resolution over a satellite photography. Both interpolations made on the basis of 5,000 sGs. The yellow circles represent the central crater, and the yellow line at the west of the east crater represents an area which collapsed during an eruptive event in late 2014. DDS is Diffuse Degassing Structures.

caused by daily meteoric and/or environmental effects. CO₂ and temperature data are log-normally distributed and exhibit clear poly-modal distribution. Partitioning of probability plots was

performed using the Sinclair methodology (Sinclair, 1974, 1976). Population parameters are summarized in **Table 1** and total gas budgets are summarized in **Table 2**. Additionally, in order to

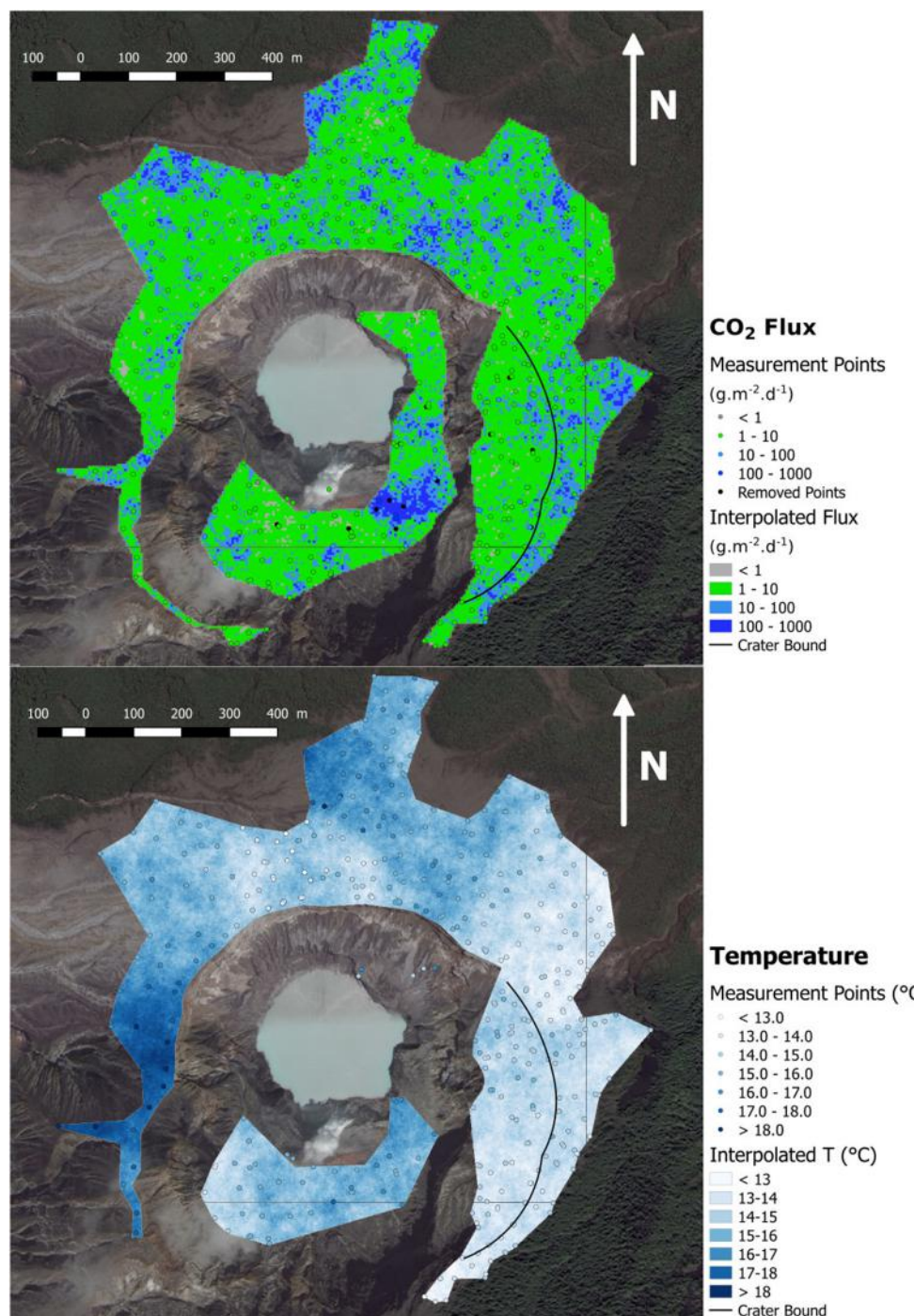


FIGURE 4 | Poás volcano main crater: measurement points and interpolation by sGs method of CO₂ flux and ground temperature at 10 cm depth with, respectively, 5 × 5 and 1 × 1 meters resolution over a satellite photography. Both interpolations made on the basis of 10,000 sGs.

check the accuracy of our mathematic model, a Monte Carlo simulation was performed according to the inferred probability law. The data histogram and Monte Carlo simulation for both CO₂ degassing and ground temperature data are shown in Figures 6, 7, respectively.

The spatial interpolation of CO₂ degassing data and the summing of all raster cells allowed us to compute the total CO₂ diffuse degassing flux. The computation of carbon flux caused by the background was computed on the basis of probability plots (Figure 6) and removed from the total flux. Indeed, populations

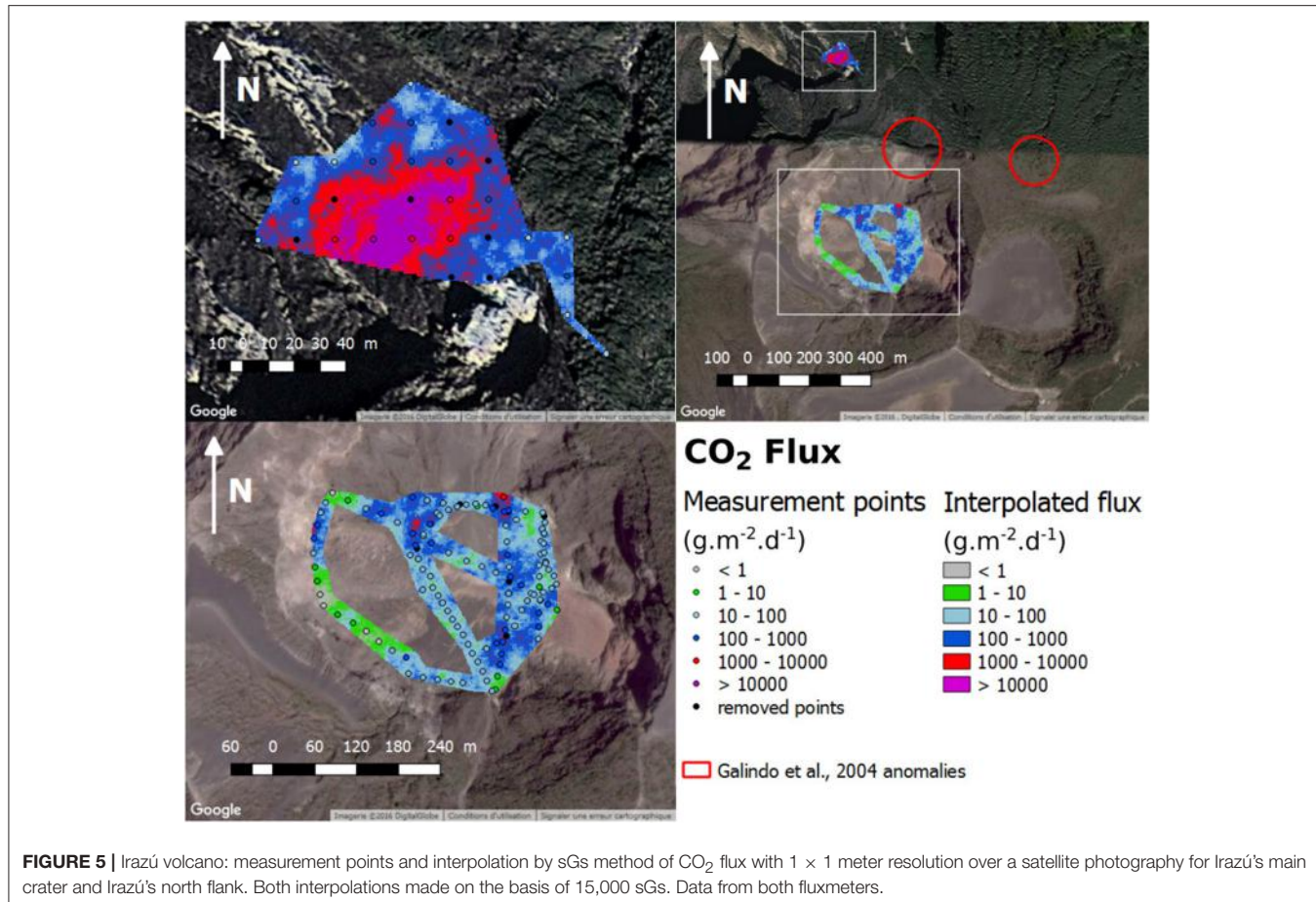


FIGURE 5 | Irazú volcano: measurement points and interpolation by sGs method of CO₂ flux with 1 × 1 meter resolution over a satellite photography for Irazú's main crater and Irazú's north flank. Both interpolations made on the basis of 15,000 sGs. Data from both fluxmeters.

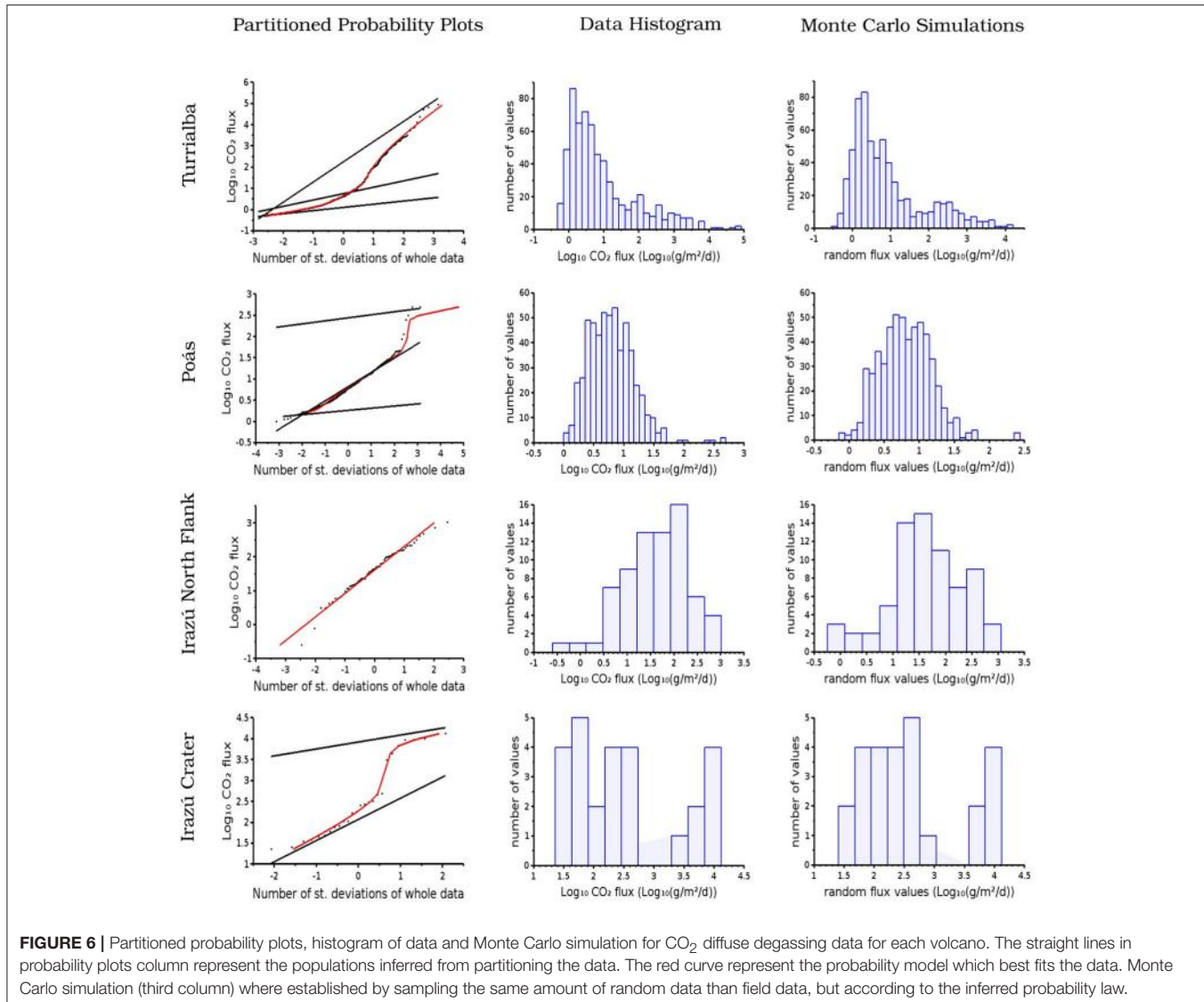
lower than 20–30 g/m²/d could be explained by biological activity (Chiodini et al., 2010) and should be removed from the database in order to get the endogenous flux only. In the case of Poás, the dome area was excluded from this investigation because it is an active degassing area (Fischer et al., 2015; de Moor et al., 2016b). Hence, the total endogenous flux for Turrialba volcano was computed as 113 ± 46 tons/d on the basis of 5,000 simulations and after withdrawing the flux caused by Pop 2 and 3 (Table 1). Poás was computed as 0.9 ± 0.5 tons/d on the basis of 10,000 simulations and after removing the flux caused by Pop 2 and 3 (Table 1). Irazú's main crater was computed as 3.8 ± 0.89 tons/d and Irazú's north flank was computed as 15 tons/d ± 12 tons/day both on the basis of 15,000 simulations. The computation of the background was not possible in the case of Irazú. First, the mean of each population (Table 1) are not relevant with typical background values (Chiodini et al., 2010). Secondly, the investigated area was targeted at the high degassing area, which are small. Hence, the background was not sampled. Uncertainties are two standard deviation intervals around the mean containing 95.4% of the statistical computed fluxes. In the case of Irazú, Diego de la Haya crater, Playa Hermosa, and the SW summit were also investigated. The southwestern area shows evidence of instability with various landslides reported since 2014, but no diffuse CO₂ flux was observed neither

here nor in the older craters of Diego de la Haya and Playa Hermosa.

DISCUSSION

Poás

Two important observations arise from our data from Poás volcano. First, the total diffuse gas was computed as 0.9 ± 0.5 t/d, which is a comparatively low value. For example, the lowest diffuse CO₂ budget found by Melián et al. (2010) was 164 ± 15 t/d in 2,000 over an area of $3,200,000\text{ m}^2$, which leads to a value of 38 ± 4 t/d when scaled to the area investigated in this work ($734,000\text{ m}^2$). A comparison of results between this survey and that of Melián et al. (2010) are presented in Table 2. The difference could be partially due to the better spatial resolution of our study which confines each anomaly to a smaller area. But such an explanation may be not sufficient to explain the observed difference. Secondly, the maximum ground temperature value among all measurement points is 19.3°C. By comparison, temperatures up to about 92°C were recorded at 40 cm depth at some locations each year of the 2000–2003 campaigns of Melián et al. (2010). Hence, no thermal anomaly was recorded in 2012. The temperature interpolation shown in Figure 4 supports this observation because no pixel



value higher than 20°C is predicted. Assuming, as mentioned above, that the populations found in the temperature probability plot are more likely to represent environmental or meteoric effects rather than authentic volcanic phenomena, temperature decrease is further evidence of a real decrease in diffuse CO₂ flux.

This is in agreement with the population flux parameters. The highest population flux was computed up to 275 g/m²/d, but contributes only to 0.5% of the total gas flux (Table 1). In comparison, Melián et al. (2010) found endogenous population between 354 g/m²/d (in 2001) and up to 4,498 g/m²/d (in 2003). Regardless of the investigated area, the Poás degassing populations pattern appears to be quite similar to Melián et al. (2010) results in 2001, suggesting that the volcano was in a similar stage in 2012. It is an indication that the boiling aquifer causing the endogenous flux (Chiodini et al., 2001) was not as active as previous years and was at a quiescent stage. In any case, the few points defining this population are located

eastward of the dome traducing the permeability of this area, which was also noticeable in Melián et al. (2010) degassing maps.

In comparison, the dome fumaroles produced 26 ± 11 t/d of CO₂ in April 2013 (Aiuppa et al., 2014) and degassing from the acid crater lake produced between ~30 ± 10 T/d in 2014 (de Moor et al., 2016b). The gas flux through the lake is directly correlated with the occurrence of phreatic eruptions, with increased magmatic gas and heat delivery driving explosive activity (de Moor et al., 2016b). Though our diffuse degassing flux estimate of 0.9 ± 0.5 t/d for 2012 is not contemporaneous with existing estimates of active degassing flux (Aiuppa et al., 2014; de Moor et al., 2016b; from measurements 2013 and 2014), we estimate the total gas flux from Poás for this period (2012–2014) to be 56 ± 22 T/d. Diffuse degassing contributes ~10% of the total gas flux.

A very weak gas anomaly to the east of the crater (Figure 4) which is known to be permeable, is also noticeable. Indeed,

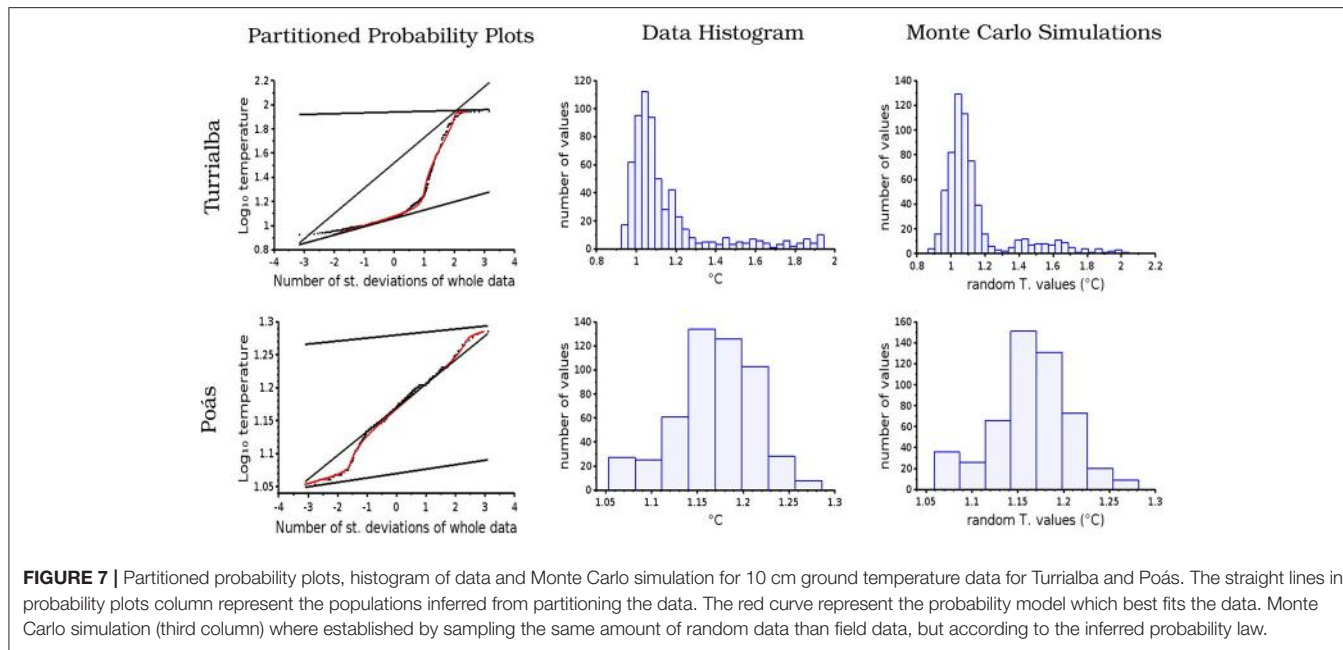


FIGURE 7 | Partitioned probability plots, histogram of data and Monte Carlo simulation for 10 cm ground temperature data for Turrialba and Poás. The straight lines in probability plots column represent the populations inferred from partitioning the data. The red curve represent the probability model which best fits the data. Monte Carlo simulation (third column) where established by sampling the same amount of random data than field data, but according to the inferred probability law.

Melián et al. (2010) detected a strong gas anomaly in this area in 2002, and this area also experienced substantial fumarolic activity (Naranja and Official fumaroles, Fischer et al., 2015). It is however intriguing to note that the Naranja and Official fumaroles disappeared in 2014 and all fumarolic activity was thereafter confined to the dome (Fischer et al., 2015), which is evidence of progressive channelization of dispersed degassing to a more centralized conduit focused at the dome and lake.

Fresh and undegassed magma in the magmatic chamber occurred at a depth of 500 m in late 2000/early 2001, defining a new magmatic cycle (Rymer et al., 2009; Fischer et al., 2015). Assuming that an injection of new magma indeed took place, there are two possibilities to explain our results.

1. Notsu et al. (2006) argue that when magma establishes open conduits to the surface, pressure decreases due to an efficient active degassing, which causes a dramatic decrease of CO₂ diffuse degassing. Consequently, Notsu et al. (2006) define five stages of activity characterized by a diffuse vs. active CO₂ degassing ratio. Stage 1 is a complete quiescence stage where neither diffuse nor active degassing occurs. When magma is rising, diffuse degassing starts (stage 2) followed by active degassing (stage 3). When magma comes close to the surface, active degassing still increases while diffuse degassing decreases strongly and could become negligible (stage 4). Finally, when magmatic chamber is flushing out, active degassing disappears and an episode of diffuse degassing may occur once again (stage 5). Observations at Poás have shown an increase in diffuse CO₂ degassing from 2000 to 2003 (Melián et al., 2010; see Table 2). By 2012, diffuse degassing had decreased to 0.9 ± 0.5 t/d. By linking these observations, we propose that Poás was at increased diffuse degassing stage (stage 2 in Notsu et al., 2006) in 2000, at increased active

channelized degassing stage (stage 3) between 2001 and 2003, and at active channelized degassing only stage (stage 4) in 2011. In April 2017 Poás produced its first phreatomagmatic eruption in over 50 years.

2. Fischer et al. (2015), through intermittent geochemical monitoring of the different fumarole between 2001 and 2014 (including currently inactive Naranja and Official fumaroles) argue that all phreatic eruptions which occurred from 2006 until the present were caused by the periodic pattern sealing, pressure increase, hydrofracturing, phreatic eruption, water infiltration and cooling generated by the 2000–2001 magmatic intrusion. The weak diffuse budget and the fact that Naranja and Official fumaroles became inactive in 2014 may be explained if the volcano was in a sealing-pressure increase stage, probably associated with increased channelization of gases to the central conduits at the dome and lake.

Turrialba

The primary observation at Turrialba is that the diffuse degassing map is in strong agreement with the ground temperature map. Secondly, we observe a strong diffuse CO₂ gas anomaly concentrated around the West Crater, particularly on its east flank near the Central Crater where a vent opened in 2012. On October 29th 2014, a powerful explosion was accompanied by the partial collapse of the crater wall along a structure priorly associated with strong diffuse degassing (Figure 3) to form the 2016 crater, suggesting that the diffuse gas emissions were demonstrating a deep degassing structure. Gas anomalies were also noticeable along SW-NE parallel lineations defining the crater graben and passing through the south of the West Crater and the Central Crater (Figure 3). These orientations have already previously been described by structural geologists (Montero, 2003). Active fumaroles at near boiling temperature were also observable along this lineation. Gas anomalies further

TABLE 1 | Summary table showing the parameters of the different computed populations for CO₂ flux and ground temperature for each volcano.

CO ₂ Degassing populations				
		Mean (g/m ² /d)	Standard deviation (g/m ² /d)	Contribution (%)
Turrialba	Pop 1	140	8.9	29
	Pop 2	5.6	2	36
	Pop 3	1.4	1.6	35
Poás	Pop 1	275	1.2	0.5
	Pop 2	6.7	2.2	94.5
	Pop 3	1.8	1.1	5
Irazú north flank	Pop 1	8,300	1.46	23.7
	Pop 2	120	3.21	76.3
Irazú Crater	Pop 1	81	4.9	100
GROUND TEMPERATURE POPULATIONS				
		Mean (°C)	Standard deviation (°C)	Contribution (%)
Turrialba	Pop 1	87	1	1.7
	Pop 2	33	1.6	16.3
	Pop 3	11	1.2	82
Poás	Pop 1	19	1	0.7
	Pop 2	15	1.1	94.3
	Pop 3	12	1	5
Irazú north flank		N.A.	N.A.	N.A.
Irazú Crater		N.A.	N.A.	N.A.

Contribution is the proportion of each assumed normal law in the whole polymodal law. N.A., Not Available.

correspond with the rim of some old craters, as for example the central crater. In contrast, no anomaly is observed toward the East Crater and a reactivation in this area appears very unlikely.

The same method as for Poás can be applied for Turrialba to estimate the proportion of diffuse degassing in the total CO₂ flux, adding the 113 ± 46 t/d diffuse flux to the 1094 ± 631 t/d of active flux measured in 2013 by Aiuppa et al. (2014), one and a half years before the volcanic activity increased. The diffuse emission would then represent between 4 and 22% of the total flux. Such a proportion is comparable with the estimation at Poás volcano.

If Turrialba volcano is following the decreasing pattern described by Notsu et al. (2006), then the 2013 diffuse degassing flux should be lower than the previous years and we could expect that it continued to decrease in the following years. Indeed, Turrialba activity increased and it experienced several vent opening in January 2010 (Campion et al., 2012), in January 2011 and in January 2012 (Alvarado et al., 2016). Furthermore, a new weak ash emission occurred in May 2013 without opening a new vent. These events correspond to the opening of conduits that have been able to channelize some of the diffuse gas (Campion et al., 2012), reducing its contribution to the total flux by transferring it to the active flux instead, particularly in 2011 when those events occurred slightly more frequently. Previous diffuse degassing survey would have been necessary to confirm this theory. However, the occurrence of energetic

phreatomagmatic eruption in October 2014, March 2015, May and September 2016 and the increase of CO₂ in the plume (Alvarado et al., 2016; de Moor et al., 2016a; Rizzo et al., 2016) comforts the idea that magma established open conduits to the surface.

The endogenous population responsible of the volcanic CO₂ flux (Figure 6) comes from the underlying boiling aquifer (Chiodini et al., 2001). However, Campion et al. (2012) have shown that the increasing volcanic activity may have opened dry channels which may feed some vents and fumaroles. Furthermore, this population appears to match well with the highest temperature population which has a mean of 87°C (Figure 3 and Table 1). It is thus not excluded that this population may be composed partly from gases rising directly from the magma. In any cases, most of the points defining this population are located on fractured and/or destabilized areas, traducing variations in permeability of the ground. For example, many high flux points are located near the west crater flank which collapsed in late 2014 (See Figure 3).

Irazú

Due to the difficult nature of the terrain (topography, weather) that limited the number of measurements, and the regularity of the grid, as well as the presence of communication antennas that were strongly interfering with the GPS signal, the results should

TABLE 2 | Comparative table summarizing total diffuse CO₂ budget measured in this study (in bold) and comparing with past and contemporary results of diffuse degassing studies.

Date	t/d	Diffuse degassing Area (m ²)	Reference
TURRIALBA			
2013	113 ± 46	705,000	
POÁS			
2011	0.9 ± 0.5	734,000	
2003	124 ± 15*	734,000*	Melián et al., 2010
2002	123 ± 16*	734,000*	Melián et al., 2010
2001	97 ± 13*	734,000*	Melián et al., 2010
2000	38 ± 4*	734,000*	Melián et al., 2010
IRAZÚ			
2015	18.3 ± 12.1	55,180	
2001	4.4*	55,180*	Galindo et al., 2004

For Poás volcano, diffuse degassing budgets of Melián et al. (2010) were in fact sampled over an area of 3,200,000 m², but were scaled here to the area investigated in this study for better comparison. The same procedure was applied to Galindo et al. (2004) work for Irazú volcano, who investigated in fact over an area of 3,500,000 m². * Means that results were normalized regarding the 2015 investigated area.

TABLE 3 | Comparative table showing the evolution over time of Irazú volcano.

	Galindo et al., 2004	Our results (2015)	
	2001	North flank	Main crater
Max value (g.m ⁻² .d ⁻¹)	316	2.71 × 10 ⁴	2.17 × 10 ³
Mean Pop 1 (g.m ⁻² .d ⁻¹)	N.A.	8,300	N.A.
Mean Pop 2 (g.m ⁻² .d ⁻¹)	28	120	81
Mean Pop 3 (g.m ⁻² .d ⁻¹)	3	N.A.	N.A.
Total flux (t.d ⁻¹)	44	15	3.8
Area investigated (km ⁻²)	3.5	5.9 × 10 ⁻³	4.9 × 10 ⁻²
Number of points	201	117	22

Results of 2001 are from Galindo et al. (2004).

Total flux is relative to the investigated area. N.A., Not Available.

be viewed with caution. However, the primary observation is that the diffuse gas anomalies are mainly concentrated on the north flank of the volcano, where extensive and intense rock alteration is visible. Gas emanation is present to a lesser extent inside the main crater as shown by measurement points in Figure 5. The rest of the investigated area, i.e., Playa Hermosa, the Diego de la Haya crater and the west flank, where a landslide is occurring, do not present any identified gas anomalies. The north flank has already been noted for its most recent activity with a debris avalanche on December 8th 1994. Initially interpreted as being the result of phreatic eruptions on the flank of the volcano (Barquero et al., 1995), new insight on the data suggests that it was more likely caused by a major landslide (Alvarado et al., 2013). In both of these hypotheses, the presence of diffuse degassing on the north flank implies an ongoing alteration process and hence a modification of the cohesion of the rocks in this steep area that increases the possibility of gravitational instability (López and Williams, 1993).

The diffuse degassing anomaly concentrated on the north flank is consistent with the study conducted in 2001 at Irazú by Galindo et al. (2004). At that time, the Main Crater, was occupied by a lake which disappeared in 2013. The anomalies identified by Galindo et al. (2004) were located to the east of the area investigated in this work, which suggests that the whole north flank is potentially porous and that the site of main degassing has migrated over time. However, those areas were not investigated by our 2015 campaign and we do not know whether those anomalies still exist. A comparison of both the studies is shown in Table 3 and a comparison of the total diffuse CO₂ budget in Table 2. Population 1 has a mean of 8,300 gm⁻²d⁻¹, which is much higher than the Galindo et al. (2004) maximum population. Nevertheless, the diffuse degassing budget in 2001 was of 4.4 t/d [277 t/d over an area of 3,500,000 m² (Galindo et al., 2004), see Table 2]. This result is very close to the lowest possible diffuse gas flux of our survey, due to the great uncertainty (15 ± 12 t/d). Hence, it is not significant and is not robust evidence of increased degassing. As previously stated, the 2015 campaign, results should be viewed with great caution. First, the 2015 data are severely affected by noise, especially for the north flank. Secondly, Galindo et al. (2004) covered a large area (3.5 km²) with only 201 points. This spatial resolution is not sufficient for seeing local anomalies and (Galindo et al., 2004) may have missed some ones.

Finally, the main crater lake disappeared in 2013. One explanation would be that evaporation may have resulted from heat input due to increasing volcanic activity. Such a phenomenon was seen at Poás during an eruptive period: indeed, the acid lake has completely disappeared at the time of writing in response to the ongoing phreatomagmatic activity. Importantly, no CO₂ flux anomaly in the crater supports increased volcanic activity as an explanation for the disappearance of the lake at Irazú. The disappearance of Irazú's crater lake is thus more likely to be structural.

The absence of volcanic plume and a weak total diffuse degassing, though with high uncertainty, supports the hypothesis that Irazú volcano is currently in a quiescent stage. Referring to Notsu et al. (2006) volcanic stages theory, Irazú volcano may be at stage 2. The major hazard currently is collapse events which could generate landslides or lahars. However, our area of investigation is very small and with a high level of uncertainty. In order to allow a better assessment of the volcanic activity, a larger area should be studied.

CONCLUSION

The investigation of diffuse CO₂ degassing allows us to observe the following:

- The total diffuse gas budget for Turrialba was computed as 113 ± 46 t/d, 0.9 ± 0.5 t/d for Poás, 3.8 ± 0.9 t/d for Irazú's main crater and 15 ± 12 t/d for Irazú's north flank. However, data from Irazú volcano and especially for the northern flank should be viewed with caution due to the significant amount of noise because of the difficulty of field measurements.

- (ii) In both the cases of Poás and Turrialba, diffuse CO₂ flux accounts for about 10% of the total volcanic CO₂ flux. At the time of diffuse degassing campaigns, both volcanoes were in a transitional stage in dynamic response to recent magma intrusions. The channelizing of gases by conduit opening is responsible for the loss in diffuse degassing and the increase of active degassing (Notsu et al., 2006).
- (iii) Structural fluid circulation controls have been observed for Turrialba through diffuse CO₂ emission and ground temperature. A strong gas anomaly was observed in 2013 at the east of West Crater (crater wall), which collapsed in 2016. This gas anomaly suggests that the ground has been deeply altered. DDS was also observed on the outer slopes of the west crater, suggesting that the upper outer cone of the volcano has been significantly altered and potentially destabilized. Such tectonic structures, interpreted as an extension of the crater graben, are altered areas which may also experience collapses or may be prone to opening of new vents in the future. No such DDS has been observed at Irazú volcano probably due to the small size of the area investigated, but such structural controls probably exist. The north flank of the volcano is highly porous and may be the source of the main volcanic risk for future flank eruptions. Irazú's crater lake probably disappeared as a result of structural controls, perhaps in response to edifice deformation associated with inflation and activity of the nearby Turrialba volcano (de Moor et al., 2016a).

Our study shows that monitoring of diffuse degassing can be a useful tool for the monitoring of long—to medium-term variations in volcanic activity and associated hazards. Evolution toward more centralized active degassing is associated with increased eruption potential and areas prone to future collapse can in some cases be identified by DDS. Our study calls for

more intensive research and monitoring of diffuse and active degassing in order to understand the dynamic volcanic gas budgets.

AUTHOR CONTRIBUTIONS

ME wrote programs for processing all the data, sampled a part of the Irazú's dataset. He drafted and wrote the different versions of paper. GA sampled the major part of the data (i.e.,) the Turrialba and the Poas dataset. He participate with JdM to the interpretation of the data. He took active part on revising and correcting the paper and approved the final version of the paper. JdM participated to the interpretation of the data. He took also part to the sampling of Irazú's dataset. He also took active part on reviewing the paper and approved the final version to be published. MM took part to the interpretation of the data and contributed to reviewing of the paper. GB participated to the sampling of Poas dataset. HB participated to the sampling of Irazú's dataset.

ACKNOWLEDGMENTS

We would like to thank Dr. Alastair J. Sinclair for his very constructive and helpful remarks about statistics and programming. We would also like to thank Dr. Melián who kindly accepted to discuss with us in further detail her papers and for having shared with us her experience of Poás. A big thank to Tullio Ricci for his words of advice and his expertise for the interpretation of volcanological data. Thanks also to Dr. C. Werner who provided us useful words of advice during the 5th NOVAC workshop. This work was also supported by Davide Continenza who provided us assistance in the use of the WestSystems fluxmeter.

REFERENCES

- Aluppa, A., Robidoux, P., Tamburello, G., Conde, V., Galle, B., Avard, G., et al. (2014). Gas measurements from the Costa Rica–Nicaragua volcanic segment suggest possible along-arc variations in volcanic gas chemistry. *Earth Planet. Sci. Lett.* 407, 134–147. doi: 10.1016/j.epsl.2014.09.041
- Allard, P., Carbonelle, J., Dajlevic, D., Le Bronec, J., Morel, P., Robe, M. C., et al. (1991). Eruptive and diffuse emissions of CO₂ from Mount Etna. *Nature* 35, 387–391. doi: 10.1038/351387a0
- Alvarado, G. E., Brenes-André, J., Barrantes, M., Vega, E., De Moor, J. M., Avard, G., et al. (2016). La actividad explosiva del volcán Turrialba (Costa Rica) en el período 2010–2016. *Rev. Geol. Amér. Central* 55, 7–60. doi: 10.15517/rgac.v55i0.26965
- Alvarado, G. E., Mora, M. M., and Ulloa, A. (2013). La caída de “ceniza” proveniente del volcán Irazú (Costa Rica) el 8 de diciembre de 1994: ¿Una explosión freática? *Rev. Geol. Am. Central* 48, 159–168. doi: 10.15517/rgac.v0i48.12241t
- Barberi, F., and Carapezza, M. L. (1994). Helium and CO₂ soil gas emission from Santorini (Greece). *Bull. Volcanol.* 56, 335–342.
- Barquero, R., Mora, M., Madrigal, L., Vargas, I., Arias, F., and Soto, G. (1995). *Resumen Anual de Sismos y Actividad Volcánica en Costa Rica Durante 1994–19 Págs.* Oficina de Sismología y Vulcanología, RSN [Inf. Interno].
- Bird, R. B., Stewart, W. E., and Lightfoot, E. N. (2001). *Transport Phenomena, 2nd Edn.* John Wiley & Sons. Available online at: <https://www.slideshare.net/Aapandove/bird-stewart-lightfoot-2002-transport-phenomena-2nd-ed>
- Campion, R., Martínez-Cruz, M., Lecocq, T., Caudron, C., Pacheco, J., Pinardi, G., et al. (2012). Space- and ground-based measurements of sulphur dioxide emissions from Turrialba Volcano (Costa Rica). *Bull. Volcanol.* 74, 1757–1770. doi: 10.1007/s00445-012-0631-z
- Carapezza, M. L., and Granieri, D. (2004). CO₂ soil flux at Vulcano (Italy): comparison between active and passive methods. *Appl. Geochem.* 19, 73–88. doi: 10.1016/S0883-2927(03)00111-2
- Carapezza, M. L., Ricci, T., Ranaldi, M., and Tarchini, L. (2009). Active degassing structures of Stromboli and variations in diffuse CO₂ output related to the volcanic activity. *J. Volcanol. Geotherm. Res.* 182, 231–245. doi: 10.1016/j.jvolgeores.2008.08.006
- Cardellini, C., Chiodini, G., and Frondini, F. (2003). Application of stochastic simulation to CO₂ flux from soil: mapping and quantification of gas release. *J. Geophys. Res.* 108, 2425. doi: 10.1029/2002JB002165
- Chiodini, G., Caliro, S., Cardellini, C., Granieri, D., Avino, R., Baldini, A., et al. (2010). Long-term variations of the Campi Flegrei, Italy, volcanic system as revealed by the monitoring of hydrothermal activity. *J. Geophys. Res.* 115: B03205. doi: 10.1029/2008JB006258
- Chiodini, G., Cioni, R., Guidi, M., Raco, B., and Marini, L. (1998). Soil CO₂ flux measurements in volcanic and geothermal areas. *Appl. Geochem.* 13, 543–552.

- Chiodini, G., Frondini, F., and Raco, B. (1996). Diffuse emission of CO₂ from the fossa crater, Vulcano Island. *Bull. Volcanol.* 58, 41–50.
- Chiodini, G., Frondini, F., Cardellini, D., Granieri, D., Marini, L., and Ventura, G. (2001). CO₂ degassing and energy release at Solfatara volcano, Campi Flegrei, Italy. *J. Geophys. Res.* 106, 213–221. doi: 10.1029/2001JB000246
- de Moor, J. M., Aiuppa, A., Avard, G., Wehrmann, H., Dunbar, N., Muller, C., et al. (2016a). Turmoil at Turrialba Volcano (Costa Rica): Degassing and eruptive processes inferred from high-frequency gas monitoring. *J. Geophys. Res. Solid Earth* 121, 5761–5775. doi: 10.1002/2016JB013150
- de Moor, J. M., Aiuppa, A., Pacheco, J., Avard, G., Kern, C., Liuzzo, M., et al. (2016b). Short-Period volcanic gas precursors to phreatic eruptions: insights from Poás Volcano, Costa Rica. *Earth Planet. Sci. Lett.* 442, 218–227. doi: 10.1016/j.epsl.2016.02.056
- Fischer, T. P., Ramirez, C., Mora-Amador, R. A., Hilton, D. R., Barnes, J. D., Sharp, Z. D., et al. (2015). Temporal variations in fumarole gas chemistry at Poás volcano, Costa Rica. *J. Volcanol. Geotherm. Res.* 294, 56–70. doi: 10.1016/j.jvolgeores.2015.02.002
- Galindo, I., Melián, G. V., Salazar, J. L. M., Hernández, P. A., Pérez, N. M., Ramírez, C., et al. (2004). Emisión difusa de dióxido de carbono en el volcán Irazú, Costa Rica. *Rev. Geol. de Am. Central* 30, 157–165. doi: 10.15517/rgac.v0i30.7284
- Gerlach, T. M. J., and Graeber, E. J. (1985). Volatile budget of Kilauea volcano. *Nature* 313, 273–277. doi: 10.1038/313273a0
- Giammanco, S., Gurrieri, S., and Valenza, M. (1998). Anomalous soil CO₂ degassing in relation to faults and eruptive fissures on Mount Etna (Sicily, Italy). *Bull. Volcanol.* 60, 252–259.
- Global Volcanism Program (2006). “Report on Poás (Costa Rica),” in *Bulletin of the Global Volcanism Network*, 31:3, ed R. Wunderman (Smithsonian Institution).
- Global Volcanism Program (2010). “Report on Turrialba (Costa Rica),” in *Bulletin of the Global Volcanism Network*, 35:2, ed R. Wunderman (Smithsonian Institution).
- Global Volcanism Program (2011). “Report on Poás (Costa Rica),” in *Bulletin of the Global Volcanism Network*, 36:4, ed R. Wunderman (Smithsonian Institution).
- Global Volcanism Program (2013). “Report on Poás (Costa Rica),” in *Bulletin of the Global Volcanism Network*, 38:9, ed R. Wunderman (Smithsonian Institution).
- Global Volcanism Program (2015a). “Report on Turrialba (Costa Rica),” in *Bulletin of the Global Volcanism Network*, 40:4, ed R. Wunderman (Smithsonian Institution).
- Global Volcanism Program (2012). “Report on Turrialba (Costa Rica),” in *Bulletin of the Global Volcanism Network*, 37:6, ed R. Wunderman (Smithsonian Institution).
- Global Volcanism Program (2015b). “Report on Poás (Costa Rica),” in *Bulletin of the Global Volcanism Network*, 40:11, ed E. Venzke (Smithsonian Institution).
- Hernández Perez, P., Notsu, K., Tsurumi, M., Mori, T., Ohno, M., Shimoike, Y., et al. (2003). Carbon dioxide emissions from soils at Hakkoda, north Japan. *J. Geophys. Res.* 108, 2210. doi: 10.1029/2002JB001847
- Hernández, P. A., Notsu, K., Salazar, J. M., Mori, T., Natale, G., Okada, H., et al. (2001). Carbon dioxide degassing by advective flow from Usu Volcano, Japan. *Science* 292, 83–86. doi: 10.1126/science.1058450
- Hernández, P. A., Perez, N. M., Salazar, J. M., Nakai, S., Notsu, K., and Wakita, H. (1998). Diffuse emission of carbon dioxide, methane, and helium-3 from Teide volcano, Tenerife, Canary Islands. *Geophys. Res. Lett.* 25, 3311–3314. doi: 10.1029/98GL02561
- Krauth, W. (2006). *Statistical Mechanics: Algorithms and Computations*. Paris: Oxford University Press.
- Lewicki, J. L., Bergfeld, D., Cardellini, C., Chiodini, G., Granieri, D., Varley, N., et al. (2005). Comparative soil CO₂ flux measurements and geostatistical estimation methods on Masaya volcano, Nicaragua. *Bull. Volcanol.* 68, 76–90. doi: 10.1007/s00445-005-0423-9
- López, D. L., and Williams, S. N. (1993). Catastrophic volcanic collapse: relation to hydrothermal processes. *Science* 260, 1794–1796. doi: 10.1126/science.260.5115.1794
- Martini, F., Tassi, F., Vaselli, O., Del Potro, R., Martinez-Cruz, M., Van del Laat, R., et al. (2010). Geophysical, geochemical and geodetical signals of reawakening at Turrialba volcano (Costa Rica) after almost 150 years of quiescence. *J. Volcanol. Geothermal Res.* 198, 416–432. doi: 10.1016/j.jvolgeores.2010.09.021
- Maxwell, J. C. (1965). On the dynamical theory of gases. *Sci. Pap. J.* 2, 26–78.
- Melián, G. V., Pérez, N. M., Hernández, P. A., Nolasco, D., Marrero, R., Fernández, M., et al. (2010). Emisión difusa de CO₂ y actividad volcánica en el volcán Poás, Costa Rica. *Rev. Geol. Am. Central* 43, 147–170. doi: 10.15517/rgac.v0i43.3462
- Melián, G., Galindo, I., Salazar, J., Hernández, P., Pérez, N., Ramirez, C., et al. (2001). “December. Spatial and secular variations of diffuse CO₂ degassing from Poás volcano, Costa Rica, Central America,” in *AGU Fall Meeting Abstracts* (San Francisco, CA), 0951.
- Minasny, B., and McBratney, A. B. (2005). The matérn function as a general model for soil variograms, *Geoderma* 128, 192–207
- Montero, W. (2003). El sistema de falla Atirro-Río sucio y la cuenca de tracción de Turrialba-Irazú: indentación tectónica relacionada con la colisión del levantamiento del Coco. *Geol. Am. Central* 28, 5–29. doi: 10.15517/rgac.v0i28.7781
- Murata, K. J., Dondoli, C., and Saenz, R. (1966). The 1963–65 eruption of Irazú volcano, Costa Rica (the period of March 1963 to October 1964). *Bull. Volcanol.* 29:763.
- Notsu, K., Mori, T., Chanchah Do Vale, S., Kagi, H., and Ito, T. (2006). Monitoring quiescent vol-canoes by diffuse CO₂ degassing: case study of Mt. Fuji, Japan. *Pure and Appl. Geophys.* 163, 825–835. doi: 10.1007/s00024-006-0051-0
- Pan, V., Holloway, J. R., and Hervig, R. L. (1991). The pressure and temperature dependence of carbon dioxide solubility in tholeiitic basalt melts. *Geochim. Cosmochim. Acta* 55, 1587–1595. doi: 10.1016/0016-7037(91)90130-W
- Papale, P., Moretti, R., and Barbato, D. (2006). The compositional dependence of the multi-component volatile saturation surface in silicate melts. *Chem. Geol.* 229, 78–95. doi: 10.1016/j.chemgeo.2006.01.013
- Peltier, A., Finizola, A., Douillet, G. A., Brothelande, E., and Garaebiti, E. (2012). Structure of an Active volcano associated with a resurgent block inferred from thermal mapping: the yasur-yenkahe volcanic complex (Vanuatu). *J. Volcanol. Geother. Res.* 243–244, 59–68. doi: 10.1016/j.jvolgeores.2012.06.022
- Rizzo, A. L., Di Piazza, A., de Moor, M., Alvarado, G. E., Avard, G., Carapezza, M. L., et al. (2016). Eruptive activity at Turrialba volcano (Costa Rica): Inferences from 3 He/ 4 He in fumarole gases and chemistry of the products ejected during 2014 and 2015. *Geochem. Geophys. Geosyst.* 17, 4478–4494. doi: 10.1002/2016GC006525
- Rymer, H., Cassidy, J., Locke, C. A., Barboza, M. V., Barquiero, J., Brenes, J., et al. (2000). Geophysical studies of the recent 15-year eruptive cycle at Poás Volcano, Costa Rica. *J. Volcanol. Geotherm. Res.* 97, 425–442. doi: 10.1016/S0377-0273(99)00166-3
- Rymer, H., Locke, C. A., Borgia, A., Martínez, M., Brenes, J., Van der Laat, R., et al. (2009). Long-term fluctuations in volcanic activity: implications for future environmental impact. *Terra Nova* 21, 304–309. doi: 10.1111/j.1365-3121.2009.00858.x
- Rymer, H., Locke, C. A., Brenes, J., and Williams-Jones, G. (2005). Magma plumbing processes for persistent activity at Poás volcano, Costa Rica. *Geophys. Res. Lett.* 32:L08307. doi: 10.1029/2004GL022284
- Salazar, J. M., Hernández, P. A., Perez, N. M., Melián, G., Alvarez, J., and Notsu, K. (2001). Diffuse emission of carbon dioxide from Cerro Negro volcano, Nicaragua, Central America, *Geo-phys. Res. Lett.* 28, 4275–4278. doi: 10.1029/2001GL013709
- Shimoike, Y., Kazahaya, K., and Shinohara, H. (2002). Soil gas emission of volcanic CO₂ at Satsuma-Iwojima Volcano, Japan. *Earth Planet. Space* 54, 239–247. doi: 10.1186/BF03353023
- Sinclair, A. J. (1974). Selection of threshold values in geochemical data using probability graphs. *J. Geochem. Explor.* 3, 129–149. doi: 10.1016/0375-6742(74)90030-2
- Sinclair, A. J. (1976). *Applications of Probability Graphs in Mineral Exploration*. Vol. 4. Vancouver, BC: Association of Exploration Geochemists. Available on line at: https://www.appliedgeochemists.org/images/stories/Members%20Area/Applications_of_Probability_Graphs_in_Mineral_Exploration.pdf
- Stein, M. L. (1999). *Interpolation of Spatial Data: Some Theory for Kriging*. New York, NY: Springer.
- Viveiros, F., Cardellini, C., Ferreira, T., Caliro, S., Chiodini, G., and Silva, C. (2010). Soil CO₂ emissions at Furnas volcano, São Miguel Island, Azores archipelago: volcano monitoring perspectives, geomorphologic studies, and land use

- planning application. *J. Geophys. Res.* 115, B12208. doi: 10.1029/2010JB007555
- Werner, C., and Cardellini, C. (2006). Comparison of carbon dioxide emissions with fluid upflow, chemistry, and geologic structures at the Rotorua geothermal system, New Zealand. *Geothermics* 35, 221–238. doi: 10.1016/j.geothermics.2006.02.006
- Werner, C., Bergfeld, D., Farrar, C. D., Doukas, M. P., Kelly, P. J., and Kern, C. (2014). Decadal-scale variability of diffuse CO₂ emissions and seismicity revealed from long-term monitoring (1995–2013) at Mammoth Mountain, California, USA. *J. Volcanol. Geotherm. Res.* 289, 51–63. doi: 10.1016/j.jvolgeores.2014.10.020

Conflict of Interest Statement: The authors declare that the research was conducted in the absence of any commercial or financial relationships that could be construed as a potential conflict of interest.

Copyright © 2017 Epiard, Avard, de Moor, Martínez Cruz, Barrantes Castillo and Bakkar. This is an open-access article distributed under the terms of the Creative Commons Attribution License (CC BY). The use, distribution or reproduction in other forums is permitted, provided the original author(s) or licensor are credited and that the original publication in this journal is cited, in accordance with accepted academic practice. No use, distribution or reproduction is permitted which does not comply with these terms.



Soil CO₂ Degassing Path along Volcano-Tectonic Structures in the Pico-Faial-São Jorge Islands (Azores Archipelago, Portugal)

Fátima Viveiros^{1*}, Márcio Marcos², Carlos Faria³, João L. Gaspar¹, Teresa Ferreira^{1,4} and Catarina Silva^{1,4}

¹ Instituto de Investigação em Vulcanologia e Avaliação de Riscos, Universidade dos Açores, Ponta Delgada, Portugal,

² Secretaria Regional da Educação, Santa Cruz da Graciosa, Portugal, ³ Secretaria Regional da Energia, Ambiente e Turismo, Horta, Portugal, ⁴ Centro de Informação e Vigilância Sismovulcânica dos Açores, Ponta Delgada, Portugal

OPEN ACCESS

Edited by:

Benjamin Alexander Black,
City College of New York (CUNY),
United States

Reviewed by:

José Madeira,
Universidade de Lisboa, Portugal
J. Maarten De Moor,
OVSICORI-UNA, Costa Rica

*Correspondence:

Fátima Viveiros
maria.fb.viveiros@azores.gov.pt

Specialty section:

This article was submitted to
Geochemistry,
a section of the journal
Frontiers in Earth Science

Received: 13 November 2016

Accepted: 01 June 2017

Published: 14 June 2017

Citation:

Viveiros F, Marcos M, Faria C, Gaspar JL, Ferreira T and Silva C (2017) Soil CO₂ Degassing Path along Volcano-Tectonic Structures in the Pico-Faial-São Jorge Islands (Azores Archipelago, Portugal).

Front. Earth Sci. 5:50.
doi: 10.3389/feart.2017.00050

The Azores archipelago is composed of nine volcanic islands located at the triple junction between the North American, Eurasian, and Nubian plates. Nowadays the volcanic activity in the archipelago is characterized by the presence of secondary manifestations of volcanism, such as hydrothermal fumaroles, thermal and cold CO₂-rich springs as well as soil diffuse degassing areas, and low magnitude seismicity. Soil CO₂ degassing (concentration and flux) surveys have been performed at Pico, Faial, and São Jorge islands to identify possible diffuse degassing structures. Since the settlement of the Azores in the fifteenth Century these three islands were affected by seven onshore volcanic eruptions and at least six destructive earthquakes. These islands are crossed by numerous active tectonic structures with dominant WNW-ESE direction, and less abundant conjugate NNW-SSE trending faults. A total of 2,855 soil CO₂ concentration measurements have been carried out with values varying from 0 to 20.7 vol. %. Soil CO₂ flux measurements, using the accumulation chamber method, have also been performed at Pico and Faial islands in the summer of 2011 and values varied from absence of CO₂ to 339 g m⁻² d⁻¹. The highest CO₂ emissions were recorded at Faial Island and were associated with the Pedro Miguel graben faults, which seem to control the CO₂ diffuse degassing and were interpreted as the pathways for the CO₂ ascending from deep reservoirs to the surface. At São Jorge Island, four main degassing zones have been identified at the intersection of faults or associated to WNW-ESE tectonic structures. Four diffuse degassing structures were identified at Pico Island essentially where different faults intersect. Pico geomorphology is dominated by a 2,351 m high central volcano that presents several steam emissions at its summit. These emissions are located along a NW-SE fault and the highest measured soil CO₂ concentration reached 7.6 vol. % with a maximum temperature of 77°C. The diffuse degassing maps show that anomalous CO₂ degassing areas are controlled essentially by the tectonic structures and the lithology of the sites since the youngest volcanic systems are characterized by very low CO₂ emissions.

Keywords: volcanic gases, diffuse degassing structures, CO₂ degassing, tectonics, Azores archipelago, Faial Island, Pico Island, São Jorge Island

INTRODUCTION

Carbon dioxide (CO₂) together with water vapor (H₂O) and sulfur dioxide (SO₂) are usually the most abundant gases released to the atmosphere during volcanic eruptions (Giggenbach, 1996; Fischer and Chiodini, 2015 and references therein). During non-eruptive periods, gas emissions are also frequent in many volcanic systems not only through the presence of permanent fumaroles, but also due to the existence of thermal and cold CO₂-rich springs, as well as soil diffuse degassing emissions (Allard et al., 1991; Chiodini et al., 1998). In the latter, the most studied gases released through volcanic soils are usually CO₂ and the radioactive gas radon (²²²Rn); in some cases the CO₂ diffusely emitted by the soils is of similar magnitude to the CO₂ released from fumaroles and crater plumes (e.g., Allard et al., 1991; Chiodini et al., 2010a; Viveiros et al., 2010; Pedone et al., 2015). Mantle-derived CO₂ can also be released away from active volcanoes through deep tectonic structures, as demonstrated by several studies (Chiodini et al., 1999, 2010b; Jung et al., 2014; Lee et al., 2016). In fact, in the last 30 years, CO₂ spatial distribution has been used worldwide to identify hidden tectonic structures, since faults/fractures act as preferential pathways (high permeability zones) for the escape of gases from the deep crust or mantle to the surface (Giammanco et al., 1999, 2006; Baubron et al., 2002; Hutchison et al., 2015; Liuzzo et al., 2015). Based on the release of soil gases in confined areas, Chiodini et al. (2001) named the anomalous CO₂ degassing areas, where hydrothermal/volcanic CO₂ is released, as diffuse degassing structures (DDS), whose shape depends on morphological, geological, and structural factors, such as the topography, existence of lithological heterogeneities, and presence of faults/fractures (Schöpa et al., 2011; Peltier et al., 2012; Pantaleo and Walter, 2014).

CO₂ has been widely used for volcanic monitoring due to its low solubility in silicate melts, being consequently one of the first gases released to the surface in case of replenishment of a magma chamber (e.g., Hernández et al., 2001; Carapezza et al., 2004; Giammanco et al., 2006; Aiuppa et al., 2010; Liuzzo et al., 2013; de Moor et al., 2016). Carbon dioxide is also an inert asphyxiant gas if present in high concentrations in the air, and above 10 vol.% can be lethal (Blong, 1984; Weinstein and Cook, 2005). Several hundreds of deaths have been reported in volcanic and non-volcanic environments due to deep-derived CO₂ emissions (Hansell and Oppenheimer, 2004) and high CO₂ concentrations have been reported in buildings located on CO₂ anomalous zones (Baxter et al., 1999; Viveiros et al., 2009, 2016a). This fact highlights the importance of identifying CO₂ anomalous areas by producing degassing maps, which should constitute valuable tools for land-use planners (Beaubien et al., 2003; Viveiros et al., 2009, 2010, 2015, 2016a). Building in high CO₂ degassing areas should be avoided, or, depending on the soil gas concentrations measured, buildings should follow few “gas-resistant” construction rules as the ones defined by Viveiros et al. (2016a).

Carbon dioxide is a colorless and odorless gas that is only detected with specific equipment. Several instruments have been developed in the last decades to detect this gas in soils

in volcanic/tectonic environments, even if the first studies started to be applied in agricultural fields to measure soil respiration rates (e.g., Kanemasu et al., 1974; Parkinson, 1981). Relatively short-time and low-cost methodologies using infrared CO₂ detectors have been implemented to measure soil CO₂ emissions since the end of the eighties, which include soil CO₂ concentration measurements (Giammanco et al., 1999, 2006; Evans and Staudacher, 2001) and soil CO₂ fluxes (dynamic concentration and accumulation chamber methods; Gurrieri and Valenza, 1988; Chiodini et al., 1998). Studies performed in diffuse degassing environments show that not only CO₂ is permanently emitted to the atmosphere from soils, but also significant variations in the amount of gases emitted are observed. Several spike-like and long term variations have been interpreted as resulting from meteorological influences and seasonal effects (Granieri et al., 2003; Viveiros et al., 2008, 2014; Rinaldi et al., 2012). Gases released from soils in hydrothermal-volcanic environments may also result from organic matter decomposition and fauna respiration, the so-called soil respiration (Luo and Zhou, 2006). Discrimination of the different CO₂ sources has been done through the use of statistical methodologies (Chiodini et al., 1998), as well as the carbon isotopic composition of the CO₂ released (e.g., Chiodini et al., 2008).

Soil CO₂ concentration surveys were performed at Faial, Pico, and São Jorge islands in the period between 2001 and 2004, and preliminary results are available in Master theses (Faria, 2002; Marcos, 2006). In 2011, sporadic soil CO₂ flux measurements were also performed in the islands of Faial and Pico, with the main scope of evaluating the stability of the previously recognized anomalous CO₂ degassing areas and select an area to install a permanent soil CO₂ flux station. This equipment is necessary to integrate with other seismo-volcanic monitoring techniques and to complement the gas geochemistry network already installed in the Azores archipelago (Viveiros et al., 2008). This study reviews the preexisting database on soil CO₂ concentration applying more recent statistical tools in order to (1) evaluate the existence of different sources for the CO₂ diffusely released from soils, (2) produce CO₂ degassing maps, (3) identify the main DDS, and (4) correlate the soil CO₂ emitted with the main volcano-tectonic structures identified in the islands.

GEOLOGICAL SETTING

The Azores archipelago is composed of nine volcanic islands located in the North Atlantic Ocean where the American, Eurasian and the Nubian plates meet at a triple junction (Searle, 1980). The main tectonic features are (1) the Mid-Atlantic Ridge (MAR) that crosses the archipelago between the islands of Flores and Faial, (2) the East Azores Fracture Zone (EAFZ), which extends E-W from the MAR to south of Santa Maria, and the Azores-Gibraltar Fault Zone that includes the E-W trending Gloria Fault, and (3) its western segment, the Terceira Rift (TR), which extends from the MAR to the island of Santa Maria along a general WNW-ESE direction, and corresponds to the present-day EU-NU plate boundary (e.g., Searle, 1980;

Madeira and Ribeiro, 1990; Vogt and Jung, 2004; Miranda et al., 2015; **Figure 1**). The main tectonic structures in the islands are normal dextral faults with a WNW-ESE trend, characteristic of the Terceira rift; the NNW-SSE conjugate fault system exhibits oblique normal left lateral displacement (Madeira and Brum da Silveira, 2003; Madeira et al., 2015). These main fault systems are also present in Faial, Pico, and São Jorge islands, with the dominant structures striking WNW-ESE and dipping 60–90° to the NNE or to the SSW controlling the general shape of some islands (Madeira and Brum da Silveira, 2003).

Most of the identified faults in the Azores archipelago are considered active (Madeira, 1998; Madeira and Brum da Silveira, 2003; Marques et al., 2013; Madeira et al., 2015) and the major faults usually have well-developed scarps; however the volcanic nature of the islands, together with differential erosion, can attenuate or amplify the tectonic slope (Madeira and Brum da Silveira, 2003) and even make the identification of tectonic structures difficult (due to scarp burial by pumice deposits, for instance). In addition, the

exuberant vegetation of some of the Azorean islands covers most of the geological structures. Tectonic structures used in the present study were mapped by Madeira and Brum da Silveira (2003) and Madeira et al. (2015) through fieldwork and vertical air-photo interpretation. All the faults in the study islands are considered active by Madeira and Brum da Silveira (2003) as they displace volcanic sequences younger than 100 ka.

The cause for the volcanism in the islands is highly debated in the literature and most studies suggest the presence of a mantle plume (e.g., Schilling, 1975; Cannat et al., 1999; Moreira et al., 1999; Jean-Baptiste et al., 2009), even if some studies argue that the addition of H₂O to the mantle together with a small temperature anomaly could be enough to induce melting (Bonatti, 1990; Asimow et al., 2004; Métrich et al., 2014).

The complex geodynamic setting of the Azores explains the frequent seismicity and volcanism in the islands. Since the settlement of the islands, in the fifteenth century, at least 28 volcanic eruptions and more than 15 major earthquakes caused

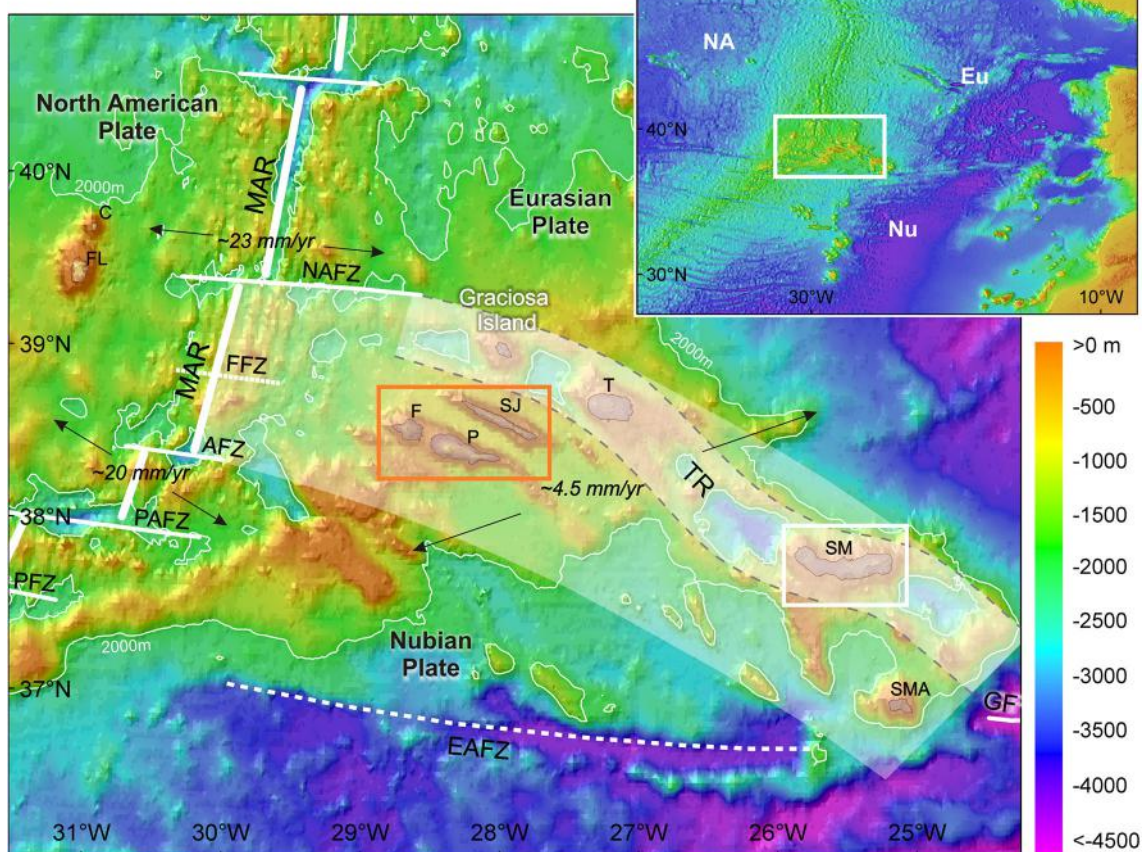


FIGURE 1 | Main morphotectonic features of the Azores region. White lines define approximately the morphological expression of each structure; white shaded area represents the sheared western segment of the Eu-Nu plate boundary, whereas the white shaded area limited by a dotted gray line represents its main structure, the Terceira Rift (TR). Tectonic structures: MAR, Mid-Atlantic Ridge; EAFZ, East Azores Fracture Zone; NAFZ, North Azores Fracture Zone; GF, Gloria Fault; FFZ, Faial Fracture Zone; AFZ, Açor Fracture Zone; PAFZ, Princesa Alice Fracture Zone; PFZ, Pico Fracture Zone. Islands: SMA, Santa Maria; SM, São Miguel; T, Terceira; SJ, São Jorge; P, Pico; F, Faial; FL, Flores; C, Corvo. Azores bathymetry adapted Lourenço et al. (1997); World topography and bathymetry from GEBCO_08 database (2010). Datum: WGS 1984 (in Hipólito et al., 2013); The red square shows the area that comprises the three studied islands.

a large number of casualties (>6,500 deaths; Gaspar et al., 2015 and references therein).

Present seismo-volcanic activity in the archipelago is characterized by almost daily record of seismic events (Gaspar et al., 2015 and references therein) and the presence of secondary manifestations of volcanism in most islands. These manifestations include hydrothermal fumaroles, cold CO₂-rich, and thermal springs, as well as soil diffuse degassing areas (Ferreira et al., 2005; Cruz et al., 2010; Viveiros et al., 2010; Caliro et al., 2015; Silva et al., 2015). Fumarolic emissions are found at Faial and Pico islands, respectively, at the remnant of the 1957–58 eruption (Capelinhos) and at the summit of Pico Volcano. São Jorge manifestations are characterized only by the presence of cold CO₂-rich springs, which are also found out at Pico and Faial (Ferreira et al., 2005).

Faial Island

Tectonic Structures and Seismicity

The eastern part of Faial Island is dominated by a WNW-ESE trending graben structure (named Pedro Miguel Graben), which is formed by seven normal dextral faults (Madeira and Brum da Silveira, 2003; **Figure 2**). Pedro Miguel graben formed as a result of the activity of transtensive dextral faults with an extension rate between ~ 3.4 and ~ 8.2 mm/y was proposed by Trippanera et al. (2014). Other important WNW-ESE tectonic structures are located south of the summit caldera and in the western part of the island (**Figure 2**). The conjugate normal left lateral faults system (trending NNW-SSE to NW-SE) shows less developed geomorphic expression (Madeira and Brum da Silveira, 2003).

In the last century Faial Island was affected by four important seismic events in 1926, 1958, 1973, and 1998, with intensities equal or higher than VII (Mercalli Modified Scale). The last destructive earthquake that caused nine casualties occurred offshore in 1998, and had a magnitude of (M_L) 5.8 (Dias et al., 2007; Matias et al., 2007).

Volcanism

Faial Island is composed by four main volcanic systems: the Ribeirinha (848 to 358 ka) and Caldeira (>440 ka) central volcanoes and two basaltic fissure systems (Horta Platform and Capelo Peninsula fissure systems; Chovelon, 1982; Demande et al., 1982; Serralheiro et al., 1989; Pacheco, 2001, 2015; Hildenbrand et al., 2012). Ribeirinha Volcano, located on the northeast sector of the island, is the oldest system and extensively dissected by the Pedro Miguel Graben (Pacheco, 2015). Caldeira Volcano dominates the morphology of the island as the summit is truncated by a 2 km wide, 400 m deep caldera (Madeira and Brum da Silveira, 2003). Hildenbrand et al. (2012) proposed a much younger age (about 120 ka ago) for the beginning of the subaerial shield-building phase of this volcanic system, when compared with the previous studies (Féraud et al., 1980). In what concerns the fissural systems, Horta Platform system should be active since at least 11 ka BP and its more recent activity is older than 6 ka BP (Serralheiro et al., 1989; Pacheco, 2015); Capelo Peninsula fissure system is the youngest volcanic system on the Island and the activity may have started between 8 and 6 ka BP (Madeira, 1998; Di Chiara et al., 2014).

Seismic tomography performed at Faial Island suggests the existence of a low P velocity between 3 and 7 km depth beneath

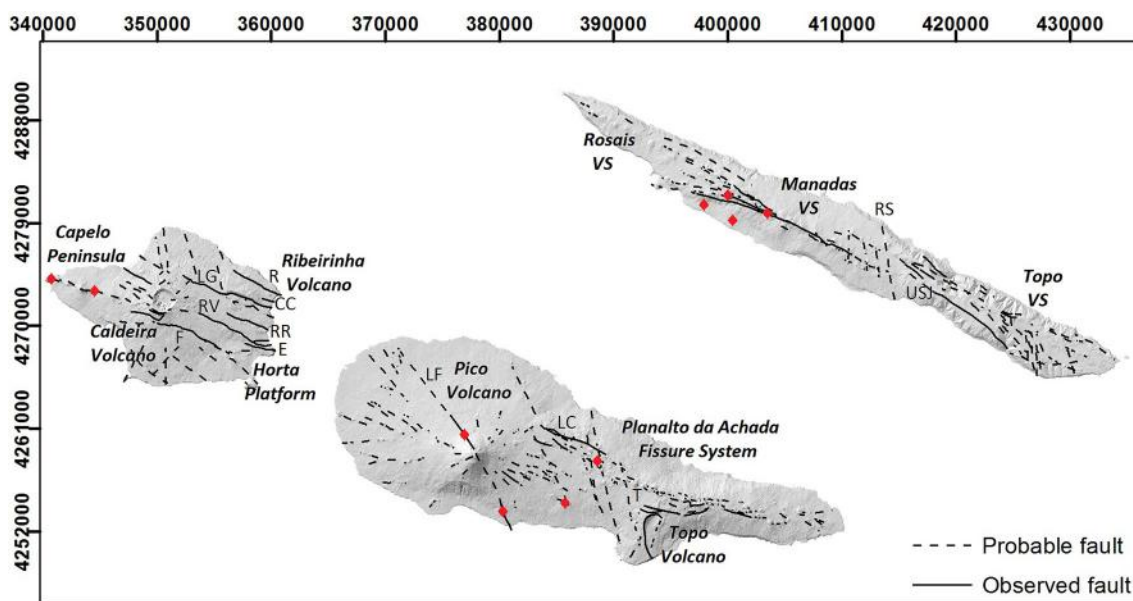


FIGURE 2 | Faial, Pico, and São Jorge digital elevation models with the identification of the volcanic systems and the main tectonic structures. Legend of the tectonic structures: Faial Island: LG, Lomba Grande; R, Ribeirinha; CC, Chã da Cruz; RR, Ribeira do Rato; RV, Rocha Vermelha; E, Espalamaca; F, Flamengos; Pico Island: LF, Lomba de Fogo-S. João; LC, Lagoa do Capitão; T, Topo; São Jorge Island: RS, Ribeira Seca; USJ, Urze-São João. VS, Volcanic System. The red diamonds represent the approximate locations of the onshore historical volcanic centers (tectonic structures modified from Madeira and Brum da Silveira, 2003).

Caldeira Volcano, which was interpreted by Dias et al. (2007) as a possible magma chamber. Zanon and Frezzotti (2013) studied CO₂-rich fluid inclusions at Faial and Pico islands and estimated different depths for magma ponding sites, which varied from 5.6 to 21.2 km. The intra-crustal ponding system of small size was proposed to be located beneath the Caldeira Volcano, in agreement with the depths obtained by the tomography studies.

Two volcanic eruptions affected the island since the settlement and both occurred in the eastern part of the island, in the Capelo Peninsula volcanic system (1672/73 and 1957/58). During this last eruptive episode, a phreatic explosion also occurred inside the caldera of the Caldeira Volcano and the fumarolic emissions associated to this event persisted from May to October 1958 (Machado et al., 1962; Madeira, 1998; Pacheco, 2001). At least three deaths were attributed to the 1672–73 volcanic eruption (Weston, 1964; Pacheco, 2001).

Nowadays, the only visible secondary manifestations of volcanism in Faial correspond to residual steam emissions from the Capelinhos eruption (1957–58) (Ferreira, 1994; Gaspar and Ferreira, 1995). Maximum temperatures of 91°C were measured in 1993, and the gases identified were CO₂, N₂, O₂, Ar, and H₂ (**Table 1**). In what concerns the origin of the volatiles, Jean-Baptiste et al. (2009) measured a value of 8.53 Ra for the ³He/⁴He on Faial water samples, which are typical MORB values and similar to the He isotopic composition measured on Faial volcanic rocks (Moreira et al., 1999).

Pico Island

Tectonic Structures and Seismicity

Several authors consider that Faial and Pico are the emerged parts of a single main volcanic ridge, the Pico–Faial ridge (Hildenbrand et al., 2012 and references therein; Quartau et al., 2015). In the present study we will analyze the degassing patterns associated to each island individually.

The main tectonic structures of Pico Island trend WNW–ESE, similarly to what is observed in Faial Island. The main structures are Lagoa do Capitão and Topo faults that progressively merge to the east and both define a graben structure, smaller than Pedro Miguel graben in Faial Island. Several other WNW–ESE and conjugated NNW–SSE faults are defined by volcanic alignments (Madeira, 1998; Nunes, 1999; Madeira and Brum da Silveira, 2003; **Figure 2**). The larger cones and Pico Volcano are located in the intersection of WNW–ESE with NNW–SSE conjugate faults (Madeira and Brum da Silveira, 2003).

A magnitude VII earthquake (EMS-98, Silva, 2005) that occurred in 1973 was the strongest earthquake with epicenter in Pico Island. However, and due to the proximity of the studied islands, strong earthquakes that occurred in Faial, São Jorge, and in the surrounding offshore areas also caused damage at Pico. This is the case of the 1757 earthquake that had epicenter close to São Jorge Island and severely damaged Pico causing 11 casualties. Damage on Pico was also reported associated with the seismic events of 1926 and 1998 that mostly affected Faial Island, and the 1980 Terceira earthquake (Silva, 2005; Gaspar et al., 2015 and references therein).

Volcanism

Pico is the youngest island of the archipelago and is formed by three volcanic systems: the Topo Volcano (186 ± 5 ka), the Planalto da Achada fissure system (270 ± 150 ka to <25 ka), and the Pico central volcano (Féraud et al., 1980; Chovelon, 1982; Madeira, 1998; Nunes, 1999; Costa et al., 2015). The older Topo Volcano is partially dismantled by landslides, displaced by faults and partially covered by more recent volcanic products (Madeira, 1998; Costa et al., 2015).

Three historic volcanic eruptions affected the island (1562–64; 1718 and 1720), and two deaths are reported for the 1718 eruption. Both 1562–64 and 1720 volcanic eruptions were associated with the Pico Island fissural system (Achada Plateau); the 1718 activity occurred at the Pico Volcano. In 1963 a submarine eruption was reported offshore the NW coast of Pico Island (Madeira, 1998; Nunes, 1999; Gaspar et al., 2015 and references therein).

Fumarolic emissions at Pico Island are located on the summit of the 2,351 m-tall Pico Volcano and a survey performed in 1994 showed that the dry gas is composed of CO₂, O₂, Ar, and N₂ (**Table 1**; Nunes, 1999). MORB-type values for the ³He/⁴He ratio (8.5 Ra) were measured by Jean-Baptiste et al. (2009) in a water well, a slightly lower value from the He isotopic composition measured in olivine crystals by Métrich et al. (2014), which varied between 10.2 and 11.1 ± 0.1 Ra.

São Jorge Island

Tectonic Structures and Seismicity

The main tectonic structures defined for São Jorge are parallel to the WNW–ESE elongation of the island (**Figure 2**). The younger western half of São Jorge is dominated by the Picos and Pico do Carvão fault zones, which are marked by alignments of cones, craters, scoria ramparts, and short fault scarps (Madeira, 1998;

TABLE 1 | Gas composition (molar%) of the fumarolic emissions from Faial and Pico islands.

Island	Sampling period	Temp. (°C)	Gas composition (molar%)							References
			CO ₂	H ₂ S	O ₂	Ar	N ₂	CH ₄	He	
Pico	Jun-16	77.0	40.45	0.00	12.96	0.54	46.05	0.00	0.00	This study
	1994	76.1	40.50	0.00	11.84	0.55	47.11	0.00	n.d.	0.00
Faial	Mar-93	91.0	1.31 × 10 ⁻²	n.d.	9.1*		90.9	n.d.	n.d.	6 × 10 ⁻⁵
*Represents the sum of the O ₂ and Ar due to limitations of the analytical procedures.										

a large number of casualties (>6,500 deaths; Gaspar et al., 2015 and references therein).

Present seismo-volcanic activity in the archipelago is characterized by almost daily record of seismic events (Gaspar et al., 2015 and references therein) and the presence of secondary manifestations of volcanism in most islands. These manifestations include hydrothermal fumaroles, cold CO₂-rich, and thermal springs, as well as soil diffuse degassing areas (Ferreira et al., 2005; Cruz et al., 2010; Viveiros et al., 2010; Caliro et al., 2015; Silva et al., 2015). Fumarolic emissions are found at Faial and Pico islands, respectively, at the remnant of the 1957–58 eruption (Capelinhos) and at the summit of Pico Volcano. São Jorge manifestations are characterized only by the presence of cold CO₂-rich springs, which are also found out at Pico and Faial (Ferreira et al., 2005).

Faial Island

Tectonic Structures and Seismicity

The eastern part of Faial Island is dominated by a WNW-ESE trending graben structure (named Pedro Miguel Graben), which is formed by seven normal dextral faults (Madeira and Brum da Silveira, 2003; **Figure 2**). Pedro Miguel graben formed as a result of the activity of transtensive dextral faults with an extension rate between ~ 3.4 and ~ 8.2 mm/y was proposed by Tripanera et al. (2014). Other important WNW-ESE tectonic structures are located south of the summit caldera and in the western part of the island (**Figure 2**). The conjugate normal left lateral faults system (trending NNW-SSE to NW-SE) shows less developed geomorphic expression (Madeira and Brum da Silveira, 2003).

In the last century Faial Island was affected by four important seismic events in 1926, 1958, 1973, and 1998, with intensities equal or higher than VII (Mercalli Modified Scale). The last destructive earthquake that caused nine casualties occurred offshore in 1998, and had a magnitude of (M_L) 5.8 (Dias et al., 2007; Matias et al., 2007).

Volcanism

Faial Island is composed by four main volcanic systems: the Ribeirinha (848 to 358 ka) and Caldeira (>440 ka) central volcanoes and two basaltic fissure systems (Horta Platform and Capelo Peninsula fissure systems; Chovelon, 1982; Demande et al., 1982; Serralheiro et al., 1989; Pacheco, 2001, 2015; Hildenbrand et al., 2012). Ribeirinha Volcano, located on the northeast sector of the island, is the oldest system and extensively dissected by the Pedro Miguel Graben (Pacheco, 2015). Caldeira Volcano dominates the morphology of the island as the summit is truncated by a 2 km wide, 400 m deep caldera (Madeira and Brum da Silveira, 2003). Hildenbrand et al. (2012) proposed a much younger age (about 120 ka ago) for the beginning of the subaerial shield-building phase of this volcanic system, when compared with the previous studies (Féraud et al., 1980). In what concerns the fissural systems, Horta Platform system should be active since at least 11 ka BP and its more recent activity is older than 6 ka BP (Serralheiro et al., 1989; Pacheco, 2015); Capelo Peninsula fissure system is the youngest volcanic system on the Island and the activity may have started between 8 and 6 ka BP (Madeira, 1998; Di Chiara et al., 2014).

Seismic tomography performed at Faial Island suggests the existence of a low P velocity between 3 and 7 km depth beneath

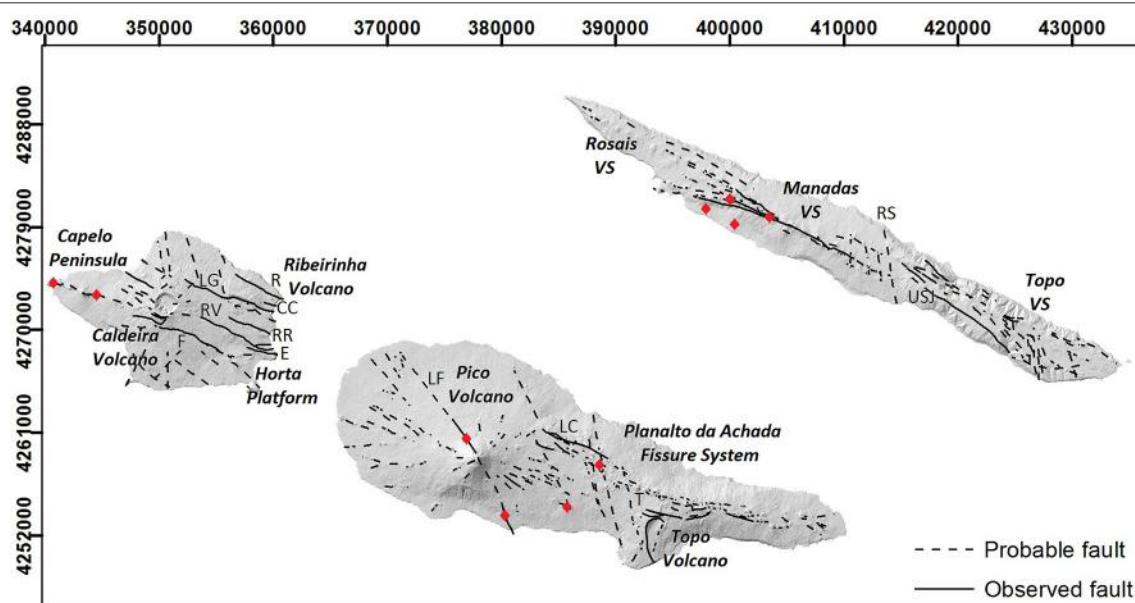


FIGURE 2 | Faial, Pico, and São Jorge digital elevation models with the identification of the volcanic systems and the main tectonic structures. Legend of the tectonic structures: Faial Island: LG, Lomba Grande; R, Ribeirinha; CC, Chá da Cruz; RR, Ribeira do Rato; RV, Rocha Vermelha; E, Espalamaca; F, Flamengos; Pico Island: LF, Lomba de Fogo-S. João; LC, Lagoa do Capitão; T, Topo; São Jorge Island: RS, Ribeira Seca; USJ, Urze-São João. VS, Volcanic System. The red diamonds represent the approximate locations of the onshore historical volcanic centers (tectonic structures modified from Madeira and Brum da Silveira, 2003).

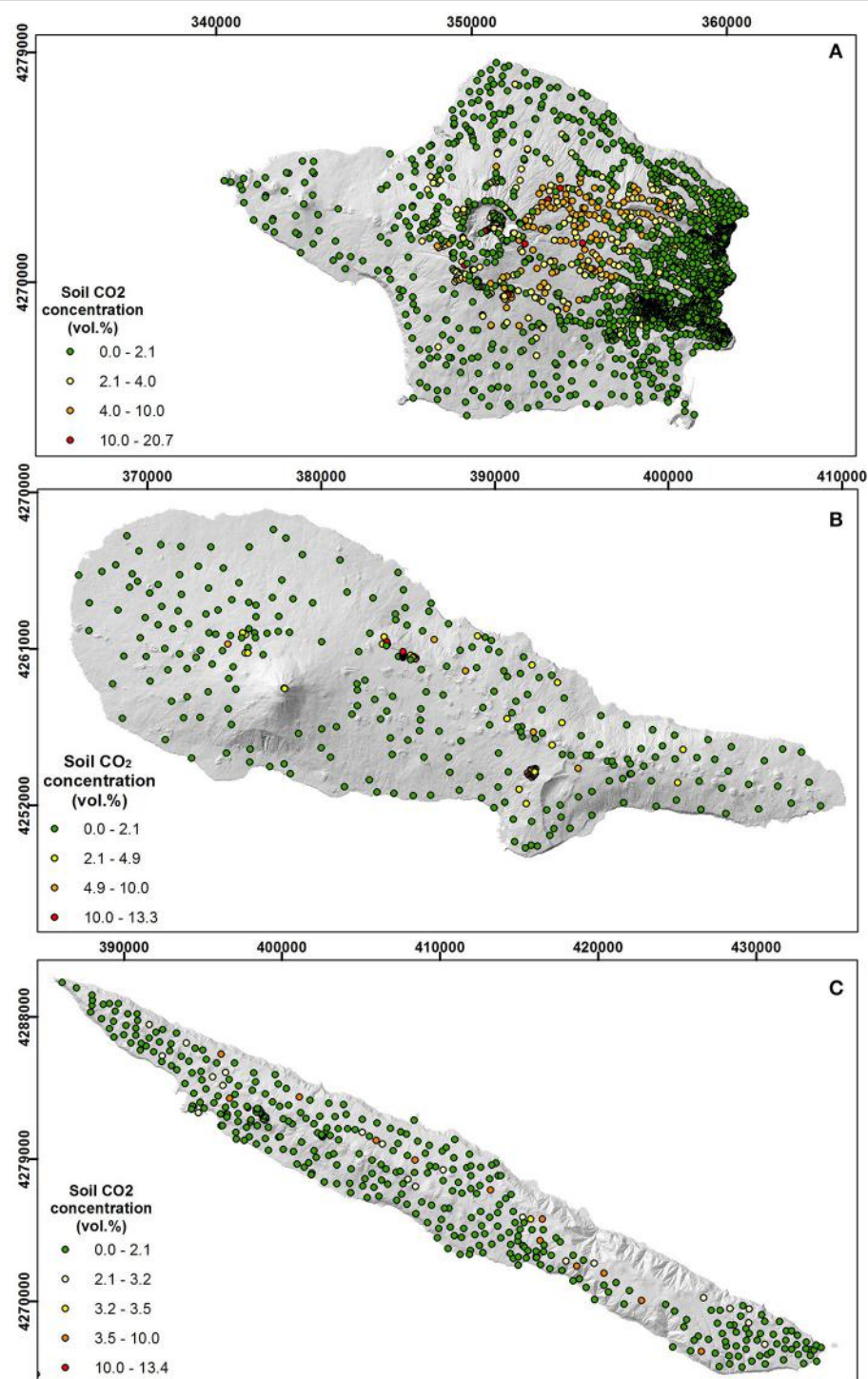


FIGURE 3 | Sampling location and soil CO₂ concentration distribution maps for the studied islands: **(A)** Faial, **(B)** Pico, and **(C)** São Jorge islands.

statistical data distribution, which results from overlapping lognormal populations, into individual populations. The mean, the standard deviation and the proportion of each partitioned lognormal population are then graphically estimated by applying the procedure proposed by Sinclair (1974). The validity of

the model and of the estimated statistical parameters of the populations is assessed by comparing, on a probability plot, the distribution resulting from the combination of the theoretical populations with the distribution of the data. Since the computed statistical parameters refer to the logarithm of the values,

the mean CO₂ flux and the 90% confidence interval of the mean are then computed with the Sichel's t-estimator (David, 1977).

TABLE 2 | Descriptive statistics of the soil CO₂ concentration/flux data.

Variables	Statistics	Faial Island	Pico Island	São Jorge Island
Soil CO ₂ concentration	Minimum (vol.%)	0.0	0.0	0.0
	Average (vol.%)	1.3	1.5	0.9
	Maximum (vol.%)	20.7	13.3	13.4
	Standard deviation (vol.%)	1.7	2.4	1.4
	Number of points	2,157	316	382
Soil CO ₂ flux	Minimum (g m ⁻² d ⁻¹)	0	0	–
	Average (g m ⁻² d ⁻¹)	170	22	–
	Maximum (g m ⁻² d ⁻¹)	339	40	–
	Standard deviation (g m ⁻² d ⁻¹)	38	9	–
	Number of points	107	93	–

The 95th percentile of the lowest values population, which usually represents the biological CO₂, is used as cutt-off for the biological (background) CO₂ fluxes. A similar criteria was used in previous studies (e.g., Chiodini et al., 1998; Cardellini et al., 2003; Viveiros et al., 2010).

Interpolated maps

Final CO₂ degassing maps have been elaborated based on the sequential Gaussian simulations (sGs) methodology (Deutsch and Journel, 1998; Cardellini et al., 2003), which consists on the production of numerous simulations of the spatial distribution of the attribute (the soil CO₂ concentration, in this study). Stochastic simulation produces realizations that respect the original data (e.g., histograms, variograms) without smoothing the extreme values. A simulated value at one location is randomly selected from the normal distribution function defined by the kriging mean and variance based on the neighborhood values. The simulation is conditional and sequential, meaning that the simulated value at the new randomly visited point is dependent upon both the original data and the previously simulated values (Deutsch and Journel, 1998; Goovaerts, 1999). The process is

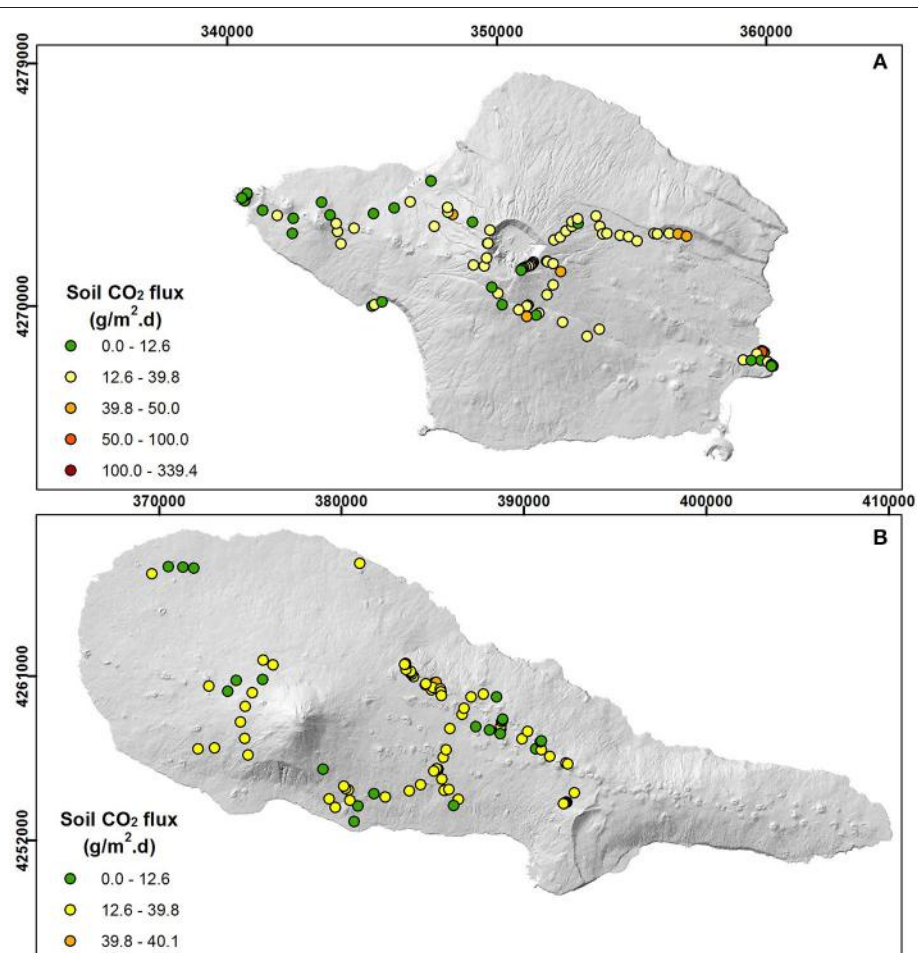


FIGURE 4 | Sampling location and soil CO₂ flux distribution maps for Faial (A) and Pico (B) islands.

repeated until all points are simulated. Considering that the sGs procedure requires a Gaussian distribution, and considering that original data do not follow the normal distribution, a normal scores transformation of the data was applied. Omnidirectional variograms (Figure 5) were also computed in order to fit the best parameters that adjust to the spatial distribution of the surveyed values (Isaaks and Srivastava, 1989), and use them in the sGs interpolation. One hundred realizations were performed per each map and results were displayed as E-type maps that show the “expected” value at any location, obtained through a point-wise linear average of all the simulations (Cardellini et al., 2003).

Fumarolic Emissions

Sampling Methodology

Gases released at Pico Volcano fumaroles were collected in June 2016 using the methodology defined by Giggenbach (1975) and Giggenbach and Goguel (1989), which consists on the use of evacuated flasks that contain a 4 N NaOH solution. A tube was

directly inserted in the main fumarolic vent and the gas guided through a silicon tube to the flask.

Analytical Procedures

The analysis of the chemical composition of the gases was carried out at the gas geochemistry laboratories of the University of the Azores, using gas chromatography and titration techniques. Gases in the headspace of the bottle (CH₄, N₂, O₂, Ar, He, and H₂) were analyzed with a Perkin Elmer Clarus 580 gas chromatograph. This chromatograph has two channels equipped with two Thermal Conductivity Detectors and both a MS 5A plot column and a MS packed column that allow using He and Ar as carrier gases to separately quantify Ar and O₂. Gases dissolved in the alkaline suspension were quantified by titration: the CO₂ was detected by potentiometric titration with an automatic titrator from Radiometer Copenhagen, model VIT90 Video Titrator and the H₂S quantified by colorimetric titration with mercury acetate using dithizone for end point detection.

RESULTS

Descriptive Statistics

Soil CO₂ concentration ranged between 0 and 20.7 vol.%, with the maximum values recorded at Faial Island (Table 2). Higher soil CO₂ fluxes were also measured at Faial Island (339 g m⁻² d⁻¹). Maximum soil CO₂ concentrations in Pico and São Jorge were lower (~13 vol.%; Figure 3).

Soil temperatures measured in the Pico and Faial fumaroles and in the surrounding areas are presented in Table 3 and maximum values were similar, i.e., 74.2 and 79.8°C, for Pico and Faial degassing areas, respectively. Higher temperatures were measured in the fumarolic/steam vents (Table 1).

Gas composition of the Pico fumarole, sampled in June 2016, is showed in Table 1. These emissions release essentially water vapor (~0.49 for the ratio dry gases/H₂O), N₂, CO₂, O₂, and Ar. The other elements, characteristic of hydrothermal fumaroles (CH₄, He, H₂, and H₂S), were not detected.

CO₂ Degassing Maps

Omnidirectional variograms of the soil CO₂ concentration data were computed and modeled for each dataset (Figure 5). Degassing maps of the CO₂ concentrations resulting from the sequential Gaussian simulation procedure for the sampled datasets are shown in Figures 6–8. The scarce data for the soil

TABLE 3 | Soil temperature measured in the fumarolic areas of Pico and Faial islands.

Island	UTM M	UTM P	Soil temperature (°C)	Average	Sampling period
Faial	340730	4274107	64.3	59.0	02/08/2011
	340730	4274110	66.8		02/08/2011
	340734	4274152	79.8		02/08/2011
	340732	4274153	77.5		02/08/2011
	340736	4274164	48.6		02/08/2011
	340733	4274173	50.4		02/08/2011
	340736	4274186	49.1		02/08/2011
	340539	4274004	35.2		02/08/2011
Pico	377894	4258704	48.6	52.5	01/07/2003
	377896	4258714	50.4		01/07/2003
	377890	4258727	54.5		01/07/2003
	377897	4258733	74.2		01/07/2003
	377892	4258739	57.9		01/07/2003
	377883	4258738	52.1		01/07/2003
	377891	4258705	36.8		01/07/2003
	377889	4258706	51.9		01/07/2003
	377893	4258714	46.0		01/07/2003

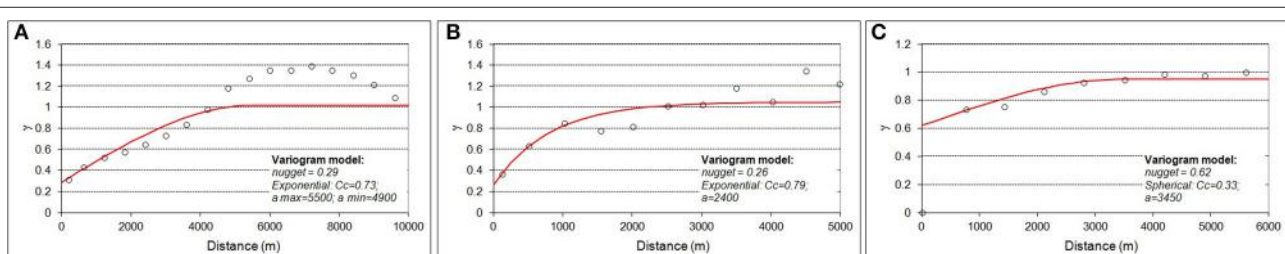


FIGURE 5 | Omnidirectional variograms of the soil CO₂ concentration data for Faial (A), Pico (B), and São Jorge (C). Cc: Partial sill; a: range (in m).

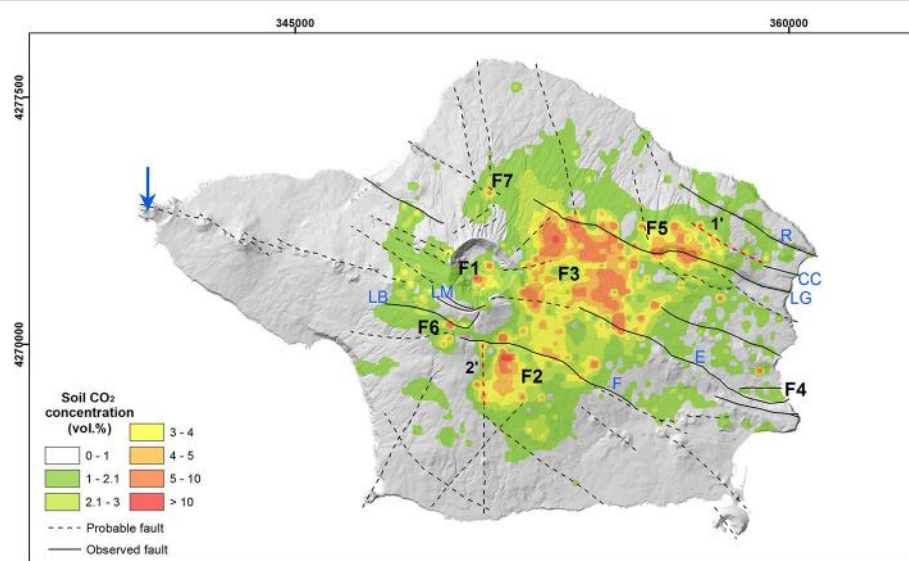


FIGURE 6 | E-type soil CO₂ concentration map for Faial Island (cell size = 50 × 50 m; interpolation method: sGs). Numbers F1–F7 represent the DDS identified at Faial Island, which correspond to areas where CO₂ is fed by hydrothermal sources (highlighted as orange and red—soil CO₂ concentration >4 vol.%) (UTM(m)-WGS84, zone 26S). The blue arrow points to the location of the Capelinhos fumarolic field and red dotted lines represent degassing lineaments. Blue letters represent tectonic structures mentioned in the text: LB, Lomba de Baixo; LM, Lomba do Meio; F, Flamengos; E, Espalamaca; LG, Lomba Grande; CC, Chã da Cruz; R, Ribeirinha.

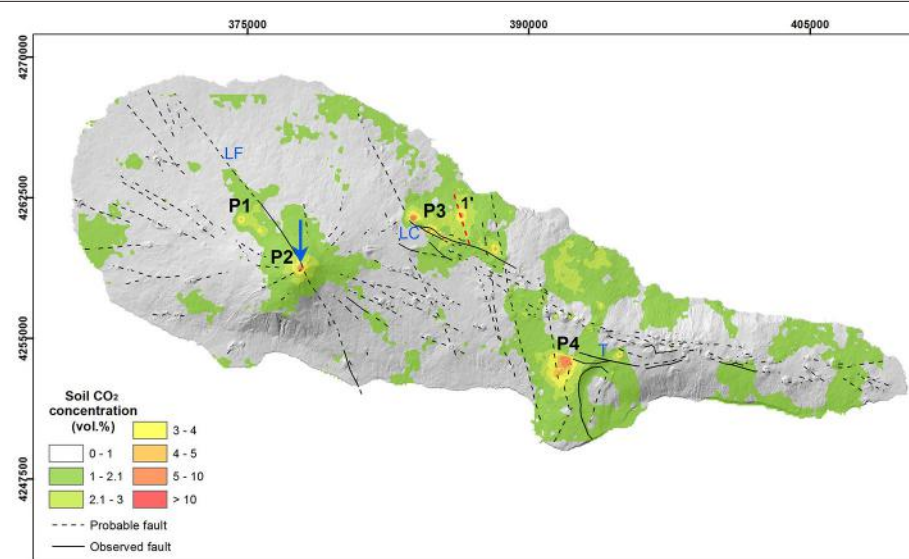


FIGURE 7 | E-type soil CO₂ concentration map for Pico Island (cell size = 50 × 50 m; interpolation method: sGs). Numbers P1–P4 represent the DDS identified at Pico Island (highlighted as orange and red colors) (UTM(m)-WGS84, zone 26S). The blue arrow represents the location of the Pico fumarolic field and red dotted line represents a degassing lineament. Blue letters represent tectonic structures mentioned in the text: LF, Lomba de Fogo-S. João; LC, Lagoa do Capitão; T, Topo.

CO₂ flux values do not allow the elaboration of an interpolated map, and for this reason only the distribution of the sampled points is showed (Figure 4).

CO₂ Populations

Logarithmic probability plots of the soil CO₂ flux/concentrations are presented in Figures 9, 10. Soil CO₂ concentration shows

bimodal populations for the data measured in the three islands, suggesting the presence of different CO₂ sources (biogenic and volcanic-hydrothermal). In what concerns the soil CO₂ flux data, polymodal distribution of the Faial Island data represents the overlapping of three log-normal populations (Figure 10).

Statistical parameters from the partitioned CO₂ populations and the 90% confidence intervals of the mean for the different



FIGURE 8 | E-type soil CO₂ concentration map for São Jorge Island (cell size = 50 × 50 m; interpolation method: sGs). Numbers SJ1–SJ4 represent the DDS identified at São Jorge Island (highlighted as orange and red colors) (UTM(m)-WGS84, zone 26S). The red dotted line represents a degassing lineament. Blue letters represent tectonic structures mentioned in the text: PC, Pico do Carvão; RS, Ribeira Seca; USJ, Urze-S. João.

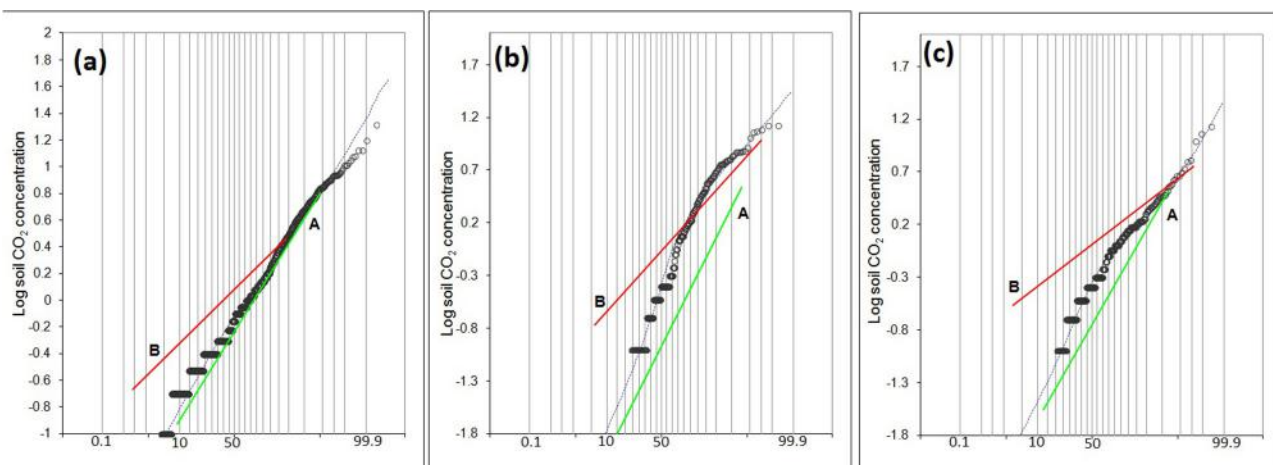


FIGURE 9 | Probability plots of soil CO₂ concentrations measured at Faial **(A)**, Pico **(B)**, and São Jorge **(C)** islands. Green and red lines represent populations A and B, respectively.

study sites are presented in **Table 4**. Populations named “A” are characterized by very low soil CO₂ flux/concentration values. Population “C” is identified only for the case of Faial Island soil CO₂ flux data.

DISCUSSION

Visible secondary manifestations of volcanism were previously recognized in the islands of Faial, Pico, and São Jorge (Ferreira et al., 2005; Cruz et al., 2010). The present study highlights the additional presence of soil CO₂ diffuse degassing areas, most of them associated to faults crossing the study sites. The maximum soil CO₂ concentration (20.7 vol.%) and flux (339 g m⁻² d⁻¹)

values were measured at Faial Island, in the Praia do Almoxarife area and are associated to the Espalamaca fault (DDS F4 in **Figure 6**). These measured soil CO₂ concentration values are comparable with the concentrations recorded at Mosteiros and Ribeira Seca villages (São Miguel Island), but significantly lower than at Furnas Volcano, where values as high as 100 vol.% were measured (Viveiros et al., 2015). The maximum soil CO₂ concentration values at Pico and São Jorge islands were similar (~13 vol.%), but lower than those recorded at Faial Island.

The measured ranges of CO₂ suggest different origins for the gases released from soils. Statistical methodologies applied to the recorded data showed different populations both for the CO₂ concentrations and fluxes, suggesting biogenic and

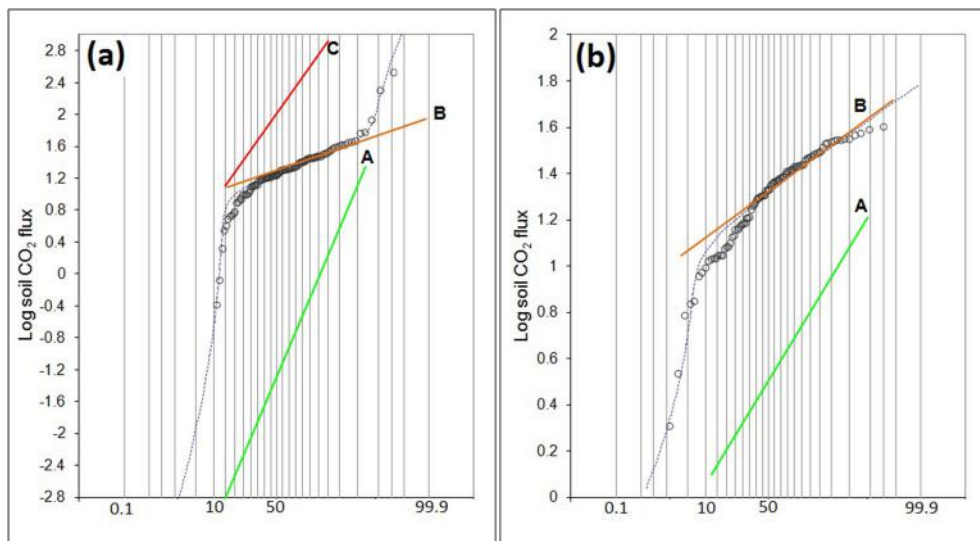


FIGURE 10 | Probability plots of soil CO₂ fluxes measured at Faial **(A)** and Pico **(B)** islands. Green, orange and red lines represent populations A, B, and C, respectively.

TABLE 4 | Statistical parameters from the partitioned CO₂ concentration/flux populations and the 90% confidence intervals of the mean.

Island	Variable	Population	CO ₂ source	Proportion of each population (%)	Mean CO ₂	Mean CO ₂ 90% confidence interval
Faial	CO ₂ flux (g m ⁻² d ⁻¹)	A	Mainly biogenic	15	0.6	–
		B	Biogenic + hydrothermal	81	22.2	20.44–24.51
		C	Hydrothermal	4	537.5	159–421,776
	CO ₂ concentration (vol.%)	A	Mainly biogenic	75	1.2	1.1–1.3
		B	Biogenic + hydrothermal	25	1.5	1.4–1.7
Pico	CO ₂ flux (g m ⁻² d ⁻¹)	A	Mainly biogenic	7	4.3	2.50–16.45
		B	Biogenic + hydrothermal	93	22.7	21.36–24.40
	CO ₂ concentration (vol.%)	A	Mainly biogenic	65	0.6	0.3–2.8
		B	Biogenic + hydrothermal	35	3.2	2.8–3.8
São Jorge	CO ₂ concentration (vol.%)	A	Mainly biogenic	65	0.7	0.5–1.1
		B	Biogenic + hydrothermal	35	1.3	1.2–1.5

volcanic-hydrothermal sources. Discrimination of these sources is particularly relevant in the Azores archipelago due to the abundant vegetation that covers the volcanic soils. Lowest CO₂ values (population “A,” **Table 4**) probably correspond to areas where biologic processes are responsible for the gas released from soils. Values very close to zero, or even zero, should represent areas where even the biologic production is scarce. Population “C,” only present in the soil CO₂ flux dataset of Faial Island, is representative of CO₂ fed by an endogenous source (volcanic-hydrothermal origin). Data associated with population “B” probably represent the mixture of biogenic and hydrothermal CO₂ contributions. Most of the measured soil CO₂ concentration data fall within populations “A” (65–75% of the data), corresponding to biogenic contribution for the emitted CO₂ (**Table 4**). In what concerns the soil CO₂ flux determinations, most of the data are interpreted as a mixture

of biogenic and hydrothermal/volcanic contributions. The high percentage of CO₂ flux data in population “B” is probably explained by the fact that the flux surveys were carried out in the areas where anomalous CO₂ values were previously detected and mostly related with the presence of faults. The main objective of the 2011 campaigns was to select an area to install permanent soil CO₂ flux stations in the islands of Pico and Faial.

The cut-off value defined for each dataset according to the criteria suggested by Sinclair (1974), i.e., the 95th percentile of a determined population, allows to establish thresholds to discriminate the biogenic contribution from a deep source (**Table 5**). The 95th percentile for population “B” is selected in this study to define the DDS (Chiodini et al., 2001). For the particular case of Faial Island, the 95th percentile of populations “A” and “B” (soil CO₂ concentrations) is similar. In what concerns the limits defined for the soil CO₂ fluxes, the thresholds

TABLE 5 | Values for the biogenic and DDS thresholds following the criteria of Sinclair (1974).

Variables	Statistics	Faial Island	Pico Island	São Jorge Island
Soil CO ₂ concentration (vol.%)	95th percentile (population A)	4.0	2.1	3.2
	95th percentile (population B) (DDS threshold)	4.0	4.9	3.5
Soil CO ₂ flux (g m ⁻² d ⁻¹)	95th percentile (population A)	12.6	12.6	–
	95th percentile (population B) (DDS threshold)	39.8	39.8	–

are the same for Pico and Faial islands (12.6 g m⁻² d⁻¹ for the biogenic contribution and 39.8 g m⁻² d⁻¹ for the definition of DDS). Scales of the distribution maps presented in **Figures 3, 4** were defined according to these limits. The final DDS proposed in the present study resulted from the integration of soil CO₂ flux and concentration values.

The thresholds proposed here are similar to data available in the literature. For instance, available data on CO₂ production from a wide variety of ecosystems show CO₂ fluxes ranging from ~0.5 to ~19 g m⁻² d⁻¹ (e.g., Raich and Schlesinger, 1992; Raich and Tufekcioglu, 2000) with maximum flux values attributed to grassland (~50 g m⁻² d⁻¹; e.g., Norman et al., 1992; Bajracharya et al., 2000; Nakadai et al., 2002). The biogenic threshold for the soil CO₂ fluxes at Faial and Pico islands is thus within the values published for other areas. At Furnas Volcano (S. Miguel Island) a value of 25 g m⁻² d⁻¹ was selected as the limit, which integrated both statistical methodologies and carbon isotopic data (Viveiros et al., 2010). The threshold defined for the DDS at Furnas Volcano was 50 g m⁻² d⁻¹, not far from the value suggested in this study (39.8 g m⁻² d⁻¹). The CO₂ sources should be better constrained by the $\delta^{13}\text{C}_{\text{CO}_2}$ data, which is not available for this study. For this reason, the evaluation of different feeding sources was only based on the cumulative probability plots.

The CO₂ degassing map for Faial Island shows an absence of CO₂ emission in the youngest part of the island (Capelo Volcanic Complex), including the areas where the recent volcanic eruptions occurred (**Figures 2, 6**). Even in areas where thermal anomalous values were measured, which are associated to the only fumarolic (steam) field in Faial, in Capelinhos Volcano, no soil CO₂ degassing (both concentration and flux) was detected. In the fumarolic field the maximum temperature measured was 91°C and the main gases released are the atmospheric constituents (N₂, O₂, and Ar), with minor amounts of CO₂ and H₂. These emissions are probably due to some remnant heat from the 1957–58 volcanic eruption that still heats some water and air in the system. Higher soil CO₂ concentrations were measured in the floor of the summit caldera (Caldeira Volcano; DDS F1, **Figure 6**), where a phreatic eruption occurred during the Capelinhos 1957–58 volcanic eruption, however no thermal anomaly was identified in the area.

Two main fault systems trending WNW-ESE and NNW-SSE were recognized in the study islands by previous works (Madeira and Brum da Silveira, 2003; Madeira et al., 2015), and most of the DDS identified in this study occur associated with the previously mapped tectonic structures. A clear correlation between distribution of the CO₂ degassing anomalies and one of the main trending pattern is not observed; instead, and similarly to the observed for volcanism that is tectonically controlled (Madeira et al., 2015 and references therein), the main degassing anomalies seem to be found out in the intersection of different fault systems.

Based on soil CO₂ concentrations coupled with the soil CO₂ flux values, seven DDS were then identified in the Faial island (**Figure 6**). Main CO₂ anomalies are located in the eastern side of the island, essentially delimited by the Pedro Miguel graben structure that affects products from the Ribeirinha and Caldeira central volcanoes. The large DDS F3, which comprises more than half of the graben floor, lays between the important WNW-ESE tectonic structures that define the Pedro Miguel graben: between the Lomba Grande Fault (LG, **Figure 2**) that dips to the south and the north-dipping Espalamaca and Flamengos faults that define the southern part of the graben structure. The presence of deeply-derived CO₂ in the Pedro Miguel graben suggests that the graben faults correspond to deep structures that link the surface to deep areas where CO₂ is trapped and then channeled to the surface. DDS F5 probably results from the intersection of the graben faults with the mapped NNW-SSE structure identified in the area. In addition, this DDS contributes to define a degassing lineament (1', **Figure 6**) that can be the prolongation of the Chã da Cruz Fault.

The graben faults do not constitute barriers to the gas traveling to the surface since diffuse degassing structures are not limited to the graben floor and, for instance, DDS F2 is identified in the upthrown block of the Flamengos Fault. Two degassing lineaments are also associated with this DDS, which argue to confirm the presence of the hidden N-S radial fracture (lineament 2'; **Figure 6**).

The DDS F6 is associated with Flamengos and Lomba de Baixo faults, which dip to the north. The main CO₂ anomaly is however observed in the top of the scarp of Lomba de Baixo Fault and should result from the high permeability of the area that is crossed by several tectonic structures. Similarly, DDS F7 is also found out in the intersection of different trending tectonic structures (WNW-ESE, NNW-SSE, and NE-SW). As mentioned before, the CO₂ anomalous areas occur, in general, where a network of faults/fractures are identified, and thus seem to result from the intersection of permeable structures that allow the gas to travel from depth and escape to the surface (see DDS F2, F5, F6, and F7 in **Figure 6**).

The highest soil CO₂ flux and concentration values, representing a clear volcanic-hydrothermal origin, were measured at Praia do Almoxarife village (DDS F4) and were detected close to a building where in 2007 lethal indoor CO₂ concentrations (>15 vol.%) were measured (Ferreira and Viveiros, 2007). This very localized DDS is aligned with submarine gas emissions offshore of Faial, along the submerged

Espalamaca Fault scarp, which are mainly constituted by cold CO₂ (Viveiros et al., 2016b).

From a public health risk assessment perspective, the DDS F4, located at Praia do Almoxarife, highlights the need to perform a detailed CO₂ flux map in that village to identify which buildings may be located over anomalous CO₂ degassing sites, with the consequent impacts that it may have on the population. Even if the other DDS are not directly associated with inhabited areas, detailed CO₂ degassing maps should also be performed to evaluate possible risks for future constructions.

A total of four DDS were identified at Pico Island. The main CO₂ degassing anomalies are located in the summit area of the youngest volcano (DDS P2), Pico Volcano, where the only fumarolic emissions of the island are found (Figure 7). DDS P1 and P2 are associated with the Lomba de Fogo-S. João NNW-SSE trending fault that crosses the summit of Pico Volcano and fed the 1718 eruption. Similarly to the central volcano, the fumarolic field occurs in the intersection of the NNW-SSE, WNW-ESE, and NE-SW structures. Chemical analyses performed on Pico fumaroles in the summer of 2016 are similar to those previously obtained in 1994, showing the stability of its feeding system across two decades. The gases emitted are mainly composed of N₂ and CO₂, with minor amounts of O₂ and Ar, whose composition suggests air contamination during the ascend of gas from the deep reservoir to the surface. This fact is probably correlated with the location of the fumaroles in the volcano's summit, allowing atmospheric air to be introduced in the system, interfering with the original gas composition in the hydrothermal reservoir.

Despite the DDS P1 and P2 the remaining anomalous CO₂ degassing sites are also associated with tectonic structures previously identified by Madeira and Brum da Silveira (2003) in older volcanic areas. These important CO₂ degassing anomalies are correlated with the Lagoa do Capitão and Topo areas (DDS P3 and DDS P4, respectively, Figure 7), where several faults intersect. DDS P3 is correlated with the important WNW-ESE trending Lagoa do Capitão Fault. This structure dips to the south, but CO₂ anomalies are observed also in the upthrown block of the fault. This behavior may be associated with a higher permeability in the top of the scarp (due to fracture along the scarp) or with the presence of not mapped tectonic structures, such as the suggested lineament 1' that can be the elongation of the probable NNW-SSE fault defined by Madeira and Brum da Silveira (2003). In what concerns DDS P4, identified in the southwestern side of the WNW-ESE Topo trending fault, it probably results from the intersection of hidden NNW-SSE and NE-SW tectonic structures (Figure 7).

Similarly to Faial, faults/fractures intersection seems to favor higher permeability for the gas to travel from depth to the surface. Madeira and Brum da Silveira (2003) suggested several probable/hidden faults for the island trending WNW-ESE and NW-SE, and the present study shows that significant CO₂ anomalies correlate well with the areas of intersection of hidden/probable NNW-SSE structures with the dominant WNW-ESE faults.

The areas associated with historical eruptions in Pico Island (1562–64, 1718 and 1720, Figure 2), similarly to what was observed for Faial (Capelo Peninsula), do not show CO₂

emissions, what can be probably explained by the low or absent coverage of soils together with the high permeability of the recent lava flows that allow ingress of atmospheric air in the sub-superficial layers and dilution of the deep gases in their traveling to the surface. Nevertheless, it cannot be excluded that lava flows may act locally as barriers to the gas ascent to the surface when they are compact and low fractured. This behavior was also observed by Padrón et al. (2013) at Timanfaya Volcano (Lanzarote, Canary Islands), where the absence of CO₂ emission along the eruptive fissures was justified by the capping nature of the lava flow fields of the 1730–36 eruptions. Even in the vent areas or in the eruptive fissures the CO₂ degassing is low. Studies performed by Giannanco et al. (1999) on Mt. Etna (Italy) justified the absence of soil degassing in recent eruptive fissures due to obstruction after magma solidification or to sealing from hydrothermal alteration.

From a hazard perspective, none of the main anomalous CO₂ sites are located in areas with buildings; nevertheless, and considering the distances between sampling sites, a detailed survey should be carried out in the villages located close to the identified DDS.

The comparison of the two surveys carried out at Pico fumarolic emissions shows that the gas composition remained quite stable in the last two decades; this fact argues for the stability of the feeding systems, and consequently can be useful for any seismo-volcanic monitoring programme.

Four main DDS were identified in São Jorge Island, where no thermal anomalous zones are known. SJ3 is the only DDS located in the intersection of different WNW-ESE trending faults (Figure 8) and probably corresponds to an area of increased permeability that allows the gas to escape at the surface. The DDS SJ1 is aligned with a WNW-ESE trending probable fault located to the west and east of the degassing anomaly and mapped by Madeira and Brum da Silveira (2003). The alignment of the soil CO₂ degassing anomalies (1', Figure 8), once again, may contribute to define the location of hidden faults. The main WNW-ESE fault zones that dominate the younger western part of the island do not show any CO₂ degassing, what can be explained by the superimposed lithological control, as mentioned also for Pico and Faial islands. In the eastern part of the island, and along the WNW-ESE north dipping Urze-São João Fault (Madeira et al., 2015) few anomalous soil CO₂ concentrations are observed, even if not directly associated with the dipping direction, and were identified as DDS SJ4.

No tectonic structure has been identified in the area surrounding the SJ2 anomaly, thus further studies are needed to better understand the permeability in the area. These future works should include soil CO₂ flux surveys that could contribute to better define the DDS here proposed and eventually identify other anomalous areas. This study does not show significant anomalous CO₂ emissions close to the probable Ribeira Seca Fault, and thus cannot contribute to support its existence, that is still under debate.

Considering that CO₂ may act as asphyxiant, a detailed survey at Ribeira Seca village is needed for land-use planning. Three of the anomalous zones (SJ2, SJ3, and SJ4) are located in the oldest volcanic system of the island (Topo Volcanic System)

and, similarly to what is observed on Pico and Faial islands, no soil CO₂ degassing was detected on the areas where historical eruptions (1580 and 1808) occurred (Figure 2), fact that should be explained by the same factors as mentioned above for Faial and Pico islands (absence of well-developed soils, permeability of the lava flows and existence of natural barriers for the gas migration and release at the surface).

Degassing phenomena during periods of quiescence may be a permanent risk in any volcanic area (Viveiros et al., 2009) and, even if no incidents were reported for the islands of Pico and São Jorge, a family was relocated in Faial Island in 2007 due to high indoor CO₂ concentrations (>90 vol.%) (Ferreira and Viveiros, 2007). As mentioned above, additional detailed surveys need to complement these studies, mainly focusing in the inhabited areas close to the DDS. For the specific case of São Jorge, and considering that no recent surveys are available, the stability of the degassing areas cannot be confirmed and as so a soil CO₂ flux survey is highly recommended. In addition, Mendes et al. (2013), based on GPS data, suggested possible magma movement in the youngest part of the island, highlighting the need to obtain complementary information from a geochemical point of view.

CONCLUDING REMARKS

Anomalous soil CO₂ degassing areas were identified at Faial, Pico, and São Jorge islands and a total of 15 diffuse degassing structures (DDS) were defined based on the integration of soil CO₂ flux and concentration measurements. Statistical methodologies applied to the measured values show distinct populations for the CO₂ emitted at the surface, which probably represent different origins (biogenic and hydrothermal-volcanic). Thresholds were defined for each population highlighting the existence of deeply-derived CO₂ that is transported to the surface through active faults. In fact, main WNW-ESE and NNW-SSE trending faults in the three study islands are usually well correlated with CO₂ degassing and constitute the pathways for the migration of CO₂ from deep reservoirs to the surface; few exceptions may be associated with the superimposed effect of the lithology. The main CO₂ emissions seem to occur in the older volcanic systems, where the development of soils reduces possible air contamination and the gases migrate to the surface through the high permeability zones that correspond to the intersection of fractures/faults. The absence of soils and the permeability of the recent lava flows, which allow the dilution of the deep gases with atmospheric air, may explain the lack of CO₂ emission in the younger volcanic systems. In addition, locally, some low permeable lava flows may act as barriers for the deep gas emissions.

For Pico and Faial islands two different methodologies were used in the present study to measure the soil CO₂ diffuse degassing. Even if no simultaneous measurements were performed, higher soil CO₂ flux values were essentially coincident with areas with anomalous soil CO₂ concentrations. The generally good spatial correlation observed between the soil CO₂ flux and concentration values in different surveyed periods shows that the anomalous CO₂ degassing areas remain stable

along time, arguing for the use of these techniques as useful tools for volcanic monitoring programmes. Considering the need to establish a permanent gas monitoring network in these islands, several DDS are here suggested as potential sites to install a permanent soil CO₂ flux station, taking into account the state of activity of the different volcanic systems. DDS F2 or F3 at Faial Island are two potential areas to install a permanent soil CO₂ flux station since they correspond to the flank of the active Caldeira central volcano. At Pico Island both DDS P1 and P2 seem to be adequate to install a permanent equipment, even if detailed soil CO₂ flux measurements should be performed to select the highest CO₂ emission site.

Considering that (a) about 32% of the historical volcanic eruptions that affected the Azores archipelago occurred inland or offshore the islands of Pico, Faial, and São Jorge (Gaspar et al., 2015), (b) some of the events were lethal causing the death of a high number of persons, even when the type of volcanism was less explosive (Hawaiian or Strombolian activity), (c) the state of activity of the volcanoes that form these three islands, and (d) the number of inhabitants (38,180, according to the Census, 2011) that can be vulnerable to a future volcanic event, the existence of a volcano monitoring programme that involves different techniques (geophysics, geochemistry) is crucial to identify periods of unrest. The CO₂ degassing maps here presented are thus important tools that characterize the CO₂ emission in quiescent periods of activity and are important to identify future periods of reactivation. Besides, several studies performed in these islands (e.g., Madeira and Brum da Silveira, 2003; Hildenbrand et al., 2012; Zanon and Frezzotti, 2013; Zanon et al., 2013; Tripanera et al., 2014) have highlighted the importance of the tectonic control on the plumbing systems of the volcanoes, and most of the main degassing areas are also tectonically controlled, what reinforces the need to integrate different geological studies to better understand the volcanic systems. On another hand, the location of some of the identified DDS close to inhabited areas highlights the need to identify hazardous CO₂ zones both for the existing and for future constructions.

AUTHOR CONTRIBUTIONS

FV revisited/processed the data and drafted the manuscript. MM, CF, FV, and CS carried out the soil diffuse degassing field surveys and contributed for the elaboration of the data. JG and TF provided important suggestions during the processing. All the authors have read and approved the final manuscript.

ACKNOWLEDGMENTS

FV is supported by a Post-Doc Grant from Fundação para a Ciência e Tecnologia (FCT, Ref. SFRH/BPD/100032/2014). This study was also a part of the MARES Project (Ref. TDC/GEO-FIQ/1088/2014), funded by the FCT. The authors would like also to thank Vittorio Zanon for sampling the Pico fumaroles during June 2016 and Lucia Moreno for performing the chemical analyses.

REFERENCES

- Aiuppa, A., Burton, M., Caltabiano, T., Giudice, G., Gurrieri, S., Liuzzo, M., et al. (2010). Unusually large magmatic CO₂ gas emissions prior to a basaltic paroxysm. *Geophys. Res. Lett.* 37, L17303. doi: 10.1029/2010GL043837
- Allard, P., Carbonnelle, J., Dajlevic, D., Le Bronec, J., Morel, P., Robe, M. C., et al. (1991). Eruptive and diffuse emissions of CO₂ from Mount Etna. *Nature* 351, 387–391. doi: 10.1038/351387a0
- Asimow, P. D., Dixon, J. E., and Langmuir, C. H. (2004). A hydrous melting and fractionation model for mid-ocean ridge basalts: application to the Mid-Atlantic Ridge near the Azores. *Geochem. Geophys. Geosys.* 5:Q01E16. doi: 10.1029/2003GC000568
- Bajracharya, R. M., Lal, R., and Kimble, J. M. (2000). Erosion effects on carbon dioxide concentration and carbon flux from an Ohio alfisol. *Soil Sci. Soc. Am. J.* 64, 694–700. doi: 10.2136/sssaj2000.642694x
- Baubron, J. C., Rigo, A., and Toutain, J. P. (2002). Soil gas profiles as a tool to characterise active tectonics areas: the Jaut Pass example (Pyrenees, France). *Earth Planet. Sci. Lett.* 196, 69–81. doi: 10.1016/S0012-821X(01)00596-9
- Baxter, P., Baubron, J. C., and Coutinho, R. (1999). Health hazards and disaster potential of ground gas emissions at Furnas Volcano, São Miguel, Azores. *J. Volcanol. Geotherm. Res.* 92, 95–106. doi: 10.1016/S0377-0273(99)00070-0
- Beaubien, S. E., Ciotoli, G., and Lombardi, S. (2003). Carbon dioxide and radon gas hazard in the Alban Hills area (central Italy). *J. Volcanol. Geotherm. Res.* 123, 63–80. doi: 10.1016/S0377-0273(03)00028-3
- Blong, R. J. (1984). *Volcanic Hazards. A Sourcebook on the Effects of Eruptions*. San Diego, CL: Academic Press.
- Bonatti, E. (1990). Not so hot “hot spots” in the Oceanic mantle. *Science* 250, 107–111. doi: 10.1126/science.250.4977.107
- Caliro, S., Viveiros, F., Chiodini, G., and Ferreira, T. (2015). Gas geochemistry of hydrothermal fluids of the S. Miguel and Terceira Islands, Azores. *Geochim. Cosmochim. Acta* 168, 43–57. doi: 10.1016/j.gca.2015.07.009
- Cannat, M., Brrias, A., Deplus, C., Escartín, J., Georgen, J., Lin, J., et al. (1999). Mid-Atlantic Ridge-Azores hotspot interactions: along-axis migration of a hotspot-derived event of enhanced magmatism 10 to 4 Ma ago. *Earth Planet. Sci. Lett.* 173, 257–269. doi: 10.1016/s0012-821X(99)00234-4
- Carapezza, M. L., and Granieri, D. (2004). CO₂ soil flux at Vulcano (Italy): comparison between active and passive methods. *Appl. Geochem.* 19, 73–88. doi: 10.1016/s0883-2927(03)00111-2
- Carapezza, M. L., Inguaggiato, S., Brusca, L., and Longo, M. (2004). Geochemical precursors of the activity of an open-conduit volcano: the Stromboli 2002–2003 eruptive events. *Geophys. Res. Lett.* 31, L07620. doi: 10.1029/2004gl019614
- Cardellini, C., Chiodini, G., and Frondini, F. (2003). Application of stochastic simulation to CO₂ flux from soil: mapping and quantification of gas release. *J. Geophys. Res.* 108, 2425–2437. doi: 10.1029/2002JB002165
- Chiodini, G., Caliro, S., Cardellini, C., Avino, R., Granieri, D., and Schmidt, A. (2008). Carbon isotopic composition of soil CO₂ efflux, a powerful method to discriminate different sources feeding soil CO₂ degassing in volcanic-hydrothermal areas. *Earth Planet. Sci. Lett.* 274, 372–379. doi: 10.1016/j.epsl.2008.07.051
- Chiodini, G., Caliro, S., Cardellini, C., Granieri, D., Avino, R., Baldini, A., et al. (2010a). Long-term variations of the Campi Flegrei, Italy, volcanic system as revealed by the monitoring of hydrothermal activity. *J. Geophys. Res.* 115: B03205. doi: 10.1029/2008JB006258
- Chiodini, G., Cioni, R., Guidi, M., Raco, B., and Marini, L. (1998). Soil CO₂ flux measurements in volcanic and geothermal areas. *Appl. Geochem.* 13, 543–552. doi: 10.1016/S0883-2927(97)00076-0
- Chiodini, G., Frondini, F., Cardellini, C., Granieri, D., Marini, L., and Ventura, G. (2001). CO₂ degassing and energy release at Solfatara Volcano, Campi Flegrei, Italy. *J. Geophys. Res.* 106, 16213–16221. doi: 10.1029/2001JB000246
- Chiodini, G., Frondini, F., Kerrick, D. M., Rogie, J., Parello, F., Peruzzi, L., et al. (1999). Quantification of deep CO₂ fluxes from Central Italy. Examples of carbon balance for regional aquifers and soil diffuse degassing. *Chem. Geol.* 159, 205–222. doi: 10.1016/S0009-2541(99)00030-3
- Chiodini, G., Granieri, D., Avino, R., Caliro, S., Costa, A., Minopoli, C., et al. (2010b). Non-volcanic CO₂ Earth degassing: the case of Mefite di Ansanto (Southern Apennines), Italy. *Geophys. Res. Lett.* 37, L11303. doi: 10.1029/2010GL042858
- Chovelon, P. (1982). *Evolution Volcanotectonique des Iles de Faial et de Pico*. Thesis, University Paris-Sud, Orsay.
- Costa, A. C. G., Hildenbrand, A., Marques, F. O., Sibrant, A. L. R., and Santos de Campos, A. (2015). Catastrophic flank collapses and slumping in Pico Island during the last 130 kyr (Pico-Faial ridge, Azores Triple Junction). *J. Volcanol. Geotherm. Res.* 302, 33–46. doi: 10.1016/j.jvolgeores.2015.06.008
- Cruz, J. V., Freire, P., and Costa, A. (2010). Mineral waters characterization in the Azores archipelago (Portugal). *J. Volcanol. Geotherm. Res.* 190, 353–364. doi: 10.1016/j.jvolgeores.2009.12.001
- David, M. (1977). *Geostatistical Ore Reserve Estimation*. Amsterdam: Elsevier Scientific Publishing Company.
- Demande, J., Fabriol, R., Gérard, A., and Iundt, F. (1982). *Prospection Géothermique des Iles de Faial e Pico (Açores)*. 82SGN003GTH. Bureau de Recherches Géologiques et Minières, Orléans.
- de Moor, J. M., Aiuppa, A., Avard, G., Wehrmann, H., Dunbar, N., Muller, C., et al. (2016). Turmoil at turrialba volcano (Costa Rica): degassing and eruptive processes inferred from high-frequency gas monitoring. *J. Geophys. Res.* 121, 5761–5775. doi: 10.1002/2016JB013150
- Deutsch, C. V., and Journel, A. G. (1998). *GSLIB: Geostatistical Software Library and User's Guide*. Applied Geostatistics Series. New York, NY; Oxford: Oxford University Press.
- Dias, N. A., Matias, L., Lourenço, N., Madeira, J., Carrilho, F., and Gaspar, J. L. (2007). Crustal seismic velocity structure near Faial and Pico Islands (Azores), from local earthquake tomography. *Tectonophysics* 445, 301–317. doi: 10.1016/j.tecto.2007.09.001
- Di Chiara, A., Speranza, F., Porreca, M., Pimentel, A., D'Ajello Caracciolo, F., and Pacheco, J. (2014). Constraining chronology and time-space evolution of Holocene volcanic activity on the Capelo Peninsula (Faial Island, Azores): the paleomagnetic contribution. *Geol. Soc. Am. Bull.* 126, 1164–1180. doi: 10.1130/B30933.1
- Evans, B. M., and Staudacher, T. H. (2001). *In situ* measurements of gas discharges across fissures associated with lava flows at Réunion Island. *J. Volcanol. Geotherm. Res.* 106, 255–263. doi: 10.1016/S0377-0273(00)00242-0
- Faria, C. (2002). *Estudo de Anomalias Geoquímicas Associadas a Processos de Desgasificação Difusa na Ilha do Faial: Contribuição Para a Cartografia de Falhas Ativas*. Master Thesis, University of the Azores.
- Féraud, G., Kaneoka, I., and Allègre, C. J. (1980). K-Ar ages and stress pattern in the Azores: geodynamic implications. *Earth Planet. Sci. Lett.* 46, 275–286. doi: 10.1016/0012-821X(80)90013-8
- Ferreira, T. (1994). *Contribuição Para o Estudo das Emanações Gasosas Associadas a Processos de Vulcanismo no Arquipélago dos Açores*. Master Thesis, University of the Azores.
- Ferreira, T., Gaspar, J. L., Viveiros, F., Marcos, M., Faria, C., and Sousa, F. (2005). Monitoring of fumarole discharge and CO₂ soil degassing in the Azores: contribution to volcanic surveillance and public health risk assessment. *Ann. Geophys.* 48, 787–796. doi: 10.4401/ag-3234
- Ferreira, T., and Viveiros, F. (2007). *Anomalia Geoquímica em Zona Residencial da Freguesia da Praia do Almoxarife (Ilha do Faial, Açores)*. Technical Report Ref. 01/CVARG/07
- Fischer, T. P., and Chiodini, G. (2015). “Volcanic, magmatic and hydrothermal gases,” in *The Encyclopedia of Volcanoes*, 2nd Edn., eds H. Sigurdsson, B. Houghton, S. R. McNutt, H. Rymer, and J. Stix (San Diego, CL: Elsevier Inc.), 779–797.
- Gaspar, J. L., and Ferreira, T. (1995). Temperatura e composição química das emanações gasosas do Vulcão dos Capelinhos no decorrer da crise sísmica que se desenvolveu a NW da ilha do Faial em 1992/93. *Açorianas* 8, 167–175.
- Gaspar, J. L., Queiroz, G., Ferreira, T., Medeiros, A. R., Goulart, C., and Medeiros, J. (2015). “Earthquakes and volcanic eruptions in the Azores region: geodynamic implications from major historical events and instrumental seismicity,” in *Volcanic Geology of S. Miguel Island (Azores archipelago)*, eds J. L. Gaspar, J. E. Guest, A. M. Duncan, F. J. A. S. Barriga, D. K. Chester (London: Geological Society, London, Memoirs), 33–49.
- Giammanco, S., Gurrieri, S., and Valenza, M. (1999). Geochemical investigations applied to active fault detection in a volcanic area: the North-East Rift on Mt. Etna (Sicily, Italy). *Geophys. Res. Lett.* 26, 2005–2008. doi: 10.1029/1999gl900396
- Giammanco, S., Gurrieri, S., and Valenza, M. (2006). Fault-controlled soil CO₂ degassing and shallow magma bodies: summit and lower east rift

- of Kilauea volcano (Hawaii), 1997. *Pure Appl. Geophys.* 163, 853–867. doi: 10.1007/s-7643-7584-1_15
- Giggenbach, W. F. (1975). A simple method for the collection and analysis of volcanic gas samples. *Bull. Volcanol.* 39, 132–145. doi: 10.1007/BF02596953
- Giggenbach, W. F. (1996). “Chemical composition of volcanic gases,” in *Monitoring and Mitigation of Volcano Hazards*, eds R. Scarpa and R. I. Tilling (Berlin; Heidelberg: Springer-Verlag), 221–253.
- Giggenbach, W. F., and Goguel, R. L. (1989). *Collection and Analysis of Geothermal Volcanic Water and Gas Discharges*. Chemistry Division, DSIR, Report no. CD 2401.
- Goovaerts, P. (1999). Geostatistics in soil science: state-of-the-art and perspectives. *Geoderma* 89, 1–45. doi: 10.1016/S0016-7061(98)00078-0
- Granieri, D., Chiodini, G., Marzocchi, W., and Avino, R. (2003). Continuous monitoring of CO₂ soil diffuse degassing at Phlegraean Fields (Italy): influence of environmental and volcanic parameters. *Earth Planet. Sci. Lett.* 212, 167–179. doi: 10.1016/S0016-821X(03)00232-2
- Gurrieri, S., and Valenza, M. (1988). Gas transport in natural porous mediums: a method for measuring CO₂ flows from the ground in volcanic and geothermal areas. *Rendiconti della Società Italiana di Mineralogia e Petrologia* 43, 1151–1158.
- Hansell, A., and Oppenheimer, C. (2004). Health hazards from volcanic gases: a systematic literature review. *Arch. Environ. Health* 59, 628–639. doi: 10.1080/00039890409602947
- Hernández, P. A., Notsu, K., Salazar, J. M., Mori, T., Natale, G., Okada, H., et al. (2001). Carbon dioxide degassing by advective flow from Usu Volcano, Japan. *Science* 292, 83–86. doi: 10.1126/science.1058450
- Hildenbrand, A., Madureira, P., Marques, F. O., Cruz, I., Henry, B., and Silva, P. (2008). Multi-stage evolution of a sub-aerial volcanic ridge over the last 1.3 Myr: S. Jorge Island, Azores Triple Junction. *Earth Planet. Sci. Lett.* 273, 289–298. doi: 10.1016/j.epsl.2008.06.041
- Hildenbrand, A., Marques, F. O., Costa, A. C. G., Sibrandt, A. L. R., Silva, P. F., Henry, B., et al. (2012). Reconstructing the architectural evolution of volcanic islands from combined K/Ar, morphologic, tectonic, and magnetic data: the Faial Island example (Azores). *J. Volcanol. Geotherm. Res.* 241–242, 39–48. doi: 10.1016/j.jvolgeores.2012.06.019
- Hipólito, A., Madeira, J., Carmo, R., and Gaspar, J. L. (2013). Neotectonics of Graciosa Island (Azores): a contribution to seismic hazard assessment of a volcanic area in a complex geodynamic setting. *Ann. Geophys.* 56:S0677. doi: 10.4401/ag-6222
- Hutchison, W., Mather, T. A., Pyle, D. M., Biggs, J., and Yirgu, G. (2015). Structural controls on fluid pathways in an active rift system: a case study of the Aluto volcanic complex. *Geosphere* 11, 542–562. doi: 10.1130/GES0119.1
- Isaaks, E. H., and Srivastava, R. M. (1989). *An Introduction to Applied Geostatistics*. New York, NY; Oxford: Oxford University Press.
- Jean-Baptiste, P., Allard, P., Coutinho, R., Ferreira, T., Fourré, E., Queiroz, G., et al. (2009). Helium isotopes in hydrothermal volcanic fluids of the Azores archipelago. *Earth Planet. Sci. Lett.* 281, 70–80. doi: 10.1016/j.epsl.2009.02.009
- Jung, N.-H., Han, W. S., Watson, Z. T., Graham, J. P., and Kim, K.-Y. (2014). Fault-controlled CO₂ leakage from natural reservoirs in the Colorado Plateau, East-Central Utah. *Earth Planet. Sci. Lett.* 403, 358–367. doi: 10.1016/j.epsl.2014.07.012
- Kanemasu, E. T., Powers, W. L., and Sij, J. W. (1974). Field chamber measurements of CO₂ flux from soil surface. *Soil Sci.* 118, 233–237. doi: 10.1097/00010694-197410000-00001
- Lee, H., Muirhead, J. D., Fischer, T. P., Ebinger, C. J., Kattenhorn, S. A., Sharp, Z. D., et al. (2016). Massive and prolonged deep carbon emissions associated with continental rifting. *Nat. Geosci.* 5, 145–149. doi: 10.1038/ngeo2622
- Liuzzo, M., Di Muro, A., Giudice, G., Michon, L., Ferrazzini, V., and Gurrieri, S. (2015). New evidence of CO₂ soil degassing anomalies on Piton de la Fournaise volcano and the link with volcano tectonic structures. *Geochem. Geophys. Geosyst.* 16, 4388–4404. doi: 10.1002/2015gc006032
- Liuzzo, M., Gurrieri, S., Giudice, G., and Giuffrida, G. (2013). Ten years of soil CO₂ continuous monitoring on Mt. Etna: exploring the relationship between processes of soil degassing and volcanic activity. *Geochem. Geophys. Geosyst.* 14, 2886–2899. doi: 10.1002/ggge.20196
- Lourenço, N., Luís, J., and Miranda, J. M. (1997). *Azores Triple Junction Bathymetry*. Map edited by Science Faculty, Lisbon and Algarve Universities, 1 sheet.
- Luo, Y., and Zhou, X. (2006). *Soil Respiration and the Environment*. San Diego, CA: Academic Press.
- Machado, F., Parsons, W., Richards, A., and Mulford, J. W. (1962). Capelinhos eruption of Fajal Volcano, Azores, 1957–1958. *J. Geophys. Res.* 67, 3519–3529. doi: 10.1029/JZ067i009p03519
- Madeira, J. (1998). *Estudos de Neotectónica nas Ilhas do Faial, Pico e S. Jorge: Uma Contribuição Para o Conhecimento Geodinâmico da Junção Tripla dos Açores*. Ph.D. thesis, Faculdade de Ciências da Universidade de Lisboa, 481.
- Madeira, J., and Brum da Silveira, A. (2003). Active tectonics and first paleoseismological results in Faial, Pico and S. Jorge islands (Azores, Portugal). *Ann. Geophys.* 46, 733–761.
- Madeira, J., Brum da Silveira, A., Hipólito, A., and Carmo, R. (2015). “Active tectonics in the Central and Eastern Azores islands along the Eurasia-Nubia boundary: a review,” in *Volcanic Geology of S. Miguel Island (Azores archipelago)*, Vol. 44, eds J. L. Gaspar, J. E. Guest, A. M. Duncan, F. J. A. S. Barriga, and D. K. Chester (London: Geological Society, London, Memoirs), 15–32.
- Madeira, J., and Ribeiro, A. (1990). Geodynamic models for the Azores triple junction: a contribution from tectonics. *Tectonophysics* 184, 405–415. doi: 10.1016/0040-1951(90)90452-e
- Marcos, M. (2006). *Estudo dos Processos de Desgaseificação Difusa nos Açores, com base na Análise de Variações Espaciais de CO₂ e Temporais de 222Rn*. Master Thesis, University of the Azores, 135.
- Marques, F. O., Catalão, J. C., DeMets, C., Costa, A. C. G., and Hildenbrand, A. (2013). GPS and tectonic evidence for a diffuse plate boundary at the Azores Triple Junction. *Earth Planet. Sci. Lett.* 381, 177–187. doi: 10.1016/j.epsl.2013.08.051
- Matias, L., Dias, N. A., Morais, I., Vales, D., Carrilho, F., Madeira, J., et al. (2007). The 9th of July 1998 Faial Island (Azores, North Atlantic) seismic sequence. *J. Seismol.* 11, 275–298. doi: 10.1007/s10950-007-9052-4
- Mendes, V. B., Madeira, J., Brum da Silveira, A., Trota, A., Elosgui, P., and Pagarete, J. (2013). Present-day deformation in São Jorge Island, Azores, from episodic GPS measurements (2001–2011). *Adv. Space Res.* 51, 1581–1592. doi: 10.1016/j.asr.2012.10.019
- Métrich, N., Zanon, V., Créon, L., Hildenbrand, A., Moreira, M., and Marques, F. O. (2014). Is the ‘Azores Hotspot’ a Wetspot? Insights from the geochemistry of fluid and melt inclusions in olivine of Pico Basalts. *J. Petrol.* 55, 377–393. doi: 10.1093/petrology/egt071
- Miranda, J. M., Luís, J. F., Lourenço, N., and Fernandes, R. M. S. (2015). “The structure of the Azores Triple Junction: implications for São Miguel Island,” in *Volcanic Geology of S. Miguel Island (Azores archipelago)*, eds J. L. Gaspar, J. E. Guest, A. M. Duncan, F. J. A. S. Barriga, and D. K. Chester (London: Geological Society, London, Memoirs), 5–13.
- Moreira, M., Doucelance, R., Kurz, M. D., Dupré B., and Allègre, C. J. (1999). Helium and lead isotope geochemistry of the Azores Archipelago. *Earth Planet. Sci. Lett.* 169, 189–205. doi: 10.1016/S0016-821X(99)00071-0
- Nakadai, T., Yokozawa, M., Ikeda, H., and Koizumi, H. (2002). Diurnal changes of carbon dioxide flux from bare soil in agricultural field in Japan. *Appl. Soil Ecol.* 19, 161–171. doi: 10.1016/S0929-1393(01)00180-9
- Norman, J. M., Garcia, R., and Verma, S. B. (1992). Soil surface CO₂ fluxes and the carbon budget of a grassland. *J. Geophys. Res.* 97, 18845–18853. doi: 10.1029/92JD01348
- Nunes, J. C. (1999). *A Actividade Vulcânica na Ilha do Pico do Plistocénico Superior ao Holocénico: Mecanismo Eruptivo e Hazard Vulcânico*. Ph.D. thesis, University of the Azores, Ponta Delgada, 356.
- Pacheco, J. (2015). ¹⁴C Ages of the last eruptive stage of Faial Island Caldeira Volcano. *Radiocarbon* 57, 1021–1027. doi: 10.2458/azu_rc.57.17957
- Pacheco, J. M. R. (2001). *Processos Associados ao Desenvolvimento de Erupções Vulcânicas Hidromagmáticas Explosivas na ilha do Faial e Sua Interpretação Numa Perspectiva de Avaliação do Hazard e Minimização do Risco*. Ph.D. thesis, Azores University, Ponta Delgada, 300.
- Padrón, E., Padilla, G., Hernández, P. A., Pérez, N. M., Calvo, D., Nolasco, D., et al. (2013). Soil gas geochemistry in relation to eruptive fissures on Timanfaya volcano, Lanzarote Island (Canary Islands, Spain). *J. Volcanol. Geotherm. Res.* 250, 91–99. doi: 10.1016/j.jvolgeores.2012.10.013
- Pantaleo, M., and Walter, T. R. (2014). The ring-shaped thermal field of Stefanos crater, Nisyros Island: a conceptual model. *Solid Earth* 5, 183–198. doi: 10.5194/se-5-183-2014

- Parkinson, K. J. (1981). An improved method for measuring soil respiration in the field. *J. Appl. Ecol.* 18, 221–228. doi: 10.2307/2402491
- Pedone, M., Viveiros, F., Aiuppa, A., Giudice, G., Grassi, F., Gagliano, A. L., et al. (2015). Total (fumarolic + diffuse soil) CO₂ output from Furnas volcano. *Earth Planets Space* 67, 174. doi: 10.1186/s40623-015-0345-5
- Peltier, A., Finizola, A., Douillet, G. A., Brothelande, E., and Garaebiti, E. (2012). Structure of an active volcano associated with a resurgent block inferred from thermal mapping: the Yasur-Yenkahe volcanic complex (Vanuatu). *J. Volcanol. Geotherm. Res.* 243–244, 59–68. doi: 10.1016/j.jvolgeores.2012.06.022
- Quartau, R., Madeira, J., Mitchell, N. C., Tempera, F., Silva, P. F., and Brandão, F. (2015). The insular shelves of the Faial-Pico Ridge (Azores archipelago): a morphological record of its evolution. *Geochem. Geophys. Geosyst.* 16, 1401–1420. doi: 10.1002/2015GC005733
- Raich, J. W., and Schlesinger, W. H. (1992). The global carbon dioxide flux in soil respiration and its relationship to vegetation and climate. *Tellus* 44B, 81–99. doi: 10.3402/tellusb.v44i2.15428
- Raich, J. W., and Tufekcioglu, A. (2000). Vegetation and soil respiration: correlations and controls. *Biogeochemistry* 48, 71–90. doi: 10.1023/A:100612000616
- Rinaldi, A. P., Vandemeulebrouck, J., Todesco, M., and Viveiros, F. (2012). Effects of atmospheric conditions on surface diffuse degassing. *J. Geophys. Res.* 117, B11201. doi: 10.1029/2012JB009490
- Schilling, J. G. (1975). Azores mantle blob: rare-earth evidence. *Earth Planet. Sci. Lett.* 25, 103–115. doi: 10.1016/0012-821X(75)90186-7
- Schöpa, A., Pantaleo, M., and Walter, T. R. (2011). Scale-dependent location of hydrothermal vents: stress field models and infrared field observations on the Fossa Cone, Vulcano Island, Italy. *J. Volcanol. Geotherm. Res.* 203, 133–145. doi: 10.1016/j.jvolgeores.2011.03.008
- Searle, R. (1980). Tectonic pattern of the Azores spreading centre and triple junction. *Earth Planet. Sci. Lett.* 51, 415–434. doi: 10.1016/0012-821X(80)90221-6
- Serralheiro, A., Forjaz, V. H., Alves, C. A. M., and Rodrigues, B. (1989). *Carta Vulcanológica dos Açores – ilha do Faial, scale 1:15000, Sheets 1, 2, 3 & 4*. Ponta Delgada: Centro de Vulcanologia do INIC, Serviço Regional de Proteção Civil dos Açores e Universidade dos Açores.
- Silva, C., Ferreira, T., Viveiros, F., and Allard, P. (2015). Soil radon (²²²Rn) monitoring at Furnas Volcano (São Miguel, Azores): applications and challenges. *Eur. Phys. J. Spec. Top.* 224, 659–686. doi: 10.1140/epjst/e2015-02398-6
- Silva, M. (2005). *Caracterização da Sismicidade Histórica dos Açores com Base na Reinterpretação de Dados de Macrossísmica: Contribuição Para a Avaliação do Risco Sísmico nas Ilhas do Grupo Central*. Master thesis, Universidade dos Açores, 146.
- Sinclair, A. J. (1974). Selection of threshold values in geochemical data using probability graphs. *J. Geochem. Explor.* 3, 129–149. doi: 10.1016/0375-6742(74)90030-2
- Tripanera, D., Porreca, M., Ruch, J., Pimentel, A., Acocella, V., Pacheco, J., et al. (2014). Relationships between tectonics and magmatism in a transtensive/transform setting: an example from Faial Island (Azores, Portugal). *Geol. Soc. Am. Bull.* 126, 164–181. doi: 10.1130/B30758.1
- Viveiros, F. (2003). *Contribuição Para o Estudo dos Processos de Desgaseificação Difusa nos Açores no âmbito da Monitorização Sismovulcânica e da Avaliação do Risco: Discriminação de Factores que Influenciam a Variação do Fluxo do CO₂*. Master thesis, University of the Azores, 140.
- Viveiros, F., Cardellini, C., Ferreira, T., Caliro, S., Chiodini, G., and Silva, C. (2010). Soil CO₂ emissions at Furnas volcano, São Miguel Island, Azores archipelago: volcano monitoring perspectives, geomorphologic studies, and land use planning application. *J. Geophys. Res.* 115:B12208, doi: 10.1029/2010JB007555
- Viveiros, F., Ferreira, T., Cabral Vieira, J., Silva, C., and Gaspar, J. L. (2008). Environmental influences on soil CO₂ degassing at Furnas and Fogo volcanoes (São Miguel Island, Azores archipelago). *J. Volcanol. Geotherm. Res.* 177, 883–893. doi: 10.1016/j.jvolgeores.2008.07.005
- Viveiros, F., Ferreira, T., Silva, C., and Gaspar, J. L. (2009). Meteorological factors controlling soil gases and indoor CO₂ concentration: a permanent risk in degassing areas. *Sci. Tot. Environ.* 407, 1362–1372. doi: 10.1016/j.scitotenv.2008.10.009
- Viveiros, F., Gaspar, J. L., Ferreira, T., and Silva, C. (2016a). Hazardous indoor CO₂ concentrations in volcanic environments. *Environ. Pollut.* 214, 776–786. doi: 10.1016/j.envpol.2016.04.086
- Viveiros, F., Gaspar, J. L., Ferreira, T., Silva, C., Marcos, M., and Hipólito, A. (2015). “Mapping of soil CO₂ diffuse degassing at São Miguel Island and its public health implications,” in *Volcanic Geology of S. Miguel Island (Azores archipelago)*, eds J. L. Gaspar, J. E. Guest, A. M. Duncan, F. J. A. S. Barriga, and D. K. Chester (London: Geological Society, London, Memoirs), 185–195.
- Viveiros, F., Moreno, L., Carreiro-Silva, M., Couto, R., Silva, C., Range, P., et al. (2016b). “Volcanic gas emissions offshore of São Miguel and Faial islands (Azores archipelago),” in *Actas das 4as Jornadas de Engenharia Hidrográfica, Instituto Hidrográfico* (Lisbon), 320–323.
- Viveiros, F., Vandemeulebrouck, J., Rinaldi, A. P., Ferreira, T., Silva, C., and Cruz, J. V. (2014). Periodic behavior of soil CO₂ emissions in diffuse degassing areas of the Azores archipelago: application to seismovolcanic monitoring. *J. Geophys. Res.* 119, 7578–7597. doi: 10.1002/2014JB011118
- Vogt, P. R., and Jung, W. Y. (2004). The Terceira rift as hyper-slow, hotspot dominated oblique spreading axis: a comparison with other slow-spreading plate boundaries. *Earth Planet. Sci. Lett.* 218, 77–90. doi: 10.1016/S0012-821X(03)00627-7
- Weinstein, P., and Cook, A. (2005). “Volcanic emissions and health,” in *Essentials of Medical Geology – Impacts of the Natural Environment on Public Health*, ed O. Selinus (Burlington, MA: Elsevier), 203–226.
- Weston, F. S. (1964). List of recorded volcanic eruptions in the Azores with brief reports. *Bol. Mus. Lab. Min. Geol. Fac. Ciências Lisboa* 10, 3–18.
- Zanon, V., and Frezzotti, M. L. (2013). Magma storage and ascent conditions beneath Pico and Faial islands (Azores Islands). A study on fluid inclusions. *Geochem. Geophys. Geosyst.* 14, 3494–3514. doi: 10.1002/ggge.20221
- Zanon, V., Kueppers, U., Pacheco, J., and Cruz, I. (2013). Volcanism from fissure zones and the Caldeira central volcano at Faial Island, Azores archipelago: geochemical processes in multiple feeding systems. *Geol. Mag.* 150, 536–555. doi: 10.1017/s0016756812000702

Conflict of Interest Statement: The authors declare that the research was conducted in the absence of any commercial or financial relationships that could be construed as a potential conflict of interest.

Copyright © 2017 Viveiros, Marcos, Faria, Gaspar, Ferreira and Silva. This is an open-access article distributed under the terms of the Creative Commons Attribution License (CC BY). The use, distribution or reproduction in other forums is permitted, provided the original author(s) or licensor are credited and that the original publication in this journal is cited, in accordance with accepted academic practice. No use, distribution or reproduction is permitted which does not comply with these terms.



Transformations and Decomposition of MnCO_3 at Earth's Lower Mantle Conditions

Eglantine Boulard^{1*†}, Yijin Liu², Ai L. Koh³, Mary M. Reagan¹, Julien Stodolna⁴, Guillaume Morard⁵, Mohamed Mezouar⁶ and Wendy L. Mao¹

¹ Geological Sciences, Stanford University, Stanford, CA, USA, ² Stanford Synchrotron Radiation Lightsource, SLAC National Accelerator Laboratory, Menlo Park, CA, USA, ³ Stanford Nano Shared Facilities, Stanford University, Stanford, CA, USA,

⁴ EDF Lab Les Renardières, Dpt MMC, Moret sur Loing, France, ⁵ Centre National de la Recherche Scientifique, UMR Centre National de la Recherche Scientifique 7590, Institut de Minéralogie, de Physique des Matériaux et de Cosmochimie, IRD, Sorbonne Universités—Université Pierre et Marie Curie, Muséum National d'Histoire Naturelle, Paris, France, ⁶ European Synchrotron Radiation Facility (ESRF), Grenoble, France

OPEN ACCESS

Edited by:

Benjamin Alexander Black,
City College of New York, USA

Reviewed by:

Matteo Alvaro,
University of Pavia, Italy

Zachary M. Geballe,
Geophysical Laboratory (CIS), USA

*Correspondence:

Eglantine Boulard
eglantine.boulard@synchrotron-soleil.fr

†Present Address:

Eglantine Boulard,
Synchrotron SOLEIL, L'Orme les
Merisiers, St. Aubin, France

Specialty section:

This article was submitted to
Geochemistry,
a section of the journal
Frontiers in Earth Science

Received: 22 August 2016

Accepted: 28 November 2016

Published: 15 December 2016

Citation:

Boulard E, Liu Y, Koh AL, Reagan MM, Stodolna J, Morard G, Mezouar M and Mao WL (2016) Transformations and Decomposition of MnCO_3 at Earth's Lower Mantle Conditions. *Front. Earth Sci.* 4:107. doi: 10.3389/feart.2016.00107

Carbonates have been proposed as the principal oxidized carbon-bearing phases in the Earth's interior. Their phase diagram for the high pressure and temperature conditions of the mantle can provide crucial constraints on the deep carbon cycle. We investigated the behavior of MnCO_3 at pressures up to 75 GPa and temperatures up to 2200 K. The phase assemblage in the resulting run products was determined *in situ* by X-ray diffraction (XRD), and the recovered samples were studied by analytical transmission electron microscopy (TEM) and X-ray absorption near edge structure (XANES) imaging. At moderate temperatures below 1400 K and pressures above 50 GPa, MnCO_3 transformed into the MnCO_3 -II phase, with XANES data indicating no change in the manganese oxidation state in MnCO_3 -II. However, upon heating above 1400 K at the same pressure conditions, both MnCO_3 and MnCO_3 -II undergo decomposition and redox reactions which lead to the formation of manganese oxides and reduced carbon.

Keywords: carbonate, phase transition, redox reaction, deep carbon cycle, high pressure

INTRODUCTION

Carbonates represent the main oxidized carbon-bearing phases which are transported into the mantle during subduction. The high-pressure behavior of carbonates can provide insight on crystal chemistry of carbon-bearing phases relevant to Earth's deep interior. In particular, the stability of carbonates vs. their decomposition and melting provides critical constraints for understanding the global carbon cycle. For all these reasons, the thermodynamic properties and phase diagrams for relevant carbonate compositions are needed down to core-mantle boundary conditions, i.e., megabar pressures and temperatures up to 3000 K.

The high-pressure behavior of various divalent cation-bearing carbonates has been the subject of a large number of studies. Systematic differences in compressibility and high pressure and high temperature polymorphs that depend on cation type have been observed in previous studies demonstrating that the polymorphism of carbonates is likely more complex than previously thought (see Shatskiy et al., 2015 and references therein). No single structural parameter or electronic property of the cation can account for the behavior of carbonates,

suggesting that a combination of factors must be considered in explaining compressibility trends among members of the calcite-structure type (Zhang et al., 1998; Zhang and Reeder, 1999). With a Mn²⁺ cation size that lies between those of Mg²⁺ and Ca²⁺, rhodochrosite (MnCO₃) represents a potential model compound for understanding the differences in the high-pressure behavior of the two main carbonate compositions (Mg and Ca carbonates). The interplay between these two species has indeed been the subject of many studies (e.g., de Capitani and Peters, 1981; Wang et al., 2011). At ambient conditions, MnCO₃ crystallizes with the calcite-type structure, R-3c. Santillán and Williams (2004) reported that MnCO₃ is stable in its rhombohedral calcite-type structure up to 50 GPa. However, more recently, Farfan et al. (2013) reported a possible electronic transition in rhodochrosite in the pressure interval 25–40 GPa which may be related to fine structural changes in the MnO₆ octahedra in the rhombohedral structure (Merlini et al., 2015). Evidence of a first order phase transition above \sim 40 GPa at room temperature in which MnCO₃ transforms into a CaCO₃-VI structure was reported by Boulard et al. (2015a) and confirmed by Merlini et al. (2015). Finally, Ono (2007) reported a phase transition at 50 GPa, after heating at 1500–2000 K and proposed an orthorhombic symmetry, the structure of which, however, could not be refined. To clarify the high pressure and high temperature behavior of MnCO₃, we combined *in situ* XRD using laser-heated diamond anvil cells and *ex situ* analyses using analytical TEM and XANES tomography for conditions up to \sim 75 GPa and 2200 K, the results of which are reported in this work.

MATERIALS AND METHODS

Sample Preparation

Powdered samples of rhodochrosite were loaded between two thermal insulating layers into symmetric diamond anvil cells (DAC) with 300 μ m diamonds culets. Both NaCl and KCl were used as the thermal insulators and also served as pressure calibrants using the thermal equations of state from Dorogokupets and Dewaele (2007) and Dewaele et al. (2012), respectively. Hot spots with a diameter larger than 20 μ m (FWHM) were obtained by two YAG lasers with excellent power stability aligned on both sides of the sample. The X-ray spot, spectrometer entrance and the heating laser spot were carefully aligned before the experiments. Temperatures were obtained by fitting the sample thermal emission spectrum from the central 2 \times 2 μ m² of the hotspot to the Planck's function using the wavelength range 600–900 nm. Reflective lenses were used for measurement in order to prevent any chromatic aberration (Benedetti and Loubeyre, 2004). Temperature stability was checked by measuring continuously during heating and X-ray acquisition. Uncertainties are of about 13% (Dewaele et al., 2012) on the pressure and 150 K on the temperature (Morard et al., 2008). For each run, the sample was first compressed at ambient temperature to the target pressure and then heated between 1000 and 2200 K using double-sided infrared laser heating. Because of their high stiffness, the high-pressure phase of NaCl and KCl do not guarantee hydrostatic conditions. Therefore, high temperature annealing of the sample have been performed in

order to partly reduce the contribution of deviatoric stresses which may have built up at high pressure. Samples were heated between 5 and 10 min at each temperature step. Some runs were performed with the addition of platinum black to the MnCO₃ sample in order to heat at a lower temperature.

In situ X-Ray Diffraction

Angle-dispersive XRD spectra were collected *in situ* at high pressure and high-temperature at beamline 12.2.2 of the Advanced Light Source (ALS), Lawrence Berkeley National Laboratory (LBNL), and beamline ID27 of the European Synchrotron Radiation Facility (ESRF) using a monochromatic incident X-ray beam with a wavelength of 0.4959 or 0.6199 \AA at ALS and 0.3738 \AA at ESRF. The monochromatic X-ray beam was focused to a smaller size than the laser heating spot in order to reduce both the radial and axial temperature gradients, typically: 3 \times 3 μ m at ID27 beamline and 10 \times 10 μ m at 12.2.2 beamline. The diffraction images were integrated with the Fit2d software (Hammersley et al., 1996), and the one-dimensional diffraction patterns were treated with the General Structure Analysis System (GSAS) software package (Larson and Von Dreele, 2004) using the LeBail method to identify the different phases and refine their lattice parameters.

X-Ray Absorption Near Edge Structure (XANES)

In order to constrain possible changes in the redox state of Mn, XANES spectra were collected on the recovered sample at the Mn-K edge using the nanoscale X-ray transmission microscope (nanoTXM) at the beamline 6-2c of the Stanford Synchrotron Radiation Lightsource (SSRL), SLAC National Acceleratory Laboratory. This microscope is equipped with optics optimized for photon energies ranging from \sim 5 to 14 keV, it provides a spatial resolution as high as 30 nm and a single flat field of view of 30 \times 30 μ m. Depth of focus is \sim 50 μ m. More details about the instrument can be found in Andrews et al. (2009) and Liu et al. (2011). NanoTXM is capable of nondestructive spectroscopic imaging, and the use of hard x-rays allows it to image the entire sample thickness avoiding possible contamination which could occur if special sample preparation were required. Transmission images were collected at small energy steps from the pre-edge region through the electronic edge (from 6470 to 6693 eV), enabling us to map out the oxidation state for Mn from its XANES signal.

Focused Ion Beam and Transmission Electron Microscopy

In order to be analyzed by TEM, the recovered samples were thinned to electron transparency (\sim 150 nm) with a Ga⁺ focused ion beam (FIB) operating at 30 kV and currents from 20 nA to 1 pA for final thinning. FIB milling was performed with a FEI Helios NanoLab 600i DualBeam FIB/SEM at the Stanford Nano Shared Facilities. FIB thin sections were extracted from the center of laser heated spots. Analytical TEM was carried out on the FIB thin sections in order to help with phase identification and to obtain chemical analyses on individual phases. TEM was performed with FEI Titan 80–300 operated at 300 keV,

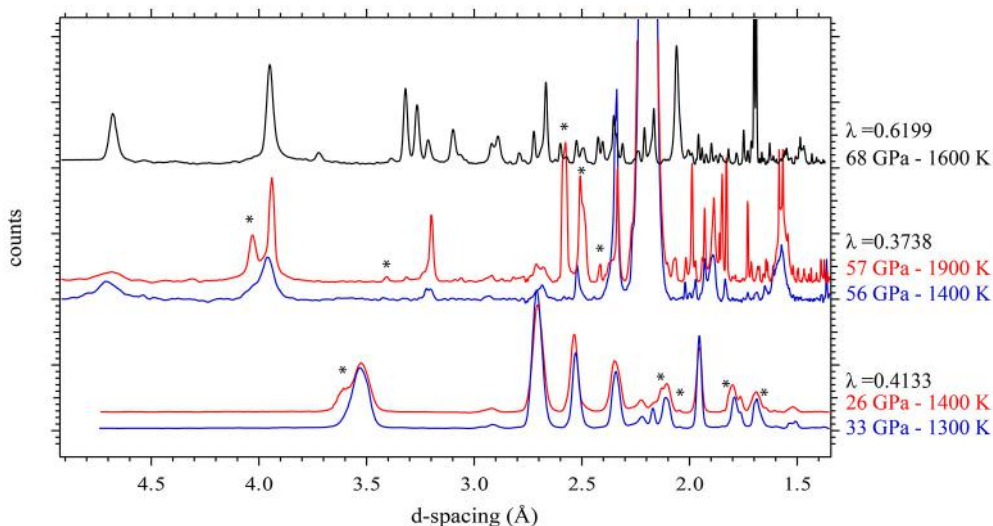


FIGURE 1 | *In situ* high P - T XRD patterns collected in the three pressure ranges: $P < 33 \text{ GPa}$, $49 < P < 65 \text{ GPa}$, $P > 65 \text{ GPa}$ at lower and higher temperature. Stars indicate the main new diffraction peaks observed upon increase in temperature.

equipped with an extra high brightness field emission gun. Semi-quantitative information on the sample chemical composition was obtained by energy dispersive X-ray spectrometry (EDXS).

RESULTS

Lower Pressure Experiments ($P < 33 \text{ GPa}$)

Figure 1 shows XRD patterns collected *in situ* at the different pressure ranges and at low or high temperature. These XRD patterns show that the rhombohedral MnCO_3 structure—rhodochrosite—is stable up to 33 GPa. For simplicity we will refer to this phase as MnCO_3 -I. When heating at relatively low temperature ($\sim 1300 \text{ K}$) only MnCO_3 -I is observed; however upon heating above 1400 K, the XRD patterns reveal the presence of another phase which does not correspond to the high pressure phase of MnCO_3 (marked by stars in Figure 1), MnO , cubic α - Mn_2O_3 (bixbyite), or Mn_3O_4 (hausmanite) manganese oxides. In a recent study, Ovsyannikov et al. (2013) reported the transformation of α - Mn_2O_3 into a perovskite-like structure (ζ - Mn_2O_3) at these pressure and temperature (P - T) conditions. Although they used a supercell in order to fit their diffraction patterns, here we found that a single cell of an orthorhombic perovskite structure can be used to index the new diffraction peaks (Figure 2 and Table 1).

Medium Pressure Experiments ($49 < P < 65 \text{ GPa}$)

Upon compressing MnCO_3 at ambient temperature and pressures above $\sim 45 \text{ GPa}$, the XRD patterns change drastically, as the rhombohedral MnCO_3 -I transforms into the high-pressure phase MnCO_3 -II which is triclinic. This is in good agreement with previous high pressure studies performed at ambient

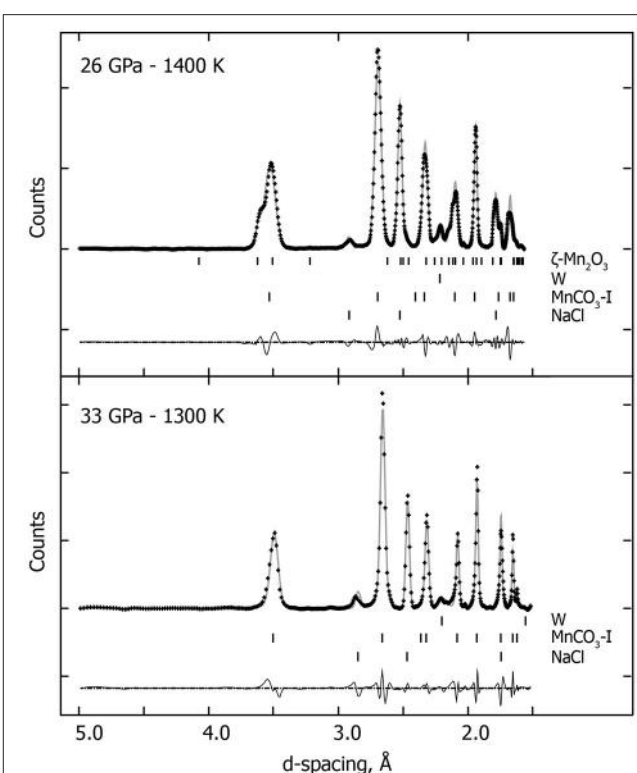


FIGURE 2 | *In situ* high P - T XRD patterns. Crosses represent observed data (background subtracted), and the gray solid lines show the profile refinements. Residuals between experiment and fit are shown below the diffraction pattern. At 33 GPa and 1300 K, we used an assemblage of NaCl and W (gasket) and rhodochrosite (MnCO_3 -I). At higher temperature (26 GPa and 1400 K), we used the same assemblage with an additional high pressure manganese oxide polymorph (ζ - Mn_2O_3).

TABLE 1 | Crystallographic data.

P-T conditions	Lattice parameters			
	$\text{MnCO}_3\text{-I}$ a, c (Å)	$V(\text{\AA}^3)$	$\zeta\text{-Mn}_2\text{O}_3$ a, b, c (Å)	
33 GPa—1300 K	4.6368(5) 14.1876(33)	264.17(5)		
26 GPa—1400 K	4.6667(4) 14.4798(14)	273.10(25)	4.9935(23) 5.2481(16) 7.0401(30)	
	$\text{MnCO}_3\text{-II}$ a, b, c (Å)	α, β, γ	$\delta\text{-Mn}_2\text{O}_3$ a, b, c (Å)	
56 GPa—1400 K	2.8116(3) 4.8083(6) 5.4533(7)	101.79(1) 91.95(1) 88.45(1)	72.11(1)	
57 GPa—1900 K	2.7759(6) 4.7620(8) 5.4408(1)	102.42(2) 92.04(2) 87.92(2)	70.16(2)	2.7137(6) 8.0501(2) 6.3973(3)

temperature (Boulard et al., 2015a; Merlini et al., 2015). Similar to the lower pressure results, when heated at moderately low temperature, i.e., 1300 K at 33 GPa, a single carbonate phase, $\text{MnCO}_3\text{-II}$ is observed (Figure 1). However upon heating above 1400 K, new XRD peaks appear which can be indexed to the high pressure manganese oxide phase, $\delta\text{-Mn}_2\text{O}_3$, with a post-perovskite like structure described by Santillán et al. (2006). We identified this assemblage ($\text{MnCO}_3\text{-II} + \delta\text{-Mn}_2\text{O}_3$) up to 57 GPa and 2100 K (Figure 3 and Table 1). When recovered to ambient pressure and temperature, XRD patterns show the back transformation of $\text{MnCO}_3\text{-II}$ into $\text{MnCO}_3\text{-I}$ as well as $\delta\text{-Mn}_2\text{O}_3$ into the cubic $\alpha\text{-Mn}_2\text{O}_3$ phase.

Highest Pressure Experiments ($P > 65 \text{ GPa}$)

Above 65 GPa, new changes in the diffraction patterns are observed as a new phase appears together with the previous assemblage (Figure 1). Above 70 GPa, the diffraction peaks from $\delta\text{-Mn}_2\text{O}_3$ disappear and we observed an assemblage of $\text{MnCO}_3\text{-II}$ plus this new phase (Figure 4). This new phase may correspond to a new high-pressure polymorph of Mn_2O_3 . To our knowledge, no experimental studies exist on Mn_2O_3 at such high pressure and temperature conditions and theoretical studies support the stability of $\delta\text{-Mn}_2\text{O}_3$ up to at least 120 GPa (Xu et al., 2015). Therefore, the composition and structure of this new phase remain unresolved. After transformation 68 GPa and 1600 K, diffraction patterns were collected on the sample once recovered to ambient pressure and temperature, and $\text{MnCO}_3\text{-I}$, $\alpha\text{-Mn}_2\text{O}_3$ as well as another unknown phase were observed.

Further, *ex situ* analyses were performed on these samples to understand the highest pressure phase assemblage. XANES imaging at the manganese K-edge (6545 eV) was conducted in order to get insight on the manganese oxidation state. These measurements were collected in the heating spot, the area that has

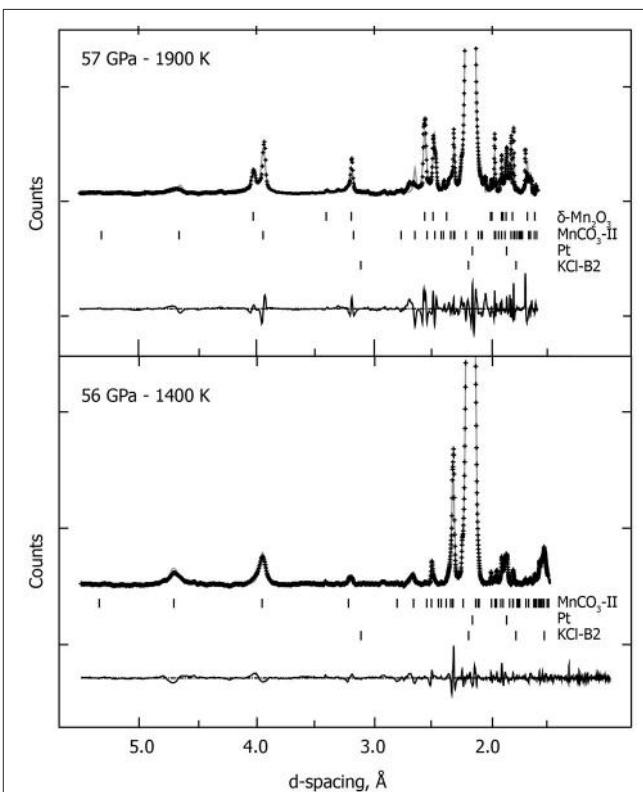
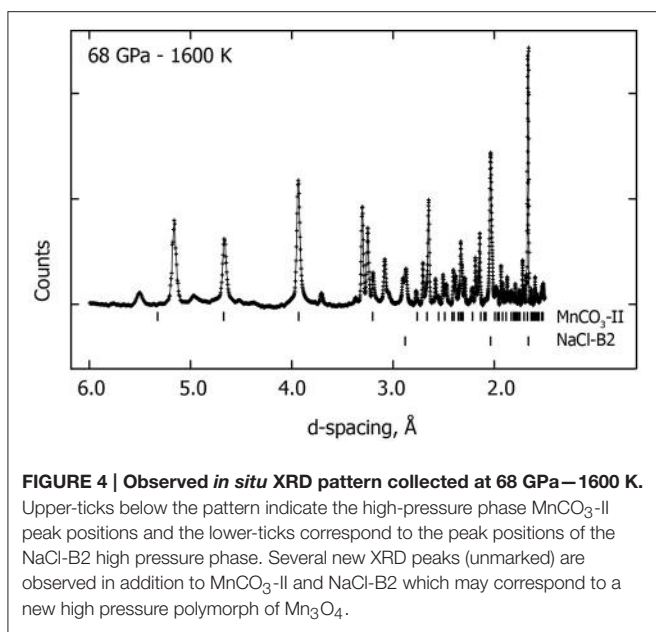
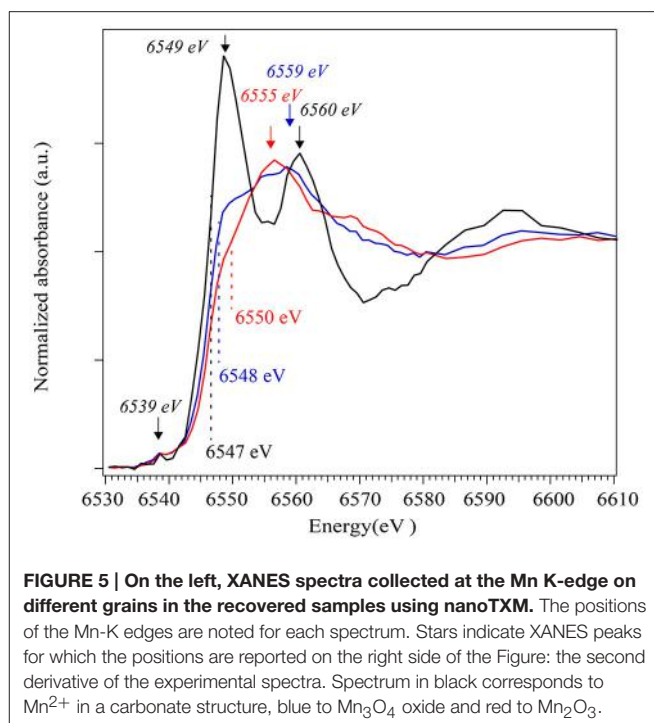


FIGURE 3 | *In situ* high P-T XRD patterns collected at 56 GPa—1400 K and at 57 GPa—1900 K. We used the following assemblage: the high-pressure polymorph $\text{MnCO}_3\text{-II}$, KCl-B2 high pressure polymorph and W (gasket), and the post-perovskite like high pressure polymorph of the manganese oxide ($\delta\text{-Mn}_2\text{O}_3$). Crosses represent observed data (background subtracted), and the solid lines show the profile refinements. Residuals between experiment and fit are shown below the diffraction pattern.



been laser heated during the *in situ* experiments, directly on the sample that had been recovered from 68 GPa and 1600 K without special sample preparation. The results indicate three areas with different absorption contrast characterized by distinct Mn-K edge spectra. The background corrected and normalized spectra are presented in Figure 5. A spectrum from the first area (shown in black in Figure 5) reveals a peak at 6549 eV, another at 6560 eV as well as a weak pre-edge peak at 6539 eV. This spectrum is consistent with Mn^{2+} in octahedral sites as in a rhodochrosite MnCO_3 -I structure. In the spectrum for the second area (show in blue in Figure 5), one can see a broad peak at \sim 6559 eV and a shift to higher energy of the Mn K-edge (from 6547 to 6548 eV) which indicate an increase in Mn oxidation state. This spectrum is consistent with the Mn-K edge for Mn_3O_4 (Ressler et al., 1999; Jiao and Frei, 2010). Finally the spectrum collected on the third area (in red in Figure 5) show an Mn-K edge at 6550 eV and broad peak at 6555 eV which is consistent with Mn_2O_3 (Nam et al., 2007; Jiao and Frei, 2010).

A thin section of the same sample was then prepared by FIB in order to perform analytical TEM. A global high-angle annular dark-field imaging scanning transmission electron microscopy (HAADF-STEM) image of the thin section is presented in Figure 6A. In this image, the grayscale is related to the mean Z of each phase. It highlights the presence of four different phases: a manganese and carbon rich phase that corresponds to the carbonate (Figure 6B); a carbon rich phase (Figure 6C) that appears in dark in the STEM image indicating the presence of a reduced form of carbon that could not be detected by *in situ* XRD; finally TEM-XEDS analyses confirm the presence of two manganese oxides (Figures 6D,E). Semi-quantitative analyses show that the experimental spectrum in Figure 6D has an O/Mn ratio of 1.68 while that from the spectrum in Figure 6E is 1.22. These numbers are consistent with the elemental ratio expected in Mn_2O_3 (theoretical O/Mn = 1.5) and Mn_3O_4 (theoretical O/Mn=1.33), respectively.



DISCUSSION

New High Pressure and Temperature Phase Diagram

The run products for all high-temperature experiments are summarized in Figure 7. The Mn_2O_3 phase diagram from Ovsyannikov et al. (2013) is also represented. To our knowledge, no study exists on manganese oxides above 25 GPa at high temperature. The *P-T* conditions of the different polymorphs α - Mn_2O_3 , ζ - Mn_2O_3 , and δ - Mn_2O_3 (respectively red, yellow, and purple *P-T* field in Figure 6) reported in the present study are in very good agreement with Ovsyannikov et al. (2013). In addition, our study shows that δ - Mn_2O_3 is stable up to at least 75 GPa–1600 K. This is in good agreement with theoretical prediction of the stability of the post-perovskite structure δ - Mn_2O_3 up to 120 GPa from Xu et al. (2015). Above 65 GPa–1700 K, we report evidences of an additional manganese oxide: a high pressure polymorph of Mn_3O_4 . The presence of a fourth phase Mn_3O_4 as observed by TEM and XANES imaging is in agreement with the *in situ* diffraction which show an unknown structure in addition to MnCO_3 -II and δ - Mn_2O_3 : a new high-pressure polymorph of Mn_3O_4 which does not back transform into the tetragonal hausmanite (Mn_3O_4). The structure of this polymorph is beyond the scope of this study and was not resolved. Further, studies on Mn_3O_4 at high pressure would be necessary in order to elucidate this new phase.

The phase transition boundary $\text{MnCO}_3 \rightarrow \text{MnCO}_3$ -II is indicated in gray on Figure 7. MnCO_3 -I is observed up to 33 GPa–1300 K (circles in Figure 7). The high pressure polymorph MnCO_3 -II appears for *P-T* condition above 49 GPa–1500 K (squares in Figure 7). This is in good agreement with previous

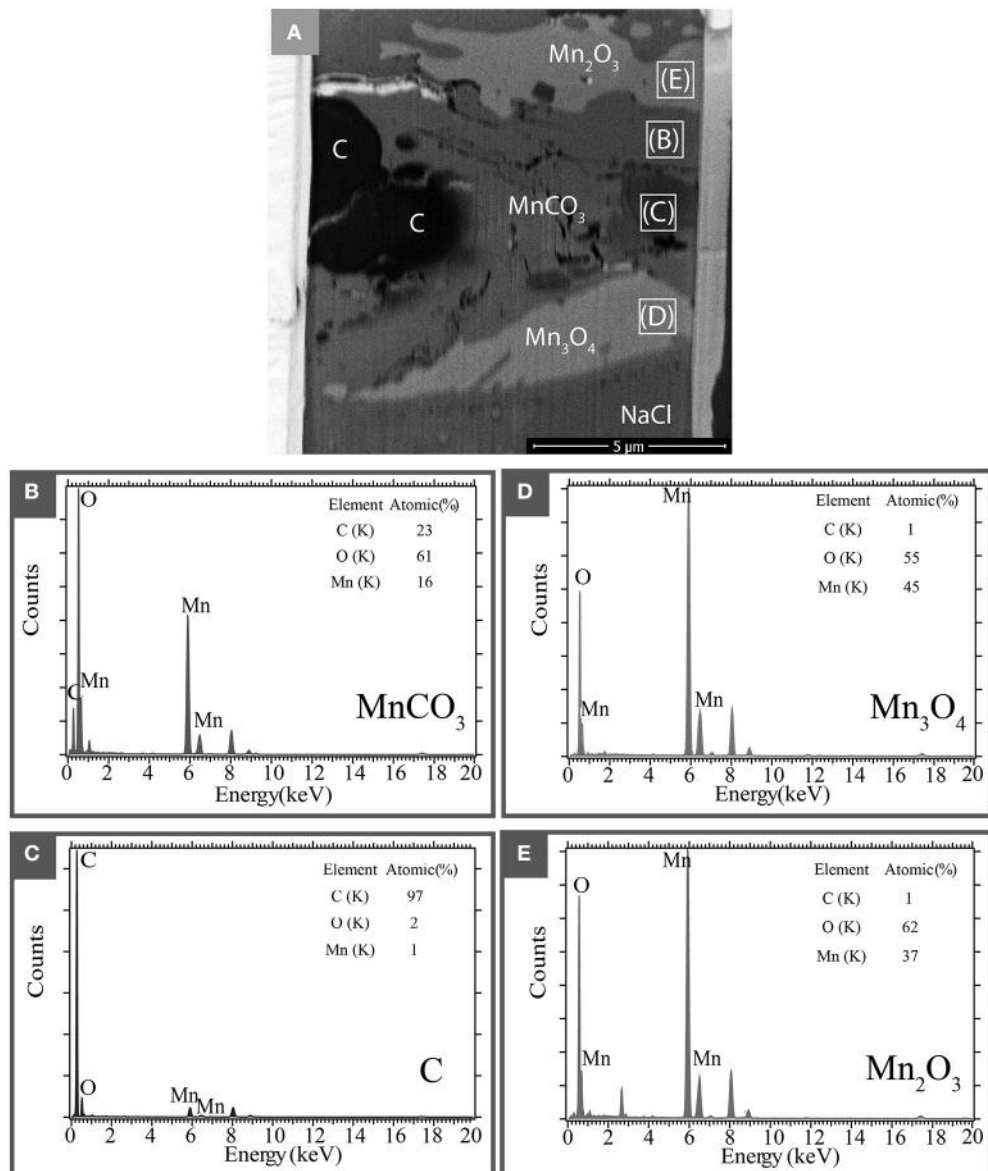
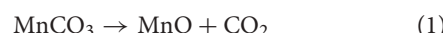


FIGURE 6 | Analytical TEM electron microscopy of a recovered sample after transformation at 68 GPa and 1600 K. (A) STEM picture of the FIB thin section. Four different phases are identified: a carbonate area marked as MnCO_3 , reduced carbon area marked by C and manganese oxides Mn_2O_3 and Mn_3O_4 . **(B–E)** show the XEDS measurements (spectra and quantification) collected in these different areas.

studies performed at room temperature that reported the phase transition of rhodochrosite into the triclinic structure MnCO_3 -II at pressure above ~40 GPa (Boulard et al., 2015a and Merlini et al., 2015). Here, we show that MnCO_3 -II is also observed at high temperature and up to 75 GPa—1700 K. This phase is isostructural to CaCO_3 -VI which is metastable for the calcium composition (CaCO_3) and only observed at room temperature. We did not observe any evidence of the aragonite or post-aragonite structures upon heating. In fact, Oganov et al. (2006) showed that the several metastable structures of CaCO_3 are similar in energy with aragonite and are almost as stable as aragonite and post-aragonite at these conditions. Due to the large cation site in aragonite it is not

surprising that MnCO_3 adopts the CaCO_3 -VI structure instead of aragonite.

Our study show that the carbonate as well as its high pressure polymorph MnCO_3 -II are stable for temperature below 1400 K. Above 1400 K, we observed the decomposition of MnCO_3 and the reduction of carbon corresponding to the two reactions:



The persistence of a carbonate phase in our experiments may indicate that the decomposition reaction was not complete by the time we stopped laser-heating.

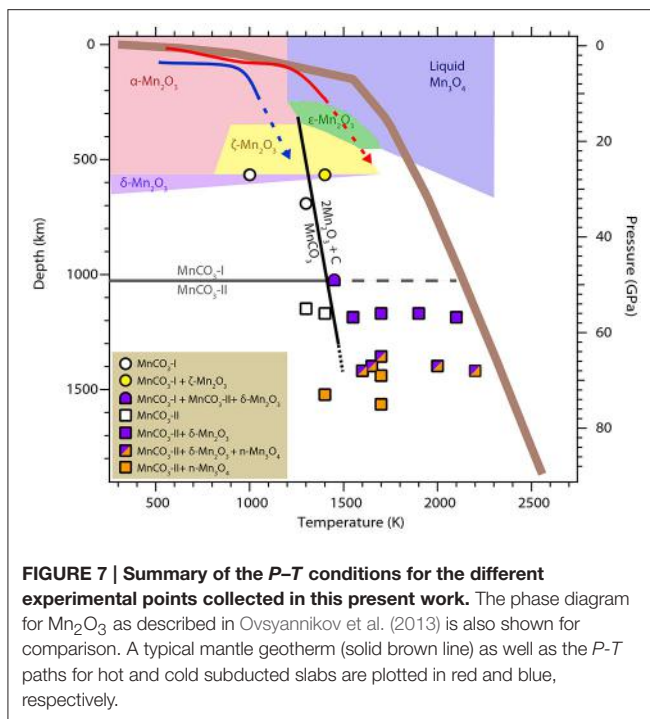


FIGURE 7 | Summary of the P - T conditions for the different experimental points collected in this present work. The phase diagram for Mn_2O_3 as described in Ovsyannikov et al. (2013) is also shown for comparison. A typical mantle geotherm (solid brown line) as well as the P - T paths for hot and cold subducted slabs are plotted in red and blue, respectively.

The corresponding decomposition line is shown in black in **Figure 7**. Liu et al. (2001) also reported the decomposition of MnCO_3 and formation of diamond at 6–8 GPa and temperatures above 2300 K. According to the Mn_2O_3 phase diagram represented in **Figure 6**, their P - T conditions falls into the liquid area (in blue in **Figure 7**) for which Ovsyannikov et al. (2013) reported that Mn_2O_3 is irreversibly reduced into Mn_3O_4 . This is in good agreement with their observations of a Mn_3O_4 , C and O_2 assemblage. Finally, Ono (2007) reported experiments at 54 GP and 1500/2000 K in which he observed new diffraction peaks and proposed a new structure for MnCO_3 . We found very good agreement between our diffraction patterns at these P - T conditions and his, however our *ex situ* analyses indicate the presence of oxides as well as carbonate at these temperatures and part of these new diffraction peaks actually belong to the manganese oxide.

Implications for the Deep Carbon Cycle

Carbon in the Earth may exist in various forms including carbides, diamond, graphite, lonsdaleite, hydrocarbons, CO_2 , and carbonates depending on the oxygen fugacity and P - T conditions (Dasgupta and Hirschmann, 2010; Hazen et al., 2013; Jones et al., 2016). Although it is generally thought that the conditions of the Earth's deep interior and of the subducting slab materials may be not compatible with the stability of carbonates or carbonate-rich liquid (Anzolini et al., 2016; Thomson et al., 2016), the observation of carbonate inclusions in diamonds potentially brought up to the Earth's surface from the deep mantle indicates that carbonates can exist at least locally in the mantle (e.g., Stachel et al., 1998, 2000; Leost et al., 2003; Bulanova et al., 2010). Carbonate compositions at the surface of the planet are

mainly calcite and dolomite. When transported into the deep Earth via subducting slabs, dolomite breaks down into aragonite and magnesite at a depth of around 250 km (e.g., Hammouda et al., 2011). These two end members display very different behavior at high pressure: magnesite is now known to be stable down to about 2000 km depth, below which it transforms into a tetrahedrally coordinated CO_4 structure (Boulard et al., 2015b) while aragonite undergoes a phase transition into a CO_3 -bearing post-aragonite structure at about 1000 km depth that remains stable down to core mantle boundary conditions (Ono et al., 2007).

Together with previous studies on MnCO_3 -II, we show that metastable structures of CaCO_3 such as CaCO_3 -VI may play an important role in the transport of carbon into our planet's deep interior as it can host intermediate sized cations such as Mn^{2+} in contrast to aragonite and post-aragonite structures. Possible miscibility between CaCO_3 and other smaller cation-bearing components, such as MnCO_3 , or MgCO_3 and FeCO_3 may make the CaCO_3 -VI structure more abundant in the planet's deep interior than previously thought. One should note that MnCO_3 and CaCO_3 display miscibility gap at ambient conditions (de Capitani and Peters, 1981) and the possibility of a miscibility in CaCO_3 -VI structure merits further investigation. However, as the slabs undergo subduction and reach temperatures closer to the mantle geotherm (brown line in **Figure 6**), this phase will decompose into manganese oxides and diamonds. Reduction of carbon into diamond at high P - T was also reported for other 3d metal-bearing carbonates such as FeCO_3 and $(\text{Mg},\text{Fe})\text{CO}_3$ (Boulard et al., 2012). However, formation of diamond in FeCO_3 and $(\text{Mg},\text{Fe})\text{CO}_3$ system is due to the fact that Fe is mainly incorporated as Fe^{3+} in their high-pressure polymorphs leading to partial reduction of carbon and a coexistence of oxidized and reduced carbon. Here, we show that there is no evidence of a change in the oxidation state of manganese in MnCO_3 -II. The redox reaction (2) that would lead to diamond formation in the subducted slabs is in fact due to decomposition of MnCO_3 into MnO and CO_2 oxides. It therefore seems probable that even if miscibility between MnCO_3 , FeCO_3 , MgCO_3 in the CaCO_3 -VI structure takes place, this structure will only be present as an intermediate stage of subduction. The high-pressure polymorph of FeCO_3 and $(\text{Mg},\text{Fe})\text{CO}_3$ would likely represent the main oxidized carbon host at lower mantle conditions.

CONCLUSIONS

Our study brings new insight into the phase diagram of MnCO_3 at high pressure and temperature. Rhombohedral MnCO_3 -I as well as its high pressure polymorph MnCO_3 -II are stable at temperatures up to 1400 K. At higher temperatures however, both MnCO_3 -I and MnCO_3 -II break down into oxides and redox reactions take place which lead to the formation of manganese oxides such as Mn_2O_3 and Mn_3O_4 and diamond. These reactions occur at P - T conditions close to the mantle geotherm. The CaCO_3 -VI structure that can host small cations at relatively high pressures can only be encountered at an intermediate stage of subduction, thus, the high pressure tetrahedral carbonate phase

of FeCO₃ and (Mg,Fe)CO₃ would represent the main mineral host for oxidized carbon in the deep Earth.

AUTHOR CONTRIBUTIONS

EB and WM designed the research project; EB, YL, AK, MR, JS, GM, and MM performed experiments and analysis; EB and YL analyzed data; and EB and WM wrote the paper with input from all co-authors.

REFERENCES

- Andrews, J. C., Brennan, S., Pianetta, P., Ishii, H., Gelb, J., Feser, M., et al. (2009). Full-field transmission x-ray microscopy at SSRL. *J. Phys.* 186:12002. doi: 10.1088/1742-6596/186/1/012002
- Anzolini, C., Angel, R. J., Merlini, M., Derzsi, M., Tokár, K., Milani, S., et al. (2016). Depth of formation of CaSiO₃-walstromite included in super-deep diamonds. *Lithos*. 265, 138–147. doi: 10.1016/j.lithos.2016.09.025
- Benedetti, L. R., and Loubeyre, P. (2004). Temperature gradients, wavelength-dependent emissivity, and accuracy of high and very-high temperatures measured in the laser-heated diamond cell. *High Press. Res.* 24, 423–445. doi: 10.1080/08957950412331331718
- Boulard, E., Goncharov, A. F., Blanchard, M., and Mao, W. L. (2015a). Pressure-induced phase transition in MnCO₃ and its implications on the deep carbon cycle. *J. Geophys. Res. Solid Earth* 120, 4069–4079. doi: 10.1002/2015JB011901
- Boulard, E., Menguy, N., Auzende, A. L., Benzerara, K., Bureau, H., Antonangeli, D., et al. (2012). Experimental investigation of the stability of Fe-rich carbonates in the lower mantle. *J. Geophys. Res.* 117, B02208. doi: 10.1029/2011jb008733
- Boulard, E., Pan, D., Galli, G., Liu, Z., and Mao, W. L. (2015b). Tetrahedrally coordinated carbonates in Earth's lower mantle. *Nat. Commun.* 6, 6311. doi: 10.1038/ncomms7311
- Bulanova, G. P., Walter, M. J., Smith, C. B., Kohn, S. C., Armstrong, L. S., Blundy, J., et al. (2010). Mineral inclusions in sublithospheric diamonds from Collier 4 kimberlite pipe, Juina, Brazil: subducted protoliths, carbonated melts and primary kimberlite magmatism. *Contrib. Miner. Petrol.* 160, 489–510. doi: 10.1007/s00410-010-0490-6
- Dasgupta, R., and Hirschmann, M. M. (2010). The deep carbon cycle and melting in Earth's interior. *Earth Planet. Sci. Lett.* 298, 1–13. doi: 10.1016/j.epsl.2010.06.039
- de Capitani, C., and Peters, T. (1981). The solvus in the System MnCO₃-CaCO₃. *Contrib. Miner. Petrol.* 76, 394–400. doi: 10.1007/bf00371481
- Dorogokupets, P. I., and Dewaele, A. (2007). Equations of state of MgO, Au, Pt, NaCl-B1, and NaCl-B2: internally consistent high-temperature pressure scales. *High Pressure Res.* 27, 431–446. doi: 10.1080/08957950701659700
- Farfan, G. A., Boulard, E., Wang, S., and Mao, W. L. (2013). Bonding and electronic changes in rhodochrosite at high pressure. *Am. Mineral.* 98, 1817–1823. doi: 10.2138/am.2013.4497
- Dewaele, A., Belonoshko, A., Garbarino, G., Occelli, F., Bouvier, P., Hanfland, M., et al. (2012). High-pressure–high-temperature equation of state of KCl and KBr. *Phys. Rev.* 85, 1–7. doi: 10.1103/physrevb.85.214105
- Hammersley, A. P., Svensson, S. O., Hanfland, M., Fitch, A. N., and Hausermann, D. (1996). Two-dimensional detector software: from real detector to idealised image or two-theta scan. *High Press. Res.* 14, 235–248.
- Hammouda, T., Andrault, D., Koga, K., Katsura, T., and Martin, A. M. (2011). Ordering in double carbonates and implications for processes at subduction zones. *Contrib. Miner. Petrol.* 161, 439–450. doi: 10.1007/s00410-010-0541-z
- Hazen, R. M., Downs, R. T., Jones, A. P., and Kah, L. (2013). Carbon Mineralogy and Crystal Chemistry. *Rev. Mineral. Geochem.* 75, 7–46. doi: 10.2138/rmg.2013.75.2
- Jiao, F., and Frei, H. (2010). Nanostructured manganese oxide clusters supported on mesoporous silica as efficient oxygen-evolving catalysts. *Chem. Commun.* 46, 2920–2922. doi: 10.1039/b921820c
- Jones, A. P., McMillan, P. F., Salzmann, C. G., Alvaro, M., Nestola, F., Prencipe, M., et al. (2016). Structural characterization of natural diamond shocked To 60GPa; implications for earth and planetary systems. *Lithos*. 265, 214–221. doi: 10.1016/j.lithos.2016.09.023
- Larson, A. C., and Von Dreele, R. B. (2004). *General Structure Analysis System (GSAS)*. Los Alamos National Laboratory Report LAUR, 86–748.
- Leost, I., Stachel, T., Brey, G. P., Harris, J. W., and Ryabchikov, I. D. (2003). Diamond formation and source carbonation: mineral associations in diamonds from Namibia. *Contrib. Miner. Petrol.* 145, 15–24. doi: 10.1007/s00410-003-0442-5
- Liu, L., Lin, C., and Yang, Y. (2001). Formation of diamond by decarbonation of MnCO₃. *Solid State Commun.* 118, 195–198. doi: 10.1016/s0038-1098(01)00068-0
- Liu, Y., Andrews, J. C., Wang, J., Meirer, F., Zhu, P., Wu, Z., et al. (2011). Phase retrieval using polychromatic illumination for transmission X-ray microscopy. *Opt. Express* 19, 540–545. doi: 10.1364/OE.19.000540
- Merlini, M., Hanfland, M., and Gemmi, M. (2015). The MnCO₃ -II high-pressure polymorph of rhodocrosite. *Am. Mineral.* 100, 2625–2629. doi: 10.2138/am-2015-5320
- Morard, G., Andrault, D., Guignot, N., Sanloup, C., Mezouar, M., Petitgirard, S., et al. (2008). *In situ* determination of Fe-Fe3S phase diagram and liquid structural properties up to 65 GPa. *Earth Planet. Sci. Lett.* 272, 620–626. doi: 10.1016/j.epsl.2008.05.028
- Nam, K., Kim, M. G., and Kim, K. (2007). *In Situ* Mn K-edge X-ray absorption spectroscopy studies of electrodeposited manganese oxide films for electrochemical capacitors. *J. Phys. Chem. C* 111, 749–758. doi: 10.1021/jp063130o
- Oganov, A. R., Glass, C. W., and Ono, S. (2006). High-pressure phases of CaCO₃. Crystal structure prediction and experiment. *Earth Planet. Sci. Lett.* 241, 95–103. doi: 10.1016/j.epsl.2005.10.014
- Ono, S. (2007). High-pressure phase transformation in MnCO₃. a synchrotron XRD study. *Mineral. Mag.* 71, 105–111. doi: 10.1180/minmag.2007.071.1.105
- Ono, S., Kikegawa, T., and Ohishi, Y. (2007). High-pressure transition of CaCO₃. *Am. Mineral.* 92, 1246–1249. doi: 10.2138/am.2007.2649
- Ovsyannikov, S. V., Abakumov, A. M., Tsirlin, A. A., Schnelle, W., Egoavil, R., Verbeeck, J., et al. (2013). Perovskite-like Mn₂O₃. A path to new manganites. *Angew. Chem. Int. Ed. Eng.* 52, 1494–1498. doi: 10.1002/anie.2012020553
- Ressler, T., Brock, S. L., Wong, J., and Suib, S. L. (1999). Multiple-Scattering EXAFS analysis of tetraalkylammonium manganese oxide colloids. *J. Phys. Chem. B* 103, 6407–6420. doi: 10.1021/jp9835972
- Santillán, J., Shim, S. H., Shen, G., and Prakapenka, B. (2006). High-pressure phase transition in Mn₂O₃: application for the crystal structure and preferred orientation of the CaIrO₃ type. *Geophys. Res. Lett.* 33, 1–5. doi: 10.1029/2006GL026423
- Santillán, J., and Williams, Q. (2004). A high-pressure infrared and X-ray study of FeCO₃ and MnCO₃: comparison with CaMg(CO₃)₂-dolomite. *Phys. Earth Planet. Interiors* 143–144, 291–304. doi: 10.1016/j.pepi.2003.06.007
- Shatskiy, A. F., Litasov, K. D., and Palyanov, Y. N. (2015). Phase relations in carbonate systems at pressures and temperatures of lithospheric

ACKNOWLEDGMENTS

EB and WM acknowledge support from the Deep Carbon Observatory. WM is supported by NSF-EAR-1055454. Portion of the XRD work was performed at the high-pressure beamline 12.2.2, ALS which is supported by the DOE-BES under contract DE-AC02-05CH11231. We thank J. Yan, J. Knight, and A. MacDowell for their assistance with XRD experiments at ALS. We also thank M. Scott for providing the rhodochrosite sample.

- mantle: review of experimental data. *Russ. Geol. Geophys.* 56, 113–142. doi: 10.1016/j.rgg.2015.01.007
- Stachel, T., Brey, G. P., and Harris, J. W. (2000). Kankan diamonds (Guinea) I: from the lithosphere down to the transition zone. *Contrib. Mineral. Petrol.* 140, 1–15. doi: 10.1007/s004100000173
- Stachel, T., Harris, J. W., and Brey, G. P. (1998). Rare and unusual mineral inclusions in diamonds from Mwadui, Tanzani. *Contrib. Mineral. Petrol.* 132, 34–47. doi: 10.1007/s004100050403
- Thomson, A. R., Walter, M. J., Kohn, S. C., and Brooker, R. A. (2016). Slab melting as a barrier to deep carbon subduction. *Nature* 529, 76–79. doi: 10.1038/nature16174
- Wang, Q., Grau-Crespo, R., and de Leeuw, N. H. (2011). Mixing thermodynamics of the calcite-structured (Mn,Ca)CO₃ solid solution: a computer simulation study. *J. Phys. Chem. B* 115, 13854–13861. doi: 10.1021/jp200378q
- Xu, C., Xu, B., Yang, Y., Dong, H., Oganov, A. R., Wang, S., et al. (2015). Prediction of a stable post-post-perovskite structure from first principles. *Phys. Rev. B* 91, 1–5. doi: 10.1103/physrevb.91.020101
- Zhang, J., Martinez, I., Guyot, F., and Reeder, R. J. (1998). Effects of Mg–Fe 2+ substitution in calcite-structure carbonates: thermoelastic properties. *Am. Mineral.* 83, 280–287.
- Zhang, J., and Reeder, R. J. (1999). Comparative compressibilities of calcite-structure carbonates: deviations from empirical relations. *Am. Mineral.* 84, 861–870.

Conflict of Interest Statement: The authors declare that the research was conducted in the absence of any commercial or financial relationships that could be construed as a potential conflict of interest.

Copyright © 2016 Boulard, Liu, Koh, Reagan, Stodolna, Morard, Mezouar and Mao. This is an open-access article distributed under the terms of the Creative Commons Attribution License (CC BY). The use, distribution or reproduction in other forums is permitted, provided the original author(s) or licensor are credited and that the original publication in this journal is cited, in accordance with accepted academic practice. No use, distribution or reproduction is permitted which does not comply with these terms.



Structure and Dynamics of Confined C-O-H Fluids Relevant to the Subsurface: Application of Magnetic Resonance, Neutron Scattering, and Molecular Dynamics Simulations

OPEN ACCESS

Edited by:

Alycia Danielle Cox,
Montana Tech of the University of
Montana, United States

Reviewed by:

Dennis D. Klug,
National Research Council Canada
(NRC-CNRC), Canada
Alfred Delville,
UMR7374 Interfaces Confinement
Matériaux et Nanostructures (ICMN),
France

***Correspondence:**

Siddharth S. Gautam
gautam.25@osu.edu

†Present Address:

Salim Ok,
Petroleum Research Center, Kuwait
Institute for Scientific Research, Safat,
Kuwait

Specialty section:

This article was submitted to
Geochemistry,
a section of the journal
Frontiers in Earth Science

Received: 14 January 2017

Accepted: 19 May 2017

Published: 06 June 2017

Citation:

Gautam SS, Ok S and Cole DR (2017)
Structure and Dynamics of Confined
C-O-H Fluids Relevant to the
Subsurface: Application of Magnetic
Resonance, Neutron Scattering, and
Molecular Dynamics Simulations.
Front. Earth Sci. 5:43.
doi: 10.3389/feart.2017.00043

Siddharth S. Gautam^{1*}, **Salim Ok**^{1,2†} and **David R. Cole**¹

¹ School of Earth Sciences, The Ohio State University, Columbus, OH, United States, ² Petroleum Research Center, Kuwait Institute for Scientific Research, Safat, Kuwait

Geo-fluids consisting of C-O-H volatiles are the main mode of transport of mass and energy throughout the lithosphere and are commonly found confined in pores, grain boundaries and fractures. The confinement of these fluids by porous media at the length scales of a few nanometers gives rise to numerous physical and chemical properties that deviate from the bulk behavior. Studying the structural and dynamical properties of these confined fluids at the length and time scales of nanometers and picoseconds, respectively forms an important component of understanding their behavior. To study confined fluids, non-destructive penetrative probes are needed. Nuclear magnetic resonance (NMR) by virtue of its ability to monitor longitudinal and transverse magnetization relaxations of spins, chemical shifts brought about by the chemical environment of a nucleus, and measuring diffusion coefficient provides a good opportunity to study dynamics and chemical structure at the molecular length and time scales. Another technique that gives insights into the dynamics and structure at these length and time scales is neutron scattering (NS). This is because the wavelength and energies of cold and thermal neutrons used in scattering experiments are in the same range as the spatial features and energies involved in the dynamical processes occurring at the molecular level. Molecular Dynamics (MD) simulations on the other hand help with the interpretation of the NMR and NS data. Simulations can also supplement the experiments by calculating quantities not easily accessible to experiments. Thus, using NMR, NS, and MD simulations in conjunction, a complete description of the molecular structure and dynamics of confined geo-fluids can be obtained. In the current review, our aim is to show how a synergistic use of these three techniques has helped shed light on the complex behavior of water, CO₂, and low molecular weight hydrocarbons. After summarizing the theoretical backgrounds of the techniques, we will discuss some recent examples of the use of NMR, NS, and MD simulations to the study of confined fluids.

Keywords: confined fluids, porous materials, diffusion, nuclear magnetic resonance, neutron scattering, MD simulations, relaxation

INTRODUCTION

All over Earth's crust, fluids have a dominating role in transporting Earth's energy and mineral reserves (Liebscher and Heinrich, 2007). Fluids with volatile carbon, hydrogen and oxygen (C-H-O) species are found in the lithosphere in large proportions besides different electrolytes and silica (Cole et al., 2013). The effects of coupled reactive-transport processes seen in geological systems vary by the properties and reactivity of these crustal fluids over wide ranges of different parameters including temperature, pressure and fluid composition. The comparative strengths of complicated molecular scale interactions in geologic fluids, and the changes in those interactions with temperature, pressure, and fluid composition, are vital keys for the observed fluid properties. Complicated intermolecular interactions of C-H-O result in their distinctive thermophysical behaviors, such as large deviations in the volumetric properties from ideality, vapor-liquid equilibria, and critical phenomena.

A fundamental goal in geochemistry is to form a comprehensive and fundamental understanding of the thermophysical properties, structures, dynamics, and reactivity of complex geologic fluids and molecules (water and other C-H-O-N-S fluids, electrolytes, and organic-biological molecules) at different length scales. Hydrocarbons, such as methane and ethane, CO_2 , and aqueous solutions can fill the pores or fractures of numerous types of complex heterogeneous Earth materials present in the systems outlined above. This accessible porosity within the solids has a range of length scales (d as pore diameter or fracture aperture) including micro-, meso-, and macroporous regimes ($d < 2.0 \text{ nm}$, $2.0 < d < 50 \text{ nm}$, and $d > 50 \text{ nm}$, respectively, as defined by IUPAC). There are a number of factors determining the way fluids, and with them reactants and products of intrapore alterations move into and through these nano-environments, wet, and finally adsorb and react with the solid surfaces. Usually, the behaviors of confined fluids are affected by the size, shape, and topology of confinement and by the competition of liquid-liquid and liquid-matrix interactions upon getting closer to the surfaces (Cole et al., 2004; Vogel, 2010). Fundamental understanding requires detailed characterization of these confinement effects. There is a common consideration that the combined structure and behaviors of bulk fluids are varied by solid substrates, confinement between two mineral surfaces, or in narrow pores due to the interplay of the length scales of the fluid and the confinement length scale (Gelb et al., 1999).

Various interactions of guest molecules, such as alkanes, CO_2 , and water with the pore walls have long been an area of research. The continued research efforts cover not only experimental but also computational studies for a better understanding of the confined systems to explore new applications in various areas ranging from catalytic conversion to selective adsorption (Kärger et al., 2014). In attempting to analyze the nanoconfined fluid behavior, there are two important aspects: detailed characterization of the nanoporous host material and deviation of confined fluid behavior from that of the bulk. In the current review article, we will summarize different aspects of confinement effects on the fluid behavior. First, we will give

a brief introduction on different nanoporous materials. Next, we describe three techniques that contribute significantly to our ability to probe fluid-solid interactions in nanoporous media or at surfaces: nuclear magnetic resonance (NMR) spectroscopy, neutron scattering (NS), and molecular dynamics (MD) simulations. Finally, we will provide some examples of contributions to a study of fluids in confined structures as studied by these techniques.

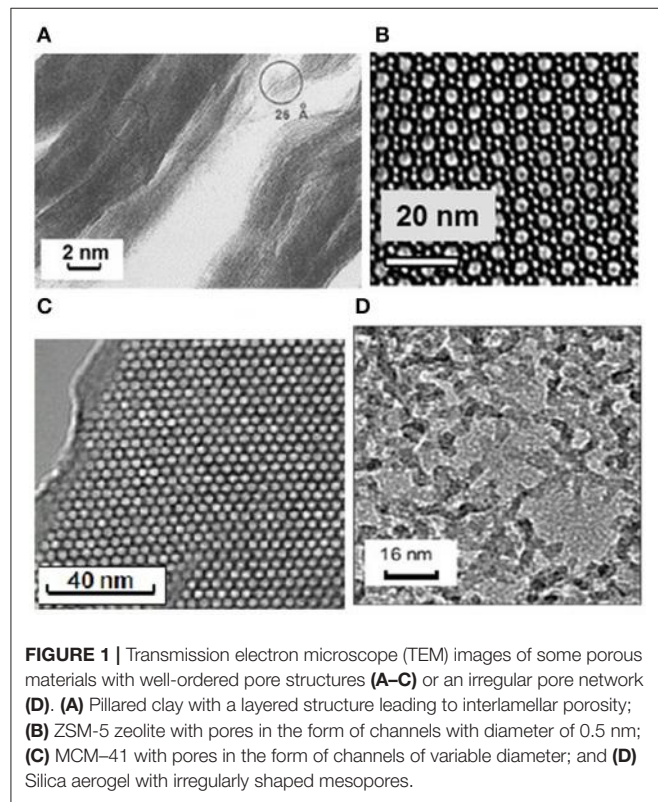
NANOPOROUS MATERIALS

Nanoporous materials can be divided into three broad groups: natural Earth materials, modified natural materials, such as select clay minerals, and engineered synthetic proxies (see Table 1). These nanoporous materials provide substrates for studying confined fluid behaviors. However, these nanoporous materials have properties, such as pore diameter, pore volume, surface chemistry, etc. that can vary or might be tuned by various ways, such as synthetic conditions or even modifications. Because of their complexity, basic characterization of the nanoporous materials in detail is required.

Among the nanoporous materials, natural clays form an important subset of porous systems with tunable properties and relatively lower surface area with respect to that of synthetic nanoporous silica-type proxies. The layered structure of the clay minerals offers the opportunity to study the interaction between different types of fluids and substrates varying in chemical and physical properties (Gupta and Bhattacharyya, 2012). Clay minerals are able to intercalate chemical species into their interlayer spaces thereby changing the layer dimensions. The layered structure of clays can be manipulated by introducing stable pillars in the interlamellar region. This leads to stability of the pore structure in pillared clays which form an ideal proxy material to study two-dimensional confinement (Cool and Vasant, 1998, see Figure 1A). In particular, kaolinite and montmorillonite clays have been used to study fluid-solid interactions at surfaces or in the interlayers. Kaolinite structure is composed of a tetrahedral silica sheet interchanging with an octahedral alumina sheet forming the 1:1 clay mineral sheet (Brigatti et al., 2013; Ok et al., 2014). Montmorillonites, an important class of clays with both swelling and shrinking abilities, are 2:1 phyllosilicates where the perfect stoichiometry is given as $[(\text{Na, Ca})_{0.33}(\text{Al, Mg})_2(\text{Si}_4\text{O}_{10})(\text{OH})_2]_{n\text{H}_2\text{O}}$. Montmorillonites can enlarge and compress the interlayer space by swelling and shrinking where the major driving force is the uptake and release of H_2O into and out of interlayers (Loring et al., 2014). In addition, acids can activate the clays so that clays are useful as solid catalysts (Breen and Moronta, 1999). It is important to note that depending on the geographical origin, clays differ in elemental composition, charge density, and locus of isomorphous substitution. For example, SWy-2 (Wyoming), STx-1 (Texas), and SAz-1 (Cheto, Arizona) bentonites have dioctahedral structure, while SWy-2 is aluminum rich, STx-1 has low iron content, and SAz-1 is magnesium rich (Breen and Moronta, 1999). These aforementioned unique properties of the clay minerals make them ideal natural

TABLE 1 | Some representative nanoporous materials discussed in the text.

Nanoporous material	Property	Relevant references
Kaolinite	A tetrahedral silica sheet alternating with an octahedral alumina sheet forming the 1:1 clay mineral sheet. Layered pore structure.	Gupta and Bhattacharyya, 2012
Montmorillonite	2:1 phyllosilicates, swelling and shrinking abilities. Layered pore structure.	Loring et al., 2014
Isoreticular metal-organic frameworks (IRMOFs)	Regular and homogeneous pores	Langmi et al., 2014
Mesoporous silica	Uniform cylindrical mesochannel and tunable pore sizes, large surface areas, and even controllable particle size and shapes.	Asefa and Tao, 2012
Mobil Catalyst Material (MCM-41)	Straight channel pores with tunable diameter up to 10 nm	Al-Othman, 2012
Santa Barbara Amorphous-15 (SBA-15)	Hexagonal channel pores with diameter above 10 nm	Al-Othman, 2012
Carbon nanotubes	Carbon materials with pores in the form of tubes with diameter in the same range as in MCM-41	Liu et al., 2014
Zeolites	A class of inorganic microporous crystalline materials with wide applications. Examples include Na-Y with spherical cages (1.2 nm diameter) and ZSM-5 with channel like pores (0.5 nm diameter).	Meng and Xiao, 2014
ZIF-8 [zeolitic zinc 2-methyl-imidazolate Zn(MeIM)2] and ZSM-58 (SiO ₂ zeolite)		Stallmach et al., 2015
Silicoaluminophosphate molecular sieves (SAPO-n)	Channel-like intracrystalline pores with diameters from 0.3 to 0.8 nm	Lok et al., 1984
AlPO ₄ -n	Family of molecular sieves synthesized without silica with channel like pores of diameters ranging between 0.3 and 0.8 nm.	Wilson et al., 1982



nanosystems, to explore wetting, transport and reactivity of confined fluids.

In addition to the porous natural clay minerals, there are also synthetic or modified natural porous proxies available for use in the studies of confined fluids. Among the synthetic porous systems, zeolites, for example, are considered a class of inorganic

microporous crystalline materials with wide applications in gas separation, catalysis, petrochemistry, magnetism, medicine, and microelectronics (Zones and Davis, 1996; Davis, 2002; Čejka et al., 2010; Meng and Xiao, 2014; Li et al., 2015). Zeolites are synthesized from silicate, aluminosilicates or kaolinites hydrothermally (Johnson and Arshad, 2014; Meng and Xiao, 2014). Zeolite framework consists of four connected frameworks of AlO₄ and SiO₄ tetrahedra, and these four frameworks are joined, by sharing oxygens (Johnson and Arshad, 2014). This gives rise to an intricate structure of connected porous networks. Further these networks give rise to various pore shapes like spherical sodalite cages found in Na-Y type zeolite or channel like pores as in ZSM-5 zeolites (Figure 1B).

Although the confined molecules may not always form ordered structure in a micropore, micropores can be organized in an ordered pattern utilizing the periodicity of a crystal. This establishes long-range regular arrangement of the molecules under confinement and collaborative molecular assembly in microporous matrix systems (Ueda et al., 2012). Such a candidate of porous system with well-defined pore structure and high crystallinity is isoreticular metal-organic frameworks (IRMOFs), a series of porous compounds with regular and homogeneous pores (Eddaoudi et al., 2001). Among the IRMOFs, [Zn₄O(BDC)₃]_n (BDC = benzene-1,4-dicarboxylate) (IRMOF-1) is the prototype of a series of these compounds where zinc oxide and terephthalic acid moieties are three-dimensionally connected with each other establishing a porous framework resembling “a jungle gym” (Ueda et al., 2012).

One of the most utilized and investigated nanoporous matrix is mesoporous silica materials, a class of nanoporous materials with tunable pore sizes, large surface areas, and even controllable particle size and shapes (Asefa and Tao, 2012). These materials can exhibit uniform cylindrical pores in the form of channels as in MCM-41 (Figure 1C) or they can have irregularly shaped

pore structure as in the case of silica aerogel (**Figure 1D**). These mesoporous materials have gained widespread interest due to their potential applications as supports for functional novel materials (Al-Othman, 2012). Because of their high surface areas, these materials might be used as hosts to confine fluids. In this regard, these materials are ideal model engineered proxies in studying fluid behavior under confinement, which has significance in different areas including physical chemistry and geochemistry.

These natural, synthetic, and originally natural but synthetically or thermally modified nanoporous matrix systems have been utilized as ideal models for studying various fluids ranging from methane, CO_2 to H_2O upon confining the fluids into the nanopores of these matrix systems. A summary of some of representative nanoporous materials is provided along with their properties in **Table 1**. In what follows, after introducing the NMR, NS, and MD simulation techniques, we discuss some examples of their use in the studies of molecular confinement in different pore types mentioned above. The intent is not to provide an exhaustive review of all such studies but rather present only a very few key examples.

NMR SPECTROSCOPY

Atomic nuclei are positively charged and have an intrinsic angular momentum. This gives rise to a magnetic dipole which is referred to as nuclear spin (James, 1998). A nuclear spin interacting with an external strong static magnetic field B_0 undergoes precession with a frequency called the Larmor frequency ω_0 around the field direction. Besides interaction with the external magnetic field, the spin experiences internal electric and magnetic fields so that the resonance frequency can be moved by a frequency ω relative to ω_0 (Macomber, 1998). For conducting NMR measurements, radio frequency (rf) pulses are employed to control the magnetization of a nuclear spin ensemble.

Upon excitation of the spin ensemble, relaxation processes restore the equilibrium magnetization. The characteristic times describing the relaxation of the magnetization vector components parallel and perpendicular to the external magnetic field (B_0) are defined as longitudinal (T_1) and transverse (T_2) magnetization relaxation times. T_1 and T_2 values of molecules depend on fluctuations of the NMR interactions (spin-lattice and spin-spin) that arise from molecular motion. Because of that, T_1 and T_2 measurements have become common and traditional methods to investigate molecular reorientation not only in pure bulk state but also in confined space (Abragam, 1961; Freedman and Heaton, 2004; Vogel, 2010; Walbrecker and Behroozmand, 2012). The T_1 distributions reflect the complex composition of different systems, such as crude oils and the distribution of pore sizes in sedimentary rocks (Freedman and Heaton, 2004). For water-saturated rocks, the surface interaction is usually dominant and provides a mechanism for estimating pore-size distributions from T_1 distributions (Allen et al., 1997). T_2 decaying curves are also correlated to viscosity of different complex mixtures as in the case of crude oil (Freedman and

Heaton, 2004). In addition, when samples of saturated porous media are measured, the amplitude of the T_2 measurements is directly proportional to porosity, and the decay rate is related to the pore size and the fluid type and its viscosity in the pore space. Short T_2 times generally indicate small pores with large surface-to-volume ratios and low permeability. Conversely, longer T_2 times indicate larger pores with higher permeability (Anovitz and Cole, 2015). **Table 2** summarizes some of the NMR techniques commonly employed for studying both nanoporous matrix systems and confined fluids relevant to geochemistry.

For NMR relaxation in liquid-dominated geologic systems, it is usually supposed that relaxation happens in the rapid diffusion regime (Behroozmand et al., 2014). In the case of rapid diffusion, the net observed relaxation rate T_1^{-1} for a single pore is as follows,

$$1/T_1 = 1/T_{1B} + \rho_1(S/V) \quad (1)$$

where $1/T_{1B}$ is the relaxation rate of bulk water, S/V is the surface-area-to-volume of the pore (inversely proportional to the pore radius r_{pore}), ρ_1 is the longitudinal surface relaxivity (Brownstein and Tarr, 1979). Similar to $1/T_1$, the transverse relaxation rate $1/T_2$ is the rate at which protons dephase during the return process to equilibrium. The expression for $1/T_2$ in this way contains an additional term to explain internal magnetic field gradients G involved by diffusing protons:

$$1/T_2 = 1/T_{2B} + \rho_2(S/V) + (D/12)(\gamma G t_E) \quad (2)$$

Here, ρ_2 is the transverse surface relaxivity, $1/T_{2B}$ is the relaxation rate of bulk water, D is the self-diffusion coefficient of water, γ is the gyromagnetic ratio of the hydrogen nucleus, and t_E is the echo time, a timing parameter of the measurement. Relaxation in geologic systems with insignificant magnetic susceptibility is governed by surface relaxation, where the expression for $1/T_2$ becomes (Grunewald and Knight, 2009):

$$1/T_2 = \rho_2(S/V) \quad (3)$$

Compared to diffusion, NMR longitudinal relaxation time (T_1) is more sensitive, and gives insight into more localized movements of confined molecules, such as translation and rotation on a time scale comparable to the reciprocal of the NMR angular frequency (approximately 1 ns) (Slichter, 1990; Corsaro et al., 2013). Longitudinal relaxation itself is an energy driven process, and is a measure of the dipolar interactions of the spins with the local environments (Corsaro et al., 2013). There are various molecular motions including dipole-dipole interactions, spin-rotation interactions, scalar-coupling, chemical shift anisotropy, and possible interaction due to presence of some paramagnetic substances in natural systems that contribute to T_1 in liquids (Inlow et al., 1975). It was also argued by Kleinberg et al. (1994) that nucleus-electron interactions rather than pore dimensions govern the proton relaxation rate of pore-confined fluids in natural systems. In attempting to characterize the porous silica glass, for instance, D’Orazio and co-workers have focused on different degrees of filling the porous material with distilled water by both diffusion

TABLE 2 | Summary of NMR techniques commonly applied in geologically relevant porous media.

NMR Technique	Property measured	Possible information obtained	References
Relaxation	Longitudinal magnetization relaxation	Pore size in rocks, pore size distribution	Allen et al., 1997; Freedman and Heaton, 2004
Relaxation	Transverse magnetization relaxation	Viscosity, fluid type, porosity	Freedman and Heaton, 2004; Anovitz and Cole, 2015
Fast field cycling (FFC) NMR relaxometry	The longitudinal magnetization relaxation rate ($1/T_1$)	Fluid dynamics at solid interface, transport in porous media	Kimmich and Anoardo, 2004; Steele et al., 2015
Cross-polarization (CP)	Polarization transfer	Surface heterogeneity	Sindorf and Maciel, 1983
Magic angle spinning (MAS)	Relaxation, Heterogeneity, dynamics, etc.	Surface heterogeneity, dynamics	Schmidt-Rohr and Spiess, 1994; Duer, 2004
Pulsed Field Gradient (PFG)	Diffusion	Deviation from bulk, viscosity	Tanner, 1970; Stallmach et al., 2000
PFG MAS	Diffusion	Adsorption processes into nanoporous host systems and possible subsequent reactions	Navarthi et al., 1994; Pampel et al., 2003

NMR and NMR relaxation measurements. Both longitudinal (T_1) and transverse (T_2) relaxation measurements revealed linear behavior with respect to the degree of fluid filling down to monolayer coverage. This was explained by the homogeneity of pore space leading to equal distribution of water (Bhattacharja et al., 1989; D’Orazio et al., 1990a,b). It is also well-known that nanoporous silica, for example, is heterogeneous with surface – OH groups as revealed by solid-state magic angle spinning (MAS) cross-polarization (CP) ^{29}Si NMR (Sindorf and Maciel, 1983).

Nuclear magnetic resonance (NMR) provides a non-invasive method of probing the geometry of porous media (Callaghan et al., 1991; Cotts, 1991; Vogt et al., 2002; Sen, 2004). NMR spectroscopy aids in the description and classification of the structures and assembly of the porous spaces over various nanometer scales, and hence contributes to a better description of how fluids are confined into the nanopores and how the fluid molecules move in the confined state within the pores (Packer, 2003). Thus, by measuring the limitation inflicted on the diffusive and relaxation activities by boundaries where particles reside, information directly related to the characteristics of the pore space is obtained (Packer, 2003; Song, 2007; Kittler et al., 2014).

Another NMR technique of interest is the pulsed field gradient (PFG) NMR. The PFG method measures translational diffusion, which is a random (stochastic) movement of molecules due to internal kinetic energy. Translational diffusion is the most basic type of transport seen in both natural and industrial systems (Hawlicka, 1995; Price, 1997). Due to heterogeneities in magnetic susceptibility of samples, such as porous materials, internal gradients will be induced, and the measured diffusion coefficient will be shorter than the real diffusion coefficient (Cotts, 1989). In order to overcome this problem, stimulated echo (STE) PFG sequence is utilized. PFGSTE sequence is considered as a three-90° pulse sequence consisting of three intervals: prepare, the store, and the read intervals (Tanner, 1970; Sørland et al., 1997). PFGSTE is a well-established NMR method, and has been utilized for measuring diffusivity in porous media. Moreover, the echo signal measured in PFGSTE is proportional to the self-intermediate scattering function (Callaghan, 1991), which, as we shall see later is accessible in a NS experiment and can be calculated from MD simulations. Thus, the measured

signal in PFGSTE provides a link between NMR and NS experiments. However, as the length and time scales accessible with the two techniques are different, they can be used to obtain complementary information. The interested reader should refer to the literature work for a detailed explanation of the technique (Tanner, 1970; Sørland et al., 1997).

It is also possible to employ MAS NMR for narrowing linewidths of NMR spectra, which could become broader due to inhomogeneity in heterogeneous systems consisting of confined fluid and nanoporous matrices. MAS NMR also helps with eliminating anisotropic contributions in NMR spectra, and extracting more information about the heterogeneous systems. In liquids, molecules reorient themselves rapidly. In solution NMR, rapid tumbling of the molecules average out molecular orientation dependent anisotropic interactions to zero on the NMR time scale yielding sharply defined spectral lines. In “true solids,” there is no such motion, and solid-state NMR, instead, gives broader spectral lines that limit most information of interest. In order to achieve similar information for a solid like we observe for liquid samples, mechanical spinning of the solid sample about an axis making a certain angle with the direction of the external magnetic field can lead to a dramatic reduction of the NMR linewidth. Mechanical rotation at any angle by itself is not sufficient enough due to the molecular orientation dependence of the form $(3\cos^2\theta-1)/2$, which is known as the second order Legendre polynomial, and where θ is the angle that describes the orientation of the spin interaction tensor by reference to the static magnetic field. When the angle is equal to 54.74 degrees, that is the sample is spun at the “magic angle” from where the name of the technique implies, it becomes possible to remove the effects of chemical shift anisotropy, both homonuclear and heteronuclear coupling effects and to narrow lines from quadrupolar nuclei (Schmidt-Rohr and Spiess, 1994; Duer, 2004).

In addition to studying confined behavior of gas molecules by NMR spectroscopy, there are also contributions on fluid behavior in liquid state under confinement. PFG NMR spectroscopy, which is sometimes described as Pulsed Gradient Spin Echo (PGSE) or Diffusion Ordered SpectroscopY (DOSY) (Galvosa et al., 2001), has become a preferred technique for exploring the behavior of confined molecules in porous systems and has been

commonly employed in scientific efforts on zeolites (Vasenkov et al., 2001) and Mobil Catalyst Material (MCM-41) based mesoporous silica systems (Stallmach et al., 2000). DOSY NMR determines diffusion coefficient based on the following equation:

$$\ln(I/I_0) = -D\gamma^2 g^2 \delta^2 (\Delta - \delta/3) \quad (4)$$

where I is the observed signal intensity for the gradient power g , I_0 is signal intensity for zero gradient power g , D is diffusion coefficient, γ is gyromagnetic ratio of the observed nuclei, δ is duration of PFG, and Δ is diffusion time (Kuchel et al., 2012).

By proper insertion of pulsed magnetic field gradients of duration δ , intensity g , and observation time t in the defocusing and refocusing period of the NMR pulse sequence, the monitored spin-echo becomes dependent on the translational motion of the molecules that move the nuclear spin under examination (Stallmach et al., 2000, 2001). Vogt et al. (2002) studied diffusion of water and hexadecane in medium and coarse sands from glacial sand deposits in central Germany. Due to the limitation of the diffusion path at the pore/grain interface, the measured diffusion coefficient in the confined area/volume of the pores depends on the observation time t . Using the “short-time diffusion” model, surface-to-volume (S/V) ratios were extracted from diffusion measurements, and it was found that the S/V ratios were independent of fluid and were in agreement with known geometrical properties of the sand grains. Simultaneous measurements of longitudinal magnetic relaxation (T_1) revealed dependence of T_1 on chemical properties of the fluid/grain interface, which did not help with quantification of geometrical characteristics of the pore/grain interface in the uncombined deposits.

However, heterogeneity limits performing diffusion NMR experiments of mixtures within porous materials (Pampel et al., 2005; Fernandez et al., 2008). In these heterogeneous porous matrices, T_2 decays due to not only a continuous dipolar interaction between the spins under investigation but also differences in the interior magnetic fields. These effects, including the limitation in the mobility of the guest molecules, broaden the NMR signal and this yields reduced resolution in the NMR spectra (Pampel et al., 2005; Fernandez et al., 2008). Applying PFG and MAS techniques on the same probe solves this problem (Nivarthi et al., 1994; Pampel et al., 2003; Gaede and Gawrisch, 2004). MAS PFG NMR allowed, for instance, investigating complex formation in an acetone-alkane mixture, which is restricted to nanoporous host systems (Fernandez et al., 2008) and molecular diffusion in zeolites (Pampel et al., 2005). A more interesting MAS probe without FG was designed to investigate the evolution of adsorption of fluids on nanoporous solids (Xu et al., 2007). The results obtained by this method showed clearly the viability of a new technique for conducting *in situ* solid-state NMR investigations of adsorption processes into nanoporous host systems and possible subsequent reactions.

One of the NMR relaxometry techniques applied for studying confined fluids is fast field-cycling (FFC). FFC NMR relaxometry is the method of choice for gaining insight into the frequency dependence of relaxation rates. Because of that it is also considered as nuclear magnetic relaxation dispersion (NMRD).

The advantage of the longitudinal relaxation rate ($1/T_1$) as a function of large frequency ranges is to isolate the typical NMR dispersion properties related to various processes of molecular dynamical behaviors (Kimmich and Anoardo, 2004; Steele et al., 2015). Fluid dynamics at the solid interface, transport in confined medium (filtration, imbibition, and conduction) (Korb, 2006), and phase transitions in confinement (Diakova et al., 2012) are some examples probed by FFC NMR technique. For the details of the FFC NMR applications on confined fluids, the interested reader could refer to the review articles by Steele et al. (2015) and Kimmich and Anoardo (2004).

NEUTRON SCATTERING

Thermal and cold neutrons, because of their characteristic wavelength being of the order of interatomic spacing in a crystal and their energy matching that of elementary excitations at molecular level, offer an ideal opportunity to study the structure and dynamics of materials with the help of NS (Bacon, 1975). Moreover, because the scattering of neutrons depends on interaction with the nucleus, rather than from the electron cloud in an atom, the NS cross sections are independent of the atomic number of the scatterer. This makes the study of lighter elements, in particular hydrogen, possible unlike in X-ray scattering where the scattering due to light elements is mostly obscured by heavier elements present in the sample. Moreover, because the NS cross sections are dependent on the nature of the nucleus, isotopic contributions in a NS experiment can be distinguished. All these properties make neutrons an ideal tool to probe the structure and dynamics in solids and liquids.

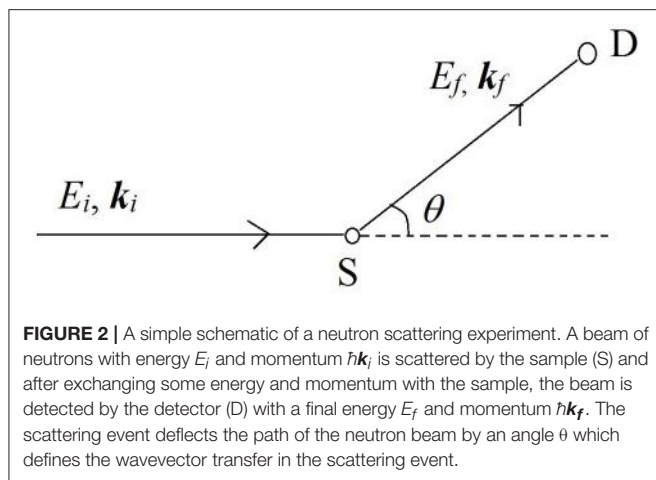
Neutron beams used to interrogate samples can be obtained from the nuclear chain reactions taking place in a nuclear reactor, after moderating them to lose energy by about six orders of magnitude to a few millielectron volts (meV)¹. Another high flux source of neutrons is a spallation source where a highly energetic proton beam strips off neutrons from a target material. Several countries run reactor based and spallation based neutron sources with user programs that cater to the study of materials. Spallation sources are present in USA, UK, Japan, Switzerland and Sweden (upcoming), whereas reactor based sources are present in USA, Canada, France, Germany, Hungary, India, Indonesia, South Korea, Japan, and Australia². The concept of a NS experiment is shown in the schematic below (see Figure 2).

Neutrons with a well-defined energy and momentum vector from the source are scattered by the material sample (S) and are detected by the detector (D). The difference in energy ($E = E_i - E_f$) and momentum ($\hbar\mathbf{Q} = \hbar\mathbf{k}_i - \hbar\mathbf{k}_f$) of the neutrons before and after the scattering event is recorded using a variety of methods³. These differences in energy and wave-vector encode the information about the structure and dynamics of molecules in the scattering sample. The reader is

¹1 meV energy corresponds to 8.067 cm⁻¹

²A list of neutron sources around the world with user programs can be found at <http://idb.neutron-eu.net/neutron-centres.html> or <http://www.ncnr.nist.gov/nsources.html>

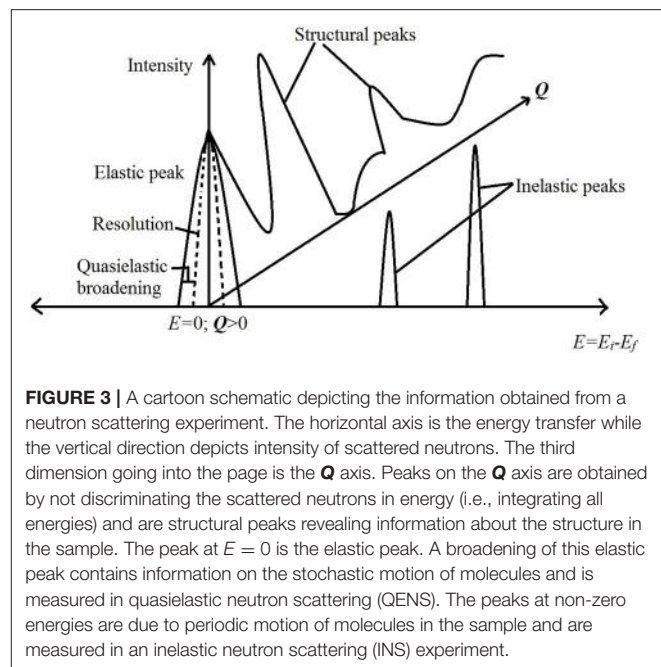
³ $\hbar = h/2\pi$ is the reduced Planck constant.



referred to literature overviews by Bacon (1975), Bée (1988), and Vogel and Priesmeyer (2006) for further technical details on the methods of recording the energy and momentum transfers.

In general, what is measured with the detector is the double differential cross section, which can be defined as the probability that a neutron with incident energy E_i is scattered in a direction Ω within a solid angle $d\Omega$ after an exchange of energy within the range $\hbar\omega = E$ and $\hbar(\omega + d\omega)$. Further, it can be shown that this double differential cross section is proportional to a quantity, called scattering law $S(\mathbf{Q}, \omega)$ which is a property of the scattering sample alone. The scattering law is related to the van Hove correlation function $G(\mathbf{r}, t)$, which gives the probability of finding a particle at a position \mathbf{r} , given that some other or the same particle was at origin at time $t = 0$. The van Hove correlation function thus contains the complete information on the structure and dynamics of molecules in a sample. Fourier transforming the van Hove correlation function in space converts it into a function in the reciprocal space, called the intermediate scattering function $I(\mathbf{Q}, t)$. Taking another Fourier transform in time gives the scattering law. As we shall see later, the intermediate scattering function can be calculated directly from the trajectories obtained in an MD simulation and thus serves a link between the experiments and simulations.

Depending on whether the neutrons detected after a scattering event are discriminated for their energies or not, the scattering experiment can be used to obtain information about dynamics or structure, respectively, in the sample. Further, the inelastic scattering experiments, in which energy discrimination is made for the scattered neutrons, can be used to study either stochastic or periodic motions of the molecules in the sample. The stochastic motion can be studied using a small exchange of energy between the neutrons and the sample leading to a broadening of the elastic line ($E = 0$ in the spectrum) on either side. In practice, the elastic line has a finite width (resolution) due to the characteristics of the instrument. The stochastic molecular motion in the sample causes a further broadening of the elastic line over resolution, which is called quasielastic



broadening (see **Figure 3**). A scattering technique, which focuses on this broadening to study stochastic molecular motions, is called quasielastic neutron scattering (QENS). Examples of stochastic motion include diffusion and random rotational jumps that make up the rotational motion. Periodic motions on the other hand include the vibrational stretching, bending of molecules. These motions give rise to a definite non-zero energy exchange between the neutrons and the molecules in the sample and lead to non-zero energy peaks in the spectrum. The scattering experiments designed to study these non-zero energy (inelastic) peaks are called inelastic neutron scattering (INS) experiments. A cartoon schematic depicting these differences is shown in **Figure 3**. Neutron spin echo (NSE) is another technique, which directly measures the difference in the energies of the neutrons before and after the scattering event instead of measuring them separately. Measuring the energy transfer directly improves the energy resolution dramatically. As it is used to measure stochastic motions, NSE is considered equivalent to QENS but with improved resolution and thus an ability to study much slower molecular motion. Further, as this technique measures the intermediate scattering function instead of scattering law, the interpretation of experimental data is more straightforward. A detailed discussion of NSE as a tool to study molecular motion can be found in Richter et al. (2005).

With a variety of instruments available, a typical NS experiment may cover a range of length scales from a few angstrom (diffraction) to a few microns (small angle neutron scattering; low \mathbf{Q} region of the \mathbf{Q} axis in **Figure 3**). The time range covered ranges between a few hundreds of femtosecond (high energy inelastic) to a few microseconds (QENS with NSE instruments). We do not include examples of neutron diffraction experiments here due to limitations of space.

MD SIMULATIONS

With the advent of economical computers, large numerical calculations have become possible. This has given rise to a large number of studies using numerical calculations for a deterministic system at small as well as large length scales. These numerical calculations can be used to model a variety of systems from quarks to galaxies and covering a variety of fields from physics to cognitive psychology and social sciences. One particular method of simulation pertinent to the study of matter at molecular level is the classical MD simulation. In a classical MD simulation, Newton's equations of motion for a system made up of molecules representing the material of interest are solved numerically to obtain the trajectories of the constituent molecules. A plethora of algorithms are available to solve these equations of motion. A detailed discussion of these algorithms and their advantages can be found elsewhere (Hoover, 1986; Allen and Tildesley, 1987; Frenkel and Smit, 2001). For a conservative system made up of a large number of molecules, the equation of motion can be written as

$$m_i \frac{d^2 \mathbf{r}_i}{dt^2} = -\nabla U_i \quad (5)$$

where U_i is the total potential energy of molecule i due to all other molecules. Once this potential energy is determined for a system, the equation can be solved numerically to yield trajectories (i.e., \mathbf{r}_i as a function of time). Thus, two important inputs for the simulation are the starting positions [$\mathbf{r}_i(0)$] of molecules comprising the system and the potential energy (U_i) of interaction of the molecules (called Force Field). The starting positions are usually defined on a regular lattice, which, takes on a more random structure as the simulation progresses. The force field is normally determined by empirical fitting of properties calculated from the simulations with their experimentally determined values. For example, Martin and Siepmann (1998) have obtained force field for alkanes by fitting the experimental data for critical temperatures and saturated liquid densities with simulated values. Similarly, a variety of force fields have been derived for water which include simple point charge (SPC) by Berendsen et al. (1987), TIP3P by Jorgensen et al. (1983) and their extensions. Guillot (2002) has compiled a list of various force fields available for modeling water. Once the starting positions have been set and the force field chosen, the equations of motions are solved numerically by choosing a time step of simulation. This is the shortest unit of time simulated by the program and is chosen in such a way that it is short enough to capture molecular processes of interest and long enough to result in a meaningful time length of simulation. Usually a time step of 1 femtosecond (fs) is used to simulate molecular processes like diffusion. After the execution of the simulation, positions of all constituent molecules at all times—trajectories [$\mathbf{r}_i(t)$]—are obtained. These trajectories can then be used to calculate various thermodynamic quantities of interest. For example, the diffusion coefficient can be obtained by calculating the mean squared displacement (MSD) of the constituent atoms from the trajectories and studying its evolution in time. Another

important quantity that can be calculated from the trajectories is the intermediate scattering function defined in the previous section. This quantity can serve as a link between the simulations and NS experiments (Gautam, 2017) and can be calculated from the simulation trajectories using the expression.

$$I(Q, t) = \overline{\langle \exp(iQ \cdot [\mathbf{r}(t + t_0) - \mathbf{r}(t_0)]) \rangle} \quad (6)$$

where angular brackets denote an average over different time origins and molecules and the bar indicates an average over different Q vectors with the same magnitude. Another quantity that can serve as the link between experiments and the simulations is the orientational correlation functions (OCF) defined as,

$$C_l(t) = \langle P_l[\mathbf{u}(t + t_0) \cdot \mathbf{u}(t_0)] \rangle \quad (7)$$

Here, \mathbf{u} is a unit vector attached to the molecule and $P_l[x]$ is the Legendre polynomial of the order l with argument x . The $l = 1$ component of OCF is the dipole correlation function and can be measured directly in a dielectric spectroscopy experiment. It can also be obtained from IR spectrum. The OCF with $l = 2$ can be measured in light scattering and NMR experiments.

SOME RECENT STUDIES ON MOLECULAR MOTION UNDER CONFINEMENT

In the following sections, some examples of the use of the above mentioned three techniques in investigating the behaviors of C-O-H based confined fluids are provided.

Methane under Confinement

Methane in Molecular Sieves and Zeolites

Methane (CH_4) is one of the most interesting and important molecule of energy relevance whose behavior under nanoporous confinement has been studied by NMR spectroscopy (Ok et al., 2017). Koskela et al. (1996) and Koskela et al. (1998) studied the behavior of methane confined into silicoaluminophosphate (SAPO) and aluminophosphate (AlPO) molecular sieves, respectively, by both static and MAS ^{13}C and $^{13}\text{C}-\{^1\text{H}\}$ NMR spectroscopy at variable temperatures. The silicoaluminophosphate molecular sieves (SAPO-n) have intracrystalline pore volumes (H_2O) from 0.18 to 0.48 cm^3/g and adsorption pore diameters from 0.3 to 0.8 nm, covering the scale of pore volumes and pore sizes known in zeolites and in silica and aluminophosphate molecular sieves (Lok et al., 1984; Table 1). When CH_4 was confined into SAPO-11 molecular sieve, there was reduction in CH_4 symmetry. This was attributed to the interactions with both the charge-compensating protons and the channel walls. However, upon confining CH_4 into AlPO4-11 molecular sieves, there were three different signals of ^{13}C -enriched methane observed. The existence of three ^{13}C NMR signals of methane was attributed to the dispersal of methane gas in four different reservoirs (Jameson et al., 1997). There were “free gas” reservoirs (I) and the adsorbed molecules existing in the inner region of the crystallites (IV) gas molecules. The rest of the nonadsorbed molecules are able to move between

the crystallites (reservoir II), some of which might be adsorbed inside the channels, but close to the crystallite surface (reservoir III). If the exchange is rapid relative to the NMR time scale, a lifetime-weighted average of shielding in the two reservoirs is detected leading to the central resonance in the ^{13}C NMR spectrum.

An example of an agreement between the NMR and QENS (spin echo) results is provided by a study of diffusion of methane in zeolites. While Caro et al. (1975) used PFG-NMR, Cohen de Lara et al. (1983) utilized spin echo QENS to obtain the diffusion coefficient of methane in A-type zeolites. A diffusion coefficient of $6 \times 10^{-6} \text{ cm}^2/\text{s}$ was obtained from the QENS data. Jobic et al. (1989) studied translational dynamics of methane in NaZSM-5 by combining NMR and QENS methods. With both techniques, the intracrystalline self-diffusion coefficients for methane at temperatures in the range 200–250 K were found to be within 10^{-5} – $10^{-4} \text{ cm}^2/\text{s}$. The activation energy of methane self-diffusion was determined to be 4–5 kJ mol^{-1} by applying both of the techniques.

Another example of the use of QENS to study confined methane is a comparative study of methane in AlPO_4 -5 and ZSM-48 channels. The channel diameters of AlPO_4 -5 and ZSM-48 are 0.8 and 0.5 nm, respectively. Thus, ZSM-48 imposes a stricter geometrical confinement on the adsorbed molecules. In the QENS study, it was observed that in AlPO_4 -5 methane molecules exhibit ordinary one dimensional diffusion. However, in ZSM-48 while a similar diffusion process was observed at lower loadings, at moderate loadings of methane, single-file diffusion of the adsorbent molecules was found in the channel pores where the molecules are forced to move in a single file in absence of enough space for a molecule to overtake other molecules (Jobic et al., 1997). This was the first instance of use of QENS to observe single-file diffusion of confined molecules which is a result of a strict geometrical confinement.

Methane Hydrate Formation/Decomposition

Among different aspects of research on natural gas, a significant focus is on capture and storage mechanisms that largely depend on hydrate-forming conditions. Most of methane on Earth is found trapped inside hydrates. The total methane content in the hydrates ranges between 2×10^3 and 4×10^6 gigatons and could be larger than the methane content from all other sources put together (Kvenvolden, 1988). Methane hydrates thus are a good potential energy resource. At the same time, they are a potential greenhouse gas threat as release into the atmosphere could accelerate global warming. Dissociation of oceanic methane hydrates has been attributed to the carbon isotope excursion at the end of Paleocene (Dickens et al., 1995). A comprehensive review of clathrate hydrates of natural gases can be found in Sloan (2003) and Sloan and Koh (2007). Here we describe a few example studies of methane clathrates using NMR, NS, and MD simulations.

The NMR technique provides insight into both qualitative and quantitative hydrate properties including structure forms, cage occupancies, and guest constituent compositions (Ripmeester and Ratcliffe, 1988; Seo and Lee, 2003). There have been several reports on NMR investigation of methane hydrate

decomposition (Dec et al., 2007; Gupta et al., 2007). For example, Seo and Lee (2003) found by acquiring ^{13}C NMR spectra of pure methane, mixed methane+tetrahydrafuran(THF), and mixed methane+neohexane hydrates that methane molecules might be existing only in a fraction of 5^{12} cages in the mixture with THF due to the existence of water-soluble THF preventing complete filling of methane molecules into small cages. One of the most important conclusions was that it was not possible to encase methane molecules at all in the $5^{12}6^4$ cages of structure II. Methane and ethane gas mixtures form two common gas hydrate structures—structure I (sI) and structure II (sII) depending on the gas-phase composition, temperature and pressure as shown in Figure 4 (Subramanian et al., 2000; Dec et al., 2007).

Using neutron diffraction, Tulk et al. (2012) studied cage occupancies in the high pressure structure H methane hydrate. The results from this experiment provided data for refinement of intermolecular potential parameters for the water-methane interactions in clathrate structures.

Recently, Casco et al. have used NS to study the growth of synthetic methane hydrates in nanoporous carbon material. The inelastic NS spectra from confined synthetic methane hydrates matched with the spectra of methane hydrates from the Pacific sea floor. The confinement of synthetic hydrates was found to result in faster growth kinetics. The synthetic hydrate formation in nanopores is thus less demanding than the formation of natural hydrates and occurs with the same stoichiometry as that found in nature (Casco et al., 2015). Myshakin et al. (2009)

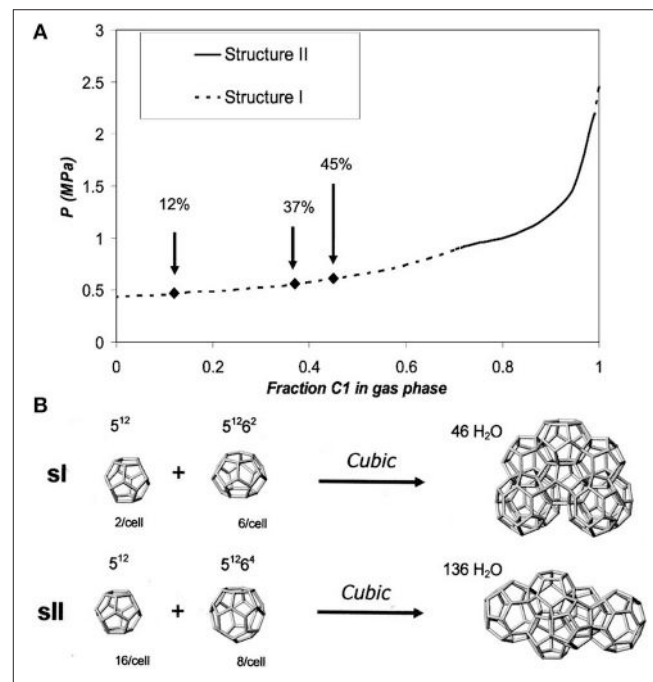


FIGURE 4 | (A) Pressure vs. methane gas phase composition for the methane + ethane + water system at 272 K. Arrows indicate methane gas phase compositions used by Dec et al. (2007). **(B)** Polyhedral cages and partial unit cells of sI and sII clathrate hydrates. Reprinted with permission from Dec et al. (2007), Copyright 2007 American Chemical Society.

studied methane hydrate decomposition using MD simulation and found a dependence of the decomposition rate on the hydration number. Further, the rate of the cage destruction indicated that it occurs via an activated mechanism.

Methane-CO₂ Replacement in Gas Hydrates

The behavior of CH₄ and CO₂ at certain temperature-pressure conditions can also produce interesting molecular interactions. Methane-CO₂ replacement in natural gas hydrates was studied by ¹³C NMR spectroscopy (Lee et al., 2013). It was shown by MD simulations that the substitution of CH₄ by CO₂ in sI hydrate cages has a negative free energy (Dornan et al., 2007). This indicated spontaneous replacement of CH₄ by CO₂ from sI hydrates, causing the release of CH₄. ¹³C NMR was used to monitor the release of CH₄ and sequestration of CO₂ (Lee et al., 2013). In addition, the CO₂ composition in the hydrate phase and the chemical formula of the mixed gas hydrate after replacement can be easily approximated from the information on the ratio of the ¹³C MAS NMR resonance lines of CH₄ in large and small cages. Contributions on the behavior of confined fluids include adsorption equilibrium of CO₂ and CH₄ into different confined systems, such as shale. Duan et al. (2016) studied the adsorption equilibrium isotherm data of CO₂ and CH₄ at 278, 298, and 318 K on rock samples from southeastern Sichuan Basin of China with a total organic carbon (TOC) of 2.58 wt%, inorganic components of quartz and orthoclase, and a wide pore size distribution. They demonstrated that the adsorption capacity of CO₂ is higher than that of CH₄ on shale. These results suggest a possible path forward for enhancing CH₄ recovery and securing CO₂ storage by injecting CO₂ into shale reservoir rocks. A fundamental understanding of competitive sorption of CO₂ and CH₄ under nanoconfinement can be explored by high-pressure MAS NMR spectroscopy. For example, Qian et al. (2011) investigated dry reformation of methane with CO₂ over 1.0 wt% Rhodium (Rh)/SBA-15 catalyst by both ¹³C and ¹H MAS NMR measurements. It was possible by ¹³C MAS NMR to track the ¹³C-labeled reactants, such as CH₃O* and CH₂O* species during the carbon exchange reaction between CH₄ and CO₂ dry reforming reaction.

Confined Water Structure and Dynamics

Water in Clays

Water transport through the terrestrial subsurface forms an important component of global water cycle. The interaction of water with subsurface minerals affects a variety of geochemical phenomena including ion adsorption and exchange, mobility of contaminants, weathering, hydrothermal alteration, soil moisture and flow of CO₂ (Brown, 2001; Wang et al., 2006). Layered clays form a major family of minerals. Structural water plays an important role in the stability of the structure in clays. This has resulted in a large number of studies of water confined in clays. Swenson et al. (2000) reported a QENS study on the dynamics of water in the vermiculite clays. This study employed orienting the clay sample in two perpendicular directions to study motion along the platelets forming the pore space in the clays and perpendicular to it. No significant water motion was detected in the direction perpendicular to the platelets thus

implying a two-dimensional motion of water along the planes of the platelets. The diffusion of this confined water was found to be only slightly reduced compared to the bulk. This study was further extended using neutron spin echo to study the slower component of water dynamics (Swenson et al., 2001). It was found that the intermediate scattering functions exhibited a stretched exponential behavior typical of a non-Arrhenius fragile liquid. This is because the confined water experiences very different environments inside the clay at different points. This gives rise to a broad distribution of the time scales of motion. Malikova et al. (2006) used a combination of QENS experiments using both time of flight and spin echo instruments and MD simulations to study water confined in clays. They found that the time of flight measurements overestimate the water dynamics. An analysis of the elastic incoherent structure factor (EISF) using the simulation data, helped interpret the QENS data. Porion et al. (2007) used a combination of NMR and multiscale modeling consisting of Monte Carlo and MD simulations and Brownian dynamics calculations to study the structure and dynamics of water in dense clay sediments. MD simulations were also used to interpret the NSE data on water dynamics in hectorite clays and resulted in good agreement (Marry et al., 2011). QENS and MD simulations studies were combined by Michot et al. (2007) to understand water dynamics in Na saponite clays. Two rotational motions with different time scales of the confined water molecules were found. The faster of these was found to be independent of the adsorbed amount of water, whereas the slower one was found to slow down further for lower adsorption of water. A similar slowing down of water translational motion with lower loading was found in the case of hydrotalcite (Mitra et al., 2007). Chakrabarty et al. (2006) studied the effect of intercalation on the dynamics of water in saponite clays. It was found that the diffusion of water in the intercalated clay is enhanced. Bordallo et al. (2008) also studied the effect of cations on the dynamics of water in the interlayer spaces. They found that the Na⁺ cations facilitate the mobility of water. Further, they found that due to the quasielastic contribution from the magnetic fluctuations caused by Fe³⁺ ions, water diffusion was overestimated.

Water in Carbon Nanotubes

The behavior of water in engineered nanoporous materials has also been of great interest in the chemistry and materials sciences arenas. For example, Liu et al. (2014) have investigated diffusion of water by PFG NMR inside multiwalled (MW) and single walled (SW) carbon nanotubes (CNT), an important model system in the field nanofluidics and for carbonaceous materials in rocks. The diffusivity of water in double-walled carbon nanotubes (DWNTs) with an average inner diameter of 2.3 ± 0.3 nm was twice that in multiwalled carbon nanotubes (MWNTs) with an average inner diameter of 6.7 ± 0.8 nm in the temperature range of 263–223 K. Moreover, the effective self-diffusion coefficient in DWNTs is an order of magnitude higher than that reported for mesoporous silica materials, such as MCM-41 with a similar pore size. The faster diffusivity of water in CNTs was attributed to the ordered hydrogen bonds formed between water molecules within the channels of CNTs and the weak interaction between water and the CNT walls. In combined NS and MD simulation

study, Kolesnikov et al. (2004) found that water inside a SWNT at 273 K exists in two different populations—one made up of a cylindrical shell concentric with the nanotube and the other making a one-dimensional chain. The confined water in this system exhibited anomalously soft dynamics. Single particle dynamics of water in both SWNT and DWNT have also been studied using QENS (Mamontov et al., 2006). Water in the nanotubes with an inner diameter of 1.4 nm was found to exhibit a fragile to strong transition at 218 K. This transition was not observed up to above 200 K for the 1.6 nm tubes. In an independent MD simulation study (Hummer et al., 2001), it was concluded that the one-dimensional chain of water confined in a carbon nanotube showed concerted pulse-like motion. This concerted rapid motion along the tube axis results from tight hydrogen bonding network.

Water in Porous Silica Materials

A large number of NMR approaches ranging from static solid-state, high-resolution MAS to PFG NMR have been used to interrogate the behaviors of small molecules in porous silica materials exhibiting either a narrow pore-size distribution with periodic structures as in MCM-41 or wider confinement pore sizes with non-periodic structures, such as in silica controlled pore glasses (CPG). Hence, for molecules with lower molecular weights, such as H_2O , the confinement dimensions investigated range from a few to a few hundred molecular diameters (Vogel, 2010).

D’Orazio et al. (1990b) conducted both longitudinal (T_1) and transverse (T_2) magnetization relaxation measurements on water in unsaturated silica pore glass. NMR relaxation measurements along with diffusion coefficient determinations of confined water in porous media helped achieve a better understanding of the dynamics of fluids in random geometries. For a loading larger than the first adsorbed monolayer, the two component fluid-solid system was homogeneous at least over a few micrometers. A linear correlation between the relaxation times and the fraction of the occupied pore volume was seen, which demonstrated that the interaction responsible for the relaxation was confined to the first monolayer. Whereas, when there was less amount of confined fluid than the corresponding monolayer of fluid on the surface of the solid, the relaxation rates increased above the values predicted by assuming no evolution of the molecular interaction during drying. It was concluded that rotational and translational degrees of freedom were correlated, indicating that an adsorbed water molecule was allowed to rotate only during a jump to a neighboring site and that, most probably; one of the O-H bonds rotates in the plane of the surface.

In addition to studying confined water behavior in random geometries with non-periodic structures, water behavior under confinement has also been explored in ordered (i.e., pores aligned in a single orientation) mesoporous silicas, such as MCM-41 with a 2–6 nm pore diameter, and SBA-15 with a 5–10 nm pore diameter (Grünberg et al., 2004; Bunkowsky et al., 2007). Grünberg et al. (2004) employed both ^1H MAS and static solid-state NMR spectroscopy in order to study the adsorption of H_2O in MCM-41 and SBA-15. Various differences have been observed in water behavior in confined state depending

on the type of porous silica. It was found that some of the H_2O molecules were strongly bound to the surface of SBA-15, and these water molecules could be removed by only heating. Stronger bounded H_2O molecules were observed in the case of SBA-15 structure but not in MCM-41. At higher filling ratios, in MCM-41 there was a bimodal-line distribution of chemical shifts of the H_2O molecules, where one signal was at the position of inner bulk H_2O , while the second peak was at the position of H_2O molecules in fast exchange with surface-SiOH groups. For SBA-15, Grünberg et al. observed only one signal continuously changing chemical shift. This outcome resulted from different filling mechanisms of the pores of MCM-41 and SBA-15. In the case of MCM-41 with a smaller pore diameter, low water loading led to the wetting of the surfaces, with subsequent higher water loadings producing more complete pore filling in the direction of the pore axis. However, because of its larger pore diameter, the filling of the pores in SBA-15 occurs radially from the pore surface to the pore center. In addition, PFG NMR results on confined water in MCM-41 demonstrated the anisotropy of the intra-particle diffusion. The components of the obtained axisymmetric diffusion tensor are assigned to diffusion parallel and perpendicular to the channel axis of the hexagonally arranged MCM-41 channel system (Stallmach et al., 2000).

Small angle neutron scattering (SANS) has been used to study the density variation of one-dimensional water trapped inside MCM-41-S channels of diameter 1.9 and 1.5 nm (Liu et al., 2008). The water inside the pore could be kept in a liquid state up to 160 K. The density of this 1-D confined water was approximately 8% higher than that of the bulk water. Using QENS it was found that diffusion of water confined in MCM-41-S was suppressed with respect to that in the bulk by a factor of about two (Takahara et al., 1999, 2005). Further, this suppression of diffusivity was found to be stronger for stronger confinement (i.e., smaller pore sizes). A much slower component of this confined water was further studied using neutron spin echo and the result on suppression of diffusivity was found consistent for slow dynamics too (Yoshida et al., 2008). Using MD simulations, Gallo et al. (2010) showed that water forms a double layered structure inside MCM-41 channels. Further, the intermediate scattering functions calculated from the MD data showed stretched exponential behavior consistent with the experimental data obtained in the QENS and NSE measurements mentioned above.

Water in Quartz Glass

Tsukahara et al. (2007) used NMR to study confined water in synthetic quartz glass containing confined (300–4,000 nm) spaces fabricated by electron-beam lithography and plasma etching. They compared the relative magnitude of the water-surface interaction, via the ^1H $1/T_1$ values, for water in a confining medium with unmodified hydrophilic surface decorated with -OH groups vs. that with a modified hydrophobic surface having -CH₃ groups. The interaction of H_2O with -CH₃ was weaker than with the -OH groups, but the confinement effect in the hydrophobic case appeared to be dominant over that in the hydrophilic case as a function of the pore size. This was explained by suggesting that the highly directional hydrogen bonding networks along with hydrophobic hydration surrounding

the $-\text{CH}_3$ groups promoted the formation of coupled H_2O molecules.

Water in Seal Rock

Diffusion of H_2O in a seal rock was studied by low-field NMR method (Fluery et al., 2009). Utilizing a MARAN 23.7 MHz from Oxford Instruments, both relaxation and diffusion experiments were conducted. Determination of continuous T_2 relaxation time distributions on two samples showed groups with three different pore sizes. Moreover, in diffusion measurements, the magnetization carried by molecules was followed, not the direct displacements of the molecules. Therefore, the lifetime of magnetization must be long enough. Because of that D_2O sample with 99.5% purity was used where no signal of D_2O was recorded, and rather a ^1H water concentration decreasing as a function of time was measured by simply recording the magnetization as a function of time. Because diffusion of CO_2 in bulk water ($2 \times 10^{-9} \text{ m}^2\text{s}^{-1}$ at 25°C) is very close to the self-diffusion of water ($2.3 \times 10^{-9} \text{ m}^2\text{s}^{-1}$) at the same temperature, these authors suggested the mobility of H in the sample could be viewed as a proxy for the upper limit of mobility of CO_2 in a porous matrices.

A Universal Scaling Law for Confined Water

A recent MD simulation study by Chiavazzo et al. (2014) attempted to generalize the behavior of water under confinement by using a universal law to predict the diffusion coefficient of water under confinement with a single parameter of the ratio of volumes of confined and total water in the pore. They simulated water in 58 different environments including nanopores, nanoparticles proteins and carbon nanotubes to obtain the diffusion coefficients of water at 300 K (see **Figure 5**). The diffusion coefficient of water in all these cases tend to fall on a single universal equation

$$D(\theta) = D_B \left(1 + \left[\frac{D_c}{D_B} - 1 \right] \theta \right) \quad (8)$$

where D is the diffusion coefficient, the subscripts C and B stand for the confined and bulk components, respectively and the parameter θ is the ratio of the volumes of water that feels the interactions with the interface and the total volume accessible to water in the pore. In a recent study, Osti et al. (2016) have applied this universal scaling law to several NS studies on the dynamics of confined water. Thus, a combination of NMR, NS, and MD simulation has not only contributed to studies of water in different confining media, but also has tried to systematically universalize the behavior of confined water.

Other Volatiles under Confinement

Low Molecular Weight Hydrocarbons in Zeolites

Low molecular weight hydrocarbons other than methane confined in several different host structures have also been studied extensively. Apart from the obvious application based interests, these have attracted attention because of the peculiar counter intuitive observations. For example, in an MD simulation study, Yashonath and Santikary (1994) observed a maximum in the translational diffusion coefficient of model

molecules as a function of molecular size in Na-Y and Na-A type zeolites. This was termed as levitation effect, where the adsorbed molecule gets levitated for a particular size as a result of a cancellation of the interactions it experiences from the opposite walls of the host. This resulted in a systematic study of a large number of low molecular weight hydrocarbons in various zeolites. A study of the intermediate scattering functions of these systems for smaller model molecules and model molecules exhibiting the diffusion maxima showed a marked difference between their behaviors (Ghorai and Yashonath, 2005). In terms of real molecules, several QENS experiments and MD simulation studies have been undertaken to study acetylene (Mitra et al., 2004; Gautam et al., 2006), ethane (Jobic et al., 1992; Chong et al., 2005), propane (Sayed et al., 2003), propylene (Sharma et al., 2009, 2010), butane (Jobic et al., 1993), butadiene (Gautam et al., 2007, 2008), and pentane (Jobic et al., 2009) in different zeolites. In addition to a focus on the translational diffusion, rotational motion of these molecules in zeolites has also been studied exclusively (Jobic et al., 1992; Mukhopadhyay et al., 2004; Gautam et al., 2010, 2016). One particular system of interest here is ethane in $\text{AlPO}_4\text{-5}$. For this system, NMR and QENS experiments reported conflicting features. While NMR measurements predicted presence of a single-file diffusion (Gupta et al., 1995), no such feature was observed in the QENS experiment (Jobic et al., 1997). To resolve this conflict, MD simulations on the system were carried out that indicated an absence of single-file diffusion in defect free $\text{AlPO}_4\text{-5}$ (Demontis et al., 2001).

PFG NMR was also utilized for investigating fluid behavior upon confining the fluid into zeolites (Gratz et al., 2009; Freude et al., 2013). Gratz et al. (2009) studied diffusional behavior of some hydrocarbons, such as propane and propylene adsorbed in NaX zeolites by PFG NMR. In Diffusion EXchange SpectroscopY (DEXSY) spectral mapping, there were on diagonal and off-diagonal peaks where the former belonged to the adsorbed phase and the latter were fingerprints of molecules migrating from exterior regions of the zeolite crystals into the crystallites and vice versa (**Figure 6**). The most interesting result was observed on the confined mixtures of hydrocarbons after the mixtures were adsorbed into the zeolites. The diffusion coefficients of the hydrocarbons in the mixture deviated only negligibly from those of the single constituent system, which emphasizes that the governing interactions happen between the adsorbed molecules and the zeolite hosts.

Effect of Pore Structure on Dynamics of Confined Hydrocarbon

Because zeolites exhibit a variety of pore structures, it is possible to study the influence of pore geometry on the dynamic behaviors of the confined fluid. Zeolites ZSM-5 and 5A were used for the comparison of dynamics of n-hexane (Stepanov et al., 2003) by combining ^2H NMR and neutron scattering. ZSM-5 is a zeolite having straight channels interconnected by zig-zag channels, each consisting of ten-membered oxygen rings (Kokotailo et al., 1978). The porous volume of zeolite 5A consists of a cubic array of α -cages (approximate diameter of 11.2 Å), interconnected through eight-membered oxygen windows of free

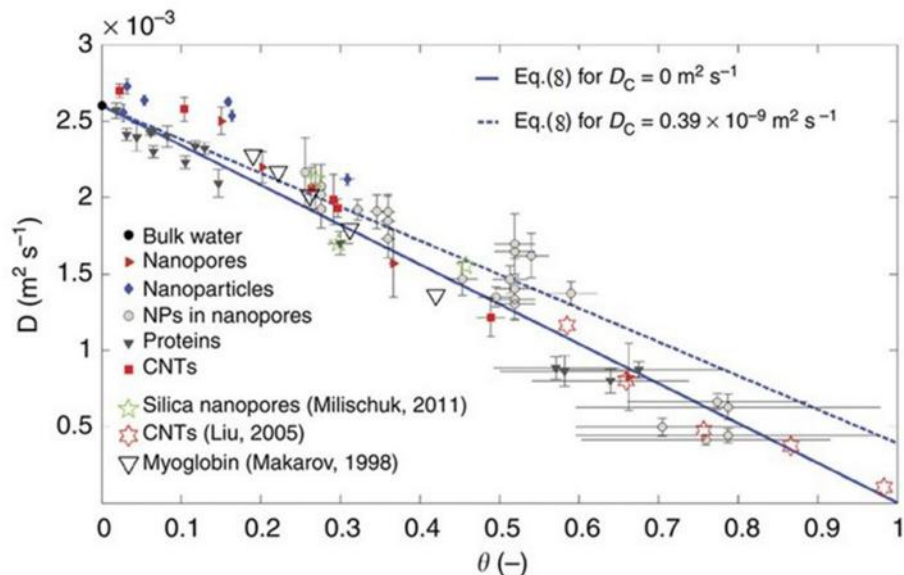


FIGURE 5 | Self-diffusion coefficient of water in different systems as a function of scaling parameter θ . Reproduced from Chiavazzo et al. (2014).

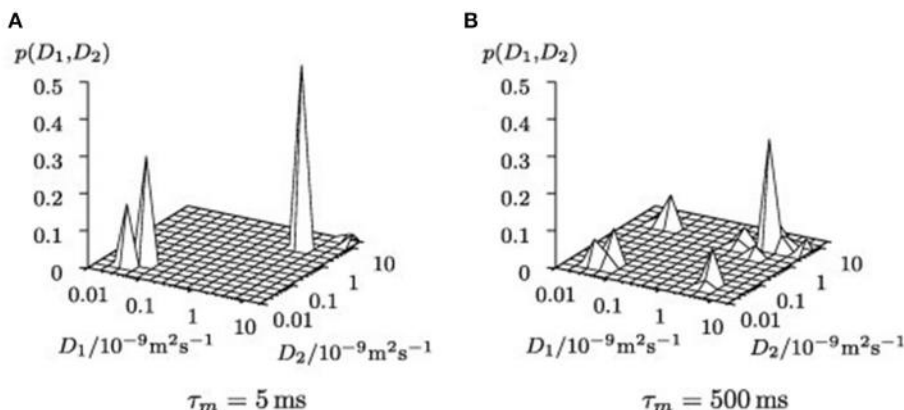


FIGURE 6 | Uncorrected 2D inverse Laplace transformed NMR signal maps of DEXSY experiments for different mixing times τ_m **(A)** $\tau_m = 5$ ms, **(B)** $\tau_m = 500$ ms. Reprinted from Gratz et al. (2009), Copyright 2009 with permission from Elsevier.

effective diameter 4.4 Å. Each α -cage has access to six similar neighbor α -cages (Adams and Haselden, 1984). The differences in the structures of the zeolites were reflected in the dynamics of confined n-hexane. In ZSM-5, the molecule sits in the channels segments and the energy barrier between two sites is small. Whereas, in 5A zeolite, the n-hexane molecule spends a longer time in the α -cages before moving to the adjacent cage. The ^2H NMR spectra indicated that the more confined adsorption geometry of n-hexane in the ZSM-5 structure, in the form of anisotropic motions, whereas isotropically reorienting molecules were evidenced in the α -cages of 5A zeolite. The diffusion coefficient of n-hexane, obtained by NS measurements at 300 K, was more than four orders of magnitude larger in ZSM-5 compared with 5A zeolite.

In another study to probe the effect of pore structure on the rotational motion of confined fluid, MD simulations of ethane in ZSM-5 were carried out (Gautam et al., 2016). As mentioned above, ZSM-5 has three different types of pores—straight channels, zig-zag channels and the intersections of these two types of channels—the last imposing the most relaxed confinement. It was found that the rotational motion of ethane in ZSM-5 was hindered. The extent of this hindrance was found to be greatest in the zig-zag channels and least in the intersections, thus indicating the importance of pore geometry. Further, the rotational motion was found to get enhanced at higher loadings, in agreement with the experimental QENS study carried out on this system earlier (Jobic et al., 1992). We note here, that this enhancement of rotational motion at higher

loading (or correspondingly, higher pressure) is consistent with an enhancement of translational diffusion at higher pressures observed for methane in carbon aerogel (Chathoth et al., 2010) and propane in silica aerogel (Gautam et al., 2015).

Hydrogen in Zeolites

Bär et al. (1999) compared hydrogen self-diffusion in zeolites by PFG NMR and QENS. In this study large zeolite crystallites, such as NaX with diameters ≥ 30 and $100\text{ }\mu\text{m}$ and NaA with diameter $\geq 15\text{ }\mu\text{m}$ were utilized. The short (T_2) times and the low spin density, put a limitation on the accuracy of the PFG NMR diffusivities. However, the PFG NMR results were in satisfactory agreement with the evidence obtained by QENS measurements. The unexpected low diffusivity of hydrogen in silicalite was explained as a result of the effect of the pentasil chains confining a significant portion of the hydrogen molecules.

Confined CO_2

CO_2 in Smectite Clays

Due to an increased concern over the rise in atmospheric CO_2 levels, CO_2 sequestration efforts have seen a dramatic increase over the past few years. This has resulted in studies on migration of CO_2 through porous networks. For example, Bowers et al. (2014) studied incorporation of supercritical CO_2 in smectite by *in situ* ^{13}C and ^{23}Na MAS NMR. They observed that there was line broadening in the $^{13}\text{CO}_2$ resonance at 90°C and 50 bar CO_2 pressure for Na-hectorite, consistent with CO_2 pressure in the interlayers. They also acquired ^{23}Na NMR spectra for the base Na-hectorite and ^{13}C and ^{23}Na NMR spectra for a composite of the Na-hectorite and Suwannee River humic acid. The ^{13}C NMR spectra indicated a progressive increase in the width of the $^{13}\text{CO}_2$ resonance from a supercritical CO_2 blank to the Na-hectorite to the composite showing progressively increasing interaction of the CO_2 and solids. The interested reader could refer to a recent review article by Kirkpatrick et al. (2015) on combined efforts of NMR and computational molecular modeling efforts on mineral surfaces and interlayer filling by H_2O , cations, anions, CO_2 , and natural organic matter (NOM).

Effect of CO_2 on Dynamics of another Confined Volatile

A number of studies have focused on how the presence of CO_2 has impacted the dynamics of confined hydrocarbons. The fact that CO_2 has a very small NS cross section compared to hydrocarbons makes it invisible in presence of hydrocarbons and thereby facilitates studying the effect of CO_2 on their dynamics. For example, Salles et al. (2013) have used QENS and MD simulations to study the effect of CO_2 on the dynamics of methane in metal organic framework type solids which are porous materials with pores about 1 nm in diameter. QENS has also been used by Chathoth et al. (2012), Patankar et al. (2016), and Gautam et al. (2015) to study the effect of CO_2 on the dynamics of methane, ethane and propane confined in mesoporous carbon aerogel, silica pore glass and silica aerogel, respectively. In all three studies, CO_2 was found to enhance the diffusion of the confined hydrocarbon. In case of ethane in CPG, the quasielastic broadening in the QENS spectra was

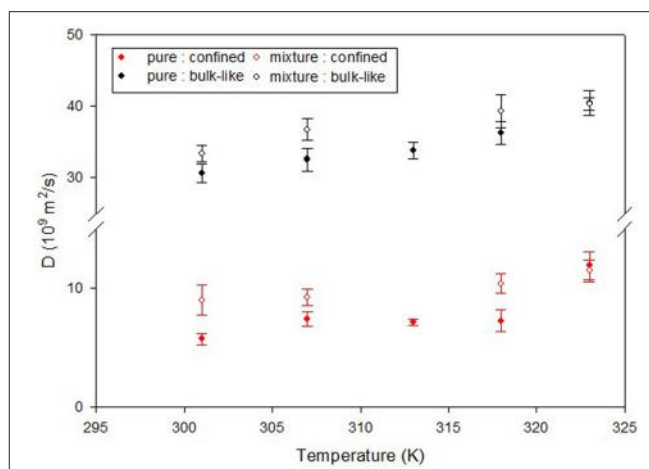


FIGURE 7 | Diffusion coefficient of ethane in CPG silica with 7.5 nm pores obtained from a QENS study. Two populations of ethane molecules were found that contributed to the quasielastic width—a bulk like population (black symbols) and another population that exhibited reduced mobility due to confinement (red symbols). The effect of CO_2 can be seen as an enhancement of the diffusivity of ethane in presence of CO_2 (open symbols) compared to that in the absence of CO_2 (solid symbols). Reprinted with permission from Patankar et al. (2016), Copyright 2016 American Chemical Society.

modeled as a sum of two Lorentzian functions which indicated presence of two different populations of molecules moving at two different time scales. These two populations represent ethane molecules that occupied the central regions of the pore which has a mean diameter of 7.5 nm and those that were close to the pore walls. A similar decomposition of two populations of ethane molecules could be observed for ethane molecules when CO_2 was added. However, the diffusion coefficients obtained by modeling of the QENS data in the latter case were higher for either population, indicating that CO_2 enhances the diffusion of ethane in CPG (Figure 7). Independent MD simulation studies have also confirmed that CO_2 enhances the diffusion of confined hydrocarbon. Le et al. (2015, 2016) have shown that presence of CO_2 enhances the diffusivity of n-butane and n-octane in silica slit nanopores, by replacing the hydrocarbons from the pore walls thereby making them free to move through the pore network.

CONCLUDING REMARKS AND FUTURE OUTLOOK

Exploring the behavior of C-O-H fluids confined in micro- and mesoporous systems provides a foundation for quantifying geologically relevant systems where mass and energy transport occur. Confinement of these fluids in porous systems gives rise to rich behavior that results from an interplay of geometrical restriction imposed by different pore sizes, the interaction between the porous material and the fluid, and the nature of the confined fluid itself. While in relatively large mesopores, the fluid motion might occur at different time scales as a function of location in the pore, for example, existence of a

bulk-like and confined components of motion in a mesoporous material, a stricter geometrical confinement can lead to a severely constrained motion, like single file molecular diffusion. Within a given porous material, time scales of motion of confined fluids can exhibit interesting dependencies on the molecular size and concentration of the confining fluid, for example levitation effect observed in the case of confined hydrocarbons. Anomalous pressure dependence has also been seen on the dynamics of gases confined in mesoporous media. Water, as a confined fluid, exhibits even richer behavior due to the effects of hydrogen bonding. A concerted motion of water molecules can result from the hydrogen bonding network. All these effects lead to a wide variety of length and time scales relevant to the study of confined fluids and as such, require versatile tools for a thorough study of behavior of geologically relevant confined fluids. Further, the techniques that probe the behavior of confined fluids at the molecular level depend heavily on the interpretation of the measured data and as such can be prone to subjective bias. Therefore, if possible it is advantageous to look at each problem from different perspectives. This is possible by using a combination of different techniques to understand the phenomena of interest. Nuclear magnetic resonance (NMR) and NS are two such techniques that can provide complimentary information on confined fluids. A synergistic use of these techniques has been successful in revealing important structural and dynamical information on fluid-substrate interactions. Further, MD simulations, which provide information in real space and time coordinates, can underpin the interpretation of the experimental data. MD simulations have been used to resolve conflicting results derived from NMR and NS. Thus, a combination of NMR, NS, and MD simulations provides a powerful “tool kit” to contribute toward a more complete understanding of confined important fluids of geological relevance.

In the current report, after a short introduction to the importance of confinement effect on fluids having significance in mass and energy transport of earth, we summarized which nano- and mesoporous matrix systems have been

utilized for investigating confined fluid behavior. Further, we provide examples of how NMR, NS, and MD approaches have been employed for studying behavior of confined fluids as a function of temperatures, pressure, confinement size, confinement dimensionality, to name a few. These examples have highlighted unusual behavior of confined fluids, including anomalous pressure or loading dependences and effects of variable pore structures. We have also discussed how MD simulation studies on water in a variety of confined spaces have helped systemize its immensely complex behavior by proposing a universal scaling law for diffusion of confined water. With ever-growing enhancement of computing power, in near future it should be possible to use MD simulations to study systems with confinement sizes larger than a few nanometers without coarse graining that is currently necessary. Similar advancements in NS and NMR instrumentation might extend the energy and time scales accessible at present. We believe that a combination of NMR, NS, and MD simulations will provide otherwise unobtainable structural and dynamical information about model confined fluid systems where fluids are confined into porous engineered proxies. Such an approach will continue contributing to understand these systems at geological conditions relevant for Earth's surface, its subsurface and the surfaces of other planets deep into the interior.

AUTHOR CONTRIBUTIONS

All authors listed, have made substantial, direct and intellectual contribution to the work, and approved it for publication.

ACKNOWLEDGMENTS

The authors (SG and DC) would like to acknowledge the support provided by the US Department of Energy, Office of Basic Energy Sciences, Division of Chemical Sciences, Geosciences and Biosciences, Geosciences Program under grant DESC0006878. SO would like to thank the Sloan Foundation-funded Deep Carbon Observatory for support of the NMR effort.

REFERENCES

- Abragam, A. (1961). *Principles of Nuclear Magnetism*. Oxford: Clarendon Press.
- Adams, J. M., and Haselden, D. A. (1984). The structure of dehydrated zeolite 5A ($\text{Si}/\text{Al} = 1.02$) by neutron profile refinement. *J. Solid State Chem.* 51, 83–90. doi: 10.1016/0022-4596(84)90318-9
- Allen, D., Crary, S., Freedman, B., Andreani, M., Klop, W., Badry, R., et al. (1997). How to use borehole nuclear magnetic resonance. *Schlumberger Oilfield Rev.* 9, 34–57.
- Allen, M. P., and Tildesley, D. J. (1987). *Computer Simulation of Liquids*. Oxford: Oxford University Press.
- Al-Othman, Z. A. (2012). A review: fundamental aspects of silicate mesoporous materials. *Materials* 5, 2874–2902. doi: 10.3390/ma5122874
- Anovitz, L. M., and Cole, D. R. (2015). Characterization and analysis of porosity and pore structures. *Rev. Mineral. Geochem.* 80, 61–164. doi: 10.2138/rmg.2015.80.04
- Asefa, T., and Tao, Z. (2012). Mesoporous silica and organosilica materials—Review of their synthesis and organic functionalization. *Can. J. Chem.* 90, 1015–1031. doi: 10.1139/v2012-094
- Bacon, G. E. (1975). *Neutron Diffraction*. Oxford: Clarendon Press.
- Bär, N. K., Ernst, H., Jobic, H., and Kärger, J. (1999). Combined quasi-elastic neutron scattering and NMR study of hydrogen diffusion in zeolites. *Magn. Reson. Chem.* 37, S79–S83. doi: 10.1002/(sici)1097-458x(199912)37:13<s79::aid-mrc545>3.0.co;2-0
- Bée, M. (1988). *Quasielastic Neutron Scattering*. Bristol: Adam Hilger.
- Behroozmand, A. A., Keating, K., and Auken, E. (2014). A review of the principles and applications of the NMR technique for near-surface characterization. *Surv. Geophys.* 36, 27–85. doi: 10.1007/s10712-014-9304-0
- Berendsen, H. J. C., Grigera, J. R., and Straatsma, T. P. (1987). The missing term in effective pair potentials. *J. Phys. Chem.* 91, 6269–6271. doi: 10.1021/j100308a038
- Bhattacharja, S., D'Orazio, F., Tarcon, J. C., and Halperin, W. P. (1989). Internal structure of porous silica: a model system for characterization

- by nuclear magnetic resonance. *J. Am. Ceram. Soc.* 72, 2126–2130. doi: 10.1111/j.1151-2916.1989.tb06043.x
- Bordallo, H. N., Aldridge, L. P., Churchman, G. J., Gates, W. P., Telling, M. T. F., Kiefer, K., et al. (2008). Quasielastic neutron scattering studies on clay interlayer space highlighting the effect of the cation in confined water dynamics. *J. Phys. Chem. C* 112, 13982–13991. doi: 10.1021/jp803274j
- Bowers, G. M., Hoyt, D. W., Burton, S. D., Ferguson, B. O., Varga, T., and Kirkpatrick, R. J. (2014). *In situ* ^{13}C and ^{23}Na magic angle spinning NMR investigation of supercritical CO_2 incorporation in smectite–Natural organic matter composites. *J. Phys. Chem. C* 118, 3564–3573. doi: 10.1021/jp410535d
- Breen, C., and Moronta, A. (1999). Influence of layer charge on the catalytic activity of mildly acid-activated Tetramethylammonium-exchanged Bentonites. *J. Phys. Chem. B* 103, 5675–5680. doi: 10.1021/jp9901646
- Brigatti, M. F., Galan, E., and Theng, B. K. (2013). “Structure and mineralogy of clay minerals, Chapter 2,” in *Handbook of Clay Science*, Vol. 5A, eds F. Bergaya and G. Lagaly (Amsterdam: Elsevier), 21–81.
- Brown, G. E. Jr. (2001). How minerals react with water. *Science* 294, 67–70. doi: 10.1126/science.1063544
- Brownstein, K. R., and Tarr, C. E. (1979). Importance of classical diffusion in NMR studies of water in biological cells. *Phys. Rev. A* 19, 2446–2453. doi: 10.1103/PhysRevA.19.2446
- Bunkowsky, G., Breitzke, H., Adamczyk, A., Roelofs, F., Emmler, T., Gedat, E., et al. (2007). Structural and dynamical properties of guest molecules confined in mesoporous silica materials revealed by NMR. *Phys. Chem. Chem. Phys.* 9, 4843–4853. doi: 10.1039/b707322d
- Callaghan, P. T. (1991). *Principles of Nuclear Magnetic Resonance Microscopy*. Oxford: Clarendon Press.
- Callaghan, P. T., Coy, A., MacGowan, D., Packer, K. J., and Zelaya, F. O. (1991). Diffraction-like effects in NMR diffusion studies of fluids in porous solids. *Nature* 351, 467–469. doi: 10.1038/351467a0
- Caro, J., Karger, J., Pfeifer, H., and Schollner, R. (1975). Zur Selbstdiffusion von Methan in 5A-Zeolithen. *Z. Phys. Chem.* 256, 698–704.
- Casco, M. E., Albero, J. S., Ramirez-Cuesta, A. J., Rey, F., Jorda, J. L., Bansode, A., et al. (2015). Methane hydrate formation in confined nanospace can surpass nature. *Nat. Comm.* 6, 6432. doi: 10.1038/ncomms7432
- Čejka, J., Corma, A., and Zones, S. (2010). *Zeolites and Catalysis: Synthesis Reactions and Applications*. Weinheim: Wiley.
- Chakrabarty, D., Gautam, S., Mitra, S., Gil, A., Vicente, M. A., and Mukhopadhyay, R. (2006). Dynamics of adsorbed water in saponite clay: neutron scattering study. *Chem. Phys. Lett.* 426, 296–300. doi: 10.1016/j.cplett.2006.05.131
- Chathoth, S. M., He, L., Mamontov, E., and Melnichenko, Y. B. (2012). Effect of carbon dioxide and nitrogen on the diffusivity of methane confined in nano-porous carbon aerogel. *Micropor. Mesopos. Mat.* 148, 101–106. doi: 10.1016/j.micromeso.2011.07.019
- Chathoth, S. M., Mamontov, E., Melnichenko, Y. B., and Zamponi, M. (2010). Diffusion and adsorption of methane confined in nano-porous carbon aerogel: a combined quasi-elastic and small-angle neutron scattering study. *Micropor. Mesopos. Mat.* 132, 148–153. doi: 10.1016/j.micromeso.2010.02.012
- Chiavazzo, E., Fasano, M., Asinari, P., and Decuzzi, P. (2014). Scaling behavior for the water transport in nanoconfined geometries. *Nat. Comm.* 5, 3565. doi: 10.1038/ncomms4565
- Chong, S. S., Jobic, H., Plazanet, M., and Sholl, D. S. (2005). Concentration dependence of transport diffusion of ethane in silicalite: a comparison between neutron scattering experiments and atomically detailed simulations. *Chem. Phys. Lett.* 408, 157–161. doi: 10.1016/j.cplett.2005.04.023
- Cohen de Lara, E., Kahn, R., and Mezei, F. (1983). Determination of the intracrystalline diffusion coefficient of methane in A zeolites by means of neutron spin-echo experiments. *J. Chem. Soc. Faraday Trans. 1* 79, 1911–1920. doi: 10.1039/f19837901911
- Cole, D. R., Gruszkiewicz, M. S., Simonson, J. M., Chialvo, A. A., and Melnichenko, Y. B. (2004). “Influence of nanoscale porosity on fluid behavior,” in *Water–Rock Interaction*, Vol. 1, eds R. Wanty and R. Seal (Rotterdam: A Balkema Publishers), 735–739.
- Cole, D. R., Ok, S., Striolo, A., and Phan, A. (2013). “Hydrocarbon behavior at nanoscale interfaces,” in *Carbon in Earth, Reviews in Mineralogy and Geochemistry*, Vol. 75, eds R. M. Hazen, A. P. Jones, and J. A. Baross (Chantilly, VA: Mineralogical Society of America), 495–545.
- Cool, P., and Vasant, E. F. (1998). “Pillared Clays: Preparation, Characterization and Applications,” in *Molecular Sieves—Science and Technology. 1. Synthesis*, eds H. G. Karge and J. Weitkamp (Berlin;Heidelberg: Springer), 265–288.
- Corsaro, C., Maisano, R., Mallamace, D., and Dugo, G. (2013). ^{1}H NMR study of water/methanol solutions as a function of temperature and concentration. *Physica A* 392, 596–601. doi: 10.1016/j.physa.2012.11.008
- Cotts, R. M. (1989). Pulsed field gradient stimulated echo methods for improved NMR diffusion measurements in heterogeneous systems. *J. Magn. Reson.* 83, 252–266. doi: 10.1016/0022-2364(89)90189-3
- Cotts, R. M. (1991). Diffusion and diffraction. *Nature* 351, 443–444. doi: 10.1038/351443a0
- Davis, M. E. (2002). Ordered porous materials for emerging applications. *Nature* 417, 813–821. doi: 10.1038/nature00785
- Dec, S. F., Bowler, K. E., Stadterman, L. L., Koh, C. A., and Sloan, E. D. Jr. (2007). NMR study of methane+ethane structure I hydrate decomposition. *J. Phys. Chem. A* 111, 4297–4303. doi: 10.1021/jp070442y
- Demontis, P., Gonzalez, J. G., Suffritti, G. B., and Tilocca, A. (2001). Statics and dynamics of ethane molecules in AlPO4-5: A molecular dynamics simulation study. *J. Am. Chem. Soc.* 123, 5069–5074. doi: 10.1021/ja003940s
- Diakova, G., Korb, J. P., and Bryant, R. G. (2012). The magnetic field dependence of water T1 in tissues. *Magn. Reson. Med.* 68, 272–277. doi: 10.1002/mrm.23229
- Dickens, G. R., O’Neil, J. R., Rea, D. K., and Owen, R. M. (1995). Dissociation of oceanic methane hydrate as a cause of the carbon isotope excursion at the end of Paleocene. *Paleoocean* 10, 965–971. doi: 10.1029/95PA02087
- D’Orazio, F., Bhattacharja, S., Halperin, W. P., and Gerhardt, R. (1990a). Fluid transport in partially filled porous sol-gel silica glass. *Phys. Rev. B* 42, 6503–6508. doi: 10.1103/PhysRevB.42.6503
- D’Orazio, F., Bhattacharja, S., Halperin, W. P., Eguchi, K., and Mizusaki, T. (1990b). Molecular diffusion and nuclear-magnetic-resonance relaxation of water in unsaturated porous silica glass. *Phys. Rev. B* 42, 9810–9818. doi: 10.1103/PhysRevB.42.9810
- Dornan, P., Alavi, S., and Woo, T. K. (2007). Free energies of carbon dioxide sequestration and methane recovery in clathrate hydrates. *J. Chem. Phys.* 127, 124510-1–124510-8. doi: 10.1063/1.2769634
- Duan, S., Gu, M., Du, X., and Xian, X. (2016). Adsorption equilibrium of CO_2 and CH_4 and their mixture on Sichuan basin shale. *Energy Fuels* 30, 2248–2256. doi: 10.1021/acs.energyfuels.5b02088
- Duer, M. J. (2004). *Introduction to Solid-State NMR Spectroscopy*. Oxford: Blackwell Science.
- Eddaoudi, M., Moler, D. B., Li, H., Chen, B., Reineke, T. M., O’Keeffe, M., et al. (2001). Modular chemistry:secondary building units as a basis for the design of highly porous and robust metal–organic carboxylate frameworks. *Acc. Chem. Res.* 34, 319–330. doi: 10.1021/ar000034b
- Fernandez, M., Pampel, A., Takahashi, R., Sato, S., Freude, D., and Kärger, J. (2008). Revealing complex formation in acetone-n-alkanes mixtures by MAS PFG NMR diffusion measurement in nanoporous hosts. *Phys. Chem. Chem. Phys.* 10, 4165–4171. doi: 10.1039/b802929f
- Fluery, M., Berne, P., and Bachaud, P. (2009). Diffusion of dissolved CO_2 in caprock. *Energy Procedia* 1, 3461–3468. doi: 10.1016/j.egypro.2009.02.137
- Freedman, R., and Heaton, N. (2004). Fluid characterization using nuclear magnetic resonance logging. *Petrophysics* 45, 241–250. Available online at: <http://cat.inist.fr/?aModele=afficheN&cpsidt=15792357>
- Frenkel, D., and Smit, B. (2001). *Understanding Molecular Simulations: From Algorithms to Applications*. San Diego, CA: Academic Press.
- Freude, D., Beckert, S., Stallmach, F., Kurzhals, R., Taschner, D., Toufar, H., et al. (2013). Ion and water mobility in hydrated Li–LSX zeolite studied by ^{1}H , ^{6}Li and ^{7}Li NMR spectroscopy and diffusometry. *Micropor. Mesopos. Mat.* 172, 174–181. doi: 10.1016/j.micromeso.2013.01.011
- Gaede, H. C., and Gawrisch, K. (2004). Multi-dimensional pulsed field gradient magic angle spinning NMR experiments on membranes. *Magn. Reson. Chem.* 42, 115–122. doi: 10.1002/mrc.1329
- Gallo, P., Roovere, M., and Chen, S.-H. (2010). Anomalous dynamics of water confined in MCM-41 at different hydrations. *J. Phys.* 22:284102. doi: 10.1088/0953-8984/22/28/284102
- Galvosa, P., Stallmach, F., Seiffert, G., Kärger, J., Kaess, U., and Majer, G. (2001). Generation and application of ultra-high-intensity magnetic field gradient pulses for NMR spectroscopy. *J. Magn. Reson.* 151, 260–268. doi: 10.1006/jmre.2001.2381

- Gautam, S. (2017). "Use of quasielastic neutron scattering and molecular dynamics simulation to study molecular dynamics under confinement," in *Horizons in World Physics*, Vol. 290, ed A. Reimer (New York, NY: Nova Science Publishers), 25–44.
- Gautam, S., Liu, T., Patankar, S., Tomasko, D., and Cole, D. (2016). Location dependent orientational structure and dynamics of ethane in ZSM5. *Chem. Phys. Lett.* 648, 130–136. doi: 10.1016/j.cplett.2016.02.021
- Gautam, S., Liu, T., Rother, G., Jalalvo, N., Mamontov, E., Welch, S., et al. (2015). Dynamics of propane in nanoporous silica aerogel: a quasielastic neutron scattering study. *J. Phys. Chem. C* 119, 18188–18195. doi: 10.1021/acs.jpcc.5b03444
- Gautam, S., Mitra, S., Chaplot, S. L., and Mukhopadhyay, R. (2008). Dynamics of 1,3-butadiene adsorbed in Na-Y zeolite: a molecular dynamics simulation studies. *Phys. Rev. E* 77:061201. doi: 10.1103/physreve.77.061201
- Gautam, S., Mitra, S., Mukhopadhyay, R., and Chaplot, S. L. (2006). Diffusion of acetylene inside Na-Y zeolite: molecular dynamics simulation studies. *Phys. Rev. E* 74:041202. doi: 10.1103/PhysRevE.74.041202
- Gautam, S., Mitra, S., Sayeed, A., Yashonath, S., Chaplot, S. L., and Mukhopadhyay, R. (2007). Diffusion of 1,3-butadiene in Na-Y zeolite: neutron scattering study. *Chem. Phys. Lett.* 442, 311–315. doi: 10.1016/j.cplett.2007.05.109
- Gautam, S., Sharma, V. K., Mitra, S., Chaplot, S. L., and Mukhopadhyay, R. (2010). Rotational dynamics of propylene in ZSM-5 zeolitic frameworks. *Chem. Phys. Lett.* 501, 345–350. doi: 10.1016/j.cplett.2010.11.080
- Gelb, L. D., Gubbins, K. E., Radhakrishnan, R., and Sliwinska-Bartkowiak, M. (1999). Phase separation in confined systems. *Rep. Prog. Phys.* 62, 1573–1659. doi: 10.1088/0034-4885/62/12/201
- Ghorai, P. K., and Yashonath, S. (2005). Levitation effect: distinguishing anomalous from linear regime of guests sorbed in zeolites through the decay of intermediate scattering function and wavevector dependence of self-diffusivity. *J. Phys. Chem. B* 109, 3979–3983. doi: 10.1021/jp046121t
- Gratz, M., Wehring, M., Galvosas, P., and Stallmach, F. (2009). Multidimensional NMR diffusion studies in microporous materials. *Micropor. Mesopos. Mat.* 125, 30–34. doi: 10.1016/j.micromeso.2009.02.014
- Grünenberg, B., Emmler, T., Gedat, E., Shenderovich, I., Findenegg, G. H., Limbach, H.-H., et al. (2004). Hydrogen bonding of water confined in mesoporous silica MCM-41 and SBA-15 studied by ^1H solid-state NMR. *Chem. Eur. J.* 10, 5689–5696. doi: 10.1002/chem.200400351
- Grunewald, E., and Knight, R. (2009). A laboratory study of NMR relaxation times and pore coupling in heterogeneous media. *Geophysics* 74, 215–221. doi: 10.1190/1.3223712
- Guillot, B. (2002). A reappraisal of what we have learnt during three decades of computer simulations on water. *J. Mol. Liq.* 101, 219–260. doi: 10.1016/S0167-7322(02)00094-6
- Gupta, A., Dec, S. F., Koh, C. A., and Sloan, E. D. (2007). NMR investigation of methane hydrate dissociation. *J. Phys. Chem. C* 111, 2341–2346. doi: 10.1021/jp066536+
- Gupta, S. S., and Bhattacharyya, K. G. (2012). Adsorption of heavy metals on kaolinite and montmorillonite: a review. *Phys. Chem. Chem. Phys.* 14, 6698–6723. doi: 10.1039/c2cp40093f
- Gupta, V., Nivarthi, S. S., McCormick, A. V., and Davis, H. T. (1995). Evidence of single-file diffusion of ethane in the molecular sieve AlPO4-5. *Chem. Phys. Lett.* 247, 596–600. doi: 10.1016/S0009-2614(95)01246-X
- Hawlicka, E. (1995). Self-diffusion in multicomponent liquid systems. *Chem. Soc. Rev.* 34, 13743–13750. doi: 10.1039/c9952400367
- Hoover, W. M. G. (1986). *Molecular Dynamics, Lecture Notes in Physics* 258. Berlin: Springer-Verlag.
- Hummer, G., Rasaiah, J. C., and Noworyta, J. P. (2001). Water conduction through the hydrophobic channel of a carbon nanotube. *Nature* 414, 188–190. doi: 10.1038/35102535
- Inlow, R. O., Joesten, M. D., and Van Wazer, J. R. (1975). Spin-lattice relaxation and hydrogen bonding in methanol-solvent mixtures. *J. Phys. Chem.* 79, 2307–2312. doi: 10.1021/j100588a016
- James, T. L. (1998). *Fundamentals of NMR. Nuclear Magnetic Resonance*. Bethesda, MD: Biophysical Society.
- Jameson, C. J., Jameson, A. K., Gerald, I. I., R. E., and Lim, H.-M. (1997). Anisotropic Xe chemical shifts in zeolites. The role of intra-and intercrystallite diffusion. *J. Phys. Chem. B* 42, 8418–8437. doi: 10.1021/jp971013a
- Jobic, H., Bée, M., and Caro, J. (1993). "Translational mobility of n-butane and n-hexane in ZSM-5 measured by quasielastic neutron scattering," in *Proceedings of the Ninth International Zeolite Conference*, Vol. II, eds R. Von Ballmos, J. B. Higgins, and M. M. J. Treacy (Montreal, QC: Butterworth Heinemann), 121–128.
- Jobic, H., Bée, M., Caro, J., Bülow, M., and Kärger, J. (1989). Molecular self-diffusion of methane in zeolite ZSM-5 by quasi-elastic neutron scattering and nuclear magnetic resonance pulsed field gradient technique. *J. Chem. Soc. Faraday Trans. 1* 85, 4201–4209. doi: 10.1039/f19898504201
- Jobic, H., Bée, M., and Kearly, G. J. (1992). Dynamics of ethane and propane in zeolite ZSM-5 studied by quasielastic neutron scattering. *Zeolites* 12, 146–151. doi: 10.1016/0144-2449(92)90075-Z
- Jobic, H., Borah, B. J., and Yashonath, S. (2009). Neutron scattering and molecular dynamics evidence for levitation effect in nanopores. *J. Phys. Chem. B* 113, 12635–12638. doi: 10.1021/jp907453a
- Jobic, H., Hahn, K., Kärger, J., Bée, M., Tuel, A., Noack, M., et al. (1997). Unidirectional and single file diffusion of molecules in one dimensional channel systems. A quasielastic neutron scattering study. *J. Phys. Chem. B* 101, 5834–5841. doi: 10.1021/jp970773i
- Johnson, E. B. G., and Arshad, S. E. (2014). Hydrothermally synthesized zeolites based on kaolinite: a review. *Appl. Clay Sci.* 97–98, 215–221. doi: 10.1016/j.clay.2014.06.005
- Jorgensen, W. L., Chandrasekhar, J., Madura, J. D., Impey, R. W., and Klein, M. L. (1983). Comparison of simple potential functions for simulating liquid water. *J. Chem. Phys.* 79, 926–935. doi: 10.1063/1.445869
- Kärger, J., Binder, T., Chmelik, C., Hibbe, F., Krautscheid, H., Krishna, R., et al. (2014). Microimaging of transient guest profiles to monitor mass transfer in nanoporous materials. *Nat. Mater.* 13, 333–343. doi: 10.1038/nmat3917
- Kimmich, R., and Anoardo, E. (2004). Field-cycling NMR relaxometry. *Prog. Nuc. Magn. Reson. Spect.* 44, 257–320. doi: 10.1016/j.pnmrs.2004.03.002
- Kirkpatrick, R. J., Kalinichev, A. G., Bowers, G. M., Yazaydin, A. O., Krishnan, M., Saharay, M., et al. (2015). NMR and computational molecular modeling studies of mineral surfaces and interlayer galleries: a review. *Am. Mineral.* 100, 1341–1354. doi: 10.2138/am-2015-5141
- Kittler, W. C., Obruchkov, S., Galvosas, P., and Hunter, M. W. (2014). Pulsed second order field NMR for real time PGSE and single-shot surface to volume ratio measurements. *J. Magn. Reson.* 247, 42–49. doi: 10.1016/j.jmr.2014.08.005
- Kleinberg, R. L., Kenyon, W. E., and Mitra, P. P. (1994). Mechanism of NMR relaxation of fluids in rock. *J. Magn. Res. Ser. A* 108, 206–214. doi: 10.1006/jmra.1994.1112
- Kokotailo, G. T., Lawton, S. L., Olson, D. H., and Meier, W. M. (1978). Structure of synthetic zeolite ZSM-5. *Nature* 272, 437–438. doi: 10.1038/272437a0
- Kolesnikov, A. I., Zanotti, J. M., Loong, C. K., Thiagarajan, P., Moravsky, A. P., Loufty, R. O., et al. (2004). Anomalously soft dynamics of water in a nanotube: a revelation of nanoscale confinement. *Phys. Rev. Lett.* 93:035503. doi: 10.1103/PhysRevLett.93.035503
- Korb, J.-P. (2006). "Surface diffusion of liquids in disordered nanopores and materials: a field cycling relaxometry approach," in *Fluid Transport Nanoporous Materials*, eds W. C. Connor, and J. Fraissard (Dordrecht: Springer), 415–437.
- Koskela, T., Ylihautala, M., Jokisaari, J., and Vaara, J. (1996). ^{13}C NMR spectroscopy of methane adsorbed in SAPO-11 molecular sieve. *Chem. Phys. Lett.* 261, 425–430. doi: 10.1016/0009-2614(96)00996-7
- Koskela, T., Ylihautala, M., Jokisaari, J., and Vaara, J. (1998). ^{13}C NMR of methane in an AlPO4-11 molecular sieve: exchange effects and shielding anisotropy. *Phys. Rev. B* 58, 14833–14836. doi: 10.1103/PhysRevB.58.14833
- Kuchel, P. W., Pages, G., Nagashima, K., and Chuang, K. H. (2012). Stejskal-tanner equation derived in full. *Concepts Magn. Reson. A* 40A, 205–214. doi: 10.1002/cmra.21241
- Kvenvolden, K. A. (1988). Methane hydrate—a major reservoir of carbon in the shallow geosphere? *Chem. Geol.* 71, 41–51. doi: 10.1016/0009-2541(88)90104-0
- Langmi, H. W., Ren, J., North, B., Mathe, M., and Bessarabov, D. (2014). Hydrogen storage in metal-organic frameworks: a review. *Electrochim. Acta* 128, 368–392. doi: 10.1016/j.electacta.2013.10.190
- Le, T., Ogbe, S., Striolo, A., and Cole, D. R. (2016). N-octane diffusivity enhancement via carbon dioxide in silica slit nanopores—a molecular dynamics simulation study. *Mole. Simu.* 42, 745–752. doi: 10.1080/08927022.2015.1089991

- Le, T., Striolo, A., and Cole, D. R. (2015). CO_2 - C_4H_{10} mixtures simulated in silica slit pores: relation between structure and dynamics. *J. Phys. Chem. C* 119, 15274–15284. doi: 10.1021/acs.jpcc.5b03160
- Lee, S., Park, S., Lee, Y., and Seo, Y. (2013). Thermodynamic and ^{13}C NMR spectroscopic verification of methane–carbon dioxide replacement in natural gas hydrates. *Chem. Eng. J.* 225, 636–640. doi: 10.1016/j.cej.2013.03.117
- Li, J., Corma, A., and Yu, J. (2015). Synthesis of new zeolite structures. *Chem. Soc. Rev.* 44, 7112–7127. doi: 10.1039/C5CS00023H
- Liebscher, A., and Heinrich, C. A. (eds.). (2007). *Fluid-Fluid Interactions. Reviews in Mineralogy and Geochemistry*. Chantilly, VA: Mineralogical Society of America.
- Liu, D., Zhang, Y., Liu, Y., Wu, J., Chen, C.-C., Mou, C.-Y., et al. (2008). Density measurement of 1-D confined water by small angle neutron scattering method: pore size and hydration level dependencies. *J. Phys. Chem. B* 112, 4309–4312. doi: 10.1021/jp70331k
- Liu, X., Pan, X., Zhang, S., Han, X., and Bao, X. (2014). Diffusion of water inside carbon nanotubes studied by pulsed field gradient NMR spectroscopy. *Langmuir* 30, 8036–8045. doi: 10.1021/la500913r
- Lok, B. M., Messina, C. A., Patton, R. L., Gajek, R. T., Cannan, T. R., and Flanigen, E. M. (1984). Silicoaluminophosphate molecular sieves: another new class of microporous crystalline inorganic solids. *J. Am. Chem. Soc.* 106, 6092–6093. doi: 10.1021/ja00332a063
- Loring, J. S., Ilton, E. S., Chen, J., Thompson, C. J., Martin, P. F., Benezeth, P., et al. (2014). *In situ* study of CO_2 and H_2O partitioning between Na–montmorillonite and variably wet supercritical carbon dioxide. *Langmuir* 30, 6120–6128. doi: 10.1021/la500682t
- Macomber, R. S. (1998). *A Complete Introduction to Modern NMR Spectroscopy*. New York, NY: John Wiley & Sons.
- Malikova, N., Cadene, A., Marry, V., Dubois, E., and Turq, P. (2006). Diffusion in water in clays on the microscopic scale: modelling and experiment. *J. Phys. Chem. B* 110, 3206–3214. doi: 10.1021/jp056954z
- Mamontov, E., Burnham, C. J., Chen, S.-H., Moravsky, A. P., Loong, C.-K., de Souza, N. R., et al. (2006). Dynamics of water confined in single- and double-walled carbon nanotubes. *J. Chem. Phys.* 124:194703. doi: 10.1063/1.2194020
- Marry, V., Dubois, E., Malikova, N., Durand-Vidal, S., Longeville, S., and Breu, J. (2011). Water dynamics in hectorite clays: influence of temperature studied by coupling neutron spin echo experiments and molecular dynamics. *Environ. Sci. Technol.* 45, 2850–2855. doi: 10.1021/es1031932
- Martin, M. G., and Siepmann, J. I. (1998). Transferable potentials for phase equilibria. 1. United-atom description of n-alkanes. *J. Phys. Chem. B* 102, 2569–2577. doi: 10.1021/jp972543+
- Meng, X., and Xiao, F.-S. (2014). Green routes for synthesis of zeolites. *Chem. Rev.* 114, 1521–1543. doi: 10.1021/cr4001513
- Michot, L. J., Delville, A., Humbert, B., Plazanet, M., and Levitz, P. (2007). Diffusion of water in a synthetic clay with tetrahedral charges by combined neutron time of flight measurements and molecular dynamics simulations. *J. Phys. Chem. C* 111, 9818–9831. doi: 10.1021/jp0690446
- Mitra, S., Pramanik, A., Chakrabarty, D., Juranyi, F., Gautam, S., and Mukhopadhyay, R. (2007). Diffusion of water adsorbed in hydrotalcite: neutron scattering study. *J. Phys.* 92:012167. doi: 10.1088/1742-6596/92/1/012167
- Mitra, S., Sumitra, S., Umarji, A. M., Mukhopadhyay, R., Yashonath, S., and Chaplot, S. L. (2004). Acetylene diffusion in Na-Y zeolite. *Pramana J. Phys.* 63, 449–453. doi: 10.1007/BF02705014
- Mukhopadhyay, R., Sayeed, A., Mitra, S., Kumar, A. V., Rao, M. N., Yashonath, S., et al. (2004). Rotational dynamics of propane in Na-Y zeolite: a molecular dynamics and quasielastic neutron scattering study. *Phys. Rev. E* 66:061201. doi: 10.1103/PhysRevE.66.061201
- Myshakin, E. M., Jiang, H., Warzinski, R. P., and Jordon, K. D. (2009). Molecular dynamics simulation of methane hydrate decomposition. *J. Phys. Chem. A* 113, 1913–1921. doi: 10.1021/jp807208z
- Nivarthi, S. S. S., McCormick, A. V., and Davis, H. T. (1994). Diffusion anisotropy in molecular sieves: a Fourier transform PFG NMR study of methane in $\text{AlPO}_4\text{-}5$. *Chem. Phys. Lett.* 229, 297–301. doi: 10.1016/0009-2614(94)01059-5
- Ok, S., Hoyt, D. W., Andersen, A., Sheets, J., Welch, S. A., Cole, D. R., et al. (2017). Surface interactions and confinement of methane: a high pressure magic angle spinning NMR and computational chemistry study. *Langmuir* 33, 1359–1367. doi: 10.1021/acs.langmuir.6b03590
- Ok, S., Sadaf, S., and Walder, L. (2014). Basic characterization and investigation of a fluorinated terpolymer in pure state and in mixtures with kaolinite at solid interphases of thin films prepared by facile solution cast and nonsolvent methods. *High Perform. Polym.* 26, 779–789. doi: 10.1177/0954008314529601
- Osti, N., Cote, A., Mamontov, E., Ramirez-Cuesta, A., Wesolowski, D. J., and Diallo, S. O. (2016). Characteristic features of water dynamics in restricted geometries investigated with quasi-elastic neutron scattering. *Chem. Phys.* 465–466, 1–8. doi: 10.1016/j.chemphys.2015.11.008
- Packer, K. J. (2003). Magnetic resonance in porous media: forty years on. *Magn. Reson. Imaging* 21, 163–168. doi: 10.1016/S0730-725X(03)00120-6
- Pampel, A., Fernandez, M., Freude, D., and Kärger, J. (2005). New options for measuring molecular diffusion in zeolites by MAS PFG NMR. *Chem. Phys. Lett.* 407, 53–57. doi: 10.1016/j.cplett.2005.03.062
- Pampel, A., Kärger, J., and Michel, D. (2003). Lateral diffusion of a transmembrane peptide in lipid bilayers studied by pulsed field gradient NMR in combination with magic angle sample spinning. *Chem. Phys. Lett.* 379, 555–561. doi: 10.1016/j.cplett.2003.08.093
- Patankar, S., Gautam, S., Rother, G., Podlesnyak, A., Ehlers, G., Liu, T., et al. (2016). Role of confinement on adsorption and dynamics of ethane and an ethane- CO_2 mixture in mesoporous CPG silica. *J. Phys. Chem. C* 120, 4843–4853. doi: 10.1021/acs.jpcc.5b09984
- Porion, P., Michot, L. J., Faugere, A. M., and Delville, A. (2007). Structural and dynamical properties of the water molecules confined in dense clay sediments: a study combining ^2H NMR spectroscopy and multiscale molecular modeling. *J. Phys. Chem. C* 111, 5441–5453. doi: 10.1021/jp067907p
- Price, W. S. (1997). Pulsed-field gradient nuclear magnetic resonance as a tool for studying translational diffusion: part 1. Basic theory. *Concepts Magn. Reson.* 9, 299–366. doi: 10.1002/(SICI)1099-0534(1997)9:5<299::AID-CMR2>3.0.CO;2-U
- Qian, L., Ren, Y., Wang, Y., Yue, B., and He, H. (2011). Controlled atmosphere ^{13}C and ^{1}H MAS NMR study of reforming route of methane with carbon dioxide over Rh/SBA-15. *Appl. Catal. A* 401, 114–118. doi: 10.1016/j.apcata.2011.05.004
- Richter, D., Monkenbusch, M., Arbe, A., and Colmenero, J. (2005). *Neutron Spin Echo in Polymer Systems*. Berlin; Heidelberg: Springer.
- Ripmeester, J. A., and Ratcliffe, C. I. (1988). Low-temperature cross-polarization/magic angle spinning ^{13}C NMR of solid methane hydrates: structure, cage occupancy, and hydration number. *J. Phys. Chem.* 92, 337–339. doi: 10.1021/j100313a018
- Salles, F., Jobic, H., Devic, T., Guillerm, V., Serre, C., Koza, M. M., et al. (2013). Diffusion of binary CO_2/CH_4 mixtures in the MIL-47(V) and MIL-53(Cr) metal–organic framework type solids: a combination of neutron scattering measurements and molecular dynamics simulations. *J. Phys. Chem. C* 117, 11275–11284. doi: 10.1021/jp403225t
- Sayeed, A., Mitra, S., Kumar, A. V. A., Mukhopadhyay, R., Yashonath, S., and Chaplot, S. L. (2003). Diffusion of propane in zeolite Na-Y: a molecular dynamics and quasielastic neutron scattering study. *J. Phys. Chem. B* 107, 527–533. doi: 10.1021/jp025576k
- Schmidt-Rohr, K., and Spiess, W. H. (1994). *Multidimensional Solid-State NMR and Polymers*. London: Academic Press.
- Sen, P. N. (2004). Time-dependent diffusion coefficient as a probe of geometry. *Concepts Magn. Reson. A* 23, 1–21. doi: 10.1002/cmr.a.20017
- Seo, Y.-T., and Lee, H. (2003). ^{13}C NMR analysis and gas uptake measurements of pure and mixed gas hydrates: development of natural gas transport and storage method using gas hydrate. *Korean J. Chem. Eng.* 20, 1085–1091. doi: 10.1007/BF02706941
- Sharma, V. K., Gautam, S., Mitra, S., and Mukhopadhyay, R. (2010). Dynamics of propylene adsorbed in Na-Y and Na-ZSM5 zeolites: a QENS and MD simulation study. *Z. Phys. Chem.* 224, 133–152. doi: 10.1524/zpch.2010.6096
- Sharma, V. K., Gautam, S., Mitra, S., Rao, M. N., Tripathi, A. K., Chaplot, S. L., et al. (2009). Dynamics of adsorbed hydrocarbon in nanoporous zeolite framework. *J. Phys. Chem. B* 113, 8066–8072. doi: 10.1021/jp9014405
- Sindorf, D. W., and Maciel, G. E. (1983). Silicon-29 NMR study of dehydrated/rehydrated silica gel using cross polarization and magic-angle spinning. *J. Am. Chem. Soc.* 105, 1487–1493. doi: 10.1021/ja00344a012
- Slichter, C. P. (1990). *Principles of Magnetic Resonance*. New York, NY: Springer Series in Solid State Science.
- Sloan, E. D. Jr. (2003). Fundamental principles and applications of natural gas hydrates. *Nature* 426, 353–359. doi: 10.1038/nature02135

- Sloan, E. D. Jr., and Koh, C. (2007). *Clathrate Hydrates of Natural Gases*. Boca Raton FL: CRC press.
- Song, Y.-Q. (2007). Novel NMR techniques for porous media research. *Cement Concrete Res.* 37, 325–328. doi: 10.1016/j.cemconres.2006.02.013
- Sørland, G. H., Hafskjold, B., and Herstadt, O. (1997). A stimulated-echo method for diffusion measurements in heterogeneous media using pulsed field gradients. *J. Magn. Reson.* 124, 172–176. doi: 10.1006/jmre.1996.1029
- Stallmach, F., Graser, A., Kärger, J., Krause, C., Jeschke, M., Oberhagemann, U., et al. (2001). Pulsed field gradient NMR studies of diffusion in MCM-41 mesoporous solids. *Micropor. Mesopos. Mat.* 44, 745–753. doi: 10.1016/S1387-1811(01)00256-6
- Stallmach, F., Kärger, J., Krause, C., Jeschke, M., and Oberhagemann, U. (2000). Evidence of anisotropic self-diffusion of guest molecules in nanoporous materials of MCM-41 type. *J. Am. Chem. Soc.* 122, 9237–9242. doi: 10.1021/ja001106x
- Stallmach, F., Pusch, A.-K., Splith, T., Horch, C., and Merker, S. (2015). NMR relaxation and diffusion studies of methane and carbon dioxide in nanoporous ZIF-8 and ZSM-58. *Micropor. Mesopos. Mat.* 205, 36–39. doi: 10.1016/j.micromeso.2014.08.034
- Steele, R. M., Korb, J. P., Ferrante, G., and Bubici, S. (2015). New applications and perspectives of fast field cycling NMR relaxometry. *Magn. Reson. Chem.* 54, 502–509. doi: 10.1002/mrc.4220
- Stepanov, A. G., Shegai, T. O., Luzgin, and Jobic, H. (2003). Comparison of the dynamics of n-hexane in ZSM-5 and 5A zeolite structures. *Eur. Phys. J. E Soft Matter* 12, 57–61. doi: 10.1140/epje/2003-10037-3
- Subramanian, S., Kini, R. A., Dec, S. F., and Sloan, E. D. Jr. (2000). Evidence of structure II hydrate formation from methane+ethane mixtures. *Chem. Eng. Sci.* 55, 1981–1999. doi: 10.1016/S0009-2509(99)00389-9
- Swenson, J., Bergman, R., and Howells, W. S. (2000). Quasielastic neutron scattering study of 2-dimensional water in a vermiculite clay. *J. Chem. Phys.* 113, 2873–2879. doi: 10.1063/1.1305870
- Swenson, J., Bergman, R., and Longeville, S. (2001). A neutron spin echo study of confined water. *J. Chem. Phys.* 115, 11299–11305. doi: 10.1063/1.1420728
- Takahara, S., Nakano, M., Kittaka, S., Kuroda, Y., Mori, T., Hamano, H., et al. (1999). Neutron scattering study on dynamics of water molecules in MCM-41. *J. Phys. Chem. B* 103, 5814–5819. doi: 10.1021/jp984136j
- Takahara, S., Sumiyama, S., Kittaka, S., Yamaguchi, T., and Bellissent-Funel, M. C. (2005). Neutron scattering study on dynamics of water molecules in MCM-41. 2. Determination of translational diffusion coefficient. *J. Phys. Chem. B* 109, 11231–11239. doi: 10.1007/s10450-005-5971-y
- Tanner, J. E. (1970). Use of the stimulated echo in NMR diffusion studies. *J. Chem. Phys.* 52, 2523–2526. doi: 10.1063/1.1673336
- Tsukahara, T., Hibara, A., Ikeda, Y., and Kitamori, T. (2007). NMR study of water molecules confined in extended nanospaces. *Angew. Chem. Int. Ed.* 46, 1180–1183. doi: 10.1002/anie.200604502
- Tulk, C. A., Klug, D. D., dos Santos, A. M., Karotis, G., Guthrie, M., Molaison, J. J., et al. (2012). Cage occupancies in the high pressure structure H methane hydrate: a neutron diffraction study. *J. Chem. Phys.* 136, 054502. doi: 10.1063/1.3679875
- Ueda, T., Kurokawa, K., Kawamura, Y., Miyakubo, K., and Eguchi, T. (2012). 1H NMR study of molecular motion of benzene and n-decane confined in the nanocavities of metal-organic frameworks. *J. Phys. Chem. C* 116, 1012–1019. doi: 10.1021/jp209746n
- Vasenkov, S., Bohlmann, W., Galvosas, P., Geier, O., Liu, H., and Kärger, J. (2001). PFG NMR study of diffusion in MFI-type zeolites: evidence of the existence of intracrystalline transport barriers. *J. Phys. Chem. B* 105, 5922–5927. doi: 10.1021/jp003899f
- Vogel, M. (2010). NMR studies on simple liquids in confinement. *Eur. Phys. J. Special Topics* 189, 47–64. doi: 10.1140/epjst/e2010-01309-9
- Vogel, S. C., and Priesmeyer, H.-G. (2006). “Neutron Production, Neutron Facilities and Neutron Instrumentation,” in *Neutron Scattering in Earth Sciences, Reviews in Mineralogy and Geochemistry*, Vol. 63, ed H.-R. Wenk (Chantilly: Mineralogical Society of America), 27–58.
- Vogt, C., Galvosas, P., Klitzsch, N., and Stallmach, F. (2002). Self-diffusion studies of pore fluids in unconsolidated sediments by PFG NMR. *J. Appl. Geophys.* 50, 455–467. doi: 10.1016/S0926-9851(02)00195-7
- Walbrecker, J. O., and Behroozmand, A. A. (2012). Surface-NMR measurements of the longitudinal relaxation time T1 in a homogenous sand aquifer in Skive, Denmark. *J. Appl. Geophys.* 87, 46–52. doi: 10.1016/j.jappgeo.2012.08.009
- Wang, J., Kalinichev, A. G., and Kirkpatrick, R. J. (2006). Effects of substrate structure, dynamics and energetics of water at mineral interfaces: a molecular dynamics modeling study. *Geochim. Cosmochim. Acta* 70, 562–582. doi: 10.1016/j.gca.2005.10.006
- Wilson, S. T., Lok, B. M., Messina, C. A., Cannan, T. R., and Flanigan, E. M. (1982). Aluminophosphate Molecular sieves: a new class of microporous crystalline inorganic solids. *J. Am. Chem. Soc.* 104, 1146–1147. doi: 10.1021/ja00368a062
- Xu, M., Harris, K. D., Thomas, J. M., and Vaughan, D. E. (2007). Probing the evolution of adsorption on nanoporous solids by *in situ* solid-state NMR spectroscopy. *Chem. Phys. Chem.* 8, 1311–1313. doi: 10.1002/cphc.200700218
- Yashonath, S., and Santikary, P. (1994). Diffusion of sorbates in zeolites Y and A: novel dependence on sorbate size and strength of sorbate-zeolite interaction. *J. Phys. Chem.* 98, 6368–6376. doi: 10.1021/j100076a022
- Yoshida, K., Yamaguchi, T., Kittaka, S., Bellissent-Funel, M. C., and Fouquet, P. (2008). Thermodynamic, structural, and dynamic properties of supercooled water confined in mesoporous MCM-41 studied with calorimetric, neutron diffraction, and neutron spin-echo measurements. *J. Chem. Phys.* 129, 054702. doi: 10.1063/1.2961029
- Zones, S. I., and Davis, M. E. (1996). Zeolite materials: recent discoveries and future prospects. *Curr. Opin. Solid State Mater. Sci.* 1, 107–117. doi: 10.1016/S1359-0286(96)80018-0

Conflict of Interest Statement: The authors declare that the research was conducted in the absence of any commercial or financial relationships that could be construed as a potential conflict of interest.

Copyright © 2017 Gautam, Ok and Cole. This is an open-access article distributed under the terms of the Creative Commons Attribution License (CC BY). The use, distribution or reproduction in other forums is permitted, provided the original author(s) or licensor are credited and that the original publication in this journal is cited, in accordance with accepted academic practice. No use, distribution or reproduction is permitted which does not comply with these terms.



An Experimental Study of the Carbonation of Serpentinite and Partially Serpentinised Peridotites

Alicja M. Lacinska^{1*}, **Michael T. Styles**¹, **Keith Bateman**¹, **Matthew Hall**² and **Paul D. Brown**²

¹ Minerals and Waste Team, British Geological Survey, Nottingham, United Kingdom, ² Faculty of Engineering, The University of Nottingham, Nottingham, United Kingdom

OPEN ACCESS

Edited by:

Benjamin Alexander Black,
City College of New York,
United States

Reviewed by:

Chiara Boschi,

Institute of Geosciences and Earth

Resources (CNR), Italy

Reinier Van Noort,

Institute for Energy Technology,

Norway

*Correspondence:

Alicja M. Lacinska
alci@bgs.ac.uk

Specialty section:

This article was submitted to
Geochemistry,
a section of the journal
Frontiers in Earth Science

Received: 14 November 2016

Accepted: 28 April 2017

Published: 02 June 2017

Citation:

Lacinska AM, Styles MT, Bateman K, Hall M and Brown PD (2017) An Experimental Study of the Carbonation of Serpentinite and Partially Serpentinised Peridotites.

Front. Earth Sci. 5:37.

doi: 10.3389/feart.2017.00037

In situ sequestration of CO₂ in mantle peridotites has been proposed as a method to alleviate the amount of anthropogenic CO₂ in the atmosphere. This study presents the results of 8-month long laboratory fluid-rock experiments on representative mantle rocks from the Oman-United Arab Emirates ophiolite to investigate this process. Small core samples (3 cm long) were reacted in wet supercritical CO₂ and CO₂-saturated brine at 100 bar and 70°C. The extent of carbonate formation, and hence the degree of carbon sequestration, varied greatly depending on rock type, with serpentinite (lizardite-dominated) exhibiting the highest capacity, manifested by the precipitation of magnesite MgCO₃ and ferroan magnesite (Mg,Fe)CO₃. The carbonate precipitation occurred predominantly on the surface of the core and subordinately within cross-cutting fractures. The extent of the CO₂ reactions appeared to be principally controlled by the chemical and mineralogical composition of the rock, as well as the rock texture, with all these factors influencing the extent and rate of mineral dissolution and release of Mg and Fe for subsequent reaction with the CO₂. It was calculated that ≈0.7 g of CO₂ was captured by reacting ≈23 g of serpentinite, determined by the mass of magnesite formed. This equates to ≈30 kg CO₂ per ton of host rock, equivalent to ≈3% carbonation in half a year. However, recycling of carbonate present in veins within the original rock sample could mean that the overall amount is around 2%. The increased reactivity of serpentinite was associated with preferential dissolution of more reactive types of serpentine minerals and brucite that were mainly present in the cross-cutting veins. The bulk of the serpentinite rock was little affected. This study, using relatively short term experiments, suggests that serpentinite might be a good host rock for CO₂ sequestration, although long term experiments might prove that dunite and harzburgite could be as effective in an engineered system of CCSM. Wet scCO₂ proved to be chemically more aggressive than CO₂-saturated brine and its ingress along fractures and grain boundaries resulted in greater host rock dissolution and subsequent carbonate precipitation.

Keywords: CO₂ sequestration, ultramafic rocks, serpentinites, carbonation, fluid-rock interaction

INTRODUCTION

In situ sequestration of CO₂ in mafic and ultramafic rocks (otherwise known as carbon capture and storage by mineralization, CCSM, or mineral carbonation) is a method proposed to alleviate the amount of anthropogenic CO₂ in the atmosphere (IPCC, 2011). Although in principle, *in situ* CCSM provides an opportunity for long-term, safe sequestration, it has yet to be implemented on an industrial scale. The barriers to large-scale deployment include concerns about the process technologies and operational costs.

The fundamental process of *in situ* CCSM involves the injection of CO₂ into a suitable geological formation, defined as a *carbon repository* (Kaszuba et al., 2005), where it reacts with the host rock to form carbonate minerals. Inevitably, a

natural rock repository constitutes a complex structural package with diverse geochemical environments, incorporating variable groundwater chemistries, host rock compositions, etc. Mafic and ultramafic rocks have been proposed as the main *host rocks* for CCSM (Kelemen and Matter, 2008; Gislason et al., 2010; Kelemen et al., 2011 and references therein). These rocks are composed largely of Mg (plus Ca and Fe, in mafic rocks) silicate minerals that exhibit relatively high reactivity, and hence are prone to dissolution in acidic and neutral environments (van Noort et al., 2013), thereby providing divalent cations (predominantly Mg²⁺) that are utilized in the precipitation of carbonate minerals for the permanent sequestration of CO₂.

Over the past couple of decades, fundamental studies on CCSM have focused largely on isolated mineral grains, such as olivine, and their interaction with CO₂ under conditions relevant

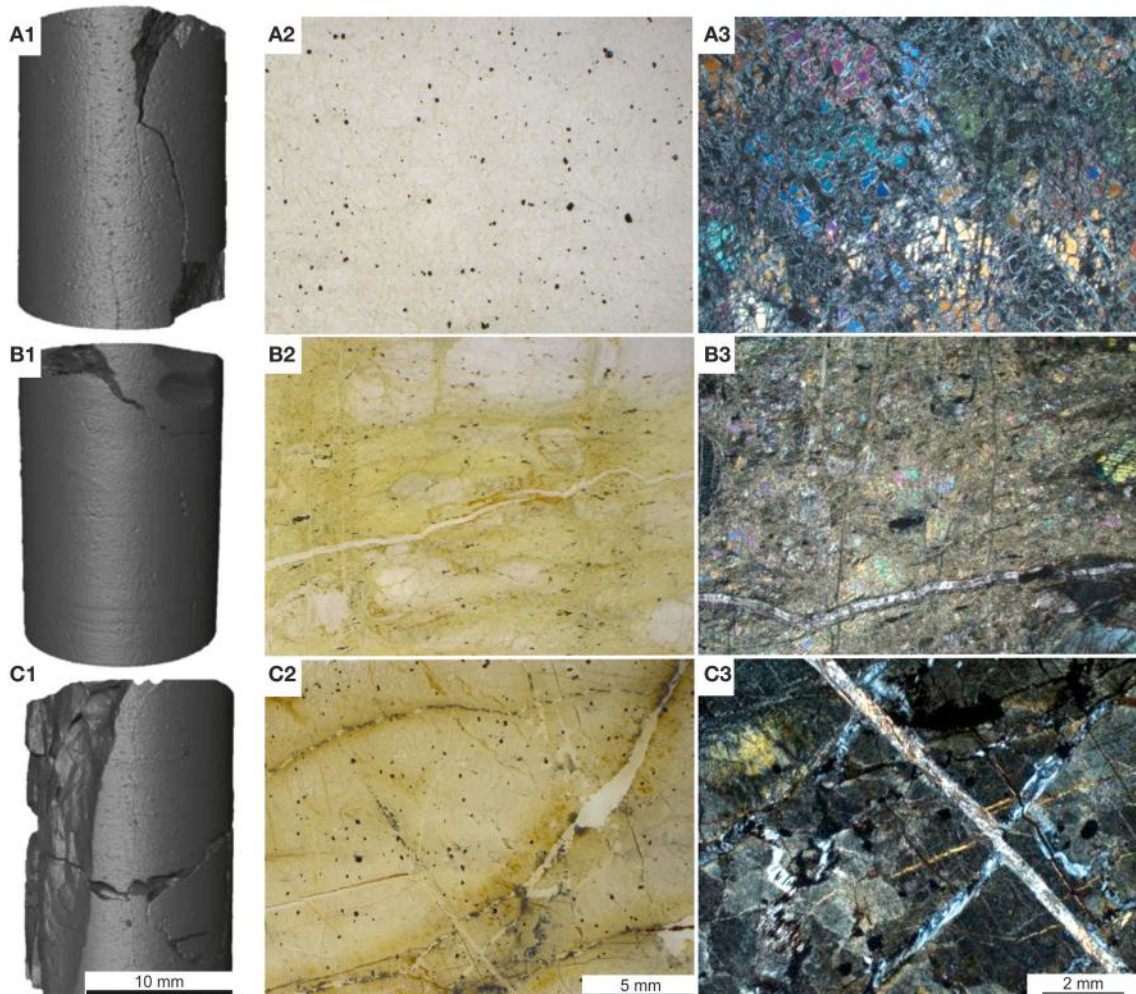


FIGURE 1 | Starting materials: **(A1–A3)** dunite core, thin section scan with scattered black crystals of chromite and crossed-polar optical image with fractured, partially serpentinised dunite; **(B1–B3)** harzburgite core, thin section scan with <5 mm large orthopyroxenes in partially serpentinized matrix and crossed-polar optical image showing partially serpentinised pyroxene+ olivine dominated rock, locally cross-cut by carbonate veins; **(C1–C3)** serpentinite core, thin section scan with scattered magnetite and localized Fe-oxide staining and crossed-polar optical image showing blocky, pseudomorphic serpentinite, cross-cut by a perpendicular array of serpentine-dominated veins. Core dimensions: 27 mm long and 17 mm diameter. Note that the fields of view of images 2 and 3 are not from the same part of the thin section.

to *in situ* injection (Giammar et al., 2005; Olsson et al., 2012; Johnson et al., 2014). Whilst such studies are essential, enabling the determination of specific reaction kinetics and the factors that control mineral dissolution under hydrothermal conditions; it is also important to perform experiments within a system that approximates more closely to the subsurface environment, i.e., that of the host rock at an injection site (Hovellmann et al., 2012; van Noort et al., 2013). The reactivity of minerals within complex rocks will not be the same as that of isolated mineral grains, being influenced by rock texture, including grain size, microfractures, and compositional heterogeneity resulting from different types of adjacent minerals and mineral veins. Hence, an understanding of the behavior of minerals in complex rock is critical to the choice of a host rock (Oelkers et al., 2008).

There is a wide range of Mg-rich rocks that could be used as a host for CCSM and Styles et al. (2014) have described the variety. To appraise the reactivity of different Mg-dominated host rocks, we devised a series of batch experiments using dunite, harzburgite, and serpentinite under conditions relevant for injection and conducted at 70°C and 100 bar CO₂ pressure. The pressure was appropriate for CO₂ injection depths, i.e., \approx 1 km. However, the temperature selected was somewhat greater than that expected at this depth (\approx 40–50°C), but chosen to enhance the probability of significant reaction within the constrained time frame available for the experiments. The experiments were run continuously for 246 days (\approx 8-months) with supercritical (sc) CO₂ or in CO₂-saturated brine (synthetic sea water), as well as under an N₂ atmosphere as a control.

MATERIALS AND METHODS

Materials

Three types of candidate host-rocks were tested, i.e., dunite (Dun), harzburgite (Hzb), and serpentinite (Srp). All samples

originated from the Oman—United Arab Emirates (UAE) ophiolite and are typical of the rocks encountered in an ophiolite mantle injection site as suggested by Kelemen and Matter (2008). The rock samples were collected from small quarries and natural outcrops where there is negligible weathering in the desert environment of the UAE and the rocks are likely to be similar to those at considerable depth. The cores used in the experiments were drilled from a single piece of each rock type but these types of rock, as do many others, show variation on a cm to mm scale. This means that the two pieces of core will be slightly different in detail and the sub-sample for analysis might be very slightly different from the pieces used in the experiment. Several thin sections were examined from each rock type and the range of variation observed is described in the following section.

Dunite (Figures 1A1–A3) was partially serpentинised and predominantly composed of olivine (forsterite) with minor interstitial clinopyroxene, trace amphibole, and scattered crystals of chromite (Table 1). The degree of serpentинisation of olivine varied slightly but is generally around 40%. A few veins traverse the samples and these are mostly serpentinite with a very few thin (10–20 μ m) veins of secondary granular carbonate.

Harzburgite (Figures 1B1–B3) samples show the most minor variation, both within and between subsamples. They consist dominantly of olivine (forsterite), with orthopyroxene (enstatite) around 20% and a small amount of clinopyroxene that ranges from around 1–4%, minor amphibole, chlorite, talc, and trace interstitial chromite (Table 1). The olivine was partially serpentинised (\approx 30–40%). The amphibole and talc are related to microshears and are only a trace component in some sections. There are several serpentinite veins and a very small number of thin carbonate veins in all samples.

Serpentinite (Figures 1C1–C3) is almost entirely composed of fine-grained massive serpentinite minerals, including lizardite and chrysotile (Table 1). The ghost texture suggests the original

TABLE 1 | Mineralogical composition of the starting materials.

	Forsterite	Enstatite	Diopside	Serpentine	Amphibole	Magnetite and *FeO(OH) _x	Chromite	Chlorite	Talc	Brucite	Dolomite	Pyroaurite	Magnesite
Dunite (A)	50	tr	3	40	tr	tr	5	–	–	–	tr	–	tr
Harzburgite (B)	35	20	5.5	31	2.5	tr	–	2	2	–	2	–	–
Serpentinite (C)	–	–	tr	mr	–	tr	tr	–	tr	tr	3	tr	tr

The data are based on a combination of XRD (semi-quantitative) and modal analysis based on OPM and SEM. Major (mr) = ($>$ 95%); Trace (tr) = ($<$ 1%). The serpentinite minerals include predominantly lizardite and lesser amount of chrysotile, the latter one mostly associated with the serpentinite sample.

*FeO(OH)_x, General term for trace amounts of iron oxide/oxyhydroxides coatings with a composition that is difficult to determine due to scarcity and fine or poor crystallinity.

TABLE 2 | Whole rock chemistry, as determined by XRF (Ti, Na, K, P, Sr, Zr, Ba, Cu, Zn, Pb, V, Hf, F, and Cl were below detection).

	SiO ₂	MgO	Al ₂ O ₃	Fe ₂ O _{3t}	Mn ₃ O ₄	CaO	Cr ₂ O ₃	NiO	Total	LOI
	Wt %									
Serpentinised Dunite	34.9	43.7	0.2	7.3	0.1	0.1	0.7	0.3	88.7	NR
Serpentinised Harzburgite	40.8	38.2	2.1	8.4	0.1	2.0	0.4	0.3	92.4	8.2
Serpentinite	34.1	39.6	0.3	8.3	0.1	0.2	0.5	0.2	83.3	17.9

The LOI of dunite is not reported here due to analytical error.

Limit of detection 0.01 wt % element.

rock type was a dunite. There are scattered chromites throughout and a few relics of clinopyroxene in one sample. The ghost textures show that the original olivine cores were replaced by relatively coarse serpentine, probably lizardite. The outer parts of the original olivine were replaced by a very fine fibrous serpentine that has thin veins (20 μm) that mark the original grain boundaries. The rock is cut by several thicker (100–200 μm) veins of secondary fibrous serpentine locally intermixed with brucite. There are probably at least three different varieties of serpentine minerals. A few thin veins that appear to be largely carbonate cut across the serpentine veins. The type and accurate amounts of serpentine minerals could not be discerned by XRD due to severe peak overlaps and poor pattern fit. However, it was inferred from optical and scanning electron microscopy (SEM) that the bulk rock serpentine is dominantly lizardite, whilst chrysotile, and possibly other serpentine polymorphs and polytypes were present in the cross-cutting veins. Dolomite and trace amounts of pyroaurite and magnesite, magnetite, and chromite were also detected.

It was difficult to estimate the proportion of the sample that comprises veins rather than the main rock type, but it is probably only a few percent. Carbonate veins appear to be less than 2% in all samples.

The whole rock chemistry of the samples selected for the experiments is summarized in **Table 2**. Prior to experimentation, cores \approx 27 mm long by 17 mm diameter were cut into each rock type and subsequently fractured to enhance the reactive surface area and enable a comparison of fresh and old mineral sealed fractures (**Figures 1A1–C1, Table 3**). The fracturing was carried out using a compression load frame applying an unconfined maximum load of 30,000 N for dunite and harzburgite, and 10,000 N for serpentinite, to form a few fractures within each core. The maximum load varied according to the strength of the rock and was controlled so that the number of fractures produced in each core was similar. Geometric surface areas, based on reconstructions of the X-ray Computed Tomography (XRCT) data, were calculated for the core samples that were

TABLE 3 | Dimensions of all the experimental cores and geometric surface areas for cores used to calculate reaction rates.

Rock type	Position in the vessel	Core length (mm)	Core diameter (mm)	Geometric surface area (mm^2)
Serpentinite CO_2	Upper	27.1	17.9	2,700
	Lower	27.8	17.9	
Serpentinite N_2	Upper	26.9	17.9	2,200
	Lower	27.5	17.9	
Dunite CO_2	Upper	18.0	17.3	
	Lower	27.6	17.3	
Dunite N_2	Upper	27.7	17.9	
	Lower	26.9	17.9	
Harzburgite CO_2	Upper	27.4	17.9	1,800
	Lower	27.2	17.5	
Harzburgite N_2	Upper	27.3	17.9	
	Lower	27.1	17.9	

used to provide data for reaction rate calculations. Accordingly, values of 0.0027 m^2 for serpentinite, 0.0022 m^2 for dunite, and 0.0018 m^2 for harzburgite were determined. The dimensions and surface area of the cores used for all experiments are shown in **Table 3**.

Experimental Methodology

Carbonation experiments were carried out in pressure vessels at 70°C ($\pm 5^\circ\text{C}$), connected to CO_2 or N_2 (control) gas lines at 100 bar (± 5 bar), for 8-months (**Figure 2**). The experimental conditions and fluid composition are summarized in **Table 4**. The vessels were made from 316 stainless steel, with wetted parts lined with polytetrafluoroethylene (PTFE); gas inlet and sampling tubes were made from 316 stainless steel or polyetheretherketone (PEEKTM) and the O-ring seals were made from Viton[®]. Each vessel contained a magnetic stirrer used for 2 min every 4 h to agitate the solution.

The fractured cores were wrapped in gold wire to hold the pieces together so that they could be mounted on the sampling tubes for insertion into the pressure vessels. Two vessels per rock type were used with one pressurized with CO_2 and the other with N_2 as a control. Each vessel contained two cores of each sample, one immersed in the aqueous phase (CO_2 -saturated or N_2 -equilibrated brine) and one located above the solution, in the headspace filled with wet supercritical CO_2 or wet N_2 . Two hundred milliliters of synthetic seawater solution was used in each vessel. The seawater composition was modified

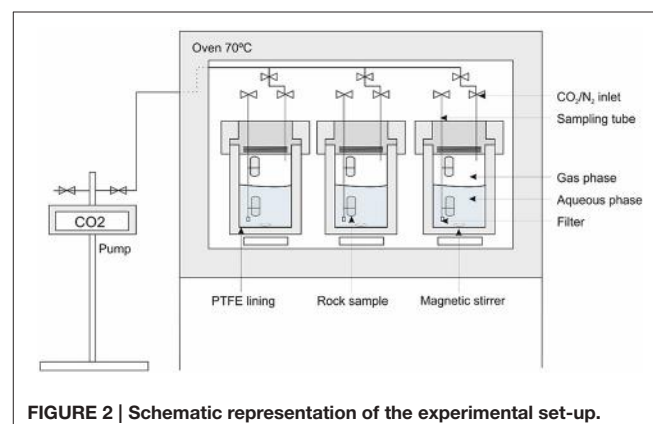


FIGURE 2 | Schematic representation of the experimental set-up.

TABLE 4 | Summary of the conditions for the CO_2 and N_2 control experiments.

T (°C)	CO_2 P and N_2 (bar)	Duration (days)	Starting fluid volume (ml)	Final fluid volume (ml)
70	100	246	200	≈ 110
STARTING FLUID COMPOSITION (mol/kg)				
Na^+	0.46		Sr^{2+}	0.0001
Mg^{2+}	0.046		SO_4^{2-}	0.028
Ca^{2+}	0.007		Cl^-	0.546
K^+	0.01			0.0001

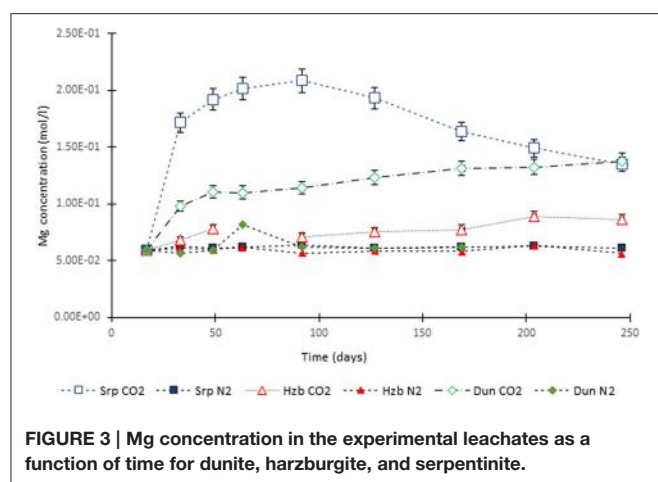


FIGURE 3 | Mg concentration in the experimental leachates as a function of time for dunite, harzburgite, and serpentinite.

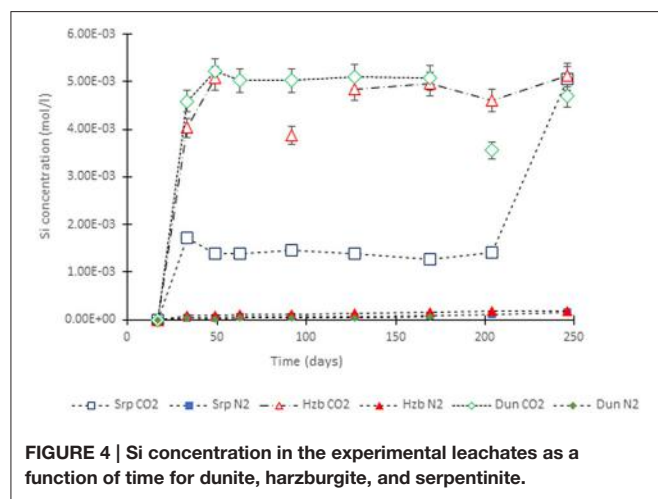


FIGURE 4 | Si concentration in the experimental leachates as a function of time for dunite, harzburgite, and serpentinite.

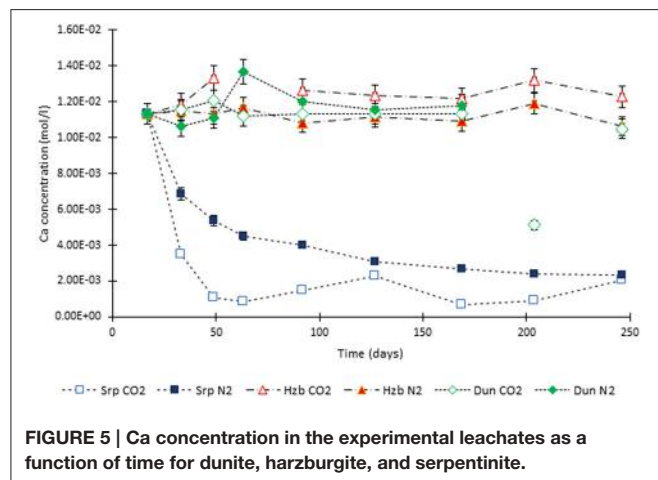


FIGURE 5 | Ca concentration in the experimental leachates as a function of time for dunite, harzburgite, and serpentinite.

from that given by Millero (1996) to contain only major cations and anions (Table 4). Each experiment was sampled 11 times (including the final solution). Approximately 10 ml of fluid was extracted for the first seven samples and ≈ 5

ml was extracted for the remaining samples. On termination of the experiments, the vessels were cooled, depressurized, and opened to collect the final solution and solid samples. The solids were photographed in their post-test state. Any precipitates were collected for analysis, whilst the cores were subsampled for microanalysis. Reference material was kept in a desiccator.

Analytical Methodology

SEM was performed using an FEI Quanta 600, with quantitative chemical analyses of mineral phases using an Oxford Instruments energy dispersive X-ray spectroscopy (EDS) system, following ASTM recommendations (ASTM E1508-12a, 2012). Samples were analyzed in the form of carbon sputter coated (≈ 25 nm thick) polished thin sections. Post-experimental, polished thin sections were cut perpendicular to the length of each core, to include the outer surface, induced and natural fractures, and the partially reacted host rock. The SEM was operated under conditions of high vacuum ($< 1 \times 10^{-5}$ torr) at 20 kV accelerating voltage, with optimal analytical 10 mm working distance and an X-ray detector take-off angle of 45° . For EDS analyses, conditions of 1.5–7 nA beam current and 30 s acquisition time were used, giving $\approx 1 \times 10^6$ total X-ray counts. These optimal conditions of beam current, acquisition time, and spot mode (rather than raster mode) provided for the analysis of major elements, free of any significant mineral damage under the electron beam.

X-ray diffractometry (XRD) was performed using a PANalytical X'Pert Pro in Bragg-Brentano geometry, equipped with a cobalt-target tube and generator operated at 45 kV and 40 mA, and an X'Celerator detector. Complementary X-ray fluorescence (XRF) spectroscopy investigations were performed by PANalytical Ltd., Environmental Science Centre, Nottingham. Nine grams of PANalytical pre-fused 66/34 Li₂B₄O₇/LiBO₂ flux was weighed into a 95/5 Pt/Au crucible and fused with 0.9000 g of sample powder at 1,200°C. Loss of ignition (LOI) was determined after 1 h at 1,050°C. The composition of the experimental leachates was determined using a Perkin Elmer Optima 7,300 DV (Dual View) Inductively Coupled Plasma—Atomic Emission Spectrometer (ICP-AES), with WinLab 32 for ICP (Version 5.5) software, in the inorganic geochemistry laboratories of the British Geological Survey (BGS). PHREEQC 3.4 geochemical code (Parkhurst and Appelo, 2013) was used to model the ionic speciation of experimental solutions, based on ionic concentrations measured in the leachates. This, in combination with data from the Bureau de Recherches Géologiques et Minières (BRGM) database for phases of interest, was used to calculate the saturation indices (SI) of potential phases.

RESULTS

Chemistry of the Experimental Leachates

The evolution of Mg, Si, and Ca in the experimental leachates is shown in Figures 3–5 as a function of time (corrected for decreasing volume), for both the CO₂ and N₂-pressurized (control) vessels. The “volume corrected time” is a term used to

account for the progressive decrease of fluid in the experimental vessel, affecting the solid to volume ratio during the experiment (Bevan and Savage, 1989). In all cases, except for Ca in the Srp experiment, the changes in elemental concentration for the N₂ control experiments were insignificant, as expected, with little visible evidence for any alteration.

For the CO₂-pressurized experiments, the most distinct concentration changes were recorded in the leachates extracted from serpentinite, as illustrated by the sudden increase in Mg concentration during the initial 2 weeks of the experiment, i.e., the 1st sampling event. The initial relatively high Mg concentration peaked at the 4th sampling event with just over 0.2 (±5%) mol/l (Figure 3). Thereafter, a steady decrease in Mg concentration continued until the end of the experiment. The Si concentration also showed distinct variations with time, marked by two distinct levels. On the 1st sampling event (≈17th day) it reached ≈0.0018 (±5%) mol/l and stayed steady. Between the 7 and 8th sampling events it increased to ≈0.005 (±5%) mol/l (Figure 4). In contrast to the Mg and Si levels, the concentration of Ca decreased with time, in both the CO₂ and N₂-pressurized vessels of serpentinite (Figure 5).

The temporal variation of Mg concentration in the leachate of dunite and harzburgite in the CO₂-pressurized vessels was less pronounced than serpentinite. A general steady increase was observed for the dunite, reaching 0.14 (±5%) mol/l at the last sampling point. The harzburgite leachate showed the lowest Mg concentration of ≈0.08 (±5%) mol/l at the end of the experiment, and although this curve displayed several small fluctuations, it maintained a general flat trend (Figure 3). The temporal evolution of Si for both dunite and harzburgite exhibited general similarities, with a rapid increase by the first sampling event up to ≈0.004–0.005 (±5%) mol/l, after which several minor fluctuations were observed, although the concentration rarely fell below 0.004 mol/l (Figure 4).

The concentration of Ca changed significantly for the serpentinite samples; the decrease of Ca in the N₂-pressurized was caused by the precipitation of aragonite on the core surface and formation of calcite in the CO₂-pressurized experiment. This was confirmed by the microanalysis.

The concentration of Ca in the dunite and harzburgite experiments remained largely invariant.

The complete data set of fluid chemistry is given in the Supplementary Tables S1, S2.

Rate of Mg Release

The rate (R) of net release of metal (i) from serpentinite, dunite, and harzburgite was calculated using the following equation (Brantley et al., 2008):

$$R_i = \left(\frac{V}{GSA} \times \frac{dC}{dt} \right)$$

Where V is the volume of the solution, corrected for its reduction with time; GSA is the geometric surface area (m²/g); and dC/dt is the change of elemental concentration (mol) with time (s).

Table 5 provides a summary of rates of net Mg release for the CO₂-pressurized experiments. In addition, **Table 5** shows pH values for all experimental solutions, corresponding to *in situ* conditions at 70°C and 100 bar, as calculated using PHREEQC, along with values obtained from direct measurement at ambient P and T. For the CO₂-pressurized experiments, the calculated pH values were 3.1–3.6 compared to the measured pH values of 6–7, with the latter being higher due to CO₂ degassing during sampling under ambient conditions. For comparison, the modeling of pH *in situ* in the N₂-pressurized vessels returned values of pH 6–8, in close agreement with the values measured in solution post-sampling.

The values for the rate of net¹ Mg release (Figure 6) gives an indication of two competing processes, with positive values indicating that Mg release dominates, whilst negative values suggest that Mg uptake prevails, i.e., mineral precipitation.

Figure 6 shows that the initial net Mg release rate was high in the serpentinite experiment, with respect to the overall rate measured throughout the experiment, reaching ≈1.3 × 10^{−8} mol/m²/s for serpentinite, ≈6 × 10^{−9} mol/m²/s for dunite, and ≈2 × 10^{−9} mol/m²/s for harzburgite. The initial release rate was approximately an order of magnitude higher for serpentinite than for the other two samples. A sudden drop in rate was observed after the 1st sampling event, with the dunite and harzburgite remaining roughly at the same level until the end of the experiments, whilst serpentinite exhibited significant variation.

The inset of **Figure 6** shows that the Mg release rate rarely dropped below zero for dunite and harzburgite, i.e., the release of Mg exceeded uptake at most time points. For serpentinite, however, the net Mg release rate fell below zero between the 4 and 5th sampling points (≈70th day of the experiment) and remained in the negative field until the end of the experiment. This shows that Mg uptake was greater than release, largely due to the precipitation of magnesite, the presence of which was confirmed by microanalysis of the final solids (Figure 8C₁).

The high initial release rates may be associated with: (a) fast dissolution of the surface layer of the cores and inner open fractures upon exposure to reactive fluid, but before any newly formed minerals could inhibit fluid interaction; and/or (b) fast dissolution of carbonate minerals present in veins within serpentinite and harzburgite (as observed for serpentinite from the N₂-pressurized experiment, Reactions in the control N₂-pressurized vessel).

Predicted Phases

The ionic speciation of the experimental solutions was modeled using PHREEQC 3.2 (Parkhurst and Appelo, 2013), based on the concentrations measured in the liquids extracted at different time points and the pH of the solution measured at 70°C and 100 bar, with the redox conditions controlled by a HS[−]/SO₄^{2−} redox couple. This data, together with data for phases of interest from

¹Net Mg release corresponds to the amount of Mg in solution, considering all reactions taking place at a specific time point in the experiment, arising from the simultaneous dissolution and precipitation of Mg-bearing minerals.

TABLE 5 | The net rates (R) of Mg release for the CO_2 -pressurized samples.

Rock sample	Rate of net Mg release (mol/m ² /s), averaged for the period up to the elapsed time point (days)									
	17 days	33	49	63	92	127	169	204	246 days	
Serpentinite CO_2 (R)	1.29×10^{-08}	4.78×10^{-10}	1.07×10^{-10}	4.17×0^{-11}	-5.40×10^{-11}	-6.11×10^{-11}	-1.98×10^{-11}	-1.23×10^{-11}	-5.9×10^{-12}	
PHREEQC calculated pH	3.3	3.2	3.2	3.3	3.1	3.1	3.2	3.6	3.1	
Measured pH (ambient P&T)	7.6	7.7	7.6	7.5	7.6	7.6	7.7	7.5	7.4	
Serpentinite N_2										
PHREEQC calculated pH	7.9	8.0	8.0	8.0	7.8	7.9	7.9	7.9	7.1	
Measured pH (ambient P&T)	7.9	8.0	8.0	8.0	8.0	8.1	8.1	8.3	8.4	
Dunite CO_2 (R)	6.07×10^{-09}	2.47×10^{-10}	-4.56×10^{-12}	2.00×10^{-11}	2.69×10^{-11}	1.31×10^{-11}	1.41×10^{-12}	3.60×10^{-12}	2.95×10^{-12}	
PHREEQC calculated pH	3.3	3.3	3.2	3.2	3.2	3.2	3.2	3.2	3.1	
Measured pH (ambient P&T)	7.3	7.4	7.1	7.4	7.3	7.5	7.8	7.6	7.6	
Dunite N_2										
PHREEQC calculated pH	7.8	7.9	7.9	7.9	8.0	8.0	8.0	8.0	7.4	
Measured pH (ambient P&T)	7.6	7.8	8.5	7.9	8.7	8.7	8.4	No sample		
Harzburgite CO_2 (R)	3.56×10^{-09}	1.72×10^{-10}	No fluid sample	3.01×10^{-10}	9.87×10^{-12}	3.59×10^{-12}	1.05×10^{-11}	-1.94×10^{-12}	-8.15×10^{-13}	
PHREEQC calculated pH	3.1	3.1		3.1	3.1	3.1	3.1	3.1	3.1	
Measured pH (ambient P&T)	7.0	6.8		6.6	6.8	7.1	7.5	7.2	7.2	
Harzburgite N_2										
PHREEQC calculated pH	6.0	7.6	7.7	6.3	6.4	7.8	7.8	7.8	6.7	
Measured pH (ambient P&T)	7.1	7	7.2	7.5	7.5	7.6	7.7	7.8	7.9	

Negative values of R indicate that Mg uptake exceeds its release. In situ pH was modeled using PHREEQC 3.3 (Parkhurst and Appelo, 2013), whilst measured pH values were obtained after sampling at ambient P and T . The 3rd fluid sample from the harzburgite experiment is missing due to a vessel leak.

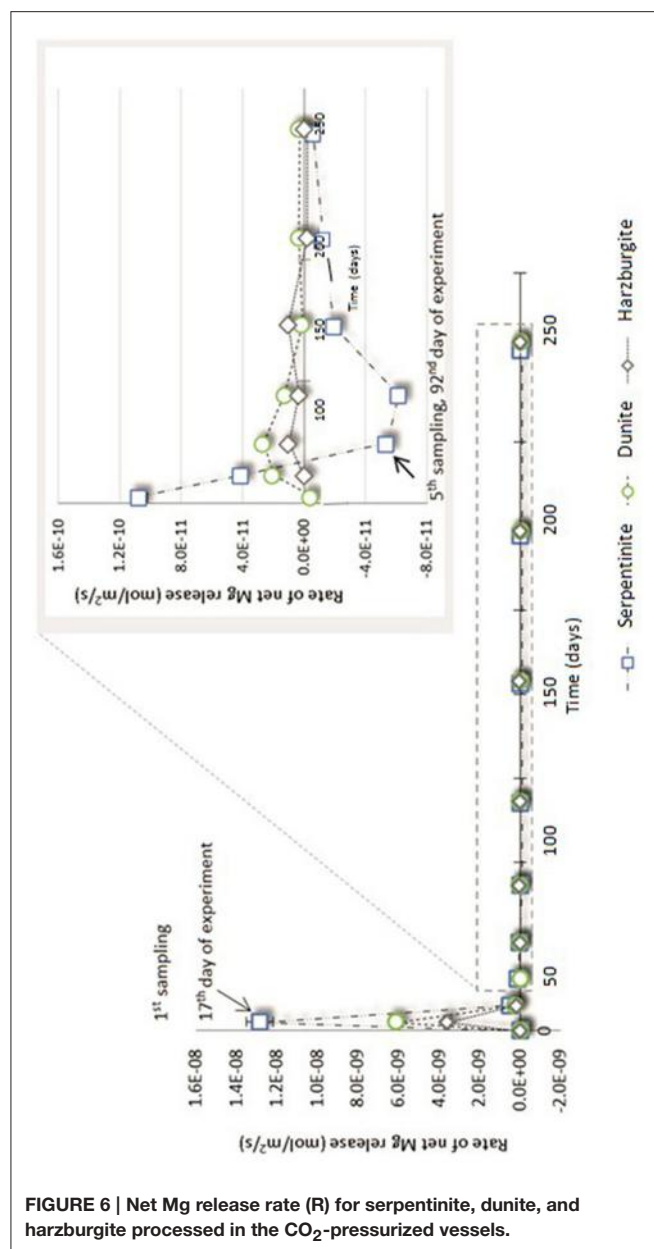


FIGURE 6 | Net Mg release rate (R) for serpentinite, dunite, and harzburgite processed in the CO_2 -purified vessels.

the BRGM database (Base de Donnee Thermoddem_V1.10), was used to calculate the saturation indices (SI) of potentially precipitating phases.

Figure 7 shows the SI for magnesite and amorphous silica, as a function of time, in the CO_2 -purified experiments.

The SI of magnesite ranged from $\text{SI} = -3.1$ to -1.2 , with the lowest values for harzburgite and the highest for serpentinite. This suggested that the solutions were close to saturation with respect to magnesite, without actually reaching it where SI is expected to be ≥ 0 . However, post-processing analyses of the cores revealed the presence of magnesite for both the dunite and the serpentinite experiments. It has been shown previously that magnesite requires a critical SI of between

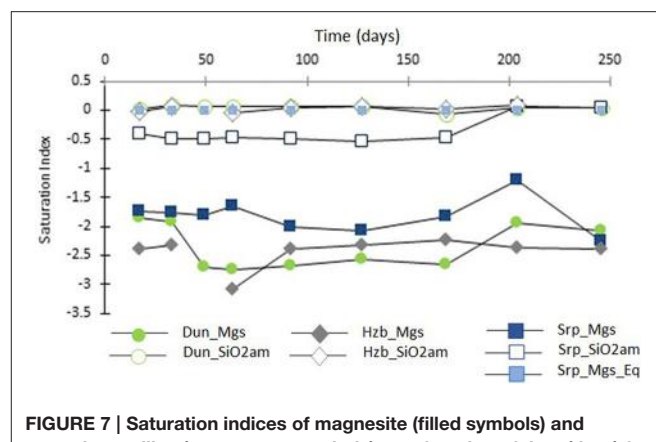


FIGURE 7 | Saturation indices of magnesite (filled symbols) and amorphous silica (transparent symbols) as a function of time (days) for the CO_2 -purified experiments.

0.25 to 1.14 to precipitate at 95°C and 100 bar pCO_2 (i.e., temperature conditions slightly higher than that used in this study; Giamar et al., 2005). The discrepancy between the presence of magnesite in the cores and negative SI could have several causes: the small variation in composition between the various sub-samples, analytical errors including those associated with sample preparation, e.g., dilution factor and the ICP AES analysis of the fluid itself. The possibility of imprecise data in the thermodynamic database when used with the combination of components encountered here must also be considered.

Figure 7 also shows that the solutions were saturated or close to saturation (in the case of serpentinite) with respect to amorphous silica; this is consistent with the microanalytical observations of the post-processing samples, as discussed in Section Post-experimental Materials.

Post-experimental Materials

Macro-Scale

The rock cores before and after 8-month reaction with CO_2 -saturated brine (lower cores) or scCO_2 (upper cores) are shown in Figure 8. For the case of dunite (Figures 8A1, A2), the transformations at a macro-scale were manifested by the presence of a thin (< 1 mm), white coating of magnesite (confirmed by XRD in all cases) on the upper core and a brown ferruginous veneer on the lower core. For the case of harzburgite, the upper core had newly formed magnesite, but it was less prominent than on the dunite; only occurring locally as scattered nodules on the surface and where some fractures intersected the core surface. The lower core was again covered by a brown ferruginous veneer.

Serpentinite (Figure 8C) showed the most prominent macro-scale transformations; a magnesite crust covered both upper and lower cores. The lower core displayed a sequence of mineral precipitation with a ferruginous veneer forming the first newly-precipitated coating, similar to those observed in dunite and harzburgite, but in this case overgrown by a carbonate crust. The carbonate crust thickness was uneven, generally < 3 mm, highly porous and friable due to loose crystal

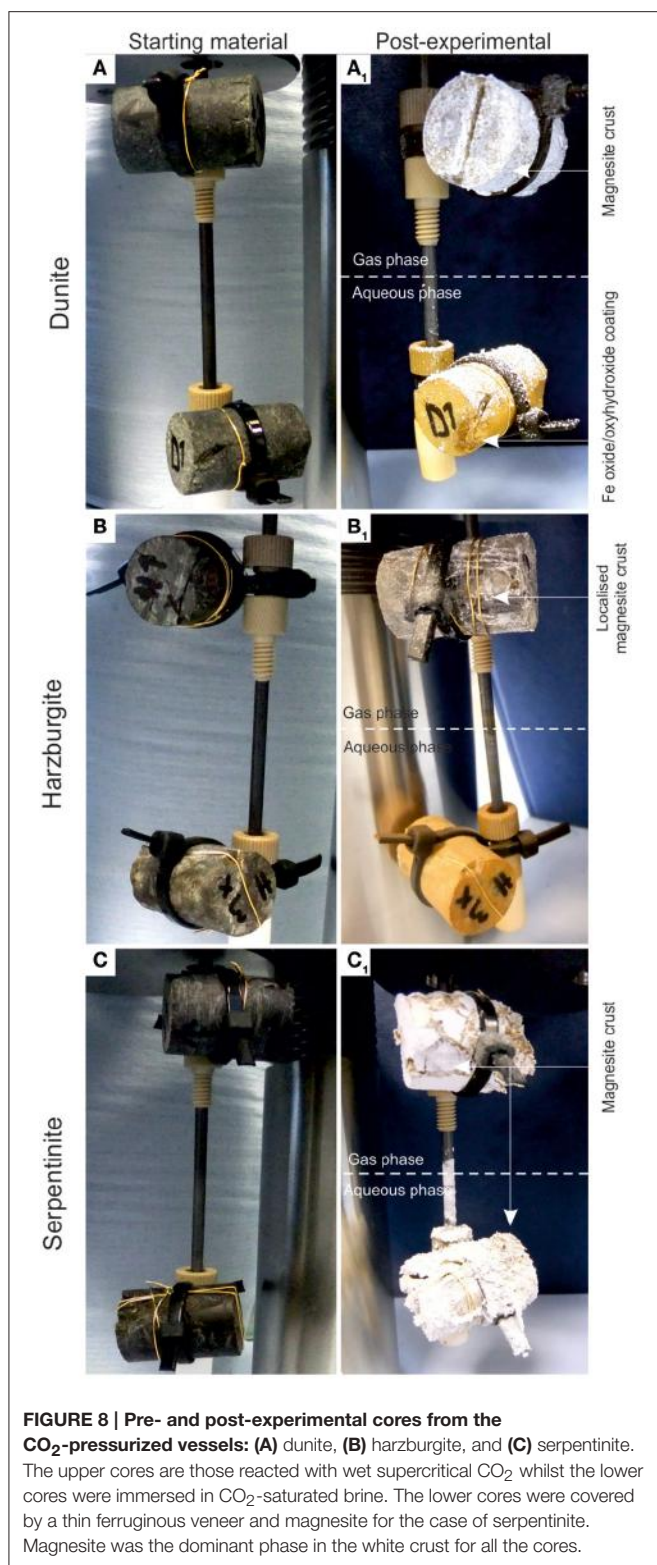


FIGURE 8 | Pre- and post-experimental cores from the CO_2 -pressurized vessels: **(A)** dunite, **(B)** harzburgite, and **(C)** serpentinite. The upper cores are those reacted with wet supercritical CO_2 whilst the lower cores were immersed in CO_2 -saturated brine. The lower cores were covered by a thin ferruginous veneer and magnesite for the case of serpentinite. Magnesite was the dominant phase in the white crust for all the cores.

packing. Interestingly, the binocular microscope observations revealed that the very first layer of carbonate mimicked the dendritic network of the original serpentine veinlets. The upper serpentinite core had undergone most textural transformation

during the experiment, resulting in the loss of $\approx 1/3$ of the core that had fallen to the base of the vessel. When the pressure vessel was opened at the end of the experiment, small fragments of serpentinite (maximum size 1–2 mm) were found amongst the carbonate debris. It is not known when or how this part of the core became detached. However, the outer surface of the upper core was completely covered by the carbonate crust and hence, it is assumed that disintegration took place sometime prior to the end of the experiment, allowing time for further carbonate growth. It is postulated that the core fragments did not come off as one large piece, but probably as several small pieces that became detached as new carbonate formed along the fractures. The sudden increase in Si concentration (Figure 4) toward the end of the experiment might indicate the timing of the major disintegration event.

The newly precipitated crust on the serpentinite core was dominated by morphologically variable magnesite and ferroan magnesite, with a lesser amount of calcite, mainly observed in the serpentinite core. Magnesite exhibited $<1 \mu\text{m}$ equant crystals and $<500 \mu\text{m}$, but mostly $<50 \mu\text{m}$, nodular crystal aggregates (Figure 9A). Calcite displayed typical dog tooth (scalenohedral) morphology (Figure 9B).

Micro-Scale

A petrographic examination was made using polished thin sections of all the cores recovered after completion of the experiments. The bulk rock visually appeared to be largely unaltered. Localized detailed changes were analyzed and a selection of BSE and SE images illustrating representative micro-scale features of the reacted cores are presented in Figures 10–12. Table 6 summarizes the compositional and textural transformations in all cores after completion of the experiments. The following paragraphs focus on the samples that exhibited the most prominent transformations (bold in Table 6).

Dunite processed under CO_2 -saturated brine

It was evident that olivine underwent preferential dissolution, resulting in the development of secondary porosity. This was observed close to the core surface (Figure 10A) and on the induced fracture surfaces where fluid access was extensive (Figure 10B). Figures 10B,C show that olivine developed $<20 \mu\text{m}$ deep etch pits. These etch pits, the larger scale secondary porosity and the fractures were partially filled with very fine-grained magnesite (Figures 10B,C). Figures 10D–F show in detail the results of olivine transformation by dissolution and precipitation of $<10 \mu\text{m}$ sized Mg carbonate nodules and $<3 \mu\text{m}$ sized amorphous silica nodules. These newly formed phases displayed preferential alignment along the olivine cleavage planes. This suggests that their precipitation position was related to the relict minerals' original structure rather than the transport of components to and from the site.

Serpentinite

Details of the micro-scale transformations in serpentinite cores following reaction with wet sc CO_2 are presented in Figures 11A,B and following reaction with CO_2 -saturated brine

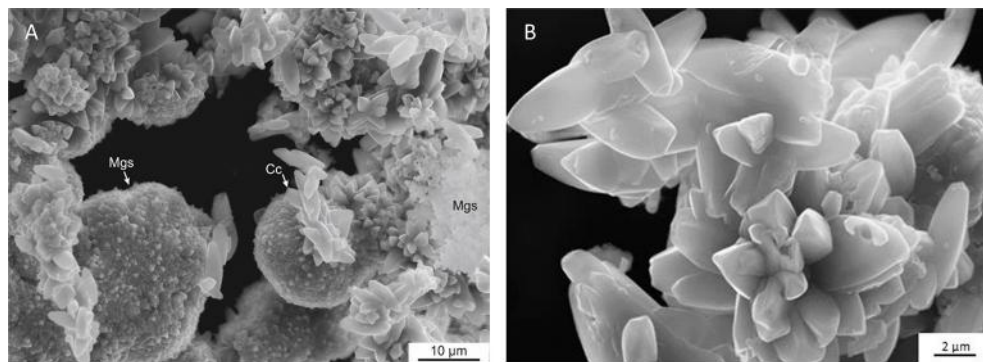


FIGURE 9 | Morphology of crystals exemplified by the serpentinite crust. Magnesite exhibited $<1\text{ }\mu\text{m}$ equant crystals and $<500\text{ }\mu\text{m}$ (here $<50\text{ }\mu\text{m}$ shown) nodular crystal aggregates (A); calcite displayed typical dog tooth (scalenohedral) morphology (B).

in **Figures 11C–E**. The first two images show an induced fracture, partially filled with reaction products, i.e., magnesite and an unidentified Mg-carbonate. The magnesite, typically exhibits a hemispherical morphology and was widely distributed, attached to the surface of the core or margins of the induced fractures. It grew in open spaces not replacing other minerals. The other Mg-carbonate occurred as partially corroded, branching aggregates of fine $<1\text{ }\mu\text{m}$ crystals. The scarcity and fine-grained nature of this mineral prevented its precise identification. However, it is evident from appraisal of the texture that this post-dated the magnesite and probably had a high crystallization force; pushing apart serpentinite slivers from the sides of the induced fracture zone (**Figure 11B**).

The mineral formation in an open induced fracture in the serpentinite core (following reaction with CO_2 -saturated brine) is shown in **Figures 11C–E** along with associated X-ray elemental distribution maps. The dolomite in this fracture is probably remnant from the thin carbonate veins observed in the starting material. Here, it appears to be partially corroded, with the crystal cores leached. The newly formed phase is an assemblage of $<3\text{ }\mu\text{m}$ rhombic crystals of Mg-carbonate that grew preferentially on the dolomite crystals (**Figure 11D**). Again, the very small size of the Mg-carbonate prevented its precise identification. The originally serpentine and brucite-filled veins became strongly Mg-depleted, and to a lesser extent Si-depleted, as evidenced by the associated X-ray elemental distribution maps (**Figure 11E**). The veins developed micropores and the components, once removed, served most probably as the main source of Mg for the precipitation of newly formed Mg-carbonates. The solid rock serpentinite, as distinct from the later veins, was not greatly affected by the dissolution. The only exception being a $<5\text{ }\mu\text{m}$ thick layer of a fibrous Si-rich phase (**Figure 11D**) that has probably crystallized from the fluid on the wall of the fracture.

Reactions in the Control N_2 -Pressurized Vessel

Micro-scale petrographical observations agree with the results of the solution chemistry, in that only negligible dissolution–carbonation reactions took place within the N_2 -pressurized vessels. Amongst the cores investigated experimentally, the only

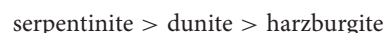
changes observed were on serpentinite that reacted with saline solution, where; a crust of acicular aragonite and lesser amounts of platy, almost rosette-like aggregates of Mg-carbonate crystals were formed. It is considered that these carbonates precipitated from components derived from the dissolution of dolomite, pyroaurite, and other minerals present in the veins of the starting materials.

DISCUSSION

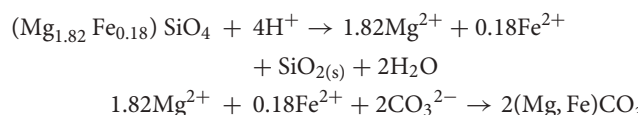
The primary aim of this study was to ascertain the extent of mineral carbonation reactions, i.e., the degree of transformation of Mg silicate to Mg carbonate, under conditions approximating to the injection of CO_2 at a depth of $\approx 1\text{ km}$ into three different types of mantle rock. It has been shown that several mineralogical and textural changes occurred during the 8-month duration of these experiments and that their extent depended greatly on the starting rock composition and the experimental conditions applied. They are summarized in **Table 6**.

Mineralogical Transformations

Evaluation of the temporal evolution of fluid chemistry, rate of net Mg release, and petrographic data for the rock samples demonstrated that most of the reactions observed were as expected, promoted by the presence of CO_2 compared to the N_2 -pressurized control experiments. The extent and rate of reaction varied between the three rock types investigated and the extent of changes decreased from:



The generic dissolution and carbonation reactions reflecting the processes observed for olivine can be written as:



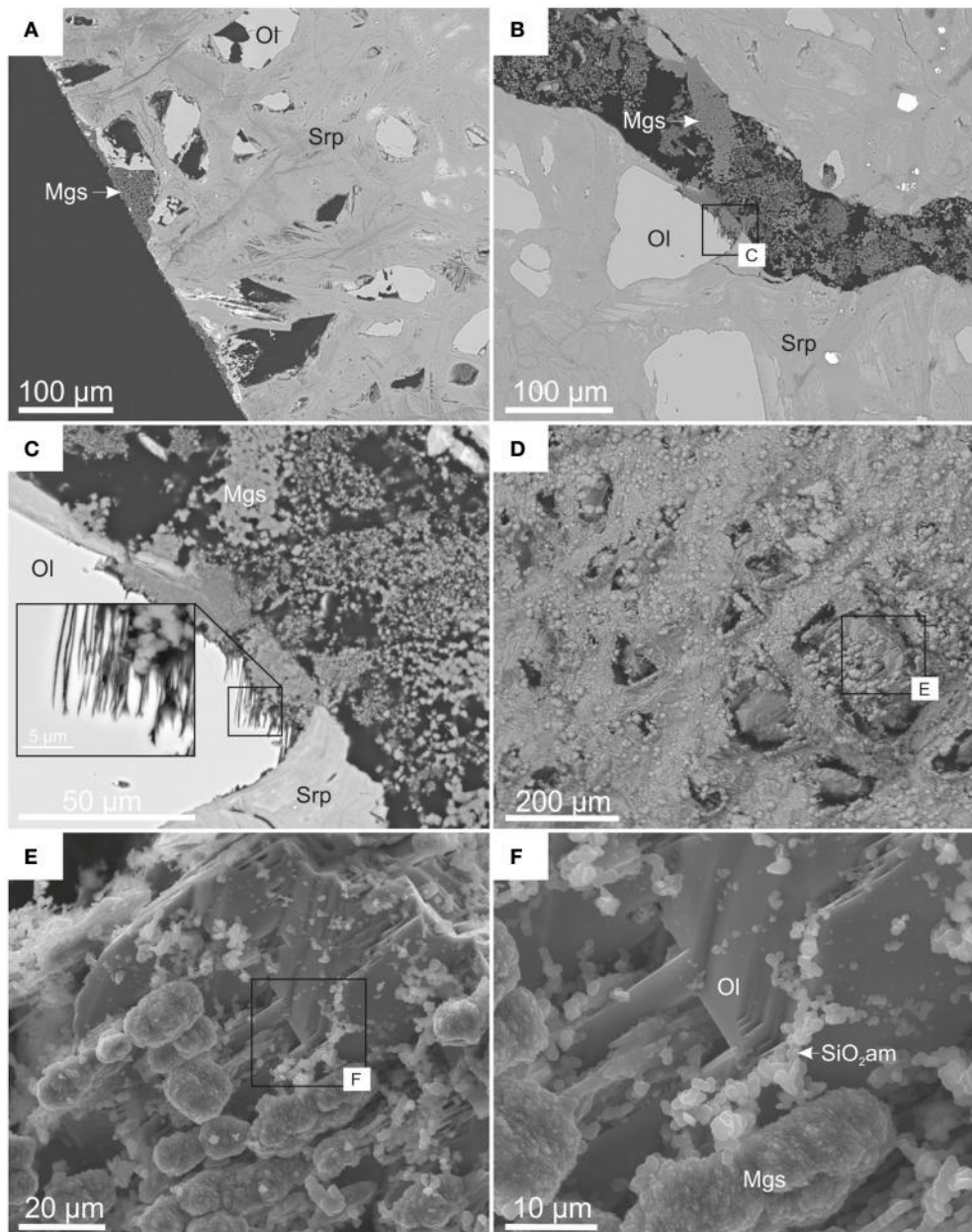
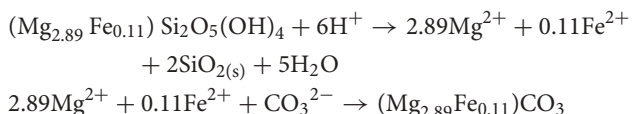


FIGURE 10 | BSE (A–C) and SE (D–F) images showing micro-scale features within reacted dunite (CO₂-pressurized vessel). (A) Preferentially dissolved olivine and associated secondary porosity; **(B)** finely crystalline magnesite within an induced fracture; **(C)** details of dissolution pits in olivine and magnesite infill; **(D)** partially dissolved olivine on the surface of an induced fracture; **(E,F)** details of newly formed phases, magnesite, and amorphous silica, displaying alignment with olivine cleavage planes.

and for serpentine:



These reactions resulted in the formation of two types of solid phases, i.e., Mg carbonate (the majority identified as magnesite) and amorphous silica, both were observed *in situ* on the surface of

partially dissolved olivine in dunite (**Figure 13A**-pre-experiment and **Figure 13B**-post-experiment).

The reactivity of the rock depended primarily on the composition and spatial relationships of the minerals. The study of the dual system of olivine-serpentine in dunite shows that at 70°C and 100 bar CO₂ pressure, olivine (Fo₈₇) dissolved partially but *congruently* (providing a substrate for *in situ* precipitation of carbonate and silica, **Figure 13**) whilst serpentinite dissolution was negligible. This is consistent with the observations made

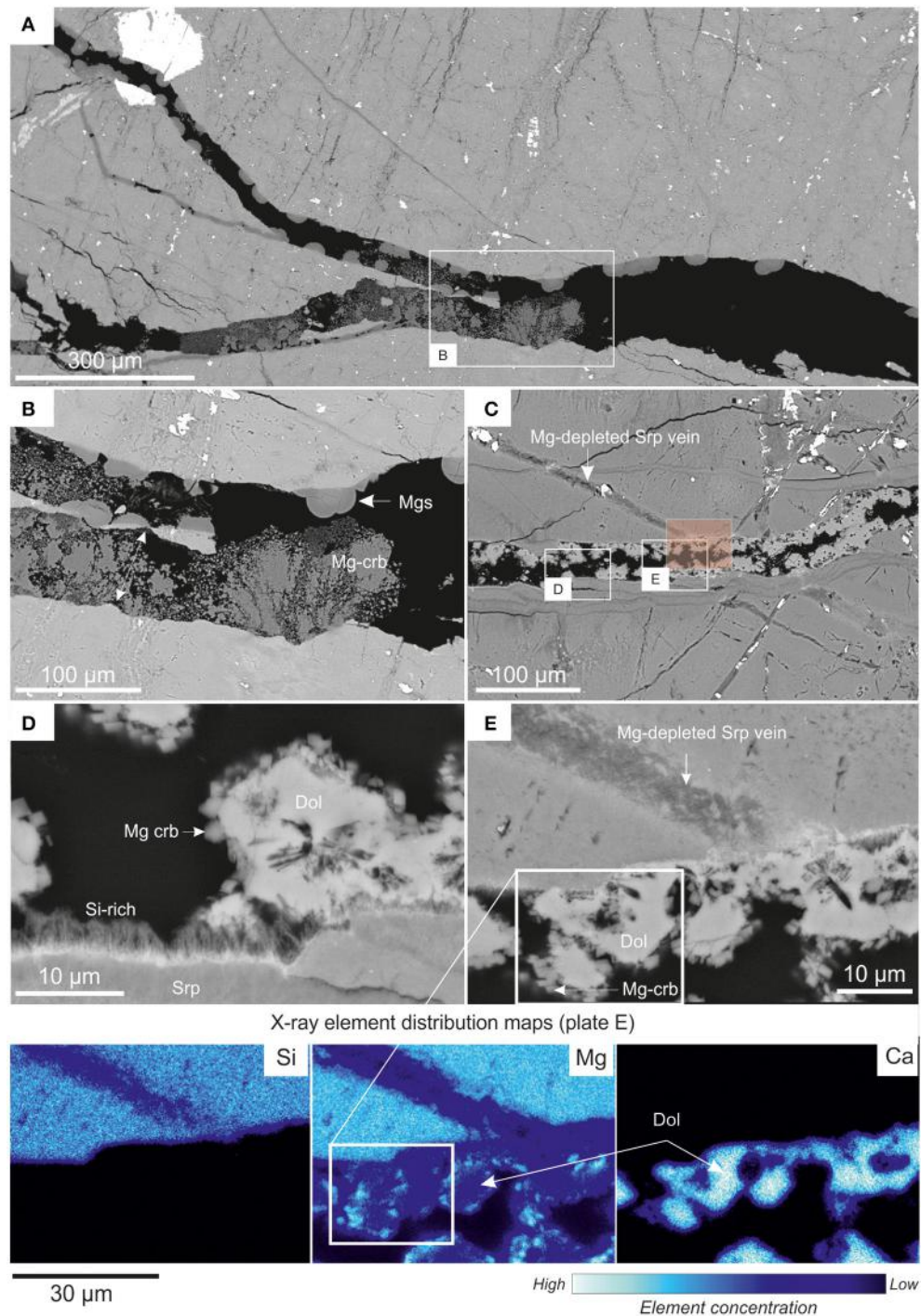


FIGURE 11 | BSE images presenting details of the micro-scale transformations in serpentinite: (A,B) from the core reacted with wet sc- CO_2 ; **(C–E)** from the core reacted with CO_2 -saturated brine. **(A)** General view of an induced fracture in serpentinite. The BSE bright phases are chromite (e.g., large crystal in top left corner) and magnetite. The fracture is infilled by several generations of Mg carbonate, including hemispherical ferroan magnesite and magnesite, and finely crystalline, generally corroded Mg carbonate (as detailed in **B**); **(B)** details of the induced fracture infill: cores of hemispherical magnesite are typically Fe-enriched. Second generation Mg carbonate, postdating magnesite, is microcrystalline and shows signs of corrosion. The double arrow shows two matching sides of host rock that has been pushed-apart; **(C,D)**, details of partially corroded dolomite (probably primary), locally overgrown by $<2\text{ }\mu\text{m}$ crystals of authigenic Mg carbonate. The Si-rich fibrous phase is probably a relic of peripheral dissolution of the serpentinite host-rock; **(E)** and associated X-ray maps show preferential Mg dissolution from the veins rather than bulk-rock serpentinite.

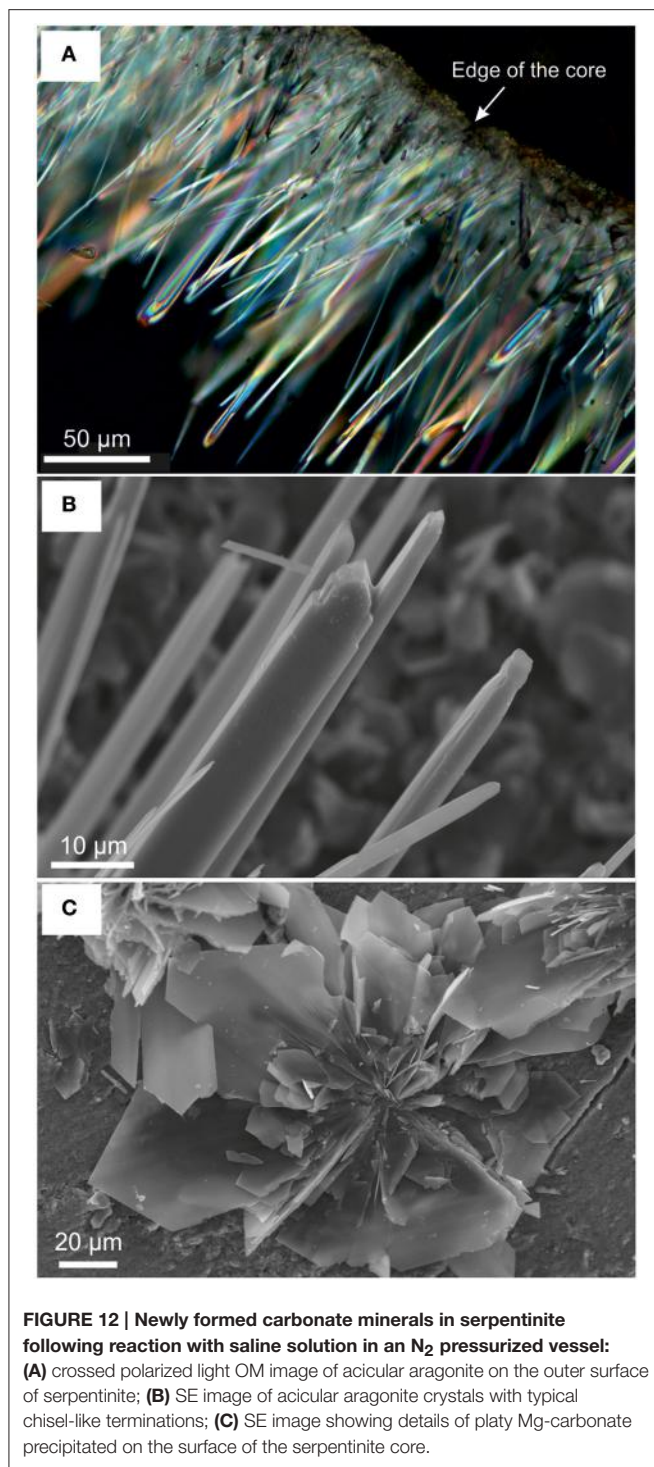


FIGURE 12 | Newly formed carbonate minerals in serpentinite following reaction with saline solution in an N_2 pressurized vessel: **(A)** crossed polarized light OM image of acicular aragonite on the outer surface of serpentinite; **(B)** SE image of acicular aragonite crystals with typical chisel-like terminations; **(C)** SE image showing details of platy Mg-carbonate precipitated on the surface of the serpentinite core.

by van Noort et al. (2013), who used Oman-UAE peridotite (partially serpentinised and containing 51% of olivine and 2–3% orthopyroxene), under experimental conditions of 150°C and 10 MPa CO_2 , and also reported the dissolution of olivine but not serpentinite. This preferential dissolution may be related to the different crystal structures of the two minerals, with the isolated Si-tetrahedra in olivine promoting faster dissolution than the

polymerised Si-tetrahedra in serpentinite. In addition, olivine is a higher temperature mineral and is thermodynamically less stable than serpentinite under the conditions applied here.

The dissolution of olivine resulted in the development of secondary porosity that provided additional pathways for fluid ingress. These pathways may have become interconnected, aiding the progressive dissolution of rock components and the release of Mg into solution.

The petrographic evidence for congruent dissolution of olivine, however, was not supported by the leachate chemistry that showed Mg concentrations up to two orders of magnitude higher than that of Si, rather than the expected similar amounts. This suggests that other components of the rock (e.g., serpentinite minerals) dissolved incongruently or significant amounts of silica had dropped out of the solution and precipitated, not only as well-defined nodules (Figure 13), but also as a fine coating layer. Such layers are considered to be passivating, limiting the number of reactive sites and having overall negative influence on the dissolution of both mineral and rock (Daval et al., 2011; Johnson et al., 2014 and references therein). Although it is possible that a passivating layer formed during the initial stages of these experiments, as proposed also by Johnson et al. (2014), no evidence for such a layer was found at this scale of observation, i.e., thickness $>1\text{ }\mu\text{m}$, and techniques with much better resolution would be required. Fibers of a Si-dominated phase ($<5\text{ }\mu\text{m}$ long) were observed on the surface of the induced fracture in serpentinite (Figure 11D), but this is a new precipitate not a passivating layer.

It is noted that although the experimental study of Johnson et al. (2014) was conducted under similar conditions to those used here, the source materials were different, i.e., isolated olivine grains vs. olivine crystals embedded in a matrix of serpentinite (dunite). As suggested by van Noort et al. (2013), the microtexture of polymimetic peridotites (such as dunite used here) may have a strong influence on the apparent dissolution rates, as compared to the dissolution of a (powdered) single mineral phase (such as the olivine, used by Johnson et al., idem.). In mineralogically heterogeneous and texturally complex rocks, the reactive fluids are never in direct and continuous contact with all the phases present, unlike isolated homogenous mineral grains. This may result in the generation of reaction fronts with varied geochemical micro-regimes, with localized pH differences and solution compositions, in turn leading to variable degrees of dissolution and precipitation, as observed in this study.

In the serpentinite that consisted of various types of serpentinite, the extent of dissolution and early reaction rates were greater than in the partially serpentinised dunite. The major cation source in serpentinite was an array of serpentinite and brucite-filled veins, rather than the bulk rock serpentinite (Figure 11, X-ray maps). Our related investigation (Lacinska et al., 2016) demonstrated that many serpentinite vein minerals are either chrysotile and/or those exhibiting wide inter-crystalline spacing or poor crystallinity. These types, due to their crystal structure, are generally less stable in the presence of acid (weak acid present here) than those formed earlier during the replacement of primary Mg-silicates that are the most abundant type in serpentinite and dunite. The preferential release of Mg

TABLE 6 | Summary of the compositional and textural transformation observed in the reacted rock cores.

	CO ₂				N ₂	
	Upper core transformations (Wet sc CO ₂)		Lower core transformations (CO ₂ saturated brine)		Upper core transformations (gaseous phase)	Lower core transformations (brine)
	Compositional	Textural	Compositional	Textural	Compositional	Compositional
Dunite	Localized crust of magnesite (<1 mm thick).	N/S	<5 μ m ferruginous veneer. Trace amount of magnesite and nodules of amorphous silica in the induced fracture (Figures 10E, F).	N/S	N/S	<2 μ m veneer of halite.
Harzburgite	Thin localized magnesite crust, mainly along pre-existing fractures.	N/S	Thin (<5 μ m) ferruginous veneer. No carbonate.	N/S	N/S	Possible formation of serpentine along pre-existing fractures.
Serpentinite	Up to 3 mm thick crust of magnesite and minor calcite (Figures 8, 9) and Mg carbonates within the fractures (Figure 11).	Partial disintegration, resulting in fragments comprising ca. 30% of the rock core falling to the bottom of the vessel. Expansion of micro-fractures, caused by push-apart growth of Mg carbonate.	<5 μ m ferruginous veneer and <3 mm magnesite-dominated crust with trace amount of halite.	N/S	N/S	Uneven crust of acicular <2 mm crystals of aragonite and <1 mm sized rosettes of Mg carbonate.

No textural transformations were observed in the N₂-pressurized vessels. The samples described in detail are shown in bold type. N/S, not significant.

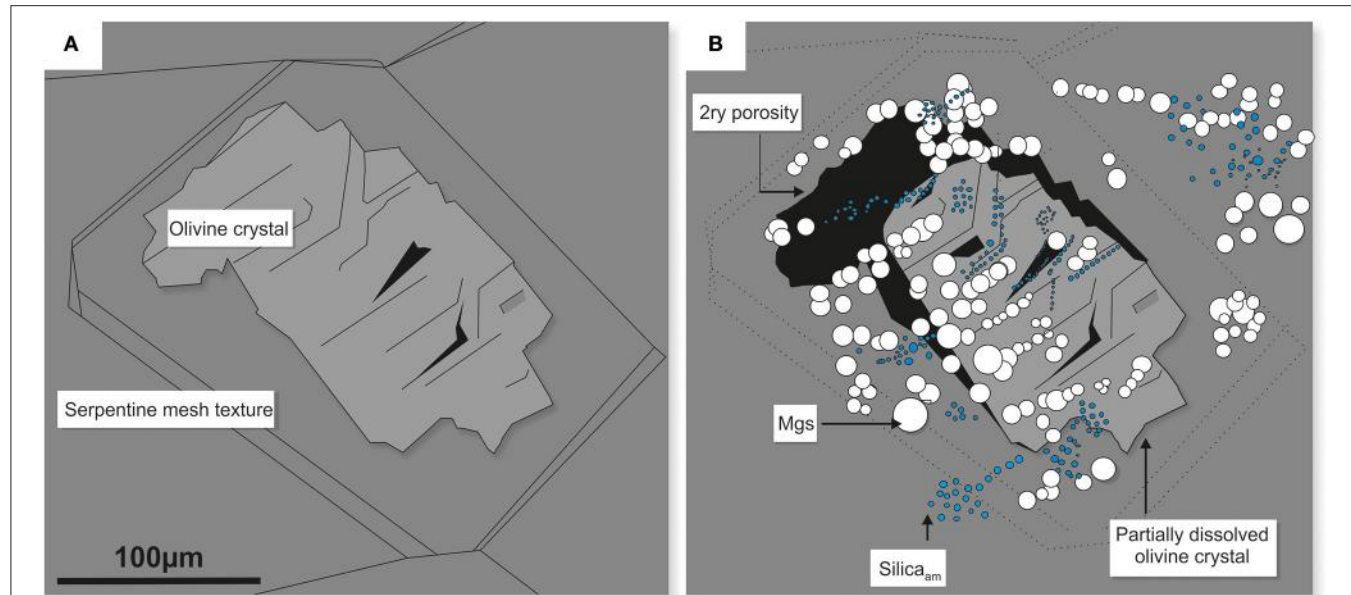


FIGURE 13 | Schematic diagram illustrating the effects of congruent dissolution of olivine in dunite. The original olivine crystal (A) dissolved stoichiometrically, providing components of Mg²⁺ and H₄SiO₄ for the subsequent *in situ* precipitation of magnesite (white) and amorphous silica nodules (blue) (B). The dissolution of olivine also resulted in the development of secondary porosity (black zones). Plate B corresponds to plate E in Figure 10.

from the original serpentine veins is also consistent with the distribution of magnesite on the surface of the reacted core that follows the distribution of the veins. Although no clear evidence was found in these experiments, it is likely that after

initial vein dissolution and with a continuous supply of fresh solution (unlike in our experiment that was run as a close system), bulk rock serpentine minerals may start to dissolve. Nevertheless, the preferential leaching of Mg from serpentine

veins resulted in a porous siliceous residuum that provided pathways for fluid ingress into deeper parts of the sample and increased the overall dissolution of the sample. This positive feedback is of high importance to the real CCSM scenario because it has the capacity of creating higher surface area for dissolution-carbonation processes.

Harzburgite, containing olivine and serpentine, in addition to the major component of pyroxene, showed the lowest extent and slowest rate of rock dissolution. The chemistry of the experimental leachates agreed with the observations of the reacted rock in hand-specimen and thin-section, with both suggesting minimal transformation. It was observed that neither serpentine nor olivine from the harzburgite reacted during the experiment. The starting harzburgite rock contained lesser amounts of original, relatively-reactive serpentine veins and a lower percentage of olivine and serpentine minerals, as well as a higher proportion of pyroxene (ortho- and clinopyroxene collectively at $\approx 23\%$), that are generally less reactive (Styles et al., 2014). All these factors contributed to the lower degree of dissolution.

Comparison between CO₂-Saturated Brine (Lower Cores) and Wet scCO₂ (Upper Cores)

One of the scenarios for industrial CCSM is to inject CO₂ as a compressed supercritical fluid (McGrail et al., 2006), at conditions exceeding the CO₂ critical point of 31.1°C and 7.38 MPa. The scCO₂ exhibits very low viscosity that makes it highly diffusive (Kwak et al., 2011) and consequently (once wet) highly reactive. Gaining improved understanding of the chemical interactions between wet scCO₂ and rocks is essential for evaluating the effectiveness and safety of CO₂ sequestration (Kerisit et al., 2012). Hence, conditions allowing for the persistence of supercritical CO₂ were used in this study, enabling the evaluation of its effect on host rock transformations.

Observations of the reacted cores in hand-specimens on the micro-scale demonstrated that the reactivity in the two CO₂-regimes, i.e., CO₂-saturated brine (lower cores) and wet scCO₂ (upper cores), was different and manifested by the presence of Fe oxide/oxyhydroxides on the lower cores and partial disintegration of the upper serpentinite core.

CO₂-Saturated Brine (Lower Core) and Goethite

Goethite was only present on the surface of cores that were immersed in CO₂-saturated brine. It formed the very first layer, $<1\text{ }\mu\text{m}$ thick, of secondary precipitate. It was subsequently overgrown by carbonate minerals, both best displayed on the serpentinite core. The temporal evolution of Fe^{total} concentration in the leachate solutions showed a rapid initial release and subsequent decrease within the first 33 days of the experiment. The absence of goethite on the surface of the upper cores, as well as the cores from the N₂ control vessels, suggests its formation resulted from a combination of dissolved oxygen and CO₂ in the brine. The CO₂ when dissolved forms carbonic acid, causing a drop of pH that may enhance the dissolution of minerals (Gaus, 2010). The ferrous iron released into saline solution reacted with the dissolved

oxygen and underwent rapid oxidation to ferric iron that then precipitated as goethite; a naturally insoluble mineral under these conditions. Several mineral phases might have provided the ferrous iron, including the original Mg, Fe silicates (serpentine and olivine), ferroan carbonate (pyroaurite), clay minerals, or Fe-oxyhydroxide formed from the earlier alteration of the primary silicates.

The dunite sample that reacted with CO₂-saturated brine showed that the goethite and Mg-carbonate precipitates were mutually exclusive. In the goethite-zone, apart from minor etch pits on the very edge of the sample, no other evidence for olivine dissolution was observed. This is consistent with observations reported elsewhere (Wogelius and Walther, 1991; Olsson et al., 2012) and as suggested by Wogelius and Walther (*idem*), the precipitation of secondary Fe³⁺-bearing phases decreases the number of rapidly reacting surface sites, thereby inhibiting further dissolution. It appears that initial minor dissolution of olivine at the very surface of the dunite core provided ferrous iron into solution. This oxidized immediately to ferric iron and precipitated as goethite, forming a barrier, and hindering further dissolution.

The initial precipitation of goethite requires further investigation because inhibiting the formation of carbonate may have a negative influence on the reactivity of rock used for CCSM and hence its capacity to sequester CO₂.

Textural Disintegration

Textural evidence showed that reactions in wet scCO₂ had an impact on sample integrity. The two serpentinite cores that reacted in the CO₂ vessel varied greatly in their resultant textures. While the lower core in CO₂-saturated brine retained its integrity, the upper core had partially but significantly disintegrated, with approximately a third of the original sample falling off during the experiment, leaving detached fragments in the lower part of the vessel. The mechanisms for chemical transformation of host rock minerals exposed to wet scCO₂ are still poorly understood (Schaef et al., 2011; Thompson et al., 2013).

It has been suggested that mineral reactions in wet supercritical CO₂ are fundamentally different to those of the same minerals in aqueous solution, being manifested by localized mineral replacements or transformations, rather than dissolution/re-precipitation involving solution phase ion transport (McGrail et al., 2009). Further, wet scCO₂-dominated fluids can drive some mineral reactions *via* dehydration or hydration processes, which could lead to a mineral volume change and thereby affecting the rock's porosity and permeability and hence long term integrity (Loring et al., 2013). Wet scCO₂ is chemically aggressive and due to its low viscosity and wetting capability has a higher relative capacity to permeate through the rock than brine. This possibly allowed a greater ingress of fluid along veins/fractures and grain boundaries and subsequent dissolution of the serpentinite sample, reducing the overall integrity of the rock and resulting in loss core from the upper sample by the end of the experiment. In addition, since the amount of oxygen dissolved in wet scCO₂ fluid was low, no goethite, a potential reaction-inhibitor was formed.

It is noted that varying degrees of textural disintegration might also be related to core sample inhomogeneity and the distribution of fractures and veins, as well as the arrangement of the gold wire cage used for sample mounting, despite attempts to keep these factors to a minimum.

Implications for Engineered *In situ* CCSM Carbonate Recycling

Several lines of petrographic evidence indicated that the stability of carbonate minerals was disturbed under the conditions investigated in this study (70°C, 100 bar CO₂). This was typically manifested by the presence of corrosion patterns on the surface of both original and secondary carbonates (Figures 11B,D), as well as the presence of newly formed carbonate minerals in the N₂-pressurized system. For example, the precipitation of aragonite and unidentified Mg-carbonates (Figure 12) on the surface of the serpentinite that had reacted with N₂-pressurized saline solution was probably facilitated by the initial dissolution of original carbonate minerals, e.g., dolomite, calcite, and/or pyroaurite that had been present in thin veins in the starting rock sample. Furthermore, microanalysis of the newly formed carbonates within the induced fractures of serpentinite (CO₂-saturated brine) showed evidence for significant crystal corrosion and dissolution during the experiment (Figures 11, 14). The extent of carbonate recycling needs to be understood more fully,

to be able to estimate the efficiency of mineral carbonation in an engineered system.

Reaction Driven Cracking

Several authors have reported on mechanisms for self-propagating fractures, induced by the force of crystallization, commonly termed reaction driven cracking (Evans, 2004; Røyne et al., 2011; Plumper et al., 2012). Recently, Kelemen and Hirth (2012) suggested that, where initial permeability is sufficient to assure the continuous supply of aqueous fluids, positive feedback between reaction-driven cracking, fluid supply and reactive surface area will result most likely in nearly 100% carbonation at 185°C (accordingly, this temperature was suggested for *in situ* accelerated CCSM). Analysis of the reacted cores in this study suggested that the force of crystallization of Mg-carbonate was sufficient to push apart slivers of weakened wall rock in the pre-existing fracture zones, but not to create new fractures (Figure 14).

Amount of Carbonate Formed

The serpentinite core that reacted with the CO₂-saturated solution showed the maximum extent of carbonation. It is desirable to estimate the extent of carbonation, but due to the nature of the friable carbonate crust it was not possible to measure it directly. Alternatively, we chose to use the changes in

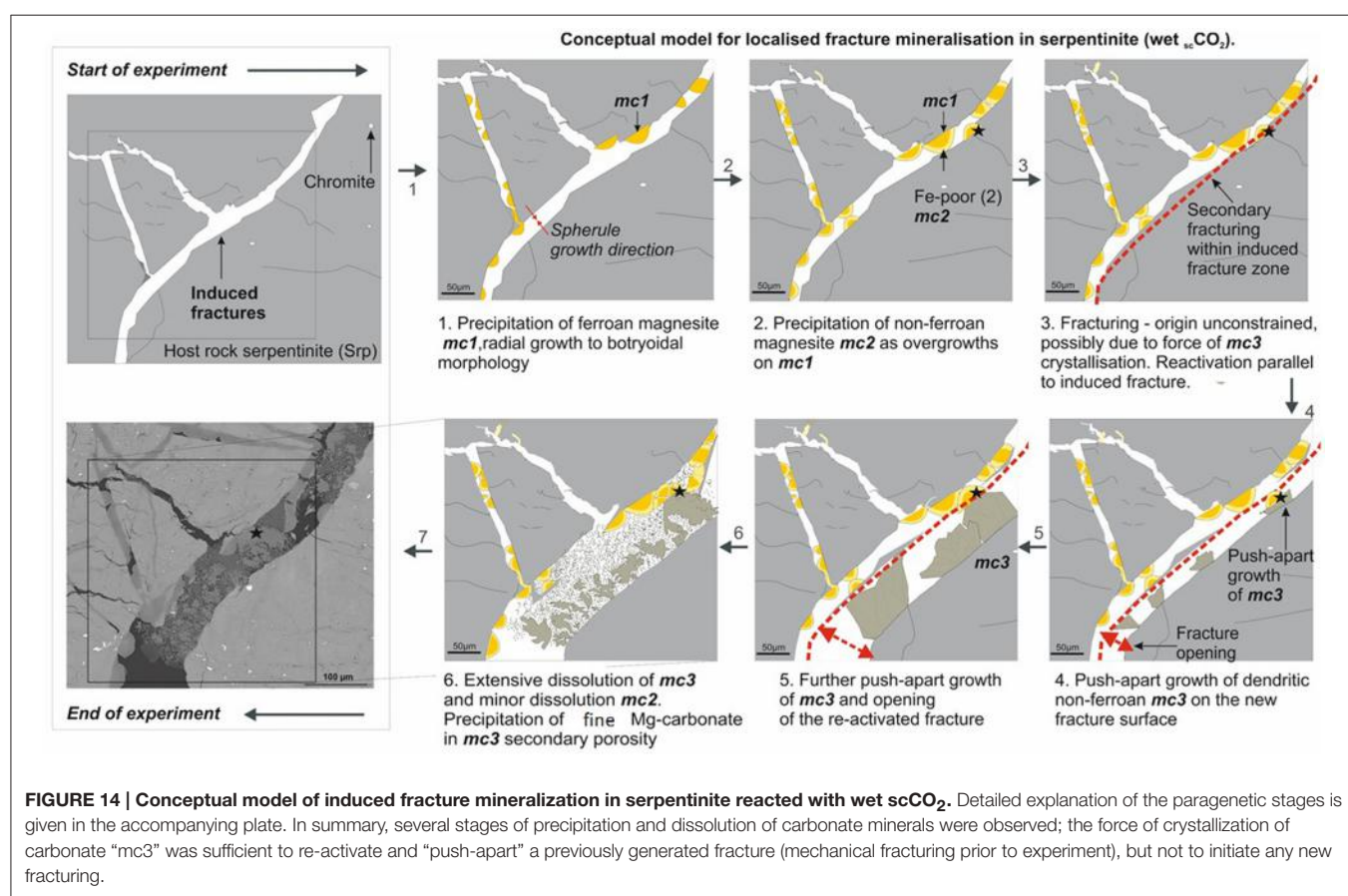


FIGURE 14 | Conceptual model of induced fracture mineralization in serpentinite reacted with wet scCO₂. Detailed explanation of the paragenetic stages is given in the accompanying plate. In summary, several stages of precipitation and dissolution of carbonate minerals were observed; the force of crystallization of carbonate "mc3" was sufficient to re-activate and "push-apart" a previously generated fracture (mechanical fracturing prior to experiment), but not to initiate any new fracturing.

composition of the leachate solution to calculate the amount of carbonate formed.

The plot of Mg concentration in the CO₂-pressurized serpentinite (**Figure 15**) is a simplification of **Figure 3** and shows that, from \approx 70th day of experiment, the Mg uptake exceeds that of release i.e., precipitation of a Mg-bearing phase was taking place. The calculation of the chemical affinities of potential phases and the analysis of post-experimental solids confirmed that the only Mg-bearing secondary phase formed in the serpentinite was magnesite. The amount formed can be calculated from the change in Mg concentration between the peak of Mg concentration (C1) at 0.21 mol Mg/l and the end of the experiment (C2).

$$\Delta C = C1 - C2$$

$$0.21 - 0.13 = 0.08 \text{ (mol Mg/l)}$$

Thus, 0.084 M Mg was utilized in the precipitation of magnesite. The weight of magnesite, as calculated from stoichiometry and adjusted to the volume of solution used in this study (i.e., 200 ml), was 1.4 g. By mass, this constitutes \approx 8% of the \approx 17.3 g starting mass of the serpentinite core. However, as revealed at the cessation of the experiment, \approx one third of the upper serpentinite core disintegrated and fell down the vessel. Although we are not able to estimate how much of the upper core contributed to lower core carbonation, we attempt to take this into account. Thus, 5.4 g from the upper core is added to the 17.3 g starting weight of the lower serpentinite.

As a result, direct measurement of the change in fluid composition showed that 0.7 g CO₂ was captured (calculated from the stoichiometry of 1.4 g magnesite), utilizing a portion of the serpentine minerals from 22.7 g (17.3 + 5.4 g) of serpentinite, in sea water at 70°C pressurized with 100 bar CO₂. If the entire rock weight of 22.7 g is used to calculate the rate of carbonation, then after conversion to the amount of CO₂ sequestered, a value

of \approx 30.8 kg of CO₂ per ton serpentinite is realized after \approx 6.5-months, corresponding to \approx 3% carbonation. In the experiments carried out here it appears that around 1% carbonate present in the starting rocks is recycled to contribute to the 3% final carbonate formed, giving an overall amount of new carbonate that captures CO₂ reduced to 2%. Due to the complexity of this fluid-rock system, there are several caveats that could affect the accuracy of this calculation:

- Chlorine was present in the original fluid, and chlorine could act as another sink for magnesium, by forming MgCl₂. This could potentially lead to an overestimate of the amount of CO₂ captured, however no evidence for any MgCl₂ precipitation was found. Hence, the assumption that magnesite was the only authigenic magnesium sink is considered reasonable.
- There is an issue with contamination of the fluid with precipitates and fragments of host rock core from the headspace that fell into the solution. It is not known at what stage of the experiment this occurred, nor the effect it might have had on solution chemistry. The estimated amount of core that fell into the solution has been taken into consideration and included as part of the total mass of serpentinite undergoing dissolution and carbonation.

The extent of laboratory carbonation was compared with two estimates of natural mineral carbonation, i.e., carbonation of chrysotile mine tailings at Clinton Creek, Canada (Wilson et al., 2006), and carbonation of peridotite in Oman (Kelemen et al., 2011), as presented in **Table 7**.

Although the values in **Table 7** represent a *rough estimate* of the extent of the reaction, the comparison shows that the laboratory carbonation of serpentinite, as pursued in this study, greatly exceeded the extent of natural carbonation of peridotite. Studies of the rate of weathering of silicate minerals in nature report that natural reactions are 1–3 orders of magnitude slower than those in laboratory experiments. This may result from differences in reactivity between freshly-crushed and weathered minerals, errors in estimating the exposed surface areas of minerals in weathered rock, and differences in solution composition (Swoboda-Colberg and Drever, 1993; Drever et al., 1994). Some parts of the weathering process are similar to carbonation and such factors could be applicable to this study.

The experiments reported here were at 70°C and 100 bar compared to ambient conditions for the natural examples and this will increase the rate of reaction. Kelemen and Matter (2008), Kelemen et al. (2011) noted that accelerated carbonation, using

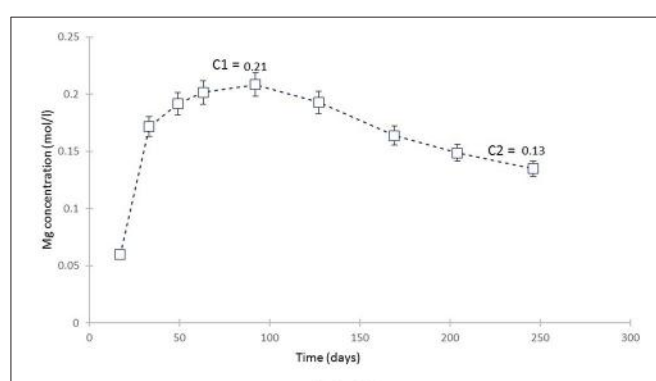


FIGURE 15 | Mg concentration in the fluid from the serpentinite CO₂ experiment. C1 marks the point from which the uptake of Mg by precipitating phase (magnesite) exceeded its release (dissolution of serpentine) and C2 is the end of experiment. The change in Mg concentration between the two points was used to calculate the amount of magnesite formed during the experiment.

TABLE 7 | Extent of laboratory mineral carbonation compared to natural processes represented by Clinton Creek chrysotile mine tailings and peridotite in Oman, data expressed as x kg CO₂ captured per ton of rock, over 6 months, assuming a linear rate.

Natural carbonation of chrysotile mine tailings (Wilson et al., 2006)	Natural carbonation of Semail peridotite (Oman) (Kelemen et al., 2011)	Experimental carbonation of Semail peridotite (UAE) (This study)
0.3	0.0001	30

conditions of 185°C and 150 bar CO₂ might result in a rate $\approx 10^6$ times higher than that of natural carbonation. Our data fits in between the two extreme rate predictions suggested by these authors.

It should be noted that the estimates above do not compare the same rock types. In this study, serpentinite might initially be much more reactive due to the preferential dissolution of serpentine minerals and brucite from the cross-cutting veins that may have contributed to the high extent of reaction. This would make it more analogous to the reaction of chrysotile mine tailings. The minimal carbonation of harzburgite would give reaction extent many orders of magnitude lower, more in line with that estimated by Kelemen et al. (2011).

What is not known from these 8-month long experiments is how much the main body of the serpentinite, or indeed the other rock types, will react given a longer period of time. This data is needed to predict behavior in a more realistic engineered CCSM scenario. It is known from natural analog studies of serpentinite and peridotite pebbles in a serpentinite sand matrix that total carbonation of serpentine and peridotite can take place in brine under near ambient conditions (Lacinska et al., 2014), but there is no control on the time taken; it could be thousands of years. Experiments over a much longer time are required to get an understanding of the likelihood of extensive proportions of the rocks being converted to carbonate and whether the carbonation rates achieved are suitable for industrial scale CO₂ injection.

CONCLUSIONS

This study has focused on the changes observed and the reactivity of dunite, harzburgite, and serpentinite during 8-month, closed-system experiments, using simulated seawater at 70°C and 100 bar CO₂. These conditions approximate the *in situ* injection of CO₂ into partially serpentinitised mantle peridotite for reaction with silicate minerals, to release Mg for the formation of carbonate and the long term capture of CO₂. We have shown that rock reactivity depends on a complex interplay between composition and texture, and the experimental conditions. Control experiments using N₂ showed essentially no changes.

We conclude that:

- Serpentinite was the most reactive—resulting in the fastest initial rates of net Mg release and the greatest amount of new carbonate formed. Dunite showed low reactivity and harzburgite was virtually unchanged.
- The increased reactivity of serpentinite was associated with the preferential dissolution of veins filled with more reactive types of serpentine minerals and brucite. The dissolution of minerals from these previously sealed fractures provided pathways for further fluid ingress, thereby enhancing overall CCSM efficiency.
- The extent of carbonation based on the analysis of serpentinite that reacted with CO₂-saturated brine was estimated to be $\approx 3\%$ per half year. This is 100 times greater than the extent of natural carbonation of Clinton Creek mine tailings in Canada (Wilson et al., 2006) and about 200,000 times greater

than the natural carbonation of peridotite in Oman (Kelemen and Matter, 2008). The estimate suggested from this study is associated with several types of uncertainty. Around 1% of the carbonate formed might be from recycling of pre-existing carbonate, giving a net figure of 2%. Further, it is stressed that the rate of serpentinite carbonation may be reduced significantly once the most reactive, i.e., vein material, is exhausted. The rate or extent of carbonation over a period of many years cannot be predicted from these experiments.

- Ferrous iron, mainly originating from the dissolution of ferromagnesian minerals present in the host-rock, undergoes rapid transformation to ferric iron upon contact with oxidative solutions. In this study, it precipitated as goethite; forming a very thin surface layer that hindered further rock dissolution by covering rapidly reacting surface sites.
- Wet scCO₂ is highly reactive and rock dissolution and carbonate precipitation, affected the integrity of the rock core, increasing the reactive surface area, and promoting further geochemical transformations.
- Although the results of PHREEQC geochemical modeling were in general agreement with the microanalysis of post-experimental solids and leachate liquids, some discrepancies were found in the values of saturation indices and the phases present. These discrepancies, albeit small, were assigned to a combination of analytical errors and possible imprecisions in the database.
- Reaction driven cracking only occurred in the zone around induced fractures, but not within previously undisturbed areas.
- The choice of the most suitable reservoir rock for *in situ* CCSM is essential and will significantly impact the efficiency of any proposed technology, as there appear to be very large differences in the likelihood of extensive carbonation. Assumptions on rock composition should not be made and detailed petrographical and geochemical studies are essential as a part of the site selection of any proposed CCSM repository. This study of relatively short term experiments suggests that serpentinite might be a very good host rock. However, although the reactivity of dunite and harzburgite was poor compared to that of serpentinite, long term experiments might prove that these rocks might be an effective host for reaction with CO₂ in an engineered system of CCSM. Longer term laboratory investigation is thus required to test this possibility.
- This study demonstrates the difficulties, complexities and uncertainties that arise when carrying out experiments on natural rocks compared to simpler systems of mineral separates. Such studies are essential to gain an understanding of the likely behavior at an industrial scale CO₂ injection site.

AUTHOR CONTRIBUTIONS

AL: carried out the experiments and interpreted the results. MS: assisted with mineralogical and petrographical study. KB: assisted with geochemical study. PB and MH: assisted with microanalysis.

ACKNOWLEDGMENTS

This research was funded by the British Geological Survey, the University of Nottingham (jointly the GeoEnergy Research Centre) and Caterpillar Inc. C. Rochelle, G. Purser, and A. Kilpatrick are acknowledged for their support in the hydrothermal laboratories at BGS; A. Kilpatrick is also thanked for reviewing the manuscript. J. Fletcher and P. Neep are thanked for the preparation of polished thin sections; D. Wagner for assistance with XRD analyses; and M. Watts and I. Mountaney

for facilitating the chemical analyses. The authors publish with the permission of the Executive Director of the British Geological Survey (NERC).

SUPPLEMENTARY MATERIAL

The Supplementary Material for this article can be found online at: <http://journal.frontiersin.org/article/10.3389/feart.2017.00037/full#supplementary-material>

REFERENCES

- ASTM E1508-12a (2012). *Standard Guide for Quantitative Analysis by Energy-Dispersive Spectroscopy*, ASTM International, West Conshohocken, PA. Available online at: www.astm.org
- Bevan, J., and Savage, D. (1989). The effect of organic acids on the dissolution of K-feldspar under conditions relevant to burial diagenesis. *Mineral. Mag.* 53, 415–425. doi: 10.1180/minmag.1989.053.372.02
- Brantley, S. L., Kubicki, J. D., and White, A. F. (2008). *Kinetics of Water-Rock Interaction*. New York, NY: Springer Science+Business Media.
- Daval, D., Sissmann, O., Menguy, N., Saldi, G. D., Guyot, F., Martinez, I., et al. (2011). Influence of amorphous silica layer formation on the dissolution rate of olivine at 90 degrees C and elevated pCO₂. *Chem. Geol.* 284, 193–209. doi: 10.1016/j.chemgeo.2011.02.021
- Drever, J. I., Murphy, K. M., and Clow, D. W. (1994). Field weathering rates versus laboratory dissolution rates: an update. *Mineral. Mag.* 58A, 239–240. doi: 10.1180/minmag.1994.58a.1.126
- Evans, B. W. (2004). The serpentinite multisystem revisited: chrysotile is metastable. *Int. Geol. Rev.* 46, 479–506. doi: 10.2747/0020-6814.46.6.479
- Gaus, I. (2010). Role and impact of CO₂-rock interactions during CO₂ storage in sedimentary rocks. *Int. J. Greenhouse Gas Control* 4, 73–89. doi: 10.1016/j.ijggc.2009.09.015
- Giammar, D. E., Bruant, R. G., and Peters, C. A. (2005). Forsterite dissolution and magnesite precipitation at conditions relevant for deep saline aquifer storage and sequestration of carbon dioxide. *Chem. Geol.* 217, 257–276. doi: 10.1016/j.chemgeo.2004.12.013
- Gislason, S. R., Wolff-Boenisch, D., Stefansson, A., Oelkers, E. H., Gunnlaugsson, E., Sigurdardottir, H., et al. (2010). Mineral sequestration of carbon dioxide in basalt: a pre-injection overview of the CarbFix project. *Int. J. Greenhouse Gas Control* 4, 537–545. doi: 10.1016/j.ijggc.2009.11.013
- Hovelmann, J., Austrheim, H., and Jamtveit, B. (2012). Microstructure and porosity evolution during experimental carbonation of a natural peridotite. *Chem. Geol.* 334, 254–265. doi: 10.1016/j.chemgeo.2012.10.025
- IPCC (2011). *Summary for Policymakers*. IPCC Special Report on Renewable Energy Sources and Climate Change Mitigation, eds by O. Edenhofer, R. Pichs-Madruga, Y. Sokona, K. Seyboth, P. Matschoss, S. Kadner et al. (Cambridge; New York, NY: Cambridge University Press).
- Johnson, N. C., Thomas, B., Maher, K., Rosenbauer, R. J., Bird, D., and Brown, G. E. Jr. (2014). Olivine dissolution and carbonation under conditions relevant for *in situ* carbon storage. *Chem. Geol.* 373, 93–105. doi: 10.1016/j.chemgeo.2014.02.026
- Kaszuba, J. P., Janecky, D. R., and Snow, M. G. (2005). Experimental evaluation of mixed fluid reactions between supercritical carbon dioxide and NaCl brine: relevance to the integrity of a geologic carbon repository. *Chem. Geol.* 217, 277–293. doi: 10.1016/j.chemgeo.2004.12.014
- Kelemen, P. B., and Hirth, G. (2012). Reaction-driven cracking during retrograde metamorphism: olivine hydration and carbonation. *Earth Planet. Sci. Lett.* 345–348, 81–89. doi: 10.1016/j.epsl.2012.06.018
- Kelemen, P. B., and Matter, J. (2008). *in situ* carbonation of peridotite for CO₂ storage. *Proc. Natl. Acad. Sci. U.S.A.* 105, 17295–17300. doi: 10.1073/pnas.0805794105
- Kelemen, P. B., Matter, J., Streit, E. E., Rudge, J. F., Curry, W. B., and Blusztajn, J. (2011). Rates and mechanisms of mineral carbonation in peridotite: natural processes and recipes for enhanced, *in situ* CO₂ capture and storage. *Annu. Rev. Earth Planet. Sci.* 39, 545–576. doi: 10.1146/annurev-earth-092010-152509
- Kerisit, S., Weare, J. H., and Felmy, A. R. (2012). Structure and dynamics of forsterite- $\text{scCO}_2/\text{H}_2\text{O}$ interfaces as a function of water content. *Geochim. Cosmochim. Acta* 84, 137–151. doi: 10.1016/j.gca.2012.01.038
- Kwak, J. H., Hu, J. Z., Turcu, R. V. F., Rosso, K. M., Ilton, E. S., Wang, C., et al. (2011). The role of H₂O in the carbonation of forsterite in supercritical CO₂. *Int. J. Greenhouse Gas Control* 5, 1081–1092. doi: 10.1016/j.ijggc.2011.05.013
- Lacinska, A. M., Styles, M. T., and Farrant, A. (2014). Near-surface diagenesis of ophiolite-derived conglomerates of the Barzaman Formation, United Arab Emirates: a natural analogue for permanent CO₂ sequestration via mineral carbonation of ultramafic rocks. *Geol. Soc. Special Edition-Tectonics of Oman Mountains*, 392, 343–360. doi: 10.1144/SP392.18
- Lacinska, A. M., Styles, M. T., Bateman, K., Wagner, D., Hall, M. R., Gowing, C., et al. (2016). Acid-dissolution of antigorite, chrysotile and lizardite for *ex situ* carbon capture and storage by mineralisation. *Chem. Geol.* 437, 153–169. doi: 10.1016/j.chemgeo.2016.05.015
- Loring, J. S., Schaeff, H. T., Thomson, C. J., Turcu, R. V., Miller, Q. R., Chen, J., et al. (2013). Clayhydration/dehydration in dry to water-saturated supercritical CO₂: implications for caprock integrity. *Energy Proced.* 37, 5443–5448. doi: 10.1016/j.egypro.2013.06.463
- McGrail, B. P., Schaeff, H. T., Glezakou, V. A., Dang, L. X., and Owen, A. T. (2009). Water reactivity in the liquid and supercritical CO₂ phase: has half the story been neglected? *Energy Proced.* 1, 3415–3419. doi: 10.1016/j.egypro.2009.02.131
- McGrail, B. P., Schaeff, H. T., Ho, A. M., Chien, Y.-J., Dooley, J. J., and Davidson, C. L. (2006). Potential for carbon dioxide sequestration in flood basalts. *J. Geophys. Res. Solid Earth* 111, B12201. doi: 10.1029/2005JB004169
- Millero, F. J. (1996). *Chemical Oceanography*. Boca Raton, FL: CRC Press.
- Oelkers, E. H., Gislason, S. R., and Matter, J. (2008). Mineral carbonation of CO₂. *Elements* 4, 333–337. doi: 10.2113/gselements.4.5.333
- Olsson, J., Bovet, N., Makovicky, E., Bechgaard, K., Balogh, Z., and Stipp, S. L. S. (2012). Olivine reactivity with CO₂ and H₂O on a microscale: implications for carbon sequestration. *Geochim. Cosmochim. Acta* 77, 86–97. doi: 10.1016/j.gca.2011.11.001
- Parkhurst, D. L., and Appelo, C. A. J. (2013). *Description of Input and Examples for Phreeqc Version 3 – a Computer Program for Speciation, Batch-Reaction, One-Dimensional Transport and Inverse Geochemical Calculations*. U.S. Geological Survey, Techniques and Methods 6–A43, 497, Denver, CO.
- Plummer, O., Royne, A., Magraso, A., and Jamtveit, B. (2012). The interface-scale mechanism of reaction-induced fracturing during serpentinization. *Geology* 40, 1103–1106. doi: 10.1130/G33390.1
- Røyne, A., Meakin, P., Maltse-Sorensen, A., Jamtveit, B., and Dysthe, D. K. (2011). Crack propagation driven by crystal growth. *Europhys. Lett.* 96:24003. doi: 10.1209/0295-5075/96/24003
- Schaeff, H., Windisch, T. C. Jr., McGrail, F. B., Martin, P. P. F., and Rosso, K. M. (2011). Brucite [Mg₉OH₂] carbonation in wet supercritical CO₂: an *in situ* high pressure x-ray diffraction study. *Geochim. Cosmochim. Acta* 75, 7458–7471. doi: 10.1016/j.gca.2011.09.029
- Styles, M. T., Sanna, A., Lacinska, A. M., Naden, J., and Maroto-Valer, M. (2014). The variation in composition of ultramafic rocks and the effect on

- their suitability for carbon dioxide sequestration by mineralization following acid leaching. *Greenhouse Gases Sci. Technol.* 4, 440–451. doi: 10.1002/ghg.1405
- Swoboda-Colberg, N. G., and Drever, J. I. (1993). Mineral dissolution rates in plot-scale field and laboratory experiments. *Chem. Geol.* 105, 51–69. doi: 10.1016/0009-2541(93)90118-3
- Thompson, C. J., Loring, J. S., Rosso, K. M., and Wang, Z. (2013). Comparative reactivity study of forsterite and antigorite in wet supercritical CO₂ by *in situ* infrared spectroscopy. *Int. J. Greenhouse Gas Control* 18, 246–255. doi: 10.1016/j.ijggc.2013.07.007
- van Noort, R., Spiers, C. J., Drury, M. R., and Kandianis, M. T. (2013). Peridotite dissolution and carbonation rates at fracture surfaces under conditions relevant for *in situ* mineralization of CO₂. *Geochim. Cosmochim. Acta* 106, 1–24. doi: 10.1016/j.gca.2012.12.001
- Wilson, S. A., Raudsepp, M., and Dipple, G. M. (2006). Verifying and quantifying carbon fixation in minerals from serpentine-rich mine tailings using the Rietveld method with X-ray powder diffraction data. *Am. Mineral.* 91, 1331–1341. doi: 10.2138/am.2006.2058
- Wogelius, R. A., and Walther, J. V. (1991). Olivine dissolution at 25°C – effects of pH, CO₂, and organic acids. *Geochim. Cosmochim. Acta* 55, 943–954. doi: 10.1016/0016-7037(91)90153-V
- Conflict of Interest Statement:** The authors declare that the research was conducted in the absence of any commercial or financial relationships that could be construed as a potential conflict of interest.
- Copyright © 2017 Lacinska, Styles, Bateman, Hall and Brown. This is an open-access article distributed under the terms of the Creative Commons Attribution License (CC BY). The use, distribution or reproduction in other forums is permitted, provided the original author(s) or licensor are credited and that the original publication in this journal is cited, in accordance with accepted academic practice. No use, distribution or reproduction is permitted which does not comply with these terms.



Improved Measurement of Extracellular Enzymatic Activities in Subsurface Sediments Using Competitive Desorption Treatment

Adrienne Hoar frost*, Rachel Snider and Carol Arnosti

Department of Marine Sciences, University of North Carolina, Chapel Hill, NC, USA

OPEN ACCESS

Edited by:

Donato Giovannelli,
Earth-Life Science Institute, Tokyo
Institute of Technology, Japan

Reviewed by:

Jason B. Sylvan,
Texas A&M University, USA
Elena Marini,
ISMAR-Istituto di Scienze Marine
(CNR), Italy

*Correspondence:

Adrienne Hoar frost
adrienne.l.hoarfrost@unc.edu

Specialty section:

This article was submitted to
Microbiological Chemistry and
Geomicrobiology,
a section of the journal
Frontiers in Earth Science

Received: 27 October 2016

Accepted: 02 February 2017

Published: 16 February 2017

Citation:

Hoarfrost A, Snider R and Arnosti C
(2017) Improved Measurement of
Extracellular Enzymatic Activities in
Subsurface Sediments Using
Competitive Desorption Treatment.
Front. Earth Sci. 5:13.
doi: 10.3389/feart.2017.00013

Extracellular enzymatic activities initiate microbially-driven heterotrophic carbon cycling in subsurface sediments. While measurement of hydrolytic activities in sediments is fundamental to our understanding of carbon cycling, these measurements are often technically difficult due to sorption of organic substrates to the sediment matrix. Most methods that measure hydrolysis of organic substrates in sediments rely on recovery of a fluorophore or fluorescently-labeled target substrate from a sediment incubation. The tendency for substrates to sorb to sediments results in lower recovery of an added substrate, and can result in data that are unusable or difficult to interpret. We developed a treatment using competitive desorption of a fluorescently-labeled, high molecular weight organic substrate that improves recovery of the labeled substrate from sediment subsamples. Competitive desorption treatment improved recovery of the fluorescent substrate by a median of 66%, expanded the range of sediments for which activity measurements could be made, and was effective in sediments from a broad range of geochemical contexts. More reliable measurements of hydrolytic activities in sediments will yield usable and more easily interpretable data from a wider range of sedimentary environments, enabling better understanding of microbially-catalyzed carbon cycling in subsurface environments.

Keywords: carbon degradation, microbial activity, deep biosphere, hydrolysis, polysaccharides

INTRODUCTION

Heterotrophic microbial communities play an important role in organic carbon cycling in subsurface sediments. Increasing genomic evidence of the predominance of heterotrophy in the subsurface environment (Biddle et al., 2006; Fry et al., 2008; Lloyd et al., 2013) suggests that heterotrophic remineralization of organic matter plays a larger role in the sedimentary environment than previously appreciated. A key first step in the heterotrophic breakdown of organic carbon is extracellular enzymatic hydrolysis, in which compounds too large to be taken up directly are hydrolyzed to sizes small enough for transport into the cell. The need for measurements of enzymatic activities to quantify heterotrophic processes in subsurface sediments is evident, but the technical challenges associated with these measurements are such that comparatively few measurements have been made, particularly in subsurface environments.

Extracellular enzymatic activity is typically measured by addition of a fluorescently labeled substrate to an environmental sample, and hydrolysis is detected either as an increase in

fluorescence as a fluorophore is cleaved (Hoppe, 1983) or as a change in molecular weight distribution as a fluorescent substrate is hydrolyzed into lower molecular weight products (Arnoldi, 1996, 2003). In both cases, adequate recovery of the amended label or labeled substrate is necessary for interpretable results.

However, adequate recovery of fluorescent labels or labeled substrates is often difficult to achieve due to the tendency of organic compounds to sorb strongly to the sediment matrix. Sorption occurs when the organic substrates interact with sediment surfaces. Interaction mechanisms can include ligand exchange, cation bridges, or weak interactions including hydrophobic interactions, van der Waals forces, or H-bonding (Theng, 1979; Lutzow et al., 2006). High molecular weight substrates often adsorb more strongly than low molecular weight compounds (Podoll et al., 1987) and so pose a particular challenge for activity measurements, yet these measurements are especially important as most natural organic matter is biosynthesized as high molecular weight compounds.

The strength of sorption is dependent on the characteristics of the organic substrate as well as the sediment composition and mineralogy (Kaiser and Guggenberger, 2000). The interaction of these factors leads to great variation in the extent to which enzyme activities in sediments can be measured: in some sediments, activities are measured relatively easily, in other sediments sorption affects the quality of measurements to an extent that may affect the accuracy of results, and in some sediments there is such poor recovery of substrate that measurements of enzyme activities are not feasible. Thus, published data likely excludes sediments for which measurements are particularly challenging to obtain. Measuring activities in such sediments may be important for capturing the range of heterotrophic activities in the subsurface, however, and exclusion of such sediments may bias our understanding of microbial effects on environmental processes.

Several strategies have been used to attempt to overcome the effect of sorption on measurements of enzyme activity in sediments. Very dilute sediment slurries, for example 20:1 ratios of aqueous media to sediment, can be used to minimize sorption surface area relative to substrate concentration (Lloyd et al., 2013). Another approach has attempted to correct for adsorption by calculating the sorption affinity constant of the target molecule from a separate set of incubation standards with known concentrations of fluorophore, and back-calculating the total concentration of substrate hydrolyzed in the enzyme activity calculation (Coolen and Overmann, 2000; Coolen et al., 2002). Both of these approaches have limitations, however. High dilution of sediments necessarily reduces microbial interactions with the sediment matrix, but such interactions may be important, since the interactions of organic matter with sediment particles can affect the bioavailability of substrates (Keil et al., 1994; Chenu and Stotzky, 2002). Moreover, phenomena such as quorum sensing are dependent upon close spatial interactions of organisms and substrates (Hmelo et al., 2011), so quorum-sensing dependent enzymatic activities likely could not be measured in a dilute slurry. Ideally, experimental conditions should reflect natural conditions as much as possible. Correcting for sorption, aside from requiring additional time and resources

to conduct incubations for sorption affinity constant calculations, assumes that sorption is at equilibrium within 8 h. Sorption can occur on both short and long timescales (Pignatello and Xing, 1996), however, and the factors affecting this vary by sediment type and characteristics, so correcting enzyme activities using sorption affinity constants may not always yield accurate results.

Here we present an alternative strategy to measure enzymatic activities in sediments, an approach that counteracts the effect of sorption by recovering adsorbed substrate. We adapted a method developed previously to measure extracellular enzymatic hydrolysis of high molecular weight organic matter in sediments and seawater (Arnoldi, 1996, 2003). The original method involves addition of a fluorescently labeled, high molecular weight substrate to sediments. After incubation, sediment subsamples are centrifuged to obtain porewater containing the partially-hydrolyzed substrate, which are analyzed chromatographically to determine the molecular weight distribution of the hydrolysis products and thereby the hydrolysis rate. We have extended this method by developing a treatment to desorb amended labeled substrate from subsamples for better detection of enzymatic activities. We tested two desorption strategies, treatment of sediment slurry subsamples with extraction solutions at elevated pH, and treatment of subsamples with extraction solutions using competitive desorption. Elevated pH was tested because adsorption via ligand exchange occurs most strongly at acidic pH (Gu et al., 1994; Kaiser and Guggenberger, 2000), and compounds bound by this means may be more easily desorbed at high pH (Kaiser and Zech, 1999). Competitive desorption, addition of unlabeled substrate to a subsample in order to desorb the adsorbed fluorescently-labeled substrate, was tested since adsorption occurs when compounds compete to adsorb to a limited number of available sorption sites in the sediment matrix (Gu et al., 1994). The adsorption of a particular molecule is often reversible, and a given molecule can be displaced by other molecules that compete for the same sorption sites (Gu et al., 1994, 1996). Competitive displacement of adsorbed compounds has been demonstrated with mixtures of natural organic matter of similar or stronger adsorption affinities (Gu et al., 1996). We tested both pH and competitive desorption strategies, optimized a desorption extraction method, and demonstrated its effectiveness with a range of marine subsurface sediments. Here, we report the efficacy of our optimized extraction method and its applicability to subsurface sediments from a range of geochemical settings.

MATERIALS AND METHODS

Sediment Collection and Characteristics

Sediments for development of the extraction treatment protocol (see below) were collected from the Marmara Sea. Once finalized, the extraction treatment was applied to sediments from a range of geochemical environments in the Eastern Mediterranean Sea and the Guaymas Basin.

Marmara Sea and Eastern Mediterranean Sediments

Sediment from the Marmara Sea and the Eastern Mediterranean were collected during R/V *Meteor* cruise M84 in February 2011

(SI Table 1). Surficial sediments from the Marmara Sea ($40^{\circ}47.97'N$, $27^{\circ}43.49'E$, 600 m water depth) were collected by multicorer, and sediments from 570–585 and 520–530 cm depth horizons were collected by gravity corer. Sediments from the Eastern Mediterranean ($33^{\circ}02.00'N$, $32^{\circ}38.00'E$, 1424 m water depth) were collected by gravity corer at 365, 385, 440, 455, 575, and 582–590 cm depth horizons. Individual depth intervals were subsampled from the cores into 50 mL centrifuge tubes, which were stored at $4^{\circ}C$ in anaerobic chambers until use. Eastern Mediterranean sediments contained five sapropel layers that were cross-referenced with those described by Calvert and Fontugne (2001). Those used in these experiments included S4 (from 385 cm), S5 (455 cm), and S7 (582–590 cm).

Guaymas Basin Sediments

Sediments from the Guaymas Basin, a spreading center within the Gulf of California, were collected aboard the R/V *El Puma* in October 2014 (Buckley et al., 2015). Sediments were collected at 5 and 55 cm sediment depth at six locations (P1, P3, P5, P8, P10, and P13) that vary in geological and environmental context (SI Table 1). Sediment intervals from cores were subsampled into airtight plastic containers and stored at $4^{\circ}C$ until use in incubations.

Sediment Incubation Preparation

Incubations with Marmara Sea sediment were used for initial development of the extraction treatment protocol in three preliminary experiments—PreX1, PreX2, and PreX3—using sediments from 0–5, 570–585, and 520–530 cm depth intervals, respectively. Autoclaved artificial seawater was added to homogenized sediments to make a 2:1 seawater:sediment slurry. Twenty-one milliliter of slurry was dispensed into each of two 50 mL-volume serum vials; one vial was autoclaved as a killed control, and one vial was used as a live experimental vial. These incubations were set up under aerobic conditions, and due to limited availability of sediments only chondroitin was used as a substrate.

In Eastern Mediterranean and Guaymas Basin sediments, all sample preparation was carried out in an anaerobic chamber under N_2 atmosphere. Each sediment sample was homogenized in a sterile beaker with a sterile spatula. Artificial seawater (Sigma S9883), autoclaved and cooled under N_2 , was added in a 2:1 ratio to homogenized sediments and mixed thoroughly. Twenty-one milliliter of sediment slurry was portioned into each 50 mL-volume, sterile serum vial using a sterile serological pipette, and sealed with a stopper and crimp. Nine serum vials were prepared from each sediment section—three live incubations and one killed control for each of two substrates (chondroitin and laminarin), and a live blank control. The sealed vials were removed from the anaerobic chamber, and two vials were autoclaved for 30 min, then cooled to room temperature to serve as killed controls. Substrate addition and subsequent subsampling of the incubations was carried out by opening the serum vials under a stream of N_2 , using aseptic technique. Substrate was added in 175 μM monomer-equivalent concentrations; three of the live incubations and one killed control received fluorescently labeled chondroitin sulfate; three

live incubations and one killed control received fluorescently labeled laminarin, and one live incubation served as a blank and did not receive substrate. Time zero samples were collected immediately after substrate addition; vials were then resealed with stoppers, crimped and stored at $4^{\circ}C$ in the dark until further subsampling. Subsamples were taken at 3, 6, and 9 week timepoints.

Development of the Extraction Protocol

The three preliminary experiments—PreX1, PreX2, and PreX3—were used to develop and optimize the extraction treatment protocol. In each case, fluorescently-labeled chondroitin substrate was added to incubations at 175 μM monomer-equivalent concentrations (PreX1) or 350 μM monomer-equivalent concentrations (PreX2 and PreX3), which is the concentration typically used in previous slurry incubations (e.g., Arnosti, 2003, 2008).

In the first experiment (PreX1), three desorption conditions were tested: competitive desorption, desorption with solution at $pH = 10$, and desorption with solution at $pH = 11$. The incubations were set up as described in section Sediment Incubation Preparation, and the fluorescently-labeled chondroitin substrate was added. Subsamples were taken at t0 and 2 days. At each subsampling point, 0.5 mL of sediment slurry was removed from each vial and added to a treatment tube containing 2 mL of either 700 μM unlabeled chondroitin (competitive desorption), carbonate buffer at $pH = 10$ (pH10), carbonate buffer at $pH = 11$ (pH11), or a no-treatment control of 2 mL DI H_2O . The no-treatment tubes were immediately centrifuged, and the supernatant was filtered through a 0.2 μm pore-size filter and stored at $-20^{\circ}C$. The treatment tubes were incubated and periodically shaken for 2 h in a $30^{\circ}C$ waterbath before centrifuging, filtering, and storing. Based on the results (see Results), competitive desorption was selected for use in subsequent experiments.

In the second experiment, PreX2, multiple concentrations of unlabeled substrate were tested for use in the competitive desorption approach. Three sediment incubations were again set up in serum vials—a live incubation, a killed incubation, and a live blank incubation, and fluorescently-labeled chondroitin substrate was added. Subsamples were taken at t0, 2 days, and 6 days. At each timepoint, 0.5 mL of sediment slurry was added to each treatment tube containing 2 mL of a solution of 700 μM unlabeled chondroitin, 1,400 μM unlabeled chondroitin, or 2,800 μM unlabeled chondroitin. There was also a no-treatment DI H_2O control. No-treatment tubes were immediately processed, while treatment tubes were incubated and periodically shaken for 2 h in a $30^{\circ}C$ waterbath before processing. Based on the results, 2,800 μM concentrations of unlabeled chondroitin was selected for subsequent experiments.

The third experiment, PreX3, tested whether the addition of sodium dodecyl sulfate (SDS) provided additional improvement to the competitive desorption treatment method developed in PreX2 and PreX1. Three sediment incubations, a live, a kill, and a live blank, were used. Subsamples were taken at t0, 7, and 14 days. At each timepoint, 0.5 mL of sediment slurry was added to each treatment tube containing 2 mL of either 2,800 μM unlabeled

chondroitin and 0.2% SDS, 2,800 μ M unlabeled chondroitin only, or a no-treatment control of DI H₂O. No-treatment tubes were immediately processed, and treatment tubes were incubated for 2 h in a 30°C waterbath before processing. Competitive desorption with addition of SDS was selected as the final extraction treatment method, and was applied to the sediments from the Eastern Mediterranean and Guaymas Basin.

Activity Measurements with Competitive Desorption Treatment

At each timepoint, subsamples were taken from each incubation to measure the potential activity of extracellular enzymes that hydrolyze chondroitin or laminarin (Figure 1). For each subsample, two 15 mL centrifuge tubes were prepared for an extraction treatment and for a no-treatment control, for a total of 18 falcon tubes per time point. Treatment tubes contained 0.5 mL of 14 mM unlabeled chondroitin or laminarin (2,800 μ M in 2.5 mL), 0.5 mL 0.5% SDS (0.2% in 2.5 mL), and 1 mL DI H₂O. No-treatment tubes contained 2 mL of DI H₂O.

One Milliliter of sediment slurry was removed with a N₂-flushed syringe from each serum vial under a N₂ stream using aseptic technique, and 0.5 mL of slurry was added to each of the treatment and no-treatment tubes. No-treatment tubes were immediately centrifuged (2,000 rpm, 4 min), and the supernatant was filtered through a 0.2 μ m pore size cellulose acetate syringe filter (Stereitech CA0225) and stored in an epi tube at -20°C until analysis. Treatment tubes were allowed to process in a 30°C waterbath for 2 h, shaking manually every 10–15 min, to allow desorption to occur. The treatment tubes were then centrifuged and syringe filtered in the same manner as the no-treatment tubes, and stored at -20°C.

The proportion of fluorescently-labeled substrate that had been hydrolyzed into lower-molecular-weight products in each subsample was analyzed using gel permeation chromatography with fluorescence detection, after Arnosti (1996, 2003).

Fluorescent Substrate Preparation and Chromatogram Interpretation

The substrates laminarin and chondroitin were labeled with the fluorophore fluoresceinamine after the method of Arnosti (1996, 2003). In short, hydroxyl groups at multiple sites along the substrate are activated with cyanogen bromide, then coupled with the fluorophore fluoresceinamine, resulting in a high molecular weight substrate labeled with a fluorescent label, typically at multiple positions. The molecular weight distribution of a fluorescently-labeled substrate can be visualized using gel permeation chromatography with fluorescence detection. When a live incubation is amended with the substrate, hydrolytic activity shifts the molecular weight distribution of the fluorescent substrate from all high- to a mixture of high- and lower-molecular-weight hydrolysis products, and the hydrolysis rate can then be calculated from the change in molecular weight distribution (relative to standards of known molecular weight).

To visualize the molecular weight distribution of the substrate and any hydrolysis products, a sample is injected onto a 21 cm G50 Sephadex gel permeation chromatography column

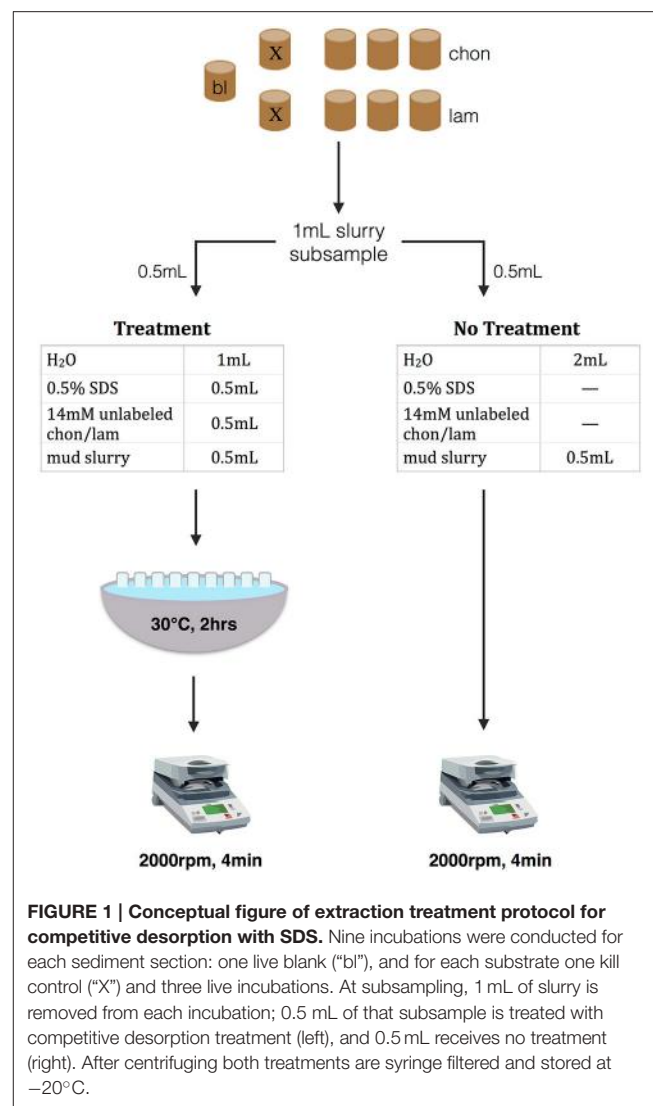


FIGURE 1 | Conceptual figure of extraction treatment protocol for competitive desorption with SDS. Nine incubations were conducted for each sediment section: one live blank ("bl"), and for each substrate one kill control ("X") and three live incubations. At subsampling, 1 mL of slurry is removed from each incubation; 0.5 mL of that subsample is treated with competitive desorption treatment (left), and 0.5 mL receives no treatment (right). After centrifuging both treatments are syringe filtered and stored at -20°C.

connected in series to a 19 cm G75 Sephadex column. These columns separate a sample by molecular weight such that the highest molecular weight compounds are excluded from the pores within a gel and the lower molecular weight compounds penetrate through the pores of the gel. The higher molecular weight compounds thus elute first from the columns, while the lower molecular weight compounds elute later. Standards of known molecular weight are used to determine elution times for different molecular weights. Elution time per sample in this study was 75 min, at a flow rate of 1 mL/min. Fluorescence of the column effluent was tracked at an emission wavelength of 530 nm (excitation at 490 nm) using a Hitachi fluorescence detector, and the molecular weight distribution was determined from the final chromatogram output of fluorescence signal vs. time. Hydrolysis rates were calculated from the change in molecular weight distribution from time zero to the time of sampling.

The added substrates, chondroitin and laminarin, are polysaccharides with different structures and characteristics: laminarin, a storage glucan in brown algae and diatoms, is a

branched polymer of β -linked glucose units, while chondroitin is a sulfated polymer of n -acetyl glucosamine and glucuronic acid. The enzymes required to hydrolyze laminarin and chondroitin sulfate have been identified in marine bacteria (Alderkamp et al., 2007; Wegner et al., 2013; Xing et al., 2015), and activities of enzymes hydrolyzing these polysaccharides have been measured in a wide range of environments (e.g., Arnosti, 2008; Arnosti et al., 2009).

Statistical Analyses

When comparing whether the treatment resulted in increased total fluorescence intensity relative to no treatment in raw fluorescence units (FU; the detector signal in millivolts), a paired, one-sided *t*-test was used to compare chromatographic fluorescence intensities of incubations subjected to no treatment and treatment conditions. When comparing a percent improvement relative to zero, the no-treatment value was subtracted from the treatment value for a particular incubation, so an unpaired, one-sided *t*-test was used to test whether the percent improvement was greater than zero.

Reproducibility

The raw data from this project is stored in the BCO-DMO database (Hoarfrost and Arnosti, 2016). The scripts used to process and analyze the data, and generate the figures in this publication, can be found at the corresponding github repository (Hoarfrost, 2016).

RESULTS

The extraction treatment presented here was developed to reduce the effects of adsorption on substrate recovery when measuring extracellular enzymatic activity in sediments using a fluorescently-labeled high molecular weight substrate, and to broaden the range of sediments in which enzyme activities can be measured using these substrates. Competitive desorption with unlabeled substrate and SDS proved to be effective in improving key chromatogram characteristics, by decreasing peak width and increasing fluorescence intensities (Figure 2, SI Figure 1). Some of the improvements in chromatogram characteristics can be summarized by the difference in area under the chromatogram, referred to here as the total integrated fluorescence intensity, between treatment and no treatment controls, which was used as an overall measure of chromatogram quality (Figures 2, 3A,B, 4, 5).

Competitive Desorption Treatment Effects on Chromatogram Quality

At all timepoints, desorption treatment improved several chromatogram characteristics (Figure 2, SI Figure 1). Overall, total integrated fluorescence intensities were higher in treatment relative to no treatment controls (Figure 3A), as can be seen by the difference in peak heights (Figure 2; note difference in scales on y axes). The desorption treatment was especially effective at desorbing the high molecular weight portion of the added substrate (Figure 3B), resulting in higher proportions of high- to low- molecular weight substrate, an effect that is particularly

evident for laminarin in core P13 from Guaymas Basin (Figures 2B,C). Finally, the chromatogram peaks are sharper and peak width is narrower, as exemplified by the incubations with chondroitin in Mediterranean 385 cm sediments (Figures 2A,C). These characteristics result in higher quality chromatograms and lead to more easily interpretable rate calculations. In some cases, samples with no treatment applied resulted in very poor recovery of substrate and such low chromatogram intensities that they would be unusable (e.g., Figure 2B, panel 1-t0). In these cases, competitive desorption treatment enables measurement of enzymatic activities in sediments where such measurements otherwise could not be made.

Although the extraction protocol includes a 2-h incubation of a subsample treatment in a 30°C waterbath, this step does not appear to stimulate an increase in activity in the treatment subsamples that would otherwise bias our results. Treatment samples, in fact, yielded lower calculated hydrolysis rates (due to improvements in substrate recovery) than no-treatment controls, which are processed immediately without incubation in the waterbath (Figure 3C). The general activity patterns in the chromatograms, which may be summarized by how quickly the fluorescence in the low molecular weight portion of the chromatogram increased over time, were similar between no treatment and treatment controls despite differences in chromatogram quality and intensity (Figure 2). The relative rate of increase in fluorescence over time of low molecular weight substrate products within a particular incubation remained the same in the no treatment and treatment conditions (result of paired *t*-test, $P = 0.98$), even in highly active sediments.

Competitive Desorption Effects on Substrate Recovery and Calculated Hydrolysis Rates

Desorption treatment increased total integrated fluorescence intensity of the resultant chromatogram by a median of 66% ($P < 0.001$) relative to a no-treatment control (Figure 3A), with a median increase in fluorescence of 8.3×10^6 mV ($P < 0.001$). The improvement in fluorescence intensity is observed in both the high- and low-molecular weight portion of the chromatogram, but is particularly effective in improving recovery of the high molecular weight portion (Figure 3B). Recovery of high molecular weight substrate products is improved by a median of 200% ($P = 0.01$), while recovery of low molecular weight substrate products is improved by a median of 39% ($P < 0.001$).

The improved recovery of the substrate from the subsample results in a higher relative proportion of high- to low-molecular weight substrate than is observed in the no-treatment controls. The desorption treatment therefore results in a lower calculated hydrolysis rate in treatment samples (Figure 3C), with a median decrease in maximum hydrolysis rate of 5 nM/h in treatment subsamples relative to no-treatment controls ($P < 0.01$).

The competitive desorption treatment improves substrate recovery in all sediments and substrates tested (Figure 4), although there is some variation in the percent improvement

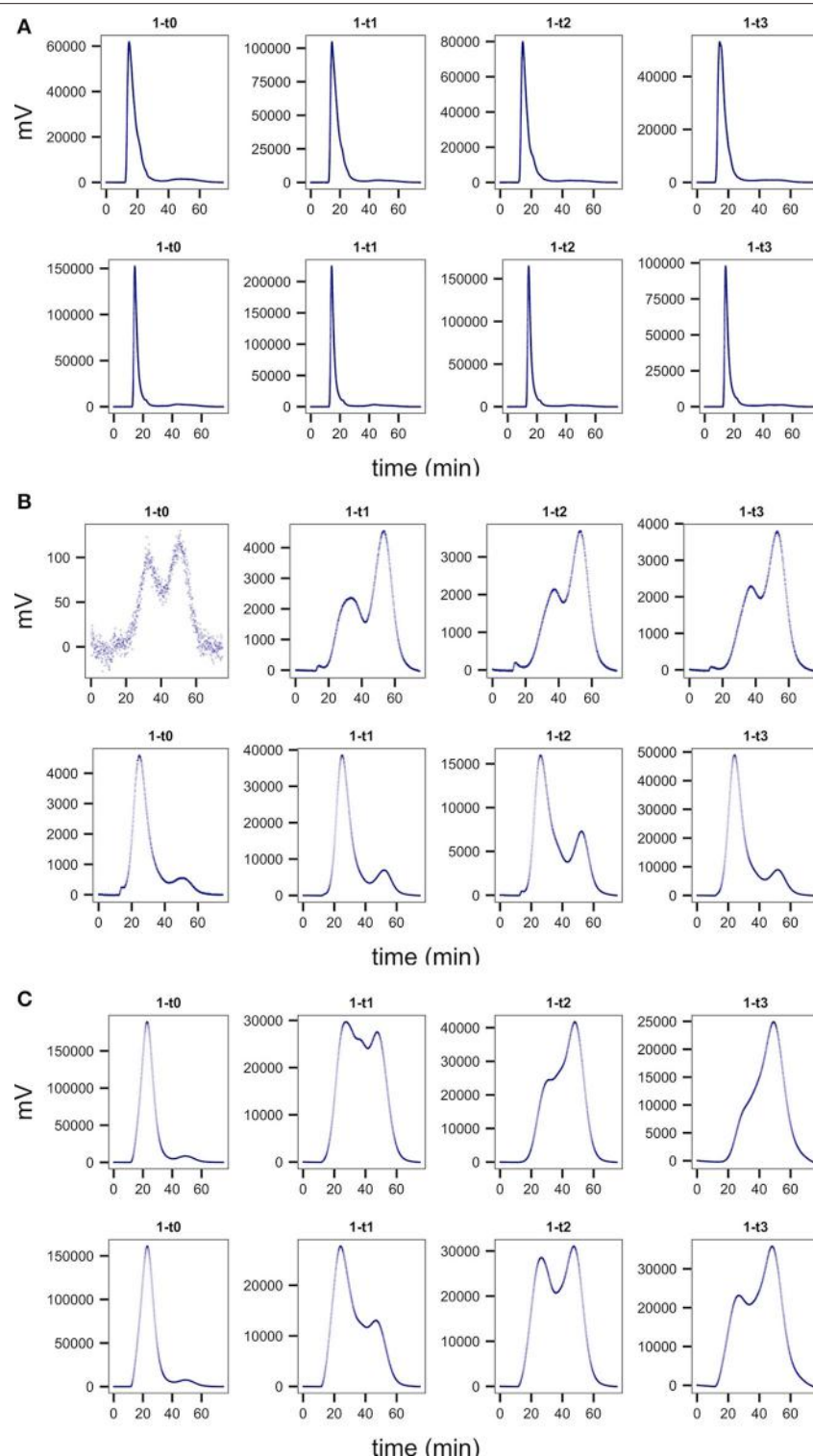


FIGURE 2 | Representative chromatograms comparing treatment (bottom row) to no treatment controls (top row) in one of the live replicate incubations for (A) Mediterranean sapropel S4, 385 cm, chondroitin incubations (B) Guaymas core P13, 55 cm, laminarin, and (C) Guaymas core P1, 55 cm, laminarin. Note differences in scales on y axes. Improved chromatogram quality is seen in treatment incubations, with narrower peak widths, higher total integrated fluorescence, and a higher proportion of high- to low-molecular-weight substrate.

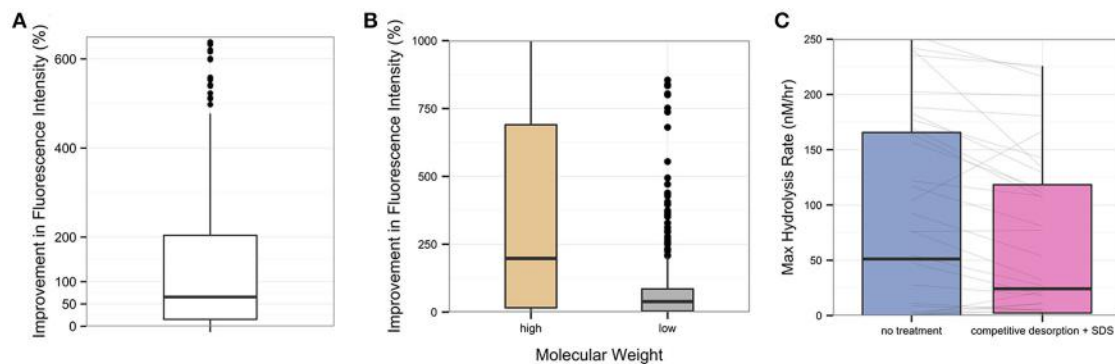


FIGURE 3 | Overall improvement in fluorescence intensity by competitive desorption and SDS treatment, for all experiments in Guaymas Basin and Eastern Mediterranean sediment. (A) The percent improvement in total integrated fluorescence intensity in desorption-treated samples relative to their no-treatment controls. **(B)** Percent improvement in total integrated fluorescence intensity using desorption treatment for the high- and low- molecular weight portions of each subsample. High molecular weight is operationally identified as the first third of a chromatogram, while low molecular weight is the last third. **(C)** Change in calculated maximum hydrolysis rate (nM/hr) in treatment versus no-treatment controls. Gray lines connect treatment and no-treatment subsamples from a single incubation.

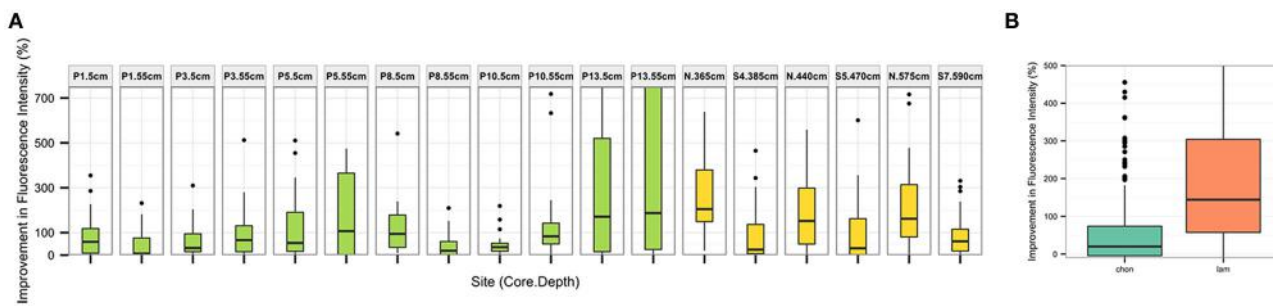


FIGURE 4 | Percent improvement in total integrated fluorescence intensity using desorption treatment method (relative to no-treatment control) (A) for each sediment section tested. Sediments from Guaymas Basin in green, Eastern Mediterranean in yellow, and **(B)** for each substrate tested.

dependent upon sampling site (Figure 4A) and substrate (Figure 4B).

Comparison of the Competitive Desorption Treatment with Low pH-Extraction

Several extraction treatment methods were tested in three preliminary experiments in order to develop and optimize the desorption protocol. Competitive desorption, using 700 μ M unlabeled substrate, was compared to alternative extraction treatments using solutions with pH of either 10 or 11, as well as a no treatment control (Figure 5A). Competitive desorption was found to be most effective at recovering chondroitin, increasing integrated fluorescence intensity by a median of 66% ($P < 0.01$), while both pH extraction treatments actually decreased substrate recovery. Based on these results, competitive desorption was chosen as the basis of the extraction treatment method.

The concentration of unlabeled substrate to use during competitive desorption treatment was optimized in a second experiment (Figure 5B), comparing 700, 1,400, and 2,800 μ M unlabeled substrate concentrations to a no-treatment control. Two thousand eight hundred micrometer concentrations improved integrated fluorescence intensity by a median of 32%

($P < 0.01$), a large improvement over 700 μ M at 20% ($P = 0.06$) and a slight improvement over 1,400 μ M concentrations at 28% ($P = 0.07$). Based on these results, competitive desorption with 2,800 μ M concentrations of unlabeled substrate was chosen as the basis of the final extraction treatment protocol.

The addition of SDS to competitive desorption was compared to a no-treatment control in a third experiment (Figure 5C) to determine whether the inclusion of SDS with competitive desorption provides additional substrate recovery. While competitive desorption both with and without SDS improved substrate recovery, the addition of SDS increased integrated fluorescence intensity by a median of 32% ($P < 0.001$), whereas competitive desorption without SDS yielded a 17% increase ($P < 0.001$). Therefore, competitive desorption with SDS was chosen as the final extraction treatment protocol.

Applicability of Competitive Desorption Treatment Using Multiple Substrates in Sediments from Diverse Environments

We measured extracellular enzymatic hydrolysis in sediments from varied settings, and were able to detect hydrolysis at activities ranging from near-zero in the Eastern Mediterranean

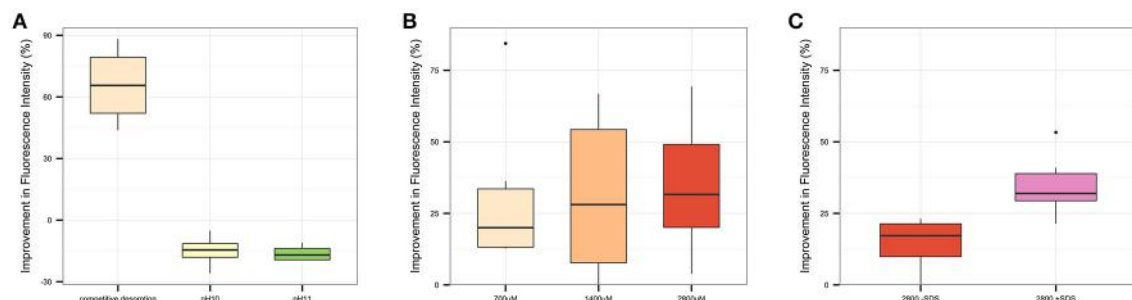


FIGURE 5 | Percent improvement in total integrated fluorescence intensity for alternative extraction treatment candidates relative to a no-treatment control for (A) PreX1, in which competitive desorption, pH = 10, and pH = 11 extraction conditions are tested, (B) PreX2, in which three candidate concentrations of unlabeled substrate (700, 1400, and 2800 μ M) in the extraction treatment are compared; and (C) PreX3, in which the presence or absence of SDS in competitive desorption are compared.

to more than 200 nM/h in parts of Guaymas Basin (**Figure 6**). The desorption treatment was more effective at increasing total integrated fluorescence intensities than a no-treatment control at every site (**Figure 4A**), with median percent improvement in total integrated fluorescence ranging from 7% (Guaymas core P1 depth 55 cm, $P = 0.02$) to 200% (Mediterranean non-sapropel, depth 365 cm, $P < 0.001$).

The greatest improvements in total integrated fluorescence intensities were observed in the sediments where the no treatment controls were uninterpretable due to very low substrate recovery. One such example is Guaymas core P13 at 55 cm (**Figure 2B**), with a median improvement in integrated fluorescence intensities of 190%. The high quality chromatograms observed after desorption treatment in these cases demonstrates that this protocol can expand the range of sediments in which enzymatic activities can be measured.

Even in cases where the median improvement in fluorescence was relatively minor, for example Guaymas core P1 at depth 55 cm, the treatment often improved the chromatogram quality in other tangible ways (**Figure 2C**). Guaymas P1-55 cm exhibited very high hydrolytic activity, but the treatment recovered a large portion of high molecular weight substrate that was not recovered in the no treatment control, such that the final calculated hydrolysis rate was 110.6 nM/hr in the treatment incubation relative to the much higher 169.8 nM/hr in the no-treatment control.

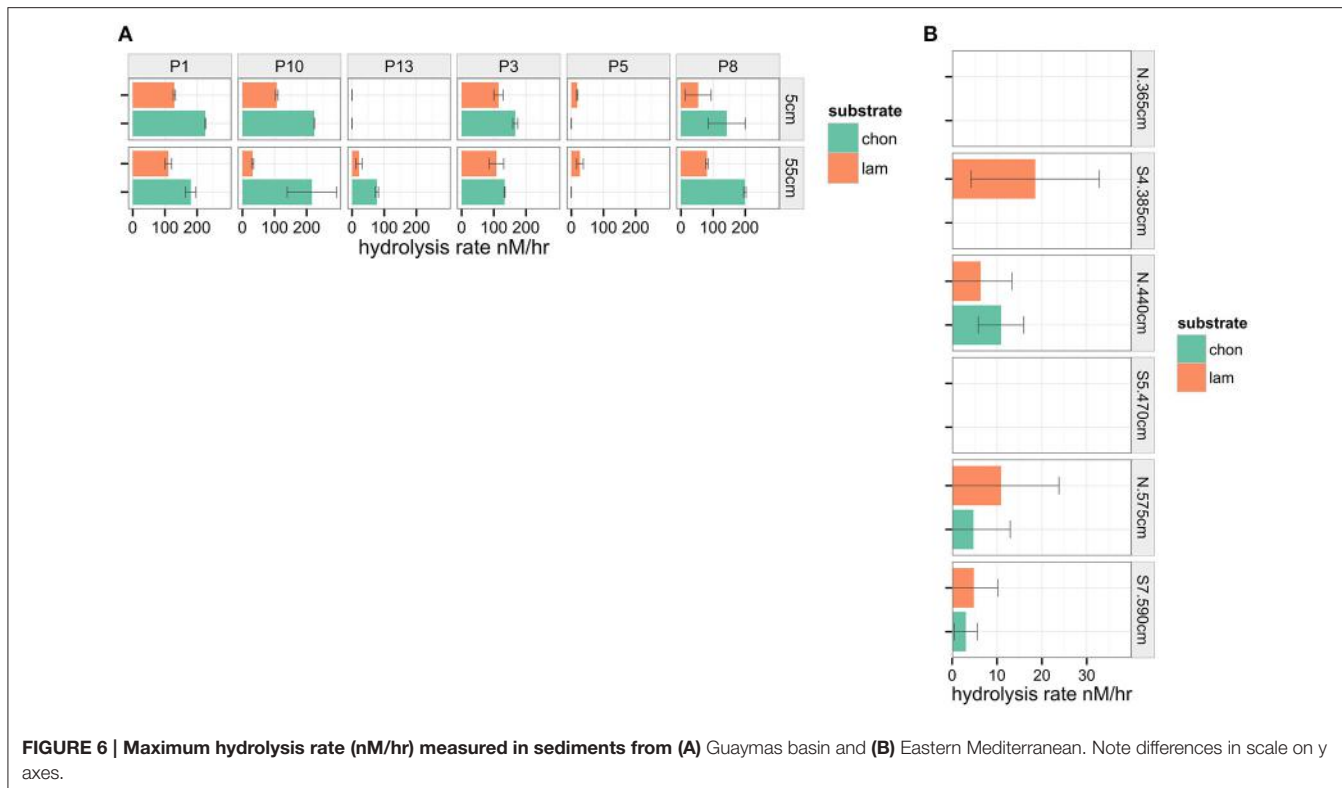
The desorption treatment was effective in improving total integrated fluorescence intensity for both chondroitin and laminarin (**Figure 4B**, e.g., **Figure 2**). The treatment had a greater effect on laminarin recovery than chondroitin recovery: laminarin integrated fluorescence intensity was improved by a median of 140% ($P < 0.001$), while chondroitin fluorescence was improved by a median of 20% ($P = 0.01$).

DISCUSSION

Microbial communities in sediments play an important role in driving key biogeochemical cycles. Organic carbon cycling is often the dominant metabolic function of microbial communities in subsurface environments (e.g., Biddle et al., 2006; Fry et al.,

2008; Lloyd et al., 2013). Reliable measurements of enzymatic activities in sediments are fundamental to our understanding of microbial carbon-cycling potential in sedimentary environments. However, our ability to measure heterotrophic enzymatic activities directly in sediments, particularly subsurface sediments, has been hampered by the tendency for amended substrates to sorb to the sediment matrix. The extraction treatment presented here facilitates the measurement of enzyme activities in sediments by improving recovery of fluorescently labeled substrates in sediments from a range of geochemical settings. This treatment further enables the measurement of enzyme activities in sediments that might not otherwise yield usable data due to effects of sorption. This approach can be used to directly link microbial potential activities to genetic potential or biogeochemical processes, to better understand the role of microbial communities in subsurface carbon cycling. This approach may also be useful in remediation applications, where, for example, one would like to quantify the bioavailability of sediment-sorbed organic contaminants (e.g., Alexander, 2000; Megharaj et al., 2011), or in agricultural applications where the rate of recycling of nitrogen- or phosphorous-containing organic substrates by soil microbial communities is of interest for applications in optimizing food production (Berg, 2009) or minimizing fertilizer use (Adesemoye and Kloepper, 2009).

Treatment of sediment-sorbed fluorescently labeled substrates using competitive desorption and SDS proved effective in all sediments and substrates tested (**Figure 4**) improving chromatogram fluorescence intensities (**Figure 3A**) and leading to hydrolysis rate measurements reflecting improved recovery on high and low molecular weight substrate products (**Figure 3B**). Both highly active and near-zero activities were detected using this procedure (**Figure 6**) and desorption treatment improved chromatogram characteristics in both types of sediments (e.g., **Figure 2A** vs. c). The geochemical and environmental contexts of the source sediments used to test the extraction treatment were varied, encompassing sapropelic sediments from the Mediterranean, with high concentrations of highly recalcitrant organic carbon; non-sapropelic, oligotrophic Mediterranean sediments; and sediments from Guaymas Basin ranging from highly compacted and sulfidic, to hemipelagic and diatom-rich,



to coarse and sandy terrestrially-influenced sediments. The two substrates tested were distinct polysaccharides with distinct compositions and conformations, but both yielded improved recoveries when treated with the competitive desorption treatment (Figure 4B). The rates obtained by the competitive desorption treatment were not significantly affected by the incubation at 30°C in extraction buffer for 2 h, while the improvements in chromatogram quality and hydrolysis rate calculations were substantial.

The hydrolysis rates measured in subsurface sediments highlighted the contrasting potential activities of sediment microbial communities in the Gulf of Mexico and Mediterranean Sea. Most locations in Guaymas Basin were much more active (ca. 100–200 nM/hr) than in the Eastern Mediterranean (ca. 0–20 nM/h, Figure 6). Both of these subsurface sites exhibited lower activities than have been observed in surficial sediments (ca. upper 15 cm of sediments) in previous studies, including Arctic sites (Arnoldi, 2008) and sediments from the Gulf of Mexico (Arnoldi et al., 2009). While the effect of desorption treatment on producing lower hydrolysis rates may have contributed to the difference in hydrolysis rates observed in this study, the 2–4 order of magnitude difference in microbial community abundance between shallow surface sediments and deeper subsurface sediments (Kallmeyer et al., 2012) likely underlies the considerable difference in measured rates. The activities measured here are potential enzymatic activities, and thus reflect the relative capacities of the nascent microbial communities to access the added substrate. The difference in rates observed between Guaymas and Mediterranean sediments suggests that

these lower rates may also be indicative of differences in microbial communities between surficial and subsurface depths.

The efficacy of the extraction treatment in all of these settings suggests that the competitive desorption approach may be useful as a general (and therefore standardizable) approach to substrate recovery in sediment enzyme activity measurements. The competitive desorption treatment was especially effective at recovering the high molecular weight fraction of substrate products (Figure 3B). Recovery of high molecular weight substrate products is particularly useful in natural settings, because high molecular weight compounds are more likely to sorb to sediment than low molecular weight compounds (Podoll et al., 1987). The rates calculated from treatment samples may better reflect the potential hydrolysis rate occurring in the incubation, whereas the higher rate calculated for the untreated sample may be exaggerated due to disproportional sorption of the high molecular weight fraction. The demonstrated applicability of this treatment in sediments from broad environmental settings may be due to the mechanism of competitive desorption, which directly competes for sorption sites with a substrate of interest, regardless of the complex combination of factors that may affect adsorption rates (Pignatello and Xing, 1996) that may vary widely depending on the sediment and substrate characteristics.

Limitations of this extraction treatment will therefore most likely occur when sorption is more irreversible, i.e., where the decrease in entropy due to complexation of a substrate with sediment is prohibitively large. In this case, once sorbed a substrate is less likely to exchange with the aqueous environment, leaving less opportunity for an unlabeled “competitive desorber”

to replace it and release the labeled substrate. Although the extraction treatment was effective in all settings, the overall percent improvement in total integrated fluorescence intensities was variable across sites (**Figure 4A**). For example, in the Eastern Mediterranean core substrate recovery was much better in the non-sapropel (“N” segments) than the sapropel (“S”) segments, perhaps due to the high concentrations of organic carbon in the sapropel segments. Future experiments may test a wider range of substrates, and additional sediments and soils with geological histories and contexts not investigated in this study, to better estimate the true variance of this extraction treatment approach and its overall applicability.

This method has been developed to improve measurements made with high molecular weight fluorescent substrates prepared after the method of Arnosti (1996, 2003), and is focused on improving recovery of hydrolyzed fragments of high molecular weight substrates. Other common methods of measuring enzymatic activities include use of low molecular weight substrate proxies, typically consisting of monomers linked to MUF or MCA fluorophores, after the method of Hoppe (1983). Measurement of enzyme activities with substrate proxies rely on the release of a fluorophore that becomes fluorescent upon hydrolysis from the attached monomer. The method is thus affected by sorption of the freed fluorophore to the sediment matrix. In this case, an adaptation of the competitive desorption treatment would require use of a non-fluorescent analog of the MCA or MUF fluorophore.

Measuring the rate at which microbial communities hydrolyze organic compounds in subsurface sediments is essential to our understanding of subsurface ecosystems and their influence on biogeochemistry, environmental remediation, and agricultural productivity. The method presented here provides a promising means to more reliably and accurately measure heterotrophic

extracellular enzymatic activities in sediments not otherwise amenable to these measurements.

AUTHOR CONTRIBUTIONS

AH and CA designed the experiments. AH and RS set up and subsampled sediment incubations, and processed subsamples. AH analysed data. AH, CA, and RS wrote the manuscript.

FUNDING

This work was supported by a CDEBI Graduate Fellowship to AH and a CDEBI research grant to CA, NSF award number OCE-0939564. Additional grants from NSF OCE-1449604 (to Andreas Teske) for sample collection in the Guaymas Basin, and NSF OCE-1332881 (to CA) provided partial support of this work. The collection (by Andreas Teske) of sediments from the Eastern Mediterranean and Marmara Sea was made possible by funding from the DARCLIFE project to Andreas Teske (UNC) and Kai Hinrichs (MARUM, Bremen).

ACKNOWLEDGMENTS

The authors would like to thank Andreas Teske and Luke McKay who collected and generously provided the sediments used in this study. This publication is CDEBI Contribution 355.

SUPPLEMENTARY MATERIAL

The Supplementary Material for this article can be found online at: <http://journal.frontiersin.org/article/10.3389/feart.2017.00013/full#supplementary-material>

REFERENCES

- Adesemoye, A., and Kloepper, J. (2009). Plant-microbe interactions in enhanced fertilizer use efficiency. *Appl. Microbiol. Biotechnol.* 85, 1–12. doi: 10.1007/s00253-009-2196-0
- Alderkamp, A.-C., van Rijssel, M., and Bolhuis, H. (2007). Characterization of marine bacteria and the activity of their enzyme systems involved in degradation of the algal storage glucan laminarin. *FEMS Microbiol. Ecol.* 59, 108–117. doi: 10.1111/j.1574-6941.2006.00219.x
- Alexander, M. (2000). Aging, bioavailability, and overestimation of risk from environmental pollutants. *Environ. Sci. Technol.* 34, 4259–4265. doi: 10.1021/es001069
- Arnosti, C. (1996). A new method for measuring polysaccharide hydrolysis rates in marine environments. *Org. Geochem.* 25, 105–115. doi: 10.1016/S0146-6380(96)00112-X
- Arnosti, C. (2003). Fluorescent derivatization of polysaccharides and carbohydrate-containing biopolymers for measurement of enzyme activities in complex media. *J. Chromatogr. B Anal. Technol. Biomed. Life Sci.* 793, 181–191. doi: 10.1016/S1570-0232(03)00375-1
- Arnosti, C. (2008). Functional differences between Arctic seawater and sedimentary microbial communities: contrasts in microbial hydrolysis of complex substrates. *FEMS Microbiol. Ecol.* 66, 343–351. doi: 10.1111/j.1574-6941.2008.00587.x
- Arnosti, C., Zier vogel, K., Ocampo, L., and Ghobrial, S. (2009). Enzyme activities in the water column and in shallow permeable sediments from the northeastern Gulf of Mexico. *Estuar. Coast. Shelf Sci.* 84, 202–208. doi: 10.1016/j.ecss.2009.06.018
- Berg, G. (2009). Plant-microbe interactions promoting plant growth and health: perspectives for controlled use of microorganisms in agriculture. *Appl. Microbiol. Biotechnol.* 84, 11–18. doi: 10.1007/s00253-009-2092-7
- Biddle, J. F., Lipp, J. S., Lever, M. A., Lloyd, K. G., Sørensen, K. B., Anderson, R., et al. (2006). Heterotrophic Archaea dominate sedimentary subsurface ecosystems off Peru. *Proc. Natl. Acad. Sci. U.S.A.* 103, 3846–3851. doi: 10.1073/pnas.0600035103
- Buckley, A., McKay, L. J., Turner, T., Chanton, J., Hensen, C., Benninger, L., et al. (2015). “Biogeochemical and Microbial Survey of Gravity Cores from the Guaymas Basin and Sonora Margin,” in *Talk and Abstract. Fall Meeting American Geophysical Union*, (San Francisco, CA), 14–18.
- Calvert, S., and Fontugne, M. (2001). On the late Pleistocene-Holocene sapropel record of climatic and oceanographic variability in the eastern Mediterranean. *Paleoceanography* 16, 78–94. doi: 10.1029/1999PA000488
- Chenu, C., and Stotzky, G. (2002). “Interactions between microorganisms and soil particles: an overview,” in *Interactions between Soil Particles Microorganisms: Impact Terrestrial Ecosystem*, eds P. M. Huang, J.-M. Bollag, and N. Senesi (John Wiley & Sons, Ltd.), 3–40.
- Coolen, M. J. L., Cypionka, H., Sass, A. M., Sass, H., and Overmann, J. (2002). Ongoing modification of Mediterranean Pleistocene sapropels mediated by prokaryotes. *Science* 296, 2407–2410. doi: 10.1126/science.1071893
- Coolen, M. J. L., and Overmann, J. (2000). Functional Exoenzymes as indicators of metabolically active bacteria in 124,000-year-old sapropel layers of

- the eastern Mediterranean Sea. *Appl. Environ. Microbiol.* 66, 2589–2598. doi: 10.1128/AEM.66.6.2589-2598.2000
- Fry, J. C., Parkes, R. J., Cragg, B. A., Weightman, A. J., and Webster, G. (2008). Prokaryotic biodiversity and activity in the deep subseafloor biosphere. *FEMS Microbiol. Ecol.* 66, 181–196. doi: 10.1111/j.1574-6941.2008.00566.x
- Gu, B. H., Schmitt, J., Chen, Z. H., Liang, L. Y., and McCarthy, J. F. (1994). Adsorption and desorption of natural organic-matter on iron-oxide - mechanisms and models. *Environ. Sci. Technol.* 28, 38–46. doi: 10.1021/es00050a007
- Gu, B., Mehlhorn, T. L., Liang, L., and McCarthy, J. F. (1996). Competitive adsorption, displacement, and transport of organic matter on iron oxide: II. Displacement and transport. *Geochim. Cosmochim. Acta* 60, 2977–2992. doi: 10.1016/0016-7037(96)00157-3
- Hmelo, L. R., Mincer, T., and Van Mooy, B. A. S. (2011). Possible influence of bacterial quorum sensing on the hydrolysis of sinking particulate organic carbon in marine environments. *Environ. Microbiol. Rep.* 3, 682–688. doi: 10.1111/j.1758-2229.2011.00281.x
- Hoarfrost, A. (2016). *SedS. Github Repository*. doi: 10.5281/zenodo.233018. Available online at: <https://github.com/ahoarfrost/SedS>
- Hoarfrost, A., and Arnosti, C. (2016). Investigating microbial activities driving organic matter transformations in the deep subsurface. *Biol. Chem. Oceanogr. Data Manag. Off.* Available online at: <http://www.bco-dmo.org/project/662055>
- Hoppe, H. (1983). Significance of exoenzymatic activities in the ecology of brackish water: measurements by means of methylumbelliferyl-substrates. *Mar. Ecol. Prog. Ser.* 11, 299–308. doi: 10.3354/meps011299
- Kaiser, K., and Guggenberger, G. (2000). The role of DOM sorption to mineral surfaces in the preservation of organic matter in soils. *Org. Geochem.* 31, 711–725. doi: 10.1016/S0146-6380(00)00046-2
- Kaiser, K., and Zech, W. (1999). Release of natural organic matter sorbed to oxides and a subsoil. *Soil Sci. Soc. Am. J.* 63:1157. doi: 10.2136/sssaj1999.6351157x
- Kallmeyer, J., Pockalny, R., Adhikari, R. R., Smith, D. C., and D'Hondt, S. (2012). Global distribution of microbial abundance and biomass in subseafloor sediment. *Proc. Natl. Acad. Sci. U.S.A.* 109, 16213–16216. doi: 10.1073/pnas.1203849109
- Keil, R., Montluçon, D., Prahl, F., and Hedges, J. (1994). Sorptive preservation of labile organic matter in marine sediments. *Nature* 370, 549–552. doi: 10.1038/370549a0
- Lloyd, K. G., Schreiber, L., Petersen, D. G., Kjeldsen, K. U., Lever, M. A., Steen, A. D., et al. (2013). Predominant archaea in marine sediments degrade detrital proteins. *Nature* 496, 215–218. doi: 10.1038/nature12033
- Lutzow, M. V., Kogel-Knabner, I., Ekschmitt, K., Matzner, E., Guggenberger, G., Marschner, B., et al. (2006). Stabilization of organic matter in temperate soils: mechanisms and their relevance under different soil conditions - A review. *Eur. J. Soil Sci.* 57, 426–445. doi: 10.1111/j.1365-2389.2006.00809.x
- Megharaj, M., Ramakrishnan, B., Venkateswarlu, K., Sethunathan, N., and Naidu, R. (2011). Bioremediation approaches for organic pollutants: a critical perspective. *Environ. Int.* 37, 1362–1375. doi: 10.1016/j.envint.2011.06.003
- Pignatello, J. J., and Xing, B. (1996). Mechanisms of slow sorption of organic chemicals to natural particles. *Environ. Sci. Technol.* 30, 1–11. doi: 10.1021/es940683g
- Podoll, R. T., Irwin, K. C., and Brendlinger, S. (1987). Sorption of water-soluble oligomers on sediments. *Environ. Sci. Technol.* 21, 562–568. doi: 10.1021/es00160a006
- Theng, B. K. G. (1979). Clay-Polymer interactions: summary and perspectives. *Clays Clay Miner.* 30, 1–10. doi: 10.1346/CCMN.1982.0300101
- Wegner, C.-E., Richter-Heitmann, T., Klindworth, A., Klockow, C., Richter, M., Achstetter, T., et al. (2013). Expression of sulfatases in *Rhodopirellula baltica* and the diversity of sulfatases in the genus *Rhodopirellula*. *Mar. Genomics* 9, 51–61. doi: 10.1016/j.margen.2012.12.001
- Xing, P., Hahnke, R. L., Unfried, F., Markert, S., Huang, S., Barbeyron, T., et al. (2015). Niches of two polysaccharide-degrading *Polaribacter* isolates from the North Sea during a spring diatom bloom. *ISME J.* 9, 1410–1422. doi: 10.1038/ismej.2014.225

Conflict of Interest Statement: The authors declare that the research was conducted in the absence of any commercial or financial relationships that could be construed as a potential conflict of interest.

Copyright © 2017 Hoarfrost, Snider and Arnosti. This is an open-access article distributed under the terms of the Creative Commons Attribution License (CC BY). The use, distribution or reproduction in other forums is permitted, provided the original author(s) or licensor are credited and that the original publication in this journal is cited, in accordance with accepted academic practice. No use, distribution or reproduction is permitted which does not comply with these terms.



Microbial Sulfide Filter along a Benthic Redox Gradient in the Eastern Gotland Basin, Baltic Sea

Mustafa Yücel^{1,2*}, Stefan Sommer¹, Andrew W. Dale¹ and Olaf Pfannkuche¹

¹ GEOMAR Helmholtz Centre for Ocean Research Kiel, Kiel, Germany, ² Middle East Technical University, Institute of Marine Sciences, Erdemli, Turkey

OPEN ACCESS

Edited by:

Cody Sheik,
University of Minnesota Duluth, USA

Reviewed by:

Judith M. Klatt,
University of Michigan, Germany

Greg Druschel,
Indiana University – Purdue University
Indianapolis (IUPUI), USA

Tom Jilbert,
University of Helsinki, Finland

*Correspondence:

Mustafa Yücel
mustyucel@gmail.com;
muyucel@metu.edu.tr

Specialty section:

This article was submitted to
Microbiological Chemistry and
Geomicrobiology,
a section of the journal
Frontiers in Microbiology

Received: 15 September 2016

Accepted: 24 January 2017

Published: 09 February 2017

Citation:

Yücel M, Sommer S, Dale AW and
Pfannkuche O (2017) Microbial Sulfide
Filter along a Benthic Redox Gradient
in the Eastern Gotland Basin, Baltic
Sea. *Front. Microbiol.* 8:169.
doi: 10.3389/fmicb.2017.00169

The sediment-water interface is an important site for material exchange in marine systems and harbor unique microbial habitats. The flux of nutrients, metals, and greenhouse gases at this interface may be severely dampened by the activity of microorganisms and abiotic redox processes, leading to the “benthic filter” concept. In this study, we investigate the spatial variability, mechanisms and quantitative importance of a microbially-dominated benthic filter for dissolved sulfide in the Eastern Gotland Basin (Baltic Sea) that is located along a dynamic redox gradient between 65 and 173 m water depth. In August-September 2013, high resolution (0.25 mm minimum) vertical microprofiles of redox-sensitive species were measured in surface sediments with solid-state gold-amalgam voltammetric microelectrodes. The highest sulfide consumption ($2.73\text{--}3.38\text{ mmol m}^{-2}\text{ day}^{-1}$) occurred within the top 5 mm in sediments beneath a pelagic hypoxic transition zone (HTZ, 80–120 m water depth) covered by conspicuous white bacterial mats of genus *Beggiatoa*. A distinct voltammetric signal for polysulfides, a transient sulfur oxidation intermediate, was consistently observed within the mats. In sediments under anoxic waters ($>140\text{ m}$ depth), signals for Fe(II) and aqueous FeS appeared below a subsurface maximum in dissolved sulfide, indicating a Fe(II) flux originating from older sediments presumably deposited during the freshwater Ancylus Lake that preceded the modern Baltic Sea. Our results point to a dynamic benthic sulfur cycling in Gotland Basin where benthic sulfide accumulation is moderated by microbial sulfide oxidation at the sediment surface and FeS precipitation in deeper sediment layers. Upscaling our fluxes to the Baltic Proper; we find that up to 70% of the sulfide flux (2281 kton yr^{-1}) toward the sediment-seawater interface in the entire basin can be consumed at the microbial mats under the HTZ (80–120 m water depth) while only about 30% the sulfide flux effuses to the bottom waters ($>120\text{ m}$ depth). This newly described benthic filter for the Gotland Basin must play a major role in limiting the accumulation of sulfide in and around the deep basins of the Baltic Sea.

Keywords: voltammetry, redox, sediments, sulfur, baltic sea, gotland basin, beggiatoa, sulfur oxidizers

INTRODUCTION

Hydrogen sulfide accumulation in marine sediments results from sulfate reduction, which is a globally important organic carbon oxidation pathway (Jørgensen and Kasten, 2006). Only a small fraction of the sulfide produced escapes to water column due to the abundantly available O₂ in the bottom waters and surface oxidized sediment layer. The flux of sulfide to bottom waters becomes

more likely under low oxygen (hypoxic) to oxygen-free (anoxic) bottom waters, the extent of which have been increasing due to eutrophication in coastal areas (Diaz and Rosenberg, 2008). Even under low-O₂ conditions, the upward fluxes of sulfide, potentially toxic to pelagic organisms, may still be dampened due to microbial sulfide oxidation and abiotic processes such as metal oxide reduction (Poulton et al., 2004). These biotic and abiotic processes can occur over such small scales (mm) that the uppermost section of the sediments may be viewed as a benthic filter, with significant consequences for the overlying water column ecosystem.

Seafloor microbial mats of sulfide-oxidizing bacteria are important in the modulation of benthic fluxes (Revsbech and Jørgensen, 1983). In order to quantify the processes occurring within these mats, high-resolution (sub mm) gradients need to be detected as sulfide is cycled very close to the sediment-water interface over spatial scales typically smaller than traditional sampling resolutions involving porewater extraction (0.5–1 cm). One approach to overcome this shortcoming is to obtain higher resolution vertical profiles using electrochemical microsensors (Taillefert et al., 2000; Kühl and Revsbech, 2001). Such profiles, mostly obtained by amperometric sulfide sensors (Kühl and Revsbech, 2001) revealed that mm-scale steep sulfide gradients close the sediment-water interface result in high sulfide fluxes (typically larger than 1 mmol m⁻² day⁻¹). These fluxes, when appropriate electron acceptors are available, can support mats of sulfide-oxidizing bacteria in shallow water marine sediments (Preisler et al., 2007), anoxic basins (Jessen et al., 2016), sediments beneath upwelling areas (Ferdelman et al., 1997), cold seeps (de Beer et al., 2006), and hydrothermal vents (Wenzhöfer et al., 2000). However, a stronger case for sulfide oxidation pathways and products can only be established if various sulfide oxidation intermediates are also documented at the same time, such as FeS, polysulfides (S_x²⁻) and thiosulfate (S₂O₃²⁻). Among electrochemical microsensors, voltammetric microsensors used in this study are particularly tailored toward sulfur oxidation studies as they are simultaneously sensitive to hydrogen sulfide, polysulfides and FeS.

Accurate quantification of benthic sulfide fluxes is particularly important for anoxic marine systems, in which euxinic conditions persist in the water column either permanently or episodically. In the modern ocean, such areas include landlocked environments such as the Black Sea and Cariaco Basin as well as intense ocean margin oxygen minimum zones (Lavik et al., 2009; Schunck et al., 2013; Sommer et al., 2016). The deeper part of the Eastern Gotland Basin (EGB) in the Baltic Sea is also such an environment. The pelagic redoxline of the EGB hosts sulfur redox processes where metal cycling (Neretin et al., 2003) coupled to sulfide oxidation by Mn(IV), Fe(III) as well as NO₃⁻ yields local concentration maxima of zerovalent sulfur (S₀) and thiosulfate (S₂O₃²⁻; Kamyshny et al., 2013). The depth distribution of these products can be variable due to seasonal physical and biogeochemical forcings (Meyer et al., 2014). In contrast to the water column, benthic sulfur cycling in the EGB has received relatively less attention with the majority of sediment geochemistry studies aiming at reconstruction of past

environmental changes, (Sohlenius et al., 1996; Sternbeck and Sohlenius, 1997; Boettcher and Lepland, 2000) and to coupled metal-nutrient cycling over the Holocene (Heiser et al., 2001; Jilbert and Slomp, 2013a,b; Scholz et al., 2013; Lenz et al., 2014). One significant recent finding has been the first observation of extensive mats of sulfide-oxidizing bacteria covering large areas of seafloor beneath a water column HTZ in the EGB (Neffke et al., 2016). This hints at a widespread yet unquantified benthic sulfide filter operating in this fragile, anthropogenically-impacted environment where seafloor elemental cycling may provide important feedback to water column biogeochemical processes.

Here we investigate benthic sulfur redox cycling in the upper sediments of the EGB using high vertical resolution (min. 0.25 mm) chemical profiles obtained with multi-analyte sensitive voltammetric microelectrodes. We supplement these microprofiles with sulfide fluxes obtained with benthic lander deployments and profiles of particulate and porewater constituents measured on vertical core sections. With these datasets, we aim to (i) resolve the vertical gradients and fluxes of electroactive porewater sulfur-iron species along a benthic redox gradient and (ii) estimate relative magnitudes of dissolved sulfide flux to the water column and sulfide retention within sediments under the hypoxic and anoxic bottom waters of the basin.

MATERIALS AND METHODS

Study Area

The Baltic Sea is a shallow, landlocked brackish marine environment and contains several deep basins where a stable water column halocline limits exchanges between upper and deeper water layers (Matthaeus, 1995). Since the last deglaciation ca 13,000 BP, the environment transformed from an ice-dammed lake to a marine environment for a brief period (Yoldia Sea, 10,000–9500 BP), followed by another lacustrine period (Ancylus Lake - Sohlenius et al., 1996; Sternbeck and Sohlenius, 1997). Since ca 8000 BP, the marine connection was established again through the Danish straits. This Littorina Sea period has been characterized by basin-wide intermittent hypoxia (Zillen et al., 2008; Jilbert and Slomp, 2013a). The deep basins were probably continuously anoxic throughout the entirety of the Littorina period as shown from laminated sediment sequences obtained from the EGB (max. depth 250 m) and Landsort Deep (max. depth 450 m). However, the EGB in particular is not permanently anoxic due to the episodic introduction of oxygenated waters originating from North Sea that leads to a temporary period (weeks–months) of deep-water oxygenation (Matthaeus, 1995). Most recent ventilation of the EGB occurred during March–December 2015 (Mohrholz et al., 2015). Prior to this, stagnant euxinic conditions prevailed for about a decade—the last major ventilation event was in 2003 (Mohrholz et al., 2015). Therefore, our results represent the final stage of the stagnant conditions (see Neffke et al., 2016 for details on water column biogeochemistry at our study sites before prior to ventilation, and see Sommer et al., 2017 for conditions after the ventilation).

Sediment Sampling and Geochemical Measurements

Sediment cores were obtained via a video-guided multiple-corer (MUC) during Alkor cruise 422 to the EGB between August 15 and September 15, 2013 (Figure 1). Typically, a sediment column 40–50 cm long and 10 cm wide was retrieved in fine-grained muddy sediment. Shorter cores were obtained where the sediment was hard clay (see Results). Different cores were used for microprofiling and sectioning. The latter were immediately transferred to a cool room (10°C) and sectioned under an argon atmosphere. Porewater was extracted by centrifugation. The core sections were used for the determination of particulate organic carbon and sulfur (POC, PS, Carlo Erba elemental analyzer), porewater sulfate (SO_4^{2-} , ion chromatography), total dissolved sulfide ($\Sigma\text{H}_2\text{S}$, colorimetry/methylene blue) and dissolved iron (Fe(II), colorimetry/ferrozine). Details on analytical methods are given in Dale et al. (2013). At certain sites, shorter sediment cores (max. 20 cm long) were taken from the benthic chamber of autonomous biogeochemical observatory lander system (BIGO; Sommer et al., 2010). A total of 8 stations between 65 and 173 m water depths were sampled (Table 1). The bottom waters of the shallowest station (65 m) were oxygenated. Four stations (82, 95, 110, and 122 m) were located under the waters of a hypoxic transition zone (HTZ, here broadly defined as the zone between 80 and 120 m, $[\text{O}_2] < 30 \mu\text{M}$, $[\text{H}_2\text{S}] < 1 \mu\text{M}$) while the “deep basin” corresponds to area beyond 120 m depth where three of our stations (140, 152, and 173 m) were located (see the companion paper Noffke et al., 2016 for the water column redox state terminology). The deep basin of the EGB is characterized by higher concentrations of reducing chemical species such as H_2S and ammonium (NH_4^+).

Voltammetric Microsensor Measurements and Diffusive Flux Calculations

We measured the electroactive redox chemical species in the sediment porewaters with a three-electrode voltammetric sensor with the gold amalgam (Au/Hg) voltammetric glass microelectrode as the working electrode (Luther et al., 1998). These electrodes can simultaneously measure porewater redox species such as O_2 , $\text{HS}^-/\text{H}_2\text{S}$, $\text{S}_2\text{O}_3^{2-}$, S_x^{2-} , S^0 , Mn^{2+} , Fe^{2+} , and qualitatively detect soluble FeS_{aq} and Fe^{3+} (Brendel and Luther, 1995; Taillefert et al., 2007; Luther et al., 2008). The three-electrode cell was calibrated separately for O_2 , Mn^{2+} , Fe^{2+} , and H_2S before the first application using standard additions. Mn^{2+} was used as a pilot ion for subsequent calibrations (Konovalov et al., 2007; Slowey and Marvin-Dipasquale, 2012; Yücel, 2013). Data were recorded from the electrodes using a bench-top potentiostat (DLK-60, AIS, Inc.).

The retrieved sediment cores were profiled with the voltammetric microelectrode within 1 h of core retrieval. Replicate profiles were obtained on different spots on the same core. The Au/Hg glass working electrode was attached to a micromanipulator (Maerzhaeuser MM33) with counter and reference electrodes placed in the overlying water of the core. The working electrode was then vertically maneuvered with a minimum step of 0.25 mm. Four voltammetric scans were taken at each depth increment. The scans were taken in cyclic voltammetry form, starting from -0.1 V to -1.8 V and back at a rate of 1000 mV s^{-1} . Before each scan the electrode was electrochemically conditioned at -0.9 V for 10 s to remove any adsorbed species (Konovalov et al., 2007; Yücel, 2013). The concentrations were calculated using triplicate measurements after discarding the first scan, which yielded standard deviations $<5\%$. Detection limits (DL) were $20 \mu\text{M}$ for O_2 , $10 \mu\text{M}$ for Mn^{2+}

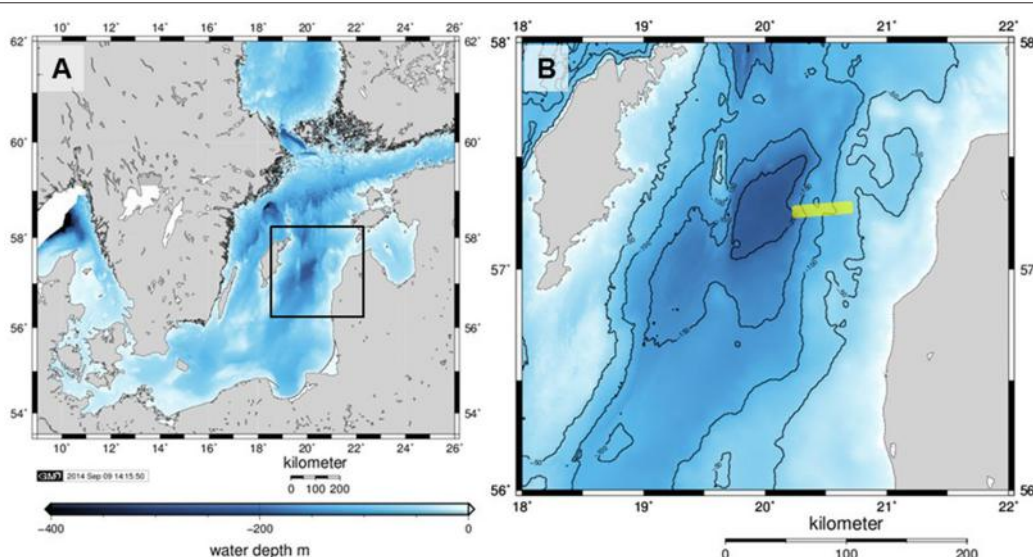


FIGURE 1 | (A) Bathymetry (m below mean sea level) of the Baltic Proper with the Eastern Gotland Basin indicated by the black rectangle and shown in detail in **(B)**. The sampled transect was on the eastern slope of the basin and its approximate location is shown as a yellow line. Axes labels denote eastings and northings. The maps were generated with Generic Mapping Tools.

TABLE 1 | Details of sediment sampling during Alkor cruise ALK 422 to Gotland Basin.

Depth, m	Gear	ALK 422 station	Date (2013)	Lat. °N	Lon. °E	Bottom water [O ₂], [H ₂ S] in μM	Visible mats
65	MUC12	653	9.9	57°26.52'	20°43.55'	>300, 0	no
65	BIGO2-6	651	10.9	57°26.26'	20°43.53'	>300, 0	yes
82	MUC5	581	23.8	57°21.81'	20°35.88'	10, 0	yes
95	MUC1	559	19.8	57°20.76'	20°35.30'	<5, 0	yes
95	MUC9	614	4.9	57°20.76'	20°35.32'	bdl	yes
95	BIGO2-1	561	21.8	57°20.76'	20°35.32'	bdl	yes
110	MUC7	596	26.8	57°20.58'	20°34.33'	bdl	yes
110	BIGO2-3	600	28.8	57°20.58'	20°34.32'	bdl	yes
123	MUC2	564	20.8	57°18.51'	20°33.00'	bdl, 9	yes
123	BIGO1-1	568	22.8	57°18.51'	20°32.99'	bdl, 9	yes
140	BIGO2-5	635	8.9	57°14.99'	20°27.13'	bdl, 46	no
152	MUC8	602	27.8	57°20.95'	20°28.99'	bdl, 77	no
152	BIGO1-3	603	29.8	57°20.98'	20°28.99'	bdl, 77	no
173	MUC6	587	24.8	57°21.05'	20°27.95'	bdl, 153	no
173	BIGO2-4	618	6.9	57°21.05'	20°27.97'	bdl, 173	no

"MUC" refers to a multicore sediment sample and BIGO stands for the "Biogeochemical Observatory" benthic lander. The first number following the BIGO operations indicates the lander used (#1 or #2) and the second to the deployment number. The redox conditions of the bottom water and the visible presence of surface bacterial mats are also given. (bdl, below detection limit).

and Fe²⁺ and 0.2 μM for H₂S. Calibration of FeS_{aq} is not possible due to lack of standards and only the signal intensity will be reported here. For sulfide, cyclic voltammetry gives two signals. On the one hand, a sharp peak proportional to the concentration of HS⁻/H₂S can be detected at ca. -0.7 V while scanning forward (toward the negative voltages). This peak shifts to more negative values (-0.9 V) with increasing sulfide concentrations. FeS_{aq} is also detectable at -1.1 V (Theberge and Luther, 1997; Buranakic et al., 2007). On the other hand, these sulfide species give a single wave-like signal during the backward scan (-1.8 V to -0.1 V) that is proportional to the sum of dissolved sulfide species (HS⁻, H₂S, S_x²⁻, and labile metal sulfides such as FeS). This is defined here as total dissolved sulfide concentration (Σ H₂S) since it represents a larger dynamic range (2–1200 μM). The forward signal is more sensitive (0.2 μM detection limit) yet typically saturated around 250 μM.

Diffusive fluxes (J , mmol m⁻² day⁻¹) were calculated from the concentration data using Fick's First Law (Equation 1), using measured linear concentration gradients and assuming steady-state conditions:

$$J = \varphi(0) \cdot D_S \cdot \frac{dC(z)}{dz} \quad (1)$$

where dC/dz is the linear concentration gradient (mmol m⁻³ m⁻¹), $\varphi(0)$ (dimensionless) is the surface sediment porosity and D_S (m² day⁻¹) is the diffusion coefficient. The latter was calculated from the diffusion coefficients in sediment-free seawater, D (m² day⁻¹), by correcting for tortuosity using the modified Weissberg relation (Boudreau, 1997):

$$D_S = D/[1 - 2\ln(\varphi(0))] \quad (2)$$

Diffusion coefficients were calculated for the ambient conditions (salinity 12, T = 10°C, 1 atm) using the Stokes-Einstein relationship with R package Marelac (Soetaert et al., 2012), leading to values of 1.36×10^{-4} , 1.02×10^{-4} , and 0.41×10^{-4} m² day⁻¹ for O₂, H₂S and Fe, respectively. The concentration gradient was estimated using the LINEST function in Excel from the concentration data covering the relevant depth range (typically the top 0–5 mm). With increasing sediment depth, positive fluxes predicted by Equation (1) imply a flux directed from seawater into the sediment. In this paper, we define positive fluxes as being directed out the sediment and vice versa. The uncertainty in the fluxes was estimated as ± 2 times the standard error (95% confidence interval).

During micro-profiling, the sediment cores were open to the atmosphere and not stirred during this procedure, which raises the possibility that the O₂ profiles (shallow site only) could have been affected by artifacts arising from (i) a change in O₂ concentrations above the diffusive boundary layer (DBL) due to atmospheric exchange, and (ii) an increase in the thickness of the DBL due a reduction in the flow regime at the sediment surface. Quantifying these artifacts is very difficult, but replicate profiles (one after the other) were very similar (see **Figure 3D**), which suggests that any alteration of the true O₂ gradient through the DBL may be minor. Nevertheless, we recognize the potential error in the O₂ fluxes, but argue that the order of magnitude is correct. Besides, the O₂ fluxes can only be treated as a snapshot of the current situation since bottom water O₂ concentrations in the oxycline regions of the EGB are extremely variable over a 24 h period, varying by tens of μM (**Figure 3** in Noffke et al., 2016). We further add that H₂S fluxes are much more likely to be reliable and representative of quasi-steady state conditions since they are less likely to be affected by short term changes in bottom water O₂ concentrations.

Benthic Chamber Sulfide Flux Measurements

Benthic flux measurements using the BIGO lander are described in detail by Sommer et al. (2010) and references therein. In short, the BIGO lander system consisted of two benthic chambers (internal diameter: 28.8 cm, area: 651.4 cm²). Four hours after the placement of the lander at the seafloor, the chambers were slowly (~ 30 cm h⁻¹) driven into the sediment. The incubation lasted 36 h during which six samples were sequentially taken from the benthic chamber using glass syringes. Upon retrieval of the lander, the syringe samples were analyzed for dissolved sulfide using the same protocol as the porewater samples (Dale et al., 2014; Noffke et al., 2016). Sulfide fluxes were calculated using the slope of the time vs. concentration data and the measured sediment-free volume of the benthic chamber.

RESULTS

General Sedimentary Properties

The changing bottom water redox conditions were reflected in the appearance of the cores. The sediment from 65 m depth underlying oxic bottom waters was light brown to brown in color at all depths. The sediments subsampled from the BIGO lander at this depth were partially covered with white bacterial mats whereas the MUC cores had no mats visible to the naked eye. Sediments in the upper 8 cm of the 82 m core were also brown to orange in color. The underlying sediment was homogeneous gray clay—a layer also present at the base of other cores (Figure S1). The sediments sampled from water depths > 90 m (anoxic) were mostly fine-grained and muddy. These sediments had a distinct dark gray-brown layer in the upper 5–20 cm followed by a light gray, more homogeneous-looking depositional layer. At 140 and 152 m cores, however, this black-organic rich zone was shallower (confined to top 5 cm) compared to others. The differences in the core characteristics, also substantiated by geochemical data described below, are due to the depositional history of EGB sediments. These sediments were previously classified as “erosion, transport and sedimentation bottoms” by Jonsson et al. (1990). It is likely that cores from 140 to 152 m represent “erosion” or “transport” bottoms which are now covered by recently deposited organic-rich sediments. Therefore, here is an abrupt transition between A cyanus Lake sediments and the modern organic-rich material. In contrast, the remainder of cores represent “sedimentation” bottoms.

A side-by-side view of cores from all sampled depths is given in Figure S1. Three of seven locations had clearly-visible mats (for 140 m we used a subcore from the BIGO chamber). Table 1 lists details on all sediment samplings. For seafloor photographs of the bacterial mats, the reader is directed to Noffke et al. (2016).

Porewater and Particulate Phase Geochemistry

Concentrations of particulate and porewater constituents measured on the core sections are shown in Figure 2. A POC-rich (> 3 wt.%) layer with a thickness of at least 10 cm (Figure 2A) was present in the upper part of the 95, 110, and

123 m cores. At 140 and 152 m cores the Holocene mud layer was shallower (5 cm) and the organic carbon levels decreased to below 1 wt.% in the underlying glacial clay. The surface sediments became progressively enriched in organic carbon with increasing water depth. Yet, the thickness of this mud layer was largest at the HTZ stations where the surfaces of the cores were almost completely covered by white bacterial mats and also in the deep basin. PS in the sediment solid phase also co-varied with POC, with downcore enrichment in the HTZ cores to about 1–2% and reaching highest values in the 173 m core (3%). PS contents decreased sharply within the gray-homogeneous zones at 140 and 152 m cores. As stated above, these sites represent erosional bottoms and a sharp transition from recent sediments (rich in POC/PS) to A cyanus Lake sediments (low in POC and PS).

Porewater sulfate concentrations generally decreased downcore with the strongest gradient in the cores sampled from the HTZ. For example, in the 95 m core sulfate decreased from 8 mM at the surface to 3.7 mM at 27 cm depth. The sulfate gradient appeared to track POC availability, which implies that microbial POC oxidation via sulfate reduction was the dominant remineralization process at the study sites, although a minor role for sulfate reduction coupled to the anaerobic oxidation of methane cannot be excluded (Jilbert and Slomp, 2013a; Egger et al., 2015). As a result, dissolved sulfide accumulated in the porewaters with the highest value of 1519 μ M (20 cm depth) at the 95 m core. In the sediments of the 174 m core, the sulfide was high downcore but the values remained < 1300 μ M. Sulfide concentrations were much lower at the stations with a thin Holocene mud layer (140 and 152 m). At the highly sulfidic cores, dissolved iron was undetectable. Downcore enrichments of dissolved iron were found only in the clay layers of sediments from 65, 82, and 152 m (140 m core not measured), with a maximum of 91 μ M in the 82 m core (15 cm depth).

Voltammetric Microprofiles

While the porewater profiles on sectioned cores revealed important trends through the basin, higher resolution microelectrode profiles resolved the fine scale processes that determine the fluxes at the sediment-water interface. Microprofiles from the permanently oxic station (65 m) revealed a quite sharp O₂ gradient across the sediment-water interface. Indeed, this was the only sampling location that had a detectable oxygen gradient across the sediment-water interface (Figure 3). Oxygen penetrated only to about 1 mm here, below which ΣH_2S gradually increased to a maximum concentration of 36 μ M at about 30 mm depth. The sub-core from the BIGO chamber obtained from the 65 m-station had a patchy distribution of microbial mats. The core subsampled from a non-microbial mat area from one the BIGO chambers had similar porewater chemistry as the MUC. However, the sediment subcore sampled over a white microbial mat had significantly higher levels of ΣH_2S with depth, with a subsurface maximum concentration of 238 μ M at 21 mm. The presence of the mat also modified the O₂ gradients such that O₂ was depleted right at the sediment-water interface just above the mat (due to high sulfide flux) but in the absence of a mat O₂ penetrated to about 0.5 mm depth (no

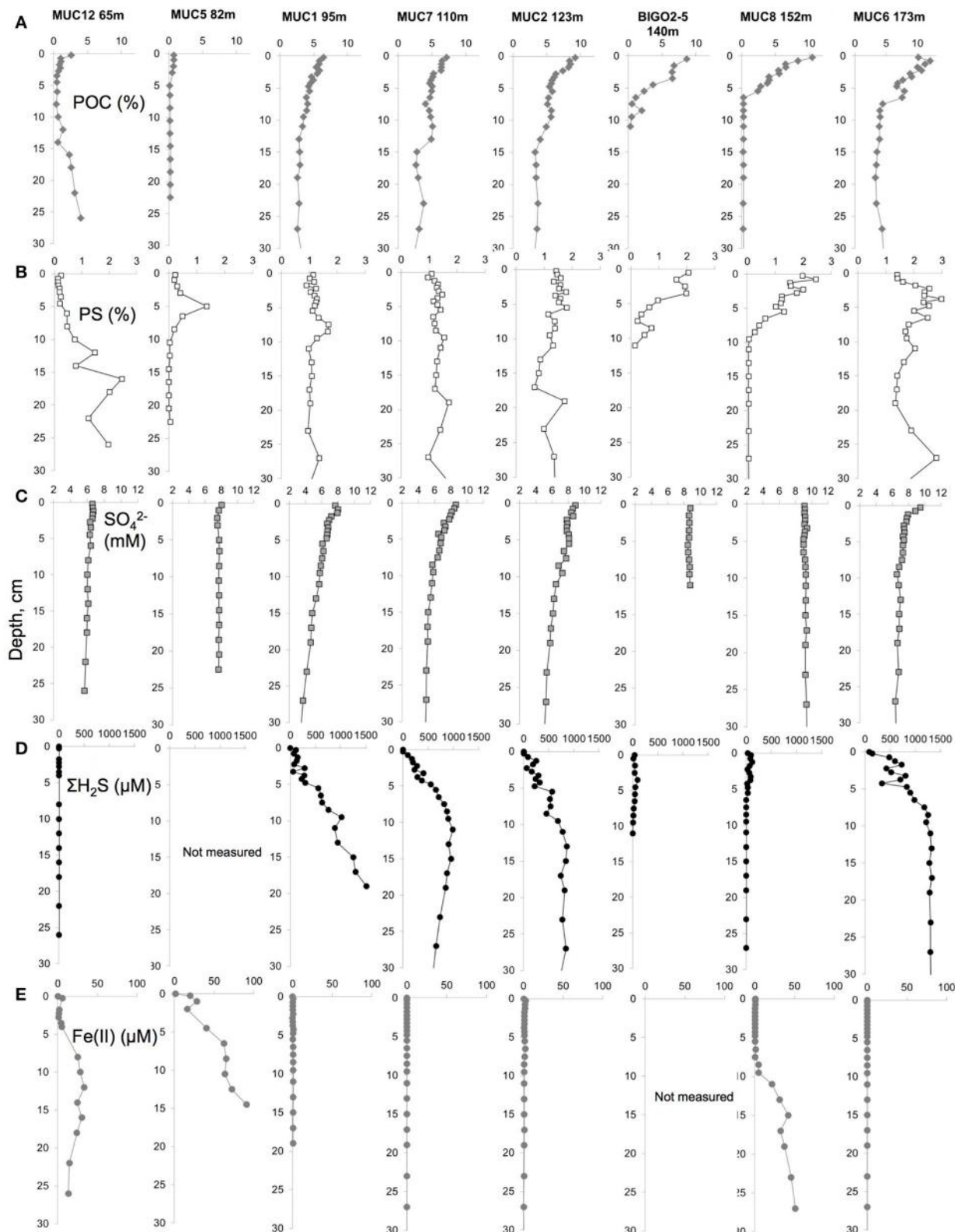


FIGURE 2 | Porewater and solid phase geochemical data for (A) Particulate organic carbon (POC) content (%), (B) particulate sulfur (PS) content (%), (C) porewater sulfate (SO_4^{2-}) concentration (mM), (D) porewater sulfide ($\Sigma\text{H}_2\text{S}$) concentration (μM) and (E) porewater dissolved iron (Fe(II)) concentration (μM) in the top 30 cm of the sediments along the transect.

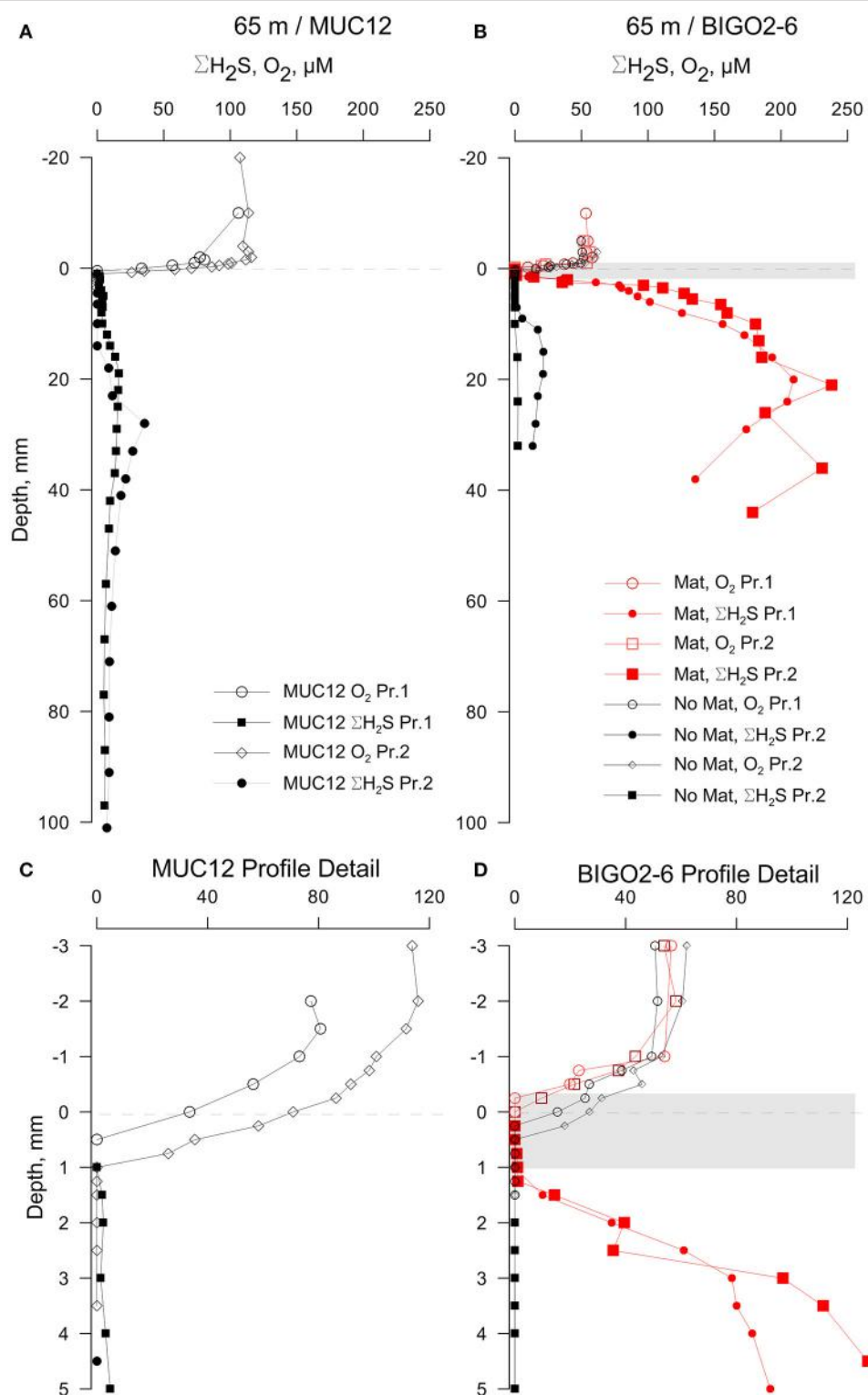


FIGURE 3 | Results of the voltammetric profiling in sediments from 65 m depth. (A) Profiles show only a moderate enrichment of sulfide in sediments with no visible bacterial mats while the BIGO cores from the same depth **(B)** had partial coverage of bacterial mats (shown as a gray band—the thickness is approximate) and a high sulfide flux. **(C,D)** shows enlarged views of the sediment-water interface shown in **(A,B)**, respectively. “Pr1” and “Pr2” refer to replicate profiles. Negative depths denote distance below the sediment-water interface (dashed line).

sulfide flux) (red and black curves in **Figures 3C–D**). In the profile with the mat, the actual oxygen depletion starts about 0.5 mm above the mat, which may point to additional oxidation pathways above the mat. The oxygen gradient may also have been modified by non-steady state effects due to increasing thickness of the DBL (see methods). Our assignment of the mat location should also be viewed with a ± 0.5 mm error. Still, we hold the view that the non-overlap of the O_2 and $\Sigma\text{H}_2\text{S}$ gradients reflect natural conditions because O_2 diffuses into the top of the mat whereas H_2S diffuses into the bottom. As will be elaborated later, within the mat H_2S can be oxidized to intermediate S oxidation states, with the additional possibility of abiotic $\text{Fe}-\text{H}_2\text{S}$ cycling. This could also contribute to the spatial separation of O_2 and H_2S gradients, as has been demonstrated in bioturbated sediments previously (e.g., Jørgensen and Nelson, 2004). Either way, our *in situ* flux measurements strongly indicate that H_2S oxidation is occurring, and that H_2S is not reaching the bottom water (see below).

The oxygen levels in the overlying waters of the cores from 82, 95, 110, and 123 m were undetectable by the voltammetric system (<20 μM). Still, micromolar levels of O_2 are known to be intermittently available in this depth range (Meyer et al., 2014; Noffke et al., 2016). Dissolved sulfide was the only voltammetric species detected whereas all other analytes remained below detection limits therefore not plotted (**Figure 4**). The core from 82 m had relatively low levels of $\Sigma\text{H}_2\text{S}$ with two subsurface maxima of about 30 μM at 2 and 70 mm. The two maxima could be due to elevated sulfate reduction rates in the very surface and deeper parts. As in all other HTZ cores, a sharp $\Sigma\text{H}_2\text{S}$ gradient was present on the top several millimeters (**Figure S2**). $\Sigma\text{H}_2\text{S}$ profiles in the 95, 110, and 123 m cores also indicate high fluxes of $\Sigma\text{H}_2\text{S}$ (highest concentration of about 400 μM at 100

mm depth), which is completely consumed in the top mm of the sediment, likely by the mediation of the sulfide-oxidizing microbial community. Strong evidence in support of this idea is the consistent appearance of a “double peak” voltammetric polysulfide signal (**Figure 5**)—which probably originates from the bacterially generated zerovalent sulfur (see Microbially Mediated Sulfide Oxidation as a Major Driver of the Benthic Filter).

The cores from water depths larger than 123 m had detectable levels of $\Sigma\text{H}_2\text{S}$ in the overlying waters (**Figure 6**, also **Figure S3**). $\Sigma\text{H}_2\text{S}$ increased to a subsurface maximum of around 120 μM in both the 140 and 152 m cores, and the levels of $\Sigma\text{H}_2\text{S}$ decreased to zero after typically 100 mm depth which denotes the top of the clay layer. The decrease in $\Sigma\text{H}_2\text{S}$ was accompanied by the appearance of dissolved iron as well as voltammetric signals for aqueous FeS (see **Figure S4** for an example voltammogram). Presumably, then, $\Sigma\text{H}_2\text{S}$ is precipitated as iron-sulfide particulates at this interface (e.g., Holmkvist et al., 2014). The profiles from the 174 m core were penetrated only until 40 mm depth; thereafter the electrochemical signals repeatedly went offscale due to very high sulfide concentrations (**Figure 2D**).

Benthic Sulfide Fluxes Across the Transect

The calculated diffusive fluxes at the sediment-mat interface indicate that $\Sigma\text{H}_2\text{S}$ consumption was between 2.5 and 3.4 $\text{mmol m}^{-2} \text{ day}^{-1}$ for the sediments located in the HTZ (**Table 2** and **Figure 7**). This flux enters the base of conspicuous white bacterial mats, thus alluding to a microbial mediation of sulfide oxidation. No $\Sigma\text{H}_2\text{S}$ efflux to the overlying waters was detected during microprofiling. At deeper locations without microbial mats, sulfide instead enters the water column, with the highest efflux occurring at the 173 m site ($3.14 \text{ mmol m}^{-2} \text{ day}^{-1}$). Due to lower

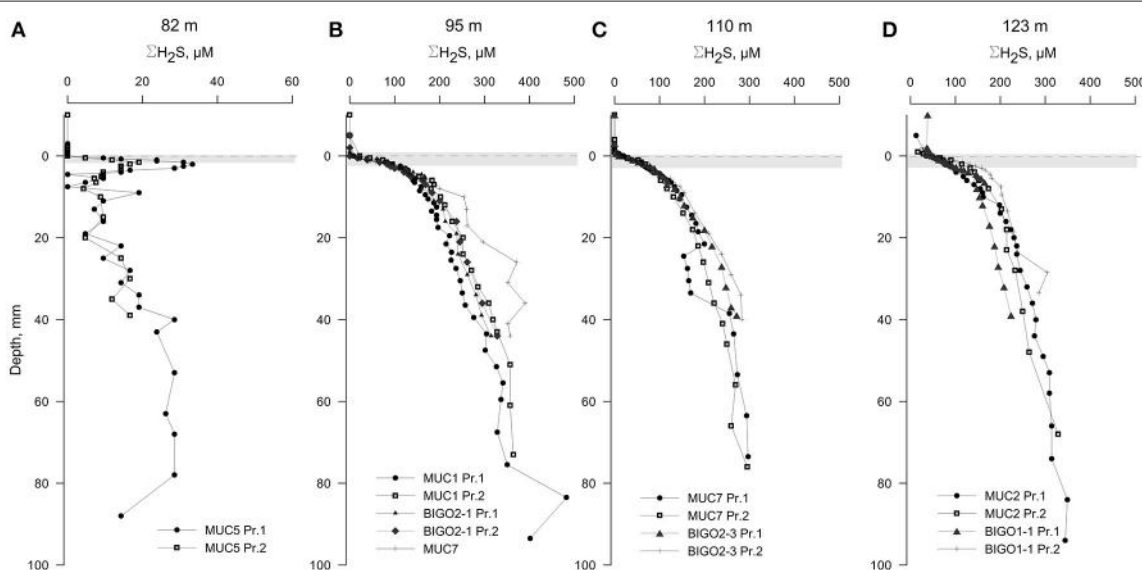


FIGURE 4 | Voltammetric profiles in sediments located along the HTZ in the EGB. Except for the 82 m site (**A**), all cores (**B–D**) displayed high sulfide fluxes near the sediment-water interface. “Pr1” or “Pr2” refers to replicate profiles. Positive depths denote distance below sediment-water interface (dashed line). The approximate locations of the bacterial mats are indicated by a gray bands. Note the expanded concentration scale in (**A**).

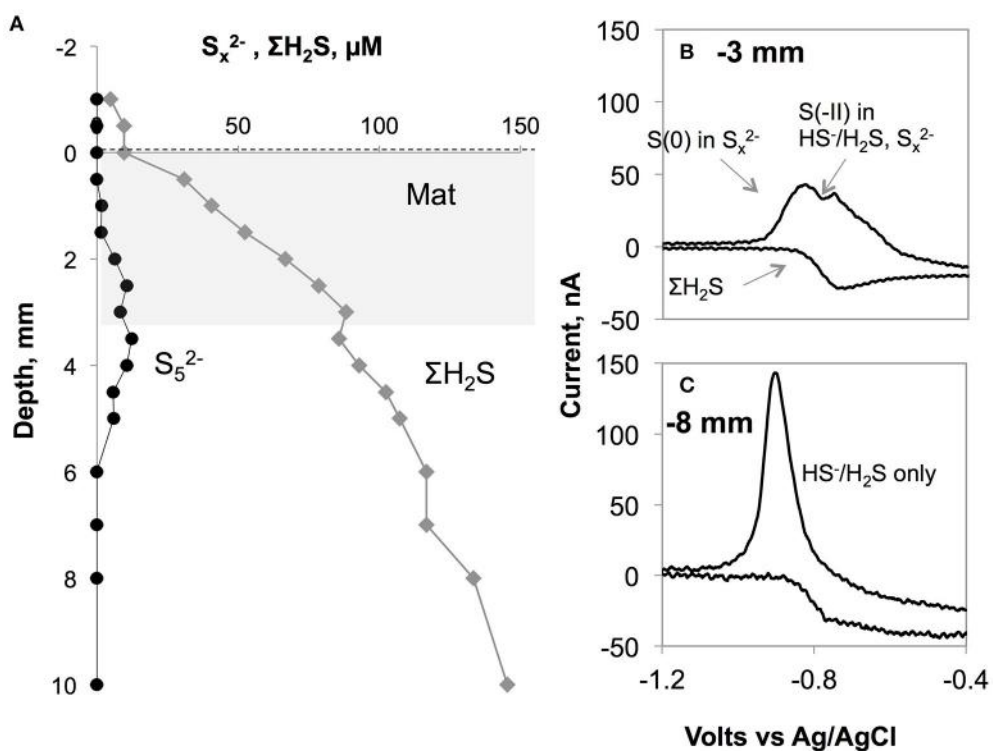


FIGURE 5 | (A) Polysulfide concentration (assumed to be S_x²⁻) plotted along with total sulfide levels in the core from BIGO2-3 from 110 m depth. The gray area shows the approximate location of the white bacterial mats. **(B)** shows a typical voltammogram with the co-existence of free sulfide and polysulfides. The double peak arises from the two different oxidation states existing in a S_x²⁻ molecule (all S have 0 valence except for the terminal S with -2 valence). The more negative peak in the forward scan corresponds to (x-1) zerovalent sulfur atoms in the polysulfides while the other peak is the sum of free sulfide plus the terminal S(-II) in S_x²⁻. On the backward scan, a wave-like signal can be used for calculation of total dissolved sulfide. This signal was obtained within or just underneath the *Beggiaota* mats. Similar signals were found within the 0–5 mm depth interval in sediments from 95, 110, and 123 m depths. The scan rate was 1000 mV s⁻¹. As shown in **(C)**, below ca. 5 mm the double peak disappeared giving rise to the single peak typical for H₂S/HS⁻.

sampling resolution compared to microprofiling, the diffusive fluxes calculated from the data (upper 10 cm) on sectioned cores were much lower. For instance, fluxes at the HTZ stations were 0.8–1.3 mmol m⁻² day⁻¹ and 1.9 mmol m⁻² day⁻¹ at the 173 m station.

High sulfide fluxes not only occurred in the HTZ and anoxic basin sediments. Despite relatively low levels of ΣH₂S in sediments from 65 m depth, the core sampled from the chamber of the BIGO lander deployed at the same location was partially covered with bacterial mats. As shown in Figure 3, these mats are characterized by a high ΣH₂S gradient such that the ΣH₂S flux toward the sediment-water interface within a mat increased to 3.4 ± 0.3 mmol m⁻² day⁻¹ whereas in an adjacent non-mat area the ΣH₂S flux was much weaker (0.14 ± 0.02 mmol m⁻² day⁻¹). This localized sulfide source apparently increases the oxygen consumption in the sediment such that in the non-mat area the O₂ flux into the sediment was 4.83 ± 1.16 mmol m⁻² day⁻¹ compared to 7.59 ± 1.89 mmol m⁻² day⁻¹ in the mat. Hence, the increase in the sulfide flux was matched by an almost equal rate of O₂ consumption.

The sulfide fluxes obtained from the benthic lander deployments also revealed a similar overall pattern (Table 3).

No sulfide flux was measurable from the HTZ sediments to bottom waters due to the benthic microbial sulfide filter. Deeper cores had sulfide fluxes to the bottom waters in the range of 5.3–10.2 mmol m⁻² day⁻¹; at least a factor of three higher than those obtained by microprofiling. This may be caused by either seafloor heterogeneity or because the large footprint of the benthic chamber provides a more complete picture of benthic fluxes than single point microprofiling measurements. Comparing our findings with previously published sulfide flux measurements to the bottom water of the EGB, we observed similar values to Noffke et al. (2016) who reported a maximum flux of 3.5 mmol m⁻² day⁻¹ using lander-based incubations in 2013 and to McGinnis et al. (2011) who reported an average flux of 1.9 mmol m⁻² day⁻¹ using an eddy correlation instrument deployment at 192 m depth.

DISCUSSION

Microbially Mediated Sulfide Oxidation as a Major Driver of the Benthic Filter

The elevated sulfide fluxes for the top 5 mm of the sediments determined from high-resolution profiling along with the

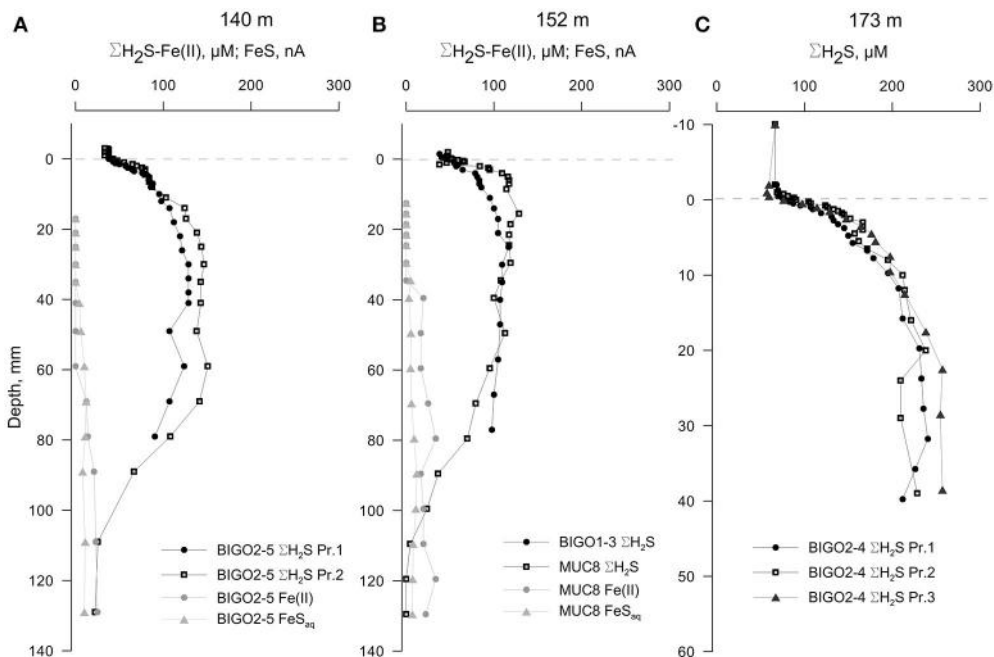


FIGURE 6 | Voltammetric profiles in sediments underlying anoxic-sulfidic waters in the EGB. (A) 140 m core, (B) 152 m core and (C) 173 m core. “Pr1” and “Pr2” refer to replicate profiles. Positive depths denote distance below the sediment-water interface (dashed line). Note that the depth-axis in (C) has an enlarged scale. The redox-active parameters that were below detection limits are not plotted.

TABLE 2 | Summary of microelectrode-derived fluxes in surface sediments.

Water depth	Component	Flux, $\text{mmol m}^{-2} \text{ day}^{-1}$	Depth Interval, mm
65m no mat	O_2	-4.83 ± 1.16	+1 to -0.5
65m no mat	$\Sigma\text{H}_2\text{S}$	$+0.14 \pm 0.05$	-5 to -20
65m with mat	O_2	-7.59 ± 1.89	+1 to 0
65m with mat	$\Sigma\text{H}_2\text{S}$	$+3.41 \pm 0.55$	-1 to -5
82m	$\Sigma\text{H}_2\text{S}$	$+0.35 \pm 0.27$	0 to -3
95m	$\Sigma\text{H}_2\text{S}$	$+3.38 \pm 0.40$	0 to -5
110m	$\Sigma\text{H}_2\text{S}$	$+2.50 \pm 0.17$	0 to -5
123m	$\Sigma\text{H}_2\text{S}$	$+2.73 \pm 0.30$	0 to -5
140m	$\Sigma\text{H}_2\text{S}$	$+1.27 \pm 0.22$	0 to -4
140m	$\Sigma\text{H}_2\text{S}$	-0.19 ± 0.04	-60 to -110
140m	Fe(II)	$+0.008 \pm 0.001$	-60 to -130
152m	$\Sigma\text{H}_2\text{S}$	$+0.84 \pm 0.23$	0 to -5
152m	$\Sigma\text{H}_2\text{S}$	-0.14 ± 0.02	-40 to -110
152m	Fe(II)	$+0.01 \pm 0.003$	-40 to -120
173m	$\Sigma\text{H}_2\text{S}$	$+3.14 \pm 0.48$	0 to -5

Positive fluxes are directed out of the sediment.

See the text for details of flux and error calculations. No flux was measurable for the components that are not listed at a given depth.

presence of microbial mats together indicate a role for biological sulfide consumption and mitigation of sulfide efflux to the bottom waters, i.e., a microbial benthic filter. As suggested

by Noffke et al. (2016), these mats are dominated by sulfide-oxidizing *Beggiatoa* sp. (also Sommer, personal observations during 2013 August and H. Schulz, pers. comm.). The HTZ waters of the EGB have variable but low levels of oxygen and nitrate (Meyer et al., 2014), both of which can be used as an electron acceptor for sulfide oxidation:



The latter equation, when coupled to chemosynthetic CO_2 fixation, is described as dissimilatory reduction of nitrate to ammonium (DNRA; Jørgensen and Nelson, 2004). Similar to denitrification, DNRA is a pathway that eliminates NO_3^- , but unlike denitrification, fixed N is not lost as N_2 but is retained as NH_4^+ . The study by Noffke et al. (2016) indicated that DNRA was pronounced in HTZ sediments sampled in 2013, yielding elevated release of NH_4^+ to bottom waters ($0.68\text{--}1.10 \text{ mmol m}^{-2} \text{ day}^{-1}$) with equal NO_3^- fluxes in the opposite direction (see Noffke et al., 2016, Figure 5). The microelectrode-derived sulfide fluxes consumed by the mat in the HTZ area, ranging from 2.78 to $3.38 \text{ mmol m}^{-2} \text{ day}^{-1}$, is nearly 3–4 times the NH_4^+ fluxes, hence supporting the view that the driver of sulfide oxidation in the HTZ is DNRA. *Beggiatoa* and other sulfide oxidizers can use sulfide also as the electron donor for CO_2 fixation. Thus, the ratio would allow for the complete oxidation of a fraction of the sulfide pool to sulfate.

The end product of equations 3 and 4, elemental sulfur (S^0), has been frequently observed within the vacuoles of the

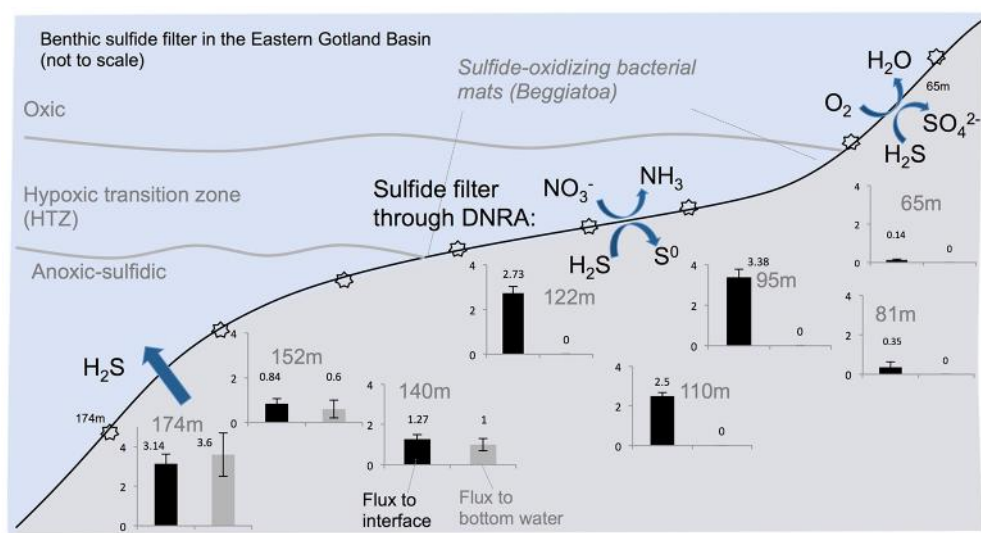
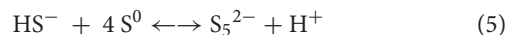


FIGURE 7 | Summary of the benthic sulfide filter in the Eastern Gotland Basin, Baltic Sea. Starbursts indicate sampling locations which are given in Table 1. Black bars denote $\Sigma\text{H}_2\text{S}$ flux to the sediment-water interface and the gray bars indicate flux ($\text{mmol m}^{-2} \text{ day}^{-1}$) to the bottom water. The gray bars are zero where the benthic sulfide filter is active.

Beggiatoa bacteria (e.g., Pasteris et al., 2001; Schwedt et al., 2012). The dissolved precursor to particulate elemental sulfur (S_8) is a polysulfide molecule (S_x^{2-}). When the chain length exceeds 8 the molecule forms an S_8 ring, releasing HS^- to solution. Polysulfides are a well-known intermediate in the oxidation of $\Sigma\text{H}_2\text{S}$ (e.g., Lichtschlag et al., 2013) and have been documented in the pelagic chemocline of the Gotland Basin (Kamyshny et al., 2013). These species are also electroactive and in our dataset voltammetric signals for them (one example shown in Figure 5) were detected in the vicinity of the mats between 1 and 5 mm depth within the surface sediment. Given that polysulfides are transient chemical products, it seems likely that the mats were actively oxidizing sulfide at the time of microprofiling.

The quantification of voltammetric polysulfide signals is rather difficult due to the undetected chemical speciation of these species due to lack of appropriate standards. Despite this drawback, an estimate is given in Figure 5 for a mat located over the sediments at 110 m depth following the method of Rozan et al. (2000). This method takes advantage of the double peak in the sulfide forward wave in the voltammogram. The double peak is due to the two oxidation states existing in a S_x^{2-} molecule (0 as in elemental sulfur but with a terminal S with -2 valence), such that it is possible to discriminate these two states with the fast voltammetric scan rates that were employed in this study ($>1000 \text{ mV s}^{-1}$) (Luther et al., 2001). The more negative peak in Figure 5B corresponds to (x-1) zerovalent sulfur atoms in the polysulfides while the other peak is the sum of free sulfide plus the terminal S(-II) in S_x^{2-} . If the polysulfides are assumed to contain 5 sulfur atoms on average (likely for a sedimentary pH range of 7–8, Kamyshny et al., 2004, 2008) and assuming that their calibration slope is the same as that of free sulfides, then we can infer a maximum of $12 \mu\text{M}$ polysulfides, accounting for 14% of total sulfide.

Similar voltammetric polysulfide signals were obtained in intertidal mats (Glazer et al., 2002), diffuse flow habitats in deep-sea hydrothermal vents (Gartman et al., 2011) and in laboratory studies of microbial S oxidizers (Sun et al., 2009). More recently, using single-cell Raman spectroscopy, Berg et al. (2014) detected intracellular polysulfide storage (in addition to S_8) in *Beggiatoa* cultures. Aside from their formation during sulfide oxidation, polysulfides can also be derived from the cleavage of the S-S bonds in the S_8 rings through intracellular enzymes (Berg et al., 2014) or chemically by the attack of HS^- (Kamyshny and Ferkelman, 2010). Taking these studies as a vantage point, the location of the subsurface polysulfide maximum (Figure 5A) in our results can be affected by two interrelated mechanisms. First, the polysulfides could be produced within the bacterial cells as a result of the utilization of the intracellular elemental sulfur and subsequent release of produced polysulfides to the porewater. Second, as the oxidation product of Equations 3, 4, elemental sulfur can be excreted from bacteria after which polysulfides can abiotically form in the porewater. For the S_5^{2-} species discussed above, this reaction can be written as (Kamyshny et al., 2008):



Shipboard microscopy observations of the bacteria (Sommer, unpubl.) revealed that their vacuoles were full of sulfur particles, implying that the release of newly produced sulfur to the porewaters is likely. The more reducing conditions below the mat may help stabilize and accumulate polysulfides, resulting in the subsurface maximum shown in Figure 5. Such a release of sulfide originating from the sulfur inclusions within a culture of *Beggiatoa* was demonstrated by Schwedt et al. (2012). Here, the sulfide release was due to the reduction of zerovalent sulfur by polyhydroxyalkanoates (PHA) inclusions that were also

TABLE 3 | Benthic fluxes in the EGB measured using benthic landers (mmol m⁻² day⁻¹).

Deployment		Water depth (m)	Incubation time (h)	ΣH_2S (mmol m ⁻² day ⁻¹)
BIGO-II-6	CH1	65	30.0	bdl
				bdl
BIGO-I-2	CH1	80	31.5	bdl
				bdl
BIGO-II-1	CH1	96	30.0	bdl
				bdl
BIGO-II-3	CH1	110	31.0	bdl
				bdl
BIGO-I-6	CH1	110	29.0	bdl
				bdl
BIGO-I-5	CH1	123	30.0	bdl
				bdl
BIGO-I-4	CH1	123	30.0	nd
				bdl
BIGO-I-1	CH1	124	30.0	bdl
				bdl
BIGO-II-5	CH1	140	29.0	7.61
				5.27
BIGO-I-3	CH1	152	35.0	3.24
				4.11
BIGO-II-4	CH1	173	31.0	10.15
				9.81

Fluxes for both chambers (CH1, CH2) of each lander deployment are provided.

Positive fluxes are directed out of the sediment. (bdl, below detection limit; nd, not determined).

synthesized in the cell during CO₂ fixation. Schwedt et al. (2012) noted “H₂S” release as a product, but it could have been the case that S_x²⁻, being more reduced than S⁰, could also form during this process. However, we cannot rule out the participation of a microbial consortium rather than *Beggiatoa* alone, that is, zero-valent sulfur may be the product of other sulfur oxidizing bacteria (e.g., *Thiobacillus*) that co-inhabit the mat. Future work will shed more light on this issue, and our findings are in parallel with emerging evidence supporting the idea that these sulfur intermediates can play important role in the benthic sulfur turnover in low-O₂ environments.

High sulfide oxidation rates have also been detected in other reducing habitats where microbial mats contribute to the formation of steep sulfide gradients. The fluxes, however, can vary within one order of magnitude. The pioneer microsensor study of Revsbech and Jørgensen (1983) found that in a shallow water setting *Beggiatoa* mat, the sulfide flux was 38 mmol m⁻² day⁻¹ whereas Preisler et al. (2007) reported a value of 5 mmol m⁻² day⁻¹ in a different coastal sediment. Recent *in-situ* microsensor studies from cold seeps at mud volcanoes yielded even higher rates. For example, in the *Beggiatoa* habitat

in the Haakon Mosby mud volcano (Barents Sea), de Beer et al. (2006) measured a flux of 18.7 mmol m⁻² day⁻¹ while Grünke et al. (2011) gave a flux of 40 mmol m⁻² day⁻¹ in a similar habitat in the Amon Mud Volcano in the Nile Fan (Eastern Mediterranean). An important contributor to these high fluxes is the sulfide production fueled by the anaerobic oxidation of methane coupled to sulfate reduction near the sediment-water interface. In continental margin sediments under upwelling areas, sulfide fluxes (associated with bacterial mats) mostly remain below 15 mmol m⁻² day⁻¹ (Zopfi et al., 2008; Sommer et al., 2016). These systems, as opposed to cold seeps, are dominated by the diffusive fluxes of sulfide generated through organic matter degradation. Taken together, our fluxes from the EGB remain at the lower end of the reported fluxes, closer to the estimates for continental margins under upwelling areas. One common finding of the above-mentioned studies is that microbial residents of sharp sulfide gradients such as *Beggiatoa* use NO₃⁻ as well as O₂ as an oxidant for energy acquisition for the production of biomass. The ability of intracellular nitrate storage gives these bacteria a significant ecological advantage in redox transition waters such as those in the EGB where O₂ and NO₃⁻ are intermittently available. Sulfide, on the other hand, is generally not limiting in these organic-rich habitats. These dynamic biogeochemical conditions can result in the widespread presence of sulfide-oxidizing benthic bacterial mats which increases the sulfide retention capacity of the seafloor (Schulz and Jørgensen, 2001). A newly discovered group of “cable bacteria,” without forming visible mats, have also been shown to oxidize sulfide in the upper sediment by shuttling electrons via cm-long filaments that connect otherwise vertically separated oxygen and sulfide gradients (Pfeffer et al., 2012; Seitaj et al., 2015). While they remain to be discovered in the EGB, we currently neglect their contribution to the benthic sulfide filter in the EGB because our measured sulfide gradients are very sharp at the sediment-water interface and lack a vertical separation from the oxygen gradient.

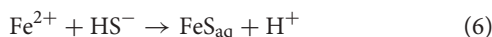
Regional Implications of Benthic Sulfide Oxidation in the Baltic Sea

The findings reported here bring forward the question of whether a similar benthic sulfide filter operates in other areas of the Baltic Sea with hypoxic-anoxic bottom waters. Towed camera observations during our cruise (ALK 422) revealed that the seafloor under the HTZ in the other parts of the Gotland Basin was also covered by extensive bacterial mats (Pfannkuche and Sommer unpubl.). Hence, sulfide oxidation at the seafloor below the redox transition zone may be important on a regional scale. Hannson et al. (2013) and Noffke et al. (2016) estimated the area of Baltic Proper seafloor under permanently anoxic waters (>120 m depth) as 18954 km² and under HTZ waters (80–120 m) as 47320 km². Using these areal estimates and the average of the measured fluxes (2.87 mmol m⁻² day⁻¹) for the 80–120 m depths and the 173 m flux (3.14 mmol m⁻² day⁻¹), we estimate that a total of 2281 kton S yr⁻¹ of this sulfide flux occurs at the sediment surface (0–5 mm) below a depth of 80 m. Of this, about 695 kton S yr⁻¹ enters the water column below 120 m. The eventual fate of the flux is oxidation in the water column chemocline (Kamyshny et al., 2013). The remaining 1586 kton S yr⁻¹, corresponding

to 70% of total flux occurring in the sediments beneath 80 m water depth, is removed in the benthic interface located under the HTZ. This analysis bears obvious uncertainties, but it suffices to highlight the important ecosystem service provided by these benthic microbial communities in the Baltic Sea.

FeS Formation in the Deep Water Sediments

In addition to sulfide oxidation at the sediment-water interface, some cores exhibited a deeper sulfur sink. The 140 and 152 m cores had a subsurface sulfide peak after which voltammetric signals for Fe(II) and FeS appeared and increased in intensity with depth. These opposing geochemical gradients also corresponded to the abrupt shift from a laminated, organic-rich surface sediment layer toward a more homogeneous, gray, low porosity layer. This points to a deep source of Fe(II) arising from the reduction of particulate Fe(III), which was reported to be in high concentration in earlier depositional periods (i.e., Ancylus Lake, Boettcher and Lepland, 2000; Holmkvist et al., 2014). We observed that FeS formation is clearly occurring in the lower part of the organic-rich sulfidic layer (Figure 6). Therefore, in addition to the removal of sulfide mediated by sulfide oxidizing bacteria on the surface sediments of the chemocline sediments, FeS precipitation acts as a second sink for sulfide (Rickard and Luther, 2007):



When compared with the downward $\Sigma\text{H}_2\text{S}$ fluxes at 140 and 152 m cores (-0.19 and $-0.14 \text{ mmol m}^{-2} \text{ day}^{-1}$), the upward Fe(II) flux of $0.01 \text{ mmol m}^{-2} \text{ day}^{-1}$, is too low to account for sulfide consumption. This indicates that H_2S must be actively consumed in further reactions with aqueous or particulate FeS to precipitate pyrite, FeS_2 (Yücel et al., 2010);



Solid phase pyrite or FeS measurements were not conducted in this study but other works such as that by Boettcher and Lepland (2000) and Holmkvist et al. (2014) already identified an iron sulfidation interface at the Ancylus-Littorina transition where the laminated organic-rich Littorina sediments are enrich in pyrite whereas the top part of the lacustrine layers are enrich in FeS. A similar iron-sulfidation front may exist in our 140 and 152 m cores at a depth of 10–15 cm only, where the transition to a gray, homogeneous layer is visible.

A likely scenario for the appearance of the gray homogeneous layer close to the sediment-water interface is that these sediments might have deposited during the freshwater Ancylus Lake (Andren et al., 2000). A first support of this idea is the very low POC-PS levels (Figure 2), which has been reported as a characteristic of pre-Littorina deposition (Boettcher and Lepland, 2000). However, this finding is rather unexpected since the presumed Ancylus Lake sediments were located 200–400 cm below the sediment-water interface (Boettcher and Lepland, 2000) whereas our results from 140 to 152 m cores suggest that this can also happen at very shallow sediment depths.

(i.e., 10–20 cm). This can be explained by the fact that earlier studies focusing on Ancylus-Littorina transition sampled from the deepest parts of the Baltic, where the accumulation rates are known to be highest (Vallius and Kunzendorf, 2001; Hille et al., 2006). In the EGB margin, especially between 100 and 150 m depth, near bottom currents are reported to be highest (Emeis et al., 1998; Hagen and Feistel, 2004), limiting the accumulation of recent material. Seismic studies in the EGB also hint at a very variable lateral distribution of depositional layers (Emeis et al., 1998), supported by reports on variable ^{210}Pb -based mass accumulation (Hille et al., 2006) and organic carbon burial rates (Winogradow and Pempkowiak, 2014). These considerations point to the possibility that the Ancylus Lake sediments may already be present at quite shallow depths at certain locations along the basin margin. In addition to the possibility that the gray homogeneous layer had a lake origin, it may also be the case that they formed during an oxic era in the Littorina Sea when the bottom sediments were bioturbated, presumably during the latest presumably “oxic” event, which occurred between ca 1200 and 1900 AD (Conley et al., 2009). Still, the very low POC levels in these depositional layers argue against a marine origin. Regardless of their provenance, these erosion bottom sediments (Jonsson et al., 1990) that underly the most recent organic-rich deposits can be a near-seafloor dissolved iron source and act as a sulfide sink in the deep basins of the Baltic.

Baltic Sea Benthic Sulfur Cycle Provides an Important Feedback to the Pelagic Ecosystem

Our combined approach using porewater measurements on sectioned cores, voltammetric microelectrode profiling and *in situ* lander incubations confirmed the presence of a highly efficient microbial hydrogen sulfide filter in the EGB. We have also found that sulfide accumulation was limited to a recent sedimentary layer that was rich in organic carbon. Not only the deep-water sediments but also the shallow water sediments contained dissolved sulfide as evidenced by patches of bacterial mats at these shallow depths. Sediments of both the deep basin and HTZ zones were highly sulfidic—however the sulfide flux was effectively consumed in the vicinity of the extensive bacterial mats beneath the HTZ. The dissolved iron flux reaching the near-surface sediments at 140–152 m cores apparently plays a role in limiting the sulfide efflux toward the water column, although quantitatively they are not be as important as the microbial filtering.

The benthic sulfur cycle in the Baltic Sea is tightly coupled to the cycles of nitrogen especially via DNRA (Noffke et al., 2016). Here, sulfide oxidation with nitrate as an electron acceptor yields elevated ammonium fluxes to bottom water (via DNRA, Noffke et al., 2016; Sommer et al., 2017) thereby leading to the retention of fixed nitrogen in the system. Understanding the intertwined cycling of C, N, and S with an integrated approach will be more important since the Baltic Sea, similar to other hypoxic coastal environments, is undergoing an accelerated change (Carstensen et al., 2014) where the intensification of the hypoxia may also elevate sulfide accumulation. In the light of these projections,

whether or not the benthic sulfide filter will remain as efficient as it is at present remains an open question.

AUTHOR CONTRIBUTIONS

MY, SS, AD, OP designed the study; OP and SS coordinated ship operations, lander deployments and sampling; MY, SS, AD took and processed samples; MY performed microelectrode measurements and analyses, MY, SS, AD performed data analyses and calculations; MY, SS, AD, and OP wrote the manuscript.

FUNDING

This research was funded by the Helmholtz Alliance Robotic Exploration of Extreme Environments (ROBEX) and partly funded by the Sonderforschungsbereich 754 “Climate—Biogeochemistry Interactions in the Tropical Ocean” (<http://www.sfb754.de>) which is supported by the Deutsche Forschungsgemeinschaft. M. Yücel also acknowledges start-up funds from Turkish Scientific and Technological Research Council (TUBITAK 2232 Program, Project No: 115C090) and from Project DEKOSIM - National Excellence Centre for Marine Ecosystem and Climate Research, funded by the Ministry

of Development of Turkey, which provided support during manuscript drafting and revision stages.

ACKNOWLEDGMENTS

We thank the captain and crew of FS Alkor, expedition ALK422 between August 15-September 15 2013. We are grateful to Sonja Kriwanek, Mathias Türk and Asmus Petersen for successful deployments of lander and multicorer and to Bettina Domeyer, Sven Trinkler, Anke Bleyer for laboratory chemical analyses. Special thanks are due to George Luther, Dan MacDonald and Allysa Findlay from University of Delaware (USA) for lending the voltammetric analyzer and microelectrodes to MY.

SUPPLEMENTARY MATERIAL

The Supplementary Material for this article can be found online at: <http://journal.frontiersin.org/article/10.3389/fmicb.2017.00169/full#supplementary-material>

Figure S1 | Photographs of the MUC cores taken from the transect.

Figure S2 | Zoomed (top 10 mm) version of the graphs in Figure 4.

Figure S3 | Zoomed (top 10 mm) version of the graphs in Figure 6.

Figure S4 | Representative voltammetric scan showing the coexistence of Fe(II) and FeS (from the 152 m-core, 100 mm).

REFERENCES

- Andren, E., Andren, T., and Sohlenius, G. (2000). The Holocene history of the southwestern Baltic Sea as reflected in a sediment core from the Bornholm Basin. *Boreas* 29, 233–250. doi: 10.1111/j.1502-3885.2000.tb00981.x
- Berg, J. S., Schwedt, A., Kreutzmann, A.-C., Kuypers, M. M. M., and Milucka, J. (2014). Polysulfides as intermediates in the oxidation of sulfide to sulfate by *Beggiatoa* spp. *Appl. Environ. Microbiol.* 80, 629–636. doi: 10.1128/AEM.02852-13
- Boettcher, M. E., and Lepland, A. (2000). Biogeochemistry of sulfur in a sediment core from the west-central Baltic Sea: evidence from stable isotopes and pyrite textures. *J. Mar. Syst.* 25, 299–312. doi: 10.1016/S0924-7963(00)00023-3
- Boudreau, B. P. (1997). *Diagenetic Models and Their Implementation, Modelling Transport and Reactions in Aquatic Sediments*. Berlin: Springer-Verlag.
- Brendel, P., and Luther, G. W. (1995). Development of a gold-amalgam voltammetric microelectrode for the determination of dissolved Fe, Mn, O2 and S(-2) in porewaters of marine and freshwater sediments. *Environ. Sci. Technol.* 29, 751–761. doi: 10.1021/es00003a024
- Bura-Nakic, E., Krznicic, D., Jurasin, D., Helz, G. R., and Ciglenecki, I. (2007). Voltammetric characterization of metal sulfide particles and nanoparticles in model solutions and natural waters. *Anal. Chim. Acta* 594, 44–51. doi: 10.1016/j.aca.2007.04.065
- Carstensen, J., Andersen, J. H., Gustafsson, B. G., and Conley, D. J. (2014). Deoxygenation of the Baltic Sea during the last century. *Proc. Natl. Acad. Sci. U.S.A.* 111, 5628–5633. doi: 10.1073/pnas.1323156111
- Conley, D. J., Björck, S., Bonsdorff, E., Carstensen, J., Destouni, G., Gustafsson, B. G., et al. (2009). Hypoxia-related processes in the Baltic Sea. *Environ. Sci. Technol.* 43, 3412–3420. doi: 10.1021/es802762a
- Dale, A. W., Bertics, V. J., Treude, T., Sommer, S., and Wallmann, K. (2013). Modeling benthic-pelagic nutrient exchange processes and porewater distributions in a seasonally-hypoxic sediment: evidence for massive phosphate release by *Beggiatoa*? *Biogeosciences* 10, 629–651. doi: 10.5194/bg-10-629-2013
- Dale, A. W., Sommer, S., Ryabenko, E., Noffke, A., Bohlen, L., Wallmann, K., et al. (2014). Benthic nitrogen fluxes and fractionation of nitrate in the Mauritanian oxygen minimum zone (Eastern Tropical North Atlantic). *Geochim. Cosmochim. Acta* 134, 234–256. doi: 10.1016/j.gca.2014.02.026
- de Beer, D., Sauter, E., Niemann, H., Kaul, N., Witte, U., and Schlu, M. (2006). *In-situ* fluxes and zonation of microbial activity in surface sediments of the Hakon Mosby Mud Volcano. *Limnol. Oceanogr.* 51, 1315–1331. doi: 10.4319/lo.2006.51.3.1315
- Diaz, R. J., and Rosenberg, R. (2008). Spreading dead zones and consequences for marine ecosystems. *Science* 321, 926–929. doi: 10.1126/science.1156401
- Egger, M., Rasigraf, O., Sapart, C. J., Jilbert, T., Jetten, M. S. M., Röckmann, T., et al. (2015). Iron-mediated anaerobic oxidation of methane in brackish coastal sediments. *Environ. Sci. Technol.* 49, 277–283. doi: 10.1021/es503663z
- Emeis, K. -C., Neumann, T., Endler, R., Struck, U., Kunzendorf, H., and Christiansen, C. (1998). Geochemical records of sediments in the Eastern Gotland Basin – products of sediment dynamics in a not-so-stagnant anoxic basin? *Appl. Geochem.* 13, 349–358. doi: 10.1016/S0883-2927(97)00104-2
- Ferdeman, T. G., Lee, C., Pantoja, S., Harder, J., Bebout, B. M., and Fossing, H. (1997). Sulfate reduction and methanogenesis in *Thioploca*-dominated sediment off the coast of Chile. *Geochim. Cosmochim. Acta* 61, 3065–3079. doi: 10.1016/S0016-7037(97)00158-0
- Gartman, A., Yücel, M., Madison, A. S., Chu, D. W., Ma, S., Janzen, C. P., et al. (2011). Sulfide oxidation across diffuse flow zones of hydrothermal vents. *Aquatic Geochem.* 17, 583–601. doi: 10.1007/s10498-011-9136-1
- Glazer, B. T., Cary, S. C., Hohmann, L., and Luther, G. W. III. (2002). “Sulfur speciation and microbial characterization of an intertidal salt marsh microbial mat,” in *Environmental Electrochemistry: Analysis of Trace Element Biogeochemistry*, Vol. 811, *American Chemical Society Symposium Series*, eds M. Taillefert and T. F. Rozan (Washington, DC), 283–304.
- Grünke, S., Felden, J., Lichtschlag, A., Girnth, A.-C., De Beer, D., Wenzhoefer, F., et al. (2011). Niche differentiation among mat-forming, sulfide-oxidizing bacteria at cold seeps of the Nile Deep Sea Fan (Eastern Mediterranean Sea). *Geobiology* 9, 330–348. doi: 10.1111/j.1472-4669.2011.00281.x
- Hagen, E., and Feistel, R. (2004). Observations of low-frequency current fluctuations in deep water of the Eastern Gotland Basin/Baltic Sea. *J. Geophys. Res.* 109, 1–15. doi: 10.1029/2003jc002017

- Hansson, M., Andersson, L., Axe, P., and Szaron, J. (2013). *Oxygen Survey in the Baltic Sea – Extent of Anoxia and Hypoxia, 1960–2012*. Report Oceanography No. 46, Swedish Meteorological and Hydrological Institute, Göteborg.
- Heiser, U., Neumann, T., Scholten, J., and Stuben, D. (2001). Recycling of manganese from anoxic sediments in stagnant basins by seawater inflow: a study of surface sediments from the Gotland Basin, Baltic Sea. *Mar. Geol.* 177, 151–166. doi: 10.1016/S0025-3227(01)00129-3
- Hille, S., Leipe, T., and Seifert, T. (2006). Spatial variability of recent sedimentation rates in the Eastern Gotland Basin (Baltic Sea). *Oceanologia* 48, 297–317.
- Holmkvist, L., Kamysny, A., Brüchert, V., and Jørgensen, B. B. (2014). Sulfidization of lacustrine glacial clay upon Holocene marine transgression (Arkona Basin, Baltic Sea). *Geochim. Cosmochim. Acta* 142, 75–94. doi: 10.1016/j.gca.2014.07.030
- Jessen, G. L., Lichtschlag, A., Struck, U., and Boetius, A. (2016). Distribution and composition of thiotrophic mats in the hypoxic zone of the Black Sea (150–170 m water depth, Crimea margin). *Front. Microbiol.* 7:1011. doi: 10.3389/fmicb.2016.01011
- Jilbert, T., and Slomp, C. P. (2013a). Rapid high-amplitude variability in Baltic Sea hypoxia during the Holocene. *Geology* 41, 1182–1186. doi: 10.1130/G34804.1
- Jilbert, T., and Slomp, C. P. (2013b). Iron and manganese shuttles control the formation of authigenic phosphorus minerals in the euxinic basins of the Baltic Sea. *Geochim. Cosmochim. Acta* 107, 155–169. doi: 10.1016/j.gca.2013.01.005
- Jonsson, P., Carman, R., and Wulff, F. (1990). Laminated sediments in the Baltic: a tool for evaluating nutrient mass balances. *Ambio* 19, 152–158.
- Jørgensen, B. B., and Kasten, S. (2006). “Sulfur cycling and methane oxidation,” in *Marine Geochemistry*, 2nd Edn., eds H. D. Schulz and M. Zabel (Berlin: Springer), 271–309.
- Jørgensen, B. B., and Nelson, D. C. (2004). “Sulfide oxidation in marine sediments: geochemistry meets microbiology,” in *Sulfur Biogeochemistry—Past and Present: Geological Society of America Special Paper*, Vol. 379, eds J. P. Amend, K. J. Edwards, and T.W. Lyons (Boulder, CO: Geological Society of America), 63–81.
- Kamysny, A. Jr., and Fertelman, T. G. (2010). Dynamics of zero-valent sulfur species including polysulfides at seep sites on intertidal sand flats (Wadden Sea, North Sea). *Mar. Chem.* 121, 17–26. doi: 10.1016/j.marchem.2010.03.001
- Kamysny, A. Jr., Goifman, A., Gun, J., Rizkov, D., and Lev, O. (2004). Equilibrium distribution of polysulfide ions in aqueous solutions at 25°C: a new approach for the study of polysulfides equilibria. *Environ. Sci. Technol.* 38, 6633–6644. doi: 10.1021/es049514e
- Kamysny, A. Jr., Yakushev, E. V., Jost, G., and Podymov, O. I. (2013). “Role of Sulfide Oxidation Intermediates in the Redox Balance of the Oxic-Anoxic Interface of the Gotland Deep, Baltic Sea,” in *Chemical Structure of Pelagic Redox Interfaces: Observations and Modeling*, ed E. V. Yakushev (Berlin: Springer), 95–119.
- Kamysny, A. Jr., Zilberbrand, M., Ekeltchik, I., Voitsekovski, T., Gun, J., and Lev, O. (2008). Speciation of polysulfides and zerovalent sulfur in sulfide-rich water wells in southern and central Israel. *Aquat. Geochem.* 14, 171–192. doi: 10.1007/s10498-008-9031-6
- Konovalov, S. K., Luther, G. W., and Yücel, M. (2007). Porewater redox processes and sediments in the Black Sea sediments. *Chem. Geol.* 245, 254–274. doi: 10.1016/j.chemgeo.2007.08.010
- Kühl, M., and Revsbech, N. P. (2001). “Biogeochemical microsensors for boundary layer studies,” in *The Benthic Boundary Layer: Transport Processes and Biogeochemistry*, eds B. P. Boudreau and B. B. Jørgensen (Oxford: Oxford University Press), 180–210.
- Lavik, G., Stührmann, T., Brüchert, V., Van der Plas, A., Mohrholz, V., Lam, P., et al. (2009). Detoxification of sulphidic African shelf waters by blooming chemolithotrophs. *Nature* 457, 581–584. doi: 10.1038/nature07588
- Lenz, C., Behrends, T., Jilbert, T., Silverira, M., and Slomp, C. P. (2014). Redox-dependent changes in manganese speciation in Baltic Sea sediments from the Holocene Therman maximum: an EXAFS, XANES and LA-ICP-MC study. *Chem. Geol.* 370, 49–57. doi: 10.1016/j.chemgeo.2014.01.013
- Lichtschlag, A., Kamysny, A. Jr., and Fertelman, T., DeBeer, D. (2013). Intermediate sulfur oxidation state compounds in the euxinic surface sediments of the Dvurechenskii mud volcano (Black Sea). *Geochim. Cosmochim. Acta* 105, 130–145. doi: 10.1016/j.gca.2012.11.025
- Luther, G. W., Brendel, P. J., Lewis, B. L., Sundby, B., Lefrancois, L., Silverberg, N., et al. (1998). Simultaneous measurement of O₂, Mn, Fe, I- and S(-II) in marine pore waters with a solid-state voltammetric microelectrode. *Limnol. Oceanogr.* 43, 325–333. doi: 10.4319/lo.1998.43.2.0325
- Luther, G. W., Glazer, B. T., Ma, S., Trouwborst, R. E., Moore, T. S., Metzger, E., et al. (2008). Use of voltammetric solid-state (micro)electrodes for studying biogeochemical processes: laboratory measurements to real time measurements with an *in situ* electrochemical analyzer (ISEA). *Mar. Chem.* 108, 221–235. doi: 10.1016/j.marchem.2007.03.002
- Luther, G. W. III, Glazer, B. T., Hohmann, L., Popp, J. I., and Taillefert, M., Rozan, T. F., et al. (2001). Sulfur speciation monitored *in situ* with solid state gold amalgam voltammetric microelectrodes: polysulfides as a special case in sediments, microbial mats and hydrothermal vent waters. *J. Environ. Monit.* 3, 61–66. doi: 10.1039/b006499h
- Matthaeus, W. (1995). Natural variability and human impacts reflected in long-term changes in the Baltic deep water conditions – A brief review. *Deutsche Hydrographische Zeitschrift* 47, 47–65. doi: 10.1007/BF02731990
- McGinnis, D. F., Cherednichenko, S., Sommer, S., Berg, P., Rovelli, L., Schwarz, R., et al. (2011). Simple, robust eddy correlation amplifier for aquatic dissolved oxygen and hydrogen sulfide flux measurements. *Limnol. Oceanogr.* 9, 340–347. doi: 10.4319/lom.2011.9.340
- Meyer, D., Prien, R. D., Dellwig, O., Waniek, J. J., and Schulz-Bull, D. (2014). Electrode measurements of the oxidation reduction potential in the Gotland Deep using a moored profiling instrumentation. *Estuarine Coast. Shelf Sci.* 141, 26–36. doi: 10.1016/j.ecss.2014.02.001
- Mohrholz, V., Naumann, M., Nausch, G., Krüger, S., and Graewe, U. (2015). Fresh oxygen for the Baltic Sea – An exceptional saline inflow after a decade of stagnation. *J. Mar. Syst.* 148, 152–166. doi: 10.1016/j.jmarsys.2015.03.005
- Neretin, L. N., Pohl, C., Jost, G., Leipe, T., and Pollehnne, F. (2003). Manganese cycling in the Gotland Deep, Baltic Sea. *Mar. Chem.* 82, 125–143. doi: 10.1016/S0304-4203(03)00048-3
- Noffke, A., Sommer, S., Dale, A. W., Hall, P. O. J., and Pfannkuche, O. O. (2016). Benthic nutrient fluxes in the Eastern Gotland Basin (Baltic Sea) with particular focus on microbial mat ecosystems. *J. Mar. Syst.* 158, 1–12. doi: 10.1016/j.jmarsys.2016.01.007
- Pasteris, J. D., Freeman, J. D., Goffredi, S. K., and Buck, K. R. (2001). Raman spectroscopic and laser scanning confocal microscopic analysis of sulfur in living sulfur-precipitating marine bacteria. *Chem. Geol.* 180, 3–18. doi: 10.1016/S0009-2541(01)00302-3
- Pfeffer, C., Larsen, S., Song, J., Dong, M., Besenbacher, F., Meyer, R. L., et al. (2012). Filamentous bacteria transport electrons over centimetre distances. *Nature* 491, 218–221. doi: 10.1038/nature11586
- Poulton, S. W., Krom, M. D., and Raiswell, R. (2004). A revised scheme for the reactivity of iron (oxyhydr)oxide minerals towards dissolved sulfide. *Geochim. Cosmochim. Acta* 68, 3703–3715. doi: 10.1016/j.gca.2004.03.012
- Preisler, A., de Beer, D., Lichtschlag, A., Lavik, G., Boetius, A., and Jørgensen, B. B. (2007). Biological and chemical sulfide oxidation in a Beggiatoa inhabited marine sediment. *ISME J.* 2007, 341–353. doi: 10.1038/ismej.2007.50
- Revsbech, N. P., and Jørgensen, B. B. (1983). Photosynthesis of benthic microflora measured with high spatial resolution by the oxygen microprofile method: capabilities and limitations of the method. *Limnol. Oceanogr.* 28, 749–756. doi: 10.4319/lo.1983.28.4.0749
- Rickard, D., and Luther, G. W. (2007). Chemistry of iron sulfides. *Chem. Rev.* 107, 514–562. doi: 10.1021/cr0503658
- Rozan, T. F., Theberge, S. M., and Luther, G. W. III. (2000). Quantifying elemental sulfur (S₀), bisulfide (HS⁻) and polysulfides (S_x2⁻) using a voltammetric method. *Anal. Chim. Acta* 415, 175–184. doi: 10.1016/S0003-2670(00)00844-8
- Scholz, F., McManus, J., and Sommer, S. (2013). The manganese and iron shuttle in a modern euxinic basin and implications for molybdenum cycling at euxinic ocean margins. *Chem. Geol.* 355, 56–68. doi: 10.1016/j.chemgeo.2013.07.006
- Schulz, H. N., and Jørgensen, B. B. (2001). Big Bacteria. *Annu. Rev. Microbiol.* 55, 105–137. doi: 10.1146/annurev.micro.55.1.105
- Schunck, H., Lavik, G., Desai, D. K., Großkopf, T., Kalvelage, T., Löscher, C. R., et al. (2013). Giant hydrogen sulfide plume in the oxygen minimum zone off Peru supports chemolithoautotrophy. *PLoS ONE* 8:e68661. doi: 10.1371/journal.pone.0068661
- Schwedt, A., Kreutzmann, A.-C., Polerecky, L., and Schulz-Vogt, H. N. (2012). Sulfur respiration in a marine chemolithotrophic Beggiatoa strain. *Front. Microbiol.* 2:276. doi: 10.3389/fmicb.2011.00276

- Seitaj, D., Schauer, R., Sulu-Gambari, F., Hidalgo-Martinez, S., Malkin, S. Y., Burdorf, L. D. W., et al. (2015). Cable bacteria generate a firewall against euxinia in seasonally hypoxic basins. *Proc. Natl. Acad. Sci. U.S.A.* 112, 13278–13283. doi: 10.1073/pnas.1510152112
- Slowey, A. J., and Marvin-Dipasquale, M. (2012). How to overcome inter-electrode variability and instability to quantify dissolved oxygen, Fe(II), Mn(II), and S(–II) in undisturbed soils and sediments using voltammetry. *Geochim. Trans.* 13:6. doi: 10.1186/1467-4866-13-6
- Soetaert, K., Petzoldt, T., and Meysman, F. (2012). *Marelac: Tools For Aquatic Sciences. R package version 2.1.2.* Available online at: <http://CRAN.R-project.org/package=marelac>
- Sohlenius, G., Sternbeck, J., Andren, E., and Westman, P. (1996). Holocene history of the Baltic Sea as recorded in a sediment core from the Gotland Deep. *Mar. Geol.* 134, 183–201. doi: 10.1016/0025-3227(96)00047-3
- Sommer, S., Clemens, D., Yücel, M., Pfannkuche, O., Hall, P., Almroth Rosell, E., et al. (2017). Major bottom water ventilation events do not significantly reduce basin-wide benthic N and P release in the Eastern Gotland Basin (Baltic Sea). *Front. Mar. Sci.* 4:18. doi: 10.3389/fmars.2017.00018
- Sommer, S., Gier, J., Treude, T., Lomnitz, U., Dengler, M., Cardich, J., et al. (2016). Depletion of oxygen, nitrate and nitrite in the Peruvian oxygen minimum zone cause an imbalance of benthic nitrogen fluxes. *Deep-Sea Res. I* 112, 113–122. doi: 10.1016/j.dsr.2016.03.001
- Sommer, S., Linke, P., Pfannkuche, O., Niemann, H., and Treude, T. (2010). Benthic respiration in a seep habitat dominated by dense beds of ampharetid polychaetes at the Hikurangi Margin (New Zealand). *Mar. Geol.* 272, 223–232. doi: 10.1016/j.margeo.2009.06.003
- Sternbeck, J., and Sohlenius, G. (1997). Authigenic sulfide and carbonate mineral formation in Holocene sediments of the Baltic Sea. *Chem. Geol.* 135, 55–73. doi: 10.1016/S0009-2541(96)00104-0
- Sun, M., Mu, Z.-X., Chen, Y.-P., Sheng, G.-P., Liu, X.-W., Chen, Y.-Z., et al. (2009). Microbe-assisted sulfide oxidation in the anode of a microbial fuel cell. *Environ. Sci. Technol.* 43, 3372–3377. doi: 10.1021/es802809m
- Taillefert, M., Luther, G. W. III, and Nuzzio, D. B. (2000). The application of electrochemical tools for *in situ* measurements in aquatic systems. *Electroanalysis* 12, 401–412. doi: 10.1002/(SICI)1521-4109(20000401)12:6<401::AID-ELAN401>3.0.CO;2-U
- Taillefert, M., Neuhuber, S., and Bristow, G. (2007). The effect of tidal forcing on biogeochemical processes in intertidal salt marsh sediments. *Geochim. Trans.* 8:6. doi: 10.1186/1467-4866-8-6
- Theberge, S. M., and Luther, G. W. (1997). Determination of the electrochemical properties of a soluble aqueous FeS cluster present in sulfidic systems. *Aquat. Geochem.* 3, 191–211. doi: 10.1023/A:1009648026806
- Vallius, H., and Kunzendorf, H. (2001). Sediment surface geochemistry of three Baltic Sea deep basins. *AMBIO* 30, 135–141. doi: 10.1579/0044-7447-30.3.135
- Wenzhöfer, F., Holby, O., Glud, R. N., Nielsen, H. K., and Gundersen, J. K. (2000). *In situ* microsensor studies of a shallow water hydrothermal vent at Milos, Greece. *Mar. Chem.* 69, 43–54. doi: 10.1016/S0304-4203(99)00091-2
- Winogradow, A., and Pempkowiak, J. (2014). Organic carbon burial rates in the Baltic Sea sediments. *Estuarine Coast. Shelf Sci.* 138, 27–36. doi: 10.1016/j.ecss.2013.12.001
- Yücel, M. (2013). Down the thermodynamic ladder: a comparative study of marine redox gradients across diverse sedimentary environments. *Estuarine Coast. Shelf Sci.* 131, 83–92. doi: 10.1016/j.ecss.2013.07.013
- Yücel, M., Luther, G. W., and Moore, W. S. (2010). Earthquake-induced turbidite deposition as a previously unrecognized sink for hydrogen sulfide in the Black Sea sediments. *Mar. Chem.* 121, 176–186. doi: 10.1016/j.marchem.2010.04.006
- Zillen, L., Conley, D. J., Andren, T., Andren, E., and Björck, S. (2008). Past occurrences of hypoxia in the Baltic Sea and the role of climate variability, environmental change and human impact. *Earth-Sci. Rev.* 91, 77–92. doi: 10.1016/j.earscirev.2008.10.001
- Zopfi, J., Böttcher, M. E., and Jørgensen, B. B. (2008). Biogeochemistry of sulfur and iron in *Thioploca*-colonized surface sediments in the upwelling area off central Chile. *Geochim. Cosmochim. Acta* 72, 827–843. doi: 10.1016/j.gca.2007.11.031

Conflict of Interest Statement: The authors declare that the research was conducted in the absence of any commercial or financial relationships that could be construed as a potential conflict of interest.

Copyright © 2017 Yücel, Sommer, Dale and Pfannkuche. This is an open-access article distributed under the terms of the Creative Commons Attribution License (CC BY). The use, distribution or reproduction in other forums is permitted, provided the original author(s) or licensor are credited and that the original publication in this journal is cited, in accordance with accepted academic practice. No use, distribution or reproduction is permitted which does not comply with these terms.



Electron Transfer between Electrically Conductive Minerals and Quinones

Olga Taran ^{*}

Department of Chemistry, Emory University, Atlanta, GA, United States

Long-distance electron transfer in marine environments couples physically separated redox half-reactions, impacting biogeochemical cycles of iron, sulfur and carbon. Bacterial bio-electrochemical systems that facilitate electron transfer via conductive filaments or across man-made electrodes are well-known, but the impact of abiotic currents across naturally occurring conductive and semiconductive minerals is poorly understood. In this paper I use cyclic voltammetry to explore electron transfer between electrodes made of common iron minerals (magnetite, hematite, pyrite, pyrrhotite, mackinawite, and greigite), and hydroquinones—a class of organic molecules found in carbon-rich sediments. Of all tested minerals, only pyrite and magnetite showed an increase in electric current in the presence of organic molecules, with pyrite showing excellent electrocatalytic performance. Pyrite electrodes performed better than commercially available glassy carbon electrodes and showed higher peak currents, lower overpotential values and a smaller separation between oxidation and reduction peaks for each tested quinone. Hydroquinone oxidation on pyrite surfaces was reversible, diffusion controlled, and stable over a large number of potential cycles. Given the ubiquity of both pyrite and quinones, abiotic electron transfer between minerals and organic molecules is likely widespread in Nature and may contribute to several different phenomena, including anaerobic respiration of a wide variety of microorganisms in temporally anoxic zones or in the proximity of hydrothermal vent chimneys, as well as quinone cycling and the propagation of anoxic zones in organic rich waters. Finally, interactions between pyrite and quinones make use of electrochemical gradients that have been suggested as an important source of energy for the origins of life on Earth. Ubiquinones and iron sulfide clusters are common redox cofactors found in electron transport chains across all domains of life and interactions between quinones and pyrite might have been an early analog of these ubiquitous systems.

OPEN ACCESS

Edited by:

Alysa Danielle Cox,
Montana Tech of the University of
Montana, United States

Reviewed by:

Mustafa Yucel,
Middle East Technical University,
Turkey

Amy Gartman,
United States Geological Survey,
United States

***Correspondence:**

Olga Taran
otarani@emory.edu

Specialty section:

This article was submitted to
Microbiological Chemistry and
Geomicrobiology,
a section of the journal
Frontiers in Chemistry

Received: 15 November 2016

Accepted: 21 June 2017

Published: 13 July 2017

Citation:

Taran O (2017) Electron Transfer
between Electrically Conductive
Minerals and Quinones.
Front. Chem. 5:49.
doi: 10.3389/fchem.2017.00049

INTRODUCTION

Sources of electrochemical energy are widespread in Nature, including hydrothermal gradients, corrosion of metal-rich rocks and minerals, concentration gradients of redox active species, and streaming currents caused by the flow of electrolyte solutions thorough porous media. Only recently, however, we began to realize that this energy is also widely used by Nature in both

biological and abiotic processes (Nakamura et al., 2010b; Revil et al., 2010) and that electrochemical redox reactions are important contributors to biogeochemical cycles (Nielsen and Risgaard-Petersen, 2015). The passage of electric currents through conductive minerals has been long-appreciated (Wells, 1914), and has gained a renewed interest due to its relevance to the biochemistry of hydrothermal vent systems and the origin of life (Karato and Wang, 2013; Malvankar et al., 2014; Yamamoto et al., 2017). Most of the redox processes across electrochemical gradients were previously associated with bacterial activity (Müller et al., 2016; Malkin et al., 2017) or human-made devices (Du et al., 2007). A detailed understanding of the extent and mechanisms of abiotic electron flows can complement our understanding of natural electrochemical systems and will be important for more accurate modeling of global biogeochemical cycles.

Many oxide and sulfide minerals are electrical conductors or semiconductors, with resistivity varying from 0.1 to $10^5 \Omega \times m$ (Karato and Wang, 2013), capable of conducting electrons over centimeter-long distances between environments of different redox potentials (Nakamura et al., 2010a; Nielsen et al., 2010). Conceivably, electrical currents transported through conductive minerals could couple chemical and biochemical reactions in physically separated environments, form natural “fuel cells” and provide the energy necessary to maintain rich biological communities on the border of oxic and anoxic zones (Jelen et al., 2016).

The efficiency of electrochemical reactions depends not only on the magnitude of an applied redox potential, but also on the properties of the electrode. In general, a good electrode must be electrically conductive, chemically stable under selected conditions and provide a catalytically active surface for the reagents. There is a growing interest in using sustainable mineral electrodes for chemical reactions (Konkena et al., 2016) and a growing awareness of the contribution of electrochemistry to natural processes (Nielsen and Risgaard-Petersen, 2015). This study was restricted to electrochemistry of common iron oxides and sulfides assuming that due to their abundance they will dominate electron flow across different geochemical settings. Iron sulfides have been used as electrodes for electrochemical CO_2 reduction in systems that simulate chemistry of hydrothermal vents related to the origin of life (Herschy et al., 2014; Yamaguchi et al., 2014; Roldan et al., 2015), while iron oxides have been extensively studied as terminal electron acceptors for bacterial respiration (Orsetti et al., 2013).

While filamentous and cable bacteria use electrochemical energy directly (Aklujkar et al., 2009; Seitaj et al., 2015), a wide range of bacteria are known to exchange electrons indirectly, using external electron mediators such as water-soluble flavines (Marsili et al., 2008), quinones (Newman and Kolter, 2000; Qiao et al., 2008) or, quinone-rich humic acid substances (Cervantes et al., 2000; Klüpfel et al., 2014). The addition of external quinones to microbial communities modifies interactions between microbes (Scheller et al., 2016) and changes the mode of respiration in bacteria (Cervantes et al., 2000). Interactions between organic mediators and conductive minerals may contribute to the overall flow of energy that

defines biogeochemical cycles, being especially important in the environments where oxygen and solar radiation are absent (D'Hondt et al., 2004; Borch et al., 2010).

As model organic molecules, I selected quinones (Q) and their reduced form, hydroquinones (H_2Q), which are key electron mediators across all domains of life (Soballe and Poole, 1999) (Figure 1). Quinones are found everywhere from interstellar clouds (Bernstein, 2006) to environmental pollutants (Mousset et al., 2016). Selection of the quinones for the study broadly represented different environmental roles that these molecules have: **1** is the simplest known hydroquinone molecule and often used for model studies of quinone-mineral interactions (Uchimiya and Stone, 2006; Klüpfel et al., 2014), **2** is 2-methoxyhydroquinone, a common component on non-soluble organic matter and a plant messenger molecule (Lynn and Chang, 1990; Yuan et al., 2016), while **3** is an oxidation product of polycyclic aromatic hydrocarbons and is both a common pollutant and a likely component of prebiotic mixtures of organic molecules delivered by comets and meteorites to early Earth (Chyba and Sagan, 1992; Bernstein et al., 1999).

Electrochemical techniques are often used to study the participation of organic molecules in redox processes of redox active clays and minerals (O'Loughlin, 2008; Sander et al., 2015). Here cyclic voltammetry (CV) was used to detect hydroquinone oxidation on the surface of electrodes made from common iron oxides and sulfides. CV is an analytical technique used to monitor trace metals in marine sediments, where an increase in current is observed when a redox process takes place on the electrode's surface at a specific applied redox potential (Luther et al., 2008; Moore et al., 2009).

Differentiating the chemical contribution of electron redox cycling from usually observed microbial redox activity would improve our understanding of global biogeochemical carbon cycles. Electron transfer between conductive minerals and soluble organics can potentially generate out-of-equilibrium systems that impact environments dependent on the abiotic redox gradients, such as microbial communities around hydrothermal vent chimneys and in anoxic marine sediments (Hedrick and White, 1986; Unden and Bongaerts, 1997; Kim et al., 2012). Quinone redox cycling can affect distribution of redox active species in water columns (Nielsen et al., 2010; Nielsen, 2016) and natural bioremediation of organic molecules (Jiang et al., 2015). Finally, redox gradients have been long considered important energy source for the origin of life (Martin et al., 2008), and a mechanism of transferring energy stored in redox gradients into chemical reactions is an important step toward better understanding processes that may lead to life on Earth and other planets.

MATERIALS AND METHODS

The reactivity between the mineral and redox species in solution depends on the amount of energy available in the system and the electrocatalytic properties of mineral surfaces. Overall, the energy available in the redox system depends on redox potential as defined by equation (1):

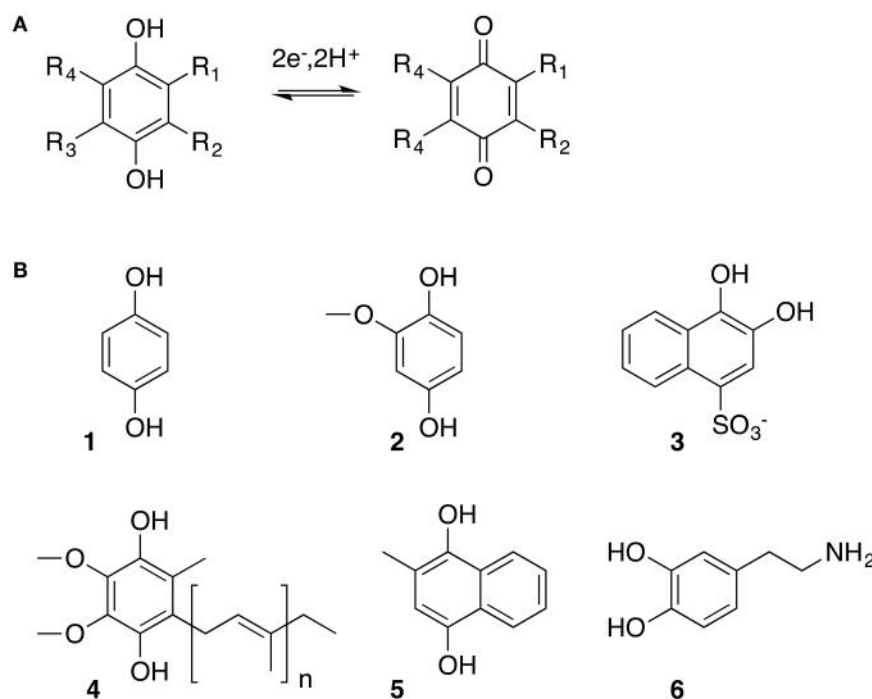


FIGURE 1 | Quinone molecules are important universal electrochemical mediators: **(A)** Reversible two electron two proton redox reaction between hydroquinone (reduced) and benzoquinone (oxidized) forms; **(B)** Example of naturally occurring quinones : **1**, p-benzoquinone (BQ), simplest quinone molecule; **2**, methoxy-p-benzoquinone (MBQ), component of humic acid mixtures; **3**, 1,2-naphthohydroxyquinone-4-sulfonate (NQ), oxidation product of polyaromatic hydrocarbons, pollutant; **4**, ubiquinone, a redox cofactor, part of electron transfer chain in living cells; **5**, menadione, extracellular mediator used in bacterial respiration; **6**, dopamine, neurotransmitter.

$$\Delta G = -nEF \quad (1)$$

E is a measurable potential difference between reacting molecules, described by the Nernst equation:

$$E = E^\circ + \frac{RT}{nF} \ln \left(\frac{[Ox]}{[Red]} \right) \quad (2)$$

Here E° is a standard redox potential of the redox reaction of interest, n is the number of electrons transferred in the reaction, T is the absolute temperature in K, and R and F are the gas and Faraday constants respectively. Naturally occurring sustained redox potentials vary from 0.2 V for marine sediments (Komada et al., 2004), 0.4 to 0.7 V for hydrothermal vents (Nakamura et al., 2010b; Ryckelynck et al., 2012) and up to 1.2 V for sulfide-rich mineral deposits (Kruger and Lacy, 1949). The naturally plausible range of redox potentials in aqueous systems is defined by the chemistry of iron and manganese, spreading from 0.7 V to -0.3 V [against a standard hydrogen electrode (SHE)] at pH 7 (Baas Becking et al., 1960). Here Ag/AgCl electrodes were used as a reference ($+0.22$ V redox potential compared to SHE), with the -0.5 to 0.5 V (Ag/AgCl) window used here broadly corresponding to the naturally occurring potential range available for redox reactions of quinone molecules.

Materials

Pyrite, pyrrhotite, magnetite, and hematite minerals were received from Harvard Natural History Museum. Mackinawite and greigite were synthesized by previously described methods (Lennie et al., 1995; Dekkers et al., 2000) and characterized by XRD (See Supplementary Information). Quinones (1–3) were bought from Sigma-Aldrich (USA) and used without further purification.

Several electrode designs were tested for the study and the most reproducible data were obtained with powder electrodes described by Almeida and Giannetti (2002). Approximately 1 g of mineral was powdered with mortar and pestle for 10 min. Powdered minerals were washed several times with acetone and dried in airflow. A mixture of 2 g of paraffin and 1 g of carbon powder were heated to 70°C and a tip of a graphite rod with 5 mm diameter was immersed into the hot mixture and then pressed against mineral powder. The lateral part of the rod was covered with Teflon tape to avoid exposure to solution.

Cyclic Voltammetry

The fundamentals of CV can be found elsewhere (Compton et al., 2014), but briefly, if a molecule is oxidized or reduced on the surface of the electrode, a change of current is registered. Analysis of the change in electrical current as a function of an applied redox potential provides information about the mechanism of the reaction.

Three-electrode arrays consisted of a Ag/AgCl reference electrode, Pt-wire counter electrode (both from CH Instruments Inc., Austin, TX, USA) and homemade working electrodes made of different minerals (see above). All potentials were compared to the Ag/AgCl reference electrode (1M KCl solution, E + 0.22 V vs. SHE). Reactions were performed in 0.1 M phosphate buffer pH 7.0 in the presence of 0.4 M KCl as an electrolyte. Unless stated otherwise, all experiments were performed under an argon atmosphere. Sample solutions were purged with nitrogen for at least 10 min at the beginning of the measurements and measurements were performed with slow nitrogen bubbling through solution. To study the effect of oxygen, air was purged through the solution for 5 min, and measurements were performed in a vial open to the air with vigorous stirring between measurements. A BAS CV-50 W Voltammetric Analyzer (BASI, West Lafayette, IN, USA) was used to perform the measurements, with each measurement reproduced at least 3 times with 3 different electrode replicas for every mineral. Electrode stability was calculated by linear sweep voltammetry with a 5 mV/s scan rate, and initial activity screening was produced with 10 mM solution of the molecule of interest with a 100 mV/s scan rate. For the pH variation experiments, a modified Britton-Robinson buffer (citrate-phosphate-borate-glycine) was used. Reactions started at pH 2 and were titrated with concentrated solution of NaOH to pH 12, with pH measured *in situ* with Toledo potentiostat (Mettler Toledo, Columbus, OH, USA) and pH electrode (Hanna Instruments, Woonsocket, RI, USA) before each measurement.

Mineral Stability Estimations

The range of thermodynamic stability of the minerals used in the discussion was calculated with HSC-7 software package (<http://www.hsc-chemistry.com>) using species concentrations found in modern ocean: $[Fe]_T$ 5.0×10^{-10} M, $[S]_T$ 2.8×10^{-2} M (Rijkenberg et al., 2014) and concentrations estimated to be found in Haedean and Archean oceans: $[Fe]_T$ 2.0×10^{-4} M, $[S]_T$ $2.0 \times$

10^{-7} M (Crowe et al., 2014). See a diagram in Supporting Information.

RESULTS

Mineral Electrode Stability

The stability of the selected naturally occurring minerals was evaluated by linear sweep voltammetry. The voltage applied to the electrode was slowly increased (5 mV/s) from -500 to 500 mV (vs. Ag/AgCl) and the current between the mineral and platinum working electrodes registered (Figure 2). The minimum value of each plot corresponds to the resting potential of the mineral, when oxidation and reduction processes on the surface are at equilibrium. The value on the abscissa axis is proportional to the number of electrons exchanged with solution and the overall redox stability of the sample. Minerals are reduced at more negative potentials and oxidized at more positive potentials than the minimum. In the potential range corresponding to oxidation, mineral surfaces are rich in electrons and are poor electron acceptors. Reduced metal sulfides greigite and mackinawite were less stable in solution than the iron oxides magnetite and hematite, while pyrite and pyrrhotite had intermediate stability values (Figure 2). Curves of the $\log |i|$ vs. E were asymmetric in the case of reduced iron sulfides, suggesting irreversible oxidation of these minerals. Iron oxides hematite and magnetite showed very low current values consistent with oxide dissolution inhibited in the presence of phosphate ions from the buffer (Biber et al., 1994).

When cyclic voltammetry was performed in air-saturated solutions, the presence of oxygen did not change the performance of the metal oxide electrodes (data not shown). In the case of pyrite, dramatic increases in the registered current was observed in the presence of oxygen, showing fast deterioration of the surface due to an oxygen-assisted cathodic iron dissolution pathway where oxygen oxidizes water soluble Fe(II) species into redox active Fe(III) species that catalyze the rate of pyrite oxidation (Rimstidt and Vaughan, 2003; Chandra and Gerson,

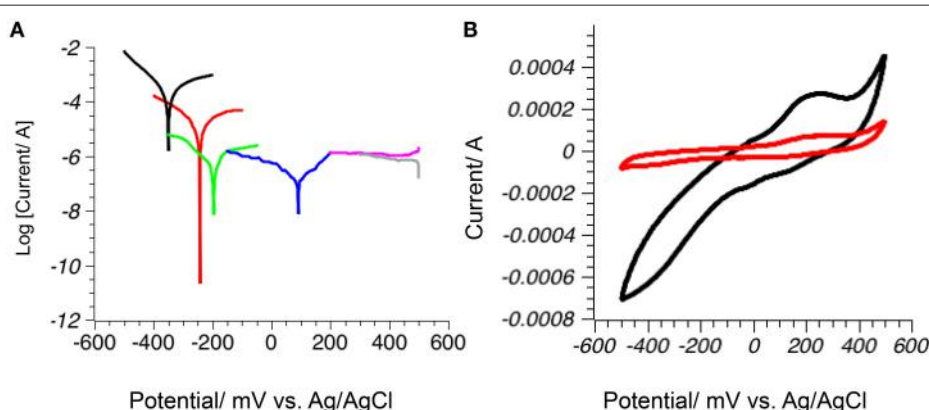


FIGURE 2 | Stability of the mineral electrodes in water: **(A)** Tafel plot ($\log |i|$ vs. Potential) for mineral electrodes in phosphate buffer pH 7: mackinawite (black), greigite (red), pyrrhotite (green), pyrite (blue), magnetite (gray) and hematite (magenta); graph minimum corresponds to rest potential where oxidation and reduction reactions are at equilibrium; **(B)** Pyrite electrode is stable in anoxic atmosphere (red), but deteriorates in the presence of oxygen (black).

2010). This process was reversed when oxygen was removed from the system (**Figure 2**).

As shown in **Figure 3**, the electrodes made of pyrrhotite, mackinawite and synthetic greigite reacted with water (black lines, all graphs). Greigite electrodes showed reversible redox process with an oxidation anodic peak at -190 mV and the corresponding reduction cathodic wave peak at -390 mV. The reversible nature of this process indicates that the electrode material was not dissolved during the scan. The peaks correspond to the reversible $\text{Fe}^{2+}/\text{Fe}^{3+}$ oxidation on the surface of the electrode (Benning et al., 2000). The pyrrhotite electrode showed two large cathodic waves at -160 and -385 mV, potentially corresponding to stepwise dissolution of polysulfur chains to sulfite ions with partial re-incorporation of the sulfur to the electrode surface during the anodic scan at -101 and 118 mV (Mikhlin, 2000). In contrast, pyrite and the metal oxides

hematite and magnetite were stable under these experimental conditions.

Electrode Interactions with Quinones

With the electrochemistry of the electrodes defined, the reduced quinones (**1–3**) were included in the measurements. While reversible oxidation and reduction waves were expected, **Figure 3** shows that only pyrite, and partially magnetite, reacted with all quinones, and there was no detectable current change on the surfaces of more reduced iron sulfides. While there was no change in electrocatalytic behavior of mackinawite with methoxyquinone **2**, the presence of more oxidizing species **1** and **3** lead to dramatic drop of electrical current over all potential range, probably due to chemical oxidation of the exposed surface. Small increases in both cathodic (reducing, negative) and anodic (oxidizing, positive) currents were detected on the surface of

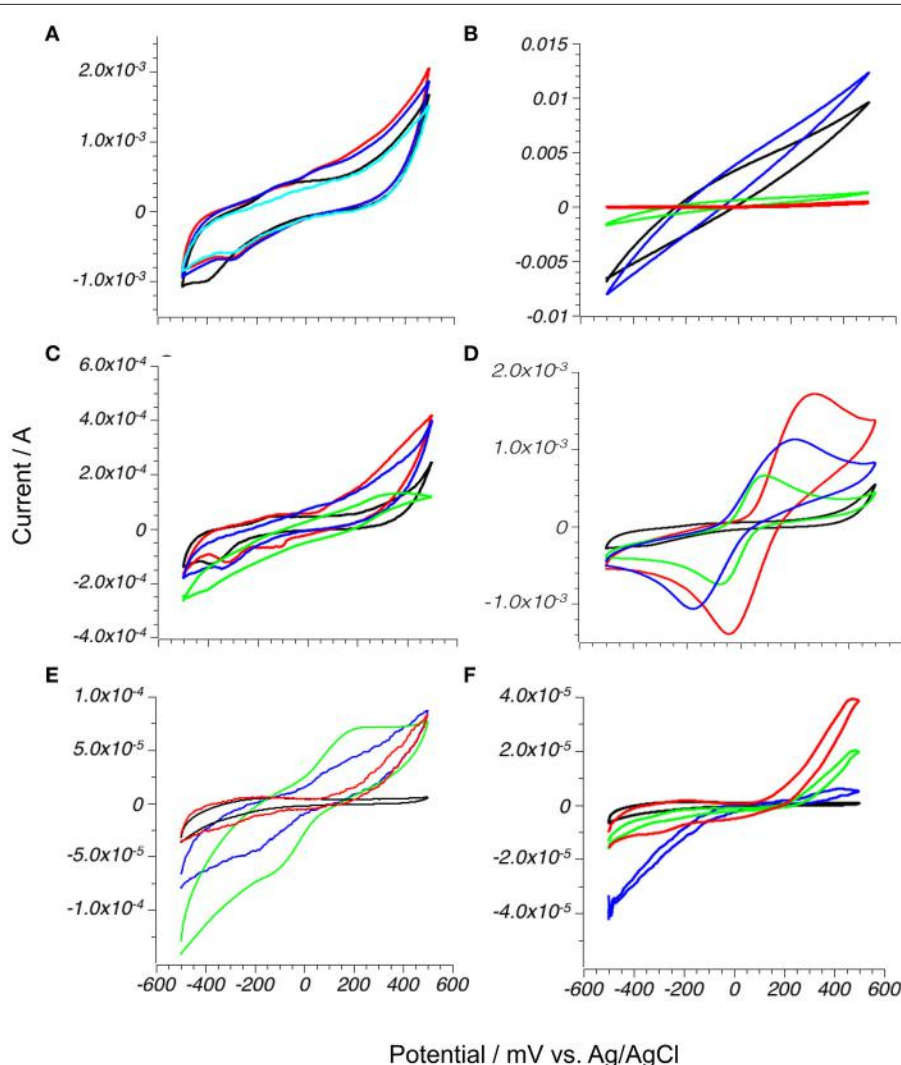


FIGURE 3 | H_2Q oxidation on mineral electrodes in anoxic environment: **1** (red), methoxy-hydroquinone **2** (blue), 1,2-hydroxynaphthoquinone-4sulfonic acid **3** (green) compared to phosphate buffer (black); **(A)** Greigite; **(B)** Mackinawite; **(C)** Pyrrhotite; **(D)** Pyrite; **(E)** Magnetite; **(F)** Hematite. All experiments are done in phosphate buffer pH 7.0 in the presence of 10 mM hydroquinones and 50 mV/s scan rate.

TABLE 1 | Summary of hydroquinone redox reactions on different mineral surfaces.

Electrode	Hydroquinone		Methoxyhydroquinone		Naphthoquinone	
	E_a (mV)/ i_a (mA)	E_c (mV)/ i_c (mA)	E_a (mV)/ i_a (mA)	E_c (mV)/ i_c (mA)	E_a (mV)/ i_a (mA)	E_c (mV)/ i_c (mA)
Pyrite	251	−3	284	−185	83	−83
	0.76	−0.48	1.12	−1.07	0.70	−0.75
Magnetite			119	−197	239	−137
			0.033	−0.045	0.07	−0.07
Glassy carbon	365	−89	306	−168	252	−145
	0.14	−0.088	0.22	−0.15	0.062	0.099

the hematite electrode, however the current never reached a maximum value, indicating that at the applied potential values, the equilibrium was shifted toward reduced hydroquinones.

Pyrite and Magnetite Electrodes

The mechanisms of redox reactions on pyrite and magnetite surfaces were then studied in more detail. As shown in **Table 1**, the electrocatalytic properties of pyrite and magnetite electrodes were tested in hydroquinone solutions of 10 mM concentration in phosphate buffer under nitrogen. The pyrite electrodes showed lower potential values of oxidation waves and higher (more positive) reduction waves for all quinones compared to magnetite, and, surprisingly, performed better than standard commercially available glassy carbon electrode. This indicates that the reaction of quinone on pyrite is more thermodynamically favorable than on other minerals. The measured value of the peak electric current (see **Table 1**) is the number of electrons flowing through electrode surface per unit of time. The current is proportional to the area of the electrode and the equilibrium constant of oxidation-reduction reaction on the electrode surface. Both mineral electrodes were composed of small particles of different sizes that contributed to roughness of the electrode, but this parameter does not significantly affect current and potential measurements (Menshykau et al., 2008). Areas of pyrite and magnetite mineral electrodes can be approximated to the geometric area covered by mineral particles, and currents registered at both electrodes under identical experimental conditions can be directly compared. Cathodic and anodic currents on pyrite electrodes were 10 to 30 times higher than on magnetite and more than 100 times higher than on hematite electrodes, suggesting that quinones were oxidized and reduced faster on pyrite than on other minerals.

The difference between the peaks corresponding to oxidation and reduction was larger than the theoretical limit of $0.059/n$ expected for a fully reversible reaction. Larger separation between peaks seems to support a stepwise oxidation mechanism where hydroquinone is oxidized via one electron step to semiquinone, which is then rapidly oxidized to benzoquinone (Uchimiya and Stone, 2006). For pyrite, the ratio between the oxidation and reduction current peaks was 0.63 for **1**, 0.95 for **2** and 0.93 for **3**, instead of 1.0 as would be expected for fully reversible processes. On pyrite surfaces, reduction occurred at lower rates than oxidation for benzoquinone **1**, probably because of the formation of poorly soluble hydroquinone-benzoquinone complex that

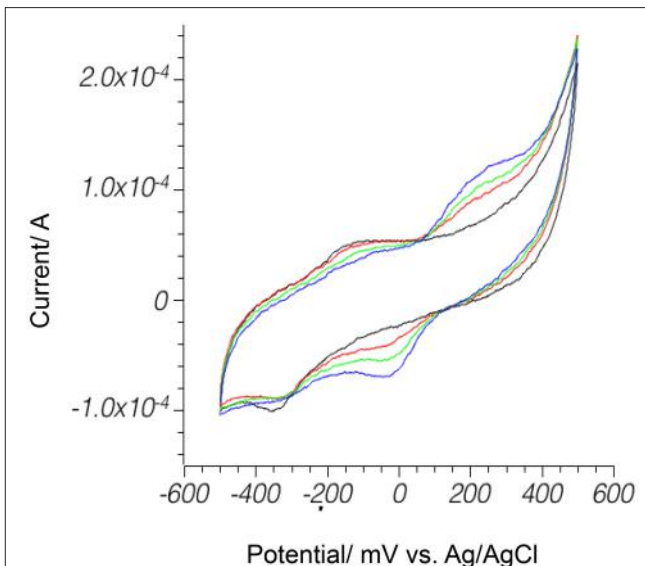


FIGURE 4 | Hydroquinone **1** oxidation on pyrite electrode in anoxic environment. Phosphate buffer pH 7.0, 50 mV/s scan rate. Black: bare pyrite; red: 0.2 mM H_2Q ; green: 0.4 mM H_2Q ; blue: 0.6 mM H_2Q .

interfered with the reaction. In case of **2** and **3**, redox reactions were close to being reversible in both directions.

Concentrations of quinone used for initial screening were much higher than the naturally occurring range of these molecules, which is usually from 0.02 to 1 mM (Uchimiya and Stone, 2006; Marsili et al., 2008). Only pyrite showed an increase in current in the naturally occurring concentration range (**Figure 4**), and further studies were limited to electrochemistry of pyrite in the presence of 1 mM or less of hydroquinones.

Mechanism of Hydroquinones Oxidation of Pyrite Electrode

On the electrode surface molecules may be oxidized by diffusion or adsorption-controlled mechanisms. To distinguish between the two, the potential scan rate was gradually increased from 10 to 1,000 mV/s (**Figure 5**), and this change caused an increase in peak current. In diffusion-controlled processes, current rise is proportional to the square root of the scan speed, while in adsorption-controlled processes, the current rise is directly proportional to the speed of the scan (Batchelor-McAuley et al.,

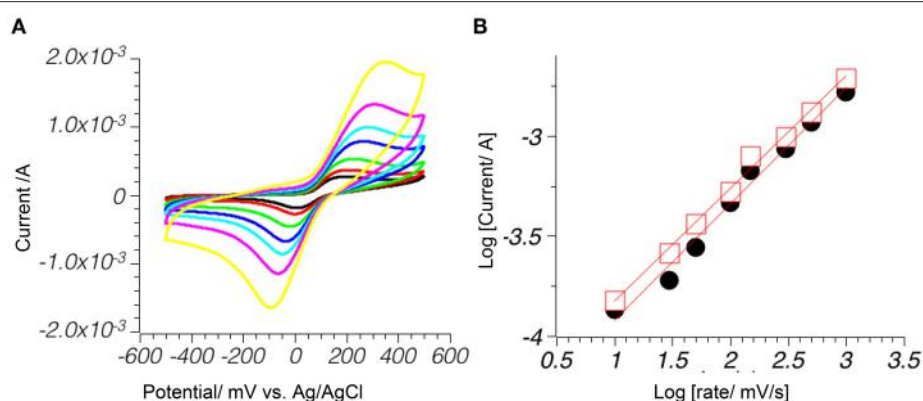


FIGURE 5 | Current rise with the increase of the scan speed indicated a diffusion controlled mechanism. 1mM **1** phosphate buffer pH 7.0. **(A)** Successive scans with (from lowest to highest) 10, 50, 100, 150, 200, 300, 500, and 1,000 mV/s; **(B)** A log/log plot of change in peak current for absolute value of cathodic (black) and anodic (red) peaks vs. change in scan rate.

2010). A mixture of both mechanisms is possible in real systems. To distinguish between both processes, $\log|i_p|$ (where $|i_p|$ is an absolute peak current value), was plotted against $\log(v)$ (where v is the scan rate in mV/s) (Gupta et al., 2012). The results showed a small contribution from the adsorption-controlled pathway in the case of unsubstituted hydroquinone **1** on pyrite surfaces, with the slope of 0.56 ($R^2 = 0.994$) for the cathodic peak and 0.58 ($R^2 = 0.985$) for the anodic peak, however slopes for **2** are 0.43 ($R^2 = 0.999$) and 0.45 ($R^2 = 0.996$) for pyrite electrode and 0.35 ($R^2 = 0.987$) and 0.42 ($R^2 = 0.992$) for **3** on magnetite electrode, showed that both processes were fully diffusion-controlled.

Variation of the redox potential with pH showed peak shifting to more reducing potentials with the increase of pH, indicating that both protons were involved in the redox process (Figure 6). Hydroquinone **1** has a pKa of 10.3, and below this pH the hydroquinone is mostly present in its diprotonated form (H_2Q). The H_2Q can be oxidized to benzoquinone (Q) or to semiquinone (Q^-), which has pKa 4.3 and is deprotonated in the studied region (Quan et al., 2007) (Figure 1). The mechanism of the first oxidation involves two electrons and two protons, while the second is a one-electron two-proton process. The change in peak potential against pH was linear in the pH range 4 to 10 with the slope of -0.064 ($R^2 = 0.990$) for anodic current and -0.058 ($R^2 = 0.995$) for cathodic current. This value is close to -0.059 , corresponding to a process where an equal number of protons and electrons are exchanged, suggesting that the process occurred via two-proton two-electron oxidation. The electrochemical oxidation of quinones on mineral surfaces has a different mechanism than quinone oxidations in solution, where hydroquinones are usually oxidized in two one-electron oxidations via a semiquinone radical intermediate.

Electrode Stability

Stability of the electrodes under an argon atmosphere was tested over 100 cycles on pyrite electrodes with hydroquinone **2**. Small shifts from 200 to 210 mV for the oxidation peak and from -160 to -168 mV for the reduction peak were observed along with

small increases (from -0.47 to -0.49 mA) in reduction current (Figure 7). Both observations are consistent with changes in electrode performance due to partial adsorption of the quinone to the surface, but the change is not significant and pyrite minerals potentially can exchange electrons with organic mediators over prolonged periods of time.

DISCUSSION

This work shows that long distance electron transfer can be coupled to abiotic organic redox reactions. To simulate processes occurring in the environments where electrochemical gradients are present, reactions on electrode surfaces made of common minerals were studied at the potential range of -500 to 500 V (vs. Ag/AgCl) expected to be found in natural environments (Baas Becking et al., 1960). Electrodes made of reduced metal sulfides are chemically unstable under the selected conditions and cannot transfer electrons to model organic molecules hydroquinones. This result is surprising: Reduced iron sulfides are usually considered to be the major catalyst of biogeochemical processes in hydrothermal vents (e.g., White et al., 2015). Observed small rises of current on the surface of metal oxides hematite and magnetite are consistent with the observation of very small effect of quinones on chemical dissolution of Fe(III) oxides (O'Loughlin, 2008). In contrast with other studied minerals, pyrite showed a significant current rise in the presence of low concentrations of quinones (0.2–1 mM), within ranges of concentration of organic matter in natural waters (Uchimiya and Stone, 2009). Electrical currents on pyrite surfaces are at least an order of magnitude higher than the maximum oxidation and reduction peak currents on other minerals, and occur at lower redox potentials, suggesting that the electron transfer between quinones and pyrite is a very efficient process that can dominate electrochemistry in natural environments.

The redox stability of pyrite in the presence of quinones can result in long term quinone cycling driven by potential differences between oxic and anoxic zones. Given the ubiquity of

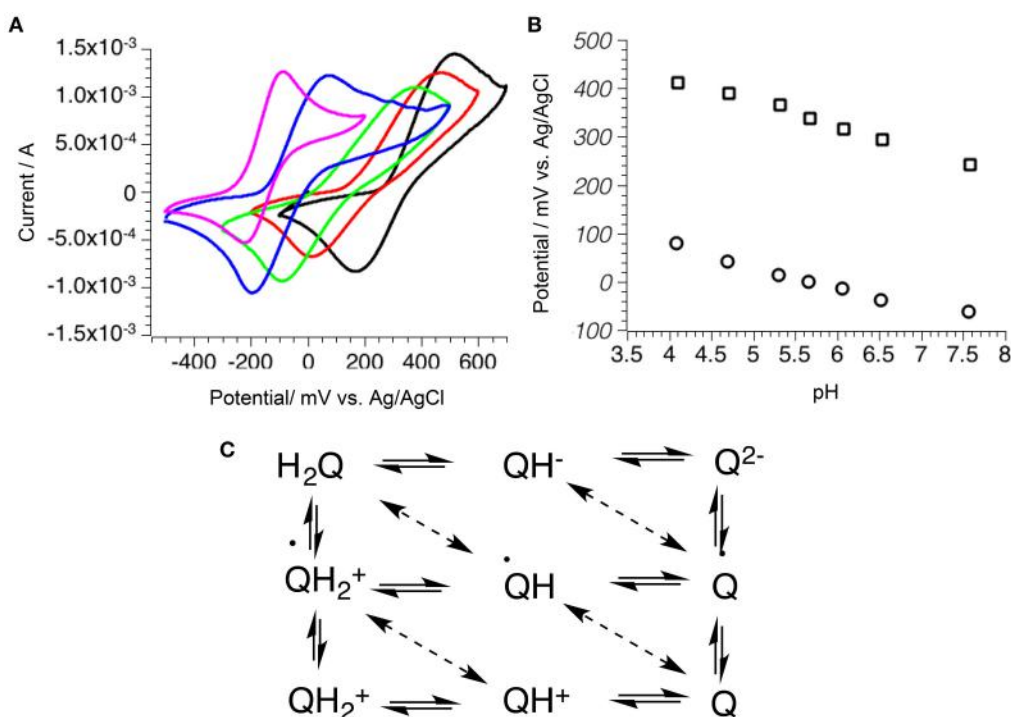


FIGURE 6 | Mechanism of hydroquinone 1 oxidation of pyrite electrode as a function of pH. **(A)** Scan samples at different pH: 2.5 (black), 5.1 (red), 6.7 (green), 9.5 (blue), 11.8 (magenta); **(B)** Decrease of maximum potential peak with increase of pH for anodic (square) and cathodic (circle) peaks; **(C)** General diagram of quinone oxidation mechanism.

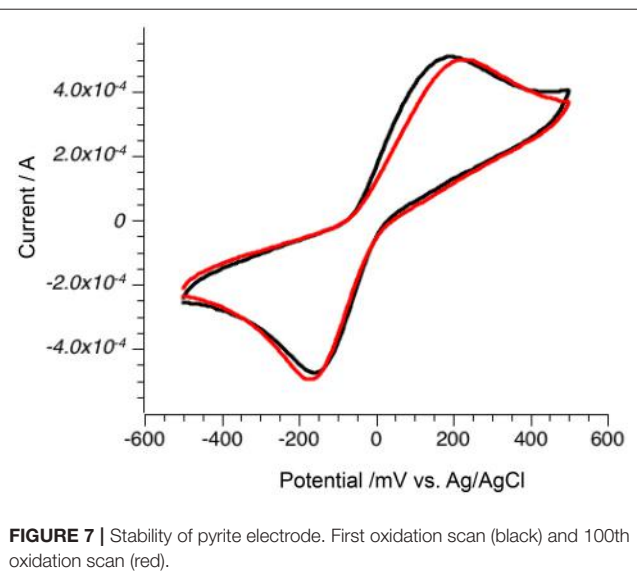


FIGURE 7 | Stability of pyrite electrode. First oxidation scan (black) and 100th oxidation scan (red).

both pyrite (Vokes, 1993) and quinones (Scott et al., 1998), the out-of-equilibrium system generated by their interactions may have multiple impacts on the environment.

It has been shown recently that cable bacteria can form millimeter-long conductive filaments that couple sulfide oxidation in anoxic sediments with oxygen reduction in

the oxygen-rich areas (Müller et al., 2016). Given that electrical current through conductive minerals can be coupled to hydroquinone oxidation, and that quinones are common external electron mediators used by a wide variety of bacteria (Hedrick and White, 1986), it is possible that other microorganisms apart from cable bacteria may also participate in biogeochemical processes involving long distance electron transfer. In this case our current models underestimate the role of abiotic electron transfer across the sediments (Seitaj et al., 2015) (**Figure 8A**).

Many naturally occurring hydroquinones are readily oxidized by dissolved oxygen to quinones. Continuous electrochemical reduction of the quinones back to the hydroquinones in the oxygen-rich areas may increase the ratio of quinone cycling and result in accelerated oxygen depletion of the solution (O'Brien, 1991) as well as abiotic generation of high local concentrations of hydrogen peroxide (Roginsky and Barsukova, 2000) (**Figure 8A**). It is possible that quinone cycling coupled to the long-range electron transfer is a complex reaction-diffusion system that can contribute to sharp seasonal oxygen variations.

Finally, hydrothermal vents and other naturally occurring zones where electrochemical gradients are found have long been considered as out-of-equilibrium systems relevant to the origins of life due to an apparent similarity between biological and geological electrochemical gradients (Martin and Russell, 2003; Amend and McCollom, 2009; Nitschke and Russell, 2009).

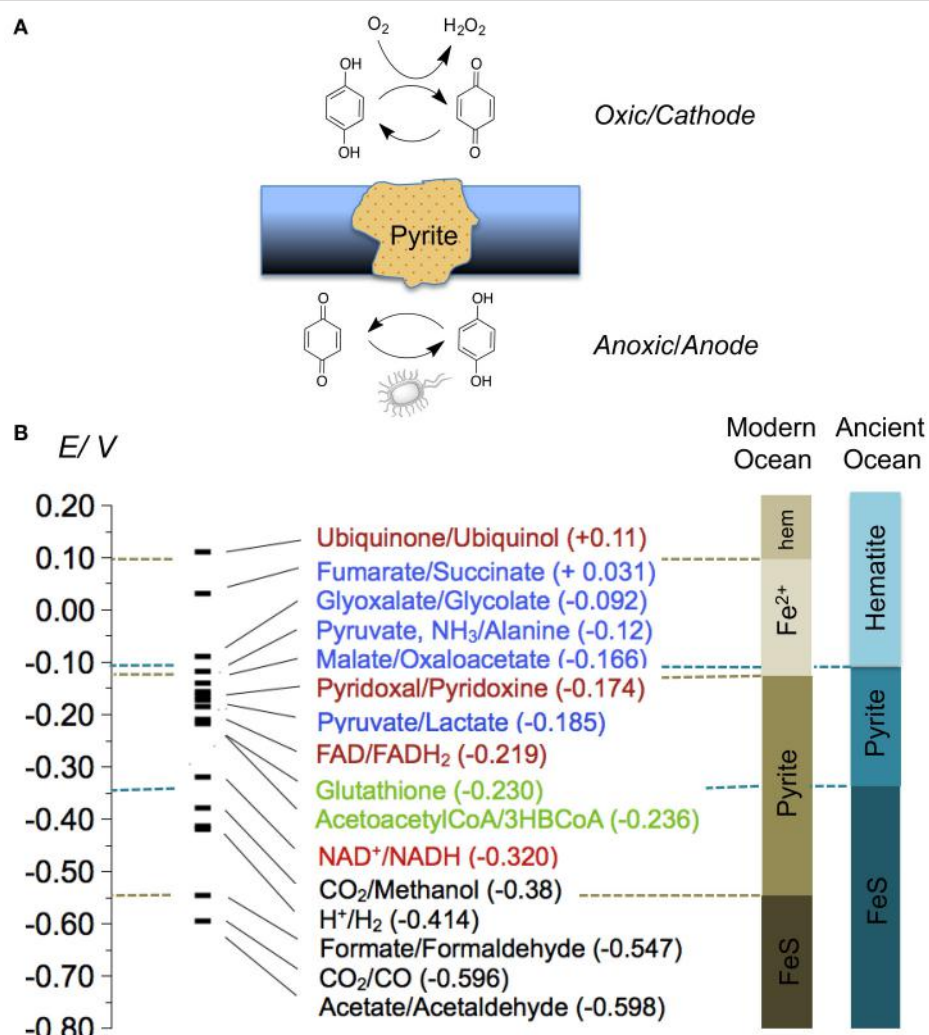


FIGURE 8 | (A) Quinone cycling maintained by pyrite in the presence of a redox gradient; above: reduction of the quinone at the cathodic surface of pyrite leads to increased quinone cycling, ROS production, and oxygen consumption; below: hydroquinone reduction at the anodic surface of pyrite generates external electron acceptors for microbial respiration; **(B)** Redox potentials (25°C , pH 7.0, vs. SHE) of biochemical reactions relevant to the origin of life, compared to the electrochemical stability regions of iron minerals in modern and ancient seawater ($[\text{Fe}]_{\text{T}} 0.5 \times 10^{-9}\text{M}$, $[\text{S}]_{\text{T}} 2.8 \times 10^{-2}\text{M}$, and $2 \times 10^{-4}\text{ M}$ and $2 \times 10^{-7}\text{ M}$, respectively); colors are used to indicate different biochemical roles of the molecules: redox cofactors (red), thiols and thioesters (green), primary metabolites (blue), and terminal electron acceptors (black); “hem” is hematite.

In general the hydrothermal vent scenarios of the origins of life suggest that reduced metal sulfides were the precursors to the biological iron-sulfur redox cofactors and the catalysts of prebiotic reactions. The exact nature of the metal sulfide catalysts as well as the range of the relevant prebiotic reactions remains a matter of debate (Orgel, 2008; Wächtershäuser, 2016).

In Wächtershäuser’s “pyrite pulled metabolism,” a model proposed almost 30 years ago, pyrite served as a catalytic surface able to adsorb and concentrate negatively charged organic molecules, but reduced metal sulfides, such as pyrrhotite and amorphous FeS, were expected to participate in the redox reactions of the system (Wächtershäuser, 1988). With few exceptions (Wang et al., 2012), reduced iron and nickel sulfides have been generally proposed as plausible minerals to catalyze

prebiotic redox reactions instead of pyrite (Cody et al., 2000; Huber et al., 2012; Novikov and Copley, 2013).

Electrochemical systems have been recently suggested as a relevant approach to study prebiotic chemistry related to hydrothermal vents scenario (de Aldecoa et al., 2013; Barge et al., 2014, 2015; Herschy et al., 2014; Yamaguchi et al., 2014; Roldan et al., 2015). The focus of these studies is usually on abiotic CO_2 reduction and reduced iron sulfides and sometimes iron oxides (green rust) are considered as possible electrode candidates. Focus on CO_2 reduction as a main model system relevant to the origin of life has been chosen because of the common assumption that life started simply and evolved toward larger synthetic complexity (Martin et al., 2008). The opposite idea that life started from complex chemical mixtures (de Duve

and Miller, 1991; Burton et al., 2012) is gaining more support with the growing realization that a large amount of organic material is formed abiotically in space and delivered to Earth with comets and meteorites (Chyba and Sagan, 1992). Under this scenario quinones, which have been produced abiotically under conditions simulating exoplanetary comet ices (Bernstein et al., 1999), are plausible first molecules relevant to the origin of life. The ubiquitous occurrence of many different quinones used by bacteria, fungi and plants suggests that quinones have a critical role in maintaining life on Earth (Szent-Gyorgyi and McLaughlin, 1983), but the role of quinones in early prebiotic reaction networks is presently underexplored.

The observed affinity between pyrite and quinones loosely resembles reactions in electron transport chain systems found across all domains of life, where redox and pH gradients across cell membranes are maintained, in part, by electron transport between metal sulfur clusters and quinone cofactors (Sun et al., 2013). Electron transport chain has a modular structure (Yankovskaya et al., 2003) and it is possible that a first primitive fragments of a biological electron transport chain appeared from abiotic electrocatalytic interactions between minerals and redox active molecules. In this case, an ability of pyrite surfaces to adsorb and concentrate amino acids and short peptides (Wachterhauser, 1988; Sanchez-Arenillas and Mateo-Marti, 2016) could have provided the link between the early redox systems and prebiotic reaction networks based on peptides and nucleic acids.

The redox processes of the living cells, with a few exceptions (Bar-Even, 2013), take place in the relatively narrow potential zone between -0.6 and 0.1 V (vs. SHE) (Weber, 2002; Bar-Even et al., 2012). If electrochemical reactions were important components of prebiotic redox systems, then minerals that acted as electrodes should have been stable in the potential window corresponding to prebiotic redox reactions, such as reactions involving redox cofactors, components of the citric acid cycle, thiols and thioesters. Side to side comparison of the redox potentials of these reactions to the stability of iron minerals at the same pH and temperature are shown on (Figure 8B). While CO_2 reduction to organic molecules can take place on surfaces of FeS minerals, pyrite stability overlaps with a large part of biochemical redox potentials. Ubiquitous pyrite surfaces likely served as natural mineral electrodes in primordial reaction networks.

The simple system presented in this paper is a model that does not yet address many questions relevant to the natural settings. The selectivity and the stability of pyrite electrodes during the quinone redox cycling in presence of other organic and inorganic compounds will be studied in the next phase of the project. To understand the global impact of abiotic

electrochemical reactions a model involving electrical currents across conductive sediments coupled with the diffusion processes at the sediment interphases has to be developed. Reduced iron sulfides are more electrically conductive than pyrite and magnetite (Telford et al., 1990), and are found at higher concentrations in the anoxic zones (Risgaard-Petersen et al., 2012). Possibly the electron flow across the sediments occurs mostly through the reduced iron sulfides, the electron transfer takes place at the pyrite interphase, and there is a competition between mineral corrosion and electrons transfer pathways. The complex pattern of the long-range electron transfer needs to be elucidated.

Present study of non-biological interactions between the organic molecules and the minerals suggests an existence of complex abiotic out-of-equilibrium systems driven by naturally occurring electrochemical gradients. These systems might contribute to global biogeochemical cycles and have an impact on different phenomena ranging from chemical pollution to the origin of life.

AUTHOR CONTRIBUTIONS

OT designed and performed the experiments, analyzed the data, and wrote the paper.

FUNDING

The postdoctoral research is supported by Neurology and the ADRC at Emory University (P50AG025688) and by grant NSF/DMR-BSF 1610377.

ACKNOWLEDGMENTS

I want to thank Prof. David Lynn for the support during the work on the project and writing of the manuscript, Prof. Craig L. Hill for providing access to the electropotentiostat used in the experiments, Dr. John Basca for the XRD analysis, Harvard Museum of Natural History for providing mineral samples for the electrodes, Prof. Y. A. Taran for the HSC-7 calculations, and Prof. M. T. Fernandez-Abedul, Dr. M. N. Tsaloglu and Dr. V.E. Campbell for the helpful discussions. Harvard Origins of Life Initiative for the financial support during the early stages of the project.

SUPPLEMENTARY MATERIAL

The Supplementary Material for this article can be found online at: <http://journal.frontiersin.org/article/10.3389/fchem.2017.00049/full#supplementary-material>

REFERENCES

- Aklujkar, M., Krushkal, J., DiBartolo, G., Lapidus, A., Land, M. L., and Lovley, D. R. (2009). The genome sequence of *Geobacter metallireducens*: features of metabolism, physiology and regulation common and dissimilar to *Geobacter sulfurreducens*. *BMC Microbiol.* 9:109. doi: 10.1186/1471-2180-9-109

- Almeida, C. M. V., and Giannetti, B. (2002). A new and practical carbon paste electrode for insoluble and ground samples. *Electrochim. Commun.* 4, 985–988. doi: 10.1016/S1388-2481(02)00511-8
- Amend, J. P., and McCollom, T. M. (2009). Energetics of biomolecule synthesis on early Earth. *ACS. Symp. Ser.* 1025, 63–94. doi: 10.1021/bk-2009-1025.ch004

- Baas Becking, L. G. M., Kaplan, I. R., and Moore, D. (1960). Limits of the natural environment in terms of pH and oxidation-reduction potentials. *J. Geol.* 68, 243–284. doi: 10.1086/626659
- Bar-Even, A. (2013). Does acetogenesis really require especially low reduction potential? *Biochim. Biophys. Acta* 1827, 395–400. doi: 10.1016/j.bbabi.2012.10.007
- Bar-Even, A., Flamholz, A., Noor, E., and Milo, R. (2012). Thermodynamic constraints shape the structure of carbon fixation pathways. *Biochim. Biophys. Acta Bioenerg.* 1817, 1646–1659. doi: 10.1016/j.bbabi.2012.05.002
- Barge, L. M., Abedian, Y., Russell, M. J., Doloboff, I. J., Cartwright, J. H. E., Kidd, R. D., et al. (2015). From chemical gardens to fuel cells: generation of electrical potential and current across self-assembling iron mineral membranes. *Angew. Chem. Int. Ed. Engl.* 54, 8184–8187. doi: 10.1002/anie.201501663
- Barge, L. M., Kee, T. P., Doloboff, I. J., Hampton, J. M., Ismail, M., Pourkashanian, M., et al. (2014). The fuel cell model of abiogenesis: a new approach to origin-of-life simulations. *Astrobiology* 14, 254–270. doi: 10.1089/ast.2014.1140
- Batchelor-McAuley, C., Gonçalves, L. M., Xiong, L., Barros, A. A., and Compton, R. G. (2010). Controlling voltammetric responses by electrode modification; using adsorbed acetone to switch graphite surfaces between adsorptive and diffusive modes. *Chem. Commun.* 46, 9037–9039. doi: 10.1039/c0cc03961f
- Benning, L. G., Wilkin, R. T., and Barnes, H. L. (2000). Reaction pathways in the Fe-S system below 100°C. *Chem. Geol.* 167, 25–51. doi: 10.1016/S0009-2541(99)00198-9
- Bernstein, M. (2006). Prebiotic materials from on and off the early Earth. *Philos. Trans. R. Soc. Lond. B. Biol. Sci.* 361, 1689–700. discussion: 1700–1702. doi: 10.1098/rstb.2006.1913
- Bernstein, M. P., Sandford, S. A., Allamandola, L. J., Gillette, J. S., Clemett, S. J., and Zare, R. N. (1999). UV Irradiation of polycyclic aromatic hydrocarbons in ices: production of alcohols, quinones, and ethers. *Science* 283, 1135–1139. doi: 10.1126/science.283.5405.1135
- Biber, M. V., dos Santos Afonso, M., and Stumm, W. (1994). The coordination chemistry of weathering: IV. Inhibition of the dissolution of oxide minerals. *Geochim. Cosmochim. Acta* 58, 1999–2010. doi: 10.1016/0016-7037(94)90280-1
- Borch, T., Kretzschmar, R., Kappler, A., Cappellen, P. V., Ginder-Vogel, M., Voegelin, A., et al. (2010). Biogeochemical redox processes and their impact on contaminant dynamics. *Environ. Sci. Technol.* 44, 15–23. doi: 10.1021/es9026248
- Burton, A. S., Stern, J. C., Elsila, J. E., Glavin, D. P., and Dworkin, J. P. (2012). Understanding prebiotic chemistry through the analysis of extraterrestrial amino acids and nucleobases in meteorites. *Chem. Soc. Rev.* 41, 5459–5472. doi: 10.1039/c2cs35109a
- Cervantes, F. J., Van der Velde, S., Lettinga, G., and Field, J. A. (2000). Competition between methanogenesis and quinone respiration for ecologically important substrates in anaerobic consortia. *FEMS Microbiol. Ecol.* 34, 161–171. doi: 10.1111/j.1574-6941.2000.tb00766.x
- Chandra, A. P., and Gerson, A. R. (2010). The mechanisms of pyrite oxidation and leaching: a fundamental perspective. *Surf. Sci. Rep.* 65, 293–315. doi: 10.1016/j.surfrep.2010.08.003
- Chyba, C., and Sagan, C. (1992). Endogenous production, exogenous delivery and impact-shock synthesis of organic molecules: an inventory for the origins of life. *Nature* 355, 125–132. doi: 10.1038/355125a0
- Cody, G. D., Boctor, N. Z., Filley, T. R., Hazen, R. M., Scott, J. H., Sharma, A., et al. (2000). Primordial carbonylated iron-sulfur compounds and the synthesis of pyruvate. *Science* 289, 1337–1340. doi: 10.1126/science.289.5483.1337
- Compton, R. G., Laborda, E., and Ward, K. R. (2014). *Understanding Voltammetry*. London: Imperial College Press.
- Crowe, S. A., Paris, G., Katsve, S., Jones, C., Kim, S. T., Zerkle, A. L., et al. (2014). Sulfate was a trace constituent of Archean seawater. *Science* 346, 735–739. doi: 10.1126/science.1258966
- de Aldecoa, A., Roldán, F., and Menor-Salván, C. (2013). Natural pyrrhotite as a catalyst in prebiotic chemical evolution. *Life* 3, 502–517. doi: 10.3390/life3030502
- de Duve, C., and Miller, S. L. (1991). Two-dimensional life? *Proc. Natl. Acad. Sci. U.S.A.* 88, 10014–10017. doi: 10.1073/pnas.88.22.10014
- Dekkers, M. J., Passier, H. F., and Schoonen, M. A. A. (2000). Magnetic properties of hydrothermally synthesized greigite (Fe₃S₄)-II. High- and low-temperature characteristics. *Geophys. J. Int.* 141, 809–819. doi: 10.1046/j.1365-246x.2000.00129.x
- D'Hondt, S., Jørgensen, B. B., Miller, D. J., Batzke, A., Blake, R., Cragg, B. A., et al. (2004). Distributions of microbial activities in deep subseafloor sediments. *Science* 306, 2216–2221. doi: 10.1126/science.1101155
- Du, Z., Li, H., and Gu, T. (2007). A state of the art review on microbial fuel cells: a promising technology for wastewater treatment and bioenergy. *Biotechnol. Adv.* 25, 464–482. doi: 10.1016/j.biotechadv.2007.05.004
- Gupta, R., Guin, S. K., and Aggarwal, S. K. (2012). A mechanistic study on the electrocatalysis of the Pu(iv)/Pu(iii) redox reaction at a platinum electrode modified with single-walled carbon nanotubes (SWCNTs) and polyaniline (PANI). *RSC Adv.* 2, 1810–1819. doi: 10.1039/c1ra01010g
- Hedrick, D. B., and White, D. C. (1986). Microbial respiratory quinones in the environment. *J. Microbiol. Methods* 5, 243–254. doi: 10.1016/0167-7012(86)90049-7
- Herschy, B., Whicker, A., Camprubi, E., Watson, C., Dartnell, L., Ward, J., et al. (2014). An origin-of-life reactor to simulate alkaline hydrothermal vents. *J. Mol. Evol.* 79, 213–227. doi: 10.1007/s00239-014-9658-4
- Huber, C., Kraus, F., Hanzlik, M., Eisenreich, W., and Wächtershäuser, G. (2012). Elements of metabolic evolution. *Chem. Eur. J.* 18, 2063–2080. doi: 10.1002/chem.201102914
- Jelen, B. I., Giovannelli, D., and Falkowski, P. G. (2016). The Role of microbial electron transfer in the coevolution of the biosphere and geosphere. *Annu. Rev. Microbiol.* 70, 45–62. doi: 10.1146/annurev-micro-102215-095521
- Jiang, C., Garg, S., and Waite, T. D. (2015). Hydroquinone-mediated redox cycling of iron and concomitant oxidation of hydroquinone in oxic waters under acidic conditions: comparison with iron-natural organic matter interactions. *Environ. Sci. Technol.* 49, 14076–14084. doi: 10.1021/acs.est.5b03189
- Karato, S. I., and Wang, D. (2013). “Electrical conductivity of minerals and rocks,” in *Physics and Chemistry of the Deep Earth*, ed S. Karato (Hoboken, NJ: John Wiley), 145–182. doi: 10.1002/9781118529492.ch5
- Kim, Y. I., Vinyard, D. J., Ananyev, G. M., Dismukes, G. C., and Golden, S. S. (2012). Oxidized quinones signal onset of darkness directly to the cyanobacterial circadian oscillator. *Proc. Natl. Acad. Sci. U.S.A.* 109, 17765–17769. doi: 10.1073/pnas.1216401109
- Klüpfel, L., Piepenbrock, A., Kappler, A., and Sander, M. (2014). Humic substances as fully regenerable electron acceptors in recurrently anoxic environments. *Nat. Geosci.* 7, 195–200. doi: 10.1038/ngeo2084
- Komada, T., Reimers, C. E., Luther, G. W., and Burdige, D. J. (2004). Factors affecting dissolved organic matter dynamics in mixed-redox to anoxic coastal sediments. *Geochim. Cosmochim. Acta* 68, 4099–4111. doi: 10.1016/j.gca.2004.04.005
- Konkena, B., Puring, J. K., Sinev, I., Piontek, S., Khavryuchenko, O., Dürholt, J. P., et al. (2016). Pentlandite rocks as sustainable and stable efficient electrocatalysts for hydrogen generation. *Nat. Commun.* 7:12269. doi: 10.1038/ncomms12269
- Kruger, F. C., and Lacy, W. C. (1949). Geological explanations of geophysical anomalies near Cerro de Pasco, Peru. *Econ. Geol.* 44, 485–491. doi: 10.2113/gsecongeo.44.6.485
- Lennie, A. R., Redfern, S. A. T., Schofield, P. F., and Vaughn, D. J. (1995). Synthesis and rietveld crystal structure refinement of mackinawite, tetragonal FeS. *Mineral. Mag.* 59, 677–683. doi: 10.1180/minmag.1995.059.397.10
- Luther, G. W., Glazer, B. T., Ma, S., Trouwborst, R. E., Moore, T. S., Metzger, E., et al. (2008). Use of voltammetric solid-state (micro)electrodes for studying biogeochemical processes: laboratory measurements to real time measurements with an *in situ* electrochemical analyzer (ISEA). *Mar. Chem.* 108, 221–235. doi: 10.1016/j.marchem.2007.03.002
- Lynn, D. G., and Chang, M. (1990). Phenolic signals in cohabitation: implications for plant development. *Annu. Rev. Plant Physiol. Plant Mol. Biol.* 41, 497–526. doi: 10.1146/annurev.pp.41.060190.002433
- Malkin, S. Y., Seitaj, D., Burdorf, L. D. W., Nieuwhof, S., Hidalgo-Martinez, S., Tramper, A., et al. (2017). Electrogenic sulfur oxidation by cable bacteria in bivalve reef sediments. *Front. Mar. Sci.* 4:28. doi: 10.3389/fmars.2017.00028
- Malvankar, N. S., King, G. M., and Lovley, D. R. (2014). Centimeter-long electron transport in marine sediments via conductive minerals. *ISME J.* 9, 527–531. doi: 10.1038/ismej.2014.131
- Marsili, E., Baron, D. B., Shikhare, I. D., Coursolle, D., Gralnick, J. A., and Bond, D. R. (2008). Shewanella secretes flavins that mediate

- extracellular electron transfer. *Proc. Natl. Acad. Sci. U.S.A.* 105, 3968–3973. doi: 10.1073/pnas.0710525105
- Martin, W., Baross, J., Kelley, D., and Russell, M. J. (2008). Hydrothermal vents and the origin of life. *Nat. Rev. Microbiol.* 6, 805–814. doi: 10.1038/nrmicro1991
- Martin, W., and Russell, M. J. (2003). On the origins of cells: a hypothesis for the evolutionary transitions from abiotic geochemistry to chemoautotrophic prokaryotes, and from prokaryotes to nucleated cells. *Philos. Trans. R. Soc. Lond. B. Biol. Sci.* 358, 59–83. discussion: 83–85. doi: 10.1098/rstb.2002.1183
- Menshykau, D., Streeter, I., and Compton, R. G. (2008). Influence of electrode roughness on cyclic voltammetry. *J. Phys. Chem. C* 112, 14428–14438. doi: 10.1021/jp8047423
- Mikhail, Y. (2000). Reactivity of pyrrhotite surfaces: an electrochemical study. *Phys. Chem. Chem. Phys.* 2, 5672–5677. doi: 10.1039/b005373m
- Moore, T. S., Mullaugh, K. M., Holyoke, R. R., Madison, A. S., Yücel, M., and Luther, G. W. (2009). Marine chemical technology and sensors for marine waters: potentials and limits. *Ann. Rev. Mar. Sci.* 1, 91–115. doi: 10.1146/annurev.marine.010908.163817
- Mousset, E., Huguenot, D., Van Hullebusch, E. D., Oturan, N., Guibaud, G., Esposito, G., et al. (2016). Impact of electrochemical treatment of soil washing solution on PAH degradation efficiency and soil respirometry. *Environ. Pollut.* 211, 354–362. doi: 10.1016/j.envpol.2016.01.021
- Müller, H., Bosch, J., Griebler, C., Damgaard, L. R., Nielsen, L. P., Lueders, T., et al. (2016). Long-distance electron transfer by cable bacteria in aquifer sediments. *ISME J.* 545, 1–8. doi: 10.1038/ismej.2015.250
- Nakamura, R., Okamoto, A., Tajima, N., Newton, G. J., Kai, F., Takashima, T., et al. (2010a). Biological iron-monosulfide production for efficient electricity harvesting from a deep-sea metal-reducing bacterium. *ChemBioChem* 11, 643–645. doi: 10.1002/cbic.200900775
- Nakamura, R., Takashima, T., Kato, S., Takai, K., Yamamoto, M., and Hashimoto, K. (2010b). Electrical current generation across a black smoker chimney. *Angew. Chemie Int. Ed.* 49, 7692–7694. doi: 10.1002/anie.20100331
- Newman, D. K., and Kolter, R. (2000). A role for excreted quinones in extracellular electron transfer. *Nature* 405, 94–97. doi: 10.1038/35011098
- Nielsen, L. P. (2016). Ecology: electrical cable bacteria save marine life. *Curr. Biol.* 26, R32–R33. doi: 10.1016/j.cub.2015.10.014
- Nielsen, L. P., and Risgaard-Petersen, N. (2015). Rethinking sediment biogeochemistry after the discovery of electric Currents. *Ann. Rev. Mar. Sci.* 7, 425–442. doi: 10.1146/annurev-marine-010814-015708
- Nielsen, L. P., Risgaard-Petersen, N., Fossing, H., Christensen, P. B., and Sayama, M. (2010). Electric currents couple spatially separated biogeochemical processes in marine sediment. *Nature* 463, 1071–1074. doi: 10.1038/nature08790
- Nitschke, W., and Russell, M. J. (2009). Hydrothermal focusing of chemical and chemiosmotic energy, supported by delivery of catalytic Fe, Ni, Mo/W, Co, S and Se, forced life to emerge. *J. Mol. Evol.* 69, 481–496. doi: 10.1007/s00239-009-9289-3
- Novikov, Y., and Copley, S. D. (2013). Reactivity landscape of pyruvate under simulated hydrothermal vent conditions. *Proc. Natl. Acad. Sci. U.S.A.* 110, 13283–13288. doi: 10.1073/pnas.1304923110
- O'Brien, P. J. (1991). Molecular mechanisms of quinone cytotoxicity. *Chem. Biol. Interact.* 80, 1–41.
- O'Loughlin, E. J. (2008). Effects of electron transfer mediators on the bioreduction of lepidocrocite (γ -FeOOH) by *Shewanella putrefaciens*. *Environ. Sci. Technol.* 42, 6876–6882. doi: 10.1021/es800686d
- Orgel, L. E. (2008). The implausibility of metabolic cycles on the prebiotic Earth. *PLoS Biol.* 6:e18. doi: 10.1371/journal.pbio.0060018
- Orsetti, S., Laskov, C., and Haderlein, S. B. (2013). Electron transfer between iron minerals and quinones: estimating the reduction potential of the Fe(II)-goethite surface from AQDS speciation. *Environ. Sci. Technol.* 47, 14161–14168. doi: 10.1021/es403658g
- Qiao, Y., Li, C. M., Bao, S. J., Lu, Z., and Hong, Y. (2008). Direct electrochemistry and electrocatalytic mechanism of evolved *Escherichia coli* cells in microbial fuel cells. *Chem. Commun.* 2008, 1290–1292. doi: 10.1039/b719955d
- Quan, M., Sanchez, D., Wasylkiw, M. F., and Smith, D. K. (2007). Voltammetry of quinones in unbuffered aqueous solution: reassessing the roles of proton transfer and hydrogen bonding in the aqueous electrochemistry of quinones. *J. Am. Chem. Soc.* 129, 12847–12856. doi: 10.1021/ja0743083
- Revil, A., Mendonça, C. A., Atekwana, E. A., Kulessa, B., Hubbard, S. S., and Bohlen, K. J. (2010). Understanding biogeobatteries: where geophysics meets microbiology. *J. Geophys. Res.* 115, 1–22. doi: 10.1029/2009JG001065
- Rijkenberg, M. J., Middag, R., Laan, P., Gerrings, L. J., van Aken, H. M., Schoemann, V., et al. (2014). The distribution of dissolved iron in the West Atlantic Ocean. *PLoS ONE* 9:e101323. doi: 10.1371/journal.pone.0101323
- Rimstidt, J. D., and Vaughan, D. J. (2003). Pyrite oxidation: a state-of-the-art assessment of the reaction mechanism. *Geochim. Cosmochim. Acta* 67, 873–880. doi: 10.1016/S0016-7037(02)01165-1
- Risgaard-Petersen, N., Revil, A., Meister, P., and Nielsen, L. P. (2012). Sulfur, iron, and calcium cycling associated with natural electric currents running through marine sediment. *Geochim. Cosmochim. Acta* 92, 1–13. doi: 10.1016/j.gca.2012.05.036
- Roginsky, V., and Barsukova, T. (2000). Kinetics of oxidation of hydroquinones by molecular oxygen. Effect of superoxide dismutase. *J. Chem. Soc. Perkin Trans. 2*, 1575–1582. doi: 10.1039/b000538j
- Roldan, A., Hollingsworth, N., Roffey, A., Islam, H.-U., Goodall, J. B. M., Catlow, C. R. A., et al. (2015). Bio-inspired CO_2 conversion by iron sulfide catalysts under sustainable conditions. *Chem. Commun.* 51, 7501–7504. doi: 10.1039/C5CC02078F
- Ryckelynck, N., Stecher, H. A., and Reimers, C. A. (2012). Understanding the anodic mechanism of a seafloor fuel cell: interactions between geochemistry and microbial activity. *Biogeochemistry* 111, 113–139. doi: 10.1007/s10533-005-2671-3
- Sanchez-Arenillas, M., and Mateo-Martí, E. (2016). Pyrite surface environment drives molecular adsorption: cystine on pyrite(100) investigated by X-ray photoemission spectroscopy and low energy electron diffraction. *Phys. Chem. Chem. Phys.* 18, 27219–27225. doi: 10.1039/C6CP03760G
- Sander, M., Hofstetter, T. B., and Gorski, C. A. (2015). Electrochemical analyses of redox-active iron minerals: a review of nonmediated and mediated approaches. *Environ. Sci. Technol.* 49, 5862–5878. doi: 10.1021/acs.est.5b00006
- Scheller, S., Yu, H., Chadwick, G. L., and Mcglynn, S. E. (2016). Artificial electron acceptors decouple archaeal methane oxidation from sulfate reduction. *Science* 351, 703–707. doi: 10.1126/science.aad7154
- Scott, D. T., McKnight, D. M., Blunt-Harris, E. L., Kolesar, S. E., and Lovley, D. R. (1998). Quinone moieties act as electron acceptors in the reduction of humic substances by humics-reducing microorganisms. *Environ. Sci. Technol.* 32, 2984–2989. doi: 10.1021/es980272q
- Seitaj, D., Schauer, R., Sulu-Gambari, F., Hidalgo-Martinez, S., Malkin, S. Y., Burdorf, L. D., et al. (2015). Cable bacteria generate a firewall against euxinia in seasonally hypoxic basins. *Proc. Natl. Acad. Sci. U.S.A.* 112, 13278–13283. doi: 10.1073/pnas.1510152112
- Soballe, B., and Poole, R. K. (1999). Microbial ubiquinones: multiple roles in respiration, gene regulation and oxidative stress management. *Microbiology* 145, 1817–1830. doi: 10.1099/13500872-145-8-1817
- Sun, F., Zhou, Q., Pang, X., Xu, Y., and Rao, Z. (2013). Revealing various coupling of electron transfer and proton pumping in mitochondrial respiratory chain. *Curr. Opin. Struct. Biol.* 23, 526–538. doi: 10.1016/j.sbi.2013.06.013
- Szent-Gyorgyi, A., and McLaughlin, J. A. (1983). The living state. *J. Bioelectric.* 2, 207–212. doi: 10.3109/15368378309009852
- Telford, W. M., Geldart, L. P., and Sheriff, R. E. (1990). “Electrical properties of rocks and minerals,” in *Applied Geophysics Monograph Series* (Cambridge University Press), 283–292.
- Uchimiya, M., and Stone, A. T. (2006). Redox reactions between iron and quinones: thermodynamic constraints. *Geochim. Cosmochim. Acta* 70, 1388–1401. doi: 10.1016/j.gca.2005.11.020
- Uchimiya, M., and Stone, A. T. (2009). Reversible redox chemistry of quinones: impact on biogeochemical cycles. *Chemosphere* 77, 451–458. doi: 10.1016/j.chemosphere.2009.07.025
- Unden, G., and Bongaerts, J. (1997). Alternative respiratory pathways of *Escherichia coli*: energetics and transcriptional regulation in response to electron acceptors. *Biochim. Biophys. Acta* 1320, 217–234. doi: 10.1016/S0005-2728(97)00034-0
- Vokes, F. M. (1993). The metamorphism of pyrite and pyritic ores: an overview. *Mineral. Mag.* 57, 3–18. doi: 10.1180/minmag.1993.057.386.02
- Wachterhauser, G. (1988). Before enzymes and templates: theory of surface. *Microbiol. Rev.* 52, 452–484.

- Wächtershäuser, G. (2016). In praise of error. *J. Mol. Evol.* 82, 75–80. doi: 10.1007/s00239-015-9727-3
- Wang, W., Qu, Y., Yang, B., Liu, X., and Su, W. (2012). Lactate oxidation in pyrite suspension: a Fenton-like process in situ generating H₂O₂. *Chemosphere* 86, 376–382. doi: 10.1016/j.chemosphere.2011.10.026
- Weber, A. L. (2002). Chemical constraints governing the origin of metabolism: the thermodynamic landscape of carbon group transformations under mild aqueous conditions. *Orig. Life Evol. Biosph.* 32, 333–357. doi: 10.1023/A:1020588925703
- Wells, R. C. (1914). *Electric Activity in Ore Deposits*. Bulletin 548, U.S. Geological Survey.
- White, L. M., Bhartia, R., Stucky, G. D., Kanik, I., and Russell, M. J. (2015). Mackinawite and greigite in ancient alkaline hydrothermal chimneys: identifying potential key catalysts for emergent life. *Earth Planet. Sci. Lett.* 430, 105–114. doi: 10.1016/j.epsl.2015.08.013
- Yamaguchi, A., Yamamoto, M., Takai, K., Ishii, T., Hashimoto, K., and Nakamura, R. (2014). Electrochemical CO₂ reduction by Ni-containing iron sulfides: how is CO₂ electrochemically reduced at bisulfide-bearing deep-sea hydrothermal precipitates? *Electrochim. Acta* 141, 311–318. doi: 10.1016/j.electacta.2014.07.078
- Yamamoto, M., Nakamura, R., Kasaya, T., Kumagai, H., Suzuki, K., and Takai, K. (2017). Spontaneous and widespread electricity generation in natural deep-sea hydrothermal fields. *Angew. Chemie Int. Ed.* 61, 5725–5728. doi: 10.1002/anie.201701768
- Yankovskaya, V., Horsefield, R., Törnroth, S., Luna-Chavez, C., Miyoshi, H., Léger, C., et al. (2003). Architecture of succinate dehydrogenase and reactive oxygen species generation. *Science* 299, 700–704. doi: 10.1126/science.1079605
- Yuan, X., Davis, J. A., and Nico, P. S. (2016). Iron-mediated oxidation of methoxyhydroquinone under dark conditions: kinetic and mechanistic insights. *Environ. Sci. Technol.* 50, 1731–1740. doi: 10.1021/acs.est.5b03939

Conflict of Interest Statement: The author declares that the research was conducted in the absence of any commercial or financial relationships that could be construed as a potential conflict of interest.

Copyright © 2017 Taran. This is an open-access article distributed under the terms of the Creative Commons Attribution License (CC BY). The use, distribution or reproduction in other forums is permitted, provided the original author(s) or licensor are credited and that the original publication in this journal is cited, in accordance with accepted academic practice. No use, distribution or reproduction is permitted which does not comply with these terms.



Reactivation of Deep Subsurface Microbial Community in Response to Methane or Methanol Amendment

Pauliina Rajala^{1*} and Malin Bomberg^{1,2*}

¹ Materials Performance, VTT Technical Research Centre of Finland, Espoo, Finland, ² Material Processing and Geotechnology, VTT Technical Research Centre of Finland, Espoo, Finland

OPEN ACCESS

Edited by:

Donato Giovannelli,
Earth-Life Science Institute, Japan

Reviewed by:

Michael J. Wilkins,
Ohio State University, USA

Zachary B. Freedman,
West Virginia University, USA

*Correspondence:

Pauliina Rajala
pauliina.rajala@vtt.fi
Malin Bomberg
malin.bomberg@vtt.fi

Specialty section:

This article was submitted to
Microbiological Chemistry and
Geomicrobiology,
a section of the journal
Frontiers in Microbiology

Received: 03 December 2016

Accepted: 28 February 2017

Published: 17 March 2017

Citation:

Rajala P and Bomberg M (2017) Reactivation of Deep Subsurface Microbial Community in Response to Methane or Methanol Amendment. *Front. Microbiol.* 8:431. doi: 10.3389/fmicb.2017.00431

Microbial communities in deep subsurface environments comprise a large portion of Earth's biomass, but the microbial activity in these habitats is largely unknown. Here, we studied how microorganisms from two isolated groundwater fractures at 180 and 500 m depths of the Outokumpu Deep Drillhole (Finland) responded to methane or methanol amendment, in the presence or absence of sulfate as an additional electron acceptor. Methane is a plausible intermediate in the deep subsurface carbon cycle, and electron acceptors such as sulfate are critical components for oxidation processes. In fact, the majority of the available carbon in the Outokumpu deep biosphere is present as methane. Methanol is an intermediate of methane oxidation, but may also be produced through degradation of organic matter. The fracture fluid samples were incubated *in vitro* with methane or methanol in the presence or absence of sulfate as electron acceptor. The metabolic response of microbial communities was measured by staining the microbial cells with fluorescent redox sensitive dye combined with flow cytometry, and DNA or cDNA-derived amplicon sequencing. The microbial community of the fracture zone at the 180 m depth was originally considerably more respiratory active and 10-fold more numerous (10^5 cells ml $^{-1}$ at 180 m depth and 10^4 cells ml $^{-1}$ at 500 m depth) than the community of the fracture zone at the 500 m. However, the dormant microbial community at the 500 m depth rapidly reactivated their transcription and respiration systems in the presence of methane or methanol, whereas in the shallower fracture zone only a small sub-population was able to utilize the newly available carbon source. In addition, the composition of substrate activated microbial communities differed at both depths from original microbial communities. The results demonstrate that OTUs representing minor groups of the total microbial communities play an important role when microbial communities face changes in environmental conditions.

Keywords: deep biosphere, deep life, carbon, methane, methanol, methanotrophy

INTRODUCTION

The Fennoscandian Shield, i.e., the exposed Precambrian northwest segment of the East European Craton, preserves some of the oldest geological records of Earth. Studies conducted in several terrestrial deep sites have reported diverse microbial communities extending several kilometers into the Earth's crystalline bedrock (Pedersen, 1997; Haveman and Pedersen, 1999; Sass and Cypionka, 2004; Wu et al., 2015). Microbial communities in deep subsurface environments have

been estimated to comprise a large portion of Earth's biomass (McMahon and Parnell, 2014) and to have a great impact on the elemental cycles in the deep biosphere (Gadd, 2010). The deep groundwater in crystalline continental crust, such as the one of the Fennoscandian Shield, is independent of photosynthetic carbon and energy production. Alternative means of carbon assimilation, such as inorganic carbon fixation or methane oxidation, may be important to support the microbial communities in these conditions. Chemolithoautotrophic organisms are thought to be the primary producers in deep crystalline bedrock environments (Pedersen, 1997, 2000).

Microorganisms in the deep, nutrient limited biosphere are believed to conduct only little metabolic activity due to low nutrient availability in these environments (Jørgensen, 2011; Hoehler and Jørgensen, 2013). Dormancy refers to an ability to enter a reversible state of low metabolic activity under unfavorable environmental conditions. By remaining in dormant state the microorganisms lower their energetic expenditures. The dormant microorganisms generate a seed bank that may activate following beneficial environmental change (Lennon and Jones, 2011). However, dormant microorganisms must invest resources into resting structures and the machinery that is needed for transitioning into and out of a dormant state (Lennon and Jones, 2011). In addition, low amount of maintenance and survival energy is still required ensure the long-term viability of dormant microorganisms (van Bodegom, 2007; Hoehler and Jørgensen, 2013).

The Outokumpu Deep Drillhole, located in eastern Finland, provides access to study isolated aquifers in the crystalline bedrock in the Paleoproterozoic part of the Fennoscandian Shield (Kukkonen, 2011). The bedrock in Outokumpu is composed of several geochemically different rock types. These include metasediments, ophiolite-derived altered ultramafic rocks and pegmatitic granite (Ahonen et al., 2011). The drillhole reaches a total depth of 2516 m and spans several fluid-filled fracture zones. Formation waters in these fracture zones are old, highly saline, reducing and have low organic carbon content. The dissolved gas phase, of which CH_4 covers up to 80 vol-%, is abundant (Kietäväinen et al., 2013). The fracture waters have been categorized to five water types, type I (180 m), type II (500–967 m), type III (1500 m), type IV (1820–2260 m) and type V (2300 m) (Kietäväinen et al., 2013). The type I water has characteristically high pH (around 10) and higher alkalinity than the other water types in Outokumpu. High pH in the drillhole water column may originate from concrete casing within the uppermost 30 m of the drillhole, and during long-term purging of the sealed-off 180 m fracture zone, the pH of the native aquifer fluid dropped to a stable level of 8.5. Water type II contains the highest amount of dissolved gases in the whole water column, of which approximately 75% (22–32 mmol 1^{-1}) is methane. A diverse bacterial and archaeal community has been detected down to 2300 m depth in the drillhole (Purkamo et al., 2013, 2015, 2016; Nyssönen et al., 2014). These communities vary at different sampling depths in response to prevailing lithology and hydrogeochemistry (Purkamo et al., 2014, 2016). Simple one-carbon compounds,

such as methane and methanol are important intermediates in the deep subsurface carbon cycle, and electron acceptors such as sulfate are critical components in the oxidation processes (Kietäväinen and Purkamo, 2015). Methane (CH_4) is a key compound in the global carbon cycle and a dominant gas in many Precambrian continental bedrock formations (reviewed by Kietäväinen and Purkamo, 2015). In the shallow subsurface CH_4 is mainly produced by anaerobic digestion of organic matter. Deeper in the geological strata CH_4 is found in large quantities within sedimentary formations (Arthur and Cole, 2014). Many aspects of origin, source, and cycling of CH_4 in deep continental bedrock environments still remain poorly understood (Kietäväinen and Purkamo, 2015). The study of methane cycling is important in order to understand deep subsurface ecosystems, such as those of the Outokumpu deep subsurface. The microbial communities in the Outokumpu deep subsurface have earlier been demonstrated to contain genes involved in methane cycling, indicating both methanogenesis and methanotrophy (Nyssönen et al., 2014; Purkamo et al., 2015; Rajala et al., 2015). Methanol may be produced through degradation of recalcitrant organic compounds present in, e.g., black schist (Petsch, 2001). Additionally, Nyssönen et al. (2014) suggested possibility of methylotrophic methanogenesis on Outokumpu deep drillhole water column.

The aim of present work was to determine the activity of microbial communities of two isolated bedrock fractures at 180 and 500 m depths of the Outokumpu deep subsurface and ability of the dormant fraction of these microbial communities to re-activate. Methane or methanol amendments were used as activating substances in the presence or absence of sulfate as an electron acceptor. The fracture fluid samples were incubated *in vitro* with methane or methanol in the presence or absence of sulfate as electron acceptor. High-throughput amplicon sequencing of bacterial and archaeal 16S rRNA genes and gene transcripts were used to identify and characterize the microorganisms that rapidly activate their metabolism in response to methane or methanol. Metabolic response was measured also by staining the microbial cells with fluorescent dyes that indicate respiratory activity. One of the main objectives of this study was thus to determine the microbial community activity and identity of microorganisms responding to methane or methanol in Outokumpu deep biosphere.

MATERIALS AND METHODS

Description of the Outokumpu Deep Drillhole

The Outokumpu deep drillhole is situated in Outokumpu, eastern Finland ($62^{\circ}43' 04''$ N, $29^{\circ}3' 43''$ E), in a Paleoproterozoic sequence consisting of metasediments, ophiolite-derived altered ultramafic rocks and pegmatitic granite (Ahonen et al., 2011). The Outokumpu mica gneiss- and granite-dominated rock association represents typical Fennoscandian bedrock. A 22 cm wide drillhole was drilled in 2004–2005 to a total depth of 2516 m and spans several independent bedrock

fracture zones (Kukkonen, 2011; Kietäväinen et al., 2013) through Paleoproterozoic, approximately 2 Ga old, bedrock. The lithology, hydrogeochemistry and gas composition of the drillhole and fracture zones have been described previously (Ahonen et al., 2011; Kietäväinen et al., 2013; Purkamo et al., 2013; Nyssönen et al., 2014). The fracture zones at 180 and 500 m depth are situated in a metasedimentary rock sequence, predominated by mica schist/biotite gneiss (Purkamo et al., 2014). The residence time for the fracture waters have been estimated to be between 20 and 50 Ma (Kietäväinen et al., 2014). The two fracture zones investigated here have previously been described in detail (Purkamo et al., 2016). In brief, the concentration of sulfate detected at 180 and 500 m was 1.5 and 1.0 mg l⁻¹, respectively, in the original fracture water. At 500 m depth, the gas to water ratio was 0.7 and methane contributed with 22 mmol l⁻¹ gas (Kietäväinen et al., 2013). The methane concentration at 180 m is not known.

Sample Collection

Deep subsurface fracture fluids were collected in October 2010 (500 m fracture) and June 2012 (180 m fracture). The fracture zones in question were isolated from the rest of the drillhole by inflatable packers (Ahonen et al., 2011). The sampling was conducted as described previously (Purkamo et al., 2013, 2016). The isolated fracture zones were purged for 21–42 days, depending on the water yield of the correspondent fracture. Care was taken to ensure that the pumping rate did not exceed the rate of inflow from the fracture zone. Temperature, pH, electrical conductivity (E_c), concentration of O₂ and redox potential (E_h) of the pumped fluid was continuously monitored in a flow-through cell and have been reported previously (Purkamo et al., 2016).

The fluid from both fracture zones was collected in the field into sterile, acid-washed 2000 ml glass bottles (Schott, Germany) in an anaerobic chamber (MBraun, Germany). Biomass for RNA and DNA extraction describing the original microbial communities was collected from two duplicate 500 ml samples for each nucleic acid fraction on 0.22 μ m filters as described earlier (Rajala et al., 2015). In order to preserve the microbial RNA, the sample processing time was kept short and filters were frozen on dry ice immediately after sample collection and maintained at -80°C until nucleic acid isolation.

Induction of Microbial Activity by Methane or Methanol

The microbial communities' response to methane (final concentration 90 mM) (referred here as CH₄) and methanol (final concentration 0.2 mM) (referred here as MetOH) was examined by introducing substrates to aliquots of sample fluid (500 ml). Sulfate (final concentration 0.375 mM, referred here as SO₄) was added in addition of CH₄ and MetOH to study if addition of possible electron acceptor changes microbial communities interactions in methane/methanol metabolisms. Sample water was divided in to sets of three parallel 500 ml subsamples to be treated with four different substrate

combinations. MetOH and SO₄ were added to samples in an anaerobic glove box and CH₄ was added through the air-tight rubber cap with N₂-flushed syringe and needle. Methanol and sulfate were made anoxic prior to use by sterile N₂ gas flush for 30 min. After the substrate addition, the samples were incubated for 2 h at 14°C in a shaker (45 rpm). The biomass from the incubated samples was collected on 0.22 μ m filters. The filters were cut from the filtration funnels with a sterile scalpel and were immediately frozen on dry ice and maintained at -80°C until RNA isolation.

Nucleic Acid Extraction

DNA was extracted from the filters containing the microbial biomass from the original fracture water (baseline situation) using the PowerWater DNA Isolation kit (MoBio Laboratories, Inc., Carlsbad, CA, USA) in accordance with the manufacturer's protocol. RNA from both original fracture water and activated samples was extracted from filter membranes using the PowerWater RNA Isolation kit (MoBio Laboratories, Inc., Carlsbad, CA, USA), including DNase, in accordance with the manufacturer's protocol. Negative reagent controls for nucleic acid extractions were included in each extraction.

Reverse Transcription

The presence of residual DNA in the RNA extracts was excluded by running a PCR with bacterial universal primers U968f and U1401r (Nübel et al., 1996) using the RNA extract as template. No PCR product was obtained, and it was thus assumed that the RNA extracts did not contain residual DNA and they were submitted to cDNA synthesis. The extracted RNA was converted to cDNA by reverse transcriptase-PCR using the Superscript III First Strand Synthesis SuperMix (Invitrogen, Carlsbad, CA, USA) as described previously (Rajala et al., 2015).

Amplicon Libraries and Sequencing

The amplification libraries for high throughput sequencing on the Ion Torrent PGM platform (Thermo Fisher Scientific) were prepared by PCR from two replicate DNA samples. Bacterial 16S rRNA genes were amplified with primers S-D-Bact-0341-b-S-17/S-D-Bact-0785-a-A-21 (Herlemann et al., 2011), targeting the variable region V3-V4 of the 16S rRNA gene, archaeal 16S rRNA genes with primers S-D-Arch-0349-a-S-17/S-D-Arch-0787-a-A-20 (Klindworth et al., 2013), targeting the V4 region of the gene. PCR amplification was performed in parallel 25 μ l reactions for every sample containing 1 \times MyTaqTM Red Mix (Bioline, London, UK), 20 pmol of each primer, up to 25 μ l nuclease-free water (Sigma, St. Louis, MO, USA) and 2 μ l of template. The PCR program consisted of an initial denaturation step at 95°C for 3 min, 35 cycles for bacteria and 40 cycles for archaea of 15 s at 95 °C, 15 s at 50°C and 15 s at 72°C. A final elongation step of 30 s was performed at 72°C. Correct size of the PCR products was verified with agarose gel electrophoresis. Amplicon libraries were sent to Bioser, University of Oulu (Finland) for sequencing on the Ion Torrent PGM equipment (Thermo Fisher Scientific), and amplicons were purified and size selected to include only 400–600 bp amplicons

on a Shimadzu capillary electrophoresis (Kyoto, Japan) prior to sequencing.

Sequence Analysis

The sequence reads obtained from Ion Torrent sequencing were subjected to quality control using the QIIME-software Version 1.9 (Caporaso et al., 2010) using a minimum quality score of 20, minimum and maximum sequence length of 200 and 600 bp, respectively, maximum primer mismatch of two nucleotides (nt) and maximum homopolymer stretches of eight nt. Adapters, barcodes and primers were removed from the sequence reads, and chimeric sequence reads were removed from the dataset with the USEARCH-algorithm (Edgar, 2010) by *de novo* detection and through similarity searches against the Greengenes reference dataset (Version gg_13_5) (DeSantis et al., 2006) with bacterial and archaeal sequences. OTUs were picked at 97% sequence homology against the Greengenes database, and *de novo* OTUs were picked from a randomly subsampled sequence subset that failed the closed-reference OTU-picking stage. Singleton OTUs, i.e., OTUs that were represented by a single sequence, were filtered from the dataset. Taxonomy from domain to species level was assigned to OTUs via representative OTU sequences with the Ribosomal Database Project (RDP) classifier algorithm at a minimum of 80% confidence (Wang et al., 2007). Sequences that did not get any taxonomic assignments were removed from the data sets. Alpha diversity calculations were performed on the absolute OUT abundance data as well as on data normalized to 1000 sequence reads per sample for better comparison between samples. Samples with less than 1000 sequence reads were not normalized.

The sequences were deposited in the European Nucleotide Archive (ENA¹) under accession number PRJEB18131.

Statistical Analyses and Data

Visualization

Alpha-diversity measures (observed OTUs, Chao1 OTU richness and Shannon diversity index) were calculated based on the OTU abundance data outputted by QIIME using the Phyloseq package in R (R Development Core Team, 2013; McMurdie and Holmes, 2015) and visualized using ggplot2. The similarity of the archaeal and bacterial communities between the different treatments was tested by principal coordinate analysis (PCoA) using the Phyloseq package in R. The analysis was performed using the OTU abundance data outputted by QIIME. The Bray-Curtis distance model was used for both analyses. Eigen values for the variance explained by the PCoA dimensions were calculated on 999 permutations using vegan (Oksanen et al., 2016) in R. An UPGMA tree clustering the samples according to similarity in the OTU profiles and a heatmap was calculated using the 1000 most abundant OTUs with the Bray-Curtis similarity model using phyloseq in R. Statistically significant differences in number of observed OTUs, Chao1-estimated richness and Shannon diversity between treatment types (original DNA and RNA, amendments) and between the different depths was analyzed

with one-way ANOVA, Tukey's pairwise test, Kruskal-Wallis and Mann-Whitney pairwise test using the PAST software (Hammer et al., 2001).

Induction of Respiration and Transcription by Addition of Substrates

The activating effect of methane or methanol on microbial communities was identified by the redox indicating dye 5-cyano-2,3-ditolyl tetrazolium chloride (CTC, Polysciences Inc., Warrington, PA, USA). 50 ml sterile, acid-washed glass serum bottles (Wheaton, NJ, USA) were flushed with sterile N₂ gas for 30 min, each containing 0.55 ml 50 mM CTC dye, and sealed with sterile butyl rubber stoppers (Bellco Glass Inc., Vineland, NJ, USA) and open top aluminum crimp caps (Sigma, St. Louis, MO, USA). Fracture fluid, after 4 weeks of starvation, was aliquoted (5 ml) under anoxic atmosphere through the butyl rubber stoppers into the sealed infusion bottles using a N₂-flushed sterile syringe and needle. The bottles were amended with filter-sterilized CH₄ (9 mM) or anoxic filter-sterilized methanol (0.2 mM) with or without sulfate (anoxic, filter-sterilized, final concentration 0.375 mM).

The samples were incubated together with the CTC dye for 6 h, according to the manufacturers recommendations, at +14°C on a shaker (45 rpm), after which 0.5 ml glycerol-TE buffer was added to the samples for preservation at -80°C according to the protocol by the Single Cell Genomics Center². Briefly the samples were divided into 1 ml aliquots in sterile cryo-tubes and immediately frozen in liquid N₂ and stored at -80°C. A non-dyed reference sample was prepared and preserved in the same way as the dyed samples.

The CTC-dyed and un-dyed fracture fluid aliquots were carefully thawed on ice prior to screening by flow cytometry (BD FACSaria flow cytometer, Becton Dickinson, Franklin Lakes, NJ, USA). Samples were injected into a sterile phosphate buffered saline (PBS) flow stream and fluorescence was detected using a 655 nm long pass and 675/20 nm band pass filters. For excitation of CTC, an argon laser was used (488 nm). To detect the active respiratory cells, simultaneous measurements of forward light scatter (relative size), side light scatter (cell granularity), and CTC fluorescence emission were used, by setting the PMT voltage to 250, 250, and 500 volts, respectively. The side scatter threshold was set to 2000. To investigate the concentration of respiratory active cells, events were acquired over a time of 30 s with a flow rate of 10 μ l min⁻¹ from each sample. The fluorescence signal was plotted to the side scatter and analyzed with the BD FACSDivaTM 5.1 software (Becton Dickinson, Franklin Lakes, NJ, USA). The CTC positive cells were gated comparing the fluorescence intensities of the dyed to the un-dyed fracture fluid sample.

For comparison total number of cells was determined by staining with 4',6-diamidino-2-phenylindole (DAPI) and microscopy as described by Purkamo et al. (2013) and Rajala et al. (2015).

¹<https://www.ebi.ac.uk/>

²https://scgc.bigelow.org/PDFs/Sample_cryopreservation_glyTE.pdf

RESULTS

Active Population

The total number of microbial cells in the fracture fluid at the time of sampling was evaluated by counting DAPI stained cells using epifluorescence microscopy (Rajala et al., 2015). In addition, the proportion of respiratory active cells was determined by staining using the redox sensitive dye, CTC, and counting the cells using flow cytometry. The number of microbial cells was $3 \times 10^5 \text{ ml}^{-1}$, of which 87% were respiratory active at the depth of 180 m. At 500 m depth the number of cells was $6 \times 10^4 \text{ ml}^{-1}$, of which only 0.3% were active (Figure 1). The microbial population from 500 m depth responded to the addition of methane and methanol by increasing metabolic activity. The largest increase in metabolic activity (16.3%) was seen in $\text{CH}_4 + \text{SO}_4$ amended sample (Figure 1). Sulfate alone did not affect the metabolic activity of the microbial community of the 500 m depth and methane amendment caused slightly lower increase in the activity (11.6%). Sulfate combined to methanol also increased the activity (9%) slightly more than methanol alone (5.2%). The microbial community from the 180 m depth where the majority of microbial community was respiratory active did not respond in the same way to the amendment of methane or methanol substrates or sulfate as the community at 500 m but the activity of community remained low (Figure 1).

Bacterial Community

Proteobacteria accounted for the majority of the bacterial communities at both 180 and 500 m depths, but substrate

addition changed the 16S rRNA profile at both depths. At the 180 m depth the original fracture water community (DNA and RNA) consisted of Betaproteobacteria, Clostridia, Bacteroidia and Anaerolineae (Figure 2A). After methane or methanol addition the detected rRNA profile of RNA contained mainly Gammaproteobacteria (mainly genus *Pseudomonas*), with Clostridia and Betaproteobacteria as minor classes (Figure 2A and Supplementary Figure S1). This indicates that the *Pseudomonas* significantly increased their production of ribosomes as a result of the addition of substrates. There were no major differences between the systems with different substrates added. At the 500 m depth the original community detected from both the DNA and RNA fractions consisted of Alphaproteobacteria, Actinobacteria and Clostridia (Figure 2B). However, after addition of substrates the 16S rRNA profile from RNA was dominated by Alphaproteobacteria (resembling mainly *Rhodobacter*, minority *Caulobacter*) and Gammaproteobacteria (resembling *Pseudomonas*) (Figure 2B and Supplementary Figure S1).

The number of bacterial sequence reads obtained varied between 1116 and 7376 reads per sample with an average number of 3862 bacterial sequence reads per sample (Table 1). The number of observed OTUs obtained from the DNA fraction of the bacterial community of the original fracture water at 180 m depth was generally higher (411–735 OTUs) than that observed at 500 m depth (258–328 OTUs) (Table 1). The OTU number detected from the RNA fraction from 180 m depth was also higher (200–492 OTUs) than that detected from the fraction at 500 m (124–281 OTUs). The number of OTUs detected in the amended samples was on average

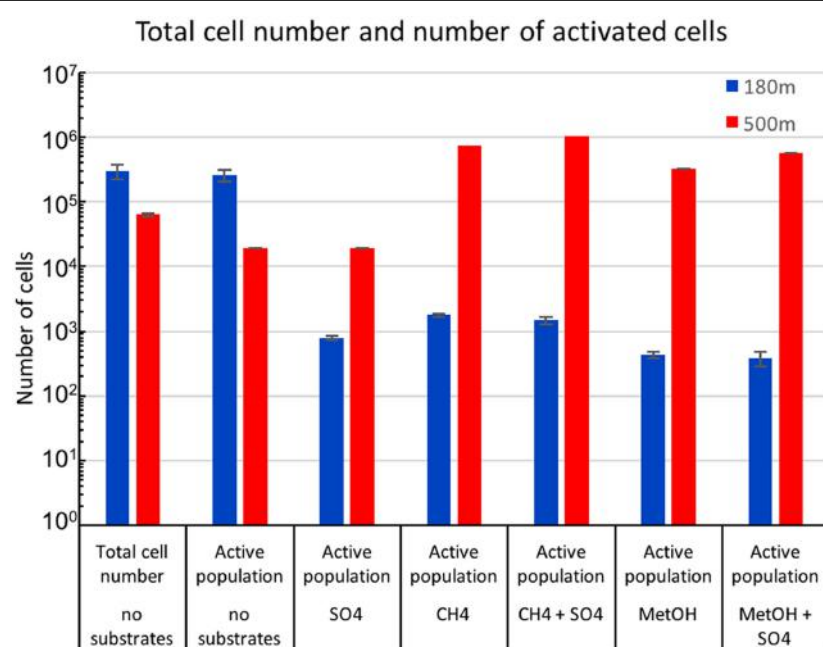


FIGURE 1 | Mean concentrations of total microbial cells from untreated fracture waters detected with DAPI staining combined to epifluorescence microscopy and active microbial population from untreated and substrate amended fracture water detected by CTC staining combined to flow cytometry.

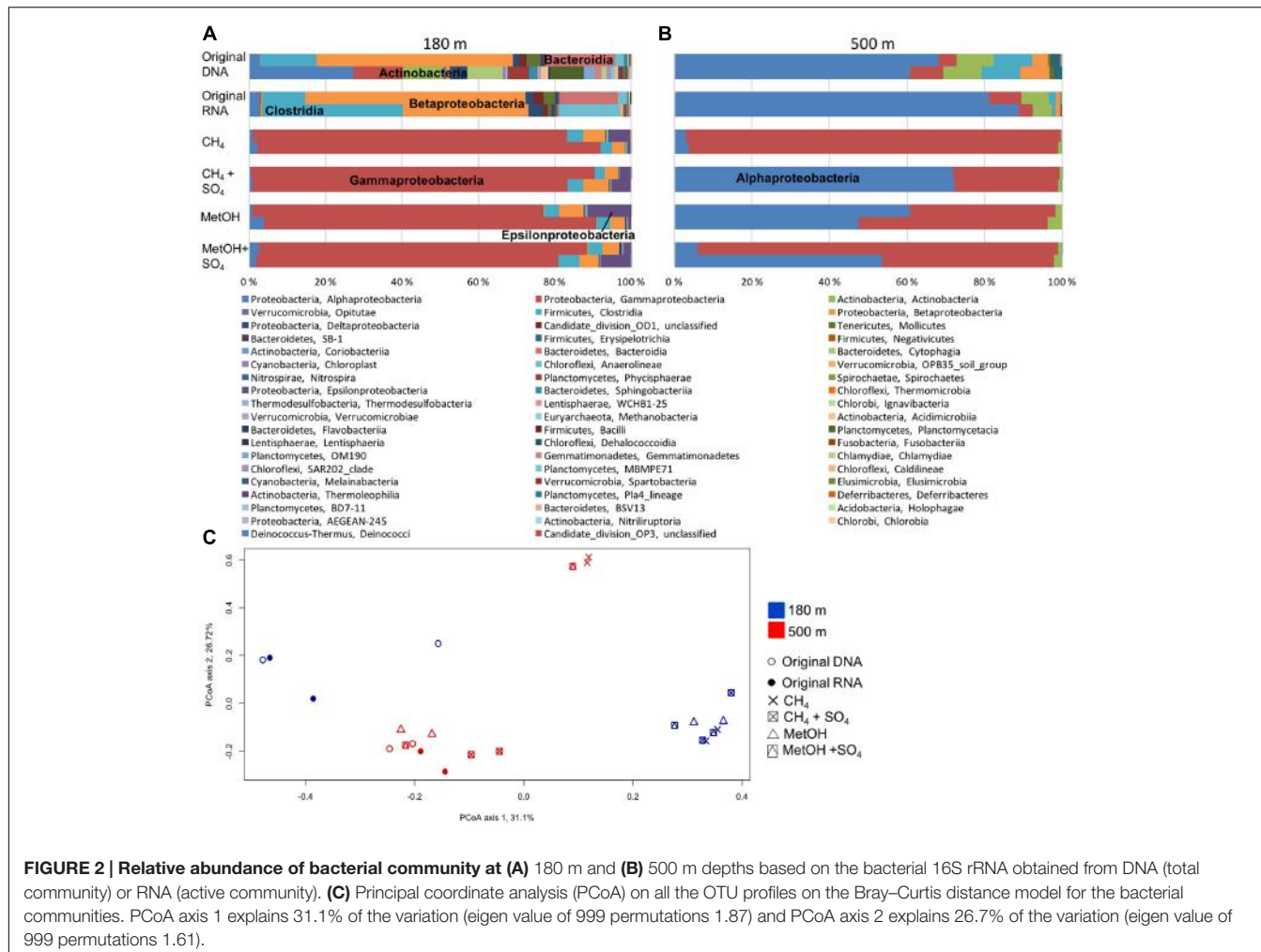


FIGURE 2 | Relative abundance of bacterial community at (A) 180 m and (B) 500 m depths based on the bacterial 16S rRNA obtained from DNA (total community) or RNA (active community). (C) Principal coordinate analysis (PCoA) on all the OTU profiles on the Bray–Curtis distance model for the bacterial communities. PCoA axis 1 explains 31.1% of the variation (eigen value of 999 permutations 1.87) and PCoA axis 2 explains 26.7% of the variation (eigen value of 999 permutations 1.61).

302 (+/– 22.6 standard error of mean SEM) OTUs in the samples from 180 m and 227 (+/– 8.1 SEM) OTUs in the samples from 500 m, which was statistically significantly lower (Tukey's pairwise $p < 0.01$, Mann–Whitney Bonferroni corrected $p < 0.05$). Taken all observed OTUs into account from the two different depths the average number of OTUs was statistically significantly lower (on average 234 OTUs per sample, SEM +/– 14.5 OTUs) in the samples from 500 m compared to the samples from 180 m (on average 355 OTUs per sample +/– 42.7 SEM), $p < 0.05$ according to Tukey's pairwise test and Mann–Whitney pairwise test with Bonferroni correction. The estimated Chao1 OTU richness was slightly higher in the samples from 180 m compared to those from 500 m (Table 1), but no statistically significant differences between the original DNA or RNA fractions or the amended samples between the two depths were observed. The Shannon diversity index H' calculated for the bacterial community of the original fracture water at the 180 m depth was 3.5–5.7 and 3.3–3.7 from the DNA and RNA fractions, respectively. In the substrate amended microcosms the H' was between 2.1 and 3.2 in all samples, and the differences were not statistically significant. However, when combining the values obtained from the same treatment of the different

depths, the average H' from the different amended samples (i.e., methane, methane+sulfate, methanol, or methanol+sulfate) were all statistically significantly lower, between 2.35 and 2.88 ($p < 0.05$) compared to the H' from the original DNA (average $H' = 4.2$) and original RNA (average $H' = 3.1$) fractions combined from both depths.

The PCoA analysis demonstrated that the community profiles from the different samples grouped into several groups. The original DNA and RNA samples from the 180 m depth fell clearly separate from the amended samples (Figure 2C). However, of the samples from 500 m, only one MetOH+SO₄ sample and both CH₄ samples fell into a different group than the original DNA and RNA samples. Of the 500 m samples the two CH₄-amended samples and one MetOH+SO₄ sample formed their own cluster separate from the other samples from the 500 m depth (Figure 2C). In addition, the samples from the two depths did not mix on the PCoA plot.

The UPGMA tree and heat map analysis, including the 1000 most abundant OTUs, based of the Bray–Curtis distance model clustered together most of the bacterial communities of the original fracture water determined by both the DNA and RNA fractions from both depths (Figure 3). The bacterial

TABLE 1 | The alpha-diversity measures (observed OTUs, Chao1 OTU richness and Shannon diversity index H') calculated for archaeal and bacterial community, numbers 1 and 2 in the sample names refer to two parallel samples included in analysis.

Depth	Sample	Number of sequences	Number of Observed OTUs	Number of Chao1-estimated OTUs	Shannon diversity index H'	*Number of Observed OTUs	*Number of Chao1-estimated OTUs	*Shannon diversity index H'
Archaea								
180 m	Original DNA1	3131	47	56	3.1	37	50	3.1
	Original DNA2	5855	36	47	2.0	25	27	2.0
	Original RNA1	7043	45	52	3.0	28	33	2.9
	Original RNA2	3443	26	28	1.7	17	17	1.6
	CH ₄ - 1	2081	22	25	1.4	17	17	1.4
	CH ₄ - 2	1505	26	35	1.5	24	30	1.4
	CH ₄ +SO ₄ - 1	310	16	18	1.7	—	—	—
	CH ₄ +SO ₄ - 2	2906	22	22	1.2	21	29	1.3
	MetOH - 1	2868	20	21	0.7	17	21	0.8
	MetOH - 2	2345	31	38	2.2	25	29	2.2
	MetOH+SO ₄ - 1	2645	19	19	1.4	16	17	1.4
	MetOH+SO ₄ - 2	2817	21	27	1.2	18	19.5	1.1
500 m	Original DNA1	891	36	66	3.0	—	—	—
	Original DNA2	66	5	6	1.5	—	—	—
	Original RNA1	—	—	—	—	—	—	—
	Original RNA2	131	8	23	1.3	—	—	—
	CH ₄ - 1	1103	25	130	2.3	24	115	2.2
	CH ₄ - 2	255	14	18	1.9	—	—	—
	CH ₄ +SO ₄ - 1	1511	24	42	2.5	22	36	2.5
	CH ₄ +SO ₄ - 2	2332	20	22	2.0	17	24	2.0
	MetOH - 1	—	—	—	—	—	—	—
	MetOH - 2	2650	58	89	2.9	37	63	2.7
	MetOH+SO ₄ - 1	3441	35	95	2.0	20	27	2.0
	MetOH+SO ₄ - 2	655	23	28	2.8	—	—	—
Bacteria								
180 m	Original DNA1	3102	735	1427	5.7	408	851	7.9
	Original DNA2	3152	411	1075	3.5	194	488	5.0
	Original RNA1	4174	492	1322	3.3	193	661	4.6
	Original RNA2	1683	200	323	3.7	161	335	5.3
	CH ₄ - 1	4143	197	497	2.1	95	179	2.9
	CH ₄ - 2	4482	246	463	2.2	103	230	3.0
	CH ₄ +SO ₄ - 1	4591	274	598	2.4	109	310	3.2
	CH ₄ +SO ₄ - 2	7376	300	534	2.4	93	254	3.2
	MetOH - 1	5005	329	676	2.3	118	268	3.2
	MetOH - 2	6981	406	767	3.1	138	383	4.4
	MetOH+SO ₄ - 1	4335	343	866	3.2	147	346	4.4
	MetOH+SO ₄ - 2	5042	325	652	2.5	127	313	3.5
500 m	Original DNA1	1771	258	789	3.6	165	565	5.0
	Original DNA2	1662	328	1268	4.0	235	760	5.6
	Original RNA1	3247	281	1101	2.7	123	278	3.9
	Original RNA2	1116	124	399	2.8	110	307	4.0
	CH ₄ - 1	3779	205	604	2.5	82	268	3.5
	CH ₄ - 2	4096	228	425	2.6	95	231	3.6
	CH ₄ +SO ₄ - 1	3883	249	579	2.8	110	280	4.0
	CH ₄ +SO ₄ - 2	4828	258	826	2.6	89	234	3.6
	MetOH - 1	3116	224	804	3.1	118	256	4.5
	MetOH - 2	4126	248	636	3.0	105	278	4.2

A dash (—) indicates missing data. *subsampled to 1000 sequence reads per sample and shown for samples with <1000 reads.

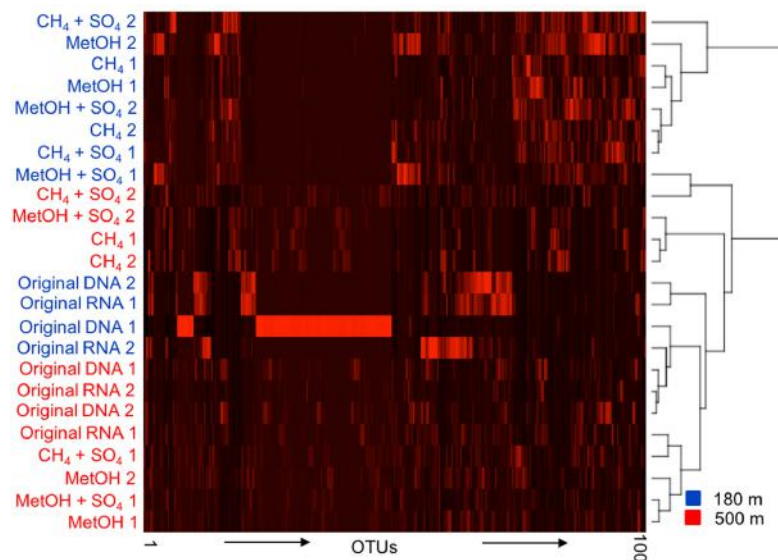


FIGURE 3 | A UPGMA cladogram clustering the samples based on the 100 most abundant OTUs of the bacterial OTU profile according to the Bray-Curtis distance model. Blue indicating 180 m depth and red indicating 500 m depth, numbers 1 and 2 refer to two parallel samples included in analysis.

communities from the substrate amended microcosms from 180 m clustered together in the heat map, while those from 500 m were split in to two different groups, one containing both CH₄-amended communities and the other containing both MetOH-amended communities, with CH₄/MetOH+SO₄ communities divided between them.

Archaeal Community

The archaeal communities consisted mostly of the Euryarchaeota at both depths. At the 180 m depth the methane or methanol did not affect the archaeal community composition (Figure 4A and Supplementary Figure S2). The major order was the Methanobacterales (Supplementary Figure S2). In addition, Methanomicrobiales, Halobacterales and thaumarcheotal Marine Group I (MGI) were detected (Supplementary Figure S2). At the 500 m depth the archaeal community structure changed due to the methane or methanol availability (Figure 4B). Methanosarcinales, Methanobacterales, Methanococcales and Methanocellales were detected from the original fracture water samples (Figure 4B and Supplementary Figure S2). As a result of methane or methanol amendments the rRNA profile of RNA changed and was dominated mainly by Halobacteriaceae that was not detected in active community of untreated fracture water, with a small portion of Methanobacteriaceae, 30% decrease in relative abundance compared to untreated RNA (Supplementary Figure S2).

The number of archaeal sequence reads obtained from the different samples varied between 0 and 4896 reads with an average of 1818 sequence reads per sample. The number of observed archaeal OTUs in the original fracture water was 30–79 and 92–100 OTUs in the DNA and RNA fractions, respectively, while in the substrate amended samples the number of OTUs varied between 26–84 archaeal OTUs. The Chao1-estimated

number of OTUs in the original fracture water was 60–130 and 149–232 OTUs in the DNA and RNA fractions, respectively and varied between 31–106 in the substrate amended samples. The H' calculated for the original fracture water was 1.9–2.1 and 2.5 in the DNA and RNA fraction, respectively and in the substrate amended samples H' varied between 1.8–2.5. At 500 m the number of observed and estimated OTUs as well as H' was generally lower than those at 180 m. The number of observed OTUs in the original fracture water was 3–24 and 4 in the DNA and RNA fractions, respectively. Nevertheless, the number of observed OTUs increased after substrate amendment to between 12–28. The Chao1-estimated number of OTUs in the original fracture water was 4–38 and 7, DNA and RNA fractions, respectively, and varied between 17–61 after substrate amendment. The H' calculated for the original fracture water at 500 m depth 0.3–2.2 and 0.2 for DNA and RNA fractions, respectively. In the substrate amended samples the H' varied between 1.3–1.7. Overall, the archaeal community had higher OTU richness and H' at 180 m than 500 m depth. Nevertheless, there were no statistically significant differences in the number of detected or Chao1-estimated OTUs or H' between the different depths or sample types.

At both depths the active archaeal community detected from the RNA fraction in the original fracture water was more diverse than that detected from DNA fractions. The PCoA plotting of the archaeal community showed clear separation between the depths (Figure 4C). The archaeal communities from the 180 m fracture zone were similar to the ones detected from the original fracture water and generally clustered together both on the PCoA plot and in the UPGMA tree (Figures 4C, 5). Nevertheless, the archaeal community profile of the substrate amended microcosms from the 500 m fracture zone clustered as a group to the left of the PCoA plot as well as in the UPGMA

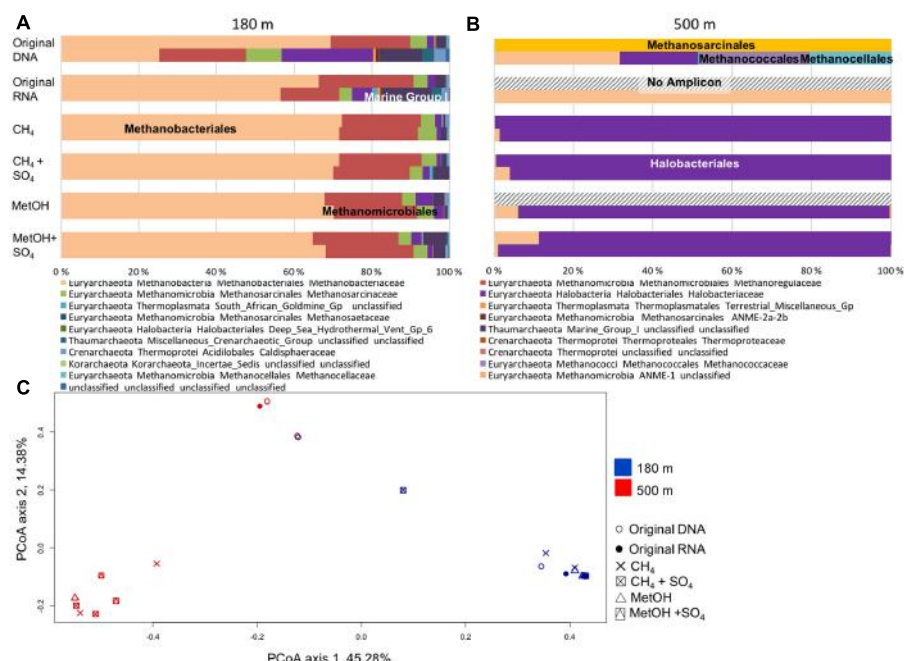


FIGURE 4 | Relative abundance of archaeal community at (A) 180 m and (B) 500 m depths based on the archaeal 16S rRNA obtained from DNA (total community) or RNA (active community). (C) PCoA on all the OTU profiles on the Bray–Curtis distance model for the archaeal communities. PCoA axis 1 explains 45.3% of the variation (eigen value of 999 permutations 3.45) and PCoA axis 2 explains 14.4% of the variation (eigen value of 999 permutations 1.11).

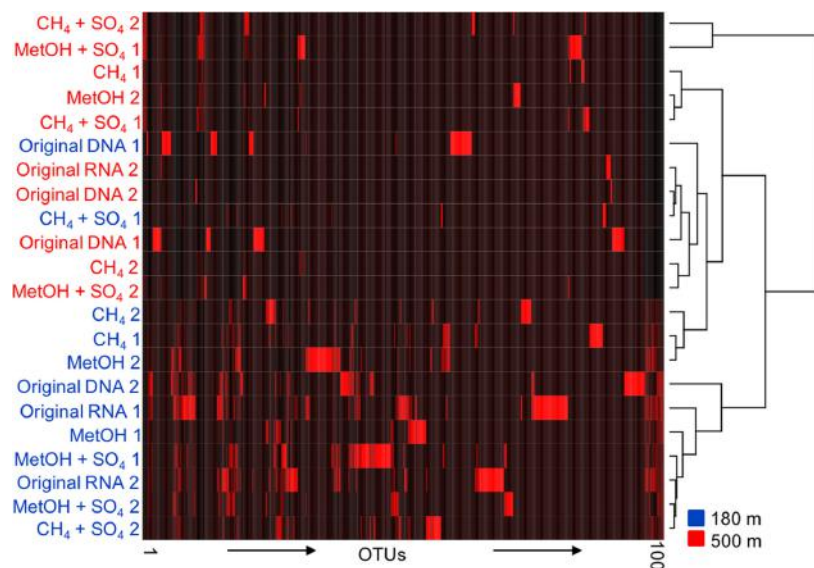


FIGURE 5 | A UPGMA cladogram clustering the samples based on the 100 biggest OTUs of the archaeal OTU profile according to the Bray–Curtis distance model. Blue indicating 180 m depth and red indicating 500 m depth, numbers 1 and 2 refer to two parallel samples included in analysis.

tree. This division indicates that a different population from that dominating in the fracture water at 500 m depth increased their transcription of ribosomes after substrate amendment allowing for more frequent detection of the ribosomal RNA of this activated population compared to the ribosomes of the dominating taxa.

DISCUSSION

Microbial communities in deep, nutrient limited subsurface environments of areas with low seismic activity are assumed to express only low metabolic activity when the environmental factors remain stable (Jørgensen and D'Hondt, 2006; Jørgensen,

2011; Hoehler and Jørgensen, 2013; Lever et al., 2015). In the present study the activity of microbial community differed largely between the two studied fracture zones, the communities of more shallow fracture, 180 m depth, being more active (87% of population active) than the communities of deeper fracture zone, 500 m depth, where only 0.3% of community was active. By remaining in dormant state the microorganisms lower their energetic expenditures. In ancient isolated subterranean fracture zones, the fluids and the surrounding rock have developed a state of equilibrium where the fluid does not leach chemical substances from the rock without external interference. Occasionally gas may be released causing a stirring in the fluid bringing a flush of nutrients or electron acceptors from the depths, but in general the deep subsurface environment is deemed stable. Nevertheless, due to land movements, such as faults on a longer geological time scale, or geological constructions, new passages for release of pressure (gas bubbles) and fluid flow may occur, and infiltration from meteoric water sources may increase. Mixing of chemically distinct fluid faces has been shown to increase microbial metabolic activity as well as change the metabolic pattern in microbial communities in deep groundwater (Pedersen, 2013). The effect of environmental changes due to for example above mentioned mechanisms was simulated by adding methane or methanol with or without sulfate to the fracture water samples. The microbial community at the 500 m depth that appeared dormant, gained respiratory activity rapidly when methane became available (11.6–16.3% activity versus only 0.3% activity of the population in untreated fracture water) demonstrating the viability and ability of long-isolated microbial communities to utilize introduced substrates, as reported also earlier (Morono et al., 2011; Pedersen, 2013; Rajala et al., 2015). However, in the shallower fracture zone, 180 m depth, where the ratio of active cells was higher, only a small sub-population was responsive to the methane or methanol amendment. Earlier, Purkamo et al. (2014) suggested that heterotrophic mechanisms such as fermenting could be community supporting strategies at certain depths of Outokumpu deep biosphere. When comparing the activated bacterial population, it was seen that at 180 m depth the *Pseudomonas* genus (Gammaproteobacteria) formed the majority of the activated community, whereas in the original community they were in minority. At 500 m depth Rhodobacterales order (Alphaproteobacteria) were enriched when methane or methanol compounds were available, in addition to *Pseudomonas*. Earlier Rhodobacterales have demonstrated to utilize methanol efficiently in seawater (Sargeant et al., 2016). Purkamo et al. (2016) suggested that the Pseudomonadaceae-related bacteria are part of the core community in deep crystalline bedrock fractures in Outokumpu and some species affiliating to *Pseudomonas* are able to grow on methanol (Riis et al., 2003).

The archaeal community at 180 m did not respond to methane or methanol amendment, whereas the archaeal community profile at 500 m depth changed from different methanogenic taxa to *Halarchaeum* after methane or methanol amendment. However, the amount of archaeal 16S rRNA sequence reads was low in untreated samples, both DNA and RNA. This is

no surprise, because the detection of archaea from these two depths is difficult as archaea have been shown to be present at only low concentrations of 6.2×10^3 and 8.6×10^1 16S rRNA gene copies ml^{-1} , while the bacterial 16S rRNA gene concentration reaches 6.3×10^6 and 1.9×10^6 gene copies ml^{-1} at 180 and 500 m, respectively (Purkamo et al., 2016). Halobacterial groups were only detected from the RNA fraction of the original groundwater, but in the DNA fraction they were not abundant enough to be detected. The fact that the *Halarchaeum* was detected in the RNA fraction of the substrate induced microcosms indicates that although their relative abundance in the community is low they are able to increase their production of ribosomes upon activation, which allows them to be detected. Our results are in accordance with Manucharova et al. (2016) who showed that archaea belonging to the Halobacteriaceae family can rapidly reactivate after long-term dormancy. The microbial community activating effect of methane addition has been demonstrated also earlier at different terrestrial deep biosphere site (Pedersen, 2013). The microbial community there responded to methane addition by increasing their metabolic activity but the activated community did not correspond to known anaerobic methane oxidizers, which would be most straight forward explanation and the full mechanisms behind activation remained unclear (Pedersen, 2013).

According to the water chemistry the two fracture zones at 180 and 500 m depth differ from each other greatly and are thought to represent distinctive water types (Kietäväinen et al., 2013). The shallower fracture zone is characterized with higher pH than the other water types in Outokumpu deep drillhole (Kietäväinen et al., 2013). The fracture water at 500 m depth, on the other hand, has been demonstrated to contain the highest amount of dissolved gases of all fracture zones crossing the deep drillhole. Approximately 75% of dissolved gases ($22\text{--}32 \text{ mmol l}^{-1}$) is methane (Kietäväinen et al., 2013). As reviewed by Kietäväinen and Purkamo (2015) the concentration of methane in Outokumpu deep bedrock is high and is in the same range as concentrations detected in the Lupin mine (Canada) and the Beatrix mine (South Africa). The fracture zones are believed to lack hydraulic connections and the exchange of the fracture fluids between the fracture zones is not considered probable (Nyyssönen et al., 2014). The prevalent rock types at these fracture zones are also different. Mica schist-biotite gneiss is the dominating rock type of the fracture at 180 m depth and Chlorite-sericite schist at 500 m depth (Purkamo et al., 2016). Despite the differences in the water chemistry and the rock types, the original microbial communities identified from DNA and RNA fractions obtained directly from the fracture waters from both depths clustered closely together in the UPGMA tree (Figures 3, 5). Purkamo et al. (2016) speculated that these two fracture zones might both be in contact with ophiolite-derived rock types and serpentinization could support microbial communities and explain the similarity of the two communities originating from separate fracture zones. In addition, the differences in the two communities was also seen as generally higher bacterial OTU numbers detected from the fracture water from 180 m compared to that from

500 m. This was also previously reported by Purkamo et al. (2016).

Even though the original microbial communities clustered together, the activity of microbial communities at these two fracture zones was very different. At 180 m 87% of the microbial cells stained active without being induced with substrates while only 0.3% did so at 500 m depth. Dormancy is estimated to be a common strategy of microorganisms in various environments, especially in deep biosphere (Jørgensen, 2011; Lennon and Jones, 2011). The low activity of the microbial community from 500 m depth is well in line with previous research, whereas an activity rate of 87% at 180 m depth might be considered unusually high for deep terrestrial biosphere (Lennon and Jones, 2011). In addition to higher activity, the cell abundance at 180 m depth was 10-fold more numerous than at 500 m depth. However, it is typical that the number of microbial cells decreases as a function of depth (Jägevall et al., 2011; Purkamo et al., 2013; Nyssönen et al., 2014). The dying of the microbial community with respiratory active dye combined to flow cytometry counting is likely not sensitive enough to detect the microbial community that is viable but respiring at extreme low level in original untreated fracture water samples. How non-sporulating microbial cells, such as those dominating in this study, might exit dormancy and how they might detect permissive environmental conditions is not clear (Dworkin and Shah, 2010; Lennon and Jones, 2011). Dormant cells need to identify growth-promoting conditions, but the wide range of possible conditions makes such a determination challenging (Dworkin and Shah, 2010). This rapid reactivation has only been tested in few studies but some evidence of reactivation within hours has been shown previously (Whitesides and Oliver, 1997).

Our results also support the idea that microorganisms present as minor groups in an environment may play an important role when microbial communities face changes in environmental conditions. These low-abundance groups may represent the so called rare biosphere (Sogin et al., 2006). The rare biosphere does not necessarily need to consist of taxa that generally are hard to find, but they may represent the minority in, for example, the fracture water habitats investigated here. The rare (or low-abundance) taxa may represent a reservoir of genetic diversity that can respond to environmental changes although the metabolic status of these taxa is unclear (Jones and Lennon, 2010). The rare biosphere may be part of the dormant microbial community and as such are thought to serve as an important reservoir to ensure the survival and diversity of a community under stressful environmental situations. These microbes may reactive and multiply following for them beneficial environmental change, a so called seed bank hypothesis (Jones and Lennon, 2010; Lennon and Jones, 2011). It is likely that both of these mechanisms support the response seen in Outokumpu fracture zone communities.

In the Outokumpu deep drillhole water the hydrogen is in isotopic equilibrium, in the system $\text{H}_2\text{O}-\text{H}_2-\text{CH}_4$ at ambient temperatures, which is thought to either indicate equilibration due to long residence time of groundwater or relatively recent *in situ* production of methane (Kietäväinen et al., 2013). In addition,

marker genes for methanogenesis have been previously detected throughout the drillhole water column (Nyssönen et al., 2014; Purkamo et al., 2016).

CONCLUSION

The respiratory activity of microbial communities in terrestrial subsurface fracture zones differed largely between fracture zones at 180 and 500 m depth. Despite apparent dormancy at the 500 m the microbial community may be able to reactivate rapidly when suitable conditions arise. The microbial community of the fracture zone at 180 m depth was originally metabolically more active than the community of the fracture zone at 500 m, and only a small sub-population was able to utilize the newly available carbon source. However, the composition of substrate activated microbial communities differed at both depths from the original communities. Our results demonstrate that the minority OTUs of the total community may play an important role when the communities face environmental changes in its living habitat.

AUTHOR CONTRIBUTIONS

PR and MB designed the work, performed the samplings, analyses, and interpreted the data. PR and MB wrote the article.

FUNDING

The sampling was funded by the Academy of Finland (DeepLife-project 133847). MB was funded by the Academy of Finland (Methano-project, 261220).

ACKNOWLEDGMENTS

Maija Nupponen-Puputti and Lotta Purkamo are thanked for the valuable help during the samplings. Mirva Pyrhönen is thanked for performing part of laboratory work. Ilmo Kukkonen, Lasse Ahonen, and Riikka Kietäväinen from Geological Survey of Finland (GTK) for providing the sampling site and tools for deep underground sampling and performing the analysis of geochemistry. Sirpa Jylhä is thanked for performing the flow cytometry analyses. Merja Itävara is acknowledged for providing the funding for the field samplings and sample preparation as well as inspiring the study of deep carbon cycling.

SUPPLEMENTARY MATERIAL

The Supplementary Material for this article can be found online at: <http://journal.frontiersin.org/article/10.3389/fmicb.2017.00431/full#supplementary-material>

FIGURE S1 | The composition of Alphaproteobacteria and Pseudomonadales communities.

FIGURE S2 | The composition of Archaeal, Methanobacterales and Halobacterales communities.

REFERENCES

- Ahonen, L., Kietäväinen, R., Kortelainen, N., Kukkonen, I. T., Pullinen, A., Toppi, T., et al. (2011). Hydrogeological characteristics of the outokumpu deep drill hole. *Spec. Pap. Geol. Surv. Finl.* 2011, 151–168.
- Arthur, M. A., and Cole, D. R. (2014). Unconventional hydrocarbon resources: prospects and problems. *Elements* 10, 257–264. doi: 10.2113/gselements.10.4.257
- Caporaso, J. G., Kuczynski, J., Stombaugh, J., Bittinger, K., Bushman, F. D., Costello, E. K., et al. (2010). QIIME allows analysis of high-throughput community sequencing data. *Nat. Methods* 7, 335–336. doi: 10.1038/nmeth.f.303
- DeSantis, T. Z., Hugenholtz, P., Larsen, N., Rojas, M., Brodie, E. L., Keller, K., et al. (2006). Greengenes, a chimera-checked 16S rRNA gene database and workbench compatible with ARB. *Appl. Environ. Microbiol.* 72, 5069–5072. doi: 10.1128/AEM.03006-05
- Dworkin, J., and Shah, I. M. (2010). Exit from dormancy in microbial organisms. *Nat. Rev. Microbiol.* 8, 890–896. doi: 10.1038/nrmicro2453
- Edgar, R. C. (2010). Search and clustering orders of magnitude faster than BLAST. *Bioinformatics* 26, 2460–2461. doi: 10.1093/bioinformatics/btq461
- Gadd, G. M. (2010). Metals, minerals and microbes: geomicrobiology and bioremediation. *Microbiology* 156, 609–643. doi: 10.1099/mic.0.037143-0
- Hammer, Ø., Harper, D. A. T., and Ryan, P. D. (2001). PAST: paleontological statistics software package for education and data analysis. *Palaeontol. Electron.* 4, 1–9.
- Haveman, S. A., and Pedersen, K. (1999). Distribution and metabolic diversity of microorganisms in deep igneous rock aquifers of Finland. *Geomicrobiol. J.* 16, 277–294. doi: 10.1080/014904599270541
- Herlemann, D. P., Labrenz, M., Jürgens, K., Bertilsson, S., Wanek, J. J., and Andersson, A. F. (2011). Transitions in bacterial communities along the 2000 km salinity gradient of the Baltic Sea. *ISME J.* 5, 1571–1579. doi: 10.1038/ismej.2011.41
- Hoehler, T. M., and Jørgensen, B. B. (2013). Microbial life under extreme energy limitation. *Nat. Rev. Microbiol.* 11, 83–94. doi: 10.1038/nrmicro2939
- Jägevall, S., Rabe, L., and Pedersen, K. (2011). Abundance and diversity of biofilms in natural and artificial aquifers of the Åspö Hard Rock Laboratory, Sweden. *Microb. Ecol.* 61, 410–422. doi: 10.1007/s00248-010-9761-z
- Jones, S. E., and Lennon, J. T. (2010). Dormancy contributes to the maintenance of microbial diversity. *Proc. Natl. Acad. Sci. U.S.A.* 107, 5881–5886. doi: 10.1073/pnas.0912765107
- Jørgensen, B. B. (2011). Deep subseafloor microbial cells on physiological standby. *Proc. Natl. Acad. Sci. U.S.A.* 108, 18193–18194. doi: 10.1073/pnas.1115421108
- Jørgensen, B. B., and D'Hondt, S. (2006). A starving majority deep beneath the seafloor. *Science* 314, 932–934. doi: 10.1126/science.1133796
- Kietäväinen, R., Ahonen, L., Kukkonen, I. T., Hendriksson, N., Nyssönen, M., and Itävara, M. (2013). Characterisation and isotopic evolution of saline waters of the Outokumpu Deep Drill Hole, Finland—implications for water origin and deep terrestrial biosphere. *Appl. Geochim.* 32, 37–51. doi: 10.1016/j.apgeochem.2012.10.013
- Kietäväinen, R., Ahonen, L., Kukkonen, I. T., Niedermann, S., and Wiersberg, T. (2014). Noble gas residence times of saline waters within crystalline bedrock, Outokumpu Deep Drill Hole, Finland—implications for water origin and deep terrestrial biosphere. *Geochim. Cosmochim. Acta* 145, 159–174. doi: 10.1016/j.gca.2014.09.012
- Kietäväinen, R., and Purkamo, L. (2015). The origin, source, and cycling of methane in deep crystalline rock biosphere. *Front. Microbiol.* 6:725. doi: 10.3389/fmicb.2015.00725
- Klindworth, A., Pruesse, E., Schweer, T., Peplies, J., Quast, C., Horn, M., et al. (2013). Evaluation of general 16S ribosomal RNA gene PCR primers for classical and next-generation sequencing-based diversity studies. *Nucleic Acids Res.* 41, 1–11. doi: 10.1093/nar/gks808
- Kukkonen, I. T. (ed.) (2011). *Outokumpu Deep Drilling Project 2003–2010*. Espoo: Geological Survey of Finland.
- Lennon, J. T., and Jones, S. E. (2011). Microbial seed banks: the ecological and evolutionary implications of dormancy. *Nat. Rev. Microbiol.* 9, 119–130. doi: 10.1038/nrmicro2504
- Lever, M. A., Rogers, K. L., Lloyd, K. G., Overmann, J., Schink, B., Thauer, R. K., et al. (2015). Life under extreme energy limitation: a synthesis of laboratory- and field-based investigations. *FEMS Microbiol. Rev.* 39, 688–728. doi: 10.1093/femsre/fuv020
- Manucharova, N. A., Trosheva, E. V., Kol'tsova, E. M., Demkina, E. V., Karaevskaya, E. V., Rivkina, E. M., et al. (2016). Characterization of the structure of the prokaryotic complex of Antarctic permafrost by molecular genetic techniques. *Microbiology* 85, 102–108. doi: 10.1134/S0026261716010057
- McMahon, S., and Parnell, J. (2014). Weighing the deep continental biosphere. *FEMS Microbiol. Ecol.* 87, 113–120. doi: 10.1111/1574-6941.12196
- McMurdie, P., and Holmes, S. (2015). Shiny-phyloseq: web application for interactive microbiome analysis with provenance tracking. *Bioinformatics* 31, 282–283. doi: 10.1093/bioinformatics/btu616
- Morono, Y., Terada, T., Nishizawa, M., Ito, M., Hillion, F., Takahata, N., et al. (2011). Carbon and nitrogen assimilation in deep subseafloor microbial cells. *Proc. Natl. Acad. Sci. U.S.A.* 108, 18295–18300. doi: 10.1073/pnas.1107763108
- Nübel, U., Engelen, B., Felske, A., Snaidr, J., Wieshuber, A., Amann, R. I., et al. (1996). Sequence heterogeneities of genes encoding 16S rRNAs in *Paenibacillus polymyxa* detected by temperature gradient gel electrophoresis. *J. Bacteriol.* 178, 5636–5643. doi: 10.1128/jb.178.19.5636-5643.1996
- Nyssönen, M., Hultman, J., Ahonen, L., Kukkonen, I., Paulin, L., Laine, P., et al. (2014). Taxonomically and functionally diverse microbial communities in deep crystalline rocks of the Fennoscandian shield. *ISME J.* 8, 126–138. doi: 10.1038/ismej.2013.125
- Oksanen, J., Blanchet, F. G., Friendly, M., Kindt, R., Legendre, P., McGlinn, D., et al. (2016). *Vegan: Community Ecology Package, R Package Version 2.4-0*. Available at: <http://CRAN.R-project.org/package=vegan> [accessed October 31, 2016].
- Pedersen, K. (1997). Microbial life in deep granitic rock. *FEMS Microbiol. Rev.* 20, 399–414. doi: 10.1016/S0168-6445(97)00022-3
- Pedersen, K. (2000). Exploration of deep interterrestrial microbial life: current perspectives. *FEMS Microbiol. Lett.* 185, 9–16. doi: 10.1111/j.1574-6968.2000.tb09033.x
- Pedersen, K. (2013). Metabolic activity of subterranean microbial communities in deep granitic groundwater supplemented with methane and H(2). *ISME J.* 7, 839–849. doi: 10.1038/ismej.2012.144
- Petsch, S. T. (2001). 14C-Dead living biomass: evidence for microbial assimilation of ancient organic carbon during shale weathering. *Science* 292, 1127–1131. doi: 10.1126/science.1058332
- Purkamo, L., Bomberg, M., Kietäväinen, R., Salavirta, H., Nyssönen, M., Nupputen-Puputti, M., et al. (2015). The keystone species of Precambrian deep bedrock biosphere belong to Burkholderiales and Clostridiales. *Biogeosci. Discuss.* 12, 18103–18150. doi: 10.5194/bgd-12-181032015
- Purkamo, L., Bomberg, M., Kietäväinen, R., Salavirta, H., Nyssönen, M., Nupputen-Puputti, M., et al. (2016). Microbial co-occurrence patterns in deep Precambrian bedrock fracture fluids. *Biogeosciences* 13, 3091–3108. doi: 10.5194/bg-13-3091-2016
- Purkamo, L., Bomberg, M., Nyssönen, M., Kukkonen, I., Ahonen, L., and Itävara, M. (2014). Heterotrophic communities supplied by ancient organic carbon predominate in deep fennoscandian bedrock fluids. *Microb. Ecol.* 69, 319–332. doi: 10.1007/s00248-014-0490-6
- Purkamo, L., Bomberg, M., Nyssönen, M., Kukkonen, I., Ahonen, L., Kietäväinen, R., et al. (2013). Dissecting the deep biosphere: retrieving authentic microbial communities from packer-isolated deep crystalline bedrock fracture zones. *FEMS Microbiol. Ecol.* 85, 324–337. doi: 10.1111/1574-6941.12126
- R Development Core Team (2013). *R: A Language and Environment for Statistical Computing*. Available at: <http://www.r-project.org/>
- Rajala, P., Bomberg, M., Kietäväinen, R., Kukkonen, I., Ahonen, L., Nyssönen, M., et al. (2015). Rapid reactivation of deep subsurface microbes in the presence of C-1 compounds. *Microorganisms* 3, 17–33. doi: 10.3390/microorganisms3010017
- Riis, V., Miethe, D., and Babel, W. (2003). Formate-stimulated oxidation of methanol by *Pseudomonas putida* 9816. *Biosci. Biotechnol. Biochem.* 67, 684–690. doi: 10.1271/bbb.67.684
- Sargeant, S., Murrell, J., Nightingale, P., and Dixon, J. (2016). Seasonal variability in microbial methanol utilisation in coastal waters of the western English Channel. *Mar. Ecol. Prog. Ser.* 550, 53–64. doi: 10.3354/meps11705

- Sass, H., and Cypionka, H. (2004). Isolation of sulfate-reducing bacteria from the terrestrial deep subsurface and description of *Desulfovibrio cavernae* sp. nov. *Syst. Appl. Microbiol.* 27, 541–548. doi: 10.1078/0723202041748181
- Sogin, M. L., Morrison, H. G., Huber, J. A., Welch, D. M., Huse, S. M., Neal, P. R., et al. (2006). Microbial diversity in the deep sea and the underexplored rare biosphere. *Proc. Natl. Acad. Sci. U.S.A.* 103, 12115–12120. doi: 10.1073/pnas.0605127103
- van Bodegom, P. (2007). Microbial maintenance: a critical review on its quantification. *Microb. Ecol.* 53, 513–523. doi: 10.1007/s00248-006-9049-5
- Wang, Q., Garrity, G. M., Tiedje, J. M., and Cole, J. R. (2007). Naive Bayesian classifier for rapid assignment of rRNA sequences into the new bacterial taxonomy. *Appl. Environ. Microbiol.* 73, 5261–5267. doi: 10.1128/AEM.00062-07
- Whitesides, M. D., and Oliver, J. D. (1997). Resuscitation of *Vibrio vulnificus* from the viable but nonculturable state. *Appl. Environ. Microbiol.* 63, 1002–1005.
- Wu, X., Holmfeldt, K., Hubalek, V., Lundin, D., Åström, M., Bertilsson, S., et al. (2015). Microbial metagenomes from three aquifers in the Fennoscandian shield terrestrial deep biosphere reveal metabolic partitioning among populations. *ISME J.* 10, 1192–1203. doi: 10.1038/ismej.2015.185

Conflict of Interest Statement: The authors declare that the research was conducted in the absence of any commercial or financial relationships that could be construed as a potential conflict of interest.

Copyright © 2017 Rajala and Bomberg. This is an open-access article distributed under the terms of the Creative Commons Attribution License (CC BY). The use, distribution or reproduction in other forums is permitted, provided the original author(s) or licensor are credited and that the original publication in this journal is cited, in accordance with accepted academic practice. No use, distribution or reproduction is permitted which does not comply with these terms.



Response of Deep Subsurface Microbial Community to Different Carbon Sources and Electron Acceptors during ~2 months Incubation in Microcosms

Lotta Purkamo^{1*†}, Malin Bomberg¹, Mari Nyssönen¹, Lasse Ahonen², Ilmo Kukkonen³ and Merja Itävaara¹

¹ VTT Technical Research Centre of Finland, Espoo, Finland, ² Geological Survey of Finland, Espoo, Finland, ³ Department of Physics, University of Helsinki, Helsinki, Finland

OPEN ACCESS

Edited by:

Donato Giovannelli,
Tokyo Institute of Technology, Japan

Reviewed by:

William D. Orsi,
Ludwig Maximilian University
of Munich, Germany
Katharina Palmer,
University of Oulu, Finland

*Correspondence:

Lotta Purkamo
lkp5@st-andrews.ac.uk

†Present address:

Lotta Purkamo,
School of Earth and Environmental
Sciences, University of St Andrews,
St Andrews, UK

Specialty section:

This article was submitted to
Microbiological Chemistry
and Geomicrobiology,
a section of the journal
Frontiers in Microbiology

Received: 15 November 2016

Accepted: 02 February 2017

Published: 20 February 2017

Citation:

Purkamo L, Bomberg M,
Nyssönen M, Ahonen L, Kukkonen I
and Itävaara M (2017) Response
of Deep Subsurface Microbial
Community to Different Carbon
Sources and Electron Acceptors
during ~2 months Incubation
in Microcosms.
Front. Microbiol. 8:232.
doi: 10.3389/fmicb.2017.00232

Acetate plays a key role as electron donor and acceptor and serves as carbon source in oligotrophic deep subsurface environments. It can be produced from inorganic carbon by acetogenic microbes or through breakdown of more complex organic matter. Acetate is an important molecule for sulfate reducers that are substantially present in several deep bedrock environments. Aceticlastic methanogens use acetate as an electron donor and/or a carbon source. The goal of this study was to shed light on carbon cycling and competition in microbial communities in fracture fluids of Finnish crystalline bedrock groundwater system. Fracture fluid was anaerobically collected from a fracture zone at 967 m depth of the Outokumpu Deep Drill Hole and amended with acetate, acetate + sulfate, sulfate only or left unamended as a control and incubated up to 68 days. The headspace atmosphere of microcosms consisted of 80% hydrogen and 20% CO₂. We studied the changes in the microbial communities with community fingerprinting technique as well as high-throughput 16S rRNA gene amplicon sequencing. The amended microcosms hosted more diverse bacterial communities compared to the intrinsic fracture zone community and the control treatment without amendments. The majority of the bacterial populations enriched with acetate belonged to clostridial hydrogenotrophic thiosulfate reducers and *Alphaproteobacteria* affiliating with groups earlier found from subsurface and groundwater environments. We detected a slight increase in the number of sulfate reducers after the 68 days of incubation. The microbial community changed significantly during the experiment, but increase in specifically acetate-cycling microbial groups was not observed.

Keywords: acetate, heterotrophy, autotrophy, deep biosphere, crystalline terrestrial bedrock, enrichment culture, competition, sulfate reducing bacteria

INTRODUCTION

After the discovery of the existence of the deep, hot biosphere in the crustal setting over 20 years ago, we have been continuously amazed by the life thriving in these harsh and extreme environments (Gold, 1992; Whitman et al., 1998; McMahon and Parnell, 2014). These anoxic, highly reducing, saline environments are commonly nutrient-depleted and oligotrophic, while

pressure and temperature increase with depth (Pedersen, 1993, 1997; Lovley and Chapelle, 1995; Amend and Teske, 2005; Fredrickson and Balkwill, 2006; Dong, 2008). Still, the carbon sources and energy substrates for the microbial life deep beneath the surface remain to be fully described. Traditional perception of the metabolism of deep-dwelling microbes is that they are chemolithotrophic using inorganic carbon and hydrogen as their carbon and energy source (Pedersen, 1993, 1997; Stevens and McKinley, 1995; Chapelle et al., 2002; Haveman and Pedersen, 2002; Amend and Teske, 2005; Lin et al., 2005a,b; Nealson et al., 2005). Autotrophs, such as methanogens and acetogens, acquire their carbon and energy sources from the deep Earth's crust, while essential nutrients such as phosphorus and nitrogen can be derived from minerals or dissolved gas, respectively (Pedersen, 1997; Rogers et al., 1998; Bennett et al., 2001; Lin et al., 2005a). However, recent studies show that deep crystalline bedrock in Finland hosts diverse heterotrophic microbial communities in its ancient fracture fluids (Purkamo et al., 2013; Kietäväinen et al., 2014; Purkamo et al., 2015, 2016).

Organic carbon can originate from abiotic or biotic sources in the bedrock. Serpentization, i.e., hydration of olivine in ultramafic rocks, leads to hydrogen generation and abiotic synthesis of organic matter (McCollom and Seewald, 2001; Proskurowski et al., 2008; Lang et al., 2010; Russell et al., 2010; Schrenk et al., 2013). Many microbial groups can use acetate and contribute significantly to the total organic carbon content and carbon cycling of the deep biosphere (Pedersen, 1997; Lever, 2012). Acetate is a key molecule in carbon cycling and can be used by microbes involved in sulfur cycling, thus linking these two important elemental cycles together (Muyzer and Stams, 2008). Sulfate reducers that are incomplete oxidizers produce acetate by metabolizing for example fatty acids, while other group of sulfate reducers completely oxidizes acetate to carbon dioxide (Rabus et al., 2006). Aceticlastic methanogenic archaea can use acetate as an electron donor and/or a carbon source (e.g., Chaudhary et al., 2013; Costa and Leigh, 2014). Microbes are responsible for biological acetate production, either by autotrophy or by fermenting organic matter. Autotrophic acetogens in the deep subsurface use CO_2 and H_2 emanating from the mantle to produce acetate (Pedersen, 1997). Organic compounds, on the other hand, can either be transported from the surface deeper to the groundwater system by fluid circulation or after being buried and metamorphosed, remain trapped in the rock record (Krumholz et al., 1997; Fredrickson and Balkwill, 2006; Strapoć et al., 2011). Organotrophic and fermenting microbes can decompose this more complex and sometimes recalcitrant organic matter to smaller compounds such as acetate (Krumholz et al., 1997; Petsch et al., 2001, 2005; Fredrickson and Balkwill, 2006; Matlakowska and Skłodowska, 2011). Recently, bacteriophages have been determined to be significantly impacting the deep crystalline bedrock biosphere by creating a viral shunt and release of organic material via bacterial cell lysis (Kyle et al., 2008; Pedersen, 2012). Thus, using acetate as a representative of small organic carbon can help us to understand the organotrophic potential of microbial communities in the deep terrestrial biosphere.

The goal of this research was to study the effect of supplying an ample source of organic carbon to a microbial community inhabiting naturally oligotrophic groundwaters in deep Fennoscandian crystalline bedrock. In addition, we aimed to understand the role of sulfate reducers in these habitats and their ability to compete with methanogens and acetogens for substrates and electron donors. Since most microorganisms in the deep subsurface cannot be cultured, we applied molecular biology methods in order to reveal changes in community structure in groundwater samples enriched with an organic carbon source/electron donor (acetate), inorganic carbon source/electron acceptor (CO_2) and/or electron acceptor (sulfate), and electron donor (H_2) over an incubation period of over 2 months. DGGE fingerprinting was used first for rough characterization of the community structure and detecting the changes in the community during the incubation. As a nested PCR approach was required to produce sufficient amount of amplicons for DGGE, we decided to confirm the results and obtain a more refined characterization of the bacterial communities with high throughput amplicon sequencing. Acetate was chosen for organic carbon source for microbial communities for two reasons: (1) in anaerobic environments, such as the deep subsurface, acetate is a key intermediate in degradation of organic matter by for example sulfate reducers and (2), acetate could sustain heterotrophic communities which have previously been detected in the Fennoscandian shield bedrock environments (Itävaara et al., 2011; Purkamo et al., 2013, 2016; Nyysönen et al., 2014). In addition, sulfate reducers can use acetate as a carbon source and as an electron donor. Sulfate reducing bacteria have been detected both in this fracture as well as in the drill hole fluids at the depth of the fracture zone, although the sulfate concentrations measured from this depth are less than 1 mg L^{-1} (Itävaara et al., 2011; Kietäväinen et al., 2013; Purkamo et al., 2016). Thus, the usability of sulfate as terminal electron acceptor for the microbial community in Outokumpu was also assessed. Autotrophic microbial groups in the microbial community were targeted with CO_2 and H_2 amendment in order to evaluate their potential in competing with heterotrophic microbes.

MATERIALS AND METHODS

Sampling and Enrichment

The Outokumpu Deep Scientific Drill Hole pierces through Palaeoproterozoic rock formation comprising of metamorphic schists and skarns, serpentized ophiolite-derived rocks and pegmatitic granite, reaching a depth of 2516 m. The fluids emanating from the 967 m fracture zone are saline: total dissolved solids are 13 g L^{-1} , with Ca, Na and Cl as main dissolved components (Ahonen et al., 2011; Kietäväinen et al., 2013). Gas is abundantly present in the fluids, comprising mainly of methane at 967 m fracture depth (Kietäväinen et al., 2013). This drill hole provides access to intrinsic, millions of years old saline fracture fluids of Fennoscandian Shield when using appropriate sampling methods (Purkamo et al., 2013). The intrinsic microbial communities have been characterized

from this fracture, and bacterial communities are comprised of phylotypes belonging to *Clostridia* and *Betaproteobacteria*. Archaeal populations at this fracture zone are dominated by *Hadesarchaea* and *Methanobacteriaceae* (Purkamo et al., 2016).

Fluid samples were collected in September 2009 from a fracture zone at the Outokumpu Deep Drill Hole. Sampling was optimized to obtain the indigenous microbial population from 967 m fracture zone with packer installation and sampling conducted as described on Purkamo et al. (2013). Briefly, two packers were positioned at 962 and 972 m depth flanking the fracture zone. The packers were expanded with tap water in order to seal the fracture zone and prevent water flow from other parts of the drill hole. After c. 4.6 m³ of fluid was pumped from the packer-isolated fracture zone, samples from indigenous fracture fluid were retrieved through a factory-clean polyamide tube. The fluid samples were collected in acid-washed, 120-mL serum bottles in a portable anaerobic chamber (MBRAUN, Garching, Germany), prepared under anoxic conditions as described in Purkamo et al. (2013). The sample bottles were first flushed with approximately 30 mL of fracture fluid in order to remove possible oxygen contamination of the bottle surfaces. After flushing, bottles were filled with 100 mL fracture fluid. The samples were amended with sodium acetate (final concentration 4 mM), sodium acetate and sodium sulfate (4 and 15 mM, respectively), only sodium sulfate (15 mM) or left unamended as controls. Vials were closed with butyl rubber stoppers and aluminum crimp caps (Sigma). The gas phase (20 mL) in the sealed bottles consisted of 80% hydrogen and 20% carbon dioxide, which was generated by gassing the headspace for approximately 1 min, and then adding a 20 mL overpressure of H₂-CO₂ gas mixture using a 50 mL syringe equipped with a needle pushed through the rubber stopper. All treatments were performed in triplicate and three similar sets were prepared, each to be sacrificed in one time point. Enrichments were incubated at 18°C, corresponding to the *in situ* temperature at 967 m in the drill hole, with slow rotation for 4, 32, or 68 days. In addition, biomass from a 100-mL sample of fracture water was collected on a Sterivex filter unit and immediately placed in dry ice in the field. A total of three of these zero-time point controls were collected and kept frozen at -80°C in the laboratory until DNA extraction.

Biomass Collection and DNA Extraction

Following the incubation, biomass of the enrichments was collected from triplicates of each treatment with Sterivex filtration units (Millipore, Billercia, MA, USA) and immediately frozen to -80°C. DNA from the biomass of the enrichments was extracted with Mobio's PowerWater DNA extraction kit (Mobio Laboratories, Inc. Carlsbad, CA, USA). Sterivex columns were thawed on ice and opened in a laminar flow hood using sterile pliers. Each filter was cut with a sterile scalpel to approximately 2 × 25 mm slices and transferred to a bead tube. DNA from the biomass was extracted according to the manufacturer's protocol. DNA was eluted in 50 µl of molecular grade H₂O. An extraction control without any sample was included in each extraction batch. Extracted DNA concentrations were measured with a NanoDrop-1000 spectrophotometer (Thermo Fisher Scientific, Waltham, MA, USA).

Quantity of Total Bacteria, Sulfate Reducing Bacteria and Methanogens in the Microcosms

The numbers of 16S rRNA, *dsrB* and *mcrA* gene copies in the enrichments was determined with quantitative PCR (qPCR). The qPCR reactions (10 µl each) consisted of Kapa SYBR FAST 2x qPCR Master Mix for Roche LightCycler 480 (Kapa Biosystems, Woburn, MA, USA), 1.5, 2.5 or 2.5 pmol (16S rRNA gene, *dsrB* gene and *mcrA* gene, respectively) of each primer and 1 µl template DNA. The 16S ribosomal RNA genes were amplified with p1 and p2 primers (Muyzer et al., 1993), *dsrB* gene with primers DSRp2060f (5'-CAACATCGTYCAYACCCAGGG-3') (Wagner et al., 1998) and DSR4r (5'-GTGTAGCAGTTACCGCA-3') (Geets et al., 2006) and *mcrA* gene with primers ME1 (5'-GCMATGCARATHGGWATGTC-3') (Hales et al., 1996) and ME3R (5'-TGTGTGAACWCKACDCCACC-3') (Nyyssönen et al., 2012). All qPCR reactions were conducted in triplicate and a negative template control was included in each run. The qPCR assays were performed with a LightCycler 480 (Roche Applied Science, Germany) using the following thermal protocol for 16S rRNA gene fragments: an initial denaturation step at 95°C for 10 min, 40 or 50 cycles of amplification with three steps: 15 s at 95°C, 30 s at 57°C and 30 s at 72°C. For *dsrB* genes, amplification was performed in 50 cycles of 10 s at 95°C, 35 s at 55°C and 30 s at 72°C. The *mcrA* genes were amplified with following protocol: 45 cycles of 10 s denaturation step at 95°C, 35 s annealing at 55°C, 30 s elongation step at 72°C. In addition, all qPCR programs contained a final elongation step for 3 min at 72°C. After the amplification, a melting curve analysis consisting of a denaturation step for 10 s at 95°C followed by an annealing step at 65°C for 1 min prior to a gradual temperature rise to 95°C at a rate of 0.11°C s⁻¹ during which the fluorescence was continuously measured, was performed. Results of the melting curves were checked immediately after each run for primer dimer formation. Primer-dimer peaks were usually detected, but those were always at distinctly lower temperature (<72°C) as the main amplification products.

The copy number of each gene was estimated by comparing the amplification result to a standard dilution series reaching from 1.8×10^2 to 1.8×10^8 of plasmids containing the 16S rRNA gene of *Escherichia coli* ATCC 31608 (total bacterial number estimate) or 2.4×10^1 to 2.4×10^7 copies of plasmids containing the *dsrB* gene from *Desulfobulbus propionicus* DSM 2554 (estimated quantity of sulfate reducers) or plasmids containing the *mcrA* (dilution series from 5 to 5.03×10^6 plasmids) of *Methanothermobacter thermoautotrophicus* strain DSM 1053.

PCR-DGGE

The 16S rRNA gene -targeted PCR for bacteria employed a nested PCR approach, where the first round PCR primers fd1 (5'-AGAGTTTGATCCTGGCTCAG-3') and rD1(5'-AAGGAGGTGATCCAGCC-3') produce an almost full length 16S rRNA gene fragment (Weisburg et al., 1991), and the nested PCR primers p1(5'-CCTACGGAGGCAGCAG-3') and p2 (5'-ATTACCGCGCTGCTGG-3') a 193-bp fragment cover

the V3 region of the gene (Muyzer et al., 1993). Primer p1 included a GC-clamp for the subsequent DGGE analysis. PCR amplification was performed in 50 μ l reactions containing Dynazyme II buffer (10 mM Tris-HCl, pH 8.8, 1.5 mM MgCl₂, 50 mM KCl, and 1% Triton-X 100), 1% formamide, 0.2 mM final concentration of each deoxynucleoside triphosphate dNTP, 20 pmol of each primer, 2 units of Dynazyme II polymerase enzyme (ThermoFisher Scientific, Waltham, MA, USA), and 1 or 2.5 μ l of template (first PCR and nested PCR, respectively). The amplification program employed consisted of an initial denaturation step at 94°C for 5 min, 35 cycles of 1 min at 94°C, 1 min at 55°C, and 1 min at 72°C. A final elongation step of 10 min was performed at 72°C. Products from 16S rRNA gene-PCR were run in denaturing gradient gel electrophoresis (DGGE) as described in Purkamo et al. (2013). Distinctive DNA bands were cut out, the DNA extracted in 20 μ l of molecular biology grade water (Sigma) overnight and frozen at -20°C before reamplification for sequencing using primers p1 and p2 as described above. PCR products were checked in 1% agarose gel and sent for sequencing to Macrogen Inc. (South Korea).

High-Throughput Sequencing

The 16S rRNA gene amplicons were prepared from triplicate microcosms for each treatment and time point for high-throughput sequencing with the Ion Torrent PGM platform. Barcode attachment was done using PCR with 1.5 x MyTaq Red Mix according to the manufacturers instructions with primers 341f and 785r (20 mM each) (Herlemann et al., 2011) and 2 μ l of template in 25 μ l total reaction volume. Duplicate PCR reactions were prepared from each triplicate DNA extract in addition to the day 0 reference samples (i.e., the fracture water sample taken in the field), and with positive control (*Paracoccus denitrificans* DSM 413) and negative controls (PCR-grade water and extraction control sample). Duplicate PCR-products were combined and sequenced at Bioser Oulu (University of Oulu, Finland) using the 316 Chip Kit v2 with Ion PGM Template IA 500 and Ion PGM Hi-Q Sequencing kits (Thermo Fisher Scientific, Waltham, MA, USA).

Accession Numbers

Retrieved sequences were deposited with the European nucleotide archive (ENA) database, DGGE band sequences with accession numbers LT634494-LT634570, and the Ion Torrent – produced amplicon sequences are deposited as data project PRJEB16746.

Sequence Data Processing

Sequences obtained from DGGE analysis were aligned with relevant reference sequences retrieved from NCBI's nucleotide database using the Geneious Pro software (v. 6.1.7, Biomatters Ltd, Auckland, New Zealand) with ClustalW and Muscle with default settings. Alignment was manually checked and edited, and phylogenetic trees were calculated using PhyML in Geneious Pro, applying the Jukes-Cantor 69 substitution model (Jukes and Cantor, 1969; Guindon and Gascuel, 2003).

The data retrieved from high-throughput sequencing (in fastq – format) was demultiplexed and quality screened with

the MOTHUR software (v.1.36.0) (Schloss et al., 2009). Only the sequences with minimum length of 200 bp and average quality score 25 were retained. Sequences were aligned to the Silva reference alignment (release 123) (Quast et al., 2013). Preclustering was performed in order to remove sequences with possible sequencing errors. Chimeric sequences were identified with chimera.slayer command using Silva gold alignment as a reference and removed from the dataset. The unique sequences were classified using SILVA reference taxonomy (release 123)¹ (Quast et al., 2013) and assigned to OTUs with phylotype command in MOTHUR. We used the alpha_diversity.py command for calculating the alpha diversity indices chao1, shannon and observed_ottus using the QIIME software (MacQIIME v. 1.9.1) (Caporaso et al., 2010) using a biom-file constructed in MOTHUR. In addition, we calculated abundance coverage-based estimator (ACE), Good's coverage and Shannon evenness metrics with MOTHUR using the command collect.single for the shared-file. Total richness and shared OTUs between sample replicates as well as samples were revealed by constructing venn-diagrams from the shared-file in MOTHUR.

Statistical Analyses

Gel images of DGGE analysis were normalized, and the similarity of the sample banding profiles was calculated with Dice's coefficient and UPGMA-dendrograms were constructed with the Bionumerics software package (v.5.10, Applied Maths, Sint-Martens-Latem, Belgium). Clustering of each treatment based on the relative amount of sequences in each OTU at each time point was analyzed with constrained Dice's similarity index and UPGMA-dendrograms were constructed with the PAST program (v. 1.0, Hammer et al., 2001).

Richness and abundance data visualization and principal coordinates analysis (PCoA) of data was done with the R program using Vegan, Phyloseq and BiodiversityR packages (Kindt and Coe, 2005; McMurdie and Holmes, 2013; Oksanen et al., 2016).

RESULTS

The Amount of Microbes in the Microcosm Enrichments

The total amount of bacteria in the enrichments was evaluated with 16S rRNA gene-targeted qPCR. The mean 16S rRNA gene copy number in the untreated fracture zone fluid was 5.59×10^2 copies mL⁻¹ (S.E. 68.5) (Figure 1A; Table 1) and increased in all treatments and the unamended controls during the incubation. In acetate-amended microcosms, the 16S rRNA gene copy number increased during the incubation from 4 to 32 days by almost two orders of magnitude. In microcosms amended with acetate and sulfate, copy numbers increased after 32 days of incubation. After 68 days of incubation, the acetate and sulfate -treated fracture water sample had 1.01×10^6 16S rRNA copies (S.E. 3.63 $\times 10^5$) mL⁻¹, which was the highest concentration of 16S rRNA gene copies observed throughout the enrichments. The microcosms amended only with sulfate

¹<https://www.arb-silva.de/documentation/release-123/>

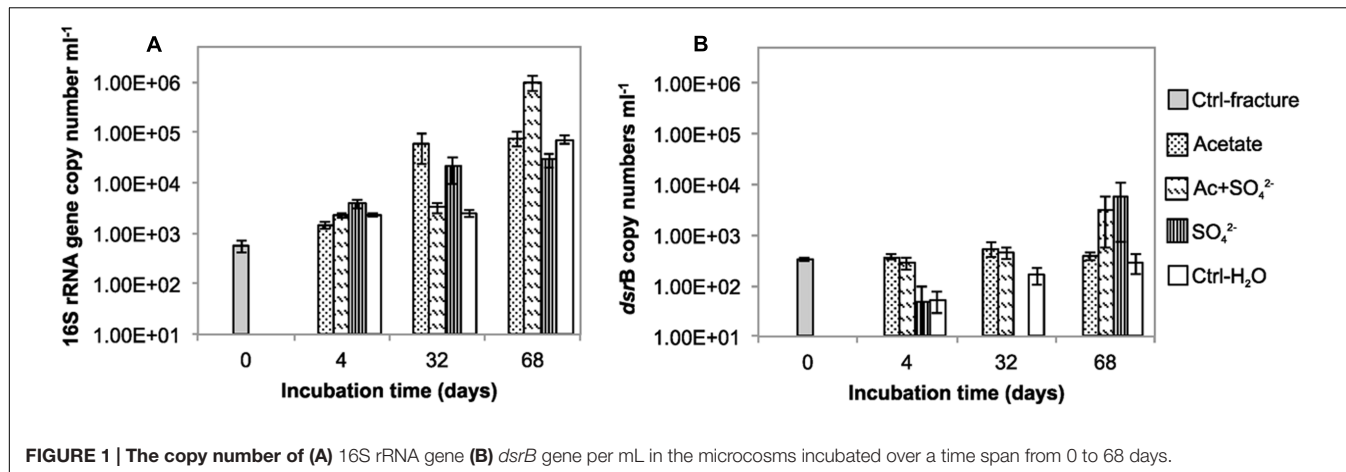
FIGURE 1 | The copy number of (A) 16S rRNA gene (B) *dsrB* gene per mL in the microcosms incubated over a time span from 0 to 68 days.

TABLE 1 | The experimental setup, qPCR results and microbial community characteristics.

Experiment name ¹	Amendments	Incubation time	16S rRNA gene copy nr mL ⁻¹	<i>dsrB</i> gene copy nr mL ⁻¹	DGGE band affiliations	Most abundant OTUs from amplicon sequencing	
Acetate	+	—	4	1,48E+03	3,69E+02	<i>Dehalobacter</i> , <i>Desulfurella</i> , unresolved	<i>Dethiobacter</i> (31%)
Acetate	+	—	32	6,13E+04	5,36E+02	<i>Pseudomonadaceae</i> , <i>Mollicutes</i> , <i>Caulobacteraceae</i>	<i>Dethiobacter</i> (32%)
Acetate	+	—	68	7,83E+04	3,88E+02	<i>Caulobacter</i> , <i>Pseudomonadaceae</i>	<i>Brevundimonas</i> (72%)
Ac + SO ₄ ²⁻	+	+	4	2,31E+03	2,82E+02	<i>Dethiosulfatibacter</i> , <i>Sulfobacillus</i> , <i>Desulfurella</i> , <i>Mollicutes</i>	<i>Dethiobacter</i> (29%)
Ac + SO ₄ ²⁻	+	+	32	3,29E+03	4,49E+02	<i>Caulobacter</i> , <i>Desulfurella</i> , <i>Novosphingobium</i>	<i>Dethiobacter</i> (28%)
Ac + SO ₄ ²⁻	+	+	68	1,01E+06	3,12E+03	<i>Rhizobium</i> , <i>Cellulomonas</i> , <i>Stenotrophomonas</i>	<i>Rhizobium</i> (39%)
SO ₄ ²⁻	—	+	4	3,91E+03	4,79E+01	<i>Desulfurella</i> , <i>Mollicutes</i>	<i>Dethiobacter</i> (40%)
SO ₄ ²⁻	—	+	32	2,13E+04	nd	<i>Desulfurella</i> , <i>Mollicutes</i>	<i>Dethiobacter</i> (31%)
SO ₄ ²⁻	—	+	68	2,91E+04	5,96E+03	<i>Pseudomonadaceae</i> , <i>Agrobacterium</i> , <i>Sulfobacillus</i> , <i>Desulfurella</i>	<i>Novosphingobium</i> (14%) <i>Nocardioides</i> (14%)
Ctrl-H ₂ O	—	—	4	2,38E+03	5,38E+01	<i>Desulfurella</i> , <i>Mollicutes</i> , <i>Desulfotomaculum</i>	<i>Dethiobacter</i> (33%)
Ctrl-H ₂ O	—	—	32	2,52E+03	1,66E+02	<i>Mollicutes</i>	<i>Dethiobacter</i> (31%)
Ctrl-H ₂ O	—	—	68	7,24E+04	2,95E+02	<i>Agrobacterium</i> , <i>Arthrobacterium</i> , <i>Cellulomonas</i>	<i>Cellulomonas</i> (41%)
Ctrl-fracture ¹	—	—	0	5,59E+02	3,24E+02	<i>Mollicutes</i> , <i>Desulfurella</i> , sequences affiliating with plastids	Unclassified <i>Chloroplast</i> (77%) <i>Dethiobacter</i> (10%)

¹All experiments were done in microcosms except Ctrl-fracture, which represents sample from the intrinsic fracture fluid. nd, not detected.

had the highest amount of the 16S rRNA gene copies in the 4 days time point but only slight increase in copy numbers was detected in the later time points. In microcosms without any amendments the 16S rRNA gene copy numbers were also highest in the last time point at 68 days, with more than one order of magnitude increase from the second time point (from 2.52×10^3 to 7.24×10^6 of cells mL⁻¹). Hence, using the 16S rRNA gene copy number counts as a proxy for total amount

of bacteria, it is presumed that cell numbers increased in all treatments during the incubation time, including the control without any amendments. The qPCR efficiency of the 16S rRNA gene amplification E was 2.035, which corresponds to efficiency slightly over 100%, most likely due to some inhibition (Callbeck et al., 2013).

The copy number of *dsrB* genes in the microcosms was used as a proxy for the amount of sulfate reducing bacteria. The *dsrB*

gene copy number in original fracture zone water was 3.24×10^2 (S.E. 2.46×10^1) copies mL^{-1} , i.e., 58% of the amount of bacterial 16S rRNA gene copies (**Figure 1B**). In acetate only - amended treatments, enrichment time did not have significant effect on *dsrB* copy numbers as copy numbers remained at the same level with that of the original fracture fluid throughout the incubation period. Microcosms amended with acetate and sulfate had significant increase in the number of *dsrB* gene copies after 32 days of incubation. Greatest fluctuation in the number of *dsrB* gene copies was detected in the sulfate-amended microcosms, where copy numbers ranging from near or below the detection limit to 5.96×10^3 (S.E. 5.22×10^3) copies mL^{-1} after 68 days of incubation. However, this should be considered cautiously, since *dsrB* copies were only detected in one of the three replicate samples of this treatment. A slight increase was detected during the incubation in the control without amendments also in the *dsrB* gene copy numbers, as was the case with the total bacterial 16S rRNA gene copy numbers. The *dsrB* amplification efficiency E was 1.802 corresponding 80% efficacy.

We also attempted to quantify methanogens in the microcosms using *mcrA* gene, the marker gene for methanogenesis as a proxy. However, *mcrA* copy numbers were all below the detection limit of the qPCR assay (<5 copies mL^{-1}).

Changes in the Bacterial Community Structure during the Experiment

Bacterial communities in the different treatments over the span of the experiment were assessed with bacterial 16S rRNA gene DGGE and high-throughput amplicon sequencing. The microbial community structure in the microcosms changed during the incubation in all treatments (**Figures 2** and **3**, **Supplementary Figure S1**). Major changes were not observed in the community structure between the different treatments after 4 and 32 days of incubation (**Figures 2** and **3**). However, after 68 days the bacterial communities in the microcosms differed significantly from one another. There was a notable dispersion in the Shannon diversity index between the communities (**Table 2**).

The DGGE profiles of each treatment showed a decrease in the number of phylotypes (i.e., bands in the fingerprint of each community) during the incubation (**Figure 2**). According to the UPGMA trees based on the DGGE band positions of each community, the bacterial communities were broadly divided into two groups, one comprising of the intrinsic fracture fluid community and microcosms incubated for 4 and 32 days and the other the bacterial community after 68 days of incubation. Similarly, according to hierarchical clustering analysis, based on the relative amount of sequences in each OTU in each sample produced by amplicon sequencing, bacterial communities after 4 and 32 days of incubation resembled each other and the communities in the original fracture water and differed from the 68-day incubations (**Supplementary Figure S2**). Correspondingly, the microbial communities after 68 days of incubation clustered together in the PCoA based on amplicon sequencing data (**Figure 4**). The eigenvalues were 3.23 (axis 1) and 1.85 (axis 2) and these dimensions explained 26.8 and 15.4% of the variation

in the data, respectively. Generally, samples tended to cluster based on the incubation time rather than the treatment in the PCoA.

The amount of observed OTUs generally diminished during the incubation (**Table 2**). After 4 days of incubation, the total number of OTUs in all treatments was 209. At this time point, there were no significant differences in the amount of shared OTUs between different treatments. Forty-four OTUs were shared between all microcosm communities. After 32 days of incubation, the number of OTUs decreased in all other treatments but those amended with acetate and sulfate. The number of shared OTUs between all treatments had decreased to 36 OTUs. After 68 days of incubation, the number of OTUs had decreased even more, to only 20 OTUs shared in all treatments. The shared OTUs between sequenced replicate microcosms was on average 21%, however, there were some samples that shared only a few OTUs between the replicates (acetate + sulfate treatment at 68 days) (**Table 2**). Good's coverage estimate was close to 100% in all sequenced communities (**Table 2**). Based on the Chao1 and ACE estimates, on average 80% of the total richness and abundance in the microcosm communities was captured with the amplicon sequencing. The Shannon diversity index ranged from 1.49 to 4.16 between treatments and time points, with a predominant trend of lower diversity after longer incubation period. The exception was the microcosms amended only with sulfate, in which the diversity increased during the incubation period and the highest Shannon diversity H' (4.16) was observed in the last time point in after 68 days. The evenness of the communities in the microcosms ranged from 0.3 to 0.6, whereas the original fracture fluid bacterial community was less even (0.3).

Sequences of selected DGGE bands were used as a rough characterization of the bacterial communities. The fingerprint of bacterial community in fracture fluid used as an inoculum for the microcosms comprised of several bands affiliating with *Mollicutes* in addition to two distinct bands closely related to *Delta proteobacteria* (*Desulfurella*). Some sequences affiliated with plastids (**Table 1**, **Figure 2**), determined by their clustering in the maximum likelihood tree (**Supplementary Figure S1**). Based on the high-throughput amplicon sequencing data, the intrinsic bacterial community in the 967 m fracture zone fluid was dominated by sequences affiliating with chloroplasts in addition to clostridia and proteobacteria. A minor proportion of the community fell with *Dethiobacter* (**Figure 3**). However, if chloroplasts were filtered from the sequence data, the remaining bacterial community was very similar with those in the microcosms after 4 days of incubation. The bacterial community fingerprint of the fracture fluid was most similar with the bacterial communities after 4 and 32 days of incubation (**Figure 2**, **Supplementary Figure S2**).

In bacterial communities of the acetate-amended microcosms, DGGE band sequences affiliating with *Dehalobacter*, *Desulfurella* and *Mollicutes* were common after four and 32 days of incubation, whereas sequences related to *Caulobacteraceae* and *Pseudomonadaceae* dominated after 68 days (**Figure 2A**, **Supplementary Figure S1**). Based on amplicon sequencing,

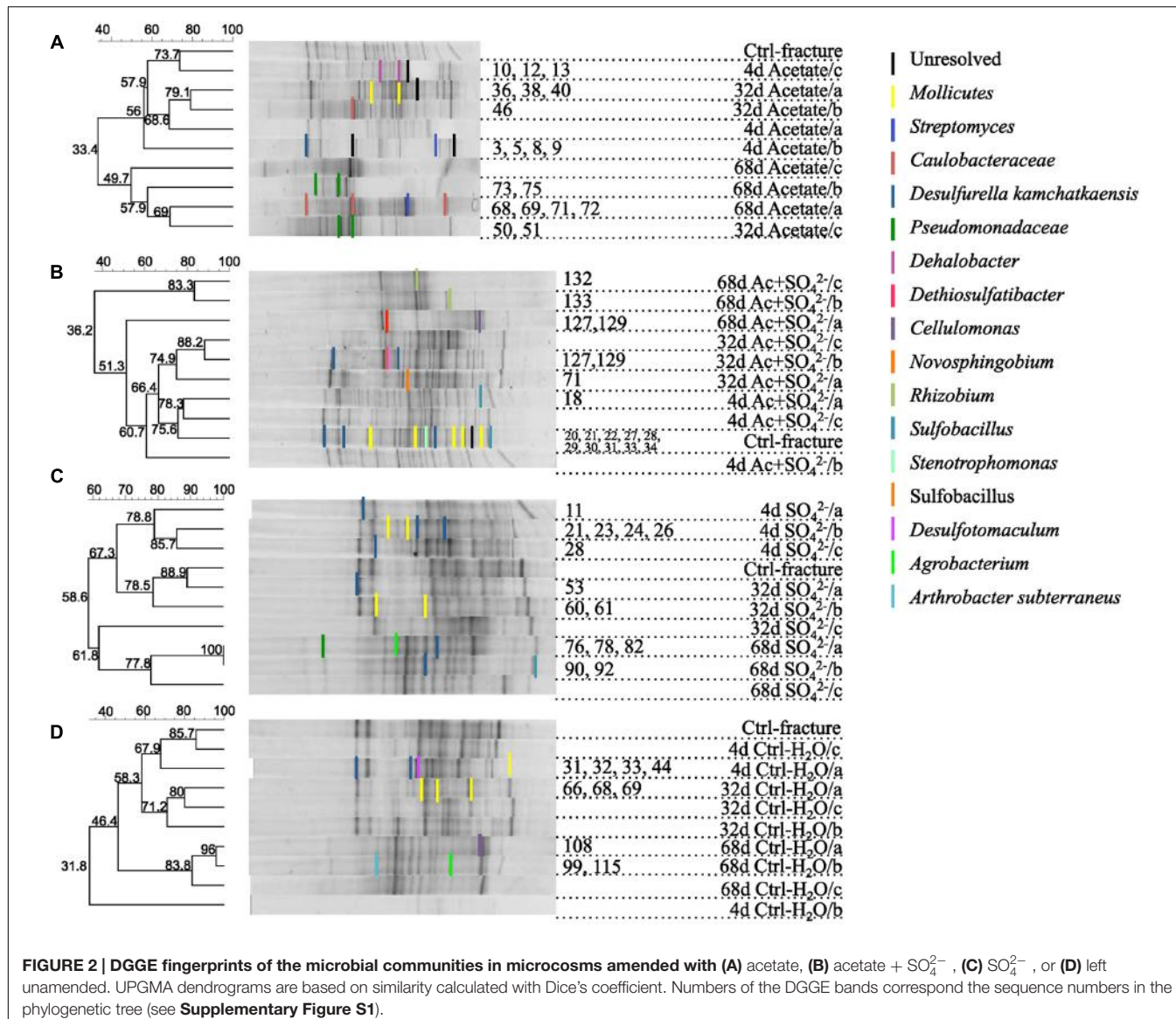


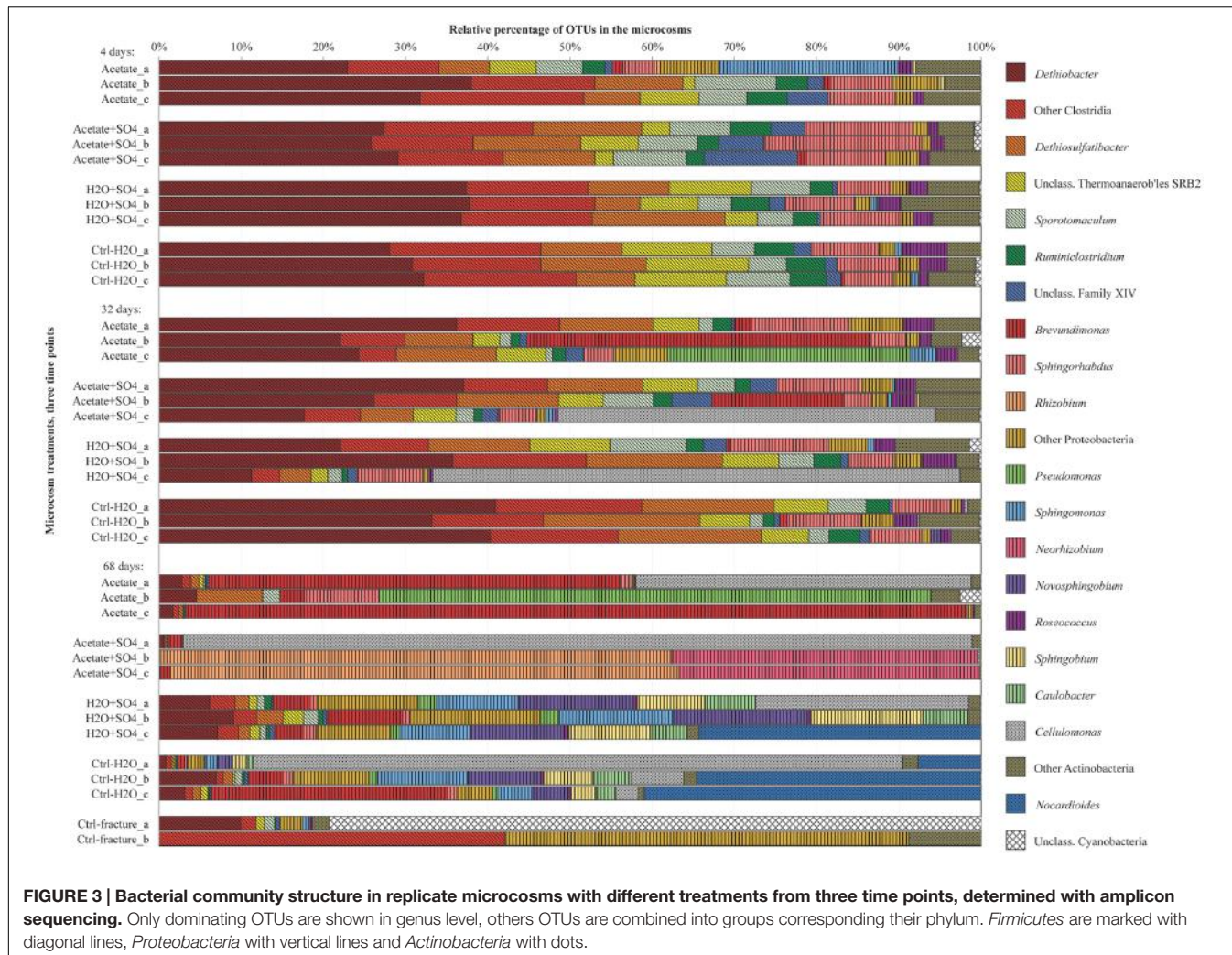
FIGURE 2 | DGGE fingerprints of the microbial communities in microcosms amended with (A) acetate, (B) acetate + SO_4^{2-} , (C) SO_4^{2-} , or (D) left unamended. UPGMA dendograms are based on similarity calculated with Dice's coefficient. Numbers of the DGGE bands correspond the sequence numbers in the phylogenetic tree (see **Supplementary Figure S1).**

on average over 30% of the sequenced community at 4- and 32-day acetate-enrichments were affiliated with *Dethiobacter* (Figure 4). Otherwise the phylotypes in these communities resembled other *Clostridiales* and alphaproteobacterial 16S rRNA gene sequences.

The bacterial community of the microcosms enriched with acetate and sulfate, assessed from the sequenced DGGE bands, consisted of phylotypes affiliating with clostridial *Sulfobacillus* and *Dethiosulfatibacter*, proteobacterial *Desulfurella*, *Mollicutes*, and especially after 68 days, phylotypes affiliating with *Rhizobium* (Figure 2B, Supplementary Figure S1). Amplicon sequencing confirmed the dominance of clostridial phylotypes such as *Dethiobacter*, *Dethiosulfatibacter*, *Sporotomaculum*, *Thermoanaerobacterales* – affiliating SRB2 phylotype, *Ruminiclostridium* and clostridial Family XIV – related bacteria after 4 and 32 days of incubation in acetate and sulfate-amended

microcosms, however, in one microcosm (replicate c) after 32 days of incubation *Cellulomonas* was dominant. After 68 days, the enrichment had a distinct community structure with phylotypes representing actinobacterial *Cellulomonas* and alphaproteobacterial *Rhizobiaceae*, Clostridia being virtually absent (Figure 3). In addition, the diversity of this community was significantly lower after 68 days ($H' 1.71$) compared to that of earlier time points.

Microcosms amended with only sulfate hosted bacterial communities resembling those of the microcosms amended with acetate and sulfate. Phylotypes of sequenced DGGE bands from day 4 and day 32 affiliated with *Desulfurella* and *Mollicutes*, and phylotypes from 68 days affiliated with *Sulfobacillus*, *Desulfurella*, *Agrobacterium*, and *Pseudomonas* (Figure 2C, Supplementary Figure S1). Amplicon sequencing revealed that after 4 and 32 days, similar phylotypes belonging to



Clostridiales that were also detected from the acetate + sulfate - amended microcosms, were the most dominant in solely sulfate-amended experiments, although in one replicate microcosm after 32 days of incubation, *Cellulomonas* phylotypes were dominating over *Clostridiales* (replicate c) (Figure 3). The bacterial community after 68 days in the sulfate-amended microcosms was the most diverse. On average, 60% of the phylotypes belonged to alphaproteobacterial groups such as *Sphingomonas*, *Sphingorhabdus*, *Sphingobium*, *Novosphingobium*, *Caulobacter*, and *Methylobacter*. Other phylotypes affiliated with *Clostridia* and *Actinobacteria*.

Microcosms left unamended hosted bacterial communities slightly dissimilar to the amended ones, especially at the last time point after 68 days. The communities detected with DGGE comprised of phylotypes affiliating with *Mollicutes*, *Actinobacteria* and *deltaproteobacterial Desulfurella* (Figure 2D). *Clostridial* phylotypes were most common after 4 and 32 days of incubation in the communities characterized with amplicon sequencing, but after 68 days, the community consisted of actinobacterial *Cellulomonas* and *Nocardioides* and of alphaproteobacterial phylotypes (Figure 3).

DISCUSSION

The Changes in the Microbial Community Structure

Previous studies have reported taxonomically and functionally diverse microbial communities dwelling in methane-rich, oligotrophic and saline groundwaters in Outokumpu (Kietäväinen et al., 2013; Purkamo et al., 2013, 2016; Nyssönen et al., 2014). Moreover, heterotrophic carbon assimilation by *Clostridia* was determined to be important for the microbial life throughout the deep drill hole water column (Purkamo et al., 2015). These data steered us to investigate further on the preferred carbon and energy sources of these microbial communities.

We provided different combinations of carbon sources, electron donors and electron acceptors to the intrinsic microbial community of the fracture fluid in order to identify the species benefiting from the amendments. Previous studies have shown that there are active sulfate reducers present in Outokumpu deep subsurface, although sulfate concentrations are low ($<1 \text{ mg L}^{-1}$ at 967 m depth) (Kietäväinen et al., 2013; Purkamo et al., 2016).

TABLE 2 | Ecological indices from amplicon sequencing.

Experiment	Incubation	No. of sequences ³	OTUs	Shared OTUs		Coverage	Shannon	Chao1	ACE	OTUs/Chao1	OTUs/ACE	Shannon evenness
				observed	between replicates ⁴							
Acetate	4	7618	99	21	21%	99.8%	4.02	106.9	91%	93%	0.6	
Acetate	32	12048	108	17	16%	99.8%	3.81	154.4	70%	81%	0.6	
Acetate	68	5449	50	5	10%	99.7%	1.49	60.9	82%	63%	0.3	
Ac + SO ₄ ²⁻	4	10334	89	23	26%	99.8%	3.77	116.1	109.7	77%	81%	0.6
Ac + SO ₄ ²⁻	32	3401	80	18	23%	99.3%	3.81	103.0	104.7	78%	76%	0.6
Ac + SO ₄ ²⁻	68	51286	43	2	5%	100.0%	1.71	48.0	51.2	90%	84%	0.3
SO ₄ ²⁻	4	16782	121	25	21%	99.9%	3.65	160.4	141.3	75%	86%	0.5
SO ₄ ²⁻	32	9763	100	18	18%	99.8%	3.76	113.9	112.6	88%	89%	0.6
SO ₄ ²⁻	68	13287	98	38	39%	99.8%	4.16	113.0	118.9	87%	82%	0.6
Ctrl-H ₂ O	4	22282	124	33	27%	99.9%	3.75	153.5	149.3	81%	83%	0.5
Ctrl-H ₂ O	32	11428	97	19	20%	99.9%	3.36	108.3	110.9	90%	87%	0.5
Ctrl-H ₂ O	68	20093	87	34	39%	99.9%	2.76	168.2	153.5	52%	57%	0.4
Ctrl-fracture	0	4659	48	5	10%	99.8%	1.62	57.0	54.1	84%	89%	0.3
Negative control ¹	—	—	80	8	na	98.8%	2.34	8.0	8.4	100%	95%	0.8
Positive control ²	—	41983	5	na	na	100.0%	0.01	6.0	11.8	83%	42%	0.0

¹Combined data from PCR-bank and DNA extraction control. ²Ampified DNA from *Paracoccus denitrificans*. ³After quality control. ⁴Shared OTUs between sample replicates. na, not available.

The dominant sulfate reducers in Outokumpu affiliate with *Desulfotomaculum*, which are commonly found from both deep terrestrial and marine subsurface environments (e.g., Moser et al., 2005; Nakagawa et al., 2006; Aüllö et al., 2013; Bomberg et al., 2015; Purkamo et al., 2016). In this study we offered an easily utilized organic carbon source together with suitable electron donor and acceptor for sulfate reducing bacteria. Our results showed an increase of *dsrB* gene copy numbers in acetate + sulfate-supplemented microcosms during the incubation period. This is in accordance with Pedersen (2012), who reported multiplication in total number of cells as well as in the most probable number of sulfate reducing bacteria in the first 30 days in in-situ flow cell cabinets amended with acetate. Although sulfate reducers were not detected with the bacterial community analyses, hydrogenotrophic thiosulfate reducers dominated the enrichments after 4 and 32 days. The detection of hydrogenotrophic bacteria and their dominance in the microcosms suggests that addition of hydrogen was in fact determining the microbial community structure more than the provided carbon source and electron acceptor. Particularly *Dethiobacter* was a major component of the bacterial communities in all microcosms, independent of whether the microcosms had received other amendments than H₂ and CO₂. *Dethiobacter* is described as a hydrogen-respiring organism using thiosulfate, elemental sulfur, and polysulfide as electron acceptors (Sorokin et al., 2008) and has previously been detected from several serpentizing, ophiolithic rock and deep terrestrial subsurface environments (Brazelton et al., 2013; Sukko et al., 2013; Tiago and Veríssimo, 2013; Crespo-Medina et al., 2014; Woycheese et al., 2015; Purkamo et al., 2016). Similar to our results, Crespo-Medina et al. (2014) reported that *Dethiobacter* was almost exclusively enriched in the microcosms originating from serpentizing groundwater, independent of nutrient addition. To our knowledge, *Dethiobacter* have not been commonly found from marine deep subsurface. Additionally, unclassifiable members of Clostridial family XIV resembling *Anaerobranca* were detected in our enrichments. *Anaerobranca* – type microorganisms, like their distant relatives *Dethiobacter*, have the capacity to reduce thiosulfate to sulfide, in addition to the reduction of elemental sulfur. These alkaliphilic bacteria essentially produce acetate by fermenting more preferred, proteinaceous compounds (Wiegel, 2015). Therefore we assume that these organisms, including *Dethiobacter* that has previously been characterized also as one of the keystone genera of Outokumpu deep biosphere, are important in converting dead biomass to acetate and thus being major players in the carbon cycling in the deep crystalline bedrock habitat (Purkamo et al., 2016). Similarly, microbial communities have been shown to preferentially use proteinaceous substrates such as amino acids originating from dead microbial biomass, i.e., necromass, in deep marine subsurface (Lomstein et al., 2012; Lloyd et al., 2013).

Another hydrogen-respiring, thiosulfate-oxidizing species, *Dethiosulfatibacter* was present in the bacterial enrichments in this study. This microorganism has been detected at several other occasions from Outokumpu deep subsurface, but to our knowledge, not from other deep continental sites

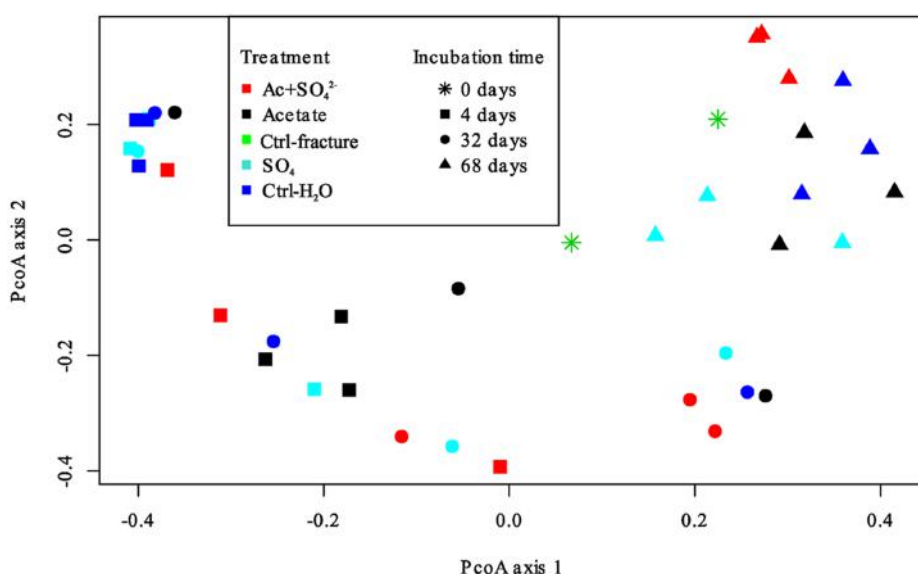


FIGURE 4 | Principal coordinates analysis plot of the microbial communities in the microcosms based on Bray-Curtis similarity model. Axis 1 explained 26.8% and axis 2 15.4% of the variation in the data. Treatments are represented by different colors; incubation time is represented by different symbols.

(Takii et al., 2007; Itävaara et al., 2011; Purkamo et al., 2013, 2016; Nyvönen et al., 2014). Consequently, a *Dethiosulfatibacter* -affiliating OTU was described to be part of the core microbial community of Outokumpu deep subsurface with only a few other species (Purkamo et al., 2016). Other relatively abundant clostridial phylotypes in the first two time points, such as *Sporotomaculum* and *Ruminiclostridium* are also not sulfate reducers but gain energy by fermentation of organic matter (Yutin and Galperin, 2014; Rainey, 2015).

While the amount of total organic carbon in Outokumpu fracture fluids is around 6 mg mL⁻¹, most of this is likely dissolved methane (80 vol-% in the fracture fluids) (Kietäväinen et al., 2013; Kietäväinen and Purkamo, 2015; Purkamo et al., 2016). Hence, methanogens could be responsible for production of this methane in deep subsurface of Outokumpu. In this study, aceticlastic methanogens were targeted with acetate amendment together with CO₂ and H₂. For comparison, other microcosms were amended with CO₂ and H₂ that would benefit specifically autotrophic methanogens and acetogens. However, methanogens were not detected in any of the microcosms. This is in agreement with Purkamo et al. (2016), where no methanogens were detected from this fracture and *Hadesarchaea* dominated the total archaeal community. Thus, we conclude that the heterotrophic community members, such as *Brevundimonas* -affiliating phylotypes whose relative abundance increased in the acetate-amended microcosms during the incubation, benefited from the acetate amendment. Alphaproteobacterial *Brevundimonas* has been identified previously in an enrichment experiment done with granitic bedrock fluids from Mizunami, Japan (Fukuda et al., 2010). A phylotype closely related to *Brevundimonas mediterranea* represented the majority of the sequences in enrichments amended with organic acids or with H₂ and CH₄. Equally to our study, Fukuda et al. (2010) detected

other α -proteobacterial phylotypes in significant amounts in their organic acid -amended enrichments. One *Brevundimonas* strain was also isolated from deep, subpermafrost subsurface brine from the Lupin Mine, Canada, with both aerobic TSA-medium and anaerobic heterotrophic medium with H₂ and CO₂ amendment (Onstott et al., 2009). The high percentage of *Alphaproteobacteria* in the end of the experiment after 68 days of incubation in our study as well as in the other studies probably results from their expertise in long-term survival in oligotrophic environments (Abraham et al., 1999). The emergence of opportunistic microbial species, such as *Alphaproteobacteria* and *Actinobacteria* toward the end of the experiment might be due to their capacity to use dead biomass for carbon and energy.

The most significant change in the bacterial communities in this study was observed after 68 days. There was a substantial increase in *Cellulomonas* phylotypes in the microcosms after 32 and especially after 68 days of incubation. *Cellulomonas* and other actinobacteria have been recurrently isolated from other deep terrestrial subsurface settings (Chang et al., 2007; Finster et al., 2009; Wouters et al., 2013; Puente-Sánchez et al., 2014). Their enrichment might indicate a succession process where an increase in cell death of *Dethiobacter*-type of microorganisms would subsequently enhance the growth of typical detritivore microbes, such as fermenters like *Cellulomonas*. In the beginning of the incubation the excess H₂ in the microcosms inhibited *Cellulomonas*, but after *Dethiobacter* and *Dethiosulfatibacter* -type of organisms consumed the H₂, the partial pressure of the hydrogen dropped enough to enable the growth of these fermenters. The measured 16S rRNA gene copy numbers stayed on the original level or increased during the incubation period. Nevertheless, it is possible that the amount of detected 16S rRNA gene copies could originate to some extent from the dead microbial biomass (Fittipaldi et al., 2011). Therefore,

we presume that the conditions in the microcosms were first more optimal for the clostridial hydrogenotrophic phylotypes but became gradually more suitable for *Cellulomonas* and *Alphaproteobacteria*.

Some phylotypes in enrichments represented unexpected bacterial groups: *Sphingorhabdus* -affiliating phylotypes composed 7–12% of the total bacterial community in the microcosms after 4 and 32 days of incubation. These bacteria contain carotenoid pigments that absorb light and are capable of anoxygenic photosynthesis (Kim et al., 2007; Jogler et al., 2013). OTUs affiliating with *Roseococcus* represented a minor component of the bacterial community. Roseococci also contain carotenoid pigments as well as bacteriochlorophyll *a*, which is used as a light-harvesting antenna. Roseococci can also produce energy by oxidation of thiosulfate to sulfate, hence Roseococci can be defined as facultative photoheterotrophs (Yurkov, 2015). The microcosms were kept in the dark, so the existence of bacteria affiliating with phototrophic organisms in the microcosms mimicking the deep, dark terrestrial subsurface remains a mystery. We did not find any sequences affiliating with roseococci or *Sphingorhabdus* from the negative controls, thus we argue that these unexpected genera can originate either from previous contamination of the groundwater fluids (possibly during the drilling) or be a real phenomenon.

Evaluation of the Used Community Detection Methods

The quantity of microbes was relatively low in the fracture fluids used as the inoculum as well as in the microcosms during the enrichment, which challenged the microbial community detection. The microbial community structure was first roughly characterized with DGGE community fingerprinting and traditional Sanger sequencing of the common phylotypes. Amplicon sequencing produced a reasonable amount of sequences, keeping in mind the low concentration of biomass of the samples. While amplicon sequencing gave a more detailed presentation of the bacterial community, the changes in the communities in the microcosms during the incubation were visible with the DGGE fingerprints. The use of nested PCR for the DGGE in order to produce enough material for the fingerprinting method is a possible source of bias (Yu et al., 2015). However, independent of the community characterization method, the microbial community structure was comparable at the order level. Especially phylotypes belonging to *Alphaproteobacteria* were detected in the microcosms with both of the community characterization methods. On the other hand, *Desulfurella* -affiliating phylotype was frequently detected with DGGE in the bacterial communities of the microcosms, but was absent in the amplicon sequencing results. In addition, sequences affiliating with *Mollicutes* were more frequently detected with DGGE than with amplicon sequencing. Similarly, *Mollicutes* were detected from the fracture fluids at the same depth characterized with DGGE using the same primers without nested PCR (Purkamo et al., 2013), as well as in amplicon sequencing of the intrinsic bacterial community of the fracture with amplicon sequencing, using fD1 and p2 -primers (Purkamo

et al., 2016). Hence, we presume that the primers used in this study for amplicon sequencing may exclude *Mollicutes* to some level. A relatively large amount of sequences affiliating with chloroplasts in the fracture fluid could be a result of PCR bias. The low amount of template material is known to generate random fluctuations in priming efficiency and lead to variable microbial community fingerprints (Chandler et al., 1997). In addition, GC-rich template sequences have been shown to have higher affinity to amplification primers (Polz and Cavanaugh, 1998), but whether the amplicon sequencing primers used in this study have higher affinity to chloroplast 16S rRNA gene is not known.

CONCLUSION

The deep subsurface is considered to be a fairly stable environment over long periods of time (Hoehler and Jørgensen, 2013), thus deep continental biosphere is providing a habitat for recalcitrant microbial life. In this study we used microcosms to study the prospective changes in the microbial community structure when abundant carbon sources, electron donors and electron acceptors were introduced. Based on the results obtained in this study, organic carbon is useful for the heterotrophic microbial groups in deep biosphere in Outokumpu. However, according to our results it appears that heterotrophic sulfate reducers or aceticlastic methanogens did not benefit from the acetate addition. Sulfate addition did not have a major effect on the number of sulfate reducers, although a minor increase in SRB marker gene copy numbers was detected. Our results show that microbial communities in the deep terrestrial crystalline bedrock subsurface are subject to transformation. The remaining bacteria in the communities toward the end of the experiment in this study are likely to ferment the organic matter for energy production as well as have the ability to use proteinaceous substrates. Overall, it is likely that the deep terrestrial subsurface microbial communities are continuously changing, depending on the available substrates and dominating metabolic processes at each time point. These changes can be cyclic, i.e., heterotrophic and fermenting microbes can produce substrates to other microbial groups that can take over when viruses or substrate limitation will decrease the numbers of heterotrophs. However, we can only detect a snapshot of these microbial communities and may miss some of the changes with only 68 days incubation period.

This work provides a basis for further studies for detecting the predominant carbon sources and cycling mechanisms in deep crystalline rock fractures. The data gathered here provides guidance for detailed studies exploring the microbial community changes through time, detecting the major carbon assimilation mechanisms and identifying the populations using specific energy and carbon metabolisms. As this study setup does not provide information about the functionality of the microbes, testing the physiological responses and activity of these microbial communities to different carbon sources will further elucidate carbon cycling in the deep Fennoscandian biosphere in the future.

AUTHOR CONTRIBUTIONS

LP, MB, and MN designed the experiments and collected the samples. All analyses were carried out by LP. LA assisted with sample collection and provided the geochemical metadata. IK provided funding and access to Outokumpu Deep Drill Hole. MI provided funding and assistance in experimental design. All authors contributed to the discussion of the results. Manuscript was written by LP with inputs from other authors.

ACKNOWLEDGMENTS

The authors acknowledge Mirva Pyrhönen from VTT Technical Research Centre of Finland for her skillful work with laboratory analyses and Arto Pullinen from Geological Survey of Finland for aiding in sampling at the Outokumpu Deep Scientific Drill Hole. Eetu Aalto and coworkers from Lapela Ltd. are acknowledged for assisting sampling at Outokumpu. Riikka Kietäväinen from Geological Survey of Finland and Maija Nuppunen-Puputti from

REFERENCES

- Abraham, W.-R., Strompl, C., Meyer, H., Lindholst, S., Moore, E. R. B., Christ, R., et al. (1999). Phylogeny and polyphasic taxonomy of *Caulobacter* species. Proposal of *Maricaulis* gen. nov. with *Maricaulis maris* (Poindexter) comb. nov. as the type species, and emended description of the genera *Brevundimonas* and *Caulobacter*. *Int. J. Syst. Bacteriol.* 49, 1053–1073. doi: 10.1099/00207713-49-3-1053
- Ahonen, L., Kietäväinen, R., Kortelainen, N., Kukkonen, I. T., Pullinen, A., Toppi, T., et al. (2011). Hydrogeological characteristics of the Outokumpu deep drill hole. *Geol. Surv. Finl. Spec. Paper* 51, 151–168.
- Amend, J. P., and Teske, A. (2005). Expanding frontiers in deep subsurface microbiology. *Palaeogeogr. Palaeoclimatol. Palaeoecol.* 219, 131–155. doi: 10.1016/j.palaeo.2004.10.018
- Aüllo, T., Ranchou-Peyruse, A., Ollivier, B., and Magot, M. (2013). *Desulfotomaculum* spp. and related gram-positive sulfate-reducing bacteria in deep subsurface environments. *Front. Microbiol.* 4:362. doi: 10.3389/fmicb.2013.00362
- Bennett, P. C., Rogers, J. R., and Choi, W. J. (2001). Silicates, silicate weathering, and microbial ecology. *Geomicrobiol. J.* 18, 3–19. doi: 10.1080/01490450151079734
- Bomberg, M., Nyysönen, M., Pitkänen, P., Lehtinen, A., and Itävaara, M. (2015). Active microbial communities inhabit sulphate-methane interphase in deep bedrock fracture fluids in Olkiluoto, Finland. *Biomed. Res. Int.* 2015:979530. doi: 10.1155/2015/979530
- Brazilton, W. J., Morrill, P. L., Szponar, N., and Schrenk, M. O. (2013). Bacterial communities associated with subsurface geochemical processes in continental serpentinite springs. *Appl. Environ. Microbiol.* 79, 3906–3916. doi: 10.1128/AEM.00330-13
- Callbeck, C. M., Sherry, A., Hubert, C. R., Gray, N. D., Voordouw, G., and Head, I. M. (2013). Improving PCR efficiency for accurate quantification of 16S rRNA genes. *J. Microbiol. Methods* 93, 148–152. doi: 10.1016/j.mimet.2013.03.010
- Caporaso, J. G., Kuczynski, J., Stombaugh, J., Bittinger, K., Bushman, F. D., Costello, E. K., et al. (2010). QIIME allows analysis of high-throughput community sequencing data. *Nat. Methods* 7, 335–336.
- Chandler, D. P., Fredrickson, J. K., and Brockman, F. J. (1997). Effect of PCR template concentration on the composition and distribution of total community 16S rDNA clone libraries. *Mol. Ecol.* 6, 475–482. doi: 10.1046/j.1365-294X.1997.00205.x
- Chang, H.-W., Bae, J.-W., Nam, Y.-D., Kwon, H.-Y., Park, J. R., Shin, K.-S., et al. (2007). *Arthrobacter subterraneus* sp. nov., isolated from deep subsurface water of the South Coast of Korea. *J. Microbiol. Biotechnol.* 17, 1875–1879.
- Chapelle, F. H., O'Neill, K., Bradley, P. M., Methé, B. A., Ciufo, S. A., Knobel, L. L., et al. (2002). A hydrogen-based subsurface microbial community dominated by methanogens. *Nature* 415, 312–315. doi: 10.1038/415312a
- Chaudhary, P. P., Brablcová, L., Buriánková, I., and Rulík, M. (2013). Molecular diversity and tools for deciphering the methanogen community structure and diversity in freshwater sediments. *Appl. Microbiol. Biotechnol.* 97, 7553–7562. doi: 10.1007/s00253-013-5102-8
- Costa, K. C., and Leigh, J. A. (2014). Metabolic versatility in methanogens. *Curr. Opin. Biotechnol.* 29, 70–75. doi: 10.1016/j.copbio.2014.02.012
- Crespo-Medina, M., Twing, K. I., Kubo, M. D. Y., Hoehler, T. M., Cardace, D., McCollom, T., et al. (2014). Insights into environmental controls on microbial communities in a continental serpentinite aquifer using a microcosm-based approach. *Front. Microbiol.* 5:604. doi: 10.3389/fmicb.2014.00604
- Dong, H. (2008). “Microbial life in extreme environments: linking geological and microbiological processes,” in *Links Between Geological Processes, Microbial Activities & Evolution of Life*, eds Y. Dilek and H. Furnes (Berlin: Springer), 237.
- Finster, K. W., Cockell, C. S., Voytek, M. A., Gronstal, A. L., and Kjeldsen, K. U. (2009). Description of *Tessaracoccus profundi* sp.nov., a deep-subsurface actinobacterium isolated from a Chesapeake impact crater drill core (940 m depth). *Antonie van Leeuwenhoek* 96, 515–526. doi: 10.1007/s10482-009-9367-y
- Fittipaldi, M., Codony, F., Adrados, B., Camper, A. K., and Morató, J. (2011). Viable real-time PCR in environmental samples: can all data be interpreted directly? *Microb. Ecol.* 61, 7–12. doi: 10.1007/s00248-010-9719-1
- Fredrickson, J. K., and Balkwill, D. L. (2006). Geomicrobial processes and biodiversity in the deep terrestrial subsurface. *Geomicrobiol. J.* 23, 345–356. doi: 10.1016/j.gambs.2015.12.001
- Fukuda, A., Hagiwara, H., Ishimura, T., Kouduka, M., Ioka, S., Amano, Y., et al. (2010). Geomicrobiological properties of ultra-deep granitic groundwater from the Mizunami Underground Research Laboratory (MIU), central Japan. *Microb. Ecol.* 60, 214–225. doi: 10.1007/s00248-010-9683-9
- Geets, J., Borremans, B., Diels, L., Springael, D., Vangronsveld, J., van der Lelie, D., et al. (2006). *DsrB* gene-based DGGE for community and diversity surveys of sulfate-reducing bacteria. *J. Microbiol. Methods* 66, 194–205. doi: 10.1016/j.mimet.2005.11.002
- Gold, T. (1992). The deep, hot biosphere. *Proc. Natl. Acad. Sci. U.S.A.* 89, 6045–6049.
- Guindon, S., and Gascuel, O. (2003). A simple, fast, and accurate algorithm to estimate large phylogenies by maximum likelihood. *Syst. Biol.* 52, 696–704.

VTT Technical Research Centre of Finland also contributed to the study. Dr. Mark Fox-Powell is thanked for the English language editing.

SUPPLEMENTARY MATERIAL

The Supplementary Material for this article can be found online at: <http://journal.frontiersin.org/article/10.3389/fmicb.2017.00232/full#supplementary-material>

FIGURE S1 | Phylogenetic affiliations of the partial 16S rRNA gene sequences retrieved from DGGE community fingerprinting analysis in relation to cultured reference strains and 16S rRNA gene sequences of uncultured environmental bacteria. Bootstrap support values were calculated from 1000 random repeats. Nodes with >40% bootstrap support are indicated. Scale bar shows the percent difference.

FIGURE S2 | UPGMA dendograms of the similarity of bacterial community structure in microcosms with different treatments, (A) acetate amended, (B) acetate + SO_4^{2-} amended, (C) only with SO_4 -amended and (D) without any amendments, based on amplicon sequencing results. Clustering was calculated using Dice similarity index.

- Hales, B. A., Edwards, C., Ritchie, D. A., Hall, G., Pickup, R. W., and Saunders, J. R. (1996). Isolation and identification of methanogen-specific DNA from blanket bog peat by PCR amplification and sequence analysis. *Appl. Environ. Microbiol.* 62, 668–675.
- Hammer, Ø., Harper, D. A. T., and Ryan, P. D. (2001). Past: Paleontological Statistics Software Package for education and data analysis. *Paleontol. Electrón.* 4, 1–9.
- Haveman, S. A., and Pedersen, K. (2002). Distribution of culturable microorganisms in Fennoscandian Shield groundwater. *FEMS Microbiol. Ecol.* 39, 129–137. doi: 10.1111/j.1574-6941.2002.tb00914.x
- Herlemann, D. P., Labrenz, M., Jürgens, K., Bertilsson, S., Wanek, J. J., and Andersson, A. F. (2011). Transitions in bacterial communities along the 2000 km salinity gradient of the Baltic Sea. *ISME J.* 5, 1571–1579. doi: 10.1038/ismej.2011.41
- Hoehler, T. M., and Jørgensen, B. B. (2013). Microbial life under extreme energy limitation. *Nat. Rev. Microbiol.* 11, 83–94. doi: 10.1038/nrmicro2939
- Itävaara, M., Nyssönen, M., Kapanen, A., Nousiainen, A., Ahonen, L., and Kukkonen, I. (2011). Characterization of bacterial diversity to a depth of 1500 m in the Outokumpu deep borehole, Fennoscandian Shield. *FEMS Microbiol. Ecol.* 77, 295–309. doi: 10.1111/j.1574-6941.2011.01111.x
- Jogler, M., Chen, H., Simon, J., Rohde, M., Busse, H. J., Klenk, H. P., et al. (2013). Description of *Sphingorhabdus planktonica* gen. nov., sp. nov. and reclassification of three related members of the genus *Sphingopyxis* in the genus *Sphingorhabdus* gen. nov. *Int. J. Syst. Evol. Microbiol.* 63, 1342–1349. doi: 10.1099/ijns.0.043133-0
- Jukes, T. H., and Cantor, C. R. (1969). “Evolution of protein molecules,” in *Mammalian Protein Metabolism*, Vol. III, ed. H. N. Munro (New York, NY: Academic Press), 21–132.
- Kietäväinen, R., Ahonen, L., Kukkonen, I. T., Hendriksson, N., Nyssönen, M., and Itävaara, M. (2013). Characterisation and isotopic evolution of saline waters of the Outokumpu Deep Drill Hole, Finland—Implications for water origin and deep terrestrial biosphere. *Appl. Geochem.* 32, 37–51. doi: 10.1016/j.apgeochem.2012.10.013
- Kietäväinen, R., Ahonen, L., Kukkonen, I. T., Niedermann, S., and Wiersberg, T. (2014). Noble gas residence times of saline waters within crystalline bedrock, Outokumpu Deep Drill Hole, Finland. *Geochim. Cosmochim. Acta* 145, 159–174.
- Kietäväinen, R., and Purkamo, L. (2015). The origin, source and cycling of methane in deep crystalline rock biosphere. *Front. Microbiol.* 6:725. doi: 10.3389/fmicb.2015.00725
- Kim, M. K., Schubert, K., Im, W. T., Kim, K. H., Lee, S. T., and Overmann, J. (2007). *Sphingomonas kaistensis* sp. nov., a novel alphaproteobacterium containing pufLM genes. *Int. J. Syst. Evol. Microbiol.* 57, 1527–1534. doi: 10.1099/ijns.0.64579-0
- Kindt, R., and Coe, R. (2005). *Tree Diversity Analysis; A Manual and Software for Common Statistical Methods for Ecological and Biodiversity Studies*. Nairobi: World Agroforestry Centre, 196. doi: 10.1198/tas.2008.s264
- Krumholz, L. R., McKinley, J. P., Ulrich, G. A., and Sulfita, J. M. (1997). Confined subsurface microbial communities in Cretaceous rock. *Nature* 386, 64–66.
- Kyle, J. E., Eydal, H. S. C., Ferris, F. G., and Pedersen, K. (2008). Viruses in granitic groundwater from 69 to 450 m depth of the Åspö hard rock laboratory, Sweden. *ISME J.* 2, 571–574. doi: 10.1038/ismej.2008.18
- Lang, S. Q., Butterfield, D. A., Schulte, M., Kelley, D. S., and Lilley, M. D. (2010). Elevated concentrations of formate, acetate and dissolved organic carbon found at the Lost City hydrothermal field. *Geochim. Cosmochim. Acta* 74, 941–952. doi: 10.1016/j.gca.2009.10.045
- Lever, M. A. (2012). Acetogenesis in the energy-starved deep biosphere - a paradox? *Front. Microbiol.* 2:284. doi: 10.3389/fmicb.2011.00284
- Lin, L. H., Hall, J., Lippmann-Pipke, J., Ward, J. A., Sherwood Lollar, B., Deflaun, M., et al. (2005a). Radiolytic H₂ in continental crust: nuclear power for deep subsurface microbial communities. *Geochim. Geophys. Geosyst.* 6:Q07003.
- Lin, L. H., Slater, G. F., Sherwood Lollar, B., Lacrampe-Coulocoume, G., and Onstott, T. C. (2005b). The yield and isotopic composition of radiolytic H₂, a potential energy source for the deep subsurface biosphere. *Geochim. Cosmochim. Acta* 69, 893–903. doi: 10.1016/j.gca.2004.07.032
- Lloyd, K. G., Schreiber, L., Petersen, D. G., Kjeldsen, K. U., Lever, M. A., Steen, A. D., et al. (2013). Predominant archaea in marine sediments degrade detrital proteins. *Nature* 496, 215–218. doi: 10.1038/nature12033
- Lomstein, B. A., Langerhuus, A. T., D'Hondt, S., Jørgensen, B. B., and Spivack, A. J. (2012). Endospore abundance, microbial growth and necromass turnover in deep sub-seafloor sediment. *Nature* 484, 101–104. doi: 10.1038/nature10905
- Lovley, D. R., and Chapelle, F. H. (1995). Deep subsurface microbial processes. *Rev. Geophys.* 33, 365–381.
- Matlakowska, R., and Skłodowska, A. (2011). Biodegradation of Kupferschiefer black shale organic matter (Fore-Sudetic Monocline, Poland) by indigenous microorganisms. *Chemosphere* 83, 1255–1261. doi: 10.1016/j.chemosphere.2011.03.003
- McCollom, T. M., and Seewald, J. S. (2001). A reassessment of the potential for reduction of dissolved CO₂ to hydrocarbons during serpentinization of olivine. *Geochim. Cosmochim. Acta* 65, 3769–3778. doi: 10.1016/S0016-7037(01)00655-X
- McMahon, S., and Parnell, J. (2014). Weighing the deep continental biosphere. *FEMS Microbiol. Ecol.* 87, 113–120. doi: 10.1111/1574-6941.12196
- McMurdie, P. J., and Holmes, S. (2013). Phyloseq: an R package for reproducible interactive analysis and graphics of microbiome census data. *PLoS ONE* 8:e61217. doi: 10.1371/journal.pone.0061217
- Moser, D. P., Gehrke, T. M., Brockman, F. J., Fredrickson, J. K., Balkwill, D. L., Dollhopf, M. E., et al. (2005). Desulfotomaculum and *Methanobacterium* spp. dominate a 4- to 5-kilometer-deep fault. *Appl. Environ. Microbiol.* 71, 8773–8783. doi: 10.1128/AEM.71.12.8773-8783.2005
- Muyzer, G., de Waal, E. C., and Uitterlinden, A. G. (1993). Profiling of complex microbial populations by denaturing gradient gel electrophoresis analysis of polymerase chain reaction-amplified genes coding for 16S rRNA. *Appl. Environ. Microbiol.* 59, 695–700.
- Muyzer, G., and Stams, A. J. M. (2008). The ecology and biotechnology of sulphate-reducing bacteria. *Nat. Rev. Microbiol.* 6, 441–454. doi: 10.1038/nrmicro1892
- Nakagawa, S., Inagaki, F., Suzuki, Y., Steinsbu, B. O., Lever, M. A., Takai, K., et al. (2006). Microbial community in black rust exposed to hot ridge flank crustal fluids. *Appl. Environ. Microbiol.* 72, 6789–6799. doi: 10.1128/AEM.01238-06
- Nealson, K. H., Inagaki, F., and Takai, K. (2005). Hydrogen-driven subsurface lithoautotrophic microbial ecosystems (SLiMEs): do they exist and why should we care? *Trends Microbiol.* 13, 405–410.
- Nyssönen, M., Bomberg, M., Kapanen, A., Nousiainen, A., Pitkänen, P., and Itävaara, M. (2012). Methanogenic and sulphate-reducing microbial communities in deep groundwater of crystalline rock fractures in Olkiluoto, Finland. *Geomicrobiol. J.* 29, 863–878.
- Nyssönen, M., Hultman, J., Ahonen, L., Kukkonen, I., Paulin, L., Laine, P., et al. (2014). Taxonomically and functionally diverse microbial communities in deep crystalline rocks of the Fennoscandian shield. *ISME J.* 8, 126–138. doi: 10.1038/ismej.2013.125
- Oksanen, J., Blanchet, F. G., Friendly, M., Kindt, R., Legendre, P., McGlinn, D., et al. (2016). Package “Vegan” Title *Community Ecology Package*. Available at: <https://github.com/vegandevels/vegan/issues> (accessed August 18, 2016).
- Onstott, T. C., McGown, D. J., Bakermans, C., Ruskeeniemi, T., Ahonen, L., Telling, J., et al. (2009). Microbial communities in subpermafrost saline fracture water at the Lupin Au mine, Nunavut, Canada. *Microb. Ecol.* 58, 786–807. doi: 10.1007/s00248-009-9553-5
- Pedersen, K. (1993). The deep subterranean biosphere. *Earth Sci. Rev.* 34, 243–260.
- Pedersen, K. (1997). Microbial life in deep granitic rock. *FEMS Microbiol. Rev.* 20, 399–414.
- Pedersen, K. (2012). Subterranean microbial populations metabolize hydrogen and acetate under in situ conditions in granitic groundwater at 450 m depth in the Åspö Hard Rock Laboratory, Sweden. *FEMS Microbiol. Ecol.* 81, 217–229. doi: 10.1111/j.1574-6941.2012.01370.x
- Petsch, S. T., Edwards, K. J., and Eglington, T. I. (2005). Microbial transformations of organic matter in black shales and implications for global biogeochemical cycles. *Palaeogeogr. Palaeoclimatol. Palaeoecol.* 219, 157–170.
- Petsch, S. T., Eglington, T. I., and Edwards, K. J. (2001). 14C-dead living biomass: evidence for microbial assimilation of ancient organic carbon during shale weathering. *Science* 292, 1127–1131. doi: 10.1126/science.1058332
- Polz, M. F., and Cavanaugh, C. M. (1998). Bias in template-to-product ratios in multitemplate PCR. *Appl. Environ. Microbiol.* 64, 3724–3730.
- Proskurowski, G., Lilley, M. D., Seewald, J. S., Früh-Green, G. L., Olson, E. J., Lupton, J. E., et al. (2008). Abiogenic hydrocarbon production at lost city hydrothermal field. *Science* 319, 604–607. doi: 10.1126/science.1151194

- Puente-Sánchez, F., Sánchez-Román, M., Amils, R., and Parro, V. (2014). *Tessaracoccus lapidicaptus* sp. nov., an actinobacterium isolated from the deep subsurface of the Iberian pyrite belt. *Int. J. Syst. Evol. Microbiol.* 64, 3546–3552. doi: 10.1099/ijss.0.060038-0
- Purkamo, L., Bomberg, M., Kietäväinen, R., Salavirta, H., Nyssönen, M., Nuppunen-Puputti, M., et al. (2016). Microbial co-occurrence patterns in deep Precambrian bedrock fracture fluids. *Biogeosciences* 13, 3091–3108. doi: 10.5194/bg-13-3091-2016
- Purkamo, L., Bomberg, M., Nyssönen, M., Kukkonen, I., Ahonen, L., and Itävaara, M. (2015). Heterotrophic communities supplied by ancient organic carbon predominate in deep fennoscandian bedrock fluids. *Microb. Ecol.* 69, 319–332. doi: 10.1007/s00248-014-0490-6
- Purkamo, L., Bomberg, M., Nyssönen, M., Kukkonen, I., Ahonen, L., Kietäväinen, R., et al. (2013). Dissecting the deep biosphere: Retrieving authentic microbial communities from packer-isolated deep crystalline bedrock fracture zones. *FEMS Microbiol. Ecol.* 85, 324–337. doi: 10.1111/1574-6941.12126
- Quast, C., Pruesse, E., Yilmaz, P., Gerken, J., Schweer, T., Yarza, P., et al. (2013). The SILVA ribosomal RNA gene database project: Improved data processing and web-based tools. *Nucleic Acids Res.* 41, D590–D596. doi: 10.1093/nar/gks1219
- Rabus, R., Hansen, T. A., and Widdel, F. (2006). “Dissimilatory sulfate- and sulfur-reducing prokaryotes,” in *The Prokaryotes*, Vol. 2, eds M. Dworkin, S. Falkow, E. Rosenberg, K.-H. Schleifer, and E. Stackebrandt (New York, NY: Springer), 659–768.
- Rainey, F. A. (2015). “*Sporotomaculum*,” in *Bergey’s Manual of Systematics of Archaea and Bacteria*, eds A. Brauman, J. A. Müller, J. L. Garcia, A. Brune and B. Schink (Hoboken, NJ: John Wiley & Sons, Inc.), 1–5.
- Rogers, J. R., Bennett, P. C., and Choi, W. J. (1998). Feldspars as a source of nutrients for microorganisms. *Am. Mineral.* 83, 1532–1540. doi: 10.2138/am-1998-11-1241
- Russell, M. J., Hall, A. J., and Martin, W. (2010). Serpentization as a source of energy at the origin of life. *Geobiology* 8, 355–371. doi: 10.1111/j.1472-4669.2010.00249.x
- Schlöss, P. D., Westcott, S. L., Ryabin, T., Hall, J. R., Hartmann, M., Hollister, E. B., et al. (2009). Introducing MOTHUR: open-source, platform-independent, community-supported software for describing and comparing microbial communities. *Appl. Environ. Microbiol.* 75, 7537–7541. doi: 10.1128/AEM.01541-09
- Schrenk, M. O., Brazelton, W. J., and Lang, S. Q. (2013). Serpentization, carbon, and deep life. *Rev. Miner. Geochem.* 75, 575–606.
- Sorokin, D. Y., Tourova, T. P., Mußmann, M., and Muyzer, G. (2008). *Dethiobacter alkaliphilus* gen. nov. sp. nov., and *Desulfurivibrio alkaliphilus* gen. nov. sp. nov.: two novel representatives of reductive sulfur cycle from soda lakes. *Extremophiles* 12, 431–439. doi: 10.1007/s00792-008-0148-8
- Stevens, T. O., and McKinley, J. P. (1995). Lithoautotrophic microbial ecosystems in deep basalt aquifers. *Science* 270, 450–455. doi: 10.1126/science.270.5235.450
- Strapoć, D., Mastalerz, M., Dawson, K., Macalady, J., Callaghan, A. V., Wawrik, B., et al. (2011). Biogeochemistry of microbial coal-bed methane. *Annu. Rev. Earth Planet. Sci.* 39, 617–656. doi: 10.1146/annurev-earth-040610-133343
- Suko, T., Kouduka, M., Fukuda, A., Nanba, K., Takahashi, M., Ito, K., et al. (2013). Geomicrobiological properties of Tertiary sedimentary rocks from the deep terrestrial subsurface. *Phys. Chem. Earth, Parts A/B/C* 58–60, 28–33. doi: 10.1016/j.pce.2013.04.007
- Takii, S., Hanada, S., Tamaki, H., Ueno, Y., Sekiguchi, Y., Ibe, A., et al. (2007). *Dethiosulfatibacter aminovorans* gen. nov., sp. nov., a novel thiosulfate-reducing bacterium isolated from coastal marine sediment via sulfate-reducing enrichment with Casamino acids. *Int. J. Syst. Evol. Microbiol.* 57, 2320–2326. doi: 10.1099/ijss.0.64882-0
- Tiago, I., and Veríssimo, A. (2013). Microbial and functional diversity of a subterrestrial high pH groundwater associated to serpentinization. *Environ. Microbiol.* 15, 1687–1706. doi: 10.1111/1462-2920.12034
- Wagner, M., Roger, A. J., Flax, J. L., Brusseau, G. A., and Stahl, D. A. (1998). Phylogeny of dissimilatory sulfite reductases supports an early origin of sulfate respiration. *J. Bacteriol.* 180, 2975–2982.
- Weisburg, W. G., Barns, S. M., Pelletier, D. A., and Lane, D. J. (1991). 16S ribosomal DNA amplification for phylogenetic study. *J. Bacteriol.* 173, 697–703.
- Whitman, W. B., Coleman, D. C., and Wiebe, W. J. (1998). Prokaryotes: the unseen majority. *Proc. Natl. Acad. Sci. U.S.A.* 95, 6578–6583. doi: 10.1073/pnas.95.12.6578
- Wiegel, J. (2015). *Anaerobranca in Bergey’s Manual of Systematics of Archaea and Bacteria*, ed. W. B. Whitman (Hoboken, NJ: John Wiley & Sons, Inc.), 1–6. doi: 10.1002/9781118960608
- Wouters, K., Moors, H., Boven, P., and Leys, N. (2013). Evidence and characteristics of a diverse and metabolically active microbial community in deep subsurface clay borehole water. *FEMS Microbiol. Ecol.* 86, 458–473. doi: 10.1111/1574-6941.12171
- Woycheese, K. M., Meyer-Dombard, D. R., Cardace, D., Argayosa, A. M., and Arcilla, C. A. (2015). Out of the dark: transitional subsurface-to-surface microbial diversity in a terrestrial serpentinizing seep (Manleluag, Pangasinan, the Philippines). *Front. Microbiol.* 6:44. doi: 10.3389/fmicb.2015.00044
- Yu, G., Fadrosh, D., Goedert, J. J., Ravel, J., and Goldstein, A. M. (2015). Nested PCR biases in interpreting microbial community structure in 16S rRNA gene sequence datasets. *PLoS ONE* 10:e0132253. doi: 10.1371/journal.pone.0132253
- Yurkov, V. V. (2015). “*Roseococcus*,” in *Bergey’s Manual of Systematics of Archaea and Bacteria*, eds V. Yurkov, E. Stackebrandt, A. Holmes, J. A. Fuerst, P. Hugenholtz, J. Golecki et al. (Hoboken, NJ: John Wiley & Sons, Inc.), 1–4. doi: 10.1002/9781118960608.gbm00887
- Yutin, N., and Galperin, M. Y. (2014). A genomic update on clostridial phylogeny: gram-negative spore-formers and other misplaced clostridia. *Environ. Microbiol.* 15, 2631–2641. doi: 10.1111/1462-2920.1217

Conflict of Interest Statement: The authors declare that the research was conducted in the absence of any commercial or financial relationships that could be construed as a potential conflict of interest.

Copyright © 2017 Purkamo, Bomberg, Nyssönen, Ahonen, Kukkonen and Itävaara. This is an open-access article distributed under the terms of the Creative Commons Attribution License (CC BY). The use, distribution or reproduction in other forums is permitted, provided the original author(s) or licensor are credited and that the original publication in this journal is cited, in accordance with accepted academic practice. No use, distribution or reproduction is permitted which does not comply with these terms.



Guar Gum Stimulates Biogenic Sulfide Production at Elevated Pressures: Implications for Shale Gas Extraction

Sophie L. Nixon^{1*}, Leanne Walker², Matthew D. T. Streets², Bob Eden², Christopher Boothman¹, Kevin G. Taylor¹ and Jonathan R. Lloyd¹

¹ School of Earth and Environmental Sciences, University of Manchester, Manchester, UK, ² Rawwater Engineering Company Limited, Culcheth, UK

OPEN ACCESS

Edited by:

Cody Sheik,
University of Minnesota Duluth, USA

Reviewed by:

Bradley Stevenson,
University of Oklahoma, USA
Kathleen Duncan,
University of Oklahoma, USA
Christopher Neil Lyles,
Northwestern State University, USA

*Correspondence:

Sophie L. Nixon
sophie.nixon@manchester.ac.uk

Specialty section:

This article was submitted to
Microbiological Chemistry
and Geomicrobiology,
a section of the journal
Frontiers in Microbiology

Received: 10 October 2016

Accepted: 03 April 2017

Published: 19 April 2017

Citation:

Nixon SL, Walker L, Streets MDT, Eden B, Boothman C, Taylor KG and Lloyd JR (2017) Guar Gum Stimulates Biogenic Sulfide Production at Elevated Pressures: Implications for Shale Gas Extraction. *Front. Microbiol.* 8:679.

doi: 10.3389/fmicb.2017.00679

Biogenic sulfide production is a common problem in the oil industry, and can lead to costly hydrocarbon processing and corrosion of extraction infrastructure. The same phenomenon has recently been identified in shale gas extraction by hydraulic fracturing, and organic additives in fracturing fluid have been hypothesized to stimulate this process. Constraining the relative effects of the numerous organic additives on microbial metabolism *in situ* is, however, extremely challenging. Using a bespoke bioreactor system we sought to assess the potential for guar gum, the most commonly used gelling agent in fracturing fluids, to stimulate biogenic sulfide production by sulfate-reducing microorganisms at elevated pressure. Two pressurized bioreactors were fed with either sulfate-amended freshwater medium, or low-sulfate natural surface water, in addition to guar gum (0.05 w/v%) and an inoculum of sulfate-reducing bacteria for a period of 77 days. Sulfide production was observed in both bioreactors, even when the sulfate concentration was low. Analysis of 16S rRNA gene sequences indicate that heterotrophic bacteria closely associated with the genera *Brevundimonas* and *Acinetobacter* became enriched early in the bioreactor experiments, followed by an increase in relative abundance of 16S rRNA genes associated with sulfate-reducing bacteria (*Desulfosporosinus* and *Desulfobacteraceae*) at later time points. Results demonstrate that guar gum can stimulate acid- and sulfide-producing microorganisms at elevated pressure, and may have implications for the potential role in microbially induced corrosion during hydraulic fracturing operations. Key differences between experimental and *in situ* conditions are discussed, as well as additional sources of carbon and energy for biogenic sulfide production during shale gas extraction. Our laboratory approach can be tailored to better simulate deep subsurface conditions in order to probe the role of other fracturing fluid additives and downhole parameters on microbial metabolisms observed in these systems. Such baseline studies will prove essential for effective future development of shale gas worldwide.

Keywords: sulfate-reducing bacteria, guar gum, bioreactor, hydraulic fracturing, organic carbon

INTRODUCTION

The recent development of shale gas in the United States has dramatically increased domestic gas supply, and the UK and other European countries are planning to follow suit in the coming decades and exploit their own shale gas reserves (Andrews, 2013; Weijermars, 2013). The lead up to this development offers the opportunity to learn from and avoid problems encountered in the US, among them the biogenic production of hydrogen sulfide. This process, known as souring, causes pitting and cracking of susceptible materials (increasing the risk of leaks), can form pyrophoric films on steel in gas lines (posing a fire risk), and necessitates costly removal from produced gas. These issues can potentially lead to environmental and reputational damage, and can ultimately shorten the life span of a shale gas well (Eden et al., 1993). Biogenic hydrogen sulfide has been reported at a number of shale gas wells in the Barnett Shale (Fichter et al., 2008, 2009), and several studies have since demonstrated the presence of sulfidogenic bacteria in produced waters from this and other shale gas plays (Davis et al., 2012; Kirk et al., 2012; Struchtemeyer and Elshahed, 2012; Mohan et al., 2013a,b; Cluff et al., 2014; Akob et al., 2015).

Shale gas exists in unconnected or poorly-connected sub-micron scale spaces within very low permeability shale. It is therefore necessary to artificially fracture the formation in order to liberate shale gas. This is achieved through hydraulic fracturing, in which water-based fluids are pumped down the well at high pressure in order to overcome confining pressures and induce fractures in the formation. Wells are first drilled vertically to the required depth in the shale formation, then horizontally to increase contact with the gas-bearing rock. The fractures generated in this process are held open by a proppant, typically sand, to allow free flow of natural gas to the well. The fluid used to fracture the host rock is water-based, and includes a host of additives in addition to sand. Each serves a particular function, and the mix of additives varies from one operation to another, depending primarily on the characteristics of the source formation, though many such additives are organic (Elsner and Hoelzer, 2016). Here we address the hypothesis that organic fracturing fluid additives stimulate biogenic sulfide production.

A number of organic fracturing fluid additives are already known to be bioavailable to microorganisms. For example, ethylene glycol is widely used as a surfactant to inhibit scale formation during shale gas extraction (Elsner and Hoelzer, 2016), but is readily degraded and used for growth by soil and sewage microorganisms (Haines and Alexander, 1975; Watson and Jones, 1977; McGahey and Bouwer, 1992). Citric acid, used as a complexing agent in almost a third of disclosed hydraulic fracturing operations to date (Elsner and Hoelzer, 2016), is readily fermented by strains of *Clostridium*, yielding further bioavailable by-products such as acetate (Walther et al., 1977; Schink, 1984). Even the most conservative fracturing fluids contain an organic polymer, which serves as a gelling agent to increase viscosity and keep the proppant in suspension. The most widely used gelling agent is guar gum (Elsner and

Hoelzer, 2016), a polysaccharide also common in the food industry, and fermented by intestinal bacteria (Tomlin et al., 1986; Crociani et al., 1994). It is therefore highly likely that fracturing fluid additives will stimulate microbial metabolism in shale gas extraction operations, and are in part responsible for the observed biogenic sulfide production in these systems (Fichter et al., 2008, 2009).

Tracking the metabolism of such organic amendments and their possible coupling to sulfate reduction *in situ* is, however, extremely challenging. Here we report on a laboratory-based procedure to test the potential for the widely used gelling agent, guar gum, to stimulate biogenic sulfide production in pressurized semi-continuous bioreactor experiments. We present evidence that guar gum stimulates sulfide production. The implications for biofouling in future shale gas extraction operations are discussed. This study employs an *ex situ* bioreactor approach and represents a first step in understanding the potential microbiological implications in shale gas extraction. This approach is more appropriate than conventional microcosm-based batch tests conducted in serum vials, and can be tailored to simulate the deep terrestrial subsurface. This method could therefore serve as a blueprint for similar “baseline” studies on, for example, the microbial metabolism of fracking additives, required to support effective large-scale shale gas extraction both in the United States, and more widely in regions considering exploitation of this resource.

MATERIALS AND METHODS

Microbial Enrichment

A sulfate-reducing enrichment culture was initiated using sediment-laden water from a drinking water reservoir near Buxton, Derbyshire in the UK. Sediment-laden water was added to 90 ml sterile (121°C 20 min) Postgate B medium (described in Tanner, 1989) amended with sodium acetate as the electron donor (31 mM), pH 7, in a sterile 100 ml serum vial. The enrichment was incubated at 30°C in the dark, and was considered positive for sulfate reduction upon the accumulation of a black precipitate (iron sulfide). Sulfate reduction was evidenced by the appearance of black precipitates (presumed iron sulfide) and was used as an inoculum for bioreactor experiments after a 17 day incubation period.

Bioreactor Design

The pressurized bioreactors are bespoke, designed and manufactured by Rawwater Engineering Company Limited. Each bioreactor comprised a 5 cm outside diameter steel tube, lined with a unplasticized polyvinyl chloride liner, grouted in place either end prior to welding end-caps in place. Within the center of each end-cap was a weldable 0.635 cm Swagelok tube fitting. The inlet of the bioreactor was connected to a Perkins-Elmer HPLC series 100 pump, supplied by a nitrogen-pressurized aspirator at 2 barg. The outlet was connected to a union-T fitting, connected to a 0–3000 psig (0–206.8 bar) pressure gauge and a 1000 psig (68.9 bar) pressure release valve, from which samples were collected. All fittings were of 316L stainless steel.

Bioreactor Experimental Setup

Bioreactor 1 was packed with glass beads, and was fed with an influent of sulfate-amended freshwater medium. Prior to injection medium was purged with nitrogen gas to drive off dissolved oxygen. The basal medium (pH 7) contained (in grams per liter deionized water): NaHCO_3 (2.0), NH_4Cl (0.25), $\text{NaH}_2\text{PO}_4 \cdot \text{H}_2\text{O}$ (0.06), KCl (0.1), $\text{MgSO}_4 \cdot 7\text{H}_2\text{O}$ (2.0), CaSO_4 (1.0), and 10 ml mineral mix. The mineral contained (in grams per liter deionized water): nitrilotriacetic acid (1.5), $\text{MgSO}_4 \cdot 7\text{H}_2\text{O}$ (6.0), NaCl (1.0), $\text{FeSO}_4 \cdot 7\text{H}_2\text{O}$ (0.1), CaCl_2 (0.076), CoCl_2 (0.054), ZnCl_2 (0.13), $\text{CuSO}_4 \cdot 5\text{H}_2\text{O}$ (0.01), $\text{AlK}(\text{SO}_4)_2 \cdot 12\text{H}_2\text{O}$ (0.01), H_3BO_3 (0.01), $\text{MnO}_4 \cdot 2\text{H}_2\text{O}$ (0.294), and $\text{NiCl}_2 \cdot 6\text{H}_2\text{O}$ (0.024). All constituents of the medium were added prior to autoclaving for 20 min at 121°C. Total concentration of sulfate in this medium was 15.7 mM.

Bioreactor 2 was packed with low-iron sand (Fisher Scientific, UK), and was fed with deoxygenated surface water collected from a seasonal pond on private land in Culcheth, Cheshire, UK (53°37'44.04"N, 2°29'44.05"W). This land was chosen as a source of readily available fresh surface water relevant to potential future hydraulic fracturing scenarios in the North of England. Formate, acetate, propionate, and butyrate concentrations were measured with ion chromatography (IC; Metrohm 930 Compact IC Flex, Daresbury, UK) and found to be below the detection limit of 0.1 mg/l. Sulfate, nitrate, and phosphate concentrations in this surface water were similarly measured with IC (Dionex ICS5000 Dual Channel, Hemel Hempstead, UK), and found to be 79.6 (0.83 mM), 0.19, and 0.1 mg/l, respectively. Bioreactor 2 therefore served as a "low sulfate" comparison to Bioreactor 1. The influent was purged with oxygen-free nitrogen gas for 24 h prior to injection.

The bioreactors were run at room temperature (15–25°C) and 1000 psi (68.9 bar) under batch conditions. Injections were made at a flow rate of 3 ml/min for a 30 min batch injection twice weekly (on days 1 and 4 of each week) until day 28, then once weekly, for a total of 77 days. For each bioreactor, the weekly influent injection volume was equal to the pore volume of the bioreactor, quantified with a fluorescein tracer (Sigma-Aldrich, UK) prior to initiating the experiments. The pore volume of Bioreactor 1 was 376 ml, and 562 ml for Bioreactor 2. Both bioreactors were flushed with 6× pore volumes of anaerobic reverse-osmosis water after fluorescein tracer tests, and before the first experimental injection. A 1% (v/v) inoculum from the sulfate-reducing enrichment culture was added to the influent of both bioreactors from the start of the experiment until day 28. Guar gum (0.05% w/v) was added to the influent of both bioreactors from the start of the experiment until day 63. Samples were collected for analysis from the effluent generated at each injection point.

Analytical Methods

Total sulfide concentrations in the effluent were measured using the methylene blue assay. Samples were collected directly onto zinc acetate crystals, which reacted with the sulfide in solution

to form a zinc sulfide precipitate, preserving the aqueous sulfide concentration. The sulfide was then regenerated in acid for a methylene blue colorimetric test (Fonselius et al., 1999). The methylene blue test was calibrated using the standard iodometric determination of sulfide titration method (limit of detection 0/5 mg/l total sulfide). The pH of the effluent was measured using pH indicator strips (pH range 4–10, Fisher Scientific).

Bacterial Community Composition

Bacterial community composition was examined by extraction of DNA from 10 ml samples of the enrichment culture influent (2 days prior to the start of experiments) and effluent using the MoBio PowerLyzer™ PowerSoil DNA Isolation Kit (MoBio Laboratories, Inc., Carlsbad, CA, USA). Sequencing of polymerase chain reaction (PCR) amplicons of 16S rRNA was conducted with the Illumina MiSeq platform (Illumina, San Diego, CA, USA) targeting the V4 hyper variable regions (forward primer, 515F, 5'-GTGY CAGCMGCCGCGGTAA-3'; reverse primer, 806R, 5'-GGA CTACHVGGGTWTCTAAT-3') for 2 × 150-bp paired-end sequencing (Illumina) (Caporaso et al., 2011, 2012). PCR amplification was performed using Roche FastStart High Fidelity PCR System (Roche Diagnostics Ltd, Burgess Hill, UK) in 50 μl reactions under the following conditions: initial denaturation at 95°C for 2 min, followed by 36 cycles of 95°C for 30 s, 55°C for 30 s, 72°C for 1 min, and a final extension step of 5 min at 72°C. The PCR products were purified and normalized to ~20 ng each using the SequalPrep Normalization Kit (Fisher Scientific, Loughborough, UK). A negative PCR control was conducted in parallel to bioreactor effluent and inoculum samples, and found to be devoid of DNA. The PCR amplicons from all samples were pooled in equimolar ratios. The run was performed using a 4 pM sample library spiked with 4 pM PhiX to a final concentration of 10% following the method of Kozich et al. (2013). Raw sequences were divided into samples by barcodes (up to one mismatch was permitted) using a sequencing pipeline. Quality control and trimming was performed using Cutadapt (Martin, 2011), FastQC¹, and Sickle (Joshi and Fass, 2011). MiSeq error correction was performed using SPADes (Nurk et al., 2013). Forward and reverse reads were incorporated into full-length sequences with Pandaseq (Masella et al., 2012). Chimeras were removed using ChimeraSlayer (Haas et al., 2011) and operational taxonomic units (OTUs) were generated with UPARSE (Edgar, 2013). OTUs were classified by Usearch (Edgar, 2010) at the 97% similarity level, and singletons were removed. Rarefaction analysis was conducted using the original detected OTUs in Qiime (Caporaso et al., 2010). Taxonomic assignment was performed by the Ribosomal Database Project (RDP) Classifier using an 80% confidence limit (Wang et al., 2007). Raw sequencing data have been submitted to NCBI Sequence Read Archive² with the project accession number SRP093359.

¹<http://www.bioinformatics.babraham.ac.uk/projects/fastqc/>

²<http://www.ncbi.nlm.nih.gov/sra/>

RESULTS

Bioreactor Experiments

Results from bioreactor experiments are summarized in **Figure 1**. Sulfide production was detected in both bioreactors. Much higher concentrations of sulfide were measured in bioreactor 1 (**Figure 1A**) compared to bioreactor 2 (**Figure 1B**). In both cases, the concentration of total sulfide was highest after inoculations had stopped, but before guar injection had ceased (**Figure 1**, points 1 and 2, respectively). In bioreactor 1, the average concentration of sulfide from day 0 to day 21 was 5.3 ± 1.6 mg/l. The average sulfide concentration for the same period in bioreactor 2 was 2.5 ± 1.4 mg/l. In both bioreactors the maximum total sulfide concentrations were recorded on day 63 (118.6 mg/l in bioreactor 1 and 12.6 mg/l in bioreactor 2). Sulfide concentrations decreased in both bioreactors after guar injections ceased. The average pH measured in bioreactors 1 and 2 was 8.3 and 7.6, respectively.

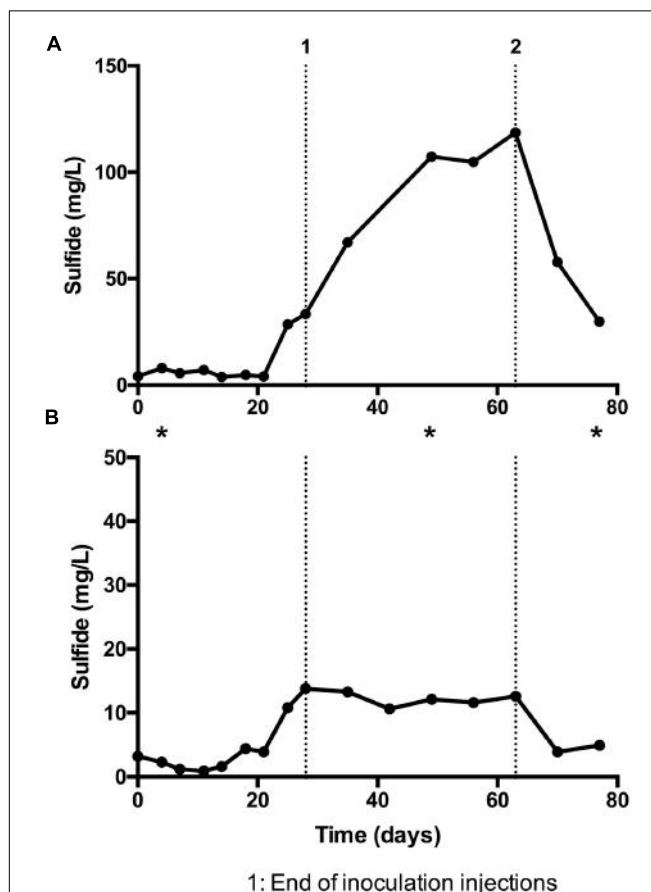


FIGURE 1 | Sulfide detected in guar gum bioreactor experiments, expressed as milligram per liter with time. **(A)** Bioreactor 1, fed with sulfate-amended freshwater medium and packed with glass beads. **(B)** Bioreactor 2, fed with low-sulfate natural surface water and packed with sand. Asterisks denote timepoints at which samples were taken for DNA extraction and 16S rRNA sequencing.

Microbial Community Analysis

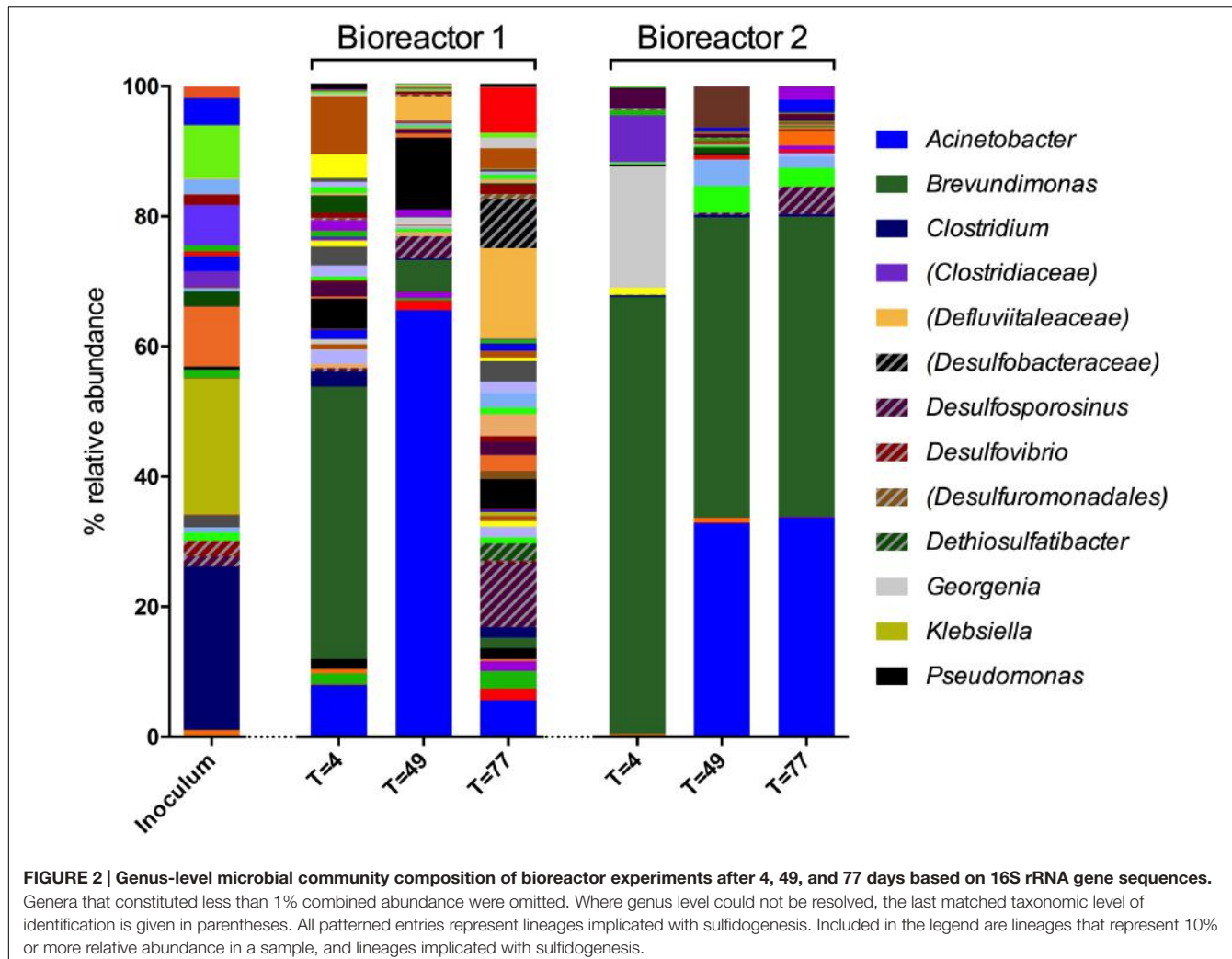
Microbial community composition was analyzed using 16S rRNA gene sequencing. A total of 281 OTUs were detected in the sulfate-reducing enrichment culture that was inoculated into both bioreactors (the inoculum). In bioreactor 1 samples, 599 OTUs were detected by day 4, 347 by day 49, and 420 by day 77. In bioreactor 2, 105 OTUs were observed by day 4, 135 by day 49, and 117 by day 77. Genus-level diversity of the inoculum and bioreactor samples is shown in **Figure 2**.

The inoculum was dominated by Firmicutes (64.0%, 78 OTUs), of which 58% of obtained sequences were affiliated to the class *Clostridiaceae* (68 OTUs). The remainder of the sequences were affiliated with the phyla Proteobacteria (30.3%, 29 OTUs) and Bacteroidetes (5.5%, 9 OTUs). Other phyla accounted for less than 0.2% of the sequences from this sample. The most abundant genera detected in the inoculum were *Clostridiaceae* (24.1%, 16 OTUs), *Klebsiella* (20.0%, 1 OTU) and *Sedimentibacter* (8.8%, 6 OTUs). Sequences of unidentified genera affiliated with the families Ruminococcaceae (7.8%, 13 OTUs), Enterobacteriaceae (5.9%, 1 OTU), Sphingobacteriaceae (4.0%, 1 OTU), and Clostridiaceae (2.4%, 2 OTUs) were also prominent. Sulfate-reducing genera detected in the inoculum include *Desulfovibrio* (2.2%, 1 OTU), *Desulfosporosinus* (1.5%, 1 OTU), and *Desulfotobacterium* (0.7%, 1 OTU), and 0.1% of sequences were assigned to the sulfur-reducing species *Geobacter sulfurreducens* (1 OTU), which is also a well known Fe(III)-reducing bacterium.

Sequences obtained from bioreactor 1 on day 4 were dominated by Proteobacteria (77.9%, 114 OTUs), most of which were affiliated to the class Alphaproteobacteria (50.1%, 28 OTUs), in addition to Gammaproteobacteria (15.2%, 20 OTUs) and Betaproteobacteria (10.1%, 46 OTUs). The most abundant genus in this sample was *Brevundimonas*, accounting for 32.2% of sequences (2 OTUs). Other prominent bacteria in this sample included members of the *Acinetobacter* (6.1%, 3 OTUs) and *Pseudomonas* (3.6%, 7 OTUs) genera. In contrast to the inoculum, sequences assigned to the *Clostridiaceae* genus only accounted for 1.8% (7 OTUs) of the community at this time point.

By day 49, the bioreactor 1 community was dominated by Proteobacteria (83.3%, 102 OTUs). The dominant genera were *Acinetobacter* (63.2%, 3 OTUs), *Pseudomonas* (10.7%, 6 OTUs), and *Brevundimonas* (4.6%, 2 OTUs). By day 77, diversity of the community had substantially increased (see **Figure 2**). Roughly two-thirds of sequences were affiliated with Firmicutes (36.0%, 92 OTUs) and Proteobacteria (35.3%, 112 OTUs). The majority of sequences assigned to the former were identified as unknown members of the *Defluvialteaceae* family, and 8.1% were assigned to the sulfate-reducing genus *Desulfosporosinus* (4 OTUs).

Bioreactor 2 was dominated with Proteobacteria throughout the experiment, accounting for 71.1% (41 OTUs), 85.6% (51 OTUs), and 80.7% (41 OTUs) of sequences by day 4, 49, and 77, respectively. Actinobacteria accounted for 18.5% of sequences at day 4 (11 OTUs), but less than 1% at the later time points. Firmicutes were less abundant than in the inoculum (64.0% 78 OTUs), but relatively stable throughout (9.4% at day



4, 18 OTUs; 7.3% at day 49, 29 OTUs; 9.8% at day 77, 29 OTUs). *Brevundimonas* was the dominant genus at every time point of the bioreactor 2 experiment, representing 65.0% of day 4 sequences (5 OTUs), 44.8% of those obtained by day 49 (4 OTUs), and 45.0% at day 77 (6 OTUs). Organisms affiliated with *Georgenia* species were also prominent by day 4, accounting for 18.2% of sequences (2 OTUs). Unknown members of the Clostridiaceae family represented 7.0% of sequences at the same time point (4 OTUs), but were not detected at later time points. Organisms most closely affiliated with *Acinetobacter* was the second-most abundant genus by day 49 (31.9%, 3 OTUs) and 77 (33.0%, 2 OTUs).

The dominant genera identified throughout both bioreactor experiments (representatives of *Brevundimonas*, *Acinetobacter*) were detected in the inoculum, albeit each accounted for less than 1% of the inoculum community. *Pseudomonas*, found to be relatively prominent in bioreactor 1, was also detected in the inoculum, although *Georgenia* (prominent in bioreactor 2) was not. The bioreactors were not sterile prior to use in these experiments, so may represent an additional source of microorganisms.

Presence of Sulfidogenic Lineages

The presence and abundance of genera associated with sulfide production are summarized in Figures 3, 4. Only assigned taxa that include known bacterial strains capable of sulfide production have been included in this analysis, however we acknowledge that other microorganisms may have contributed to sulfide production. The acetate oxidizing sulfate-reducing enrichment used to inoculate the bioreactors appeared to select for organisms most closely related to *Desulfovibrio* and *Desulfosporosinus* species, though only the latter appeared to increase in relative abundance in the bioreactor experiments (see Figure 2).

The most abundant sulfate-reducing genus in the inoculum was *Desulfovibrio*, although it only accounted for 2.4% of sequences (1 OTU) obtained from this sample, and less than 1% of the community in both bioreactor experiments at every time point. Close relatives of known *Desulfosporosinus* species were also present in the inoculum (1.6%, 3 OTUs), although less abundant than *Desulfovibrio* species. The relative abundance of *Desulfosporosinus* species increased in the later stages of the bioreactor 1 experiment, representing 10.2% (4 OTUs) of the day

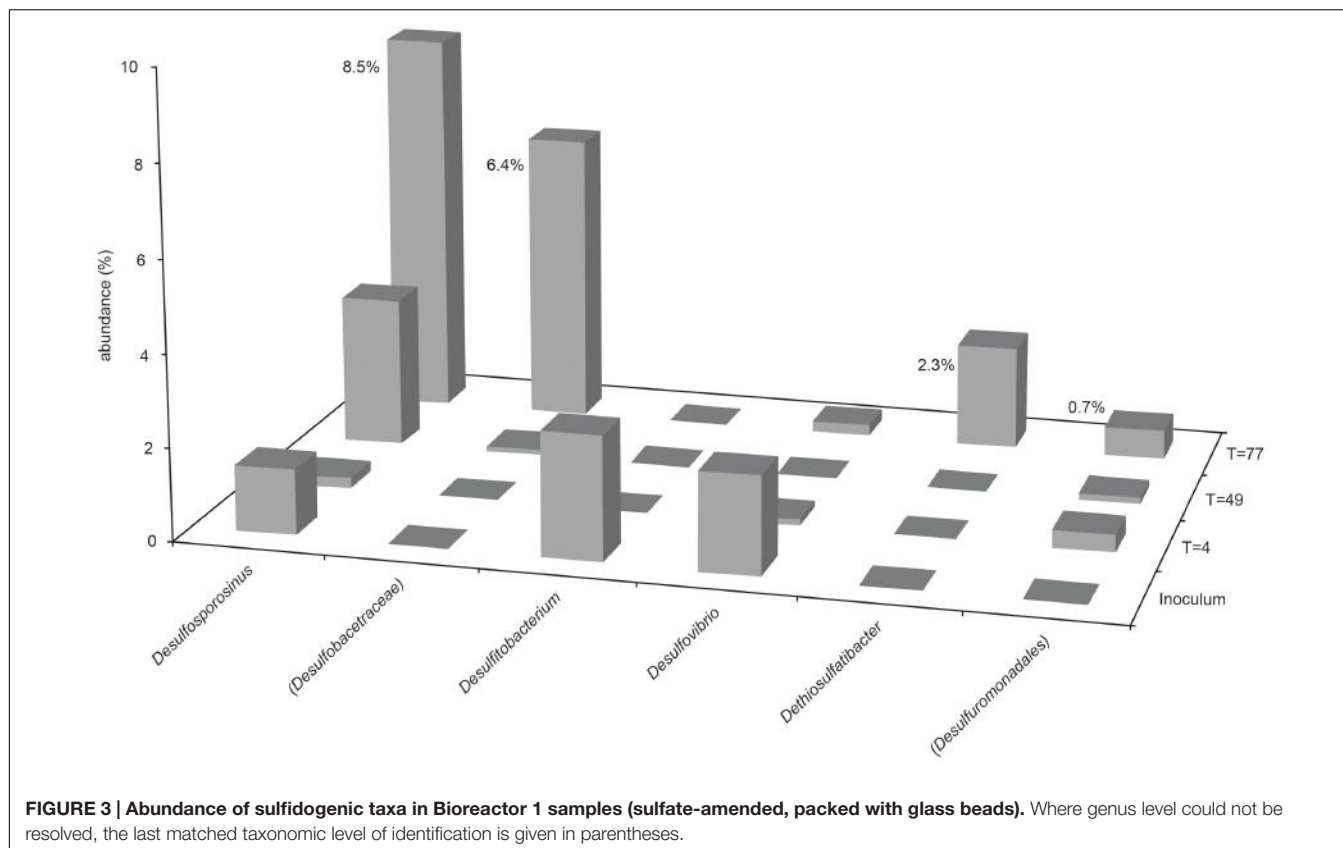


FIGURE 3 | Abundance of sulfidogenic taxa in Bioreactor 1 samples (sulfate-amended, packed with glass beads). Where genus level could not be resolved, the last matched taxonomic level of identification is given in parentheses.

77 community (see **Figures 2, 3**). The thiosulfate-reducing genus *Dethiosulfatibacter* was also detected in bioreactor 1 samples (2.7% of day 77 community, 1 OTU), but was not detected in the inoculum, presumably due to very low abundance, though its presence in the bioreactor prior to inoculation cannot be ruled out.

In bioreactor 2, *Desulfosporosinus* species were enriched by day 77, representing 4.1% of the community (1 OTU). *Desulfobacterium* species were not detected in any samples from bioreactor 2. Organisms most closely affiliated with *Dethiosulfatibacter* and *Desulfobulbus* genera were both detected at day 4, but each accounted for less than 0.1% of the community, and were not detected in the inoculum or at later time points, either due to their low abundance in the inoculum or because they were already present in the bioreactor.

DISCUSSION

A number of organic additives are used in hydraulic fracturing fluid, and whether these additives stimulate deleterious microbial activity is poorly understood. The results from this study demonstrate that guar gum, a widely used gelling agent in disclosed hydraulic fracturing operations, can stimulate heterotrophic microorganisms including sulfate-reducing bacteria under conditions relevant to the terrestrial subsurface, even with low sulfate concentrations typical of surface water sources, ultimately fuelling biogenic sulfide production.

The enrichment of heterotrophic taxa in both bioreactor experiments (**Figure 2**) suggests that guar gum is readily bioavailable for microbial metabolism. Consistent with this was the detection of high concentrations of volatile fatty acids in both bioreactors at day 28 (principally acetate and propionate at 182.6 and 75.4 mg/l, respectively in bioreactor 1, and 169.4 mg/l acetate and 109.8 mg/l propionate in bioreactor 2), which depleted over the course of the experiment (data not shown). *Brevundimonas*, the most abundant genus detected early in the bioreactor 1 experiment and throughout the bioreactor 2 experiment (**Figure 2**), is a non-fermentative Gram-negative genus in the alpha subdivision of the Proteobacteria, able to draw upon a wide range of organic compounds for non-fermentative respiration and is known to produce organic acids as by-products (Segers et al., 1994). At least one strain of *Brevundimonas* is known to metabolize mannose and galactose, the two sugars that make up the guar gum galactomannan polysaccharide (Segers et al., 1994). It therefore seems likely that strains of *Brevundimonas* were able to metabolize guar gum and its potential degradation products in these experiments. This hypothesis warrants further investigation, including culturing experiments with and without guar. *Acinetobacter* was also prominent in later stages of both bioreactor experiments. Strains of this genus are similarly non-fermentative and metabolically versatile, capable of using an array of organic compounds as sole energy and carbon sources (Doughari et al., 2011). A large number of strains have been successfully isolated using acetate

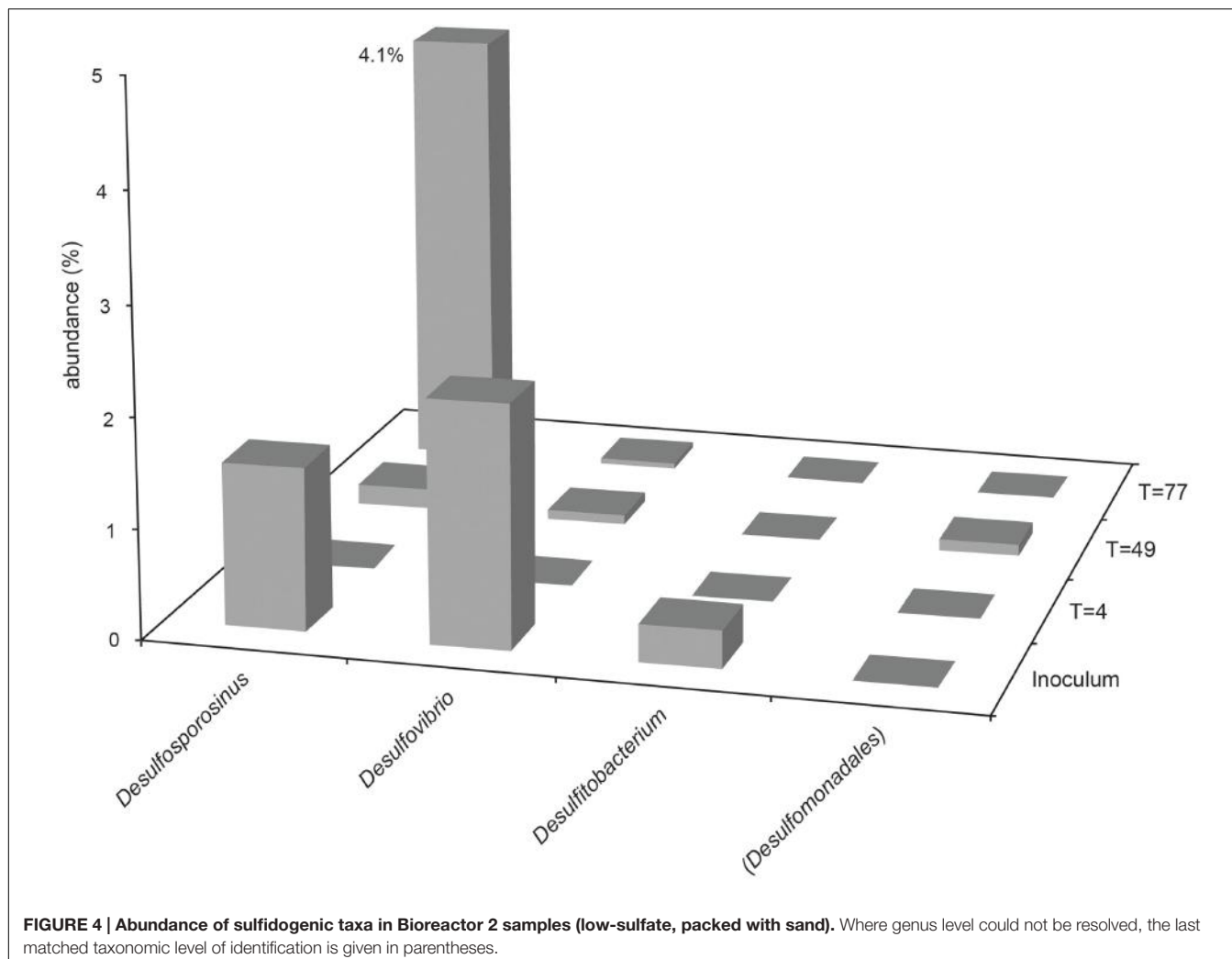


FIGURE 4 | Abundance of sulfidogenic taxa in Bioreactor 2 samples (low-sulfate, packed with sand). Where genus level could not be resolved, the last matched taxonomic level of identification is given in parentheses.

as the sole source of carbon and energy (Warskow and Juni, 1972), which may be present as a guar degradation product in the bioreactors. It is therefore feasible that strains of *Acinetobacter* are also able to use guar gum, directly or via its degradation products, in the experiments. Both genera were detected in the inoculum, and are assumed to originate from the reservoir water used to initiate the sulfate-reducing enrichment culture.

Unsurprisingly, sulfidogenic genera were more numerous and abundant in samples taken from bioreactor 1 (injected with sulfate-amended medium) compared with bioreactor 2 (injected with low-sulfate surface water). The most abundant sulfate-reducing genera in bioreactor 1 were *Desulfosporosinus*, *Dethiosulfatibacter* and unidentified members of the Desulfobacteraceae family (Figures 2, 3). Of these, only *Desulfosporosinus* was detected in the inoculum. It is possible that these other taxa were in fact present but in such small numbers that they were not detected during sequencing. Interestingly, *Dethiosulfatibacter* species are unable to reduce sulfate to sulfide, and instead utilize thiosulfate and elemental sulfur as electron acceptors (Takii et al., 2007), neither of which were supplied to the bioreactor. It is therefore

likely that *Dethiosulfatibacter* strains were not contributing directly to sulfide production, and were instead operating a fermentative metabolism (Takii et al., 2007), contributing to the breakdown of guar gum. Some sulfate-reducing genera that were enriched in the inoculum did not prosper in the bioreactor experiment, such as *Desulfobacterium* and *Desulfovibrio* (Figure 3). The data therefore suggest that *Desulfosporosinus* and members of the sulfate-reducing family Desulfobacteraceae were responsible for sulfide production measured in the bioreactor 1 experiment. The sulfide production measured in bioreactor 2 (Figure 1) can most likely be attributed to *Desulfosporosinus*, the only sulfidogenic taxon that increased in abundance throughout the course of the experiment (Figure 4). In both cases it is possible that taxa other than those discussed here may have contributed to sulfide production.

The sulfide production measured in both bioreactors does not appear to be limited by the amount of sulfate available. Based on a 1:1 ratio of sulfate reduced to sulfide produced (whether direct or via intermediate sulfur species), the maximum amount of sulfide that could be produced is equal to the concentration of

sulfate available in each bioreactor, assuming the supply of electron donors is not limiting. Therefore, 15.7 mM sulfate added to bioreactor 1 has the potential to liberate 15.7 mM (519 mg/l) sulfide, yet the maximum concentration measured was almost five times lower. Similarly, only 12.6 mg/l total sulfide was measured in bioreactor 2, more than six times lower than the maximum concentration that could be produced from the direct reduction of 79.6 mg/l sulfate measured in the pond water. In both cases it therefore appears that the supply of electron donors was limiting.

Results Compared to *In Situ* Studies of Shale Gas Plays

A number of other studies have identified sulfidogenic microorganisms obtained from active shale gas plays in the US. Struchtemeyer and Elshahed (2012) conducted 16S rRNA diversity analysis on flowback fluids from shale gas wells in the Barnett shale, and identified sequences affiliated with the sulfate-reducing genera *Desulfosporosinus*, *Desulfotomaculum*, as well as thiosulfate- and sulfur-reducing genera *Dethiosulfovibrio*, *Thermotoga*, *Petrotoga*, *Thermovirga*, and *Halanaerobium*. Davis et al. (2012) monitored the change in microbial communities in post-fracturing fluids stored in tanks in the Barnett shale formation over a 6-month period using 16S rRNA gene sequencing, and found the number of sequences affiliated with *Desulfovibrio* increased over time. However, their results indicate that the thiosulfate-reducing *Halanaerobium* genus was more abundant, and likely contributed to the biogenic sulfide production reported in this area (Fichter et al., 2008, 2009). Indeed, it is common that microorganisms other than those traditionally thought of as sulfate-reducing bacteria are the dominant sulfide-producers in conventional hydrocarbon reservoirs, especially at elevated temperature and pressure (Gittel et al., 2009; Stevenson et al., 2011). *Desulfovibrio* was found to be abundant in flowback fluids from one well in the Antrim shale gas play (Kirk et al., 2012), consistent with results reported by Davis et al. (2012). *Desulfovibrio halotolerans* was abundant in a flowback impoundment in the Marcellus shale, despite treatment with biocide, though *Halanaerobium congolense* accounted for more than half of sequences obtained from 16S rRNA analysis (Mohan et al., 2013b). *Halanaerobium* is a genus of halophilic bacteria, capable of fermentation of wide array of organics as well as thiosulfate- and sulfur-reduction (Zeikus et al., 1983), and was also found to dominate sequences from produced waters in other studies of the same shale gas play (Mohan et al., 2013a; Cluff et al., 2014; Daly et al., 2016). Strains of the same genus in flowback fluids were later shown to be viable (Akob et al., 2015), and, more recently, capable of degrading guar gum (Liang et al., 2016).

It is clear that sulfidogenic taxa are common in flowback and produced fluids from active shale gas plays, though the overlap with those identified in our experiments is limited to *Desulfosporosinus* species (Struchtemeyer and Elshahed, 2012). In addition, a number of studies have identified the prominence of non-sulfate-reducing sulfidogenic taxa, especially strains of *Halanaerobium*. This genus was absent from our bioreactor

samples, in part owing to the lack of thiosulfate and high salt concentrations in the systems.

Bioreactor Compared with *In Situ* Conditions

In this study, we sought to simulate conditions more relevant to the deep terrestrial subsurface compared with conventional serum bottle substrate utilization tests. In particular, bioreactor experiments were run at high pressure (1000 psi, 68.9 bar, 6.89 MPa), and bioreactor 2 was fed with terrestrial surface water which represents a plausible source of fracturing fluid water in future UK shale gas extraction (CIWEM, 2016). Furthermore, the sulfate-reducing enrichment culture was initiated with water from a drinking water reservoir, a similarly plausible source of water for UK hydraulic fracturing operations, and thus the microbial community introduced to the bioreactor experiments could be considered highly appropriate.

A number of parameters at play in the hydraulic fracturing of shale formations were not, however, represented in the experiments reported here. These parameters are likely to impact on bacterial community composition, and can account for the major differences in our study compared with *in situ* studies. For example, hydraulic fracturing leads to significant changes in fracturing fluid composition that were not reflected in the bioreactor experiments. During shale gas extraction, input fluids are subjected to temperatures above 50°C, and pressures greater than 30 MPa (Fichter et al., 2012; Picard and Daniel, 2013). Upon contact with freshly fractured shale, these fluids are influenced by the chemical composition of the formation, observed in flowback and produced waters as high concentrations of total dissolved solids, dissolved organic carbon, naturally-occurring radioactive minerals, lower pH, and salinities that can reach several times that of seawater (Struchtemeyer and Elshahed, 2012; Mohan et al., 2013a; Akob et al., 2015; Liang et al., 2016). Furthermore, the increased temperatures encountered by hydraulic fracturing fluids at depth may alter the properties (and hence the bioavailability) of organic additives, including guar gum. Significant changes in microbial diversity can be seen as a result of these well-documented chemical changes, from a typical freshwater aerobic community in input fluids, to a less diverse anaerobic community in flowback fluids. The predominance of halotolerant and halophilic taxa in flowback waters indicates that salinity is a significant contributing factor to changes in microbial ecology (Struchtemeyer and Elshahed, 2012; Mohan et al., 2013a; Cluff et al., 2014; Akob et al., 2015; Daly et al., 2016), and most likely accounts for the lack of halophilic sulfidogens, such as *Halanaerobium* (Zeikus et al., 1983), in our experiments. It is worth noting, however, that relatively few shale gas plays have been assessed with regard to microbial activity, and it remains unclear to what extent the predominance of certain taxa over others are controlled by factors such as the choice of source water used for fracturing fluids, the characteristics of the shale formations, the mix of additive used, and operational parameters chosen. These factors may change significantly in shale gas extraction development outside of the US. The experiments reported here thus serve as a blueprint for an *ex situ* method

superior to simple microcosm tests. This methodology can be applied extensively to better constrain the factors that contribute to souring and other deleterious microbial activities during shale gas extraction operations.

Sources of Carbon and Energy for Biogenic Sulfide Production during Shale Gas Extraction

In this study, we have demonstrated that guar gum, a commonly used gelling agent added to fracturing fluids, has the potential to stimulate biogenic sulfide production. However guar gum is not the only potential electron donor for microbial activity during shale gas extraction. An alternative gelling agent to guar is cellulose, readily fermented by heterotrophic bacteria (e.g., Weimer and Zeikus, 1977), the by-products of which could serve as electron donors for sulfidogenesis. Acetate is a well-known electron donor for microbial sulfate reduction (e.g., Laanbroek and Pfennig, 1981), and is added to fracturing fluids to control pH (Elsner and Hoelzer, 2016). It is also plausible that other fracturing fluid additives known to be bioavailable to microorganisms, such as polyacrylamide (Nakamiya and Kinoshita, 1995; Wen et al., 2010) and ethylene glycol (Haines and Alexander, 1975; Watson and Jones, 1977; McGahey and Bouwer, 1992), would be broken down into directly available electron donors during hydraulic fracturing.

Another source of organic carbon and energy is the formation itself. Shale is organic rich, and whilst its nanodarcy permeability is thought to render it uninhabitable, the organic compounds they host are thought to support microbial communities at the interface of more permeable strata (Frederickson et al., 1997; Krumholz et al., 2002). It is clear from the organic chemistry of flowback and produced fluids that hydraulic fracturing liberates hydrocarbons from the formation (Strong et al., 2014). These hydrocarbons could conceivably serve as an indirect source of electron donors after undergoing fermentation by heterotrophic bacteria (e.g., species of *Halanaerobium*, Zeikus et al., 1983). Additionally, highly oxidizing peroxide compounds are added to fracturing fluids to reduce fluid viscosity and allow for fluid recovery prior to gas flow, and these compounds may render otherwise recalcitrant kerogen more bioavailable through oxidation.

Struchtemeyer et al. (2011) demonstrated that organic polymers in drilling waters were degraded by a community of anaerobic microorganisms present in drilling muds. Barite (BaSO_4) and sulfonates, added to drilling mud to add weight and reduce viscosity, respectively, were also found to stimulate sulfate-reducing microorganisms and biogenic sulfide production (Struchtemeyer et al., 2011). The act of drilling into shale formations prior to hydraulic fracturing can therefore introduce additional carbon and energy sources for sulfidogenesis before organic-rich fracturing fluids are injected.

Additional sources of sulfur compounds can also be found in injection fluids, though to a much lesser extent than organic carbon. In a thorough review of disclosed fracturing fluid additives, Elsner and Hoelzer (2016) report the use of organo

sulfonates as surfactants in 4% of operations, sodium sulfate to control ionic strength in 2.4% of operations, ammonium sulfate as a friction reducer in 1.1%, and ferric sulfate as a crosslinker in less than 1%. The source of water used to make up fracturing fluid may also harbor sulfate concentrations sufficient to lead to detectable biogenic sulfide production, though this will vary with operation location. In addition, it is plausible that oxidizing agents added to fracturing fluids to reduce viscosity for fluid recovery (breakers) could oxidize any reduced sulfur native to the formation [either as pyrite (Raiswell and Berner, 1986; Gross et al., 2015) or organo-sulfur compounds (Tissot and Welte, 1978; Sinnighe Damsté and de Leeuw, 1989)], thereby rendering it available to support sulfidogenesis through sulfate-, thiosulfate-, or sulfur-reduction.

CONCLUSION

Using bespoke high-pressure bioreactor systems, we have demonstrated that guar gum, the most commonly used gelling agent in hydraulic fracturing fluids, can serve as a carbon and electron donor source for a sulfate-reducing microbial community, leading to biogenic sulfide production. These results have important implications for our understanding of the critical factors controlling souring during shale gas extraction, and highlight the value of adopting a bespoke bioreactor methodology to study these constraints in isolation. Future research should seek to accurately simulate the elevated pressures, temperatures and aqueous geochemistry encountered during shale gas extraction. This approach could be used to assess the potential for other additives to stimulate sulfidogenesis and other microbial processes, for example, biofilm formation and clogging, using the pressurized bioreactor model employed here, in order to better define the least problematic fracturing fluid composition, and to identify the microorganisms that need to be controlled prior to re-use of flowback fluids. The methodology adopted in this study offers the opportunity to probe the microbial metabolisms observed recently to be active in hydraulic fracturing produced waters in more detail (Daly et al., 2016). In particular, our approach allows for the relative influence of fracturing fluid additives on the activity of these metabolisms to be constrained beyond what is possible through *in situ* studies.

AUTHOR CONTRIBUTIONS

SN, BE, KT, and JL designed the experiments. SN, LW, and MS conducted the experiments. CB carried out DNA extractions and sequencing. SN carried out data analysis, prepared figures, and wrote the manuscript with contributions from all authors.

FUNDING

SN was supported through NERC Impact Acceleration Account NE/L012723/1.

REFERENCES

- Akob, D. M., Cozzarelli, I. M., Dunlap, D. S., Rowan, E. L., and Lorah, M. M. (2015). Organic and inorganic composition and microbiology of produced waters from Pennsylvania shale gas wells. *Appl. Geochem.* 60, 116–125. doi: 10.1016/j.apgeochem.2015.04.011
- Andrews, I. J. (2013). *The Carboniferous Bowland Shale Gas Study: Geology and Resource Estimation*. London: British Geological Survey for Department of Energy and Climate Change, 64.
- Caporaso, J. G., Kuczynski, J., Stombaugh, J., Bittinger, K., Bushman, F. D., Costello, E. K., et al. (2010). QIIME allows analysis of high-throughput community sequencing data. *Nat. Methods* 7, 335–336. doi: 10.1038/nmeth.f.303
- Caporaso, J. G., Lauber, C. L., Walters, W. A., Berg-Lyons, D., Huntley, J., Fierer, N., et al. (2012). Ultra-high-throughput microbial community analysis on the Illumina HiSeq and MiSeq platforms. *ISME J.* 6, 1621–1624. doi: 10.1038/ismej.2012.8
- Caporaso, J. G., Lauber, C. L., Walters, W. A., Berg-Lyons, D., Lozupone, C. A., Turnbaugh, P. J., et al. (2011). Global patterns of 16S rRNA diversity at a depth of millions of sequences per sample. *Proc. Natl. Acad. Sci. U.S.A.* 108(Suppl. 1), 4516–4522. doi: 10.1073/pnas.1000080107/-/DCSupplemental
- CIWEM (2016). *Shale Gas and Water: An Independent Review of Shale Gas Extraction in the UK and the Implications for the Water Environment*. London: Chartered Institution of Water and Environmental Management (CIWEM).
- Cluff, M. A., Hartsock, A., MacRae, J. D., Carter, K., and Mouser, P. J. (2014). Temporal changes in microbial ecology and geochemistry in produced water from hydraulically fractured Marcellus shale gas wells. *Environ. Sci. Technol.* 48, 6508–6517. doi: 10.1021/es501183p
- Crociani, F., Alessandrini, A., Mucci, M. M., and Biavati, B. (1994). Degradation of complex carbohydrates by *Bifidobacterium* spp. *Int. J. Food Microbiol.* 24, 199–210. doi: 10.1016/0168-1605(94)90119-8
- Daly, R. A., Borton, M. A., Wilkins, M. J., Hoyt, D. W., Kountz, D. J., Wolfe, R. A., et al. (2016). Microbial metabolisms in a 2.5-km-deep ecosystem created by hydraulic fracturing in shales. *Nat. Microbiol.* doi: 10.1038/nmicrobiol.2016.146 [Epub ahead of print].
- Davis, J. P., Struchtemeyer, C. G., and Elshahed, M. S. (2012). Bacterial communities associated with production facilities of two newly drilled thermogenic gas wells in the Barnett Shale (Texas, USA). *Environ. Microbiol.* 64, 942–954. doi: 10.1007/s00248-012-0073-3
- Doughari, H. J., Nidakidemi, P. A., Human, I. S., and Benade, S. (2011). The ecology, biology and pathogenesis of *Acinetobacter* spp.: an overview. *Microbes Environ.* 26, 1–12. doi: 10.1264/jmse2.ME10179
- Eden, B., Laycock, P. J., and Fielder, M. (1993). *Oilfield Reservoir Souring*. Sudbury: HSE Books.
- Edgar, R. C. (2010). Search and clustering orders of magnitude faster than BLAST. *Bioinformatics* 26, 2460–2461. doi: 10.1093/bioinformatics/btq461
- Edgar, R. C. (2013). UPARSE: highly accurate OTU sequences from microbial amplicon reads. *Nat. Methods* 10, 996–998. doi: 10.1038/nmeth.2604
- Elsner, M., and Hoelzer, K. (2016). Quantitative survey and structural classification of hydraulic fracturing chemicals reported in unconventional gas production. *Environ. Sci. Technol.* 50, 3290–3314. doi: 10.1021/asc.est.5b02818
- Fichter, J., Moore, R., Braman, S., Wunch, K., Summer, E., and Holmes, P. (2012). “How hot is too hot for Bacteria? A technical study assessing bacterial establishment in downhole drilling, fracturing and stimulation operations,” in *Proceedings of the NACE International Conference and Expo, March 11–15, Salt Lake City, UT*.
- Fichter, K., Johnson, K., French, K., and Oden, R. (2008). “Use of microbicides in Barnett shale gas well fracturing fluids to control bacterially-related problems,” in *Proceedings of the NACE International Conference and Expo, Paper 08658, March 16–19, New Orleans, LA*.
- Fichter, K., Johnson, K., French, K., and Oden, R. (2009). Biocides control Barnett Shale fracturing fluid contamination. *Oil Gas J.* 107, 38–44.
- Fonselius, S. H., Dryissen, D., and Yhlen, B. (1999). “Determination of hydrogen sulphide,” in *Methods of Seawater Analysis*, 3rd Edn, eds K. Grasshoff, K. Kremling, and M. Ehrhardt (New York, NY: Wiley), 91–100.
- Frederickson, J. K., McKinley, J. P., Bjornstad, B. N., Long, P. E., Ringelberg, D. B., White, D. C., et al. (1997). Pore-size constraints on the activity and survival of subsurface bacteria in the late cretaceous shale-sandstone sequence, northwestern New Mexico. *Geomicrobiol. J.* 14, 183–202. doi: 10.1080/01490459709378043
- Gittel, A., Sørensen, K. B., Skovhus, T. L., Ingvorsen, K., and Schramm, A. (2009). Prokaryotic community structure and sulfate reducer activity in water from high-temperature oil reservoirs with and without nitrate treatment. *Appl. Environ. Microbiol.* 75, 7086–7096. doi: 10.1128/AEM.01123-09
- Gross, D., Sachsenhofer, R. F., Bechtel, A., Pytlak, L., Rupprecht, B., and Wegerer, E. (2015). Organic geochemistry of Mississippian shales (Bowland Shale Formation) in central Britain: implications for depositional environment, source rock and gas shale potential. *Mar. Pet. Geol.* 59, 1–21. doi: 10.1016/j.marpetgeo.2014.07.022
- Haas, B. J., Gevers, D., Earl, A. M., Feldgarden, M., Ward, D. V., Giannoukos, G., et al. (2011). Chimeric 16S rRNA sequence formation and detection in Sanger and 454-pyrosequenced PCR amplicons. *Genome Res.* 21, 494–504. doi: 10.1101/gr.112730.110
- Haines, J. R., and Alexander, M. (1975). Microbial degradation of polyethylene glycols. *Appl. Environ. Microbiol.* 29, 621–625.
- Joshi, N. A., and Fass, J. N. (2011). *Sickle: A Sliding-Window, Adaptive, Quality-Based Trimming Tool for FastQ Files (Version 1.33) [Software]*. Available at <https://github.com/najoshi/sickle>
- Kirk, M. F., Martinin, A. M., Breecker, D. O., Colman, D. R., Takacs-Vesback, C., and Petsch, S. T. (2012). Impact of commercial natural gas production on geochemistry and microbiology in a shale-gas reservoir. *Chem. Geol.* 33, 15–25. doi: 10.1016/j.chemgeo.2012.08.032
- Kozich, J. J., Westcott, S. L., Baxter, N. T., Highlander, S. K., and Schloss, P. D. (2013). Development of a dual-index sequencing strategy and curation pipeline for analyzing amplicon sequence data on the MiSeq illumina sequencing platform. *Appl. Environ. Microbiol.* 79, 5112–5120. doi: 10.1128/AEM.01043-13
- Krumholz, L. R., Harris, S. H., and Suflita, J. M. (2002). Anaerobic microbial growth from components of Cretaceous Shales. *Geomicrobiol. J.* 19, 593–602. doi: 10.1080/01490450290098559
- Laanbroek, H. J., and Pfennig, N. (1981). Oxidation of short-chain fatty acids by sulfate-reducing bacteria in freshwater and in marine sediments. *Arch. Microbiol.* 128, 330–335. doi: 10.1007/BF00422540
- Liang, R., Davidova, I. A., Marks, C. R., Stamps, B. W., Harriman, B. H., Stevenson, B. S., et al. (2016). Metabolic capability of a predominant *Halanaerobium* sp. in hydraulically fractured gas wells and its implication in pipeline corrosion. *Front. Microbiol.* 7:988. doi: 10.3389/fmicb.2016.00988
- Martin, M. (2011). Cutadapt removes adapter sequences from high-throughput sequencing reads. *EMBnet J.* 17, 10–12. doi: 10.14806/ej.17.1.200
- Masella, A. P., Bartram, A. K., Truszkowski, J. M., Brown, D. G., and Neufeld, J. D. (2012). PANDAseq: paired-end assembler for illumina sequences. *BMC Bioinformatics* 13:31. doi: 10.1186/1471-2105-13-31
- McGahey, C., and Bouwer, E. J. (1992). Biodegradation of ethylene glycol in simulated subsurface environments. *Water Sci. Technol.* 26, 41–49.
- Mohan, A. M., Hartsock, A., Bibby, K. J., Hammack, R. W., Vidic, R. D., and Gregory, K. B. (2013a). Microbial community changes in hydraulic fracturing fluids and produced water from shale gas extraction. *Environ. Sci. Technol.* 47, 13141–13150. doi: 10.1021/es402928b
- Mohan, A. M., Hartsock, A., Hammack, R. W., Vidic, R. D., and Gregory, K. B. (2013b). Microbial communities in flowback water impoundments from hydraulic fracturing for recovery of shale gas. *FEMS Microbiol. Ecol.* 86, 567–580. doi: 10.1111/1574-6941.12183
- Nakamiya, K., and Kinoshita, S. (1995). Isolation of polyacrylamide-degrading bacteria. *J. Ferment. Bioeng.* 80, 418–420. doi: 10.1111/1574-6941.12183
- Nurk, S., Bankevich, A., Antipov, D., Gurevich, A., Korobeynikov, A., Lapidus, A., et al. (2013). “Assembling genomes and mini-metagenomes from highly chimeric reads,” in *Proceedings of the 17th Annual International Conference, RECOMB 2013: Research in Computational Molecular Biology, Beijing, China, April 7–10, 2013*, eds M. Deng, R. Jiang, F. Sun, and X. Zhang (Berlin: Springer), 158–170.
- Picard, A., and Daniel, I. (2013). Pressure as an environmental parameter for microbial life – a review. *Biophys. Chem.* 183, 30–41. doi: 10.1016/j/bpc.2013.06.019

- Raiswell, R., and Berner, R. A. (1986). Pyrite and organic matter in Phanerozoic normal marine shales. *Geochim. Cosmochim. Acta* 50, 1967–1976. doi: 10.1016/0016-7037(86)90252-8
- Schink, B. (1984). *Clostridium magnum* sp. nov., a non-autotrophic homoacetogenic bacterium. *Arch. Microbiol.* 137, 250–255. doi: 10.1007/BF00414553
- Segers, P., Vancanneyt, M., Pot, B., Torck, U., Hoste, B., Dewettinck, D., et al. (1994). Classification of *Pseudomonas diminuta* Leifson and Hugh 1954 and *Pseudomonas vesicularis* Büsing, Döll, and Freytag 1953 in *Brevundimonas* gen. nov. as *Brevundimonas diminuta* comb. nov. and *Brevundimonas vesicularis* comb. nov., respectively. *Int. J. Syst. Bacteriol.* 44, 499–510. doi: 10.1099/00207713-44-3-499
- Sinninghe Damsté, J. S., and de Leeuw, J. W. (1989). Analysis, structure and geochemical significance of organically-bound sulphur in the geosphere: state of the art and future research. *Org. Geochem.* 16, 1077–1101. doi: 10.1016/0146-6380(90)90145-P
- Stevenson, B. S., Drilling, H. S., Lawson, P. A., Duncan, K. E., Parisi, V. A., and Suflita, J. M. (2011). Microbial communities in bulk fluids and biofilms of an oil facility have similar composition but different structure. *Environ. Microbiol.* 13, 1078–1090. doi: 10.1111/j.1462-2920.2010.02413.x
- Strong, L. C., Gould, T., Kasinkas, L., Sadowsky, M. J., Aksan, A., and Wackett, L. P. (2014). Biodegradation in waters from hydraulic fracturing: chemistry, microbiology, and engineering. *J. Environ. Eng.* 140:B4013001. doi: 10.1061/(ASCE)EE.1943-7870.0000792
- Struchtemeyer, C. G., Davis, J. P., and Elshahed, M. S. (2011). Influence of the drilling mud formulation process on the bacterial communities in thermogenic natural gas wells of the Barnett Shale. *Appl. Environ. Microbiol.* 77, 4744–4753. doi: 10.1128/AEM.00233-11
- Struchtemeyer, C. G., and Elshahed, M. S. (2012). Bacterial communities associated with hydraulic fracturing fluids in thermogenic natural gas wells in North Central Texas, USA. *FEMS Microbiol. Ecol.* 81, 13–25. doi: 10.1111/j.1574-6941.2011.01196.x
- Takii, S., Hanada, S., Tamaki, H., Ueno, Y., Sekiguchi, Y., Ibe, A., et al. (2007). *Dethiosulfatibacter aminovorans* gen. nov., sp. nov., a novel thiosulfate-reducing bacterium isolated from coastal marine sediment via sulfate-reducing enrichment with Casamino acids. *Int. J. Syst. Evol. Microbiol.* 57, 2320–2326. doi: 10.1099/ijss.0.64882-0
- Tanner, R. S. (1989). Monitoring sulfate-reducing bacteria: comparison of enumeration media. *J. Microbiol. Methods* 10, 83–90. doi: 10.1016/0167-7012(89)90004-3
- Tissot, B., and Welte, D. H. (1978). *Petroleum Formation and Occurrence*. Berlin: Springer.
- Tomlin, J., Read, N. W., Edwards, C. A., and Duerden, B. I. (1986). The degradation of guar gum by a faecal incubation system. *Br. J. Nutr.* 55, 481–486. doi: 10.1079/BJN19860055
- Walther, R., Hippe, H., and Gottschalk, G. (1977). Citrate, a specific substrate for the isolation of *Clostridium sphenoides*. *Appl. Environ. Microbiol.* 33, 955–962.
- Wang, Q., Garrity, G. M., Tiedje, J. M., and Cole, J. R. (2007). Naïve Bayesian classifier for rapid assignment of rRNA sequences into the new bacterial taxonomy. *Appl. Environ. Microbiol.* 73, 5261–5267. doi: 10.1128/AEM.00062-07
- Warskow, A., and Juni, E. (1972). Nutritional requirements of *Acinetobacter* strains isolated from soil, water and sewage. *J. Bacteriol.* 112, 1014–1016.
- Watson, G. K., and Jones, N. (1977). The biodegradation of polyethylene glycols by sewage bacteria. *Water Res.* 11, 95–100. doi: 10.1016/0043-1354(77)90189-0
- Weijermars, R. (2013). Economic appraisal for shale gas plays in Continental Europe. *Appl. Energy* 106, 100–115. doi: 10.1016/j.apenergy.2013.01.025
- Weimer, P. J., and Zeikus, J. G. (1977). Fermentation of cellulose and cellobiose by *Clostridium thermocellum* in the absence of *Methanobacterium thermoautotrophicum*. *Appl. Environ. Microbiol.* 33, 289–297.
- Wen, Q., Chen, Z., Zhao, Y., Zhang, H., and Feng, Y. (2010). Biodegradation of polyacrylamide by bacteria isolated from activated sludge and oil-contaminated soil. *J. Hazard. Mater.* 175, 955–959. doi: 10.1016/j.hazmat.2009.10.102
- Zeikus, J. G., Hegge, P. W., Thompson, T. E., Phelps, T. J., and Langworthy, T. A. (1983). Isolation and description of *Haloanaerobium prevalens* gen. nov. and sp. nov., an obligate halophile common to Great Salt Lake sediments. *Curr. Microbiol.* 9, 225–233. doi: 10.1007/BF01567586

Conflict of Interest Statement: The authors declare that the research was conducted in the absence of any commercial or financial relationships that could be construed as a potential conflict of interest.

Copyright © 2017 Nixon, Walker, Streets, Eden, Boothman, Taylor and Lloyd. This is an open-access article distributed under the terms of the Creative Commons Attribution License (CC BY). The use, distribution or reproduction in other forums is permitted, provided the original author(s) or licensor are credited and that the original publication in this journal is cited, in accordance with accepted academic practice. No use, distribution or reproduction is permitted which does not comply with these terms.



Serpentinization-Influenced Groundwater Harbors Extremely Low Diversity Microbial Communities Adapted to High pH

Katrina I. Twing^{1,2*}, William J. Brazelton², Michael D. Y. Kubo³, Alex J. Hyer², Dawn Cardace⁴, Tori M. Hoehler⁵, Tom M. McCollom⁶ and Matthew O. Schrenk¹

¹ Department of Microbiology and Molecular Genetics, Michigan State University, East Lansing, MI, USA, ² Department of Biology, University of Utah, Salt Lake City, UT, USA, ³ SETI Institute, Mountain View, CA, USA, ⁴ Department of Geosciences, University of Rhode Island, Kingston, RI, USA, ⁵ Exobiology Branch, NASA Ames Research Center, Moffett Field, CA, USA, ⁶ Laboratory for Atmospheric and Space Physics, University of Colorado, Boulder, CO, USA

OPEN ACCESS

Edited by:

Cody Sheik,
University of Minnesota Duluth, USA

Reviewed by:

Thomas L. Kieft,
New Mexico Institute of Mining
and Technology, USA
Wesley Douglas Swingley,
Northern Illinois University, USA

*Correspondence:

Katrina I. Twing
katrinatwing@gmail.com

Specialty section:

This article was submitted to
Microbiological Chemistry
and Geomicrobiology,
a section of the journal
Frontiers in Microbiology

Received: 14 January 2017

Accepted: 14 February 2017

Published: 01 March 2017

Citation:

Twing KI, Brazelton WJ, Kubo MDY, Hyer AJ, Cardace D, Hoehler TM, McCollom TM and Schrenk MO (2017) Serpentinization-Influenced Groundwater Harbors Extremely Low Diversity Microbial Communities Adapted to High pH. *Front. Microbiol.* 8:308.

doi: 10.3389/fmicb.2017.00308

Serpentinization is a widespread geochemical process associated with aqueous alteration of ultramafic rocks that produces abundant reductants (H_2 and CH_4) for life to exploit, but also potentially challenging conditions, including high pH, limited availability of terminal electron acceptors, and low concentrations of inorganic carbon. As a consequence, past studies of serpentinites have reported low cellular abundances and limited microbial diversity. Establishment of the Coast Range Ophiolite Microbial Observatory (California, U.S.A.) allowed a comparison of microbial communities and physicochemical parameters directly within serpentinization-influenced subsurface aquifers. Samples collected from seven wells were subjected to a range of analyses, including solute and gas chemistry, microbial diversity by 16S rRNA gene sequencing, and metabolic potential by shotgun metagenomics, in an attempt to elucidate what factors drive microbial activities in serpentinite habitats. This study describes the first comprehensive interdisciplinary analysis of microbial communities in hyperalkaline groundwater directly accessed by boreholes into serpentinite rocks. Several environmental factors, including pH, methane, and carbon monoxide, were strongly associated with the predominant subsurface microbial communities. A single operational taxonomic unit (OTU) of Betaproteobacteria and a few OTUs of Clostridia were the almost exclusive inhabitants of fluids exhibiting the most serpentinized character. Metagenomes from these extreme samples contained abundant sequences encoding proteins associated with hydrogen metabolism, carbon monoxide oxidation, carbon fixation, and acetogenesis. Metabolic pathways encoded by Clostridia and Betaproteobacteria, in particular, are likely to play important roles in the ecosystems of serpentinizing groundwater. These data provide a basis for further biogeochemical studies of key processes in serpentinite subsurface environments.

Keywords: serpentinization, alkaliphile, extremophile, groundwater, borehole

INTRODUCTION

The Earth's subsurface is predicted to be an expansive habitat for microorganisms (Whitman et al., 1998; Edwards et al., 2012; Kallmeyer et al., 2012). Unlike surface biomes, the subsurface is largely decoupled from photosynthetic primary production; instead, many subsurface ecosystems are influenced by carbon and energy liberated from the Earth's mantle and crust. However, given the inherent lack of accessibility, direct sampling of subsurface, rock-hosted environments has been limited. In continental settings, researchers have used caves (Northrup and Lavoie, 2001; Engel et al., 2004), mines (Onstott et al., 2003; Chivian et al., 2008), springs (Brazelton et al., 2012, 2013; Suzuki et al., 2013; Cardace et al., 2015), and isolated boreholes (Stevens and McKinley, 1995; Itävaara et al., 2011) as windows into the subsurface environment. These features grant access to an otherwise inaccessible environment, but they represent opportunistic sampling locations. In the present study, a series of wells were drilled directly into serpentinization-influenced aquifers of the Coast Range Ophiolite, a portion of ancient seafloor in northern California, USA, to sample microbial communities in serpentinizing rocks and groundwater. This observatory represents the first opportunity to investigate microbial communities with direct access to the range of conditions in the serpentinizing subsurface (Cardace et al., 2013).

Serpentinization is a widespread geochemical process involving the aqueous alteration of peridotite to serpentine minerals, resulting in an abundance of potential reductants, in the form of hydrogen, methane, and small organic molecules (McCollom and Seewald, 2007; Proskurowski et al., 2008; Schrenk et al., 2013). Serpentinization also releases hydroxyl ions, which creates extremely high pH fluids ($\text{pH} > 10$). At high pH, bicarbonate and carbonate are the dominant species of dissolved inorganic carbon (DIC), and the latter can precipitate out of solution as carbonate minerals when in the presence of divalent cations, such as Ca^{2+} and Mg^{2+} commonly found in serpentinite fluids. Thus, fluids associated with serpentinization are characteristically low in DIC, particularly dissolved CO_2 . Compared to the abundance of reductants in these systems, there is a lack of corresponding oxidants, which likely limits the range of potential microbial metabolisms. Thus subsurface serpentinite environments are characterized by unusual challenges to life, such as extreme pH (>10), limited availability of dissolved carbon, and a lack of potential terminal electron acceptors.

The best-characterized serpentinite-hosted microbial ecosystem to date is the Lost City Hydrothermal Field, located 15 km from the Mid-Atlantic Ridge (Kelley et al., 2005). The tall carbonate chimneys at Lost City are dominated by methane-cycling archaea in the anoxic chimney interiors (Schrenk et al., 2004) and by methanotrophic and sulfur-oxidizing bacteria in the chimney exteriors (Brazelton et al., 2006). More recently, researchers have started exploring life within continental serpentinite environments by using natural springs, such as the Tablelands Ophiolite in Newfoundland, Canada (Brazelton et al., 2012, 2013) and The Cedars site in northern California (Suzuki

et al., 2013, 2014), or previously established wells, such as at the Cabeço de Vide Aquifer (CVA) in Portugal (Tiago and Veríssimo, 2013). In these studies of continental serpentinite sites, microbial communities were dominated by clades of Betaproteobacteria and Firmicutes (Schrenk et al., 2013).

Surveys of the Tablelands Ophiolite suggest that subsurface serpentinite communities are dominated by Erysipelotrichia, a class within the phylum Firmicutes, in the deep, anoxic source-waters and microaerophilic H_2 -oxidizing Betaproteobacteria at the shallow, oxic/anoxic interface (Brazelton et al., 2013). Microcosm experiments from the Coast Range Ophiolite Microbial Observatory (CROMO), the location of this study, have indicated that Betaproteobacteria closely related to *Hydrogenophaga pseudoflava* and *Clostridia* (phylum Firmicutes) closely related to *Dethiobacter alkaliphilus*, are stimulated by small organic molecules that are expected to be available in the serpentinite environment (Crespo-Medina et al., 2014). Furthermore, recently published genomes of cultivated isolates of the proposed genus *Serpentinomonas*, which are most closely related to the genus *Hydrogenophaga*, are consistent with a role for these organisms at oxic/anoxic interfaces in serpentinizing systems (Suzuki et al., 2014).

While these previous studies suggest that distinct microbial communities inhabit different physico-chemical regimes in serpentinizing groundwater, these relationships have not yet been studied directly. Furthermore, little genomic or metagenomic data for organisms other than *Serpentinomonas* are available from serpentinizing environments. This study combines environmental 16S rRNA gene sequencing, shotgun metagenomic analyses, and geochemical monitoring across a range of conditions in order to relate patterns in microbial diversity and metabolic potential to underlying geochemical processes in serpentinite subsurface environments. This work improves our understanding of the physiology and ecology of the dominant bacteria in these ubiquitous ecosystems, and it will facilitate our integration of these systems into models of carbon cycling.

MATERIALS AND METHODS

Site Description and Sample Collection

The Coast Range Ophiolite is a 155–170 million year old ophiolite located in northern California, containing numerous calcium-hydroxide rich springs, indicating serpentinizing activity below the surface (Barnes and O'Neil, 1971). The CROMO, which is located at the UC-Davis McLaughlin Natural Reserve in Lower Lake, CA and was established in August 2011 and using clean drilling techniques to enable subsequent monitoring of the microbial communities and associated geochemistry within the serpentinite subsurface (Cardace et al., 2013). CROMO consists of two sets of wells located 1.4 km apart: the Core Shed Wells (CSW), and the Quarry Valley wells (QV). CSW consists of five wells, drilled to depths between 9 and 31 m. QV consists of three wells, drilled to depths between 15 and 46 m.

Preliminary lithostratigraphic interpretations of CROMO cores indicate that both sites (CSW and QV) are characterized

by intercalated serpentine-rich units with variable contributions of other clay minerals; lizardite and magnetite are common in serpentine-rich units (Cardace et al., 2013). At specific intervals, minerals indicative of altered mafic rocks (e.g., albite, chlorite, quartz, rarely calcite) co-occur with serpentine minerals, such as at ~28 m depth at the primary CSW site (CSW1.1), and at 18–22 m and 34–36 m depth at the primary QV site (QV1.1). Very thin serpentine-rich soil cover exists at the QV1.1 site (<1 m), while ~4 m of soil cover occurs at CSW1.1 (Cardace et al., 2013). Taken together, these data indicate that CROMO scientific monitoring wells sample fluids interacting with tectonically reworked ultramafic units very near the surface, with some entrainment of altered mafic materials from adjacent units of the Coast Range Ophiolite.

The samples described here were collected from seven wells at CROMO in August 2012. For the current study, well QV1.3 was not sampled due to complications with sediments clogging the filters. Well fluids were collected using positive displacement Teflon bladder pumps (Geotech Environmental Equipment, Denver, CO, USA) and pumped through a YSI 3059 flow cell fitted with a YSI 556 multiprobe (Yellow Springs, OH, USA), which measured water temperature, specific conductance, pH, dissolved oxygen (DO) and oxidation-reduction potential (ORP) once the DO measurement stabilized at a minimum value. Samples were collected for dissolved gas analyses (CH_4 , CO, and H_2) and aqueous phase species (DIC and organic acids), as previously described Crespo-Medina et al. (2014).

For DNA analyses, fluids were filtered through a 0.22 μm Sterivex filter cartridge (Millipore, Billerica, MA, USA) using a Masterflex E/S peristaltic pump (Cole Parmer, Vernon Hills, IL, USA). Field replicate samples, ranging between two to eight filters per well, were collected in succession (labeled A, B, C, etc.). Sterivex filter cartridges were flash frozen with liquid nitrogen and stored at -80°C until DNA extraction. For microbial cell quantification, replicate samples of 45 mL of fluids were preserved at a final concentration of 3.7% formaldehyde and stored at 4°C . All publicly available data generated from this project can be found¹.

Geochemistry

Dissolved gasses (H_2 , CH_4 , and CO) were extracted into an inert (N_2) gas phase of known volume and analyzed for CH_4 via a SRI 8610C GC-FID and dissolved H_2 and CO with a Trace Analytical RGA3 Reduced Gas Analyzer. DIC was measured by acidifying a known volume of well fluid within a sealed vial, and analyzing the concentration of liberated CO_2 in the headspace by GC-FID (SRI 8610) following passage through a “methanizer,” which catalyzes the in-line conversion of CO and CO_2 to methane in the presence of H_2 over a heated Ni catalyst, thus allowing sensitive detection of these species by flame ionization detector following their separation by gas chromatography. Organic acid samples were analyzed by HPLC with UV/VIS detection, following derivatization with 2-nitrophenylhydrazide (Albert and

Martens, 1997). All sample vials were analyzed with duplicate injections.

Microbial Cell Counts

Fluids preserved for cell counts were filtered through 0.2 μm black polycarbonate filters (Millipore, Billerica, MA, USA). The cells were stained with 1 $\mu\text{g}/\text{ml}$ of 4',6-diamidino-2-phenylindole (DAPI) and were counted by epifluorescence microscopy using appropriate filter sets according to previously published protocols (Hobbie et al., 1977; Schrenk et al., 2003).

DNA Extraction

DNA extractions from Sterivex filter cartridges were performed by lysis via freeze/thaw cycles and lysozyme/Proteinase K treatment and purified with phenol-chloroform extractions, precipitation in ethanol, and further purification with QiaAmp (Qiagen, Hilden, Germany) columns according to the manufacturer's instructions for purification of genomic DNA, as described previously by Brazelton et al. (2013).

16S rRNA Gene Amplicon Sequencing and Data Analysis

Samples were submitted to the DOE Joint Genome Institute (JGI) for 16S rRNA amplicon sequencing of the V4 region on an Illumina MiSeq instrument, as described by Caporaso et al. (2011). Briefly, the amplification reaction contained 5 PRIME's HotMasterMix, custom V4 16S rRNA gene primers, and Illumina sequencing adapters and unique barcodes. The individual amplicon libraries were quantified, normalized, and pooled. The pooled multiplex reactions were then quantified using KAPA Biosystem's next-generation sequencing library qPCR kit and run on a Roche LightCycler 480 real-time PCR instrument. The quantified, multiplexed amplicon pool was then loaded on an Illumina MiSeq instrument utilizing the v3 reagent mix and a 2×300 indexed recipe mix.

Sequence reads were aligned to the SILVA SSURel alignment (v119), and taxonomic classifications were assigned using mothur (Pruesse et al., 2007; Schloss et al., 2009). Sequences were clustered into operational taxonomic units (OTUs) at the 3% distance threshold using the cluster.split command and the average-neighbor clustering algorithm in mothur (Schloss and Westcott, 2011). Prior to calculating measures of diversity, data were subsampled to the sample with the fewest sequences (77,580). Beta (between sample) diversity of the microbial communities was assessed by calculation of the Bray-Curtis index and displayed in a multi-dimension scaling (MDS) plot with geochemical data overlay in Primer-6 (Clarke, 1993; Clarke and Gorley, 2006). Alpha (within sample) diversity was assessed with the Inverse Simpson diversity index and rarefaction analysis. Sequence identification of reads belonging to the top OTUs compared with 16S rRNA sequences from other serpentinite studies (Brazelton et al., 2013; Suzuki et al., 2013; Tiago and Veríssimo, 2013) was performed using MatGAT with the default settings (Campanella et al., 2003). The 16S rRNA sequence data are publicly available in the NCBI Sequence Read Archive under the accession number SRA280854.

¹<https://nai.nasa.gov/research/data-sharing/>

Metagenomic Sequencing and Data Analysis

Samples were submitted to JGI for metagenomic sequencing on an Illumina HiSeq2000 instrument, as described by Hawley et al. (2014). Briefly, 200 ng of DNA was used for each sample and sheared to 270 bp fragments via a Corvaris LE220 focused-ultrasonicator and size selected by SPRI. Fragments were then end-repaired, A-tailed, and ligated with Illumina-compatible adapters with barcodes unique for each library. Libraries were quantified with KAPA Biosystem's next-generation sequencing library qPCR kit and run on a Roche LightCycler 280 real-time PCR instrument. Quantified libraries were combined into 10-library pools and prepared for sequencing on the Illumina instrument in one lane each, using the TruSeq paired-end cluster kit (v3) and Illumina's cBot instrument to generate clustered flowcells, which were sequenced on the Illumina HiSeq2000 sequencer using TruSeq SBS sequencing kit v3 and a 2×150 indexed run recipe.

Metagenomic assembly was conducted by JGI as described by Hawley et al. (2014) and briefly described again here. Raw reads were trimmed with a minimum quality score cutoff of 10, and the trimmed paired-end reads were assembled with SOAPdenovo v1.05, with the default settings and a variety of kmers (i.e., 81, 85, 89, 93, 97, 101; Luo et al., 2012; Hawley et al., 2014). Contigs were sorted into pools based on length: contigs < 1800 bp were further assembled by Newbler (Life Technologies, Carlsbad, CA, USA) and contigs > 1800 bp, including those produced from Newbler run, were combined using minimus 2 (flags: $-D$ MINID = 89 $-D$ OVERLAP = 80; Sommer et al., 2007). BWA was used to estimate read depth, based on mapping of trimmed, screened, paired-end Illumina reads to assembled contigs (Li and Durbin, 2009). These data are publicly available in the JGI IMG/M database² under the project IDs: 1021918, 1021921, 1021924, and 1021927; and in the MG-RAST database (Meyer et al., 2008) under the following sample IDs: 4569549.3, 4569550.3, 4569551.3, and 4569552.3.

The Prokka pipeline (Seeman, 2014) was used for gene prediction and functional annotation of contigs. The arguments $-metagenome$ and $-proteins$ were used with Prokka v.1.12 to indicate that genes should be predicted with the implementation of Prodigal v.2.6.2 (Hyatt et al., 2010) optimized for metagenomes. Predicted protein-coding sequences were aligned to the last free version (2011) of the Kyoto Encyclopedia of Genes and Genomes (Ogata et al., 1999) using BLASTP v2.3, and any coding sequences that remained un-annotated were then aligned to Prokka's default databases. Predicted protein abundances (in units of reads per kilobase) were calculated with HTSeq v.0.6.1 (Anders et al., 2014), and the final normalized coverage was calculated by normalizing to the total number of bases in the smallest metagenome.

To assign taxonomy to specific contigs of interest, a consensus taxonomic classification was manually determined by examining the taxonomic classifications associated with the best BLAST hits for each predicted gene. Specifically, for each contig-of-interest, all (Prokka-predicted) coding sequences (CDSs) on

the contig were aligned against the NCBI NR database (v. 2016-10-01), and the taxonomy of the best hit was taken to be the taxonomy of the CDS. The taxonomy of the whole contig was manually determined by identifying the lowest common ancestor on the NCBI Taxonomy Tree where half of all CDS taxonomic assignments agreed (Hanson et al., 2016). The full list of CDS taxonomic assignments can be found in Supplementary Dataset S1.

Statistical Analyses

Correlation network analyses were constructed from statistically significant pairwise Pearson's correlations among environmental variables and sequence data (Fuhrman and Steele, 2008) and visualized in Cytoscape v 2.8.3 (Shannon et al., 2003). A matrix containing environmental data and relative OTU (97% similarity) abundance for each sample was used as input for pairwise Pearson's correlation analysis computed with the rcor.test function in the R package lmt (Rizopoulos, 2006). The false-discovery rate (q -value) was computed for the distribution of Pearson's p -values to account for multiple tests. Pairwise correlations with both p - and q -values of < 0.05 were considered significant and included in network analyses. Network models of significant correlations were created using Cytoscape v2.8.3 (Shannon et al., 2003).

The ANOSIM test using a Bray-Curtis resemblance matrix, with sequence data subsampled to 77,580 sequences (the size of the smallest 16S rRNA amplicon library), was used to test whether individual environmental parameter categories had significant effects on the community composition of samples (Clarke, 1993). To statistically determine which combinations of numerical environmental variables best described the community composition variation within the dataset, the BEST analysis was performed in PRIMER-6 (Clarke, 1993; Clarke and Gorley, 2006).

RESULTS

Sampling Site and Geochemistry

Fluids were collected from seven wells within the CROMO, which were drilled for the purpose of monitoring biogeochemistry and microbial community dynamics with high temporal and spatial resolution (Cardace et al., 2013). To identify which bacterial taxa are most influenced by geochemical indicators of serpentinization, geochemical and microbiological data from these seven wells were compared.

Geochemical data associated with the well fluids from August 2012 are summarized in **Table 1**. Samples from wells CSW1.1 and QV1.1 are characterized by extremely high pH (12.2 and 11.5, respectively) and generally reducing character (**Table 1**). These wells are depleted in DIC, containing one to two orders of magnitude less DIC than a nearby well with circumneutral pH, CSW1.4 (**Table 1**). CSW1.1 also had higher concentrations of H₂ and organic acids, relative to the other wells (**Table 1**). QV1.1, the deepest well, contained the highest cell abundance and exhibited the lowest dissolved O₂ measurement. Wells CSW1.4 and QV1.2 exhibited circumneutral pH, low conductivity and higher DIC (**Table 1**) than the other wells. These circumneutral pH wells

²www.img.jgi.doe.gov

TABLE 1 | Environmental and geochemical parameters associated with samples collected in August 2012.

	CSW1.1	CSW1.2	CSW1.3	CSW1.4	CSW1.5	QV1.1	QV1.2
Depth (mbs)	31.1	19.2	23.2	8.8	27.4	45.7	14.9
Temp (°C)	17.2	18.5	16.9	15.2	16.2	17.9	18.4
pH	12.2	9.3	10.1	7.9	9.7	11.5	7.9
ORP (mV)	-284	-32	-83	-35	-121	-155	-30
DO (mg/L)	0.05	0.41	0.06	1.05	0.03	0.03	0.03
Conductivity (μS/cm)	5200	3710	4500	1560	4220	2068	1655
DIC (μM)	253 ± 8	605 ± 268	172 ± 16	5046 ± 531	545 ± 13	96 ± 2	979 ± 32
Dissolved H ₂ (μM)	0.289 ± 0.004	0.140 ± 0.001	0.283 ± 0.018	0.271 ± 0.013	0.138 ± 0.020	0.075 ± 0.001	0.076 ± 0.009
Dissolved CH ₄ (mM)	0.524 ± 0.132	1.625 ± 0.055	0.969 ± 0.529	0.002 ± 0.0003	1.266 ± 0.032	0.301 ± 0.021	0.303 ± 0.030
Dissolved CO (μM)	0.089 ± 0.002	0.158 ± 0.001	0.115 ± 0.013	0.187 ± 0.005	0.124 ± 0.008	0.142 ± 0.004	0.150 ± 0.008
Acetate (μM)	70.79 ± 1.26	<1.55	<1.55	<3.04	<3.04	10.20 ± 0.33	<2.01
Formate (μM)	15.74 ± 0.99	<1.39	<1.39	<1.79	<1.79	<1.39	<2.23
Propionate (μM)	3.49 ± 0.003	<0.01	<0.01	<0.01	<0.01	0.16 ± 0.05	0.22 ± 0.01
Butyrate (μM)	20.99 ± 0.45	<1.11	<1.11	<2.75	<2.75	5.97 ± 0.30	<1.89
Microbial cells (cells/mL)	1.8 × 10 ⁵	6.6 × 10 ⁵	2.3 × 10 ⁵	1.0 × 10 ⁵	3.9 × 10 ⁵	1.0 × 10 ⁶	9.5 × 10 ⁵

Values reported are averages of replicate measurements taken throughout sampling. Specific parameter values associated with specific field replicate samples can be found in **Supplementary Figure S2**.

also had elevated concentrations of H₂ and CO comparable to the wells with higher pH. CSW1.2 (pH 9.3) had the highest concentration of methane (1.6 mM; **Table 1**).

Unsurprisingly, many of the environmental parameters of the system (**Table 1**) were correlated with one another (Supplementary Table S1). Higher pH was correlated with more negative ORP, and lower concentrations of carbon monoxide (CO), DO, and DIC, and was positively correlated with depth and organic acid concentration (Supplementary Table S1). The concentrations of the organic acids acetate, formate, propionate, and butyrate were all positively correlated with one another and were negatively correlated with ORP (Supplementary Table S1). CO concentration was positively correlated with ORP (i.e., positively correlated with a more positive ORP value) and DO, and was negatively correlated with conductivity and H₂ concentration (Supplementary Table S1). The concentration of methane was not significantly correlated with any other environmental parameters.

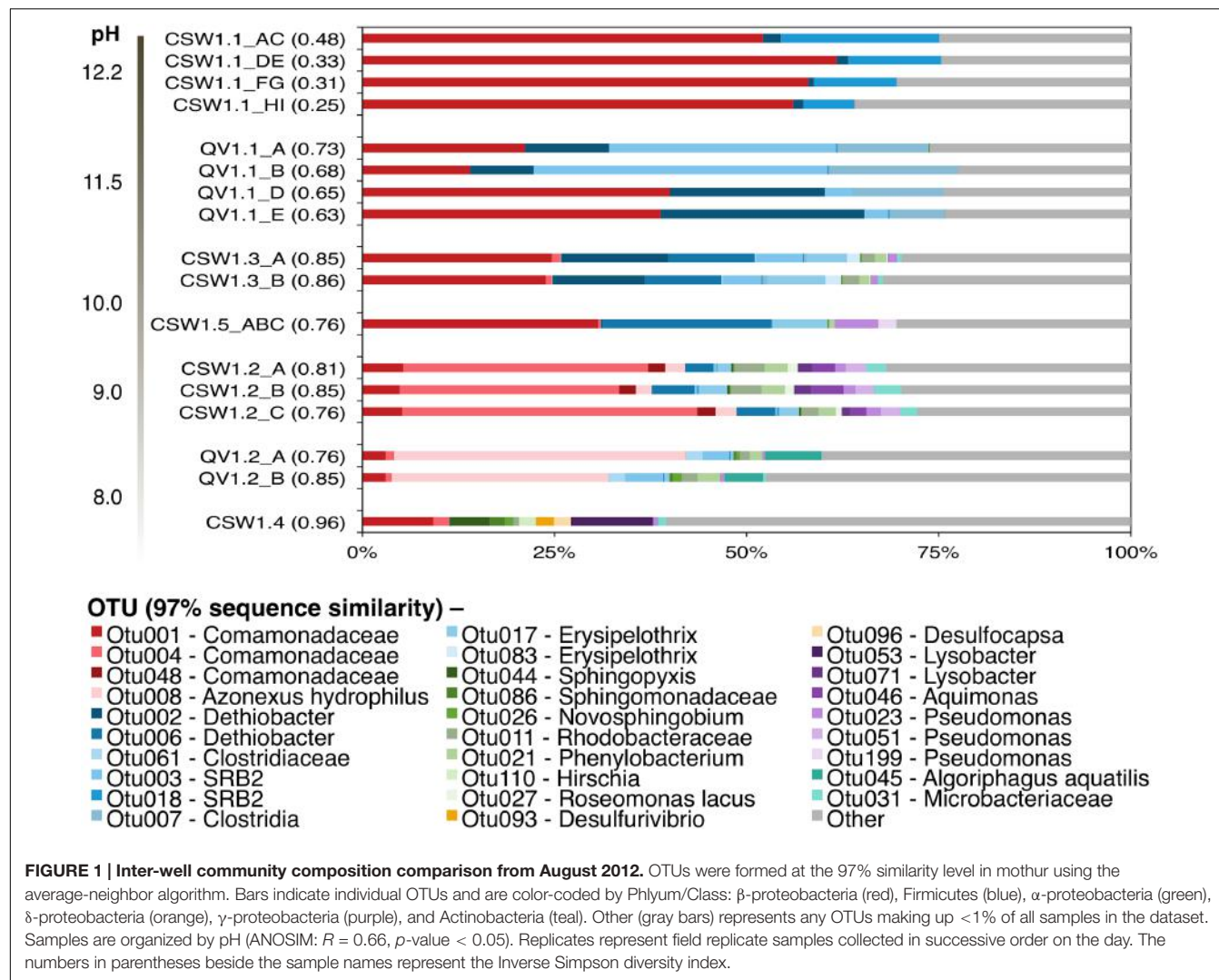
16S rRNA Gene Diversity and Community Composition

Bacterial diversity was assessed in fluids collected in August 2012 from the seven CROMO wells. Environmental sequences of 16S rRNA gene amplicons were obtained with an Illumina MiSeq platform, yielding between 78,000 and 179,000 merged paired-end sequences per sample, for a total of 2,528,572 16S rRNA sequences in this study. These sequences were clustered into 11,454 OTUs at a 97% sequence similarity threshold, and only 30 of these OTUs comprised greater than 1% of the sequences in any of the samples analyzed. All diversity analyses in this study were conducted with OTUs, instead of relying solely on taxonomic annotations, in order to avoid the biases and limitations inherent to database-dependent classifications that are magnified when studying poorly characterized microbial communities. Field replicates of samples were collected and

analyzed in parallel and were statistically indistinguishable from one another, as determined by a SIMPROF test of community similarities among all samples (**Supplementary Figure S1**). The community compositions of samples from different wells were clearly distinct from each other (ANOSIM, $R = 0.96$, p -value = 0.001).

Alpha diversity of the samples, as measured by the Inverse Simpson diversity index, decreased with increasing pH (**Figure 1**). The wells with the highest pH, CSW1.1 and QV1.1, exhibited extremely low diversity, containing almost exclusively Betaproteobacteria and Firmicutes (**Figure 1**). Well CSW1.1 was dominated by a single betaproteobacterial OTU (OTU001), classified as a member of family Comamonadaceae with 100% sequence identity over 250 bp of the 16S rRNA gene's V4 region (calculated with MatGAT) to strain B1 from the proposed genus *Serpentinomonas* isolated from The Cedars serpentinite site (Suzuki et al., 2014; **Table 2**). The second most abundant OTU in CSW1.1 (OTU018), which comprised 12.5 ± 5.8% of the sequences from that well, was classified as Thermoanaerobacterales SRB-2, and exhibited 99% sequence identity to a Clostridia clone from a well in Cabeço de Vide (CVA) in Portugal (Tiago and Veríssimo, 2013; **Table 2**). The third most-abundant OTU detected in CSW1.1 (OTU002), which accounted for only 1% of the sequences from that well, was classified as *Dethiobacter*, and shared 100% sequence identity to a clone from CVA (Tiago and Veríssimo, 2013; **Table 2**), enriched in a microcosm from CROMO (Crespo-Medina et al., 2014), and a clone from the deep groundwater site at The Cedars (Suzuki et al., 2013). The remaining 29.0 ± 5.3% of the CSW1.1 microbial community was made up of rare species, defined as OTUs comprising less than 1% of the total sequences in any sample.

Well QV1.1 was dominated by three Clostridia OTUs (OTU003, OTU002, and OTU007) that together accounted for 47.1 ± 13.4% of the bacterial community (**Figure 1**).



Both OTU003 (classified as Thermoanaerobacterales SRB-2) and OTU002 (classified as *Dethiobacter*) exhibited 99–100% sequence identity to clones from CVA in Portugal (Tiago and Veríssimo, 2013; **Table 2**). The same betaproteobacterial OTU from CSW1.1 (OTU001) made up $28.5 \pm 12.9\%$ of the QV1.1 community, and the remaining bacterial taxa were rare, accounting for $24.3 \pm 1.6\%$ of the community (**Figure 1**). A time-series analysis of samples collected quarterly from QV1.1 (data not shown) indicated that community composition within wells is relatively constant over time, with no significant difference between time points (ANOSIM, $R = 0.2$, p -value = 0.902).

While Betaproteobacteria made up a large proportion of all samples above neutral pH, the diversity and composition of the Betaproteobacteria shifted with pH (**Figure 1**). As expressed above, OTU001 made up $42.7 \pm 17.6\%$ of the extremely high pH wells. However, in samples with $pH \leq 10$, OTU001 was replaced by OTU004 (classified as Comamonadaceae and 100% identical to *Alicycliphilus denitrificans*; **Table 2**) and OTU008 (classified as *Azonexus hydrophilus*; **Table 2**) as the dominant betaproteobacterial taxa.

Clostridia, which accounted for up to 64% of the bacteria in the highest pH fluids, were also found in the moderately high pH wells (defined here as wells with pH 8.5–10). *Dethiobacter* OTUs made up $13.9 \pm 10.1\%$ of samples with a pH 9.5–11.0. *Erysipelotrichia* (another class of the phylum Firmicutes) made up 8 and 2% of CSW1.5 (pH 9.7) and CSW1.2 (pH 9.3), respectively, but was not detected in any other CROMO samples. OTUs classified as Thermoanaerobacterales SRB-2 were detected in QV1.2, as well as CSW1.1 and QV1.1. No Firmicutes OTUs were detected in the wells with pH less than 9 (**Figure 1**). In addition to Betaproteobacteria and Firmicutes, the moderately high pH (pH 8.5–10) wells contained Bacteroidetes as well as Alpha-, Delta-, and Gammaproteobacteria (**Figure 1**). The circumneutral pH wells contained a greater complement of rare taxa and many taxa that were not present in the high pH wells (**Figure 1**).

No archaea were detected in any of the 16S rRNA amplicon libraries, which were created with the universal primers targeting the V4 region of the 16S rRNA gene used by the DOE Joint Genome Institute (Caporaso et al., 2011). In

TABLE 2 | Summary of significant correlations (p -value < 0.05) between top OTUs (making up $> 25\%$ of the sample in which they are most abundant) and environmental parameters.

OTU	Variable	R	Cor*	Max Sample (% of sample)	Max Abundance (% of sample)	Class	Order	Family	Closest Relative (NCBI accession number)	% Identity†
OTU001	Butyrate	0.88	+	CSW1.1	61.7	Beta proteobacteria	Burkholderiales	Comamonadaceae	<i>Serpinimonas</i> B1 (AP014569.1) ^a	100%
	pH	0.86	+							
	Acetate	0.86	+							
	Propionate	0.83	+							
	Formate	0.82	+							
	Conductivity	0.63	+							
	Hydrogen	0.54	+							
	ORP	0.91	-							
	CO	0.86	-							
OTU004	Methane	0.81	+	CSW1.2	38.4	Beta proteobacteria	Burkholderiales	Comamonadaceae	<i>Alicyclophilus denitrificans</i> (NR_074585.1) ^b	100%
	DO	0.53	+	QV1.1	38.2	Clostridia	Thermoanaerobacterales	SRB2	<i>CV/CloAm3Ph15</i> (AM778006) ^c	99.6%
OTU003	Depth	0.54	+							
OTU008	pH	0.61	-	QV1.2	38.0	Beta proteobacteria	Rhodocyclales	<i>Azonus Hydrophilus</i> (EF158391.1) ^d	100%	
OTU002	Depth	0.67	+	QV1.1	26.5	Clostridia	Clostridiales	<i>Syntrophomonadaceae</i> <i>Rhodocyclales</i>	<i>CV/CloAm2Ph135</i> (AM777954) ^c	100%
OTU006	Methane	0.60	+	CSW1.5	21.9	Clostridia	Clostridiales	<i>Syntrophomonadaceae</i>	<i>CV/CloAm2Ph135</i> (AM777954) ^c	98.2%
OTU018	Formate	0.91	+	CSW1.1	20.6	Clostridia	Thermoanaerobacterales	SRB2	<i>CV/CloAm3Ph98</i> (AM778028) ^c	99.1%
	Propionate	0.91	+							
	Acetate	0.90	+							
	Butyrate	0.88	+							
	Conductivity	0.64	+							
	Hydrogen	0.60	+							
	pH	0.60	+							
	ORP	0.85	-							
	CO	0.74	-							

^aSuzuki et al., 2013; ^bOosterkamp et al., 2011; ^cTiago and Veríssimo, 2013; ^dChou et al., 2008. This is a subset of the data used to make the correlation network (Figure 4).

*Corr, correlation relationship.

†Percent identity, as determined by MATTGAT (Campanella et al., 2003).

addition to 16S rRNA amplicon sequencing, a subset of the samples (CSW1.1AC, CSW1.3A, QV1.1A, and QV1.2A) underwent shotgun metagenomic sequencing. To further investigate the potential presence of archaea in CROMO fluids the relative abundance of archaea was also assessed by counting archaeal sequences in the metagenomic datasets. The number of metagenomic sequences classified as archaea by MG-RAST (Meyer et al., 2008) did not exceed 1% of the total sequences in any sample (Table 3). Furthermore, none of these archaeal metagenomic reads included a 16S rRNA gene. The bacterial diversity of the metagenomes exhibited similar abundances of Betaproteobacteria, but expressed a lower abundance of Clostridia and greater diversity of other taxa, compared to the 16S rRNA amplicon data (Figures 1, 2).

Biogeochemical Relationships

One of the main goals of this study was to identify the geochemical drivers of microbial community composition within serpentinite subsurface environments. Several physical and chemical factors are overlain on a multi-dimensional scaling (MDS) plot of community composition (as measured by shared 16S rRNA OTUs; Figure 3). The figure highlights

TABLE 3 | Microbial communities at CROMO are dominated by Bacteria.

Well	Bacteria	Archaea	Eukaryotes	Viruses	Unassigned
CSW1.1	98.3	0.2	1.2	0.1	0.2
QV1.1	97.9	1.1	0.8	0.0	0.1
CSW1.3	98.8	0.7	0.3	0.0	0.1
QV1.2	99.1	0.2	0.5	0.1	0.1

Relative abundance is expressed as percentage of metagenomic sequence reads assigned to different domains of life via the M5NR database in MG-RAST.

the geochemical variability among the wells and visually displays the correlated parameters (Figure 3 and Supplementary Table S1). Community-level differences in the samples can be seen, such as a differentiation between high pH and moderate/circumneutral pH samples (Figure 3). A combination of pH, CO₂, and CH₄ concentrations best explain the bacterial community composition variability across wells, as determined by the multivariate BEST test in Primer-6 ($R = 0.83$, p -value = 0.001); Clarke, 1993; Clarke and Gorley, 2006). Therefore, pairwise Pearson's correlations among these three environmental parameters and the relative abundances of all associated OTUs were visualized with a correlation network diagram (Figure 4).

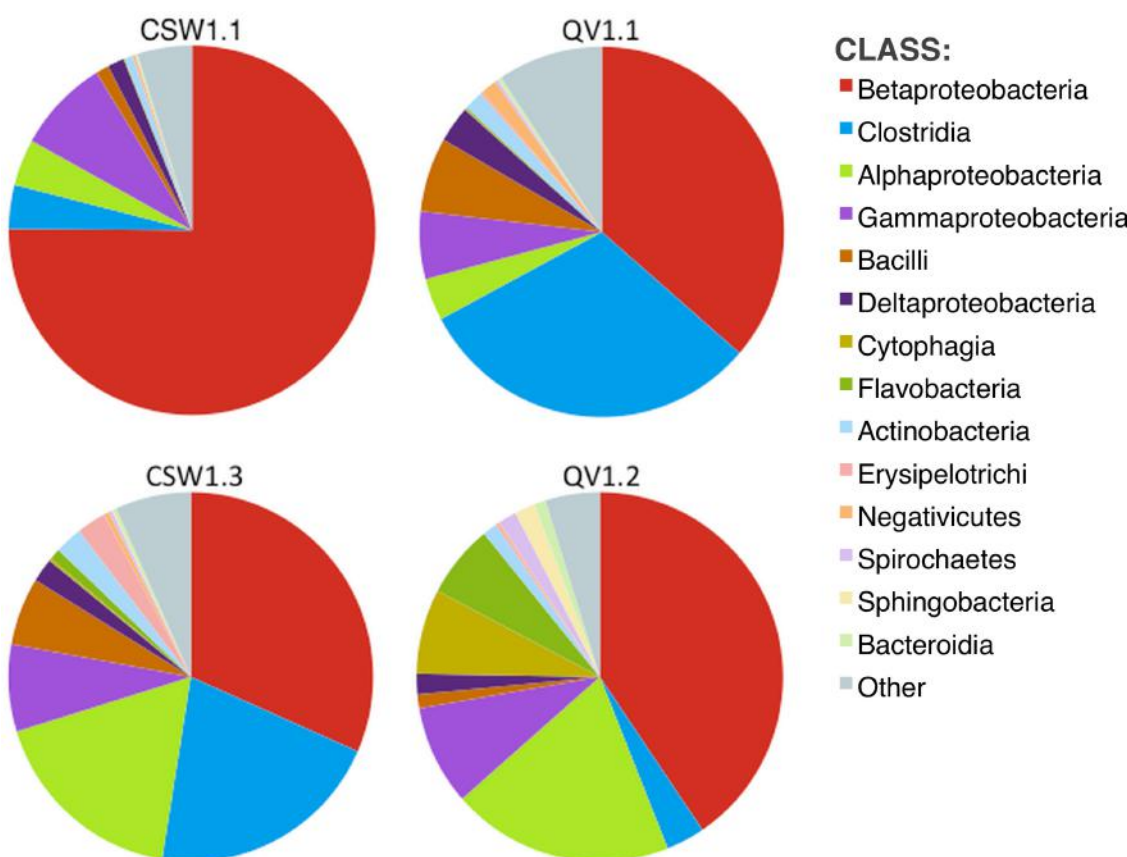


FIGURE 2 | Diversity (at class level) within metagenomic assemblies, as determined by MG-RAST (Meyer et al., 2008). Other represents classes with relative abundance <1% in any sample. No archaeal classes comprised more than 1% of any sample.

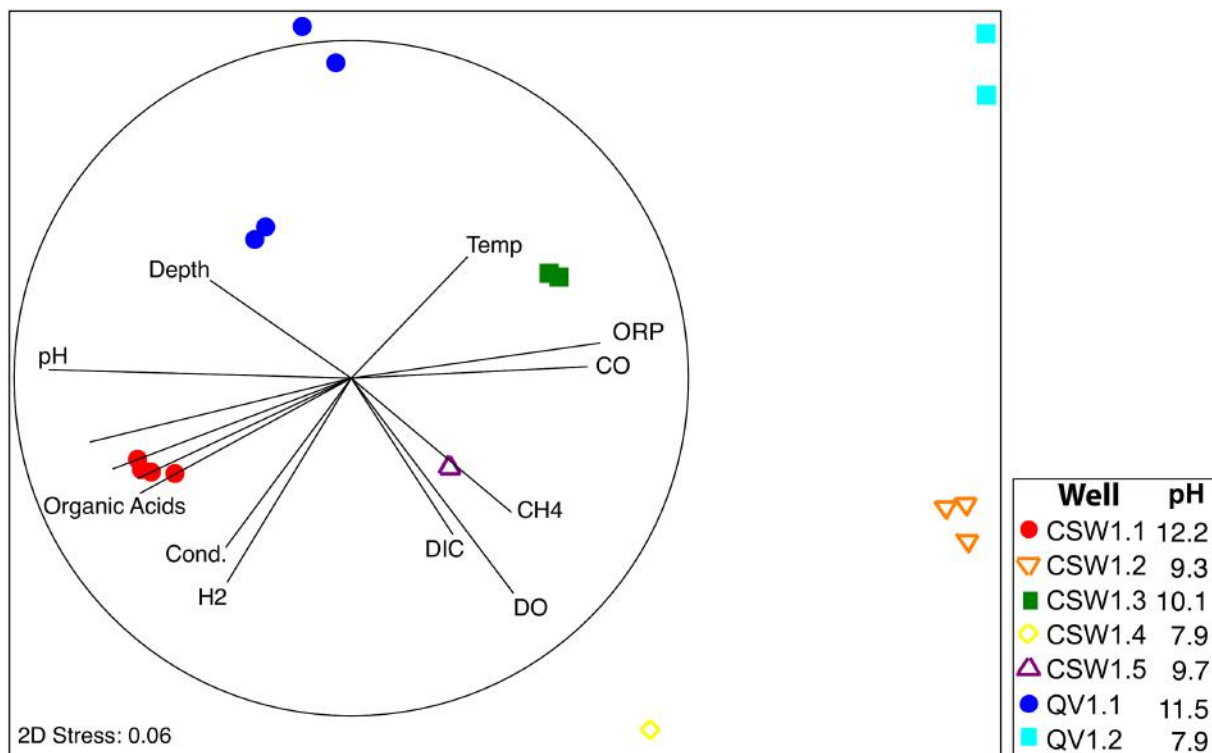


FIGURE 3 | Non-parametric Multi Dimensional Scaling (MDS) plot of microbial community diversity based upon bacterial 16S rRNA gene sequences using the Bray–Curtis similarity index. Environmental variables that correlated with community composition are represented by vectors in two-dimensional space. The dark circle represents the length of a vector with perfect correlation ($R = 1$).

Fluid pH was positively correlated with the two most abundant OTUs in CSW1.1 (OTU001 and OTU018, classified as Comamonadaceae and Thermoanaerobacterales SRB-2, respectively) and negatively correlated with OTU008 (classified as *Azonexus hydrophilus*), the dominant betaproteobacterial OTU in wells with a pH below 10 (Table 2 and Figure 4). The top OTUs from CSW1.1, OTU001 (classified as Comamonadaceae) and OTU018 (classified as Thermoanaerobacterales SRB-2), were negatively correlated with CO concentration. Except for the betaproteobacterial OTU033, all other OTUs that were positively correlated with CO concentration belonged to the alphaproteobacterial order Sphingomonadaceae (Figure 4). Among the OTUs positively correlated with the abundance of methane were Betaproteobacteria OTU004, most abundant in CSW1.2, and Clostridia OTU006, most abundant in CSW1.5 (Table 2 and Figure 4). Additionally, five Gammaproteobacteria OTUs and three Alphaproteobacteria OTUs, two classes known to contain aerobic methanotrophs, were also positively correlated with methane concentration (Figure 4). It should be stressed, however, that correlation does not necessarily indicate utilization or production of this compound by the microorganisms.

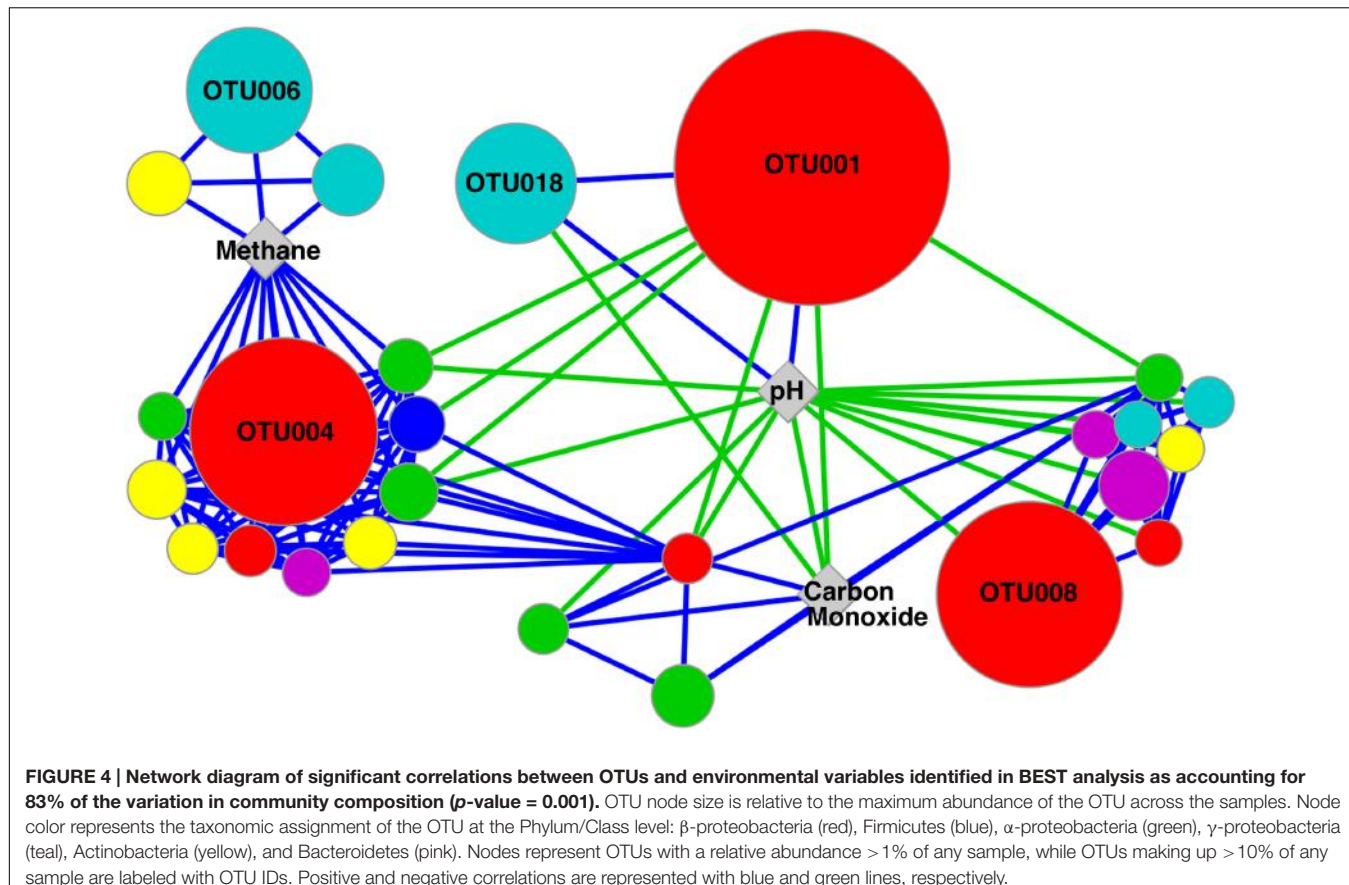
The most abundant OTUs in CSW1.1, OTU001 (classified as Comamonadaceae) and OTU018 (classified as Thermoanaerobacterales SRB-2), were positively correlated with conductivity, organic acid concentrations, and H_2

concentrations, and were negatively correlated with ORP (Table 2). Two of the most abundant Clostridia OTUs (OTU002 and OTU003), both dominant in QV1.1, were significantly correlated only with well depth (Table 4). While Table 2 and the discussion above denote the sample in which each OTU was most abundant, it should be mentioned that many of those abundant OTUs were found in multiple samples, though at lower abundances (Supplementary Figure S2).

Metabolic Potential

To elucidate whether microbes within the serpentinite subsurface environments are capable of metabolizing the geochemical products of serpentinization (specifically hydrogen, methane, acetate, and carbon monoxide) and other environmentally relevant compounds (specifically carbon dioxide and sulfur compounds), assembled and annotated metagenomes from four of the wells were searched for sequences predicted to encode proteins potentially diagnostic of specific metabolic pathways of interest (Figure 5). The metagenomes came from samples CSW1.1AC (pH 12.2), QV1.1A (pH 11.5), CSW1.3A (pH 10.1), and QV1.2A (pH 7.9). A summary of the metagenomic assembly statistics can be found in Supplementary Table S2.

To assess the potential for H_2 metabolism, genes encoding [FeFe]-hydrogenase (KEGG ID: K00533) and [NiFe]-hydrogenases (KEGG ID: K0628, K00436) were sought in the assembled metagenomes. [FeFe]-hydrogenases, often found



in fermentative Clostridia species, are typically involved in the production of H_2 (Vignais et al., 2001; Vignais and Billoud, 2007). [NiFe]-hydrogenases are divided into functional groups: Group 1 includes membrane-bound uptake hydrogenases; Group 2 includes H_2 -sensing hydrogenases; Group 3 includes cytoplasmic hydrogenases catalyzing reversible hydrogen-oxidation; and Group 4 includes archaeal H_2 production (Vignais et al., 2001; Vignais and Billoud, 2007). The [NiFe]-hydrogenases targeted in this analysis are *hyaB* (K06281), which is a Group 1 (H_2 -oxidizing) hydrogenase, and *hoxH* (K00436), which is a Group 3d (cytoplasmic) hydrogenase.

The [FeFe]-hydrogenase gene was detected in all four metagenomes, but was most abundant in QV1.1A (Figure 5). All of the contigs containing the [FeFe]-hydrogenase sequences were classified as Clostridia (Table 4). The Group 1 [NiFe]-hydrogenase (*hyaB*) was only detected in the moderate pH CSW1.3A and QV1.2A metagenomes (Figure 5), and the contigs that contained the gene were classified as Clostridia, Flavobacteria, Cyanobacteria, and Proteobacteria (Alpha-, and Beta-; Table 4). The Group 3d [NiFe]-hydrogenase (*hoxH*), on the other hand, was detected in all four metagenomes (Figure 5) and was found on contigs belonging to Betaproteobacteria, Clostridia, and Alphaproteobacteria. The betaproteobacterial contigs it was present on were identified as belonging to *Serpentinomonas* in CSW1.1AC, QV1.1A, and CSW1.3A (Table 4).

The metagenomic assemblies were searched for representative genes of bacterial aerobic methane oxidation (particulate methane monooxygenase (*pmoA*; K10944) and methanol dehydrogenase (*mxaf*; K14028) and for a representative gene of archaeal methanogenesis (*mcrA*; K00399). No *pmoA* or *mcrA* genes were identified in any of the metagenomes. CSW1.3A (pH 10.1) contained *mxaf* genes (Figure 5) on contigs belonging to members of the Alphaproteobacteria (Table 4), likely of the family Methylbacteriaceae, a group of methylotrophs (Lau et al., 2013) found in low abundance in samples from CSW1.3 (Figure 1).

The acetyl-coA synthase gene (*acsB*; K14138), suggestive of acetogenesis via the Wood/Ljungdahl pathway (or reductive acetyl-coA pathway; Ragsdale and Pierce, 2008), was only detected in QV1.1A (acetate = 11.2 μM ; Table 1) and CSW1.3A (acetate < 1.55 μM ; Table 1 and Figure 5). All instances of the contigs containing the gene were classified as being closely related to the clostridium *Dethiobacter alkaliphilus* (Table 4), which makes up 11 and 25% of the QV1.1A and CSW1.3A communities, respectively (Figure 1).

The high pH of the serpentinite environment limits the availability of CO_2 , potentially leading to the use of CO as both an electron donor and an inorganic carbon source. To assess CO metabolism at CROMO, two forms of CO dehydrogenase were sought in the metagenomes; *coxL* (K03520) and *cooS* (K00198) were used to identify aerobic and anaerobic CO oxidation,

TABLE 4 | Taxonomy (at the Class level) of metagenomic contigs containing genes-of-interest.

<i>mxAF</i> K14028	<i>[Fe]₂[ej-hyd</i> K00533	<i>hyAB</i> K06281	<i>hoxH</i> K00436	<i>acsB</i> K14138	<i>rbcl</i> K01601	<i>coxL</i> K03320	<i>cooS</i> K00198	<i>aprA</i> K00394	<i>dsrA</i> K11180
CSW1.1AC	Clostridia	Beta-pb*	Beta-pb*	Beta-pb*	Beta-pb*	Beta-pb*	Beta-pb*	Clostridia ⁺	Clostridia
QV1.1A	Clostridia ⁺	Beta-pb*	Clostridia ⁺	Beta-pb*	Beta-pb*	Beta-pb*	Beta-pb*	Clostridia ⁺	Clostridia ⁺
CSW1.3A	Alpha-pb	Clostridia ⁺	Beta-pb	Beta-pb*	Beta-pb*	Beta-pb*	Beta-pb*	Clostridia ⁺	Clostridia ⁺
QV1.2A		Clostridia	Flavobacteria	Alpha-pb	Beta-pb	Beta-pb	Beta-pb	Clostridia	
			Cyanobacteria	Beta-pb	Beta-pb	Beta-pb	Beta-pb		

Serpentinomonas* B1. *Serpentinomonas* A1. +*Dethiobacter alkophilus*.

respectively. Neither gene was detected in CSW1.1AC, and both were most abundant in QV1.1A (CO = 0.142 μ M; **Table 1** and **Figure 5**). All of the *cooS* genes detected were on contigs that belonged to Clostridia, while the *coxL* genes were more diverse, belonging to contigs identified as Betaproteobacteria and Alphaproteobacteria in the moderate to circumneutral wells, and to the Betaproteobacteria closely related to *Serpentinomonas* strain A1 in the high pH wells (**Table 4**; Suzuki et al., 2014).

Sequences encoding the *rbcl* gene (K01601) of the RuBisCo enzyme used in the Calvin–Benson–Bassham cycle were detected in all four metagenomes (**Figure 5**). In CSW1.1AC and QV1.1A, *rbcl* genes were found on contigs with high similarity to *Serpentinomonas* strain B1 (**Table 4**; Suzuki et al., 2014). The sequences detected in CSW1.3A also belonged to Betaproteobacteria, but of the family Burkholderiaceae (unlike the Comamonadaceae found in the higher pH wells), and the *rbcl* sequences from QV1.2A were more diverse, identified on contigs as coming from Sphingobacteria and Bacilli, as well as Betaproteobacteria (**Table 4**).

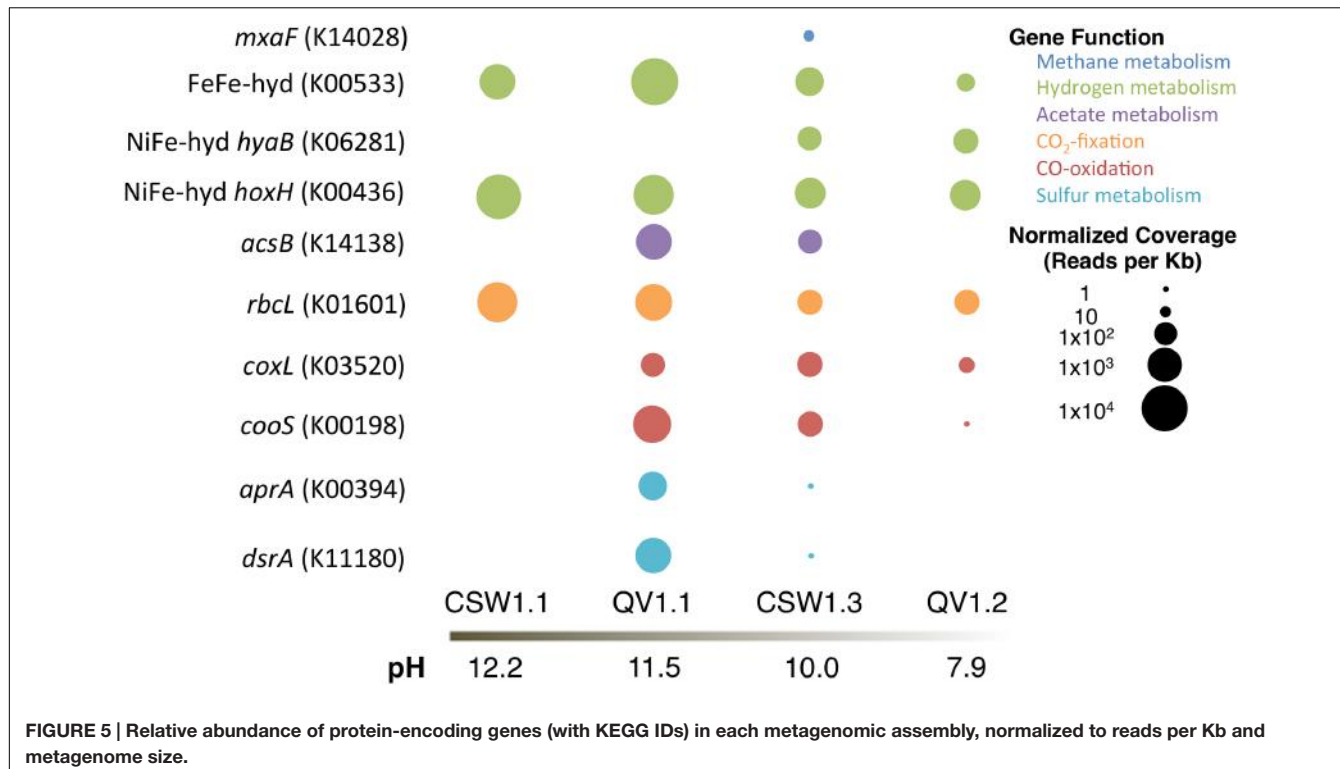
The potential metabolism of sulfur compounds was assessed by searching for dissimilatory sulfite reductase (*dsrA*; K11180) and dissimilatory adenosine-5'-phosphosulfate reductase (*aprA*; K00394). Both genes were detected at high abundance in QV1.1A and at low abundance in CSW1.3A (**Figure 5**). In both QV1.1A and CSW1.3A the contigs containing *aprA* and *dsrA* were classified as Clostridia (**Table 4**), and both of these samples contained a relatively high abundance of *Dethiobacter* sp. and SRB-2 (**Figure 1**). In contrast, neither gene was detected in wells CSW1.1AC or QV1.2A.

DISCUSSION

Serpentinite Environment at CROMO

The geochemical variability among multiple wells at CROMO allowed us to distinguish groundwater with varying degrees of influence from subsurface serpentinization processes. For example, the shallow CSW1.4 and QV1.2 wells produced pH \sim 8 water that had comparatively high levels of DO, DIC, and ORP (**Table 1**), which is consistent with oxygenated water that was recently exposed to the surface and was not noticeably affected by serpentinization. In contrast, the CSW1.1 well (pH 12.2) exhibited high conductivity and high concentrations of H₂ and small organic molecules (**Table 1**), consistent with water heavily influenced by subsurface serpentinization-associated reactions. Furthermore, CSW1.1 has remarkably low bacterial diversity, suggesting that it represents the most extreme window into the serpentinite subsurface. Other wells have weaker serpentinization signatures, such as that of CSW1.3, which is almost as deep as CSW1.1 and has almost as much H₂, but its water is pH \sim 10, suggesting a dilution of serpentinization-influenced water with shallower, surface-influenced water.

It should be noted that all of the wells, save CSW1.1 and QV1.1, were cased with PVC pipe upon drilling, essentially isolating the flow of water into the wells (Cardace et al., 2013). The larger diameter CSW1.1 and QV1.1 wells remained uncased,



and therefore, could experience some fluid input from above the drilled depth, which suggests that true serpentinite end-member fluids could be even more extreme than those measured here.

Bacterial diversity trends across the CROMO wells are remarkably consistent with the geochemistry of the wells. The overall bacterial community compositions of water from the most serpentinization-influenced (CSW1.1 and QV1.1) wells are tightly correlated with pH, organic acid concentrations, and low ORP values (Figure 3). Conversely, the community compositions of shallow, pH 7.8–9 wells (CSW1.2, CSW1.4 and QV1.2) are more tightly coupled to higher ORP, DO, and DIC, which is consistent with the interpretation of geochemistry data that these wells represent mixing of surface waters and serpentinization-influenced groundwater.

The distributions of individual genes, as measured by metagenomic sequencing, are also consistent with these biogeochemical trends. For example, genes involved in CO oxidation were completely absent in the well (CSW1.1) with the lowest concentration of CO, and these genes were present in each of the other three metagenomes (Table 1 and Figure 5). Genes associated with methane metabolism were surprisingly rare in the CROMO metagenomes, but one gene involved in bacterial methane oxidation (*mxAF*) was found in CSW1.3, which contains higher methane concentrations than the other three wells with metagenomes (Table 1 and Figure 5).

Betaproteobacteria

Serpentinomonas is a newly proposed genus within family Comamonadaceae currently represented by three strains isolated from the Cedars, another site of subsurface serpentinization in

northern California (Suzuki et al., 2014). An OTU with 100% sequence identity to *Serpentinomonas* B1 comprised over 50% of environmental 16S rRNA gene sequences from CSW1.1 (pH 12.2) and over 25% of sequences from QV1.1 (pH 11.5) and has been detected in CROMO wells at other time points (Crespo-Medina et al., 2014). The abundance of this OTU was positively correlated with pH, H₂, conductivity, and organic acids and negatively correlated with ORP and CO (Figure 1 and Table 2).

Each strain of *Serpentinomonas* (A1, B1, and H1) from the Cedars contains slightly different genes with regards to nitrate reduction, hydrogen oxidation, and carbon fixation (Suzuki et al., 2014). All strains are capable of CO₂-fixation via the Calvin–Benson–Bassham cycle and contain the *rbcL* gene coding for the RuBisCo enzyme, which was detected in all four metagenomes from CROMO wells and was most abundant in CSW1.1 (Figure 5). The *coxL* gene (involved in aerobic CO oxidation) is found only in *Serpentinomonas* A1 and was detected in QV1.1, but not CSW1.1 in this study, suggesting different phylotypes of the abundant organism in different wells (Figure 5 and Table 4). Only the H1 strain of *Serpentinomonas* contains the Group 1 [NiFe]-hydrogenase hydrogen-oxidation gene *hyaB*, which was not detected in either of the wells with extreme pH (Figure 5). However, Group 3d [NiFe]-hydrogenases, which are cytoplasmic hydrogenases capable of reversible H₂-oxidation, are found in all three strains of *Serpentinomonas* (Suzuki et al., 2014) and were detected in all four CROMO wells (Figure 5). *Serpentinomonas* strains containing Group 3d (and not Group 1) [NiFe]-hydrogenase genes were experimentally shown to oxidize hydrogen to support autotrophic growth, so it has been speculated that Group 3d [NiFe]-hydrogenase genes, such as

hoxH, might be the key to H₂ metabolism in these organisms (Suzuki et al., 2014). None of the *Serpentinomonas* strains contain ACS, *cooS*, *aprA*, or *dsrA* (Suzuki et al., 2014), and none of those genes were detected in CSW1.1, where *Serpentinomonas* dominated the community (Figures 1, 5). These data support interpretations (Schrenk et al., 2013) that *Serpentinomonas*-like organisms are hydrogen-oxidizing, carbon-fixing members of serpentinite-hosted ecosystems, able to persist at extreme pH and thrive on the chemical disequilibrium of the mixing zone between anoxic end-member and oxygenated surface fluids.

The most abundant betaproteobacterial OTU found in QV1.2 (pH 7.9) was OTU008, which made up $33.1 \pm 6.8\%$ of the total community and exhibited 100% sequence identity to *Azonexus hydrophilus* (family Rhodocyclaceae; Table 2 and Figure 1). This organism is a motile, non-spore-forming aerobe isolated from freshwater springs in Taiwan and Korea (Chou et al., 2008), and it has a circumneutral optimal growth pH. In this study, OTU004 exhibited a negative correlation with pH, which is consistent with a circumneutral optimal growth pH. It has been detected in sewage treatment facilities (Auguet et al., 2015; Yan et al., 2015) and coal bed methane environments (Guo et al., 2012), as well as in the deep subsurface (Ise et al., 2016; Jangir et al., 2016). In QV1.2A, Group 1 [NiFe]-hydrogenase gene *hyaB* and the *rbcL* gene of RuBisCo were detected on contigs identified as *Azonexus hydrophilus* (Supplementary Dataset S1), suggesting that these Betaproteobacteria are involved in H₂-oxidation and carbon fixation in the moderate wells.

Alicycliphilus denitrificans made up 32.9% of CSW1.2 (pH 9.3), making it the most abundant betaproteobacterial OTU in the sample (Figure 1 and Table 2). This organism is a facultative denitrifying bacterium that can use acetate as a carbon source (Mechichi et al., 2003). OTU004 (classified as *A. denitrificans*) was positively correlated with methane (Table 2), but this organism is not known to be involved in methane cycling.

Clostridia

Clostridia have been detected at sites of continental serpentinization around the world (Brazelton et al., 2012, 2013; Suzuki et al., 2013; Tiago and Veríssimo, 2013; Woycheese et al., 2015), where they are thought to inhabit the anoxic end-member serpentinite fluids (Schrenk et al., 2013). An abundance of [FeFe]-hydrogenases belonging to Clostridia in metagenomic data from serpentinite springs (Brazelton et al., 2012) suggests that these abundant organisms are producing H₂, but additional clues to their physiology and ecology are lacking.

Operational taxonomic units classified as Clostridia were very abundant in the high pH wells at CROMO. The clostridial OTUs at CROMO were either classified as *Dethiobacter*, Thermoanaerobacterales SRB-2, or unclassified Clostridia. The most extreme well, CSW1.1 (pH 12.2), contained $13.9 \pm 6.5\%$ Clostridia, mostly represented by an OTU classified as SRB-2. QV1.1 (pH 11.5) displayed a greater abundance and diversity of Clostridia, as well as a shift in clostridial community composition between field replicates (Figure 1). The deeper QV1.1 samples (field replicates A/B) had more SRB-2 and fewer *Dethiobacter*

than in waters naturally found higher up in the well (i.e., filtered later as water was drawn down).

Dethiobacter alkaliphilus is an anaerobic alkaliphile that was originally isolated from a Mongolian soda lake; it utilizes H₂ as an electron donor, sulfur compounds (S⁰, thiosulfate, polysulfide) as electron acceptors, and acetate as a carbon source (Sorokin et al., 2008). *Dethiobacter* has been detected at sites of continental serpentinization and is hypothesized to live in the deep, anoxic serpentinite end-member fluids (Brazelton et al., 2012; Suzuki et al., 2013; Tiago and Veríssimo, 2013; Crespo-Medina et al., 2014; Woycheese et al., 2015). Crespo-Medina et al. (2014) detected growth in CROMO microcosms dominated by *D. alkaliphilus* with H₂-headspace and the addition of thiosulfate with either acetate or methane as a carbon source. It should be noted that since there is no known mechanism for Clostridia to consume methane, it is believed there was a cryptic organism within the microcosms making methane-derived carbon bioavailable to *Dethiobacter* (Crespo-Medina et al., 2014). In the QV1.1A metagenome, the genes attributed to *Dethiobacter* are *hoxH* (H₂ sensing), FeFe-hydrogenase (H₂-production), *acsB* (acetogenesis), and *cooS* (anaerobic CO-oxidation) (Table 4). These data suggest that the abundant *Dethiobacter* encode several metabolic pathways that might allow them to adapt to changing conditions in the subsurface or in the well water.

Members of the family Thermoanaerobacterales, identified as belonging to the SRB-2 lineage, were abundant in CSW1.1 and QV1.1 (Figure 1). The SRB-2 OTUs share high sequence identity with clones from CVA fluids and the Cedars (Table 2; Suzuki et al., 2013; Tiago and Veríssimo, 2013). Not much is known about this uncultivated group, but the Thermoanaerobacterales include organisms capable of sulfate reduction (Pereira et al., 2011), fermentative acetate oxidation (Oehler et al., 2012), fermentative hydrogen production (Rittmann and Herwig, 2012), and homoacetogenesis (Ljungdahl, 1994). The [FeFe]-hydrogenase and *acsB* genes detected in the metagenomes could not be classified at the family level (with some exceptions, see Table 4) but they were all classified as Clostridia, consistent with SRB-2 and perhaps other unclassified Clostridia as potentially acetogenic, sulfur-reducing alkaliphiles in the subsurface serpentinite fluids.

Sequences belonging to Erysipelotrichia (another class of the phylum Firmicutes) were inferred to represent the most likely inhabitants of serpentinite end-member fluids exiting from springs at the Tablelands, Newfoundland (Brazelton et al., 2013). An OTU classified as genus *Erysipelothrix* was found in three moderately high pH CROMO wells, but in none of the other wells (Figure 1). None of the protein-coding genes in the CROMO metagenomes were classified as *Erysipelothrix* (Table 4).

Other Community Members

All of the OTUs in CSW1.1 and QV1.1 that made up greater than 1% of sequences in either well belonged to the Betaproteobacteria or Clostridia. Furthermore, all of the metagenomic contigs containing key genes of interest from these two wells were classified as one of these two classes of bacteria (Table 4). The

moderately high pH and circumneutral wells exhibited slightly higher diversity in not only 16S rRNA genes (**Figure 1**), but also in the variety and taxonomic classification of protein-encoding genes (**Figure 5** and **Table 4**). Additional bacterial taxa in these wells included Alphaproteobacteria, Deltaproteobacteria, and Bacteroidetes. These results suggest that a breadth of organisms are capable of using products of serpentinization, but might be restricted by the extreme pH conditions in wells containing a greater degree of end-member fluids.

It is notable that archaea were absent from all CROMO 16S rRNA sequences and were very rare (1% or less of sequences) in the metagenomic data (**Table 3**). Studies of other sites of continental serpentinization, in contrast, have detected methanogenic Euryarchaeota (Suzuki et al., 2013; Tiago and Veríssimo, 2013). Methane isotopologue analyses have suggested that the methane at CROMO displays a thermogenic signature, while methane from the nearby Cedars site (from which *Serpentinomonas* was isolated) has a more microbial signature (Wang et al., 2015). These isotope geochemistry results are consistent with the lack of methanogens in CROMO wells. Additionally, OD-1 and Chloroflexi, both of which are bacteria that Suzuki et al. (2013) hypothesized to be endemic to end-member serpentinite fluids, were not detected in any of the CROMO fluids. Therefore, the subsurface fluids in CROMO wells appear to be an unfavorable environment for several microorganisms that are abundant in other sites of serpentinization.

CONCLUSION

By studying groundwater with a range of geochemical characteristics, we were able to identify the bacterial taxa with the strongest correlations to the environmental variables (such as pH, CO, and CH₄) indicative of subsurface serpentinization processes. These data suggest that various Clostridia taxa are potentially capable of anaerobic CO-oxidation, acetogenesis, and the reduction of sulfur compounds in extremely high pH, anoxic subsurface fluids heavily influenced by serpentinization, while microaerophilic *Serpentinomonas* (Betaproteobacteria) are capable of H₂-oxidation and CO₂-fixation (and in some cases, aerobic CO-oxidation) in mixing zones where deep, anoxic fluids interact with oxygenated surface waters. These data provide tractable targets for further biogeochemical and microbiological analyses of serpentinite-hosted microbial ecosystems at CROMO and elsewhere.

The results of this study support those of other recent studies of serpentinite-hosted ecosystems that have identified a few key bacterial taxa that are common to such systems. Furthermore, our results significantly expand our current understanding of the microbial ecology of subsurface, serpentinite-hosted ecosystems. Previously, studies of the microbiology of continental serpentinites have focused on opportunistic sampling from a small number of surface-exposed sites (Brazelton et al., 2012; Suzuki et al., 2013; Tiago and Veríssimo, 2013). Because these studies must sample the surface expression of subsurface processes, identifications of taxa that are truly endemic to the

subsurface must be indirect inferences that rely on assumptions of hydrology and sampling methodology. By directly accessing the serpentinite subsurface using wells at CROMO, we were able to observe subsurface microbial communities that had not directly experienced the surface processes that influence the composition of microbial communities sampled from springs. Furthermore, access to the groundwater revealed the absence of several taxa that were identified as key members of other serpentinite-hosted ecosystems, which highlights the remarkably low diversity of organisms apparently capable of thriving in these high pH subsurface fluids.

AUTHOR CONTRIBUTIONS

KT, WB, and MS designed the study. WB, MK, and DC performed field sampling. KT, WB, and AH performed the bioinformatic analyses and interpretations. KT and WB performed statistical analyses. MK, DC, TH, and TM contributed to the geochemical analyses and interpretations. KT, WB, MK, AH, DC, TH, TM, and MS wrote the manuscript.

FUNDING

The establishment of CROMO was funded by the NASA Astrobiology Institute and the research conducted was funded by the Alfred P. Sloan Foundation's Deep Carbon Observatory (2011-12-01). All of the sequencing was performed by the DOE Joint Genome Institute (supported by the Office of Science of the U.S. Department of Energy under the contract DE-AC02-05CH11231).

ACKNOWLEDGMENTS

We thank C. Koehler and P. Aigner at the UC-Davis McLaughlin Nature Reserve and S. Moore and Homestake Mining Company for support in the establishment of CROMO. Thank you to D. Carnevale for help with field sampling, C. Thornton for data analysis assistance, and D. Morgan-Smith, M. Crespo-Medina, and D. Wang for insightful discussions.

SUPPLEMENTARY MATERIAL

The Supplementary Material for this article can be found online at: <http://journal.frontiersin.org/article/10.3389/fmicb.2017.00308/full#supplementary-material>

FIGURE S1 | Microbial community structure. **(A)** Rarefaction analysis of 16S rRNA amplicon sequences. Multiple samples from the same well represent field replicates. **(B)** Community similarity dendrogram calculated from Bray-Curtis index. Samples connected by red lines are not distinguishable from one another by a SIMPROF test and ANOSIM analysis indicated that there is a significant difference in community composition between wells ($R = 0.9$, p -value < 0.05).

FIGURE S2 | Heatmap of most abundant OTUs and geochemical parameters across all samples. Dendrogram at the top represents community similarity between samples and red lines indicate no statistical difference between field replicates, as determined by SIMPROF (Clarke, 1993).

REFERENCES

- Albert, D., and Martens, C. (1997). Determination of low-molecular-weight organic acid concentrations in seawater and pore-water samples via HPLC. *Mar. Chem.* 56, 27–37. doi: 10.1016/S0304-4203(96)00083-7
- Anders, S., Pyl, P. T., and Huber, W. (2014). HTSeq: a Python framework to work with high-throughput sequencing data. *Bioinformatics* 31, 166–169. doi: 10.1093/bioinformatics/btu638
- Auguet, O., Pijuan, M., Guasch-Balcells, H., Borrego, C. M., and Gutierrez, O. (2015). Implications of downstream nitrate dosage in anaerobic sewers to control sulfide and methane emissions. *Water Res.* 68, 522–532. doi: 10.1016/j.watres.2014.09.034
- Barnes, I., and O’Neil, J. R. (1971). Calcium-magnesium carbonate solid solutions from Holocene conglomerate cements and travertines in the Coast Range of California. *Geochim. Cosmochim. Acta* 35, 699–718. doi: 10.1016/0016-7037(71)90068-8
- Brazelton, W. J., Morrill, P. L., Szponar, N., and Schrenk, M. O. (2013). Bacterial communities associated with subsurface geochemical processes in continental serpentinite springs. *Appl. Environ. Microbiol.* 79, 3906–3916. doi: 10.1128/AEM.00330-13
- Brazelton, W. J., Nelson, B., and Schrenk, M. O. (2012). Metagenomic evidence for H₂ oxidation and H₂ production by serpentinite-hosted subsurface microbial communities. *Front. Microbiol.* 2:268. doi: 10.3389/fmicb.2011.00268
- Brazelton, W. J., Schrenk, M. O., Kelley, D. S., and Baross, J. A. (2006). Methane- and sulfur-metabolizing microbial communities dominate the Lost City Hydrothermal Field ecosystem. *Appl. Environ. Microbiol.* 72, 6257–6270. doi: 10.1128/AEM.00574-06
- Campanella, J. J., Bitincka, L., and Smalley, J. (2003). MatGAT: an application that generates similarity/identity matrices using protein or DNA sequences. *BMC Bioinformatics* 4:29. doi: 10.1186/1471-2105-4-29
- Caporaso, J. G., Lauber, C. L., Walters, W. A., Berg-Lyons, D., Huntley, J., Fierer, N., et al. (2011). Ultra-high-throughput microbial community analysis on the Illumina HiSeq and MiSeq platforms. *ISME J.* 6, 1621–1624. doi: 10.1038/ismej.2012.8
- Cardace, D., Hoehler, T. M., McCollom, T. M., Schrenk, M. O., Carnevale, D., Kubo, M. D., et al. (2013). Establishment of the Coast Range ophiolite microbial observatory (CROMO): drilling objectives and preliminary outcomes. *Sci. Drill.* 16, 45–55. doi: 10.5194/sd-16-45-2013
- Cardace, D., Meyer-Dombard, D. R., Woycheese, K. M., and Arcilla, C. A. (2015). Feasible metabolisms in high pH springs in the Philippines. *Front. Microbiol.* 6:10. doi: 10.3389/fmicb.2015.00010
- Chivian, D., Brodie, E. L., Alm, E. J., Culley, D. E., Dehal, P. S., Desantis, T. Z., et al. (2008). Environmental genomics reveals a single-species ecosystem deep within Earth. *Science* 322, 275–278. doi: 10.1126/science.1155495
- Chou, J. H., Jiang, S. R., Cho, J. C., Song, J., Lin, M. C., and Chen, W. M. (2008). *Azonexus hydrophilus* sp. nov., a novel nifH gene-harboring bacterium isolated from freshwater. *Int. J. Syst. Evol. Microbiol.* 58, 946–951. doi: 10.1099/ijss.0.65434-0
- Clarke, K. R. (1993). Non-parametric multivariate analyses of changes in community structure. *Aust. J. Ecol.* 18, 117–143. doi: 10.1111/j.1442-9993.1993.tb00438.x
- Clarke, K. R., and Gorley, R. N. (2006). *PRIMER v6: User Manual/Tutorial*. Plymouth, MN: PRIMER-E.
- Crespo-Medina, M., Twining, K. I., Kubo, M. D., Hoehler, T. M., Cardace, D., McCollom, T. M., et al. (2014). Insights into environmental controls on microbial communities in a continental serpentinite aquifer using a microcosm-based approach. *Front. Microbiol.* 5:604. doi: 10.3389/fmicb.2014.00604
- Edwards, K. J., Fisher, A. T., and Wheat, C. G. (2012). The deep subsurface biosphere in igneous ocean crust: frontier habitats for microbiological exploration. *Front. Microbiol.* 3:8. doi: 10.3389/fmicb.2012.00008
- Engel, A. S., Stern, L. A., and Bennett, P. C. (2004). Microbial contribution to cave formation: new insights into sulfuric acid speleogenesis. *Geology* 32, 369–372. doi: 10.1130/G20288.1
- Fuhrman, J., and Steele, J. (2008). Community structure of marine bacterioplankton: patterns, networks, and relationships to function. *Aquat. Microb. Ecol.* 53, 69–81. doi: 10.3354/ame01222
- Guo, H., Yu, Z., Liu, R., Zhang, H., Zhong, Q., and Xiong, Z. (2012). Methylotrophic methanogenesis governs the biogenic coal bed methane formation in Eastern Ordos Basin, China. *Appl. Microbiol. Biotechnol.* 96, 1587–1597. doi: 10.1007/s00253-012-3889-3
- Hanson, N. W., Konwar, K. M., and Hallam, S. J. (2016). LCA: an entropy-based measure for taxonomic assignment within assembled metagenomes. *Bioinformatics* 32, 3535–3542. doi: 10.1093/bioinformatics/btw400
- Hawley, E. R., Piao, H., Scott, N. M., Malfatti, S., Pagani, I., Huntemann, M., et al. (2014). Metagenomic analysis of microbial consortium from natural crude oil that seeps into the marine ecosystem offshore Southern California. *Stand. Genomic Sci.* 9, 1259–1274. doi: 10.4056/sigs.5029016
- Hobbie, J. E., Daley, R. J., and Jasper, S. (1977). Use of nucleopore filters for counting bacteria by fluorescence microscopy. *Appl. Environ. Microbiol.* 33, 1225–1228.
- Hyatt, D., Chen, G. L., Locascio, P. F., Land, M. L., Larimer, F. W., and Hauser, L. J. (2010). Prodigal: prokaryotic gene recognition and translation initiation site identification. *BMC Bioinformatics* 11:119. doi: 10.1186/1471-2105-11-119
- Ise, K., Sasaki, Y., Amano, Y., Iwatsuki, T., Nanjo, I., Asano, T., et al. (2016). The succession of bacterial community structure in groundwater from a -250-m gallery in the Horonobe Underground Research Laboratory. *Geomicrobiol. J.* doi: 10.1080/01490451.2016.1152329
- Itäväära, M., Nyssönen, M., Kapanen, A., Nousiainen, A., Ahonen, L., and Kukkonen, I. (2011). Characterization of bacterial diversity to a depth of 1500 m in the Outokumpu deep borehole, Fennoscandian Shield. *FEMS Microbiol. Ecol.* 77, 295–309. doi: 10.1111/j.1574-6941.2011.01111.x
- Jangir, Y., French, S., Momper, L. M., Moser, D. P., Amend, J. P., and El-Naggar, M. Y. (2016). Isolation and characterization of electrochemically active subsurface *Deltia* and *Azonexus* species. *Front. Microbiol.* 7:756. doi: 10.3389/fmicb.2016.00756
- Kallmeyer, J., Pockalny, R., Adhikari, R. R., Smith, D. C., and D’Hondt, S. (2012). Global distribution of microbial abundance and biomass in subseafloor sediments. *Proc. Natl. Acad. Sci. U.S.A.* 109, 16213–16216. doi: 10.1073/pnas.1203849109
- Kelley, D. S., Karson, J. A., Früh-Green, G. L., Yoerger, D. R., Shank, T. M., Butterfield, D. A., et al. (2005). A serpentinite-hosted ecosystem: the Lost City Hydrothermal Field. *Science* 307, 1428–1434. doi: 10.1126/science.1102556
- Lau, E., Fisher, M. C., Steudler, P. A., and Cavanaugh, C. M. (2013). The methanol dehydrogenase gene, *mxaF*, as a functional and phylogenetic marker for proteobacterial methanotrophs in natural environments. *PLoS ONE* 8:e56993. doi: 10.1371/journal.pone.0056993
- Li, H., and Durbin, R. (2009). Fast and accurate short read alignment with Burrows-Wheeler Transform. *Bioinformatics* 25, 1754–1760. doi: 10.1093/bioinformatics/btp324
- Ljungdahl, L. G. (1994). “The acetyl-CoA pathway and the chemiosmotic generation of ATP during acetogenesis,” in *Acetogenesis*, ed. H. L. Drake (New York, N.Y: Chapman & Hall), 63–87. doi: 10.1007/978-1-4615-1777-1_2
- Luo, R., Liu, B., Xie, Y., Li, Z., Huang, W., Yuan, J., et al. (2012). SOAPdenovo2: an empirically improved memory-efficient short-read denovo assembler. *GigaScience* 1:18. doi: 10.1186/2047-217X-1-18
- McCollom, T. M., and Seewald, J. S. (2007). Abiotic synthesis of organic compounds in deep-sea hydrothermal environments. *Chem. Rev.* 107, 382–401. doi: 10.1021/cr0503660
- Mechichi, T., Stackebrandt, E., and Fuchs, G. (2003). *Alicucliphilus denitrificans* gen. nov. sp. nov., a cyclohexanol-degrading, nitrate-reducing β-proteobacterium. *Int. J. Syst. Evol. Microbiol.* 53, 147–152. doi: 10.1099/ijss.0.02276-0
- Meyer, F., Paarmann, D., D’Souza, M., Olson, R., Glass, E. M., Kubal, M., et al. (2008). The metagenomics RAST server: a public resource for the automatic phylogenetic and functional analysis of metagenomes. *BMC Bioinformatics* 9:386. doi: 10.1186/1471-2105-9-386
- Northrup, D. E., and Lavoie, K. H. (2001). Geomicrobiology of caves: a review. *Geomicrobiol. J.* 18, 199–222. doi: 10.1080/01490450152467750
- Oehler, D., Poehlein, A., Leimbach, A., Muller, N., Daniel, R., Gottschalk, G., et al. (2012). Genome-guided analysis of physiological and morphological traits of the fermentative acetate oxidizer *Thermoacetogenium phaeum*. *BMC Genomics* 13:723. doi: 10.1186/1471-2164-13-723

- Ogata, H., Goto, S., Sato, K., Fujibuchi, W., Bono, H., and Kanehisa, M. (1999). KEGG: kyoto encyclopedia of genes and genomes. *Nucleic Acids Res.* 27, 29–34. doi: 10.1093/nar/27.1.29
- Onstott, T. C., Moser, D. P., Pfiffner, S. M., Fredrickson, J. K., Brockman, F. J., Phelps, T. J., et al. (2003). Indigenous and contaminant microbes in ultradeep mines. *Environ. Microbiol.* 5, 1168–1191. doi: 10.1046/j.1462-2920.2003.00512.x
- Oosterkamp, M. J., Veuskens, T., Plugge, C. M., Langenhoff, A. A., Gerritse, J., van Berkel, W. J., et al. (2011). Genome sequences of *Alicycliphilus denitrificans* strains BC and K601. *J. Bacteriol.* 193, 5028–5029. doi: 10.1128/JB.00365-11
- Pereira, I. A., Ramos, A. R., Grein, F., Margques, M. C., de Silva, S., and Venceslau, S. S. (2011). A comparative genomic analysis of energy metabolism in sulfate reducing bacteria and archaea. *Front. Microbiol.* 2:69. doi: 10.3389/fmicb.2011.00069
- Proskurowski, G., Lilley, M. D., Seewald, J. S., Früh-Green, G. L., Olson, E. J., Lupton, J. E., et al. (2008). Abiogenic hydrocarbon production at Lost City Hydrothermal Field. *Science* 319, 604–607. doi: 10.1126/science.1151194
- Pruesse, E., Quast, C., Knittel, K., Fuchs, B. M., Ludwig, W., Peplies, J., et al. (2007). SILVA: a comprehensive online resource for quality checked and aligned ribosomal RNA sequence data compatible with ARB. *Nucleic Acids Res.* 35, 7188–7196. doi: 10.1093/nar/gkm864
- Ragsdale, S. W., and Pierce, E. (2008). Acetogenesis and the Wood-Ljungdahl pathway of CO₂ fixation. *Biochim. Biophys. Acta* 1784, 1873–1898. doi: 10.1016/j.bbapap.2008.08.012
- Rittmann, S., and Herwig, C. (2012). A comprehensive and quantitative review of dark fermentative biohydrogen production. *Microb. Cell Fact.* 11:115. doi: 10.1186/1475-2859-11-115
- Rizopoulos, D. (2006). ltm: an R package for latent variable modeling. *J. Stat. Softw.* 17:5. doi: 10.18637/jss.v017.i05
- Schloss, P. D., and Westcott, S. L. (2011). Assessing and improving methods used in operational taxonomic unit-based approaches for 16S rRNA gene sequence analysis. *Appl. Environ. Microbiol.* 77, 3219–3226. doi: 10.1128/AEM.02810-10
- Schloss, P. D., Westcott, S. L., Ryabin, T., Hall, J. R., Hartmann, M., Hollister, E. B., et al. (2009). Introducing mothur: open-source, platform-independent, community-supported software for describing and comparing microbial communities. *Appl. Environ. Microbiol.* 75, 7537–7541. doi: 10.1128/AEM.01541-09
- Schrenk, M. O., Brazelton, W. J., and Lang, S. Q. (2013). Serpentinization, carbon and deep life. *Rev. Miner. Geochem.* 75, 575–606. doi: 10.2138/rmg.2013.75.18
- Schrenk, M. O., Kelley, D. S., Bolton, S. A., and Baross, J. A. (2004). Low archaeal diversity linked to subseafloor geochemical processes at the Lost City Hydrothermal Field, Mid-Atlantic Ridge. *Environ. Microbiol.* 6, 1086–1095. doi: 10.1111/j.1462-2920.2004.00650.x
- Schrenk, M. O., Kelley, D. S., Delaney, J. R., and Baross, J. A. (2003). Incidence and diversity of microorganisms within the walls of an active deep-sea sulfide chimney. *Appl. Environ. Microbiol.* 69, 3580–3592. doi: 10.1128/AEM.69.6.3580-3592.2003
- Seeman, T. (2014). Prokka: rapid prokaryotic genome annotation. *Bioinformatics* 14, 2069–2069. doi: 10.1093/bioinformatics/btu153
- Shannon, P., Markiel, A., Ozier, O., Baliga, N. S., Wang, J. T., Ramage, D., et al. (2003). Cytoscape: a software environment for integrated models of biomolecular interaction networks. *Genome Res.* 13, 2498–2504. doi: 10.1101/gr.1239303
- Sommer, D. D., Delcher, A. L., Salzberg, S. L., and Pop, M. (2007). Minimus: a fast, lightweight genome assembler. *BMC Bioinformatics* 8:64. doi: 10.1186/1471-2105-8-64
- Sorokin, D. Y., Tourova, T. P., Mußmann, M., and Muyzer, G. (2008). *Dethiobacter alkaliphilus* gen. nov. sp. nov., and *Desulfurivibrio alkaliphilus* gen. nov. sp. nov.: two novel representatives of reductive sulfur cycle from soda lakes. *Extremophiles* 12, 431–439. doi: 10.1007/s00792-008-0148-8
- Stevens, T. O., and McKinley, J. P. (1995). Lithoautotrophic microbial ecosystems in deep basalt aquifers. *Science* 270, 450–454. doi: 10.1126/science.270.5235.450
- Suzuki, S., Ishii, S., Wu, A., Cheung, A., Tenney, A., Wanger, G., et al. (2013). Microbial diversity in The Cedars, an ultrabasic, ultrareducing, and low salinity serpentinizing ecosystem. *Proc. Natl. Acad. Sci. U.S.A.* 110, 15336–15341. doi: 10.1073/pnas.1302426110
- Suzuki, S., Kuenen, J. G., Schipper, K., van der Velde, S., Ishii, S., Wu, A., et al. (2014). Physiological and genomic features of highly alkaliphilic hydrogen-utilizing Betaproteobacteria from a continental serpentinizing site. *Nat. Commun.* 5:3900. doi: 10.1038/ncomms4900
- Tiago, I., and Veríssimo, A. (2013). Microbial and functional diversity of a subterrestrial high pH groundwater associated to serpentinization. *Environ. Microbiol.* 15, 1687–1706. doi: 10.1111/1462-2920.12034
- Vignais, P. M., and Billoud, B. (2007). Occurrence, classification, and biological function of hydrogenases: an overview. *Chem. Rev.* 107, 4206–4272. doi: 10.1021/cr050196r
- Vignais, P. M., Billoud, B., and Meyer, J. (2001). Classification and phylogeny of hydrogenases. *FEMS Microbiol.* 25, 455–501. doi: 10.1111/j.1574-6976.2001.tb00587.x
- Wang, D. T., Gruen, D. S., Lollar, B. S., Hinrichs, K. U., Stewart, L. C., Holden, J. F., et al. (2015). Nonequilibrium clumped isotope signals in microbial methane. *Science* 348, 428–431. doi: 10.1126/science.aaa4326
- Whitman, W. B., Coleman, D. C., and Wiebe, W. J. (1998). Prokaryotes: the unseen majority. *Proc. Natl. Acad. Sci. U.S.A.* 95, 6578–6583. doi: 10.1073/pnas.95.12.6578
- Woycheese, K. M., Meyer-Dombard, D. R., Cardace, D., Argayosa, A. M., and Arcilla, C. A. (2015). Out of the dark: transitional subsurface-to-surface microbial diversity in a terrestrial serpentinizing seep (Manleluag, Pangasiana, the Philippines). *Front. Microbiol.* 6:44. doi: 10.3389/fmicb.2015.00044
- Yan, P., Wang, J., Chen, Y.-P., Ji, F.-Y., Shen, Y., Fang, F., et al. (2015). Investigation of microbial community structure in an advanced activated sludge side-stream reactor process with alkaline treatment. *Int. Biodeter. Biodegr.* 104, 356–362. doi: 10.1016/j.ibiod.2015.07.003

Conflict of Interest Statement: The authors declare that the research was conducted in the absence of any commercial or financial relationships that could be construed as a potential conflict of interest.

Copyright © 2017 Twining, Brazelton, Kubo, Hyer, Cardace, Hoehler, McCollom and Schrenk. This is an open-access article distributed under the terms of the Creative Commons Attribution License (CC BY). The use, distribution or reproduction in other forums is permitted, provided the original author(s) or licensor are credited and that the original publication in this journal is cited, in accordance with accepted academic practice. No use, distribution or reproduction is permitted which does not comply with these terms.



Methane Dynamics in a Tropical Serpentinizing Environment: The Santa Elena Ophiolite, Costa Rica

Melitza Crespo-Medina¹, Katrina I. Twing², Ricardo Sánchez-Murillo³, William J. Brazelton², Thomas M. McCollom⁴ and Matthew O. Schrenk^{5*}

¹ Center for Education, Conservation and Research, Inter-American University of Puerto Rico, San Juan, PR, United States

² Department of Biology, University of Utah, Salt Lake City, UT, United States, ³ Stable Isotope Research Group, School of Chemistry, National University of Costa Rica, Heredia, Costa Rica, ⁴ Laboratory for Atmospheric and Space Physics, Center for Astrobiology, University of Colorado Boulder, Boulder, CO, United States, ⁵ Department of Earth and Environmental Sciences, Michigan State University, East Lansing, MI, United States

OPEN ACCESS

Edited by:

Cody Sheik,
University of Minnesota Duluth, United
States

Reviewed by:

Maggie Lau,
Princeton University, United States
D'Arcy Renee Meyer-Dombard,
University of Illinois at Chicago, United
States

*Correspondence:

Matthew O. Schrenk
mattoschrenk@gmail.com

Specialty section:

This article was submitted to
Microbiological Chemistry and
Geomicrobiology,
a section of the journal
Frontiers in Microbiology

Received: 17 January 2017

Accepted: 04 May 2017

Published: 23 May 2017

Citation:

Crespo-Medina M, Twing KI, Sánchez-Murillo R, Brazelton WJ, McCollom TM and Schrenk MO (2017) Methane Dynamics in a Tropical Serpentinizing Environment: The Santa Elena Ophiolite, Costa Rica. *Front. Microbiol.* 8:916.
doi: 10.3389/fmicb.2017.00916

Uplifted ultramafic rocks represent an important vector for the transfer of carbon and reducing power from the deep subsurface into the biosphere and potentially support microbial life through serpentinization. This process has a strong influence upon the production of hydrogen and methane, which can be subsequently consumed by microbial communities. The Santa Elena Ophiolite (SEO) on the northwestern Pacific coast of Costa Rica comprises ~250 km² of ultramafic rocks and mafic associations. The climatic conditions, consisting of strongly contrasting wet and dry seasons, make the SEO a unique hydrogeological setting, where water-rock reactions are enhanced by large storm events (up to 200 mm in a single storm). Previous work on hyperalkaline spring fluids collected within the SEO has identified the presence of microorganisms potentially involved in hydrogen, methane, and methanol oxidation (such as *Hydrogenophaga*, *Methylbacterium*, and *Methylibium* spp., respectively), as well as the presence of methanogenic Archaea (such as *Methanobacterium*). Similar organisms have also been documented at other serpentinizing sites, however their functions have not been confirmed. SEO's hyperalkaline springs have elevated methane concentrations, ranging from 145 to 900 μM, in comparison to the background concentrations (<0.3 μM). The presence and potential activity of microorganisms involved in methane cycling in serpentinization-influenced fluids from different sites within the SEO were investigated using molecular, geochemical, and modeling approaches. These results were combined to elucidate the bioenergetically favorable methane production and/or oxidation reactions in this tropical serpentinizing environment. The hyperalkaline springs at SEO contain a greater proportion of Archaea and methanogens than has been detected in any terrestrial serpentinizing system. Archaea involved in methanogenesis and anaerobic methane oxidation accounted from 40 to 90% of total archaeal sequences. Genes involved in methanogenic metabolisms were detected from the metagenome of one of the alkaline springs. Methanogenic activities are likely to be facilitated by the movement of nutrients, including dissolved inorganic carbon (DIC), from surface water and their infiltration into serpentinizing groundwater. These data provide new insight into methane cycle in tropical serpentinizing environments.

Keywords: tropical serpentinization, methane, methanogenesis, metagenomics, bioenergetics

INTRODUCTION

Serpentinization is the aqueous alteration of low-silica ultramafic rocks, mainly olivine and pyroxenes, into serpentinite, brucite, magnetite, and other minerals (Moody, 1976). This reaction produces hydrogen gas (H_2) and the reducing conditions that favor the abiogenic synthesis of methane and higher molecular weight hydrocarbons through Fischer-Tropsch-type reactions (e.g., McCollom and Seewald, 2007; Proskurowski et al., 2008). Serpentinization also produces favorable conditions for the potential biogenic formation of methane through the activity of chemolithoautotrophic microorganisms, however the occurrence and relative importance of abiogenic vs. biogenic methanogenesis processes is enigmatic (Wang et al., 2015; Etiope, 2016; Kohl et al., 2016; Miller et al., 2016).

The relationship between serpentinization and life has been relatively well studied in submarine hydrothermal systems (Schrenk et al., 2004; Kelley et al., 2005; Brazelton et al., 2006; Quéméneur et al., 2014). The study of the microbiology and geochemistry of terrestrial serpentinites has accelerated in the past several years at numerous locations globally, where meteoric water infiltrates and interacts with obducted ultramafic rock and mixes with serpentinizing fluids. Such settings have been described in the Sultanate of Oman (Barnes and O’Neil, 1978; Bath et al., 1987; Miller et al., 2016), Italy (Cipolli et al., 2004), Portugal (Marques et al., 2008; Tiago and Veríssimo, 2013), Spain (Etiope et al., 2016), Canada (Brazelton et al., 2013; Szponar

et al., 2013), the Philippines (Abrajano et al., 1990; Cardace et al., 2015; Woycheese et al., 2015), and California (Barnes et al., 1967; Cardace et al., 2013; Morrill et al., 2013; Suzuki et al., 2013), among other locations.

More recently, a terrestrial serpentinization site was described in a tropical setting at the Santa Elena Ophiolite (SEO), which comprises over 250 km² of ultramafic rocks and mafic associations along the northwestern Pacific coast of Costa Rica (Sánchez-Murillo et al., 2014; **Figure 1**). This system is characterized by warm air temperature (up to 38°C during the dry season months) and extreme variation in precipitation conditions between wet (May–November) and dry (December–April) seasons, resulting in a distinctive hydrogeological setting (Sánchez-Murillo et al., 2014). These dynamic hydroclimatic conditions make the hyperalkaline springs at SEO unique, and potentially enhance rock weathering processes and the delivery of nutrients and oxidants likely stimulating subsurface microbial activity.

Microorganisms involved in the methane cycle are abundant in marine hydrothermal serpentinizing systems (Brazelton et al., 2006). At terrestrial serpentinization sites, however, even though there is abundant methane (Wang et al., 2015), there is less evidence of the presence and activity of methanogenic and methanotrophic microorganisms. Sequences related to the anaerobic methanotrophic archaea ANME-1a have been previously detected from the springs in Cabeço de Vide aquifer in Portugal (Tiago and Veríssimo, 2013). Methanogenic taxa have

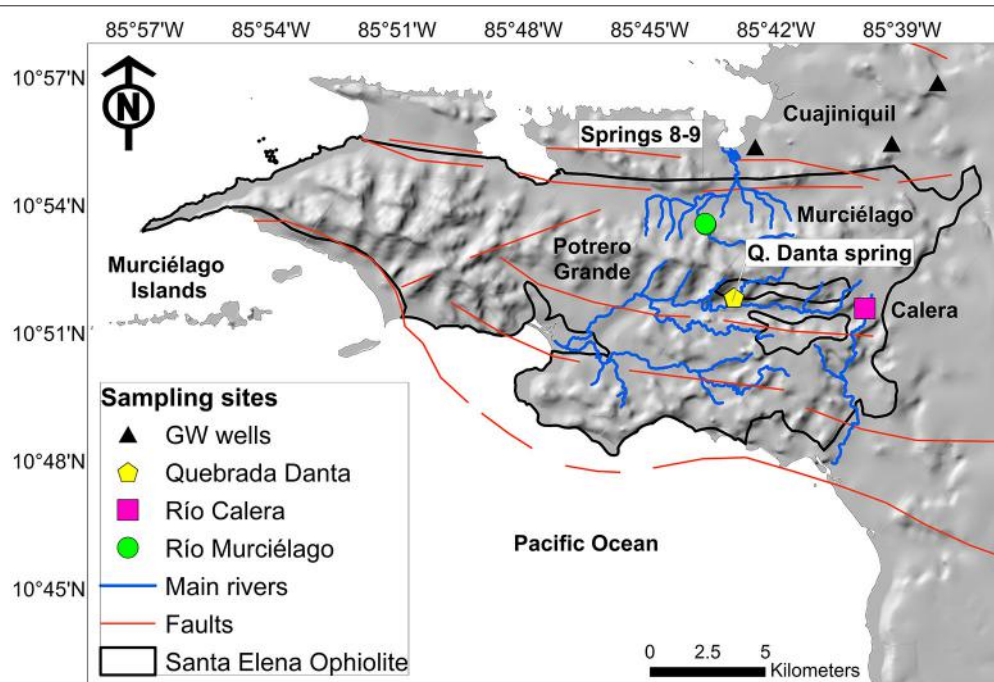


FIGURE 1 | Map of the study area. The bold-black line denotes the Santa Elena Ophiolite boundary, dominated by ultramafic mantle rocks based on Gazel et al. (2006). Sample locations are color-coded: alkaline spring systems within Murciélagos and Potrero Grande watersheds are identified by green and yellow symbols, respectively; black triangles denote groundwater wells; pink square stands for a control surface water site. Blue and orange lines are the main perennial rivers and faults, respectively.

been detected in springs from the Voltri Massif, Italy (Brazelton et al., 2017) and wells from the Samail Ophiolite in the Sultanate of Oman (Miller et al., 2016) and from carbonate samples collected from serpentinizing seeps in Manleluag Spring National Park, Philippines (Woycheese et al., 2015). Microcosm studies using ^{13}C -labeled substrates demonstrated that native microbial communities from The Cedars (California, USA) spring water and sediments were capable of methanogenesis and acetogenesis (Kohl et al., 2016). Previous work in SEO detected the presence of microorganisms involved in the methane cycle, such as methanotrophic bacteria from the families *Methylcoccaceae*, *Methylbacteriaceae*, and *Methylocystaceae*, and methanogenic archaea from the orders *Methanobacteriales*, *Methanocellales*, and *Methanomicrobiales* (Sánchez-Murillo et al., 2014). Here we investigate in more detail the presence of these organisms and their metabolic potential in fluids collected from different sites within this tropical serpentinizing setting, using molecular, geochemical, and modeling approaches. The results are discussed in light of the unique precipitation and hydrological processes within the SEO.

Hydroclimatic Conditions at SEO

Four regional air circulation processes predominantly control the climate of the SEO: NE trade winds, the latitudinal migration of the Intertropical Convergence Zone (ITCZ), cold continental outbreaks, and sporadic influence of tropical cyclones (Waylen et al., 1996; Sáenz and Durán-Quesada, 2015). These circulation processes produce two predominant rainfall maxima, one in May and June and the second one in August-September-October, which are interrupted by a relative minimum in July known as the Mid-Summer Drought (Magana et al., 1999; Maldonado et al., 2013). In addition to these circulation processes, the continental divide (i.e., a mountainous range that extends from NW to SE) also influences precipitation patterns across the country, dividing the territory into the Caribbean and Pacific slopes. The SEO (located on the northwestern Pacific slope) receives on average 1,464 mm/year of rainfall (based on 10 years of historical records at the Santa Rosa climatological station, Sánchez-Murillo et al., 2014). This region is highly dependent on the variations of the El Niño/Southern Oscillation cycles. For instance, La Niña (cold and wet phase) produces a considerable rainfall increase up to 3,000 mm, while El Niño (warm and dry phase) years are characterized by annual precipitation below 1,200 mm and a dry period usually covering 5–7 months. Seasonal temperature variation is low; mean annual maximum and minimum ambient temperatures are 31 and 23°C, respectively. During the dry period, maximum temperatures can reach up to 38°C (Sánchez-Murillo et al., 2014). The northwestern Pacific region of Costa Rica has estimated regional groundwater recharge rates of <300 mm/year (Mulligan and Burke, 2005). Baseflow recession starts in November and reaches its minimum in late April. Most of the groundwater recharge in the SEO occurs between May and October. Commonly, terrestrial serpentinization and alkaline spring studies have been conducted in temperate regions (e.g., Tablelands, Canada; California Coast Range, USA; Gruppo di Voltri, Italy; Othrys, Greece) and at subtropical sites (e.g., Samail, Oman). In these regions precipitation is mostly composed of

snow and rainfall events, meteoric recharge occurs in a short time during spring runoff or in relatively slow snowmelt rates. Coastal temperate sites might experience intermittent rainfall at relatively low intensities. Furthermore, in arid and semi-arid areas where precipitation events are scarce and isolated, infiltration is limited due to large evaporation losses. Contrary to the previous scenarios, in tropical environments like the SEO (Sánchez-Murillo et al., 2015), the Zambales Ophiolite and the Palawan Ophiolite (Abrajano et al., 1988; Cardace et al., 2015; Woycheese et al., 2015) precipitation amounts and rainfall intensities are usually greater and occur throughout several months, which facilitate infiltration and deep percolation, and thus, water-rock reactions, may be enhanced. The SEO differs from the Philippines serpentinites in that rainfall and recharge is punctuated into a short (few-month) interval.

MATERIALS AND METHODS

Site Description and Sample Collection

During a field sampling campaign in February 2014 (dry season), fluid and gas samples were collected from three hyperalkaline springs: Spring 9 and Spring 8, located at the Murciélagos river watershed, and Quebrada Danta (Q. Danta) located in the Potrero Grande watershed (Figure 1). Upstream locations to the springs were sampled (Murciélagos Upstream and Q. Danta Upstream, respectively) for comparison purposes. Three private and municipal wells located nearby the SEO were also sampled (30–70 m depth): Pozo Murciélagos (P. Murciélagos), Pozo Nuevo (P. Nuevo), and Pozo Aguas Calientes (P. Aguas Calientes), as well as one control location at Río Calera (R. Calera) (Figure 1). Although the groundwater wells are located outside SEO, their recharge and flow paths originate within the ophiolite complex (Sánchez-Murillo et al., 2014).

Potrero Grande watershed (Figure 1) is characterized by a 10.3 km long floodplain with very steep tributaries (~33% slope), such as Q. Danta. Active erosion processes resulted in greater peridotite exposure among all watersheds in the SEO. Vegetation (i.e., deciduous trees) is mostly located in riparian areas, whereas tropical dry forest grass is common on the upper part of the stream canyons. Carbon and nutrient contributions from the topsoil layer are negligible during baseflow periods, and it solely represents subsurface conditions. The hyperalkaline system (Q. Danta) within Potrero Grande is located in the headwaters about 121 m a.s.l. Murciélagos River is characterized by a relatively narrow valley and a greater presence of riparian vegetation. The hyperalkaline springs within the Murciélagos watershed are located at the bottom portion of the catchment (78 m a.s.l.). Overall, field evidence suggests that hyperalkaline seepages are numerous and are active late in the baseflow period of perennial streams (December to April). Hyperalkaline springs often form shallow pools characterized by moderate turbidity, thin white films of carbonate precipitates, and extensive yellow-brown carbonate deposits.

Surface waters were exclusively collected at the flowing sections of streams to avoid stagnant ponds with biased evaporative signals (Sánchez-Murillo and Birkel, 2016). Groundwater samples were collected using Teflon sterile and

disposable geobailers (Geotech Environmental Equipment, Colorado, USA) and automated pumping (P. Murciélagos). Spring samples were collected according to following criteria: evidence of continuous water flow from the rock, close to bubbling zones, and near the most reductive point. The sampling campaign was designed to target baseflow conditions. Baseflow is described as the cumulative outflow from all upstream riparian aquifers during rainless periods (Brutsaert, 2005), therefore, it represents the most average geochemical characteristics of any particular watershed or aquifer (Sánchez-Murillo et al., 2015).

Fluid and gas samples were collected from all sites following methods in the subsections below. Standard physicochemical measurements (i.e., water temperature, pH, Eh, electrical conductivity (EC), total dissolved solids, and salinity) were recorded using handheld probes (Oakton PC Testr 35 and Oakton Testr 10), which were calibrated twice a day using standard solutions.

Gas and Aqueous Geochemical Characterization

Water samples for dissolved methane concentration and isotopic composition analyses were collected from the spring source using a bubble-free 60 mL syringe with Tygon tubing attached. The samples were carefully transferred to a He-purged 160 mL serum bottle and crimp sealed immediately. For H₂, a 10 mL sample was collected following the same protocol and transferred to a 14 mL serum vial. For dissolved inorganic carbon (DIC), a 14 mL serum vial, containing one NaOH pellet, was filled to the top, capped with a butyl rubber stopper, and microbial activity was arrested using saturated ZnCl₂ (80 μ M final conc.). All samples were collected in triplicate and were sent for analysis as a contracted service to JBL Analytical Services (<http://www.joyeresearchgroup.uga.edu>; University of Georgia, GA, USA).

The filtrate from the 0.2 μ m Sterivex filter cartridges (EMD Millipore, Billerica, MA) used for molecular sampling (see methods below) was collected into an acid-cleaned 30 mL Nalgene bottle (Tupas et al., 1994; Joye et al., 2010) for dissolved organic carbon (DOC) and nitrogen and phosphorous species: total dissolved nitrogen (TDN), ammonium (NH_4^+), nitrite (NO_2^-), nitrite + nitrate ($\text{NO}_2^- + \text{NO}_3^-$), total dissolved phosphorous (TDP), and orthophosphate (PO_4^{3-}). Samples were transported in cold bags from the field and were frozen at -20°C immediately upon arrival to the field station (2–6 h after sampling). Samples were sent for analysis to JBL Analytical Services (University of Georgia, GA, USA).

Samples for water stable isotope analysis were collected in 30 mL glass E-C borosilicate bottles with tetrafluoroethylene (TFE)-lined caps (Wheaton Science Products, USA). Bottles were filled completely, leaving no head space, covered with parafilm (Thermo Scientific, USA) avoiding exchange with atmospheric moisture, and stored upside down at 5°C until analysis. Water stable isotope analyses were conducted at the Stable Isotope Research Group facilities of the National University (Heredia, Costa Rica) using a Cavity Ring Down Spectroscopy (CRDS) water isotope analyzer L2120-i (Picarro, USA). The secondary standards were: Moscow Tap Water, MTW ($\delta^2\text{H} = -131.4\text{\textperthousand}$,

$\delta^{18}\text{O} = -17.0\text{\textperthousand}$), Deep Ocean Water, DOW ($\delta^2\text{H} = -1.7\text{\textperthousand}$, $\delta^{18}\text{O} = -0.2\text{\textperthousand}$), and Commercial Bottled Water, CAS ($\delta^2\text{H} = -64.3\text{\textperthousand}$, $\delta^{18}\text{O} = -8.3\text{\textperthousand}$). MTW and DOW standards were used to normalize the results to the VSMOW2-SLAP2 scale, while CAS was used as a quality control and drift control standard. The analytical long-term precision was: $\pm 0.5\text{\textperthousand}$ (1 s) for $\delta^2\text{H}$ and $\pm 0.1\text{\textperthousand}$ (1 s) for $\delta^{18}\text{O}$.

Cell Counts

Fluids were preserved in 3.7% (v/v) formaldehyde (final concentration) for enumeration of cell abundances and stored at 4°C until processing. The preserved fluids were filtered through a 0.2 μ m black polycarbonate filters (Whatman; PA, USA), and cells were stained with 1 μ g/ml of 4',6-diamidino-2-phenylindole (DAPI) and counted by epifluorescence microscopy using appropriate filter sets according to previously published protocols (Hobbie et al., 1977; Schrenk et al., 2003).

DNA Extraction

For molecular characterization of the microbial communities, between one to three liters of fluids were filtered in the field though 0.22 μ m SterivexTM -GV filter units (EMD Millipore, MA, USA) using a Masterflex[®] E/S portable sampler (Cole-Parmer, IL, USA). Filters were covered with ice during the filtration process, then capped and flash frozen in liquid nitrogen, and stored at -80°C until processing. Extraction of total genomic DNA followed previously described protocols (Huber et al., 2002; Sogin et al., 2006). DNA extracts were purified with the DNA Clean and Concentrator^{TM-5} kit (Zymo Research, CA, USA) according to the manufacturer's instructions. DNA extracts were quantified with a Qubit[®] dsDNA High Sensitivity Assay kit in a Qubit[®] 2.0 Fluorometer (Life Technologies, NY, USA).

16S rRNA Gene Enumeration

Quantification of 16S rRNA gene copies were determined by quantitative polymerase chain reaction (q-PCR) on a BioRad C-1000 thermo-cycler with a q-PCR module using the SsoAdvanced SybrGreen Assay (BioRad; CA, USA). Domain-specific primers, 958F and 1048R for Archaea and 967F and 1064R for Bacteria, targeted the V6 hypervariable region of the 16S rRNA gene (Sogin et al., 2006). Gene copy numbers were calculated using standard curves generated by amplification of DNA from *Methanocaldococcus jannaschii* for Archaea and *Escherichia coli* for Bacteria. Amplification efficiencies were 70% for the Archaeal and 93% for the Bacteria qPCR reactions, respectively.

16S rRNA Gene Tag Sequencing and Data Analysis

Purified DNA was submitted to the Josephine Bay Paul Center, Marine Biological Laboratory (<http://www.mbl.edu/jbpc/>) for amplicon sequencing of archaeal and bacterial 16S rRNA genes with an Illumina MiSeq instrument with domain-specific primers targeting the V4-V5 hypervariable regions of the 16S rRNA gene (518F-926R for bacteria and 517F-958R for archaea), following the methods described by Nelson et al. (2014). Quality-filtering of the sequences was conducted via the Visualization and Analysis of Microbial Population Structures (VAMPS) pipeline (Huse

et al., 2014). These data are publicly available at <https://vamps.mbl.edu/> under the project code DCO_BRZ and the sample code Serp_SEO as well as the NCBI SRA database under SRP096759 and Bioproject accession number PRJNA361138.

The 16S rRNA gene amplicon sequences were processed as described previously by Brazelton et al. (2017). Briefly, further quality-control of the sequences was completed in mothur (v. 1.36.1; Schloss et al., 2009) to remove sequences with homopolymers >9 and ambiguous bases >0. The mothur command pre.cluster (diff = 1) was run, reducing the number of unique samples from 1,531,396 to 1,044,544 for Bacteria and 862,835 to 616,217 for Archaea. The resulting unique sequences were considered operational taxonomic units (OTUs) for this study. Taxonomic classification of all OTUs was performed with mothur using the SILVA reference alignment (SSURef v.123.1) and taxonomy outline (Pruesse et al., 2007).

This current study focuses on the methane cycling members within the bacterial and archaeal communities. To assess the abundance of methanotrophic bacteria, the following genera were searched within the taxonomic dataset: *Methylococcus*, *Methylocaldum*, *Methylohalobius*, *Methyothermus*, *Methylobacter*, *Methylomicrobium*, *Methylomonas*, *Methylosarcina*, *Methylosoma*, *Methylosphaera*, *Crenothrix*, and *Clonothrix* of the family *Methylococcaceae* within the Gammaproteobacteria; *Methylocystis* and *Methylosinus* of the family *Methylocystaceae* and *Methylocella* and *Methylocapsa* of the family *Beijerinckiaceae* within the Alphaproteobacteria (Hanson and Hanson, 1996; Op den Camp et al., 2009 and the references therein). Additionally, the members of the genus *Methylacidiphilum* within phylum Verrucomicrobia (Op den Camp et al., 2009) and the Ca. genus *Methylomirabilis* of the candidate phylum NC10 (Ettwig et al., 2010) were also searched for within the bacterial taxonomic dataset. Archaea classified as belonging to Anaerobic Methane Oxidizing Archaea (ANME) were identified as potential methanotrophs. For methanogenic archaea, sequences taxonomically classified as belonging to the orders Methanopyrales, Methanococcales, Methanobacterales, Methanomicrobiales, Methanocellales (Sakai et al., 2008), Methanoplasmatales (Paul et al., 2012), and Methanosarcinales (Thauer et al., 2008) were identified. The relative abundances of these taxa were calculated with the get.relabund command in mothur.

Metagenomic Sequencing and Data Analysis

Purified DNA from two samples (Spring 9 and Murciélagos Upstream) was submitted to the Josephine Bay Paul Center, Marine Biological Laboratory for shotgun metagenomic sequencing. Metagenomic libraries were constructed with the Nugen Ultralow Ovation kit according to the manufacturer's instructions. Paired-end sequencing with a 100 cycle Illumina HiSeq run generated partial ~30 bp overlaps, and six libraries were multiplexed per lane. The raw metagenomic sequence data are publicly available in the NCBI SRA database under the BioProject accession number PRJNA340462.

Quality control of the metagenomic reads was performed to remove low quality and sequencing artifact reads. Cutadapt v.1.9 (Martin, 2011) was used to identify and remove reads with Illumina adapters at the 5'-end of the sequence and to trim Illumina adapters at the 3'-end of the sequence. Identical and 5'-prefix replicates were also removed (Gomez-Alvarez et al., 2009). Nucleotides (0–3) at the beginning and end of reads were cropped from all reads in that sample if those positions exhibited nucleotide frequencies inconsistent with the nucleotide frequency distribution for the rest of the read. Low-quality bases were removed from the ends of the reads, and the remaining sequence was scanned 6 base pairs at a time and trimmed where the mean quality score fell below a score of 28. Reads that did not pass a minimum length threshold of 62 bp after quality and adapter trimming were removed from the dataset. Metagenomic assembly of each sample was performed by Ray Meta v.2.3.1 (Boisvert et al., 2012). A kmer of 61 was chosen after manual inspection of assemblies with kmer values of 31, 41, 51, and 61. High-quality reads from each sample were mapped onto each assembly with Bowtie2 v.2.2.6 (Langmead and Salzberg, 2012). Metagenomic assembly statistics can be found in Table S1. The Prokka pipeline (Seeman, 2014) was used for gene prediction and functional annotation, with the arguments –metagenome and –proteins in Prokka v.1.12 with gene prediction by Prodigal v.2.6.2 (Hyatt et al., 2010). The database provided was the Kyoto Encyclopedia of Genes and Genomes, release 2016-09-26 (Ogata et al., 1999). Predicted protein abundances (in units of reads per kilobase) were calculated with HTSeq v.0.6.1 (Anders et al., 2014), and the final normalized coverage was calculated by normalizing to the total number of fragments in the smallest metagenome. A summary of the methane-cycling genes and their KEGG IDs searched for within this dataset can be found in Table S2.

Bioenergetics Calculations

To assess the amount of chemical energy potentially available to support chemolithoautotrophic organisms at the study sites, a series of calculations were performed to estimate the Gibbs energy of several metabolic reactions based on the measured fluid compositions. For the calculations, fluid speciation calculations were first performed with Geochemist's Workbench (Aqueous Solutions LLC, Champaign, IL) to estimate activities of dissolved species involved in the metabolic reactions, such as dissolved CO₂. The default thermo.com.V8.R6+tdat database supplied with the program was used for the calculations. Since data were available for only some components of the fluid, nominal amounts of Na and Cl (10–15 mM for Na and Cl) were included in the calculations to account for the measured salinity and achieve charge balance since these are typically the major dissolved ion components at sites of terrestrial serpentinization (e.g., Morrill et al., 2013).

The amount of energy available from several potential metabolic reactions involving methane (Tables S3, S4) was then calculated according to the familiar equation:

$$\Delta G = \Delta G^\circ + RT \ln Q \quad (1)$$

where ΔG is the Gibbs energy of reaction (J/mol), ΔG° the standard Gibbs energy, R the universal gas constant (J/mole K), T the temperature (K), and Q the activity quotient of the compounds involved in the reaction. The latter factor, Q, takes into account the contribution of the fluid composition to the Gibbs energy of each reaction, and was calculated using the activities determined by the fluid speciation models. Values of the ΔG° were calculated using SUPCRT92 (Johnson et al., 1992) with the default database. Since measurements of dissolved O₂ were not available, calculations for aerobic methanotrophy were performed assuming concentrations equivalent to 0.1 and 1.0% of saturation with respect to air (Table S3). Similarly, calculations for acetoclastic methanogenesis assume acetate accounts for 1 or 10% of measured DOC concentrations (Table S4), which are within the range previously reported for the Coast Range Ophiolite (Crespo-Medina et al., 2014). To better facilitate comparisons between different metabolic pathways, the total amount of energy available from each of these reactions per liter of fluid was estimated by multiplying the Gibbs energy by the concentrations of the reaction components in the fluids, taking

into account which of the reactants was the limiting component (e.g., McCollom and Shock, 1997).

RESULTS

Aqueous, Volatile, and Stable Isotope Geochemistry

Fluids from SEO's springs are highly alkaline with pH ranging between 11.2 and 11.6 and highly reducing, with an oxidation-reduction potential (ORP) ranging from -380 to -251 mV. Overall, surface water from upstream sites and groundwater in proximity of SEO are relatively alkaline with pH values ranging from 7.54 up to 8.90. Upstream sites and groundwater wells exhibited oxidizing conditions with ORP values ranging from +66 up to +97 mV. These conditions are consistent with springs sampled at other terrestrial serpentinization sites (Schrenk et al., 2013, and reference therein). The fluid temperature ranged from 26.1° to 29.2°C, with the temperature at the springs measuring 1–3°C greater than the respective upstream counterparts (Table 1). Electrical conductivity (EC) ranged from 470 up to 700

TABLE 1 | Physicochemical, geochemical, and isotopic analysis of samples collected from Santa Elena Ophiolite*.

Sample name	Q. Danta	Q. Danta Upstream	Spring 8	Spring 9	Murciélagos Upstream	R. Calera	P. Murciélagos	P. Nuevo	P. Aguas Calientes
Sample type	Spring	River	Spring	Spring	River	River	Well	Well	Well
PHYSICOCHEMICAL PARAMETERS									
pH	11.59	8.42	11.54	11.54	8.9	8.61	7.54	8.3	7.26
Temp. (°C)	29.2	27.9	26.1	26.4	24	25.3	28	30.2	30.2
Conductivity (μS/cm)	542	470	543	466	492	493	700	696	603
TDS (ppm)	358	334	386	333	306	349	498	535	428
Salinity (ppm)	412	357	414	351	326	372	535	496	459
ORP (mV)	-251	66	-331	-348	35	148	97	76	70
AVERAGE GEOCHEMICAL PARAMETERS (μM)									
DOC	5.6	103.0	73.2	41.2	67.1	59.5	11.6	20.2	25.9
DIC (μM)	126.3	597.3	227.0	254.3	533.7	663.3	748.0	417.7	644.3
δ ¹³ C-CO ₂ (‰)	-20.1	-17.9	-17.9	-20.8	-19.8	-18.6	-19.5	-18.6	-18.7
TDN	0.4	6.6	14.2	1.7	1.7	2.6	62.4	3.5	39.2
NOx	0.8	2.5	0.3	0.2	0.3	1.8	58.3	0.2	36.8
NO ₂	0.0	0.1	0.0	0.0	0.1	0.0	0.0	0.0	0.0
NH ₄ ⁺	1.3	0.6	1.7	0.8	0.1	0.1	2.1	4.1	1.5
DON	bdl ^{**a}	3.5	12.2	1.1	1.3	0.7	2.0	bdl	0.9
PO ₄ ³⁻	0.1	1.6	0.2	0.3	1.6	1.9	2.7	1.7	2.7
TDP	0.1	0.2	0.1	0.1	0.2	0.2	0.4	0.6	1.1
AVERAGE GASEOUS GEOCHEMISTRY AND ISOTOPIC COMPOSITION									
CH ₄ (μM)	145.0	0.3	870.7	912.3	14.3	0.3	0.3	0.3	0.2
δ ¹³ C-CH ₄ (‰)	-44.0	bdl ^b	-0.9	-2.2	1.3	bdl	bdl	bdl	bdl
H ₂ (μM)	38.3	9.2	10.9	53.1	0.8	23.7	1.0	0.8	1.0
WATER ISOTOPES									
δ ¹⁸ O (‰)	-7.18	-4.33	-7.22	-7.18	-7.02	-6.65	-7.12	-6.84	-6.65
δ ² H (‰)	-50.0	-33.4	-50.4	-50.4	-45.7	-45.1	-47.6	-48.9	-45.1

*Complete data set is presented in Table S5.

^{**}bdl, below detection level.

^aLimit of detection for DON was 0.1 μM.

^bSamples with methane concentration of 0.3 μM or less were within the limit of the detection of the instrument, but did not give a reliable δ¹³C-CH₄ signature (measurements with high standard deviation) and thus were not taken into consideration in this analysis.

$\mu\text{S}/\text{cm}$. EC values upstream from the hyperalkaline springs were consistently lower, while groundwater wells presented the greatest EC values. The DOC concentration in the spring fluids ranged from 5.6 to 73.2 μM (Table 1), while upstream sites ranged from 67.1 to 103.0 μM . Groundwater wells presented low DOC values ranging from 11.6 up to 25.9 μM . The fluids are enriched in nitrogen and phosphorous species compared to other terrestrial serpentinizing sites (Tiago et al., 2004; Morrill et al., 2013; Cardace et al., 2015), though to a lesser extent than was previously reported for fluids from the Coast Range Ophiolite in California (Crespo-Medina et al., 2014). Both DOC and nutrients (nitrogen and phosphorous species) were slightly elevated at Spring 8 and Spring 9 compared to Q. Danta (Table 1). Hyperalkaline springs and groundwater wells presented a nearly uniform $\delta^{18}\text{O}$ (-6.65 to $-7.22\text{\textperthousand}$) and $\delta^2\text{H}$ (-45.1 to $-50.4\text{\textperthousand}$) composition. The sampling site upstream from Q. Danta spring was more enriched ($\delta^{18}\text{O} = -4.33\text{\textperthousand}$ and $\delta^2\text{H} = -33.4\text{\textperthousand}$).

Methane concentrations in SEO's spring fluids ranged from 145 to 912 μM , which is in the same range as previously described for the Coast Range Ophiolite (CA, USA) (210–1832 μM ; Crespo-Medina et al., 2014), serpentinite springs at Voltri Massif (155–733 μM ; Brazelton et al., 2017), and at tropical springs from Zambales and Palawan Ophiolites in Philippines 0–400 μM ; Cardace et al., 2015), but slightly elevated when

compared to springs at Tablelands (20.0–26.2 μM ; Szponar et al., 2013). Methane concentrations were 0.3 μM at the Q. Danta upstream and 14.3 μM at the Murciélagos upstream sites (Table 1). However, it is important to highlight that several bubbling sites within the Murciélagos River's upstream channel were observed, which may have contributed to the methane concentrations measured in this stream. Methane concentrations in the control stream (R. Calera) and nearby groundwater wells were consistently below 0.3 μM . Hydrogen concentrations at the springs were elevated, ranging from 10.9 up to 53.1 μM , which is greater than previously described for the California site (CROMO, 0.2–0.7 μM ; Crespo-Medina et al., 2014), and consistent with what has been previously observed at Voltri Massif (0.5–26.8 μM ; Brazelton et al., 2017), but lower to that reported from Tablelands (585–747 μM ; Szponar et al., 2013), and from Zambales Ophiolite (0–495.5 μM ; Cardace et al., 2015). Spring 9 had the greatest methane and hydrogen concentrations (Table 1). Groundwater wells presented lower hydrogen concentrations ($<0.8\text{ }\mu\text{M}$). The spring samples contain lower DIC concentration (ranging between 126 and 254 μM) than the background samples (417–748 μM). Even though DIC at the SEO springs is greater than at most terrestrial serpentinizing sites; e.g. in the Voltri Massif springs in Italy, DIC ranged from 7.8 to 29 μM (Brazelton et al., 2017), at

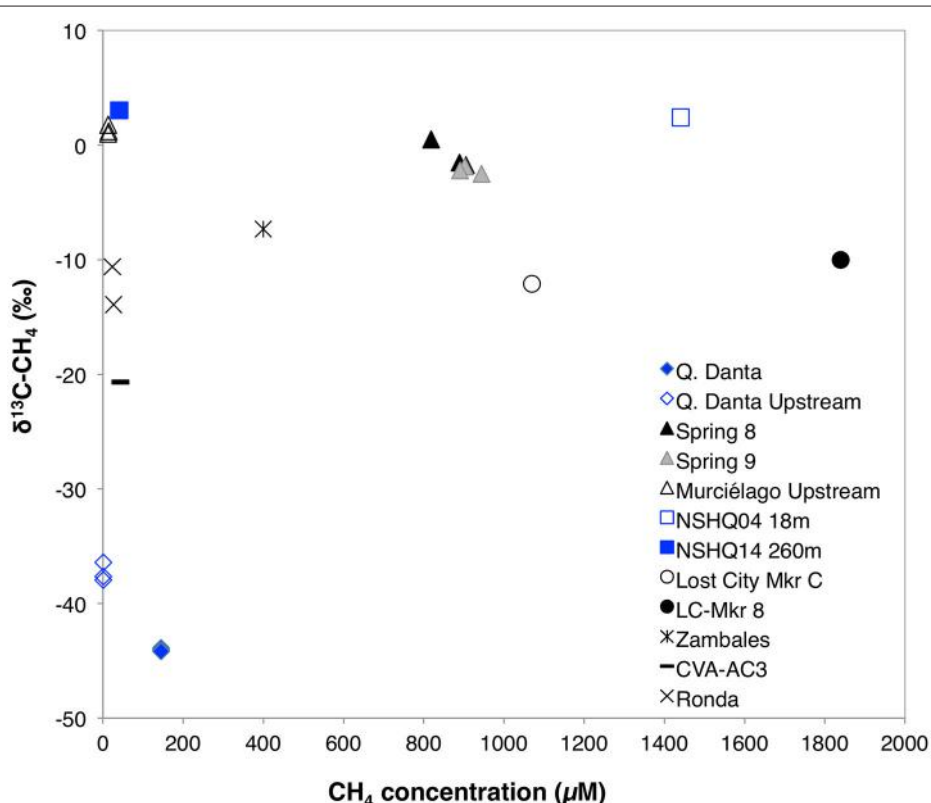


FIGURE 2 | Concentration vs. stable isotopic signature for dissolved methane in fluids from SEO in comparison with other serpentinizing fluids. Samail Ophiolite data (red squares) was obtained from Miller et al. (2016) and Etiope (2016); Lost City data (circles) was obtained from Proskurowski et al. (2008); Zambales Ophiolite data (blue cross) was obtained from Cardace et al. (2015); and Cabeço de Vide data (black asterisk) was obtained from Etiope et al. (2013).

The Cedars' springs it ranged from 6 to 70 μM (Morrill et al., 2013), while at CROMO, it ranged from 21 to 63 μM in fluids collected from established wells and 194–210 μM in a newly-drilled well (Crespo-Medina et al., 2014), the levels are 2–15 times lower than what was previously reported from another tropical serpentinizing site in Phillipines (250–3216 μM ; Cardace et al., 2015). Samples with greater methane concentrations (Springs 8 and 9 within Murciélagos river) were enriched in $^{13}\text{CH}_4$ (Table 1, Figure 2), relative to a spring with moderate methane concentrations (Q. Danta) (Table 1, Figure 2). A detailed table with the geochemistry results from individual replicates is presented as a supplementary material (Table S5).

DNA Yields and Cell Abundances

In general, the hyperalkaline springs had slightly lower biomass than their respective upstream samples, as suggested from the DNA yield (ng/L) and cell count data (cells/ml) (Table 2), and slightly higher abundances than neutral pH groundwater wells. Conversely, the wells had the highest average abundances of archaeal amplicons, followed by the springs, and the upstream “background” samples (Table 2).

Abundance of Methanotrophs and Methanogens from 16S rRNA Gene Sequencing

Based upon tag sequencing of 16S rRNA marker genes, sequences related to known methanotrophic bacteria comprise <2% of the total bacterial 16S rRNA gene sequences in all the samples, except in the fluids from P. Aguas Calientes, where sequences related to these microorganisms represent ~3–7% of the total sequences (Figure 3). From 1 to 2% of the sequences in P. Aguas Calientes belong to the Phylum NC10, whose members are capable of NO-dismutation coupled to methane oxidation (Ettwig et al., 2010).

On the other hand, archaeal sequences related to the methane cycling (methanogenesis and AOM), accounted for ~40 to 90% of the archaeal 16S rRNA gene sequences in spring water samples, 15 to 40% in the upstream samples, and 0–15% in the control river sample (R. Calera) and in groundwater well samples (Figure 4) suggesting the importance of methane-metabolizing organisms in this system. The majority of the archaeal sequences in the Spring 8 sample belong to the order Methanosaecinales, which for the most part include methanogenic Archaea. However, it should be noted that Methanoperedens, a member of the ANME-2d clade, falls within Methanosaecinales and was detected in Spring 8 in low abundances within the 16S rRNA amplicon dataset. The majority of the sequences in Spring 9 and Q. Danta belong to the ANME-1b group, a group that is thought to represent obligate methanotrophs (Hinrichs et al., 1999).

Metagenomic Analysis of the Methanogenesis Pathway

Metagenomic sequences were obtained from Spring 9 and Murciélagos Upstream, and the analysis described here focuses only on the identification of genes involved in the methane cycle (Table S2). Genes involved in aerobic methanotrophy, such

TABLE 2 | Microbial biomass abundance data for samples collected from Santa Elena Ophiolite.

Sample name (replicate)	DNA yield (ng/L)	Archaeal 16S copies per mL of sample	Bacterial 16S copies per mL of sample	Cell counts (cells/mL)
Q. Danta (1)	34.4	2.00×10^3	1.05×10^4	2.90×10^4
Q. Danta (2)	57.7	8.24×10^3	2.74×10^4	4.15×10^4
Q. Danta (3)	78.2	4.92×10^3	2.68×10^4	3.37×10^4
Q. Danta	767.8	2.96×10^4	2.29×10^5	8.64×10^4
Upstream (1)				
Q. Danta	2111.4	3.51×10^4	4.47×10^5	1.94×10^4
Upstream (2)				
Q. Danta	1004.1	2.99×10^1	9.63×10^3	1.63×10^4
Upstream (3)				
Spring 8 (1)	68.3	5.40×10^3	1.66×10^4	3.44×10^4
Spring 8 (2)	1499.0	5.55×10^4	2.71×10^5	4.39×10^4
Spring 8 (3)	366.6	1.74×10^4	8.37×10^4	7.18×10^4
Spring 8 (4)	559.7	9.73×10^3	6.90×10^4	2.66×10^4
Spring 9 (1)	501.8	3.34×10^4	1.74×10^5	1.90×10^5
Spring 9 (2)	552.3	3.11×10^4	1.63×10^5	1.09×10^5
Spring 9 (3)	518.3	3.74×10^4	2.15×10^5	1.33×10^5
Murciélagos	972.0	5.54×10^4	7.20×10^5	2.29×10^5
Upstream (1)				
Murciélagos	1096.4	5.71×10^4	7.55×10^5	2.21×10^5
Upstream (2)				
Murciélagos	1185.1	3.58×10^4	6.30×10^5	7.15×10^4
Upstream (3)				
R. Calera (1)	439.3	2.01×10^4	7.18×10^4	7.76×10^4
R. Calera (2)	283.4	3.46×10^3	1.20×10^4	5.17×10^4
R. Calera (3)	224.7	3.14×10^3	1.07×10^4	1.14×10^4
P. Murciélagos (1)	97.6	1.02×10^4	1.41×10^4	7.49×10^3
P. Murciélagos (2)	11.4	1.82×10^3	2.45×10^3	Bdl*
P. Murciélagos (3)	13.1	2.06×10^3	2.76×10^3	Bdl
P. Nuevo (1)	748.5	6.84×10^4	1.55×10^5	9.39×10^4
P. Nuevo (2)	677.5	ND	1.57×10^5	7.88×10^4
P. Nuevo (3)	599.9	6.21×10^4	1.58×10^5	1.90×10^5
P. Aguas	168.5	2.07×10^4	2.87×10^4	2.54×10^4
Calientes (1)				
P. Aguas	159.9	1.27×10^4	2.03×10^4	Bdl
Calientes (2)				
P. Aguas	309.1	1.79×10^4	8.03×10^4	4.51×10^4
Calientes (3)				

ND, not determined; bdl, below detection limit.

*detection limit for cell counts was 6.98×10^3 cells per mL.

as particulate methane monooxygenase (*pmoA*) or methanol dehydrogenase (*mxfA*) were not detected in the metagenomic assemblies (Table S2). However, when investigating genes involved in methanogenesis pathways (Figure 5), we were able to detect all the key genes involved in acetoclastic methanogenesis, hydrogenotrophic methanogenesis, and methanogenesis from formate in the Spring 9 metagenome. The genes for methylotrophic methanogenesis were not detected in either metagenome. The metagenome of the Murciélagos Upstream sample contained only genes involved in initial steps of methanogenesis, such as those involved in the conversion

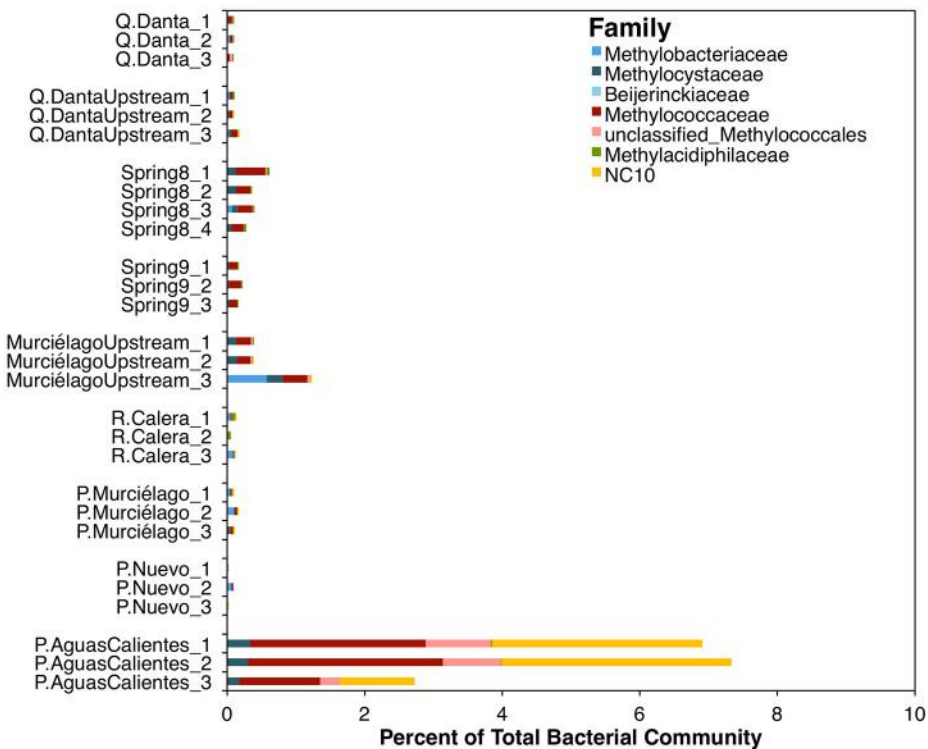


FIGURE 3 | Relative abundance of methanotrophic OTUs within the bacterial 16S rRNA amplicon dataset.

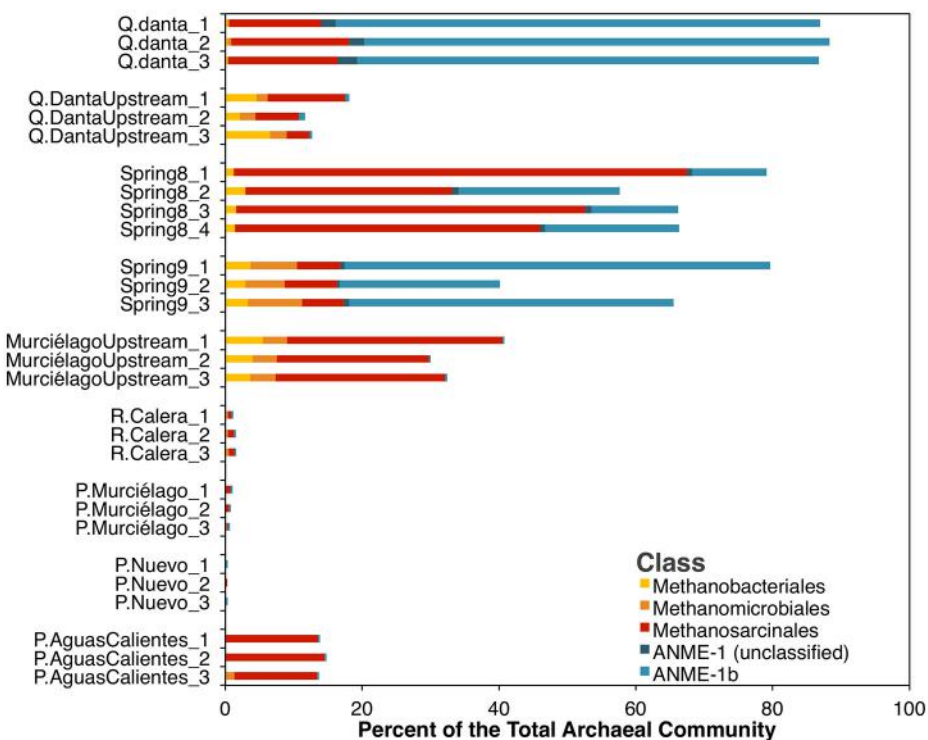
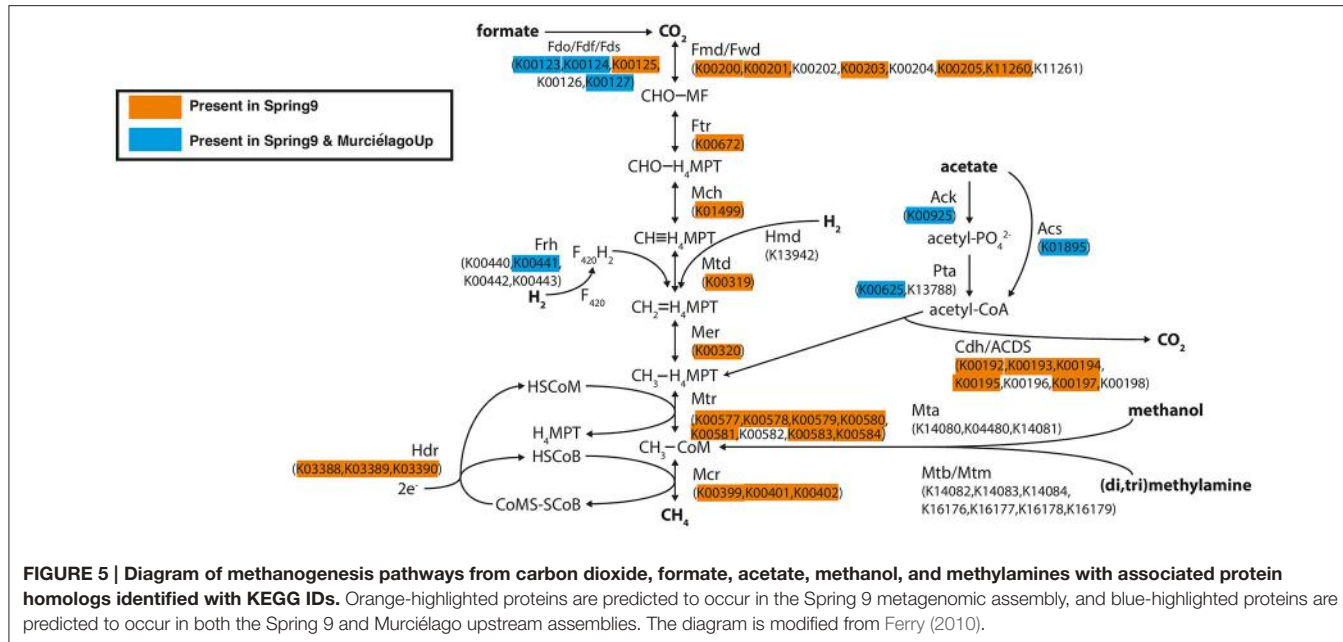


FIGURE 4 | Relative abundance of methane-cycling archaea within the archaeal 16S rRNA amplicon dataset. Families generally associated with methanogenesis are in shades of yellow and red, while taxa generally associated with anaerobic methane-oxidation are in blue.



of formate to CO_2 , of acetate to acetyl Co-A and for the incorporation of H_2 into di-iron flavoprotein F_{420}H_2 oxidase.

Bioenergetics of Methane Metabolism

For Spring 8 and Spring 9, the bioenergetics calculations reflect that there is more energy (kJ per L) from acetoclastic methanogenesis than hydrogenotrophic methanogenesis (although that depends, in part, on assumptions about the composition of DOM; **Figure 6**, Table S4), and both have greater energy yields than anaerobic methane oxidation. For Q. Danta the bioenergetics calculations reflect that there is more energy available from hydrogenotrophic methanogenesis than acetoclastic methanogenesis. Bioenergetic calculations for this system demonstrate that anaerobic methane oxidation is limited by the abundance of electron acceptors (**Figure 6**, Table S3).

DISCUSSION

As in other serpentinization-influenced ecosystems, the springs at SEO have fluids that are highly alkaline, reduced, and enriched in methane and hydrogen. The fluids at SEO had elevated concentrations of DIC and nutrients when compared to previously studied serpentinizing springs, this might be due in part by the large input of meteoric water to the system and short mean residence times. Microorganisms involved in methane cycling were detected in all three alkaline springs studied. Aerobic methanotrophic bacteria were less prevalent than ANME or methanogenic archaea in spring fluids. These results are consistent with our bioenergetics calculations, which indicate that aerobic methanotrophy is not likely to be a favorable process at depth in this system. Sequences related to ANME-1b methanotrophic archaea and to methanogens from the orders Methanosaecinales, Methanomicrobiales and

Methanobacteriales accounted for 40–90% of the total archaeal sequences in all three hyperalkaline spring fluids.

The enriched $\delta^{13}\text{C-CH}_4$ signature of the Spring 8 and Spring 9 samples suggests that a majority of methane in these samples is likely to be abiotically generated (Whiticar, 1999), although biological methanogenesis from $\delta^{13}\text{C}$ -enriched substrates cannot be excluded with the current data set (Etiope, 2016). At Spring 8 and Spring 9, the biological signal of methanogenesis may be overshadowed by abiogenic contributions. On the other hand, the detection of a ^{13}C depleted stable isotope signature ($\sim -40\text{\textperthousand}$) in methane from *Q. Danta* may represent contributions from acetoclastic methanogenesis (Whiticar, 1999).

Bioenergetic calculations indicate that methanogenesis (acetoclastic and hydrogenotrophic) yields more energy than anaerobic methanotrophy, but the sample with the most depleted $\delta^{13}\text{C-CH}_4$ (Q. Danta) was dominated by ANME-1b. The detection of ANME-1 archaea in methanogenic sediments from White Oak River estuary, however, suggests that these organisms are not exclusively methanotrophs and that they might be capable of methanogenesis (Lloyd et al., 2011). Alternatively, the isotopic signature may represent a combination of hydrogenotrophic methanogenesis and subsequent methane oxidation, resulting in the relatively “heavy” isotopic signature of methane from Q. Danta.

The fact that methanogenesis is a relatively favorable bioenergetic process and that methanogens and ANME-1 were abundant at Spring 8 and Spring 9, even though the $\delta^{13}\text{C-CH}_4$ in these samples is very enriched, might be explained by the hydrology of the system. Spring 8 and Spring 9 are located at the bottom of Murciélagos watershed, where water flow paths from the recharge zone (~700 m a.s.l.) to the hyperalkaline springs outflow (78 m a.s.l.) are expected to be longer. Q. Danta is located in a steeper watershed but closer to the recharge

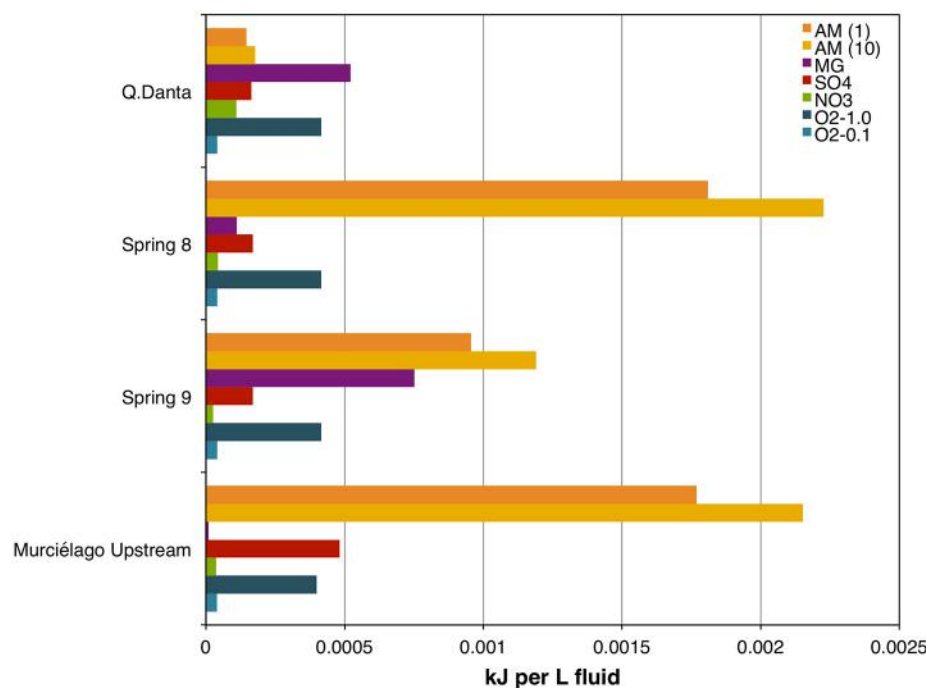


FIGURE 6 | Free energy yield (kJ per L of fluids) for methanogenic and methanotrophic processes in SEO's fluids. AM (1), acetoclastic methanogenesis assuming 1% of DOM is acetate; AM (10), acetoclastic methanogenesis assuming 10% of DOM is acetate; MG, hydrogenotrophic methanogenesis; SO₄, Anaerobic oxidation of methane (AOM) coupled to SO₄²⁻ reduction; NO₃, AOM coupled to NO₃⁻ reduction; O₂-1.0, aerobic methane oxidation assuming 1% saturation with respect to air; O₂-0.1, aerobic methane oxidation assuming 0.1% saturation with respect to air.

zone, resulting in potentially shorter flow paths. In terms of water mean residence time (MRT), the expected longer MRT in Spring 8 and 9 might result in a stronger abiotic methane signature, by allowing abiogenic methane to accumulate, which in turn, may mask the biological methane signature. While in Q. Danta, having shorter water flow paths from the recharge zone to the spring outflow and consequently shorter MRT, biological methanogenesis likely impacts the bulk methane signal.

The hyperalkaline springs at SEO contain a greater abundance of Archaea and a higher proportion of methanogens than has been detected in any terrestrial serpentinizing system to date. The conditions at SEO appear to sustain a predominantly methanogenic ecosystem, where biological methanogenesis is sustained by acetoclastic and hydrogenotrophic processes, in concert with abiogenic methane formation. Methanogenic activities are likely to be facilitated by the dynamic flux of nutrients, including DIC, from surface water and their infiltration into serpentinizing groundwater during intense seasonal cycles of rainfall and recharge. However, in addition to methanogenic process, anaerobic methane oxidation may be superimposed and influence the resulting gas flux. These data provide new insight into methane cycle in a tropical serpentinizing environment, and context to the patterns in methane occurrence in terrestrial serpentinites in various hydrological and climatic settings.

AUTHOR CONTRIBUTIONS

MC and KT contributed equally to this study. MC, RS, and MS designed the project and planned the field campaign. MC and RS were in charge of sample collection. MC and MS were in charge of geochemical characterization of the fluids, RS of isotopic analysis, KT and WB of sequence analysis, TM of the bioenergetics calculations. All authors contributed to the writing and editing of the manuscript.

FUNDING

Metagenomic analysis was funded by the Census of Deep Life (CoDL) project PRJNA340462 to MC and RS. RS would like to thank the support of the Research Office of the National University of Costa Rica through grants SIA-0482-13, SIA-0378-14, and SIA-0101-14. Travel support, geochemical, and 16S rDNA sequence analyses were supported by MSU new faculty startup funds to MS. Postdoctoral salary support was provided to MC through a grant by the Deep Carbon Observatory (Alfred P. Sloan Foundation).

ACKNOWLEDGMENTS

We would like to thank Ms. María Marta Chavarría, Mr. Roger Blanco, and Mr. Alejandro Masís from the Research Program of the Área de Conservación Guanacaste, Costa Rica

(<https://www.acguanacaste.ac.cr/>) for their help in the field and with related sampling logistics. Special thanks to Alex Hyer, Christopher Thornton, Pham Nguyen, and Michaela Lemen for their help with bioinformatic analyses; to Hilary Morrison and Mitch Sogin from MBL for their expertise and technical assistance; and to personnel from JBL Analytical Services at the University of Georgia for their advice during the geochemical sampling. The authors declared that all biological samples were collected under the authorized 2014 permission given

to MC and RS from the Comisión Nacional para la Gestión de la Diversidad de Costa Rica, Ministerio de Ambiente y Energía.

SUPPLEMENTARY MATERIAL

The Supplementary Material for this article can be found online at: <http://journal.frontiersin.org/article/10.3389/fmicb.2017.00916/full#supplementary-material>

REFERENCES

- Abrajano, T. A., Sturchio, N. C., Bohlke, J. K., Lyon, G. L., Poreda, R. J., and Stevens, C. M. (1988). Methane-hydrogen gas seeps, Zambales ophiolite, Philippines: deep or shallow origin? *Chem. Geol.* 71, 211–222. doi: 10.1016/0009-2541(88)90116-7
- Abrajano, T. A., Sturchio, N. C., Kennedy, B. M., Lyon, G. L., Muehlenbachs, K., and Bohlke, J. K. (1990). Geochemistry of reduced gas related to serpentinization of the Zambales ophiolite, Philippines. *Appl. Geochem.* 19, 787–802. doi: 10.1016/0883-2927(90)90060-i
- Anders, S., Pyl, P. T., and Huber, W. (2014). HTSeq: a Python framework to work with 805 high-throughput sequencing data. *Bioinformatics* 31, 166–169. doi: 10.1101/002824
- Barnes, I., Lamarche, V. C. Jr., and Himmelberg, G. (1967). Geochemical evidence of present-day serpentinization. *Science* 156, 830–832. doi: 10.1126/science.156.3776.830
- Barnes, I., and O'Neil, J. R. (1978). Present day serpentinization in New Caledonia, Oman, and Yugoslavia. *Geochim. Cosmochim. Acta* 42, 144–145. doi: 10.1016/0016-7037(78)90225-9
- Bath, A. H., Christofi, N., Philp, J. C., Cave, M. R., McKinley, I. G., and Berner, U. (1987). *Trace Element and Microbiological Studies of Alkaline Groundwaters in Oman, Arabian Gulf: A Natural Analog for Cement Pore-Waters*. FFLPU Report 87-2. British Geological Survey.
- Boisvert, S., Raymond, F., Godzarczuk, E., Laviolette, F., and Corbeil, J. (2012). Ray meta: scalable de novo metagenome assembly and profiling. *Genome Biol.* 13:R122. doi: 10.1186/gb-2012-13-12-r122
- Brazelton, W. J., Morrill, P. L., Szponar, N., and Schrenk, M. O. (2013). Bacterial communities associated with subsurface geochemical processes in continental serpentinite springs. *Appl. Environ. Microbiol.* 79, 3906–3916. doi: 10.1128/AEM.00330-13
- Brazelton, W. J., Schrenk, M. O., Kelley, D. S., and Baross, J. A. (2006). Methane- and sulfur-metabolizing microbial communities dominate the Lost City hydrothermal field ecosystem. *Appl. Environ. Microbiol.* 72, 6257–6270. doi: 10.1128/AEM.00574-06
- Brazelton, W. J., Thornton, C. H., Hyer, A., Twing, K. I., Longino, A. A., Lang, S. Q., et al. (2017). Metagenomic identification of active methanogens and methanotrophs in serpentinite springs of the Voltri Massif, Italy. *Peer J* 5:e2945. doi: 10.7717/peerj.2945
- Brutsaert, W. (2005). *Hydrology: An Introduction*. Cambridge: Cambridge University Press.
- Cardace, D., Hoehler, T., McCollom, T., Schrenk, M., Carnevale, D., Kubo, M., et al. (2013). Establishment of the Coast Range Ophiolite Microbial Observatory (CROMO): drilling objectives and preliminary outcomes. *Sci. Dril.* 16, 45–55. doi: 10.5194/sd-16-45-2013
- Cardace, D., Meyer-Dombard, D. R., Woycheese, K. M., and Arcilla, C. A. (2015). Feasible metabolism in high pH springs in the Philippines. *Front. Microbiol.* 6:10. doi: 10.3389/fmicb.2015.00010
- Cipolli, F., Gambardella, B., Marini, L., and Ottonello, G. (2004). Geochemistry of high-pH waters from serpentinites of the Gruppo di Voltri (Genova, Italy) and reaction path modeling of CO₂ sequestration in serpentinite aquifers. *Appl. Geochem.* 19, 787–802. doi: 10.1016/j.apgeochem.2003.10.007
- Crespo-Medina, M., Twing, K. I., Kubo, M. D. Y., Hoehler, T. M., Cardace, D., McCollom, T., et al. (2014). Insights into environmental controls on microbial communities in a continental serpentinite aquifer using a microcosm-based approach. *Front. Microbiol.* 5:604. doi: 10.3389/fmicb.2014.00604
- Etiope, G. (2016). Comment: methane origin in the Samail ophiolite: comment on “modern water/rock reactions in Oman hyperalkaline peridotite aquifers and implications for microbial habitability.” *Geochim. Cosmochim. Acta* 19, 787–802. doi: 10.1016/j.gca.2016.08.001
- Etiope, G., Vadillo, I., Whiticar, M. J., Marques, J. M., Carreira, P. M., Tiago, I., et al. (2016). Abiotic methane seepage in the Ronda peridotite massif, southern Spain. *Appl. Geochem.* 66, 101–113. doi: 10.1016/j.apgeochem.2015.12.001
- Etiope, G., Vance, S., Christensen, L. E., Marques, J. M., and Ribeiro da Costa, I. (2013). Methane in serpentized ultramafic rocks in mainland Portugal. *Mar. Petrol. Geol.* 45, 12–16. doi: 10.1016/j.marpetgeo.2013.04.009
- Ettwig, K. F., Butler, M. K., Le Paslier, D., Pelletier, E., Mangenot, S., Kuypers, M. M., et al. (2010). Nitrite-driven anaerobic methane oxidation by oxygenic bacteria. *Nature* 464, 543–548. doi: 10.1038/nature08883
- Ferry, J. G. (2010). How to make a living by exhaling methane. *Annu. Rev. Microbiol.* 64, 453–473. doi: 10.1146/annurev.micro.112408.134051
- Gazel, E., Denyer, P., and Baumgartner, P. O. (2006). Magmatic and geotectonic significance of Santa Elena Peninsula, Costa Rica. *Geol. Acta* 4, 193–202. doi: 10.1344/105.000000365
- Gomez-Alvarez, V., Teal, T. K., and Schmidt, T. M. (2009). Systematic artifacts in metagenomes from complex microbial communities. *ISME J.* 3, 1314–1317. doi: 10.1038/ismej.2009.72
- Hanson, R. S., and Hanson, T. E. (1996). Methanotrophic bacteria. *Microbiol. Rev.* 60, 439–471.
- Hinrichs, K.-U., Hayes, J. M., Sylva, S. P., Brewer, P. G., and DeLong, E. F. (1999). Methane-consuming archaeabacteria in marine sediments. *Nature* 398, 802–805. doi: 10.1038/19751
- Hobbie, J. E., Daley, R. J., and Jasper, S. (1977). Use of nucleopore filters for counting bacteria by fluorescence microscopy. *Appl. Environ. Microbiol.* 33, 1225–1228.
- Huber, J. A., Butterfield, D. A., and Baross, J. A. (2002). Temporal changes in archaeal diversity and chemistry in a mid-ocean ridge subseafloor habitat. *Appl. Environ. Microbiol.* 68, 1585–1594. doi: 10.1128/AEM.68.4.1585-1594.2002
- Huse, S. M., Mark Welch, D. B., Voorhis, A., Shipunova, A., Morrison, H. G., Eren, A. M., et al. (2014). VAMPS: a website for visualization and analysis of microbial population structures. *BMC Bioinformatics* 15:41. doi: 10.1186/1471-2105-15-41
- Hyatt, D., Chen, G. L., Locascio, P. F., Land, M. L., Larimer, F. W., and Hauser, L. J. (2010). Prodigal: prokaryotic gene recognition and translation initiation site identification. *BMC Bioinformatics*. 11:119. doi: 10.1186/1471-2105-11-119
- Johnson, J. W., Oelkers, E. H., and Helgeson, H. C. (1992). SUPCRT92: a software package for calculating the standard molal thermodynamic properties of minerals, gases, aqueous species, and reactions from 1 to 5000 bar and 0 to 1000°C. *Comput. Geosci.* 18, 899–947. doi: 10.1016/0098-3004(92)90029-q
- Joye, S. B., Bowles, M. W., Samarkin, V. A., Hunter, K. S., and Niemann, H. (2010). Biogeochemical signatures and microbial activity of different cold-seep habitats along the Gulf of Mexico deep slope. *Deep Sea Res. Part II* 57, 1990–2001. doi: 10.1016/j.dsr2.2010.06.001
- Kelley, D. S., Karson, J. A., Früh-Green, G. L., Yoerger, D. R., Shank, T. M., Butterfield, D. A., et al. (2005). A serpentinite hosted ecosystem: the Lost City hydrothermal field. *Science* 307, 1428–1434. doi: 10.1126/science.1102556
- Kohl, L., Cumming, E., Cox, A., Rietze, A., Morrissey, L., Lang, S. Q., et al. (2016). Exploring the metabolic potential of microbial communities in ultrabasic,

- reducing springs at The Cedars, CA, USA: experimental evidence of microbial methanogenesis and heterotrophic acetogenesis. *J. Geophys. Res. Biogeosci.* 121, 1203–1220. doi: 10.1002/2015JG003233
- Langmead, B., and Salzberg, S. (2012). Fast gapped-read alignment with Bowtie 2. *Nat. Methods* 9, 357–359. doi: 10.1038/nmeth.1923
- Lloyd, K. G., Alperin, M. J., and Teske, A. (2011). Environmental evidence for net methane production and oxidation in putative Anaerobic MEthanotrophic (ANME) archaea. *Environ. Microbiol.* 13, 2548–2564. doi: 10.1111/j.1462-2920.2011.02526.x
- Magana, V., Amador, J. A., and Medina, S. (1999). The midsummer drought over Mexico and Central America. *J. Clim* 12, 1577–1588. doi: 10.1175/1520-0442(1999)012<1577:TMDOMA>2.0.CO;2
- Maldonado, T., Alfaro, E., Fallas-López, B., and Alvarado, L. (2013). Seasonal prediction of extreme precipitation events and frequency of rainy days over Costa Rica, Central America, using Canonical Correlation Analysis. *Adv. Geosci.* 33, 41–52. doi: 10.5194/adgeo-33-41-2013
- Marques, J. M., Carreira, P. M., Carvalho, M. R., Matias, M. J., Goff, F. E., Basto, M. G., et al. (2008). Origins of high pH mineral waters from ultramafic rocks, Central Portugal. *Appl. Geochem.* 23, 3278–3289. doi: 10.1016/j.apgeochem.2008.06.029
- Martin, M. (2011). Cutadapt removes adapter sequences from high-throughput sequencing reads. *EMBnet. J.* 17, 10–12. doi: 10.14806/ej.17.1.200
- McCollom, T. M., and Seewald, J. S. (2007). Abiotic synthesis of organic compounds in deep-sea hydrothermal environments. *Chem. Rev.* 107, 382–401. doi: 10.1021/cr0503660
- McCollom, T. M., and Shock, E. L. (1997). Geochemical constraints on chemolithoautotrophic metabolism by microorganisms in seafloor hydrothermal systems. *Geochim. Cosmochim. Acta* 61, 4375–4391. doi: 10.1016/S0016-7037(97)00241-X
- Miller, H. M., Matter, J. M., Kelemen, P., Ellison, E. T., Conrad, M. E., Fierer, N., et al. (2016). Modern water/rock reactions in Oman hyperalkaline peridotite aquifers and implications for microbial habitability. *Geochim. Cosmochim. Acta* 179, 217–241. doi: 10.1016/j.gca.2016.01.033
- Moody, J. B. (1976). Serpentinization: a review. *Lithos* 9, 125–138. doi: 10.1016/0024-4937(76)90030-X
- Morrill, P. L., Kuenen, G. J., Johnson, O. J., Suzuki, S., Rietze, A., Sessions, A. L., et al. (2013). Geochemistry and geobiology of a present day serpentinization site in California: the Cedars. *Geochim. Cosmochim. Acta* 109, 222–240. doi: 10.1016/j.gca.2013.01.043
- Mulligan, M., and Burke, S. M. (2005). *Fog Interception for the Enhancement of Streamflow in Tropical Areas (90 m Resolution Hydrological Model)*. Available online at: <http://www.ambiotek.com/fiesta> (Accessed September 30, 2013).
- Nelson, M. C., Morrison, H. G., Benjamins, J., Grim, S. L., and Graf, J. (2014). Analysis, optimization, and verification of Illumina-generated 16S rRNA gene amplicon surveys. *PLoS ONE* 9:e94249. doi: 10.1371/journal.pone.0094249
- Ogata, H., Goto, S., Sato, K., Fujibuchi, W., Bono, H., and Kanehisa, M. (1999). KEGG: Kyoto Encyclopedia of Genes and Genomes. *Nucleic Acids Res.* 27, 29–34. doi: 10.1093/nar/27.1.29
- Op den Camp, H. J. M., Islam, T., Stott, M. B., Harhangi, H. R., Hynes, A., Schouten, S., et al. (2009). Environmental, genomic and taxonomic perspectives on methanotrophic *Verrucomicrobia*. *Environ. Microbiol. Rep.* 1, 293–306. doi: 10.1111/j.1758-2229.2009.00022.x
- Paul, K., Nonoh, J. O., Mikulski, L., and Brune, A. (2012). “Methanoplasmatales,” Thermoplasmatales-related archaea in termite guts and other environments, are the seventh order of methanogens. *Appl. Environ. Microbiol.* 78, 8245–8253. doi: 10.1128/AEM.02193-12
- Proskurowski, G., Lilley, M. D., Seewald, J. S., Früh-Green, G. L., Olson, E. J., Lupton, J. E., et al. (2008). Abiogenic hydrocarbon production at lost city hydrothermal field. *Science* 319, 604–607. doi: 10.1126/science.1151194
- Pruesse, E., Quast, C., Knittel, K., Fuchs, B. M., Ludwig, W., Peplies, J., et al. (2007). SILVA: a comprehensive online resource for quality checked and aligned ribosomal RNA sequence data compatible with ARB. *Nucleic Acids Res.* 35, 7188–7196. doi: 10.1093/nar/gkm864
- Quéméneur, M., Bes, M., Postec, A., Mei, N., Hamelin, J., Monnin, C., et al. (2014). Spatial distribution of microbial communities in the shallow submarine alkaline hydrothermal field of the Prony Bay, New Caledonia. *Environ. Microbiol. Rep.* 6, 665–674. doi: 10.1111/1758-2229.12184
- Sáenz, F., and Durán-Quesada, A. M. (2015). A climatology of low level wind regimes over Central America using weather type classification approach. *Front. Earth Sci.* 3:15. doi: 10.3389/feart.2015.00015
- Sakai, S., Imachi, H., Hanada, S., Ohashi, A., Harada, H., and Kamagata, Y. (2008). *Methanocella paludicola* gen. nov., sp. nov., a methane-producing archaeon, the first isolate of the lineage ‘Rice Cluster I’, and proposal of the new archaeal order *Methanocellales* ord. nov. *Int. J. Syst. Evol. Microbiol.* 58, 929–936. doi: 10.1099/ijss.0.65571-0
- Sánchez-Murillo, R., and Birkel, C. (2016). Groundwater recharge mechanisms inferred from isoscapes in a complex tropical mountainous region. *Geophys. Res. Lett.* 43, 5060–5069. doi: 10.1002/2016GL068888
- Sánchez-Murillo, R., Brooks, E. S., Elliot, W. J., and Boll, J. (2015). Isotope hydrology and baseflow geochemistry in natural and human-altered watersheds in the Inland Pacific Northwest, USA. *Isotope Environ. Health Sci.* 51, 231–254. doi: 10.1080/10256016.2015.1008468
- Sánchez-Murillo, R., Gazel, E., Schwarzenbach, E. M., Crespo-Medina, M., Schrenk, M. O., Boll, J., et al. (2014). Geochemical evidence for active tropical serpentinization in the Santa Elena Ophiolite, Costa Rica: an analog of a humid early Earth? *Geochem. Geophys. Geosyst.* 15, 1783–1800. doi: 10.1002/2013GC005213
- Schloss, P. D., Westcott, S. L., Ryabin, T., Hall, J. R., Hartmann, M., Hollister, E. B., et al. (2009). Introducing mothur: open-source, platform-independent, community-supported software for describing and comparing microbial communities. *Appl. Environ. Microbiol.* 75, 7537–7541. doi: 10.1128/AEM.01541-09
- Schrenk, M. O., Brazelton, W. J., and Lang, S. Q. (2013). Serpentinization, carbon, and deep life, *Rev. Mineral. Geochem.* 75, 575–606. doi: 10.2138/rmg.2013.75.18
- Schrenk, M. O., Kelley, D. S., Bolton, S. A., and Baross, J. A. (2004). Low archaeal diversity linked to subseafloor geochemical processes at the Lost City Hydrothermal Field, Mid-Atlantic Ridge. *Environ. Microbiol.* 6, 1086–1095. doi: 10.1111/j.1462-2920.2004.00650.x
- Schrenk, M. O., Kelley, D. S., Delaney, J. R., and Baross, J. A. (2003). Incidence and diversity of microorganisms within the walls of an active deep-sea sulfide chimney. *Appl. Environ. Microbiol.* 69, 3580–3592. doi: 10.1128/AEM.69.6.3580-3592.2003
- Seeman, T. (2014). Prokka: rapid prokaryotic genome annotation. *Bioinformatics* 30, 2068–2069. doi: 10.1093/bioinformatics/btu153
- Sogin, M. L., Morrison, H. G., Huber, J. A., Mark Welch, D., Huse, S. M., Neal, P. R., et al. (2006). Microbial diversity in the deep sea and the underexplored “rare biosphere.” *Proc. Natl. Acad. Sci. U.S.A.* 103, 12115–12120. doi: 10.1073/pnas.0605127103
- Suzuki, S., Ishii, S., Wu, A., Cheung, A., Tenney, A., Wanger, G., et al. (2013). Microbial diversity in The Cedars, an ultrabasic, ultrareducing, and low salinity serpentinizing ecosystem. *Proc. Natl. Acad. Sci. U.S.A.* 110, 15336–15341. doi: 10.1073/pnas.1302426110
- Szponar, N., Brazelton, W. J., Schrenk, M. O., Bower, D. M., Steele, A., and Morrill, P. L. (2013). Geochemistry of a continental site of serpentinization, the Tablelands Ophiolite, Gros Morne National Park: a Mars analogue. *Icarus* 224, 286–296. doi: 10.1016/j.icarus.2012.07.004
- Thauer, R. K., Kaster, A. K., Seedorf, H., Buckel, W., and Hedderich, R. (2008). Methanogenic archaea: ecologically relevant differences in energy conservation. *Nat. Rev. Microbiol.* 6, 579–591. doi: 10.1038/nrmicro1931
- Tiago, I., Chung, A. P., and Veríssimo, A. (2004). Bacterial diversity in a nonsaline alkaline environment: heterotrophic aerobic populations. *Appl. Environ. Microbiol.* 70, 7378–7387. doi: 10.1128/AEM.70.12.7378-7387.2004
- Tiago, I., and Veríssimo, A. (2013). Microbial and functional diversity of a subterrestrial high pH groundwater associated to serpentinization. *Environ. Microbiol.* 15, 1687–1706. doi: 10.1111/1462-2920.12034
- Tupas, L. M., Popp, B. N., and Karl, D. M. (1994). Dissolved organic carbon in oligotrophic waters: experiments on sample preservation, storage and analysis. *Mar. Chem.* 45, 207–216. doi: 10.1016/0304-4203(94)90004-3
- Wang, D. T., Gruen, D. S., Lollar, B. S., Hinrichs, K. U., Stewart, L. C., Holden, J. F., et al. (2015). Nonequilibrium clumped isotope signals in microbial methane. *Science* 348, 428–431. doi: 10.1126/science.aaa4326

- Waylen, P. R., Caviedes, C. N., and Quesada, M. E. (1996). Interannual variability of monthly precipitation in Costa Rica. *J. Clim.* 9, 2606–2613. doi: 10.1175/1520-0442(1996)009<2606:IVOMPI>2.0.CO;2
- Whiticar, M. J. (1999). Carbon and hydrogen isotope systematics of bacterial formation and oxidation of methane. *Chem. Geol.* 161, 291–314. doi: 10.1016/S0009-2541(99)00092-3
- Woycheese, K. M., Meyer-Dombard, D. R., Cardace, D., Argayosa, A. M., and Arcilla, C. A. (2015). Out of the dark: transitional subsurface-to-surface microbial diversity in a terrestrial serpentinizing seep (Manleluag, Pangasian, the Philippines). *Front. Microbiol.* 6:44. doi: 10.3389/fmicb.2015.00044

Conflict of Interest Statement: The authors declare that the research was conducted in the absence of any commercial or financial relationships that could be construed as a potential conflict of interest.

Copyright © 2017 Crespo-Medina, Twing, Sánchez-Murillo, Brazelton, McCollom and Schrenk. This is an open-access article distributed under the terms of the Creative Commons Attribution License (CC BY). The use, distribution or reproduction in other forums is permitted, provided the original author(s) or licensor are credited and that the original publication in this journal is cited, in accordance with accepted academic practice. No use, distribution or reproduction is permitted which does not comply with these terms.



Evaluating the Role of Seagrass in Cenozoic CO₂ Variations

Marco Brandano^{1,2*}, **Marco Cuffaro**², **Giovanni Gaglianone**¹, **Patrizio Petricca**³,
Vincenzo Stagno¹ and **Guillem Mateu-Vicens**^{4,5}

¹ Dipartimento Scienze della Terra, Università Roma La Sapienza, Rome, Italy, ² Istituto di Geologia Ambientale e

Geoingegneria, CNR, Rome, Italy, ³ GFZ German Research Centre for Geosciences, Telegrafenberg, Potsdam, Germany,

⁴ Cátedra Guillem Colom Casasnovas, Universitat de les Illes Balears, Palma de Mallorca, Spain, ⁵ Laboratorio de Zoología, Departament de Biología, Universitat de les Illes Balears, Palma de Mallorca, Spain

OPEN ACCESS

Edited by:

Cody Springer Sheik,
University of Minnesota Duluth, USA

Reviewed by:

John Senko,
University of Akron, USA
Alberto Saez,
University of Barcelona, Spain

*Correspondence:

Marco Brandano
marco.brandano@uniroma1.it

Specialty section:

This article was submitted to
Microbiological Chemistry and
Geomicrobiology,
a section of the journal
Frontiers in Environmental Science

Received: 13 July 2016

Accepted: 24 October 2016

Published: 11 November 2016

Citation:

Brandano M, Cuffaro M, Gaglianone G, Petricca P, Stagno V and Mateu-Vicens G (2016) Evaluating the Role of Seagrass in Cenozoic CO₂ Variations. *Front. Environ. Sci.* 4:72.
doi: 10.3389/fenvs.2016.00072

Marine seagrass angiosperms play an important role in carbon sequestration, removing carbon dioxide from the atmosphere and binding it as organic matter. Carbon is stored in the plants themselves, but also in the sediments both in inorganic and organic forms. The inorganic component is represented by carbonates produced by calcareous organisms living as epiphytes on seagrass leaves and rhizomes. In this paper, we find that the rate of seagrass epiphyte production (leaves and rhizomes) averages 400 g m⁻² yr⁻¹, as result of seagrass sampling at seven localities along the Mediterranean coasts, and related laboratory analysis. Seagrasses have appeared in the Late Cretaceous becoming a place of remarkable carbonate production and C sequestration during the whole Cenozoic era. Here, we explore the potential contribution of seagrass as C sink on the atmospheric CO₂ decrease by measuring changes in seagrass extent, which is directly associated with variations in the global coastal length associated with plate tectonics. We claim that global seagrass distribution significantly affected the atmospheric composition, particularly at the Eocene-Oligocene boundary, when the CO₂ concentration fell to 400 ppm, i.e., the approximate value of current atmospheric CO₂.

Keywords: seagrass, atmospheric CO₂, cenozoic, plate reconstructions, coast

INTRODUCTION

Seagrasses are marine angiosperms that form extensive submarine meadows in the photic zone along temperate to tropical coastlines worldwide (Short and Wyllie-Echeverria, 1996; Short et al., 2007). They first (*Posidonia cretacea*) appeared during the Late Cretaceous (Brasier, 1975; den Hartog and Polderman, 1975; Eva, 1980; Ivany et al., 1990) in the Tethys Ocean. Since the early Eocene this ecosystem became well established and spread throughout the Tethys (Brasier, 1975; Čosović et al., 2004; Zamagni et al., 2008; Tomás et al., 2016; Tomassetti et al., 2016), the Western Atlantic-Caribbean (Vélez-Juarbe, 2014) and in the Indo-Pacific realm when they colonized the euphotic zone of coastal environments as well as carbonate platforms.

Until the 2000s only few works focus on geological record of seagrass (Brasier, 1975; Eva, 1980; Wanless, 1981; Ivany et al., 1990). This is likely a consequence of the scarcity of fossil remains of seagrasses, due to the low potential of preservation of these plants (Brasier, 1975; Reich et al., 2015 and references therein). On the contrary, in these last years many works have focused on the identification of paleo-seagrasses through the recognition of indirect sedimentological and biological indicators, by comparison with modern seagrass habitats (e.g.,

Mateu-Vicens et al., 2008, 2012; Reich et al., 2015; Darroch et al., 2016). These works well evidence the extensive colonization by seagrass in the photic zone of coastal environment and carbonate platforms at global scale (Reich et al., 2015 and reference therein).

Seagrasses have two clearly distinguishable levels, rhizomes and blades. Rhizomes run in sediments beneath the seabed, and have regularly spaced nodes, each bearing roots below and an erect stem or shoot with the blades above. Each level has characteristic associated communities living attached to the plant (Langer, 1988; Mateu-Vicens et al., 2008). A diverse array of biota dwells in seagrass meadows as epiphytic (foraminifers, bryozoans, serpulids and encrusting coralline algae) or infaunal forms (echinoids, mollusks) (Figures 1A,B). Many of these organisms secrete calcareous skeletons (Perry and Beavington-Penney, 2005; Brandano et al., 2009; Mateu-Vicens et al., 2010, 2012), consequently seagrasses hosted a significant carbonate production.

The distribution of seagrass species is the result of combined plant sexual reproduction and clonal growth (Figure 1C) influenced by dispersal and environmental limitations (Spalding et al., 2003). All seagrass species are capable of asexual reproduction, giving rise to modular units known as ramets, through horizontal growth of the rhizome genetically identical to the parent plant, the genet. The reproductive strategy, which involves clonal growth and production of long-lived, locally dispersed seeds may provide an evolutionary advantage to plants growing in environments subject to temporally unpredictable major disturbances (Rasheed, 2004).

Lastly, seagrasses play an important role in carbon sequestration as they remove carbon dioxide from the atmosphere and bind it as organic matter (Fourqurean et al., 2012). The carbon (C) sequestered in vegetated coastal ecosystems, specifically mangrove forests, seagrass beds and salt marshes, has been termed “blue carbon” (Nellemann et al., 2009). Blue carbon is sequestered over the short term (decennial) in biomass and over longer (millennial) time-scales in sediments (Duarte et al., 2005; Lo Iacono et al., 2008). Carbon is stored above the seabed on plant tissues, underneath the seabed on roots and rhizomes, and in sediments in both organic and inorganic forms, the latter represented by carbonates. Much attention has focused on the quantification of organic C sequestration, and the latest estimates indicate that seagrasses can store 4.2–8.4 Pg C (Fourqurean et al., 2012), and total global C burial by seagrasses may reach 112 Tg C yr⁻¹ (McLeod et al., 2011). However, we point out here that less attention has been paid to C stored by carbonates (inorganic C) produced by epiphytic calcareous organisms that, live on seagrass leaves and rhizomes. This inorganic C, unlike organic C, is locked away..

METHODS

Estimates of Seagrass Carbonate Production

Posidonia oceanica shoots were collected by scuba divers at 5, 11, and 15 mwd (mean water depth) from seagrass meadows in seven locations on the Tyrrhenian coast (Maratea, Ponza, S. Marinella,

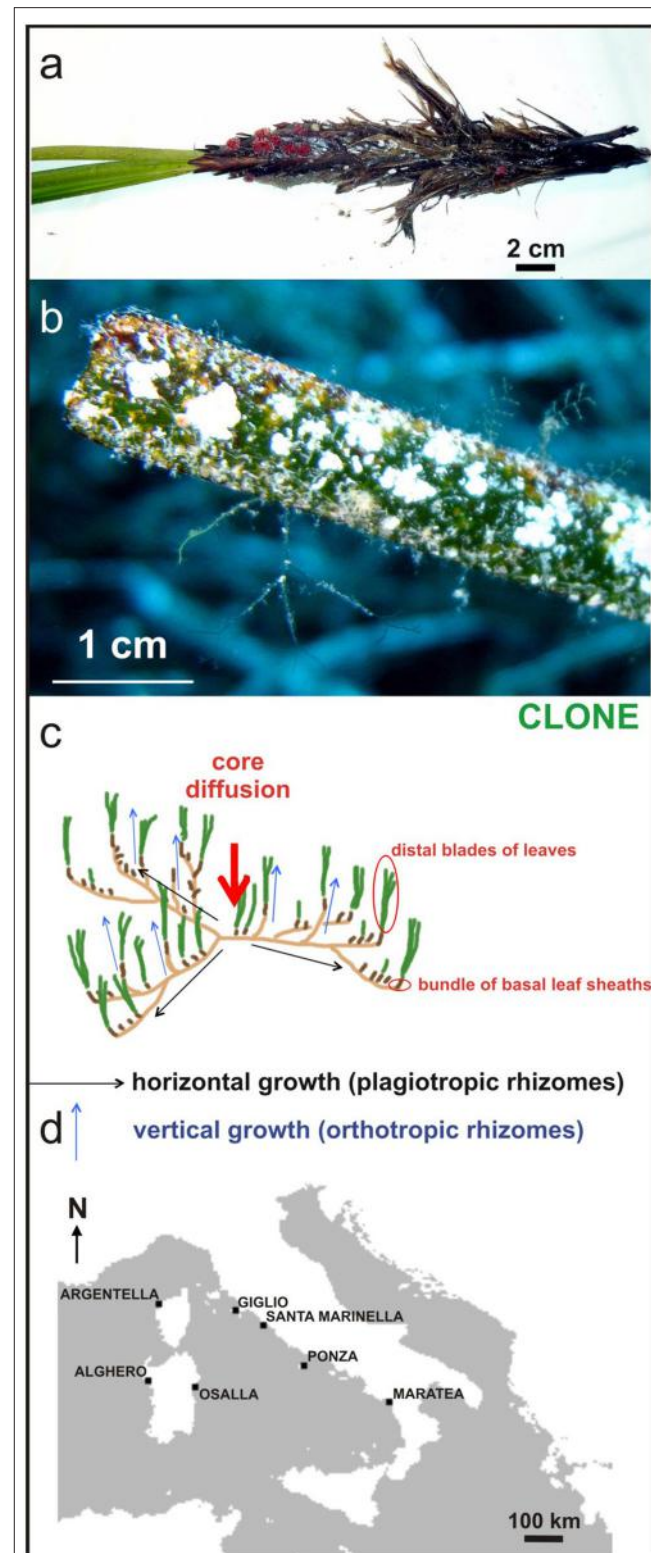


FIGURE 1 | (A) Biota dwelling vertical rhizome (*Miniacina miniae*) and **(B)** leaves as epiphytic forms; **(C)** clonal growth reproductive strategy involves the development of modular units, knowns as ramets, through horizontal growth of the rhizome, genetically identical to the parent plant, the genet; **(D)** Location map of sampling sites for measurement of seagrass carbonate production.

Isola del Giglio, Osalla, Alghero, Crovani see **Figure 1D**) during spring and autumn 2012 after evaluation of meadow shoot density near the sampling points. The sampling period was chosen taking into account the seagrass growth dependence on seasons (Short et al., 2006). The main morphometric measurements (length, width, and leaf area, leaf length, Leaf Area Index) were performed on 200 leaves from seagrass bundles. The annual production of epiphytic carbonate in the meadows was evaluated independently for the leaves (blades) and its common basal parts (bundle of leaf-sheaths), as well as on the whole leaf bundles. Calcium carbonate content was assessed by geochemical calcimetric analysis on ash from plant parts, previously dried at 105°C for 24 h and weighed, burned in an oven at 550°C for 4 h (LOI₅₅₀ method; (Dean, 1974)), and determination of calcium carbonate content by calcimetric analysis on ash. The epiphytic foliar content of calcium carbonate was converted into epiphytic foliar annual average following Canals and Ballesteros (1997), that is multiplying by 1.88. This process was also extended to the carbonate contribution from basal parts, and then to whole bundles. On whole parts (leaves and basal parts), the annual production of epiphytic carbonate per surface meadow unit of *P. oceanica* was estimated to be about 400 g m⁻² yr⁻¹.

Plate Reconstructions and Coastline Lengths

Absolute plate reconstructions with respect to the Pacific Hotspot Reference frame during the Cenozoic were performed by combining global plate models and finite rotations provided by Seton et al. (2012). The reconstructed positions of continents (Figure S1) were obtained with GPlates software (<http://www.gplates.org>), and closely coincide with magnetic Chrons, crucial geological events (e.g., the Messinian salinity crisis) and global variation trends of atmospheric CO₂, as reported by Beerling and Royer (2011). The coastline polygons from Seton et al. (2012) were used to compute global coastline lengths at each selected stage. Coastal data were digitalized and simplified due the complexity of several uneven areas (such as Polynesia and Indonesia), underestimating the actual total lengths of the coastlines. Polygon borders presumed to be in contact with seas and oceans were selected and considered as a single boundary according to the reconstruction by Seton et al. (2012). Total coastline lengths and areas of seagrass emplacement were computed at each selected age.

Global CO₂ Estimates

In this work, the Cenozoic CO₂ variations according to Beerling and Royer (2011) are used with one proxy (phytoplankton) to obtain a better comprehension of changes in atmospheric CO₂ concentrations. Our purpose is to quantify the contribution from both inorganic and organic carbon sequestration due to seagrass extent variations during the Cenozoic, and compare them with the reference changes of Beerling and Royer (2011) to evaluate the role of seagrass in CO₂ atmospheric composition. At this aim we consider that,

$$\frac{V_{CO_2}}{V_{atm}} = C \quad (1)$$

where V_{CO_2} is the partial volume of the CO₂ in the atmosphere, V_{atm} is the total volume of the atmosphere, and $C = 400$ ppmv is the current value of the global concentration of carbon dioxide in the atmosphere, expressed in parts per million by volume.

Under the same conditions of temperature T and pressure P , we can write:

$$\frac{PV_{CO_2}}{PV_{atm}} = \frac{n_{CO_2}RT}{n_{atm}RT} \quad (2)$$

where n_{CO_2} and n_{atm} are the CO₂ and the atmosphere number of moles respectively, and R is the universal gas constant, so that we have:

$$\frac{V_{CO_2}}{V_{atm}} = \frac{M_{CO_2}}{M_{atm}} \frac{m_{atm}}{m_{CO_2}} \quad (3)$$

where M_{CO_2} is the mass in grams of the carbon dioxide in the atmosphere, $M_{atm} = 5.1480 \times 10^{21}$ g is the total mean mass of the atmosphere (Trenberth and Smith, 2005), $m_{CO_2} = 44.00$ g mole⁻¹ and $m_{atm} = 28.97$ g mole⁻¹ are the CO₂ molecular weight and the mean molecular weight of the atmosphere (NASA Earth Fact Sheet, <http://nssdc.gsfc.nasa.gov/planetary/factsheet/earthfact.html>), respectively

Using equation (3), we are able to compute the variation of the ratio V_{CO_2}/V_{atm} during the Cenozoic, and evaluate the inorganic and organic carbon sequestration in terms of carbon dioxide mass M_{CO_2} (in grams) in the atmosphere.

The quantity M_{CO_2} depends on the seagrass areal extent, being estimated for the Present using the lower global area of $A_1 = 300,000$ km² (Charpy-Roubaud and Sournia, 1990), and an upper global area $A_2 = 600,000$ km² (Duarte et al., 2005). The area depends by the extension of seagrass from the coast, that in turn is under control of the light requirement for photosynthesis Short et al. (2007). The upslope limit of seagrasses is imposed by their necessity of constant immersion in seawater and low hydrodynamic conditions because high energy superficial wave inhibits its growth and development. As seagrass may colonize rocky and sandy substrates in the photic zone (Green and Short, 2003; Mateu-Vicens et al., 2012) the areal extent of seagrass meadows depends by steep gradient of marine seafloor. These requirements suggest that it is not necessary a flat and wide seafloor surface for seagrass meadows colonization, and also steep rocky substrate may host productive seagrasses (Green and Short, 2003). Modern examples of such substrate are represented by the northeastern coast of Philippines or northeastern coast of Haiti in the Caribbean (Green and Short, 2003). On the contrary are well known examples of large continental platforms not colonized by seagrass such as the southwestern Africa or southeastern South America continental platforms.

During the Cenozoic, we expect that seagrass area varied according to plate tectonics. Mantle—reference plate reconstructions with respect to the Pacific hotspot framework during the Cenozoic were performed by combining global plate models and finite rotations provided by Seton et al. (2012). The reconstructed positions of continents (Figure S1) were obtained with GPlates software (<http://www.gplates.org>), chosen here to

coincide as closely as possible with magnetic chrons, crucial geological events (e.g., the Messinian salinity crisis) and global variation trends of atmospheric CO₂, as reported by Beerling and Royer (2011). The coastline polygons of Seton et al. (2012) are used to compute global coastline lengths L at each selected stage in a range of latitude [−65°N, 65°N] in which seagrasses are presumed to have existed based on paleontological record-IPSlS-, Reich et al. (2015) (see **Figure 1**, Table S1). Offshore distance d is assumed constant during the Cenozoic, and is varied to obtain lower and upper global estimates of the seagrass areal extent for the present-day, so that:

$$A_i = L_0 d_i \quad (4)$$

where $i = 1, 2$, and L_0 is the current total coastline length obtained with coastal polygon model by Seton et al. (2012), at age $t = 0$ Ma, resulting in $d_1 = 0.889625$ km and $d_2 = 1.779249$ km. Cenozoic coast lengths and seagrass areal extent variations are reported in Table S1.

To compute current inorganic carbon sequestration, laboratory experiments carried out in this study suggest that present-day seagrass coverage produces CaCO₃ carbonate with the rate $a = 400$ g m^{−2} yr^{−1}, which results in the 44% of CO₂ stored in seagrass carbonates, corresponding to the coefficient $b = 176$ g m^{−2} yr^{−1}. The mass in grams of CO₂ over a year, due to inorganic carbon sequestration, produced by seagrass coverage A_i , with $i = 1, 2$ is obtained for the Present-day, as it follows:

$$M_{CO_2}^{CaCO_3}(i) = b L_0 d_i \quad (5)$$

Combining Equation (5) with Equation (3), we obtain the carbon dioxide removal (CDR) due to inorganic (CaCO₃) carbon sequestration, during the Cenozoic. At each selected age, results are reported in Table S2 and Table S3, for lower and upper seagrass areal extent A_1 and A_2 , respectively.

To calculate the present-day value of organic carbon sequestration, the estimate procedure of Duarte et al. (2010), Kennedy et al. (2010) and Waycott et al. (2009) were followed. Those authors estimated an organic C sink of $c_1 = 160$ g C m^{−2} yr^{−1} and $c_2 = 186$ g C m^{−2} yr^{−1} related to the A_1 (300,000 km²) and A_2 (600,000 km²) seagrass areal extent, respectively. The mass in grams of C over a year, due to the organic carbon sequestration, produced by seagrass coverage A_i , with $i = 1, 2$ is obtained for the present-day, as it follows:

$$M_c^{Org}(i) = c_i L_0 d_i \quad (6)$$

Then, from Rasheed (2004), we know that:

$$M_{CO_2} = M_c \frac{m_{CO_2}}{m_c} \quad (7)$$

where $m_{CO_2} = 44.00$ g mole^{−1} and $m_c = 12.00$ g mole^{−1} are the CO₂ and C molar mass, respectively.

Combining Equation (7), Equation (6), and Equation (3) we obtain the carbon dioxide removal (CDR) due to organic carbon sequestration during the Cenozoic. At each selected age, results

are reported in Tables S2, S3, for lower and upper seagrass areal extent A_1 and A_2 , respectively.

Finally, to have an estimate of the global amount of C sink due to both inorganic and organic contributions, we define the cumulative carbon dioxide removal (CDR), as it follows:

$$M_{CO_2}^{cum.}(i) = M_{CO_2}^{CaCO_3}(i) + M_{CO_2}^{Org.}(i), \quad (8)$$

where $i = 1, 2$. Combining equation (8) with equation (3) we obtain the carbon dioxide removal (CDR) due to cumulative effect of carbon sequestration (i.e., inorganic and organic), during the Cenozoic. At each selected age, results are reported in Tables S2, S3, for lower and upper seagrass areal extent A_1 and A_2 , respectively. A third model for the upper seagrass areal extent $A_3 = 100,000$ km² with $d_3 = 2.965415$ km can be used to calculate the present-day values of inorganic and organic carbon sequestration taking into account the seagrass loss of 29% worldwide (Waycott et al., 2009), also including the inorganic C sink estimate of $b = 176$ g m^{−2} yr^{−1}, and the organic C sink estimate of $c_2 = 186$ g C m^{−2} yr^{−1} respectively. Again, combining Equation (5), Equation (6), Equation (7) with Equation (3), and using Equation (8) we obtain results as in Table S4.

Storage of C by seagrasses may be calculated over 1000-year periods as seagrasses work and live for 1000 of years (Arnaud-Haond et al., 2012). This carbon dioxide removal over 1000 yr (KCDR) is reported in Tables S2–S4, for the inorganic, organic and cumulative contributions of lower and upper seagrass areal extent A_1 , A_2 , and A_3 .

Cenozoic coastal variations, associated with inorganic, organic and cumulative contribution for C sink for Area A_1 and A_3 are reported in Figures S2, S3, respectively.

Linear regressions on CO₂ Cenozoic variations CO₂ and KCDR models (i.e., A_1 , A_2 , and A_3), are reported in Table S5 and Figure S4, and represent the rate of variations, showing a decrease of CO₂ with respect an increase of carbon dioxide removal over 1000 yr.

Partial time interval linear regressions are reported in Table S5 and Figure S5, showing that rates of variations suggest a correspondence at 45% between CO₂ decrease and cumulative KCDR increase during the Cenozoic whereas, if we consider the 41–7 Ma interval, correspondence increases to 66% (Table S5, and Figure S5).

RESULTS AND DISCUSSION

The Mediterranean shelf has classically hosted seagrass sites used to investigate both calcareous production and carbon burial capacity (Canals and Ballesteros, 1997; Duarte et al., 2013). In this paper, carbonate content and (epiphytic) production have been quantified both from seagrass leaves (blades) and from bundles of persistent basal leaf-sheaths resembling “shaving brushes” (Larkum et al., 2006), where the most important seagrass is *Posidonia oceanica* in terms of calcareous epiphyte production (**Figure 1A**). The seagrass biomass exerts a predominant control on the relative abundance of calcareous epiphytes. The most

abundant of these are geniculate (articulated) and non-geniculate (encrusting) coralline algae that, together, comprise up to 50% of epiphytic carbonate. Other significant epiphytes are bryozoans and benthic foraminifers, which contribute approximately in equal amounts (~25% each) to the carbonate production. Calcareous epiphyte abundance peaks at water depths of ~10 meters. The rate of epiphyte production (leaves and rhizomes) averages 400 g m⁻² yr⁻¹. Today, seagrass meadows are widespread in many tropical and temperate, shallow marine, and estuarine environments. Data from leaf carbonate production are available from both tropical and temperate environments (Nelsen and Ginsburg, 1986; Bosence, 1989; James et al., 2012), showing that the total epiphytic production for seagrass is within the range of the Tyrrhenian seagrass. Throughout the world, seagrasses are estimated to cover 0.6×10^6 km², equivalent to 10% of the coastal ocean surface, an area comparable to that covered by coral reefs and mangroves (Charpy-Roubaud and Sournia, 1990; Hemminga and Duarte, 2000). Consequently, with an average carbonate production of 400 g m⁻² yr⁻¹, the CO₂ stored in seagrass carbonates may be estimated at up to 105 Tg yr⁻¹ (10.5×10^7 t).

Seagrasses have been integral components of shallow marine ecosystems since their appearance in the Late Cretaceous (den Hartog, 1970; Brasier, 1975; Ivany et al., 1990). Because the calcareous skeletons of many seagrass dwellers contribute significantly to the sediment of photic shallow water environments, seagrass meadows have become host of substantial carbonate production and C (organic and inorganic) sequestration since the Cenozoic era.

Reconstructions of atmospheric CO₂ concentrations for the Cenozoic have improved greatly in the last few decades (e.g., Beerling and Royer, 2011), although many uncertainties still exist, with CO₂ estimates varying greatly within the same time interval used as a proxy (Royer et al., 2012). However, the review of CO₂ concentration estimates by Beerling and Royer (2011) documented a consistent pattern of CO₂ change. According to the above authors' compilation in the early Paleogene atmospheric CO₂ was about 400 ppm, followed by a first peak to nearly 1900 ppm at 50 Ma and two others above 1200 ppm until the Eocene-Oligocene boundary when a decreasing trend began, with values around 400 ppm throughout the Oligocene. During the Miocene a few data points exceed 400 ppm, but most fall in the range 200–350 ppm. The bulk of the data from the Pliocene are in the range 250–400 ppm, followed by a general decrease during the Pleistocene.

The causes of the reduction in atmospheric CO₂ levels at the Eocene-Oligocene boundary are still debated (Willenbring and von Blanckenburg, 2010). According to Allen and Armstrong (2008), the decrease in atmospheric CO₂ was the result of complementary mechanisms, such as waning pre-collision arc magmatism, increased weathering of silicate, storage of organic carbon in Paratethyan basins, and oceanographic changes producing upwelling.

Changes in the atmospheric CO₂ concentrations, however, may have had severe consequences for marine ecosystems. Elevated atmospheric CO₂ phases in the Earth's history had

induced important crisis and extinctions of marine calcifiers (Weissert and Erba, 2004; Erba et al., 2010; Črne et al., 2011; Hönisch et al., 2012). However, with the exception of PETM (Paleocene Eocene Thermal Maximum) event, the Cenozoic interval was not affected by important changes of CaCO₃ saturation (Hönisch et al., 2012).

The role of modern seagrasses as global C sinks was demonstrated and quantified once the total area of Earth covered by seagrass meadows was estimated. Seagrasses grow over a large range of latitudes, from the tropics to close to Arctic regions (N70°, Norway) in coastal waters, with a seafloor illuminated by 1.0–29% of surface irradiance, in water depths of up to ~60 m, average ~25 m (Green and Short, 2003). On the other hand, the global extent of seagrasses is directly linked to global coastal length. As a consequence, changes in the latter over time may influence global seagrass coverage and its contribution to C storage.

The potential contribution of seagrasses in reducing atmospheric CO₂ during the Cenozoic can be evaluated by measuring changes in seagrass extent, which is directly associated with variations in global coastal length due to plate tectonics. Estimates of coastal length changes are provided here by means of plate tectonic reconstructions. During the Cenozoic the position and shape of the continents were modified by the movement of lithospheric plates with respect to the underlying mantle (Figure 2).

Using the rotation vector, plate polygon and coastline data proposed by Seton et al. (2012), we computed global plate reconstructions at several key-time points (Figure S1)

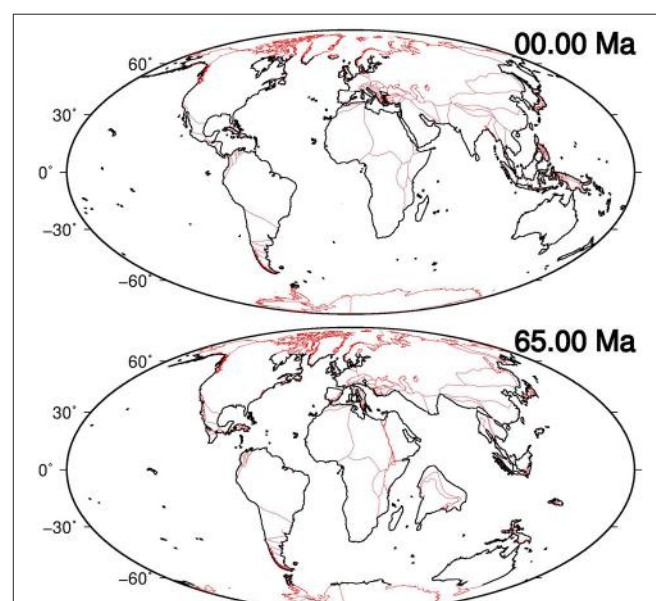


FIGURE 2 | Present-day (0 Ma) and reconstructed (65 Ma) positions of continents using models provided by Seton et al. (2012) (red polygons).

Black lines represent digitalized, and simplified data, estimated in a range of latitude [-65°N, 65°N] in which seagrasses are presumed to have existed, and utilized to compute global coastal lengths at several key-time points.

overlapping possible magnetic Chrons, crucial geological events (e.g., the Messinian salinity crisis) and trends of variations in atmospheric CO₂, as reported by Beerling and Royer (2011). Then, with the reconstructed positions of continents, we estimated the total length of the global coastlines in a range of latitude [−65°N, 65°N] in which seagrasses are presumed to have existed over the entire investigated period of time (see Methods paragraph).

From 65 to 41 Ma we observe a general increase in the coastline length (Figure 3), mostly due to the southward movement of North America and Eurasia over the latitude hypothesized for seagrass growth, at 65°N. The appreciable decrease in coastlines at 34 Ma can be attributed to the evolution of the India-Eurasia continental collision: a relevant increase in coastline lengths between 34 and 28 Ma is observed, probably due to the opening of the Gulf of Aden and the beginning of continental rifting in the Red Sea between the Africa and Arabia plates. Lastly, a steady decrease in length is noted after 14 Ma, mainly due to the continental collision of the Arabia and Eurasia plates, with the exception of a singular increase at 5 Ma, ascribed to the closure of North America and South America. The curves of CaCO₃ carbonate production and organic contribution to carbon dioxide removal (CDR) and their cumulative curve (i.e., CaCO₃ plus organic C) during the Cenozoic are shown in Figure 3 and compared with variations in coastline length (31.0×10^4 to 36.7×10^4 km). Here, we present 3 models (A_{1–3}) that take into account the dependence of CO₂ sequestration on the seagrass areal extent, being evaluated for the Present-day with a lower global estimate of $A_1 = 300,000$ km² (29), an upper global estimate of $A_2 = 600,000$ km² (19) and an overestimation of $A_3 = 1,000,000$ km². We report the result of calculation for the A₂ model, for A₁ and A₂ see Figures 3, 4.

The contribution of CaCO₃ to CO₂ sequestration in the A₂ was found to vary from 12.45×10^{-3} to 14.72×10^{-3} ppm yr^{−1}. Higher values were observed for the organic component, which ranged from 48.26×10^{-3} to 57.52×10^{-3} ppm yr^{−1}. The cumulative contribution of the two components was in the range 60.71×10^{-3} to 71.79×10^{-3} ppm yr^{−1}.

Storage of C by seagrasses may be calculated over 1000-year periods, because seagrasses work and live for 1000 of years (Arnaud-Haond et al., 2012). This cumulative carbon dioxide removal over 1000 years (KCDR) (80.43–95.11 ppm) throughout the Cenozoic is shown in Figure 4 and compared with the value of atmospheric CO₂ reported by Beerling and Royer (2011), including values for the key time used to calculate plate reconstructions and coastline lengths. Figure 3A shows the general match between increased C sequestration and increased coastal length. Linear regressions on both curves, i.e., cumulative KCDR and atmospheric CO₂, show a general increase in seagrass contributions with respect to a global decrease in atmospheric CO₂ during the Cenozoic (Figure S4).

Nowadays, the role of the oceans as carbon sinks is widely documented (Duarte et al., 2005; McLeod et al., 2011; Fourqurean et al., 2012; Karl et al., 2012). Phytoplankton photosynthesis is one of the mechanism leading to C sequestration through the deposition and burial of the particulate organic material at the ocean floor formed by phytoplankton (Raven and Falkowski,

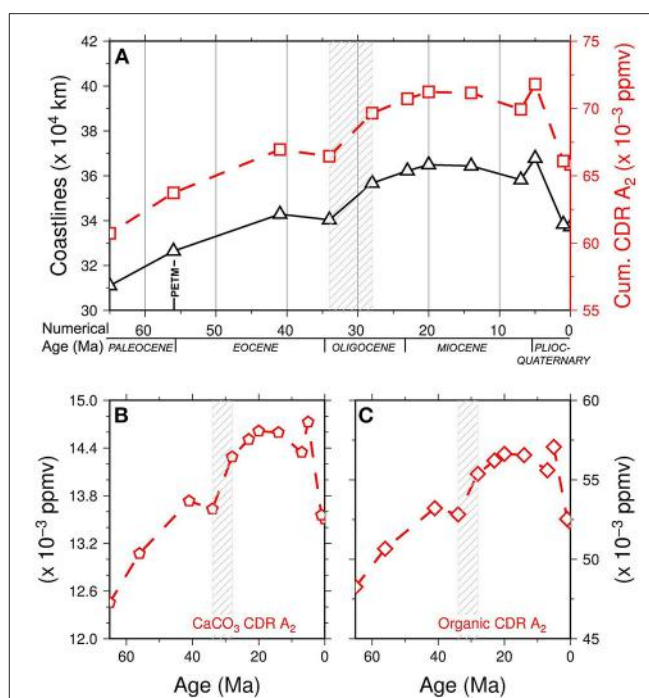


FIGURE 3 | (A) Cenozoic cumulative carbon dioxide removal (CDR) for model A_2 (red line, open squares, compared with variations of coastline length (black line open triangles). **(B)** Cenozoic inorganic (CaCO₃) carbon dioxide removal (CDR) for model A_2 . **(C)** Cenozoic organic carbon dioxide removal (CDR) for model A_2 . Dashed pattern represents the Eocene-Oligocene time interval. Data are reported in Table S3.

1999). However, the carbon burial capacity of coastal vegetated habitats (seagrass, mangroves and salt marshes) is 180 times greater than the average burial rate in the open ocean (Duarte et al., 2005), reaching 233 Tg C yr^{−1} (McLeod et al., 2011), values comparable with the C burial in lakes and peatlands that is about 300 Tg C yr^{−1} (Dean and Gorham, 1998). Consequently, it is out of question that blue carbon sinks play a key role in the oceanic carbon cycle (Duarte et al., 2005; McLeod et al., 2011; Fourqurean et al., 2012). On the contrary, it is more difficult to prove the role of blue carbon and, more in general, of the ocean as C sink in the fossil record. The obtained data for seagrass are in agreement with the present day role of ocean as natural sink. The obtained values of carbon dioxide sequestration are in the order of atmospheric CO₂ fluctuations during glacial cycles (Kohfeld et al., 2005).

By looking at the specific time-points and analyzing each rate of the two curves compared (i.e., cumulative KCDR increase and CO₂ decrease, Figure S5) with linear regressions for each time interval, the correspondence decreases to 45%, probably due to the lack of accuracy of CO₂ data from 65 to 41–34 Ma. In addition, after the Late Miocene (5 Ma), the lack of correspondence may be due to the development of the Arctic ice cap, marked by decreasing temperature and consequent decreasing atmospheric CO₂. The resulting increase of CO₂ solubility in ocean seawater, together with the

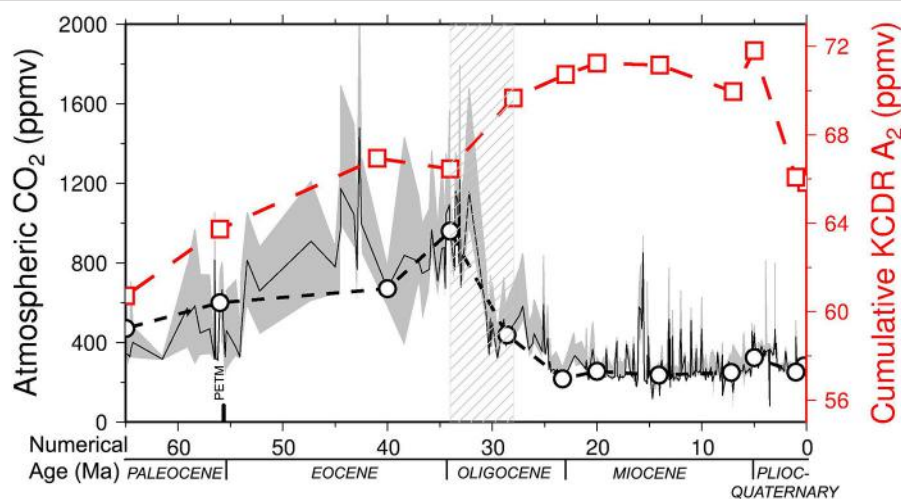


FIGURE 4 | Cenozoic cumulative (i.e., inorganic—CaCO₃ – and organic) carbon dioxide removal carbon dioxide removal over 1000 yr (KCDR) (red line, open squares) for model A₂ = 600,000 km², compared with the values of atmospheric CO₂ reported by Beerling and Royer (2011) (solid black line, gray confidence band), including CO₂ selected values at the key times used to calculate plate reconstructions and coastline lengths (dashed black line, open circles). Note the general match between CO₂ decrease and KCDR increase due to seagrass extent as a consequence of increase of coastal length. Dashed pattern represents the Eocene-Oligocene time interval.

Mediterranean Messinian crisis, probably reduced the seagrass extent.

It should also be noted that the Red Sea syn-rift Miocene evaporative event and the Mediterranean Messinian salinity crisis were included in our computation of coastlines, although a decreased seagrass productivity is expected in these areas during those specific periods. This means that 4000 km² of seagrass production in the Red Sea should be neglected in our record, almost from 28 to 5 Ma. In addition, at 5 Ma, we have an over-estimated length of coastlines producing seagrasses in the Mediterranean, so that non-accurate comparisons can be made for the 7–5 and 5–1 time intervals. Focusing on those key-time intervals, for which CO₂ data are well constrained (e.g., from 41 to 7 Ma) the global correspondence rises up to 66% except for the time ranges 23–20 and 20–14 Ma. The most evident shift occurs with the Eocene-Oligocene CO₂ decline (Figure 4). Both curves, i.e., increasing cumulative KCDR and decreasing CO₂ (Figure 4 and Figure S5), plot on higher rates of the considered time intervals, estimated with linear regressions to be 5.32 ppm Ma⁻¹ and -87.00 ppm Ma⁻¹, respectively (Figure S5). In conclusion, we provide an initial estimate of the contribution of seagrass meadows as C sink since their occurrence at the end of the Cretaceous. We admit that this result might be underestimated due to the simplified models used for coastal length computations, and it would need of more specific regional tectonic investigations and ecological constraints associated with eustatic processes in order to improve the accuracy of seagrass involvement to CO₂ decline. However, we are confident that this study represents a valid quantitative and global estimate of C sequestration by seagrass in the

geological record since Cretaceous time, to date missing in literature.

AUTHOR CONTRIBUTIONS

MB, MC, VS, and GM developed the ideas and the methods for this study. GG carried out sampling and laboratory analyses. MC and PP carried out plate tectonic reconstructions and coastline length computations. MB and MC wrote jointly the paper. All the authors discussed extensively the results and the interpretations

FUNDING

Funding by Sapienza University of Rome and IGAG-CNR.

ACKNOWLEDGMENTS

Discussions with Marco Ligi and Fabio Trippetta were appreciated. Many of the figures were made with the Generic Mapping Tools of Wessel and Smith (1995) (<http://gmt.soest.hawaii.edu/>). Criticisms by two reviewers and A. Editor Cody Sheik greatly improved the manuscript.

SUPPLEMENTARY MATERIAL

The Supplementary Material for this article can be found online at: <http://journal.frontiersin.org/article/10.3389/fenvs.2016.00072/full#supplementary-material>

REFERENCES

- Allen, M. B., and Armstrong, H. A. (2008). Arabia-Eurasia collision and the forcing of mid Cenozoic global cooling. *Paleoecol. Palaeogeogr. Palaeocl.* 265, 52–58. doi: 10.1016/j.palaeo.2008.04.021
- Arnaud-Haond, S., Duarte, C. M., Diaz-Almela, E., Marbà, N., Sintes, T., and Serrão, E. A. (2012). Implications of extreme life span in clonal organisms: millenary clones in meadows of the Threatened Seagrass: *Posidonia oceanica*. *PLoS ONE* 7:e30454. doi: 10.1371/journal.pone.0030454
- Beerling, D. J., and Royer, D. L. (2011). Convergent cenozoic CO₂ history. *Nat. Geosci.* 4, 418–420. doi: 10.1038/ngeo1186
- Bosence, D. (1989). Biogenic carbonate production in florida bay. *Bull. Mar. Sci.* 44, 419–433.
- Brandano, M., Frezza, V., Tomassetti, L., Pedley, M., and Matteucci, R. (2009). Facies analysis and paleoenvironmental interpretation of the Late Oligocene Attard Member (Lower Coralline Limestone Formation), Malta. *Sedimentology* 56, 1138–1158. doi: 10.1111/j.1365-3091.2008.01023.x
- Brasier, M. D. (1975). An outline history of seagrass communities. *Palaeontology* 18, 681–702.
- Canals, M., and Ballesteros, E. (1997). Production of carbonate particles by phytoplanktonic communities on the Mallorca-Menorca shelf, northwestern mediterranean sea. *Deep Sea Res. II*, 44, 611–629. doi: 10.1016/s0967-0645(96)00095-1
- Charpy-Roubaud, C., and Sournia, A. (1990). "The comparative estimation of phytoplanktonic, microphytobenthic and macrophytobenthic primary production in the oceans," in *Microalgal Growth: Inputs and Losses, Practical Approaches: Marine Microbial Food Webs*, eds S. Y. Maestrini and F. Rassoulzadegan (Rome: Sapienza Press), 31–57.
- Ćosović, V., Drobne, K., and Moro, A. (2004). Paleoenvironmental model for Eocene foraminiferal limestones of the Adriatic carbonate platform (Istrian Peninsula). *Facies* 50, 61–75. doi: 10.1007/s10347-004-0006-9
- Črne, A. E., Weissert, H., Goričan, Š., and Bernasconi, S. M. (2011). A biocalcification crisis at the Triassic-Jurassic boundary recorded in the Budva Basin (Dinarides, Montenegro). *Geol. Soc. Am. Bull.* 123, 40–50. doi: 10.1130/B30157.1
- Darroch, S. A., Locatelli, E. R., McCoy, V. E., Clark, E. G., Anderson, R. P., Tarhan, L. G., et al. (2016). Taphonomic disparity in foraminifera as a paleo-indicator for seagrass. *Palaios* 31, 242–258. doi: 10.2110/palo.2015.046
- Dean, W. E. (1974). Determination of carbonate and organic matter in calcareous sediments and sedimentary rocks by loss on ignition: comparison with other methods. *J. Sed. Petrol.* 44, 242–248.
- Dean, W. E., and Gorham, E., (1998). Magnitude and significance of carbon burial in lakes, reservoirs, and peatlands. *Geology* 26, 535–538.
- den Hartog, C. (1970). The sea-grasses of the World. North-Holland Publ. Co: *Verh kon Ned Akad Wet Af'd Natuurkundem* 59, 275.
- den Hartog, C., and Polderman, P. J. G. (1975). Changes in the seagrass populations of the Dutch Wadden Zee. *Aquat. Bot.* 1, 141–147.
- Duarte, C. M., Kennedy, H., Marbà, N., and Hendriks, I. (2013). Assessing the capacity of seagrass meadows for carbon burial: current limitations and future strategies. *Ocean Costal Manage* 83, 32–38. doi: 10.1016/j.ocecoaman.2011.09.001
- Duarte, C. M., Marbà, N., Gacia, E., Fourqurean, J. W., Beggins, J., Barrón, C., et al. (2010). Seagrass community metabolism: assessing the carbon sink capacity of seagrass meadows. *Glob. Biogeochem. Cycles* 24:GB4032. doi: 10.1029/2010GB003793
- Duarte, C. M., Middelburg, J. J., and Caraco, N. (2005). Major role of marine vegetation on the oceanic carbon cycle. *Biogeosciences* 2, 1–8. doi: 10.5194/bg-2-1-2005
- Erba, E., Bottini, C., Weissert, H., and Keller, C. E. (2010). Calcareous nannoplankton response to surface water acidification around Oceanic Anoxic Event 1a. *Science* 329, 428–432. doi: 10.1126/science.1188886
- Eva, A. N. (1980). Pre-miocene seagrass communities in the Caribbean. *Palaeontology* 23, 231–236.
- Fourqurean, J. W., Duarte, C. M., Kennedy, H., Marbà, N., Holmer, M., Mateo, M. A., et al. (2012). Seagrass ecosystems as a globally significant carbon stock. *Nat. Geosci.* 5, 505–509. doi: 10.1038/ngeo1477
- Green, E. P., and Short, F. T. (2003). *World Atlas of Seagrasses. Prepared by the UIMEP World Conservation Monitoring Centre*. Berkeley, CA: University of California Press.
- Hemming, M., and Duarte, C. M. (2000). *Seagrass Ecology*. Cambridge: Cambridge University Press.
- Hönisch, B., Ridgwell, A., Schmidt, D. N., Thomas, E., Gibbs, S. J., Sluijs, A., et al. (2012). The geological record of ocean acidification. *Science* 335, 1058–1063. doi: 10.1126/science.1208277
- Ivany, L. C., Portell, R. W., and Jones, D. S. (1990). Animal-plant relationships and paleobiogeography of an Eocene seagrass community from Florida. *Palaios* 5, 244–258. doi: 10.2307/3514943
- James, N. P., Bone, Y., Brown, K. M., and Cheshire, A. (2012). "Calcareous epiphyte production in cool-water carbonate seagrass depositional environments; Southern Australia," in *Perspectives in Carbonate Geology: A Tribute to the Career of Robert Nathan Ginsburg* (London: Special Publication 41 of the IAS), 123–148.
- Karl, D. M., Church, M. J., Dore, J. E., Letelier, R. M., and Mahaffey, C., (2012). Predictable and efficient carbon sequestration in the North Pacific Ocean supported by symbiotic nitrogen fixation. *Proc. Natl. Acad. Sci. U.S.A.* 109, 1842–1849. doi: 10.1073/pnas.1120312109
- Kennedy, H., Beggins, J., Duarte, C. M., Fourqurean, J. W., Holmer, M., Marbà, N., et al. (2010). Seagrass sediments as a global carbon sink: isotopic constraints. *Glob. Biogeochem. Cycles* 24:GB4026. doi: 10.1029/2010GB003848
- Kohfeld, K. E., Le Quéré, C., Harrison, S. P., and Anderson, R. F., (2005). Role of marine biology in glacial-interglacial CO₂ cycles. *Science* 308, 74–78. doi: 10.1126/science.1105375
- Langer, M. R. (1988). Recent epiphytic foraminifera from Vulcano (Mediterranean Sea). *Rev. Paléobiol. BENTHOS'86 Special* 2, 827–832.
- Larkum, A. W. D., Orth, R. J., and Duarte, C. M. (2006). *Seagrasses: Biology, Ecology and Conservation*. Dordrecht: Springer, 691.
- Lo Iacono, C., Mateo, M. A., Gracia, E., Guasch, C. R., Serrano, L., and Dañobeitia, J. (2008). Very high-resolution seismo-acoustic imaging of seagrass meadows (Mediterranean Sea): implications for carbon sink estimates. *Geophys. Res. Lett.* 35:L18601. doi: 10.1029/2008GL034773
- Mateu-Vicens, G., Box, A., Deudero, S., and Rodríguez, B. (2010). Comparative analysis of epiphytic foraminifera in sediments colonized by seagrass *Posidonia oceanica* and invasive macroalgae *Caulerpa* spp. *J. Foramin. Res.* 40, 134–147. doi: 10.2113/gsjfr.40.2.134
- Mateu-Vicens, G., Brandano, M., Gaglione, G., and Baldassarre, A. (2012). Seagrass-meadow sedimentary facies in a mixed siliciclastic-carbonate temperate system in the Tyrrhenian Sea (Pontinian Islands, Western Mediterranean). *J. Sediment. Res.* 82, 451–463. doi: 10.2110/jsr.2012.42
- Mateu-Vicens, M., Hallock, P., and Brandano, M. (2008). A depositional model and paleoecological reconstruction of the lower Tortonian distally steepened ramp of Menorca (Balearic Islands, Spain). *Palaios* 23, 465–481. doi: 10.2110/palo.2007.p07-061r
- McLeod, E., Chmura, G. L., Bouillon, S., Salm, R., Björk, M., Duarte, C. M., et al. (2011). A blueprint for blue carbon: toward an improved understanding of the role of vegetated coastal habitats in sequestering CO₂. *Front. Ecol. Environ.* 9, 552–560. doi: 10.1890/110004
- Nellemann, C., Corcoran, E., Duarte, C. M., Valdés, L., De Young, C., Fonseca, L., et al. (2009). *Blue Carbon. A Rapid Response Assessment*. Arendal: GRID-Arendal: United Nations Environment Programme.
- Nelsen, J. E., and Ginsburg, R. N. (1986). Calcium carbonate production by epibionts on thalassia in florida bay. *J. Sediment. Petrol.* 56, 622–628.
- Perry, C. T., and Beavington-Penney, S. J. (2005). Epiphytic calcium carbonate production and facies development within sub-tropical seagrass beds, Inhaca Island, Mozambique. *Sediment. Geol.* 174, 161–176. doi: 10.1016/j.sedgeo.2004.12.003
- Rasheed, M. A. (2004). Recovery and succession in a multi-species tropical seagrass meadow following experimental disturbance: the role of sexual and asexual reproduction. *J. Exp. Mar. Biol. Ecol.* 310, 13–45. doi: 10.1016/j.jembe.2004.03.022
- Raven, J. A., and Falkowski, P. G. (1999). Oceanic sinks for atmospheric CO₂. *Plant Cell Environ.* 22, 741–755.

- Reich, S., Di Martino, E., Todd, J. A., Wesselingh, F. P., and Renema, W. (2015). Indirect paleo-seagrass indicators (IPSI): a review. *Earth Sci. Rev.* 143, 161–186. doi: 10.1016/j.earscirev.2015.01.009
- Royer, D. L., Pagani, M., and Beerling, D. J. (2012). Geobiological constraints on Earth system sensitivity to CO₂ during the Cretaceous and Cenozoic. *Geobiology* 10, 298–310. doi: 10.1111/j.1472-4669.2012.00320.x
- Seton, M., Müller, R. D., Zahirovic, S., Gaina, D., Torsvik, T., Shepard, G., et al. (2012). Global continental and ocean basin reconstructions since 200 Ma. *Earth Sci. Rev.* 113, 212–270. doi: 10.1016/j.earscirev.2012.03.002
- Short, F. T., Carruthers, T., Dennison, W., and Waycott, M. (2007). Global seagrass distribution and diversity: a bioregional model. *J. Exp. Mar. Biol. Ecol.* 350, 3–20. doi: 10.1016/j.jembe.2007.06.012
- Short, F. T., Koch, E., Creed, J. C., Magalhaes, K. M., Fernandez, E., and Gaeckle, J. L. (2006). SeagrassNet monitoring across the Americas: case studies of seagrass decline. *Mar. Ecol.* 27, 277–289. doi: 10.1111/j.1439-0485.2006.0095.x
- Short, F. T., and Wyllie-Echeverria, S. (1996). Natural and human-induced disturbances of seagrass. *Environ. Conserv.* 23, 17–27.
- Spalding, M., Taylor, M., Ravilious, C., Short, F., and Green, E. (2003). “Global overview: the distribution and status of seagrasses,” in *World Atlas of Seagrasses*, eds E. P. Green and F. T. Short (Berkeley, CA: University of California Press), 5–26.
- Tomassetti, L., Benedetti, A., and Brandano, M. (2016). Middle Eocene seagrass facies from Apennine carbonate platforms (Italy). *Sediment. Geol.* 335, 136–149. doi: 10.1016/j.sedgeo.2016.02.002
- Tomás, S., Frijia, G., Bömelburg, E., Zamagni, J., Perrin, C., and Mutti, M. (2016). Evidence for seagrass meadows and their response to paleoenvironmental changes in the early Eocene (Jafnayn Formation, Wadi Bani Khalid, N Oman). *Sediment. Geol.* 341, 189–202. doi: 10.1016/j.sedgeo.2016.05.016
- Trenberth, K. E., and Smith, L. (2005). The mass of the atmosphere: a constraint on global analyses. *J. Clim.* 18, 864–875. doi: 10.1175/jcli-3299.1
- Vélez-Juarbe, J. (2014). Ghost of seagrasses past: using sirenians as a proxy for historical distribution of seagrasses. *Palaeogeogr. Palaeoclimatol. Palaeoecol.* 400, 41–49.
- Wanless, H. R. (1981). Fining-upwards sedimentary sequences generated in seagrass beds. *J. Sediment. Res.* 51, 445–454.
- Waycott, M., Duarte, C. M., Carruthers, T. J. B., Orth, R. J., Dennison, W. C., Olyarnik, S., et al. (2009). Accelerating loss of seagrasses across the globe threatens coastal ecosystems. *Proc. Natl. Acad. Sci. U.S.A.* 106, 12377–12381. doi: 10.1073/pnas.0905620106
- Weissert, H., and Erba, E. (2004). Volcanism, CO₂ and palaeoclimate: a Late Jurassic–Early Cretaceous carbon and oxygen isotope record. *J. Geol. Soc.* 161, 695–702.
- Wessel, P., and Smith, W. H. (1995). *The Generic Mapping Tools, GMT, Version 3: Technical Reference and Cookbook*. Manoa: School of Ocean and Earth Science and Technology, University of Hawaii at Manoa.
- Willenbring, J. K., and von Blanckenburg, F. (2010). Long-term stability of global erosion rates and weathering during late-Cenozoic cooling. *Nature* 465, 211–214. doi: 10.1038/nature09044
- Zamagni, J., Mutti, M., and Košir, A. (2008). Evolution of shallow benthic communities during the late Palaeocene–earliest Eocene transition in the Northern Tethys (SW Slovenia). *Facies* 54, 25–43. doi: 10.1007/s10347-007-0123-3

Conflict of Interest Statement: The authors declare that the research was conducted in the absence of any commercial or financial relationships that could be construed as a potential conflict of interest.

Copyright © 2016 Brandano, Cuffaro, Gaglianone, Petricca, Stagno and Mateu-Vicens. This is an open-access article distributed under the terms of the Creative Commons Attribution License (CC BY). The use, distribution or reproduction in other forums is permitted, provided the original author(s) or licensor are credited and that the original publication in this journal is cited, in accordance with accepted academic practice. No use, distribution or reproduction is permitted which does not comply with these terms.



The Hyperarid Core of the Atacama Desert, an Extremely Dry and Carbon Deprived Habitat of Potential Interest for the Field of Carbon Science

Armando Azua-Bustos^{1,2*}, Carlos González-Silva³ and Gino Corsini²

¹ Centro de Astrobiología (Consejo Superior de Investigaciones Científicas-Instituto Nacional de Técnica Aeroespacial), Madrid, Spain, ² Instituto de Ciencias Biomédicas, Facultad de Ciencias de la Salud, Universidad Autónoma de Chile, Santiago, Chile, ³ Centro de Investigación del Medio Ambiente, Universidad Arturo Prat, Iquique, Chile

OPEN ACCESS

Edited by:

Donato Giovannelli,
Earth-Life Science Institute of Tokyo
Institute of Technology, Japan

Reviewed by:

Sara Borin,
Università degli Studi di Milano, Italy
Mustafa Yucel,
Middle East Technical University,
Turkey

*Correspondence:

Armando Azua-Bustos
aazua@cab.inta-csic.es

Specialty section:

This article was submitted to
Microbiological Chemistry and
Geomicrobiology,
a section of the journal
Frontiers in Microbiology

Received: 24 January 2017

Accepted: 17 May 2017

Published: 08 June 2017

Citation:

Azua-Bustos A, González-Silva C and Corsini G (2017) The Hyperarid Core of the Atacama Desert, an Extremely Dry and Carbon Deprived Habitat of Potential Interest for the Field of Carbon Science. *Front. Microbiol.* 8:993.
doi: 10.3389/fmicb.2017.00993

The Atacama Desert in Chile is the driest and oldest desert on Earth, also considered one of the best Mars analog models. Here, several heterotrophic microbial communities have been discovered in its driest regions, with the ones present in the soil subsurface being one of the most interesting due to its existence in a habitat with almost no water available and almost undetectable organic carbon sources. Our recent discovery of the driest site of the Atacama known to date (and the heterotrophic microbial species that are able to survive in this site) reaffirms the opportunity to better characterize the physiological and molecular mechanisms that these species use to detect, mobilize, incorporate and use carbon under these extremely harsh conditions. Here we summarize what has been reported up to date on the organic carbon concentrations in different sites of the hyperarid core of the Atacama Desert, proposing that due to the meager amounts of carbon and extremely dry conditions, the microbial communities of the hyperarid core of the Atacama Desert may be of interest for the field of carbon science.

Keywords: Atacama Desert, organic carbon, desert ecosystems, Mars, carbon science

INTRODUCTION

The Atacama Desert, located in northern Chile (Figure 1), encompasses about 105,000 square kilometers. It is bordered on the east by the Andes Mountains and on the west by the Coastal Range. The Atacama is well known for being the driest (McKay et al., 2003; Azua-Bustos et al., 2015) and oldest desert on Earth, estimated to be arid of the past 150 million years and hyperarid for the past 15 million years (Pueyo et al., 2001; Houston and Hartley, 2003; Hartley et al., 2005; Rech et al., 2006).

It was thought that no lifeforms could survive the extremely dry and high UV radiation levels of the hyperarid core of the Atacama (Navarro-González et al., 2003), however, several heterotrophic microbial species were later reported living in this extremely harsh environment (reviewed in Azua-Bustos et al., 2012a). Although the current interest of the scientific community is to understand how these microorganisms are able to tolerate the extreme desiccation and high UV radiation conditions of the Atacama (Wierzchos et al., 2006; Azua-Bustos et al., 2009, 2010, 2011; Paulino-Lima et al., 2016), nothing has yet been reported on how heterotrophic species are able to obtain, mobilize and use organic carbon in a place where carbon and water are virtually absent. In this short hypothesis paper, we review the reports up to date on organic carbon concentrations

in soils of the Atacama, proposing that due to the meager amounts of organic carbon and extremely dry conditions, the microbial communities of the hyperarid core of the Atacama Desert may be of interest for the field of carbon science (for a review on the biodiversity of heterotrophic microbial species reported in the hyperarid core of the Atacama see Azua-Bustos et al., 2012a,b).

WHAT HAS BEEN REPORTED ABOUT ORGANIC CARBON AND LIFE IN THE ATACAMA DESERT

Navarro-González et al. (2003) were the first to report organic carbon concentrations of soils of the hyperarid core of the Atacama. Using samples from the Yungay region, these authors used Pyrolysis-Gas Chromatography-Mass Spectrometry to report that soil samples from the Yungay region were almost depleted of organic molecules, with only minor amounts of formic acid (1 mmol g^{-1}) and benzene (1 mmol g^{-1}), compounds typically released by the thermal treatment of various types of organic molecules. The formic acid/benzene ratio suggested that the organic matter present in this region was highly oxidized and probably composed of refractory organics such as aliphatic and aromatic mono/polycarboxylic acids. Interestingly, these authors reported that samples from the Yungay region contained extremely low levels of heterotrophic bacteria detected by dilution plating (only one colony per every 10 plates), with no DNA recovered from these soils.

Later, Glavin et al. (2004) using a new method to estimate bacterial cell counts analyzed surface and subsurface samples from the Flat Top Hill site, located approximately 12 km south east of Yungay. These authors found only trace levels of nucleobases ($0.04\text{--}0.6 \text{ nmol/g}$) in subsurface soil samples, corresponding to a total bacterial concentration of 4.4×10^6 of *Escherichia coli* cell equivalents (ECE)/g of soil. In the case of the superficial samples, no adenine was detected, suggesting levels below 5×10^6 ECE/g.

In a later report, Glavin et al. (2006) analyzed surface soil samples from Yungay, finding adenine concentrations of 0.04 nmol/g corresponding to about 4×10^6 *E. Coli* cell equivalents/g. This value was two orders of magnitude higher than total viable counts of culturable bacteria previously measured by serial dilution plating in Yungay samples by Navarro-González et al. (2003) suggesting that these soil samples contained mostly non-culturable bacteria.

Buch et al. (2006) using a novel extraction procedure coupled with chemical derivatization to target organic compounds by gas chromatography mass spectrometry (GC-MS) also analyzed soil samples from the hyperarid core. GC-MS analysis of water and isopropanol (1:1 mixture) extracts showed that both amino (alanine; 1.1×10^{-9}) and carboxylic acids (benzoic acid; 2.7×10^{-9}) were readily extracted, supporting the hypothesis of Benner et al. (2000) in that carboxylic acids such as benzenecarboxylic acid are abundant in oxidizing soils like the

ones found in the Atacama, as well as other organic compounds of biological importance like urea and amino acids.

Amashukeli et al. (2007) also addressed the organic composition and oxidation chemistry of soils of the Yungay region. Using soil surface samples, amino acids like glycine, alanine, valine, aspartic acid, serine and glutamic acid were readily extracted in the range of 1–70 ppb. The number of cell equivalents in one gram of soil calculated from this data was estimated to be slightly higher (10^5) than the ones previously reported for surface samples, owing to the alleged ability of their method to extract amino acids from both viable and non-viable cells.

Lester et al. (2007) also analyzed surface and subsurface soil samples of the Yungay region, finding extremely low total organic carbon contents, ranging between 560 and 765 mg/g. PLFA analysis unveiled surface concentrations of about 1.0×10^7 cells/g, five times higher than that of subsurface samples, which ranged from 2.0×10^6 to 2.4×10^6 cells/g.

Connon et al. (2007) similarly analyzed surface and subsurface soil samples in the Yungay area, focusing in two sites that were previously analyzed by Navarro-González et al. (2003) and Lester et al. (2007). These authors found that the total organic carbon content of these soils was extremely low, ranging between 200 and 700 mg per g of soil. PLFA analysis showed values ranging from 2×10^5 to 7×10^6 cell equivalents per gram of soil.

Barros et al. (2008) also examined soils samples from the hyperarid core of the Atacama by using Calorimetry, reporting that total carbon in these soils ranged from 0.17 to 2.66 g per 100 g of soil, with the lowest values measured at the driest sites.

In one of the most focused studies on this topic, Fletcher et al. (2012) investigated the variability of surface soil organic carbon within the Yungay region. They reported labile organic carbon values that ranged from 2 to 73 mg/g of soil, consistent with the variability of other studies in the Yungay area. Crits-Christoph et al. (2013) also analyzed samples from six locations in the hyperarid core, reporting TOC values of less than 0.01%.

In 2015 we reported the discovery of Maria Elena South ($22^{\circ}15'39''\text{S}$, $69^{\circ}43'29''\text{W}$) the driest site of the already hyperarid Atacama (Azua-Bustos et al., 2015). We found that soil samples from Maria Elena South showed extremely low, albeit variable levels of organics (0.1–1.1%). Depending on the depth from where samples were taken, we proposed that this variability may represent the number of microbial species (*Streptomyces*, *Bacillus*, *Geodermatophilus*) found along the soil profile.

In an interesting approach to analyze microhabitats in the hyperarid core of the Atacama, Warren-Rhodes et al. (2006) examined the occurrence of heterotrophic and autotrophic hypolithic microorganisms colonizing translucent stones along an aridity gradient. These authors found that total organic carbon was five times more in the soil under the hypolithic community ($46 \pm 15 \text{ mmol g}^{-1}$) than in the surface soil ($9 \pm 3 \text{ mmol g}^{-1}$), suggesting that these colonized stones are extreme types of “islands of fertility” in the Atacama.

In a similar approach toward microhabitats colonized by heterotrophic and autotrophic microorganisms, Ziolkowski et al. (2013) reported total organic carbon concentrations in samples from gypsum, Ignimbrite, and halites from a salt pan close to

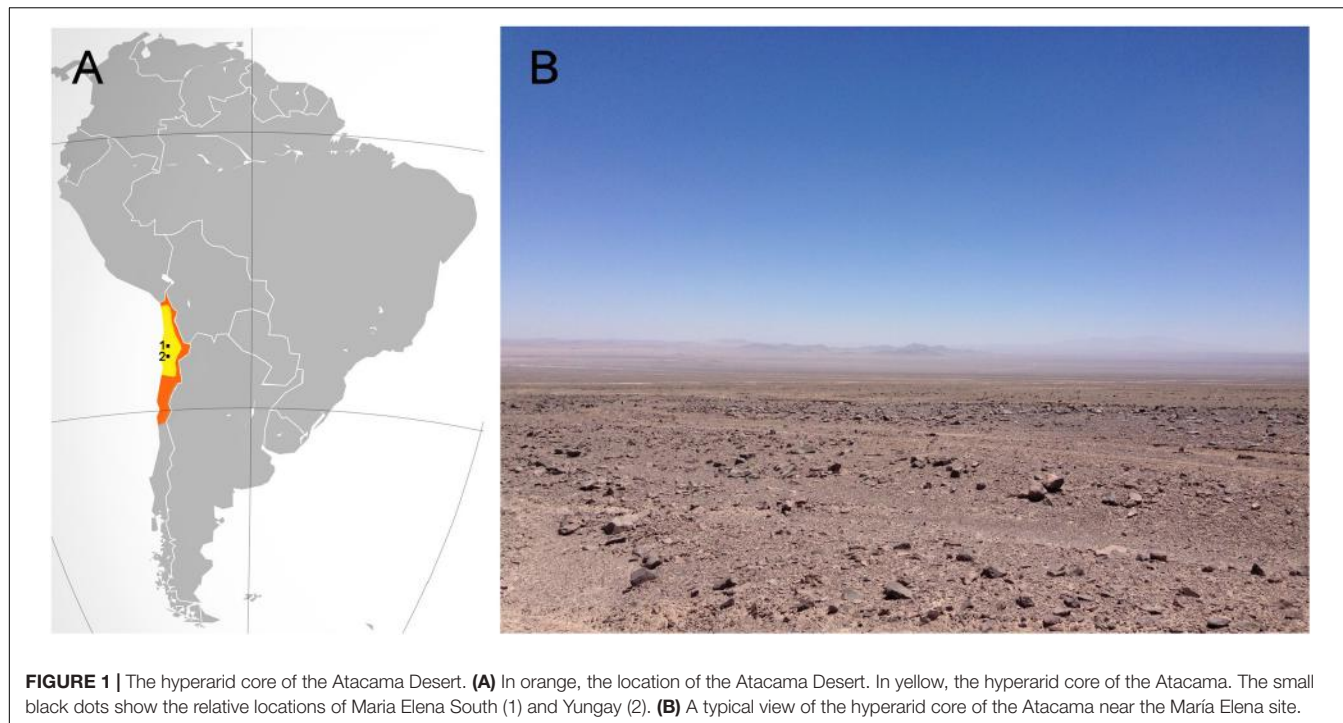


FIGURE 1 | The hyperarid core of the Atacama Desert. **(A)** In orange, the location of the Atacama Desert. In yellow, the hyperarid core of the Atacama. The small black dots show the relative locations of María Elena South (1) and Yungay (2). **(B)** A typical view of the hyperarid core of the Atacama near the María Elena site.

the Coastal Range and Yungay of 0.2, 0.1, and 0.4% respectively. These values also matched those reported by Robinson et al. (2015) on halites samples colonized by cyanobacteria and heterotrophic species collected at different sites of the hyperarid core of the Atacama, including Yungay, all with less than 0.7%.

HOW IS LIFE ABLE TO SURVIVE IN THE HYPERARID CORE WITH SUCH MEAGER CARBON SOURCES?

Dissolved and particulate organic carbon are critical components in the global carbon cycle and serve as a primary food sources for all Earth's ecosystems. When considering the characteristics of the hyperarid core, a number of questions arise that may be brought to the attention of the researchers of the field of carbon science (the objective of this hypothesis paper), leading to a number of testable hypothesis and research directions:

(A) Sources of organic carbon:

- What fraction of the organic carbon detected in soils of the hyperarid core is native and how much comes from external sources? There are no reports that have directly tackled this question. However, Ewing et al. (2007) showed that nitrogen and organic carbon concentrations measured in airborne samples at the hyperarid core are consistent with marine aerosols, suggesting long-term non-anthropogenic depositions. In addition, these authors proposed that atmospheric nitrogen deposition dominates nitrogen inventories, which would also probably be the case for organic carbon.

- If a fraction of the organic carbon comes from external sources, where it comes from and how is transported to the

hyperarid core? Wang et al. (2014) did not measure the transport of organic carbon as did Ewing et al. (2007), nevertheless these authors showed that different types of salts (Na^+ , Cl^- , SO_4^{2-} , Mg^{2+} , Ca^+ , etc.) reach the hyperarid core as seawater droplets and anthropogenic emissions transported by the wind in a west to east direction from the Pacific Ocean. This suggestion coincides with the general wind patterns observed in this area provided by the US National Weather Service's National Centers for Environmental Prediction's Environmental Modeling Center.

If so, a carbon-focused set of transects along a west to east transect across the hyperarid core of the Atacama would confirm the sources and rates of atmospheric depositions of organic carbon coming from the Pacific Ocean.

Hypothesis N1: The main fraction of organic carbon in the soils of the hyperarid core come transported by the winds coming from the Pacific Ocean.

- What are the native sources of organic carbon? As the Atacama has been an extremely arid place for a long time, most of the native organic carbon in the hyperarid core probably comes from the few microbial species that were able to adapt to its soils million of years ago. This possibility agrees with recent findings of very ancient microorganisms in the Coastal Range of the Atacama (Azua-Bustos et al., 2009), closely related to aquatic species (Azua-Bustos et al., 2012b) thus endorsing a west to east colonization of the hyperarid core by species that migrated with the prevailing winds.

Hypothesis N2: The native organic fraction in soils of the hyperarid core of the Atacama Desert come from ancient native microorganisms.

- What fraction of the native organic carbon detected in soils of the hyperarid core represents living soil biota and dead biotic material? Fletcher et al. (2011) directly approached this question using several molecular methods, and concluded that it was difficult to determine whether organic carbon in soils of the hyperarid core comes from dead or living cells, as different methods underestimate or overestimate cell concentrations. Nevertheless, Ewing et al. (2007), suggested that phospholipid fatty acid analysis (PLFA) may be a proper method to solve this question, as PLFA likely represent only viable biomass even at the driest sites.

Hypothesis N3: The native organic fraction in soils of the hyperarid core of the Atacama Desert can be determined by phospholipid fatty acid analysis.

(B) Persistence of the organic carbon:

- For how long is organic carbon able to persist in surface soils of the hyperarid core given the presence of oxidizing agents like perchlorates and the continuous exposition to high levels of UV radiation? The Hyperarid core of the Atacama is well known for the widespread presence of a variety of salts, including highly oxidizing species like iodates, chromates and the largest natural deposit of perchlorates (ClO_4^-) known on Earth (Erickson, 1981). In the hyperarid core of the Atacama, perchlorate concentrations can reach up to 0.6 wt % (Erickson, 1981), which origin is probably atmospheric (Bao and Gu, 2004; Catling et al., 2010). As already mentioned, Navarro-González et al. (2003) determined the presence of strong oxidants in soils of the Yungay region, but without identifying them. Later, Valdivia-Silva et al. (2009) showed that organics mixed with hyperarid soils are oxidized to CO_2 , suggesting the presence of at least two unidentified types of oxidants; a thermolabile highly oxidative oxidant and a thermostable oxidant with minor oxidative activity. Quinn et al. (2005) also approached this question by characterizing the oxidizing agents present in soil samples of the region of Yungay. These authors found that NO_x , SO_2 and O_3 are oxidized through gas-phase reactions into sulfuric acid and nitric acid, which then adsorb onto aerosols and deposit as dust particles transported by the wind. The levels of these acids in the dust are not high, but their dissolution on the soil surface affect the soil pH which can get highly acidic during periods of higher relative humidity, which in the case of Yungay, are frequent at night time.

Quinn et al. (2007) then directly measured the decomposition of organic compounds by adding ^{13}C -labeled alanine, formate and glucose solutions to Yungay soils. These authors reported that during the first days of incubation alanine and glucose decomposed at rates of 0.1–0.2 $\mu\text{mol}/\text{d}$, with formate decomposing at rates of 0.4 $\mu\text{mol}/\text{d}$. These authors also observed equal $^{13}\text{CO}_2$ production rates by soils treated with D-glucose and L-alanine (compared to soils treated with L-glucose and D-alanine) suggesting a non-biological chemical decomposition. Interestingly, an increase in the decomposition rates of D-glucose and L-alanine (compared to L-glucose and D-alanine) was later observed, suggesting

a second phase of biological decomposition of the added organics.

Pertaining the effects of the UV radiation, there are several reports on the level of tolerance by different species of microorganisms to UV radiation, both native of the Atacama and also introduced as models (Cockell et al., 2008; Paulino-Lima et al., 2013, 2016). However, there are no reports on how specific organic molecules degrade in time when exposed to the daily fluxes of UV radiation typical the hyperarid core of the Atacama. Thus, any organic compound that arrives to the soil surface will most likely be quickly degraded by oxidizing salts and UV radiation, while subsurface organic compounds will be mainly degraded by oxidizing salts. An experiment using different types of organic molecules to measure how long this degradation process takes and what are the products of such degradation will be informative on this point.

Hypothesis N4: Organic compounds that arrive to the soil surface of the hyperarid core of the Atacama Desert are quickly degraded by oxidizing salts and UV radiation.

Hypothesis N5: Organic compounds present below the surface of the soils of the hyperarid core of the Atacama Desert are mainly degraded by oxidizing salts.

- Does the origin of the organic carbon (external/native) influence its range of persistence in soils of the hyperarid core? As mentioned before, several species of microorganisms highly tolerant to UV radiation have been found in the hyperarid core of the Atacama (Paulino-Lima et al., 2013, 2016), and may be assumed that most of the organic compounds of such species should persist for a longer time in these soils. If so, the organic compounds found in these hyperarid soils should mainly come from native microorganisms, also supporting hypothesis N2.

- Independent of its source, is organic carbon able to move along the soil column of the hyperarid core, how and at what rates?

Given the previous remarks, little or no exogenous organic compounds should be able to move along the soil column at the hyperarid core of the Atacama, as for this not only these compounds should be able to survive the processes of oxidation and UV at its surface, but also would depend on enough rains to move down column (the interaction of organics, oxidizing salts and water have not yet been approached in these sites). A similar assertion would apply for the native organic compounds already present in the soil profile. Altogether this may explain the extremely low organics typically reported in the hyperarid core of the Atacama. However, this interpretation does not answer on how these organic compounds got into the soil depth in the first place.

(C) Metabolism of the organic carbon:

- How are heterotrophic microorganisms able to mobilize and incorporate soil organic carbon given the extremely low amounts of water availability typical of the hyperarid core of the Atacama?

This is an extremely interesting question, and up to date there have been no approaches in this subject. It may be assumed that the microorganisms close enough to the soil surface may use the meager amounts of water that is able to infiltrate in the extremely infrequent rain events in this region, and that under these conditions they may access the organic compounds in the close vicinity. An additional possibility is that some of the salts typically present in the hyperarid core of the Atacama are known to be highly hygroscopic, and that through deliquescence they may absorb water under infrequent conditions of high relative humidity (Davila et al., 2008; Robinson et al., 2015). However, this process would only work in the first centimeters of the soil surface, and would not impact the microorganisms present beyond 15 cm of depth. This again leaves the question open on what is the source of water of the microorganisms deeper in the soil profile.

- Can inorganic carbon be used by soil heterotrophic microbial species of the hyperarid core? It is well known that autotrophic nitrifiers are able to reduce inorganic carbon to form organic carbon (Kindaichi et al., 2004). Nitrifying bacteria have been reported in the hyperarid core of the Atacama (Cameron et al., 1966; Erickson, 1981), thus providing a mechanism on the use of inorganic carbon by heterotrophic bacteria. If so, a bacterial consortia may be expected to be found in the hyperarid core of the Atacama containing the aforementioned metabolic routes.

REFERENCES

- Amashukeli, X., Pelletier, C. C., Kirby, J. P., and Grunthaner, F. J. (2007). Subcritical water extraction of amino acids from atacama desert soils. *J. Geophys. Res.* 112:G04S16. doi: 10.1029/2006jg000308
- Azua-Bustos, A., Caro-Lara, L., and Vicuña, R. (2015). Discovery and microbial content of the driest site of the hyperarid atacama desert. *Chile. Environ. Microbiol. Rep.* 7, 388–394. doi: 10.1111/1758-2229.12261
- Azua-Bustos, A., González-Silva, C., Arenas-Fajardo, C., and Vicuña, R. (2012b). Extreme environments as potential drivers of convergent evolution by exaptation: the atacama desert Coastal Range case. *Front. Microbiol.* 3:426. doi: 10.3389/fmicb.2012.00426
- Azua-Bustos, A., González-Silva, C., Mancilla, R. A., Salas, L., Gómez-Silva, B., McKay, C. P., et al. (2011). Hypolithic cyanobacteria supported mainly by fog in the coastal range of the atacama desert. *Microb. Ecol.* 61, 568–581. doi: 10.1007/s00248-010-9784-5
- Azua-Bustos, A., González-Silva, C., Mancilla, R. A., Salas, L., Palma, R. E., Wynne, J. J., et al. (2009). Ancient photosynthetic eukaryote biofilms in an atacama desert coastal cave. *Microb. Ecol.* 58, 485–496. doi: 10.1007/s00248-009-9500-5
- Azua-Bustos, A., González-Silva, C., Salas, L., Palma, R. E., and Vicuña, R. (2010). A novel subaerial *Dunaliella* species growing on cave spiderwebs in the atacama desert. *Extremophiles* 14, 443–452. doi: 10.1007/s00792-010-0322-7
- Azua-Bustos, A., Urrejola, C., and Vicuña, R. (2012a). Life at the dry edge: microorganisms of the atacama desert. *FEBS Lett.* 586, 2939–2945. doi: 10.1016/j.febslet.2012.07.025
- Bao, H., and Gu, B. (2004). Natural perchlorate has a unique oxygen isotope signature. *Environ. Sci. Technol.* 38, 5077–5077. doi: 10.1021/es049516z
- Barros, N., Feijóo, S., Salgado, J., Ramajo, B., García, J. R., and Hansen, L. D. (2008). The dry limit of microbial life in the atacama desert revealed by calorimetric approaches. *Eng. Life Sci.* 8, 477–486. doi: 10.1002/elsc.200820236
- Benner, S. A., Devine, K. G., Matveeva, L. N., and Powell, D. H. (2000). The missing organic molecules on Mars. *Proc. Natl. Acad. Sci. U.S.A.* 97, 2425–2430. doi: 10.1073/pnas.040539497
- Buch, A., Glavin, D. P., Sternberg, R., Szopa, C., Rodier, C., Navarro-González, R., et al. (2006). A new extraction technique for in situ analyses of amino and carboxylic acids on Mars by gas chromatography mass spectrometry. *Planet. Space Sci.* 54, 1592–1599. doi: 10.1016/j.pss.2006.05.041
- Cameron, R. E., Gensel, D. R., and Blank, G. B. (1966). Soil studies -desert microflora xii. Abundance of microflora in soil samples from the chile atacama desert. space programs summary. *Jet Propulsion Lab.* IV, 37.
- Catling, D. C., Claire, M., Zahnle, K. J., Quinn, R. C., Clark, B. C., Hecht, M. H., et al. (2010). Atmospheric origins of perchlorate on mars and in the Atacama. *J. Geophys. Res. Planets* 115:E00E11. doi: 10.1029/2009je003425
- Cockell, C. S., McKay, C. P., Warren-Rhodes, K., and Horneck, G. (2008). Ultraviolet radiation-induced limitation to epilithic microbial growth in arid deserts—Dosimetric experiments in the hyperarid core of the atacama desert. *J. Photochem. Photobiol.* 90, 79–87. doi: 10.1016/j.jphotobiol.2007.11.009
- Connon, S. A., Lester, E. D., Shafaat, S. H., Obenhuber, D. C., and Ponce, A. (2007). Bacterial diversity in hyperarid atacama desert soils. *J. Geophys. Res.* 112:G04S17. doi: 10.1029/2006jg000311
- Crits-Christoph, A., Robinson, C. K., Barnum, T., Fricke, W. F., Davila, A. F., Jedynak, B., et al. (2013). Colonization patterns of soil microbial communities in the atacama desert. *Microbiome* 1:28. doi: 10.1186/2049-2618-1-28
- Davila, A. F., Gómez-Silva, B., de los Rios, A., Ascaso, C., Olivares, H., McKay, C. P., et al. (2008). Facilitation of endolithic microbial survival in the hyperarid core of the atacama desert by mineral deliquescence. *J. Geophys. Res.* 113:G01028. doi: 10.1029/2007jg000561
- Erickson, G. E. (1981). Geology and origin of the chilean nitrate deposits. *Paper presented at the U. S. Geological Survey Professional Paper No. 1188*: Washington DC, 12.
- Ewing, S. A., Michalski, G., Thiemens, M., Quinn, R., Macalady, J., Kohl, S., et al. (2007). Rainfall limit of the N cycle on earth. *Glob. Biogeochem. Cycles* 21, GB3009. doi: 10.1029/2006gb002838
- Fletcher, L. E., Conley, C. A., Valdivia-Silva, J. E., Perez-Montaña, S., Condori-Apaza, R., Kovacs, G. T., et al. (2011). Determination of low bacterial concentrations in hyperarid Atacama soils: comparison of biochemical and

Hypothesis S6: Heterotrophic microbial communities present in the soils of the hyperarid core of the Atacama Desert are able to use inorganic carbon with the aid of native nitrifying bacteria.

Overall, a similar set of core questions are found in field of carbon research, as carbon science explores how much carbon is in Earth, how it moves, what form it takes, where and how it originated, and how it has changed over billions of years. Similarly to the case of carbon research, in order to answer these proposed questions an interdisciplinary approach will be required, integrating the knowledge of chemists, physicists, geologists, and biologists in the case of the hyperarid core of the Atacama Desert.

AUTHOR CONTRIBUTIONS

AA-B, CG-S, and GC wrote and reviewed the submitted manuscript.

FUNDING

GC received funding from the Fondo de Apoyo a la Investigación, Proyecto DIP 39-2015 from the Universidad Autónoma de Chile. AA-B thanks the European Research Council, Starting Grant no 307496.

- microscopy methods with real-time quantitative PCR. *Can. J. Microbiol.* 57, 953–963. doi: 10.1139/w11-091
- Fletcher, L. E., Valdivia-Silva, J. E., Perez-Montaño, S., Condori-Apaza, R. M., Conley, C. A., and McKay, C. P. (2012). Variability of organic material in surface horizons of the hyper-arid Mars-like soils of the atacama desert. *Adv. Space. Res.* 49, 271–279. doi: 10.1016/j.asr.2011.10.001
- Glavin, D. P., Cleaves, H. J., Buch, A., Schubert, M., Aubrey, A., Bada, J. L., et al. (2006). Sublimation extraction coupled with gas chromatography-mass spectrometry: a new technique for future in situ analyses of purines and pyrimidines on Mars. *Planet. Space Sci.* 54, 1584–1591. doi: 10.1016/j.pss.2005.12.023
- Glavin, D. P., Cleaves, H. J., Schubert, M., Aubrey, A., and Bada, J. L. (2004). New method for estimating bacterial cell abundances in natural samples by use of sublimation. *Appl. Environ. Microbiol.* 70, 5923–5928. doi: 10.1128/AEM.70.10.5923-5928.2004
- Hartley, A. J., Chong, G., Houston, J., and Mather, A. (2005). 150 million years of climatic stability: evidence from the atacama desert, Northern Chile. *J. Geol. Soc. Lond.* 162, 421–424. doi: 10.1144/0016-764904-071
- Houston, J., and Hartley, A. (2003). The central Andean west-slope rainshadow and its potential contribution to the origin of hyperaridity in the atacama desert. *Int. J. Climatol.* 23, 1453–1464. doi: 10.1002/joc.938
- Kindaichi, T., Ito, T., and Okabe, S. (2004). Ecophysiological interaction between nitrifying bacteria and heterotrophic bacteria in autotrophic nitrifying biofilms as determined by microautoradiography-fluorescence in situ hybridization. *Appl. Environ. Microbiol.* 70, 1641–1650. doi: 10.1128/AEM.70.3.1641-1650.2004
- Lester, E. D., Satomi, M., and Ponce, A. (2007). Microflora of extreme arid atacama desert soils. *Soil. Biol. Biochem.* 39, 704–708. doi: 10.1016/j.soilbio.2006.09.020
- McKay, C. P., Friedmann, E. I., Gómez-Silva, B., Cáceres-Villanueva, L., Andersen, D. T., and Landheim, R. (2003). Temperature and moisture conditions for life in the extreme arid region of the atacama desert: four years of observations including the El Niño of 1997–1998. *Astrobiology* 3, 393–406. doi: 10.1089/153110703769016460
- Navarro-González, R., Rainey, F. A., Molina, P., Bagaley, D. R., Hollen, B. J., de la Rosa, J., et al. (2003). Mars-like soils in the atacama desert, Chile, and the dry limit of microbial life. *Science* 302, 1018–1021. doi: 10.1126/science.1089143
- Paulino-Lima, I. G., Azua-Bustos, A., Vicuña, R., González-Silva, C., Salas, L., Teixeira, L., et al. (2013). Isolation of UVC-tolerant bacteria from the hyperarid atacama desert, Chile. *Microb. Ecol.* 65, 325–335. doi: 10.1007/s00248-012-0121-z
- Paulino-Lima, I. G., Fujishima, K., Navarrete, J. U., Galante, D., Rodrigues, F., Azua-Bustos, A., et al. (2016). Extremely high UV-C radiation resistant microorganisms from desert environments with different manganese concentrations. *J. Photochem. Photobiol. B* 163, 327–326. doi: 10.1016/j.jphotobiol.2016.08.017
- Pueyo, J. J., Chong, G., and Jensen, A. (2001). Neogene evaporites in desert volcanic environments: atacama desert, northern Chile. *Sedimentology* 48, 1411–1431. doi: 10.1046/j.1365-3091.2001.00428.x
- Quinn, R., Zent, A., Grunthaner, F., Ehrenfreund, P., Taylor, C., and Garry, J. (2005). Detection and characterization of oxidizing acids in the atacama desert using the Mars Oxidation Instrument. *Planet. Space Sci.* 53, 1376–1388. doi: 10.1016/j.pss.2005.07.004
- Quinn, R. C., Ehrenfreund, P., Grunthaner, F. J., Taylor, C. L., and Zent, A. P. (2007). Decomposition of aqueous organic compounds in the atacama desert and in Martian soils. *J. Geophys. Res.* 112:G04S18. doi: 10.1029/2006JG000312
- Rech, J. A., Currie, B. S., Michalski, G., and Cowan, A. M. (2006). Neogene climate change and uplift in the atacama desert, Chile. *Geology* 34, 761–764. doi: 10.1130/G22444.1
- Robinson, C. K., Wierzchos, J., Black, C., Crits-Christoph, A., Ma, B., Ravel, J., et al. (2015). Microbial diversity and the presence of algae in halite endolithic communities are correlated to atmospheric moisture in the hyper-arid zone of the atacama desert. *Environ. Microbiol.* 17, 299–315. doi: 10.1111/1462-2920.12364
- Valdivia-Silva, J. E., Navarro-González, R., and McKay, C. (2009). Thermally evolved gas analysis (TEGA) of hyperarid soils doped with microorganisms from the atacama desert in southern Peru: implications for the Phoenix mission. *Adv. Space Res.* 44, 254–266. doi: 10.1016/j.asr.2009.02.008
- Wang, F., Michalski, G., Seo, J. H., and Ge, W. (2014). Geochemical, isotopic, and mineralogical constraints on atmospheric deposition in the hyper-arid atacama desert, Chile. *Geochim. Cosmochim. Acta* 135, 29–48. doi: 10.1016/j.gca.2014.03.017
- Warren-Rhodes, K. A., Rhodes, K. L., Pointing, S. B., Ewing, S. A., Lacap, D. C., Gómez-Silva, B., et al. (2006). Hypolithic cyanobacteria, dry limit of photosynthesis, and microbial ecology in the hyperarid atacama desert. *Microb. Ecol.* 52, 389–398. doi: 10.1007/s00248-006-9055-7
- Wierzchos, J., Ascaso, C., and McKay, C. P. (2006). Endolithic cyanobacteria in halite rocks from the hyperarid core of the atacama desert. *Astrobiology* 6, 415–422. doi: 10.1089/ast.2006.6.415
- Ziołkowski, L. A., Wierzchos, J., Davila, A. F., and Slater, G. F. (2013). Radiocarbon evidence of active endolithic microbial communities in the hyperarid core of the Atacama Desert. *Astrobiology* 13, 607–616. doi: 10.1089/ast.2012.0854

Conflict of Interest Statement: The authors declare that the research was conducted in the absence of any commercial or financial relationships that could be construed as a potential conflict of interest.

Copyright © 2017 Azua-Bustos, González-Silva and Corsini. This is an open-access article distributed under the terms of the Creative Commons Attribution License (CC BY). The use, distribution or reproduction in other forums is permitted, provided the original author(s) or licensor are credited and that the original publication in this journal is cited, in accordance with accepted academic practice. No use, distribution or reproduction is permitted which does not comply with these terms.



Weaving a Knowledge Network for Deep Carbon Science

Xiaogang Ma^{1,2*}, **Patrick West**², **Stephan Zednik**², **John Erickson**², **Ahmed Eleish**², **Yu Chen**², **Han Wang**², **Hao Zhong**² and **Peter Fox**²

¹ Department of Computer Science, University of Idaho, Moscow, ID, USA, ² Tetherless World Constellation, Rensselaer Polytechnic Institute, Troy, NY, USA

OPEN ACCESS

Edited by:

Donato Giovannelli,
Earth-Life Science Institute – Tokyo
Institute of Technology, Japan

Reviewed by:

Alessandro Sarretta,
Consiglio Nazionale delle Ricerche –
Istituto di Scienze Marine, Italy
Christian Schröder,
University of Stirling, UK
Holly M. Bik,
University of California, Riverside, USA

*Correspondence:

Xiaogang Ma
max@uidaho.edu
xgmachina@gmail.com

Specialty section:

This article was submitted to
Geochemistry,
a section of the journal
Frontiers in Earth Science

Received: 13 January 2017

Accepted: 28 April 2017

Published: 15 May 2017

Citation:

Ma X, West P, Zednik S, Erickson J, Eleish A, Chen Y, Wang H, Zhong H and Fox P (2017) Weaving a Knowledge Network for Deep Carbon Science. *Front. Earth Sci.* 5:36.
doi: 10.3389/feart.2017.00036

Geoscience researchers are increasingly dependent on informatics and the Web to conduct their research. Geoscience is one of the first domains that take lead in initiatives such as open data, open code, open access, and open collections, which comprise key topics of Open Science in academia. The meaning of being open can be understood at two levels. The lower level is to make data, code, sample collections, and publications, etc., freely accessible online and allow reuse, modification, and sharing. The higher level is the annotation and connection between those resources to establish a network for collaborative scientific research. In the data science component of the Deep Carbon Observatory (DCO), we have leveraged state-of-the-art information technologies and existing online resources to deploy a web portal for the over 1,000 researchers in the DCO community. An initial aim of the portal is to keep track of all research and outputs related to the DCO community. Further, we intend for the portal to establish a knowledge network, which supports various stages of an open scientific process within and beyond the DCO community. Annotation and linking are the key characteristics of the knowledge network. Not only are key assets, including DCO data and methods, published in an open and inter-linked fashion, but the people, organizations, groups, grants, projects, samples, field sites, instruments, software programs, activities, meetings, etc., are recorded and connected to each other through relationships based on well-defined, formal conceptual models. The network promotes collaboration among DCO participants, improves the openness and reproducibility of carbon-related research, facilitates accreditation to resource contributors, and eventually stimulates new ideas and findings in deep carbon-related studies.

Keywords: data stewardship, knowledge network, eScience, semantic web, ontologies

INTRODUCTION

Recent advances in cyberinfrastructure facilitate the culture of open science (Nosek et al., 2015) and also provide a space for conducting scientific work in a more efficient way. The geoscience community has taken an active role in the discussion and efforts on open access publication (Harnad and Brody, 2004), open samples (Lehnert et al., 2006), open source software (Hey and Payne, 2015), and open data (Glaves, 2017). Geoscience researchers are increasingly dependent on information technologies and the World Wide Web to conduct and communicate their research. The keyword “open” in those open science efforts does not mean to publish individual works or resources as separated fragments. Instead, those resources can be categorized, annotated, and

connected to each other, and thus form a knowledge network (Ma et al., 2014b). In such a network, each node has its resource type and is described with detailed and meaningful information, such as a rock sample registered at a museum (Devaraju et al., 2016). There are also various types of relationships connecting among nodes. For instance, there could be a relationship “registrant” which connects a rock sample to a researcher. In turn, there could be another relationship “author of” which connects the researcher to a number of publications (Figure 1). Such an open knowledge network has a lot of potential uses in resource discovery and access, program administration, research collaboration, scientometrics, research trend analysis, and more. To build and implement such a network, however, needs cross-disciplinary collaboration to identify the information to be covered as well as state-of-the-art methodologies and technologies to realize the network in an operable platform. In a recent research program called Deep Carbon Observatory (DCO), under the Data Science activity, we successfully carried out a study in that direction and put it into practical use for the DCO community.

DCO is a 10-year (2009–2019) global scientific initiative focusing on the study of carbon in deep Earth. More than 1,000 researchers across the world have been participated in this initiative, and the research is organized into four science communities—Deep Energy, Deep Life, Extreme Physics, and Chemistry and Reservoirs and Fluxes. Funded activities include computational model development, new instrument design, novel technology application, exploratory research, and fieldwork, scientific conferences, and early career summer school/meetings. Facing the opportunities enabled by the cyberinfrastructure and open science, the DCO community has been seeking new ways of data management and data analytics

through various DCO data science activities led by the team at Rensselaer Polytechnic Institute. A most recent achievement of those activities is a knowledge network, which is now in its practical version. The platform for the implementation of this network, called the Deep Carbon Virtual Observatory (DCvO), has the following characteristics and functions: a schema categorizing various concepts in DCO scientific works, a capability to define, and describe provenance information such as key entities, agents, and activities in a workflow, a repository for storing research datasets and the metadata annotating them, tools for scientific communication, and collaborations, and an integrated portal with friendly user interface for managing all those resources and applications. DCvO sets up an environment to facilitate open science within the DCO Community (Fox, 2015).

DCvO provides a means to collaborate, seek out and access education, and research materials such as publications and datasets, view community activities, view DCO field sites, learn about funded projects, and more. The intent of the DCvO, just like DCO itself, is to stimulate new ways to conduct and share deep carbon-related research. Underlying DCvO is the application of ideas, practices, and technologies from the fields of information science, data management, data analytics, computer science, and physical sciences using contemporary cyberinfrastructure and information technologies. DCvO promotes collaboration among DCO participants, improves the openness and reproducibility of carbon-related research, facilitates accreditation to resource contributors, and eventually stimulate new ideas and findings in deep carbon-related studies. The rest of the paper will introduce the methods and technological components applied to construct the DCO knowledge network, and features of a few realized modules in DCvO.

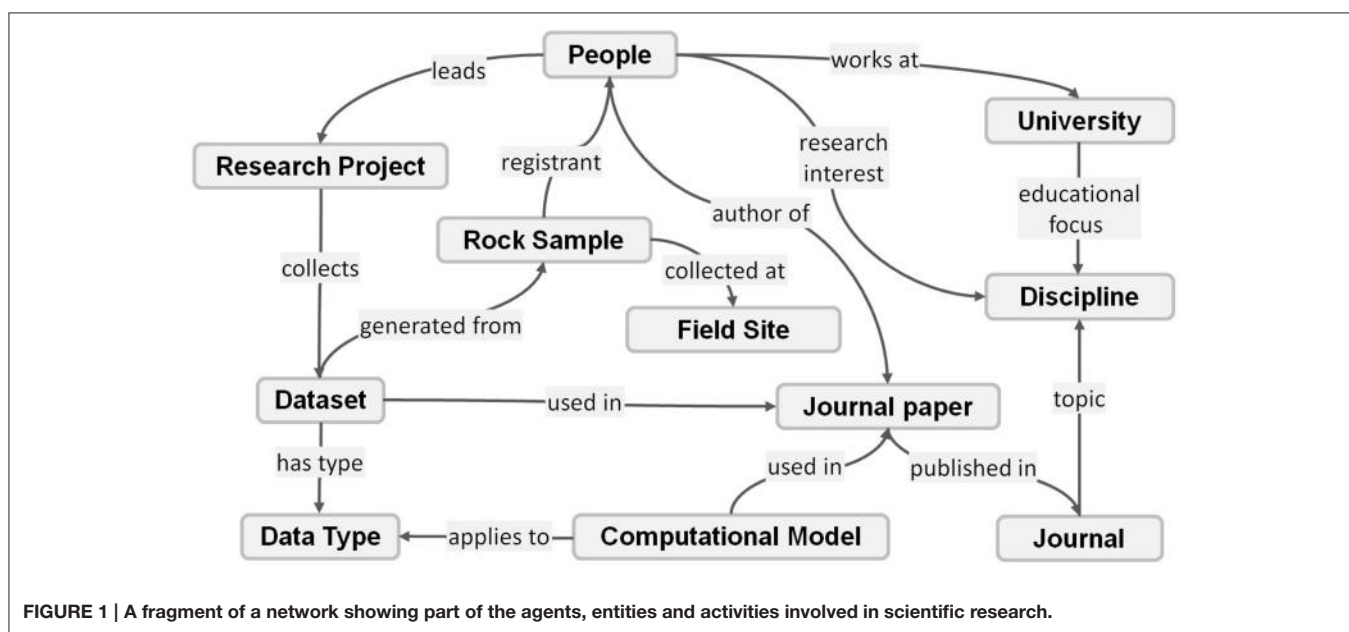


FIGURE 1 | A fragment of a network showing part of the agents, entities and activities involved in scientific research.

METHODS AND TECHNOLOGIES

Add Structures and Meanings to Content

To make the output of our work easily accessible by geoscientists and address the features of open science, we conducted our work within the context of the World Wide Web and used state-of-the-art web technologies. More specifically, the context of our work is the Semantic Web, which is defined as an extension to the current Web by adding machine readable structures, meanings, and context to information on the Web (Berners-Lee et al., 2001). The Web is now in the transition from a Web of Documents to a Web of Data because of the embedded structures and meanings that did not exist before. Nevertheless, to add structure and meaning to the information on the Web, formal specifications of concepts and the interrelationships among concepts are needed. In the Semantic Web such formal specifications are called ontologies. Each ontology is the formal specification of the shared conceptualization (Gruber, 1995) of a domain of study. In an inter-disciplinary context there thus could be a large number of ontologies. While those ontologies each address a certain topic, there could be interrelationships among them, which are the key to weave a bigger knowledge graph. In our work for the DCO science and the DCvO, a primary work is to recognize domain specific ontologies to be reused or developed, and the integration of all those ontologies into an umbrella ontology called the DCO ontology (<http://info.deepcarbon.net/schema>). The core of DCO ontology is the VIVO ontology (Mitchell et al., 2011), which reuses and extends a list of ontologies to support information management in the academia. In DCO ontology we further extended the VIVO ontologies by adding concepts and relationships recognized from the DCO science needs (Ma et al., 2015) and also by reusing several other ontologies (Table 1), including the PROV Ontology (Lebo et al., 2013) for provenance documentation and DCAT (Maali and Erickson, 2014) to represent data catalogs.

As noted above, those sub-ontologies within the DCO ontology are not isolated from each other but are inter-connected as a knowledge network for representing the objects in the scientific workflow (cf. PROV-O core model) as well as their interrelationships for the DCO scientific community. The reuse and adaptation of those ontologies is driven by needs in the DCO science community and we applied a use case-driven approach (Fox and McGuinness, 2008) to analyze the needs. Subsequently, we identified and collected the ontologies to be reused, or created new concepts and relationships as an extension to existing ontologies. The inter-mappings among those ontologies (Table 1) set up the foundation for the DCO science knowledge network. For example, four ontologies bibo, c4o, cito, and fabio were used to record individual records and the network of bibliographic information, foaf was used for individuals and the network of researchers and organizations. Then vivo and dco ontologies were used to extend the inter-connections among researchers and publications, as well as other objects such as projects, grants, keywords, funding awards, and more. Our work of provenance records in DCvO leveraged the W3C standard prov (<https://www.w3.org/TR/prov-o/>), which represents a high level framework. Components in a few domain ontologies, such

TABLE 1 | Ontologies and schemas used in DCvO.

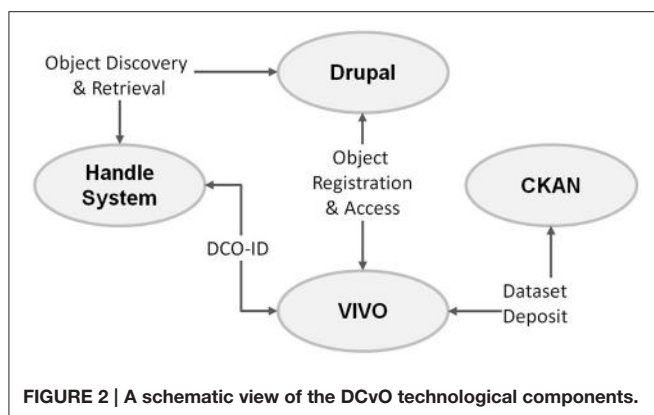
Name	Namespace URL	Prefix
Bibliographic ontology	http://purl.org/ontology/bibo/	bibo
Citation counting and context characterization ontology	http://purl.org/spar/c4o/	c4o
Citation typing ontology	http://purl.org/spar/cito/	cito
Data catalog vocabulary	http://www.w3.org/ns/dcat#	dcat
DCMI metadata terms	http://purl.org/dc/terms/	dct
DCO schema	http://info.deepcarbon.net/schema#	dco
Dublin core metadata element set	http://purl.org/dc/elements/1.1/	dc
Event ontology	http://purl.org/NET/c4dm/event.owl#	event
FRBR-aligned bibliographic ontology	http://purl.org/spar/fabio/	fabio
Friend of a friend	http://xmlns.com/foaf/0.1/	foaf
Geopolitical ontology	http://aims.fao.org/aos/geopolitical.owl#	geo
PROV ontology	http://www.w3.org/ns/prov#	prov
Simple knowledge organization system	http://www.w3.org/2004/02/skos/core#	skos
vCard ontology	http://www.w3.org/2006/vcard/ns#	vcard
VIVO core	http://vivoweb.org/ontology/core#	vivo
VIVO scientific research ontology	http://vivoweb.org/ontology/scientific-research#	scires

as dco, foaf, and vivo can be mapped as subclasses or sub-properties of corresponding parts in prov (Ma et al., 2014c).

A Technological Framework for DCvO

The knowledge graph realized by the DCO ontology set up a framework for filling in detailed records from the DCO community. Through the knowledge graph those records will have structured description and are interconnected with meaningful relationships, which as whole we referred to as the DCO knowledge network. To weave that knowledge network and implement it in DCvO, a technological framework was developed (Figure 2), which consisted of four major parts: Drupal (<https://www.drupal.org>) was used to develop the main front-end portal where users can contribute and access various types of information; The Global Handle System (<https://www.handle.net>) was used to assign a unique identifier called DCO-ID, to the records in the knowledge network; VIVO (<http://vivoweb.org>) was used as the main knowledge store for archiving the ontologies and the detailed records; and CKAN (<http://ckan.org>) was used for the storage of datasets and other media files.

DCvO enables individual researchers or collaborative groups to record and connect most objects in the procedure their research life cycle, from funding applications, instrument proposal, field investigation, data processing, experiment documentation, to publication archival, and project report, and more. In the virtual environment of DCvO, researchers can



register details about their previous activities and publications as well as current research interests. Such information will enable researchers sharing similar interests to discover and communicate with each other and propose future works. In DCvO, each DCO-ID represents an object and corresponds to a Web address (URL). Once a researcher knows the DCO-ID of a certain object, he can easily access more detailed information in the DCvO by resolving a DCO-ID in a Web browser. All instance object records in the knowledge network can be annotated with selected subjects from one or a few common ontologies and vocabularies. In this way, those objects are linked directly or indirectly to each other. For instance, a researcher tags a dataset uploaded by him with a few labels as its keywords. Some of those labels are used by another researcher as his research interests. For the latter researcher, he can easily find that the dataset can be of interest by using those labels in data search. Similarly, those labels can also be used as keywords for other resources such as funded projects, journal papers and research institutions and will make it easier for the researcher to find those resources. Such features of annotated and interconnected resources in DCvO can help expand researchers' understanding of his research and promote efficient conduction.

IMPLEMENTATION AND RESULTS

For end users of the knowledge network, either from the DCO community or the general public, the most familiar site is the DCO community portal (**Figure 3**) which was developed based on Drupal. As a member of the community, i.e., registered, one can submit ad hoc content like news and information of events to the community website, and via the menu bar item “Data Portal” can explore and use resources associated with the knowledge network. All content in the knowledge network is open to the public, including the DCO community. However, in order to be able to add and/or update records in the knowledge network one needs to be a registered member, which can be done through a member registration process. The following sections introduce a few of the functions enabled by using the knowledge network.

Semantically Enriched Faceted Browsers

To enhance the publication search capability in the DCvO, faceted browsing (Ellis and Vasconcelos, 1999) has been utilized. This interface is accessible on the DCO website (**Figure 4**) and undergoes regular enhancements. For example, in the last year more facets were added (including DCO Community, author, and year) to expand selection choices, and more information about selections such as publication type and related DCO community is displayed in the result set, and more features available to enhance the users' ability to search for and retrieve publications. Along the left of the browser shown in **Figure 4** are expandable facets, which can be used to create a specific search of the database. Each facet represents a certain type of object in DCO. The appearance of linked entries among those facets represent a view of the DCO knowledge network and that such linked content can appear on many pages or in browsers under different contexts (e.g., publications, field sites, etc.). For example, if a user wants to search by authors, he can expand the author facet. Or, the user can search using keywords after expanding that facet. The search box at the top allows free text search and queries all information. In another example, if a user wants to find all the publications related to “molecular biology,” he can just type that word in the search box. Or if he wants to see all publications authored by Robert Hazen, he can just type the last name “Hazen” in the search box and hit the search button.

The search and retrieve mechanism of the faceted browser greatly speeds up information discovery and access. The DCO knowledge network is recorded in a Semantic Web triple store where all DCO metadata are stored as linked data. That store can handle complex queries for discovering concepts and the relationships among them, retrieving complex information and relationships, and more and rendered on almost all of the web pages on the DCO website. The disadvantage of the particular triple store in use, in most cases, is that as more and more information is stored, the slower text-based searches become. Although the technology has taken great leaps forward in performance and scalability over the last couple of years, it is still relatively slow. Triple stores are best suited to relationship queries and not free-text.

As a result, the improved publications browser information is ingested from the triple store into an inverted index, using an open source product called ElasticSearch (<https://www.elastic.co>). Using an inverted index approach (Seo et al., 2003) allows for searching over a great amount of text including keywords, abstracts, descriptions, author names, etc., very quickly. Thus, in the publications faceted search, information is displayed much faster than a browser that queries the triple store directly. Using the same technologies we also developed faceted browsers for other objects, such as datasets, people, grants, field studies, and more.

Scientific Data Types for DCO Data

DCO data come in all shapes and forms. Tables, for example, contain data but often lack context, or mix data with metadata. Such context might include the meanings of quantity names and units, acronyms, or community jargon, or the inter-relatedness of data columns or rows. To address such issues, we have

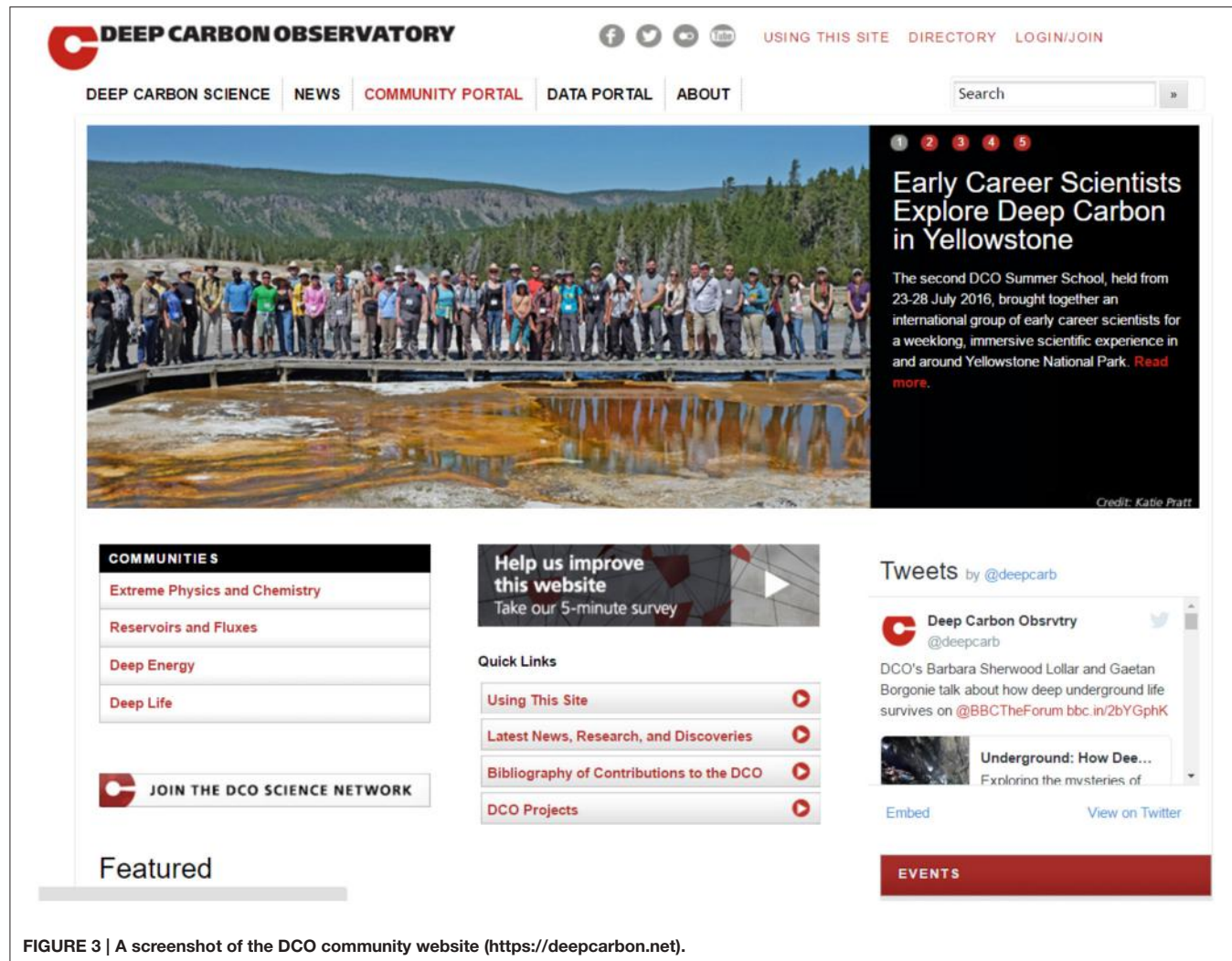


FIGURE 3 | A screenshot of the DCO community website (<https://deepcarbon.net>).

been working on ways to make disparate datasets accessible to scientists in diverse scientific disciplines by focusing on scientific context (Ma et al., 2016).

Traditional data types typically are limited to the numerical type of the datum, such as integer, float, array, char (character), or string. For example, a researcher might receive a table of numbers from a colleague, the title of which includes the word “Thermodynamics”; data that are relevant to their research. Beyond this, the table’s data may be represented only by column headers, typically acronyms, one hopes well-known in the particular scientific domain. Moreover, any description of the relationships between the table’s columns is not obvious, let alone explicit. However, many researchers think of categories of data, i.e., higher level ways of describing data they generate. For example: Volcanic Gas Composition. To enable such science context in computer-enabled data environments, the notion of “data type” must be extended so that a given data type represents a scientifically useful description of what the datasets associated with the category name actually represents. The ability to specify data types in this fashion enables researchers to better understand

the meaning and ultimately usefulness or relevance, of datasets in a given scientific context.

The large number of DCO datasets currently registered by many scientists in DCO’s four communities include a wide variety of formats and quantities with associated metadata about basic data types spanning Earth sciences, biological sciences, and beyond. The metadata (collected when datasets are registered with DCO) enables researchers to find and access DCO datasets via the Dataset Browser. A scientist might have a very specific request in mind though, such as “I need thermodynamic data from the DCO Extreme Physics and Chemistry Community that includes Mineral Name and Molecular Weight.” Without proper metadata annotations, addressing this specific, but likely common, request is difficult, not only among DCO scientists but across scientific domains. Until recently, no widely agreed upon approach had been taken to address requests with scientific context, and researchers had to resort to other means of finding/assessing datasets.

Such broad issues in data management are the focus of initiatives such as the Research Data Alliance (RDA,

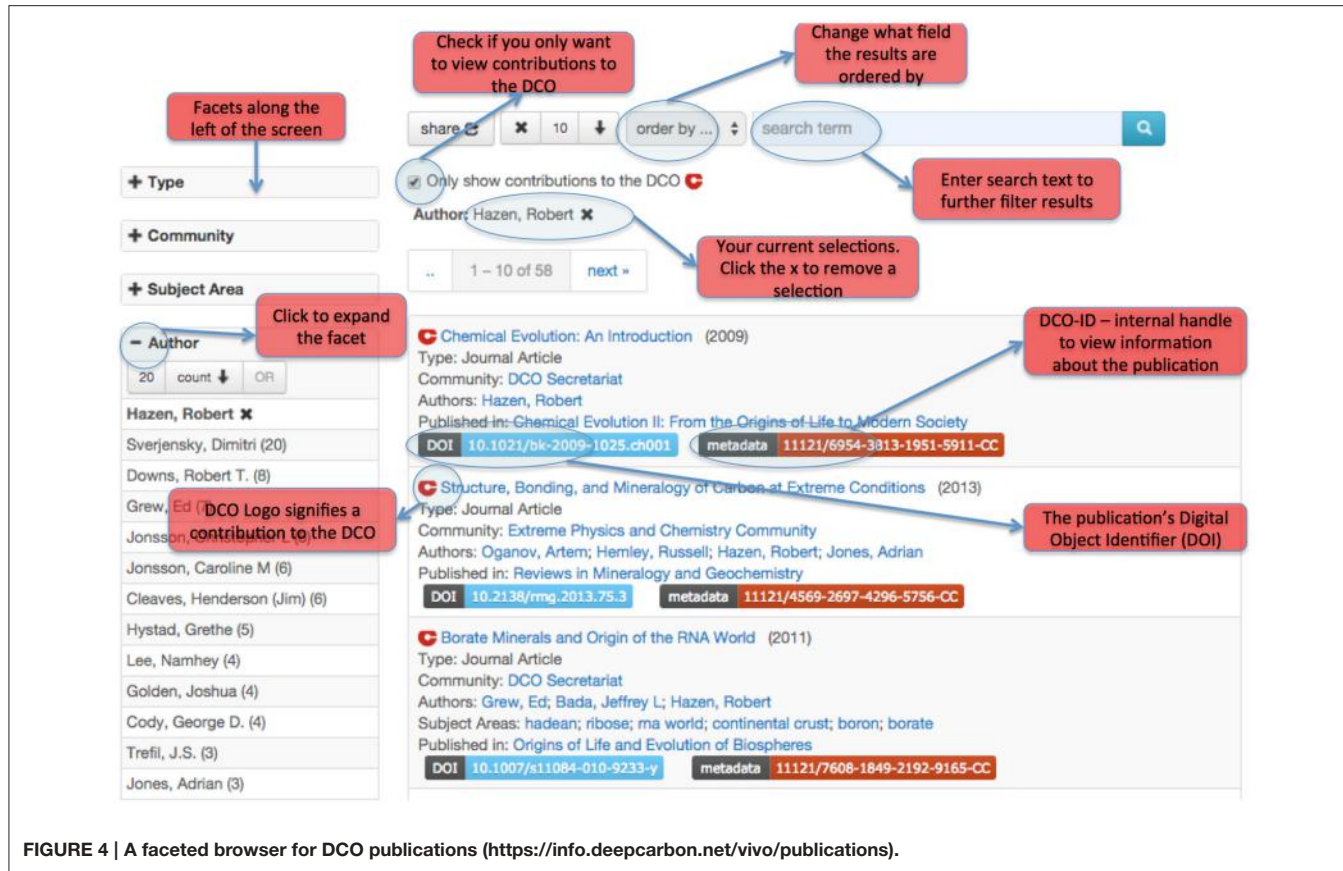


FIGURE 4 | A faceted browser for DCO publications (<https://info.deepcarbon.net/vivo/publications>).

<https://www.rd-alliance.org>). RDA is an international effort whose mission is to "... build the social and technical bridges that enable open sharing of data across technologies, disciplines, and countries." One of the bridge-building efforts to improve data sharing and data use in science communities involves a framework for developing "scientific data types." In 2015, we leveraged some funding from the National Science Foundation, via the RDA to make the DCvO one of the first platforms adopting two key RDA recommendations that greatly improved the modeling of scientific data types. The RDA deliverables adopted by DCO are the Data Type Registry (DTR) and Persistent Identifier Information Types (PIT). The first addresses a core interoperability problem among data management systems: the ability to parse, understand, and potentially reuse data retrieved from others. Scientific data types are visible to users. The second addresses the essential types of information associated with persistent identifiers [e.g., identifiers for people such as ORCID (<https://orcid.org>) are of a different "type" than identifiers for publications such as DOIs]. Permanent identifier types are largely invisible to users.

The curation and reuse of registered datasets within DCvO was well suited for testing deployments of RDA DTR and PIT because it helps address the challenges described in the above example of searching for thermodynamic datasets of interest, and provided valuable experience for other science communities who face the same issues.

In its implementation of RDA DTR and PIT, we first made updates to the DCO ontology, the backbone of DCvO, to incorporate concepts of data type and associated attributes. We collected data type instances from the DCO community and used them to annotate some initial datasets currently registered with DCvO. Results from this work are evident in the faceted DCO dataset browser and data type browser (Figure 5).

The above example, a researcher looking for thermodynamic data that includes Mineral Name and Molecular Weight, can first look for a corresponding data type using the data type browser. In that browser he can search Mineral Name and Molecular Weight in the facet window for Parameters and through which he can locate a data type, such as Thermodynamics of Chemicals and Minerals. Once the researcher finds that information, he can go to the dataset browser and retrieve all relevant datasets using that known data type. The researcher can also use the DCO Communities facet to restrict results to a subset, i.e., those generated by the DCO Extreme Physics and Chemistry Community. Using and expanding the registered (science context) data types, we foresee some future innovation, such as recommending datasets to a user based on his research interests and recommending tools for data analysis for specific data types. Such efforts will significantly facilitate work on data curation and promote the sharing and usability of deposited data. DCvO is also open for DCO science communities to add or suggest new data types for their datasets.

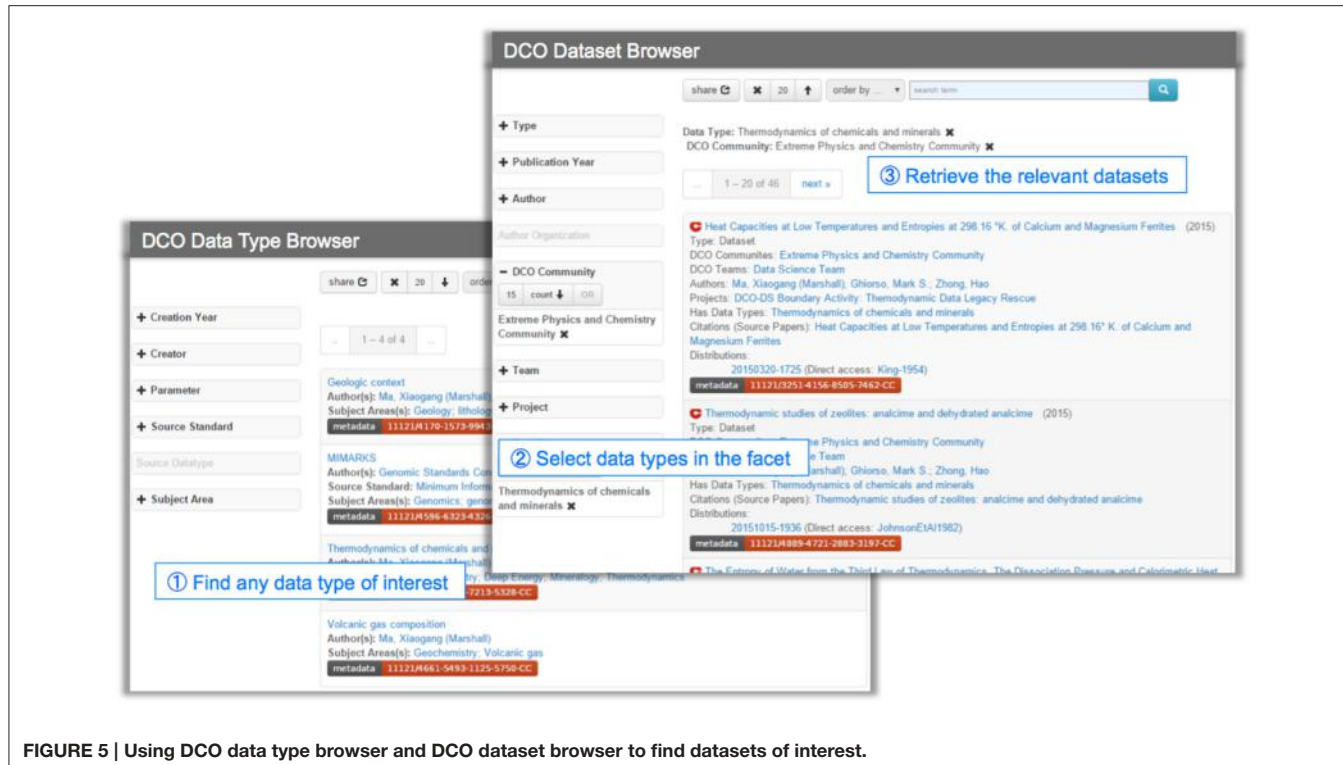


FIGURE 5 | Using DCO data type browser and DCO dataset browser to find datasets of interest.

Thermodynamic Data Rescue

A huge number of legacy datasets are contained in geoscience literature, often in the form of tables, and figures. Extracting, organizing, and reusing these datasets is valuable for many within the Earth and planetary science community. To explore methods and techniques for data rescue and management, we and Prof. Mark Ghiorso, and Extreme Physics and Chemistry community member identified thermodynamic datasets related to carbon as a proof of principle analysis, with a focus on records about the enthalpy and entropy of chemicals. The team developed a semi-automatic method for doing this. First, Ghiorso collected papers of focused themes in the fields of mineralogy, geochemistry, and petrology. We then extracted, reviewed, and registered the datasets via DCvO following the guidelines listed in the DCO data policy (<https://deepcarbon.net/page/dco-open-access-and-data-policies>). Most of those collected papers were published before the 1980s. Although provided in PDF format, their contents were scanned from printed copies and were saved as images. The workflow ensures extracted records are correct, well-organized and are saved in known formats. The resulting datasets are published and made discoverable through the DCO dataset browser (Figure 6).

To date, the team has dealt with three main types of datasets: (1) heat content or enthalpy data determined for a given compound as a function of temperature using high-temperature calorimetry, (2) heat content or enthalpy data determined for a given compound as a function of temperature using adiabatic calorimetry, and (3) direct determination of heat capacity of a compound as a function of temperature using

differential scanning calorimetry. We have collected publications with additional thermodynamic sources, and an effort to rescue more datasets is ongoing. This will lead to a comprehensive characterization of the thermodynamics of carbon and carbon-related materials.

During the work, the team preserved individual datasets from various “frozen” and “dark” places as an open and stable data legacy via DCvO. Besides data registration and deposit (Figure 2), DCvO retains essential metadata for data discovery, use, and citation, as well as connections from the datasets to their original sources. The team archived each paper as a distinct data source, and collectively these data sources are searchable in DCvO. The “inter-connection” feature of the DCO knowledge network provides a mechanism for connecting rescued datasets beyond their individual data sources, to research domains, DCO Communities, and more; all of which make data discovery and retrieval more effective.

Leveraging Existing Resources to Create a Deep Carbon Data Legacy

The data portal in DCvO was designed to be a place for registering and archiving datasets that are generated from the DCO community as well as the global geoscience community. The “open access” feature of the portal has a meaning of 2-fold. First, the datasets on the portal are open for global access following the DCO data policy. Second, the portal is open for registering metadata of datasets that are stored in other data repositories, such as EarthChem, Pangaea, and National Centers for Environmental Information (NCEI), and others. The

DCO Community: Extreme Physics and Chemistry Community **Data Type: Thermodynamics of chemicals and minerals**

1 – 20 of 42 [next »](#)

C Heat Capacities at Low Temperatures and Entropies at 298.16 °K. of Calcium and Magnesium Ferrites (2015)

Type: Dataset
DCO Communities: Data Science Team; Extreme Physics and Chemistry Community
Authors: Ma, Xiaogang (Marshall); Ghiorso, Mark S.; Zhong, Hao
Projects: DCO-DS Boundary Activity: Thermodynamic Data Legacy Rescue
Has Data Types: Thermodynamics of chemicals and minerals
Citations (Source Papers): Heat Capacities at Low Temperatures and Entropies at 298.16° K. of Calcium and Magnesium Ferrites
Distributions:
20150320-1725 [Direct access: King-1954](#)
metadata [11121/3251-4156-8505-7462-CC](#)

C The Entropy of Water from the Third Law of Thermodynamics. The Dissociation Pressure and Calorimetric Heat of the Reaction Mg(OH)2 = MgO + H2O. The Heat Capacities of Mg(OH)2 and MgO from 20 to 300 °K (2015)

Type: Dataset
DCO Communities: Extreme Physics and Chemistry Community; Data Science Team
Authors: Ma, Xiaogang (Marshall); Ghiorso, Mark S.; Zhong, Hao
Projects: DCO-DS Boundary Activity: Thermodynamic Data Legacy Rescue
Has Data Types: Thermodynamics of chemicals and minerals
Citations (Source Papers): The Entropy of Water from the Third Law of Thermodynamics. The Dissociation Pressure and Calorimetric Heat of the Reaction Mg(OH)2 = MgO + H2O. The Heat Capacities of Mg(OH)2 and MgO from 20 to 300°K
Distributions:
20150320-1659 [Direct access: Giauque-1937](#)
metadata [11121/4849-9105-6683-1153-CC](#)

C High-temperature Heat Contents of Ferrous Oxide, Magnetite and Ferric Oxide (2015)

Type: Dataset
DCO Communities: Extreme Physics and Chemistry Community; Data Science Team
Authors: Ma, Xiaogang (Marshall); Ghiorso, Mark S.; Zhong, Hao
Projects: DCO-DS Boundary Activity: Thermodynamic Data Legacy Rescue
Has Data Types: Thermodynamics of chemicals and minerals
Citations (Source Papers): High-temperature Heat Contents of Ferrous Oxide, Magnetite and Ferric Oxide 1
Distributions:
20150320-1652 [Direct access: Coughlin-1951](#)
metadata [11121/2493-7424-7112-1550-CC](#)

FIGURE 6 | Accessing rescued thermodynamic datasets in the DCO dataset browser. Rectangles indicate key selection concepts and returned results (the datasets themselves).

registration does not retrieve and archive a copy of the dataset in DCvO. Instead, it only deals with metadata. By using the original identifier (e.g., DOI) of the dataset, DCvO generates a redirection to the dataset in its original repository. The strategy of having DCO data collections already stored in existing and sustained community repositories increases the likelihood that these data legacies will continue to be available and valued well after the end of the DCO decade in 2019.

A recent example is the Legacy Russian Volcanic and Hydrothermal Gas Data. The datasets include gas samples from 20 publications, which were previously inaccessible to the non-Russian speaking community. In early 2015, Prof. Tobias Fischer (DCO DECADE program leader), together with expert Russian gas geochemist Yuri Taran (Universidad Autonoma de Mexico), Elena Kalacheva (IVS, Kamchatka), and Nicole Thomas (UNM), translated and compiled those datasets and archived them in EarthChem (See: <http://earthchem.org/featured/fischer>). As those datasets are of interest to the DCO Reservoirs & Fluxes community, their metadata were also registered in DCvO.

The EarthChem DOIs of those datasets allow users navigate from DCvO pages to the dataset download links on EarthChem (Figure 7).

On the data portal of DCvO, each registered dataset has a DCO-ID. The portal also provides several other metadata items that can be used to enrich the description of the dataset, such as associated DCO community, subject area, geographic focus, data type, and more. The enriched metadata description will support users, whether a DCO community member or not, to discover and access datasets of interest. By registering datasets from external repositories in the DCO data portal and enriching their annotation, the DCO data portal facilitates the reuse and circulation of existing data resources in the field of geosciences. Moreover, it leverages the existing data resources to create a unique data legacy for the global deep carbon-related research.

For researchers in the DCO community, by keeping their profile in DCvO up-to-date, adding publications, updating projects throughout the year for easier report generation, and adding datasets into the system, the researcher enables linking

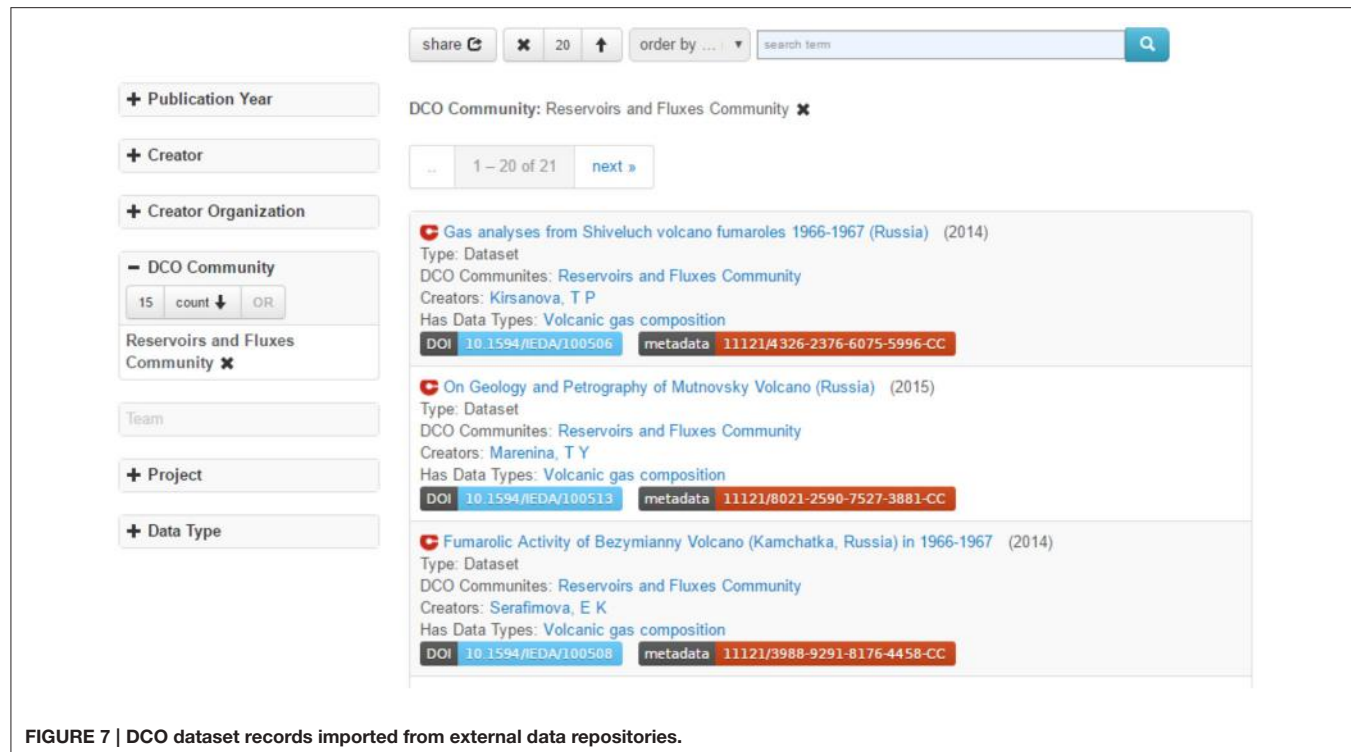


FIGURE 7 | DCvO dataset records imported from external data repositories.

people, organizations, publications, events, projects, grants, data, and more. Whenever a researcher enters information into DCvO they are contributing an ever-increasing network of linked information and documentation of the legacies of the DCO.

DISCUSSION

With the introduction of the Web in the early 1990's the world realized the value of linking documents together and scientific research communities were among the first adopters. In Web 2.0 we saw a quick increase in the use of the Web for social media, e-commerce, and the dynamic creation of pages. With the advent of Semantic Web technologies (Berners-Lee et al., 2001), Web 3.0 became possible, a combination of principles and technology that enables us to link various objects and resources together in ways that both humans and computers can understand. In the Semantic Web, structure and interoperability of datasets are facilitated by the use and reuse of ontologies (Ma and Fox, 2013; Ma et al., 2014a). The reuse of ontologies on the one hand lower the technical burden for ontology maintenance, and on the other hand also promote the sustainability of the knowledge network in the DCvO.

The geoscience community is starting to understand that data, knowledge, and services are linked together, rather than distinct areas of focus or worse isolated. Such linkage is what the DCvO offers in providing dissemination of all outputs of the DCO both for the DCO science community, the broader geoscience community, and the general public. With a knowledge network of interconnected objects and resources we are able to facilitate more and better collaborations, find colleagues working

on similar projects, contribute data that can be useful to others, discover methods, or tools that can analyze data in new ways, and study the patterns in scientific activities and outputs. The accessibility of resources in the DCO knowledge network is significantly improved by using the DCO-ID, which assigns a persistent and stable Web identifier to every resource that is part of DCvO. The DCO-ID will always be valid, even if the underlying resource changes. A researcher's profile is available via a DCO-ID and can be linked to external identifiers such as ORCID, ResearcherID, etc. Each publication of the researcher is available via a DCO-ID, in addition to a DOI if the DOI exists. Moreover, the datasets published by the researcher are also available via their DCO-ID. Our aim is to keep the resources in DCvO as a legacy of the DCO community, which will serve future works of deep carbon science even after the end of the DCO program.

The framework of DCvO presented in this paper, to our knowledge, is the first attempt to connect the platforms Drupal, VIVO, CKAN, and the Handle system. The aim is to leverage the advantage of each platform, such as Drupal for the front end, VIVO for object registration and connection, CKAN for data deposit and the Handle system for persistent identifiers. Many works in this framework was the first technical practice. Data and service standards developed by communities such as those W3C ontologies significantly reduced burdens in the technological development and implementation. Other standards, such as those developed by the Open Geospatial Consortium and the International Organization for Standardization (ISO), although not being described in detail in this paper, also play essential roles in the data flow within the DCvO framework and the communication between DCvO and external systems. The built

system is modularized and is highly reusable. The framework, or parts of it, can be easily deployed at a program or institutional level to address needs similar to DCvO.

There are already data resources on the Web that provide structured information for focused topics such as publications, datasets, geologic samples, and researchers. Some of those resources provide information service via persistent identifiers such as DOI. Such information can be a significant contribution to the DCO knowledge network. The organization CrossRef (<http://www.crossref.org>) provides an interface where machines can retrieve the metadata record of publications using their DOI. DataCite (<https://www.datacite.org>) has been providing a similar service for datasets (sometimes called data publications). ORCID (<https://orcid.org>) has been working on structured information for uniquely identifying researchers, and the International Geo Sample Number (IGSN)’s focus is on the structured records and identification of physical samples. One can see that in the future it will be easier to access detailed and authentic information of an object using a persistent identifier. Such capability will unlock individual records that can become part of many knowledge networks. Nevertheless, there is still the challenge to weave those various topics of information into a specific network such as the DCO knowledge network. Most data resources on the Web, such as those mentioned above, are only able to provide records in literal values, though those values may be structured and well-organized. In contrast, in the knowledge network each object or resource is regarded as a node in the network. To match literal values to nodes in the knowledge network we have developed some semi-automatic techniques in DCvO. For example, one function is matching an author from a CrossRef record to a person in the DCvO. Due to the issues of same names or using initial for first name, a data curator will verify the matching results and choose the correct match. A remaining challenge is to robustly recognize entities from literal values, address ever-present ambiguities in records and weave them into a knowledge network. There is still work to be done.

REFERENCES

- Berners-Lee, T., Hendler, J., and Lassila, O. (2001). The semantic web. *Sci. Am.* 284, 34–43. doi: 10.1038/scientificamerican0501-34
- Devaraju, A., Klump, J., Cox, S. J., and Golodoniu, P. (2016). Representing and publishing physical sample descriptions. *Comput. Geosci.* 96, 1–10. doi: 10.1016/j.cageo.2016.07.018
- Ellis, D., and Vasconcelos, A. (1999). Ranganathan and the net: using facet analysis to search and organise the World Wide Web. *Aslib Proc.* 51, 3–10. doi: 10.1108/EUM0000000006956
- Fox, P. (2015). “Why we need to get smart about data to be better stewards: making smarter virtual observatories,” in *2015 IEEE International Geoscience and Remote Sensing Symposium* (Milan: IGARSS), 1351–1353.
- Fox, P., and McGuinness, D. L. (2008). *TWC Semantic Web Technology*. http://twc.edu/web/doc/TWC_SemanticWebMethodology (Accessed 05.04.17).
- Glaves, H. (2017). “Developing a common global framework for marine data management,” in *Oceanographic and Marine Cross-Domain Data Management for Sustainable Development*, eds P. Diviacco, A. Leadbetter, and H. Glaves (Hershey, PA: IGI Global), 47–68.
- Gruber, T. R. (1995). Toward principles for the design of ontologies used for knowledge sharing. *Int. J. Hum. Comput. Stud.* 43, 907–928. doi: 10.1006/ijhc.1995.1081

CONCLUSION

The work presented in this paper gives a glimpse at one of the first initiatives that deployed leading-edge Semantic Web technologies for large, international research collaborations in the geoscience community. The aim for DCvO is to create more than just a data repository, but a knowledge portal. By using a knowledge network underpinned by ontologies and leveraging state-of-the-art methods in data stewardship, DCvO is able to support various aspects of collaborative geoscience research. The information in DCvO were collected from both the DCO community contributions and several extramural data resources. Detailed records were stored in a way that both humans and machines can read and understand. In the environment of the Semantic Web, a key feature of DCvO is the inter-connections among various registered objects and resources as well as the flexible ways to discover and access them. With the knowledge network the DCO community members are able to add publications and datasets that can be useful to others, find colleagues working on similar projects, discover methods and tools that can be used to analyze data in new ways, and create more and better research collaborations.

AUTHOR CONTRIBUTIONS

XM participated in the research and led the writing of the manuscript. PW, SZ, JE, AE, YC, HW, and HZ participated in the research and contributed to the manuscript writing. PF led the research and contributed to the manuscript writing.

ACKNOWLEDGMENTS

This work was funded by Alfred P. Sloan Foundation through the Deep Carbon Observatory [Award numbers: APS: 2012-10-02 (RPI) and APS: 2014-06-02 (RPI)].

- Harnad, S., and Brody, T. (2004). Comparing the impact of open access (OA) vs. non-OA articles in the same journals. *D-lib Mag.* 10, doi: 10.1045/june2004-harnad
- Hey, T., and Payne, M. C. (2015). Open science decoded. *Nat. Phys.* 11, 367–369. doi: 10.1038/nphys3313
- Lebo, T., Sahoo, S., and McGuinness, D. (2013). *PROV-O: The PROV Ontology*. Accessible online at: <http://www.w3.org/TR/prov-o/>
- Lehnert, K. A., Vinayagamoorthy, S., Djapic, B., Klump, J. (2006). “The digital sample: metadata, unique identification, and links to data and publications,” in *American Geophysical Union Fall Meeting 2006* (San Francisco, CA) Abstract # IN53C-07.
- Ma, X., Erickson, J. S., Zednik, S., West, P., and Fox, P. (2016). Semantic specification of data types for a world of open data. *ISPRS Int. J. Geo Inf.* 5:38. doi: 10.3390/ijgi5030038
- Ma, X., and Fox, P. (2013). Recent progress on geologic time ontologies and considerations for future works. *Earth Sci. Inform.* 6, 31–46. doi: 10.1007/s12145-013-0110-x
- Ma, X., Fox, P., Rozell, E., West, P., and Zednik, S. (2014a). Ontology dynamics in a data life cycle: challenges and recommendations from a Geoscience Perspective. *J. Earth Sci.* 25, 407–412. doi: 10.1007/s12583-014-0408-8

- Ma, X., Fox, P., Tilmes, C., Jacobs, K., and Waple, A. (2014b). Capturing provenance of global change information. *Nat. Clim. Change* 4, 409–413. doi: 10.1038/nclimate2141
- Ma, X., West, P., Erickson, J., Zednik, S., Chen, Y., Wang, H., et al. (2015). “From data portal to knowledge portal: Leveraging semantic technologies to support interdisciplinary studies,” in *Proceedings of the Diversity++ Workshop at ISWC 2015*, (Bethlehem), 6.
- Ma, X., Zheng, J. G., Goldstein, J., Zednik, S., Fu, L., Duggan, B., et al. (2014c). Ontology engineering in provenance enablement for the National Climate Assessment. *Environ. Model. Softw.* 61, 191–205. doi: 10.1016/j.envsoft.2014.08.002
- Maali, F., and Erickson, J. (2014). *Data Catalog Vocabulary (DCAT)*. Available online at: <http://www.w3.org/TR/vocab-dcat/>
- Mitchell, S., Chen, S., Ahmed, M., Lowe, B., Markes, P., Rejack, N., et al. (2011). “The VIVO ontology: enabling networking of scientists,” in *Proceedings of the ACM WebSci’11* (Koblenz), 2.
- Nosek, B. A., Alter, G., Banks, G. C., Borsboom, D., Bowman, S. D., Breckler, S. J., et al. (2015). Promoting an open research culture. *Science* 348, 1422–1425. doi: 10.1126/science.aab2374
- Seo, C., Lee, S. W., and Kim, H. J. (2003). An efficient inverted index technique for XML documents using RDBMS. *Inf. Softw. Technol.* 45, 11–22. doi: 10.1016/S0950-5849(02)00157-X

Conflict of Interest Statement: The authors declare that the research was conducted in the absence of any commercial or financial relationships that could be construed as a potential conflict of interest.

The reviewer AS and handling Editor declared their shared affiliation, and the handling Editor states that the process nevertheless met the standards of a fair and objective review.

Copyright © 2017 Ma, West, Zednik, Erickson, Eleish, Chen, Wang, Zhong and Fox. This is an open-access article distributed under the terms of the Creative Commons Attribution License (CC BY). The use, distribution or reproduction in other forums is permitted, provided the original author(s) or licensor are credited and that the original publication in this journal is cited, in accordance with accepted academic practice. No use, distribution or reproduction is permitted which does not comply with these terms.

Advantages of publishing in Frontiers



OPEN ACCESS

Articles are free to read, for greatest visibility



COLLABORATIVE PEER-REVIEW

Designed to be rigorous – yet also collaborative, fair and constructive



FAST PUBLICATION

Average 85 days from submission to publication (across all journals)



COPYRIGHT TO AUTHORS

No limit to article distribution and re-use



TRANSPARENT

Editors and reviewers acknowledged by name on published articles



SUPPORT

By our Swiss-based editorial team



IMPACT METRICS

Advanced metrics track your article's impact



GLOBAL SPREAD

5'100'000+ monthly article views and downloads



LOOP RESEARCH NETWORK

Our network increases readership for your article

Frontiers

EPFL Innovation Park, Building I • 1015 Lausanne • Switzerland
Tel +41 21 510 17 00 • Fax +41 21 510 17 01 • info@frontiersin.org
www.frontiersin.org

Find us on

